

THE UNIVERSITY OF HULL



Nanoparticle Mediated Toxicity and Antimicrobial Action

being a Thesis submitted for the Degree of

Doctor of Philosophy

in the University of Hull

by

Mohammed Jabber Khleaf Al-Awady

BSc (University of Babylon, Iraq, 2000)

MSc (University of Baghdad, Iraq, 2003)

December 2015

Abstract

Nanomaterials are either inorganic or organic nanosized particles which have many industrial and biological applications such as in cosmetics, environmental remediation, electronics, biosensing and imaging and in drug delivery. Some have toxic effect upon release to the environment causing death of microorganisms and others are biodegradable and nontoxic to the living beings. In this work, two types of nanoparticles were investigated: inorganic titania nanoparticles which have been shown to have toxic effects and organic Carbopol Aqua SF1 microgel particles which were shown to be nontoxic and biodegradable organic nanoparticles for drug delivery.

Chapter one explores the current literature relating to nanoparticles. The types, chemical and physical properties, methods of synthesis, characterization and functionalization are discussed along with general applications and the toxicity of titania nanoparticles. The role of nanomaterials as drug delivery systems and their design in terms of stability, swelling studies, encapsulation, drug loading and release, response to stimuli and targeting is also discussed. Finally the use of microfluidics for screening nanoparticle activity is discussed including microfabrications of chips cell trapping methods and microfluidic cell based assay methods.

Chapter two is the experimental chapter describing the chemicals and instrumentation used. It also includes the methods used for the synthesis of titania nanoparticles and effects of pH on the zeta potential measurement. In addition to that, methods for the testing of the cytotoxic effects of uncoated and coated titania nanoparticles are described. Finally the methods employed for studying the optimization of the encapsulation of berberine and chlorhexidine into Carbopol Aqua SF1 are also included.

Chapter three describe the synthesis of titania nanoparticles (TiO_2NPs) and their characterization, including crystallite size, particle size distribution, surface area measurement and zeta potential. It was found that as the temperature increased from 100°C to 800°C , the crystallite size and particle size increased while the surface area decreased. At 100°C , the crystallite size, particle size, surface area and zeta potential of the titania nanoparticles were 5 nm, 25 ± 20 nm, $163\text{ m}^2\text{ g}^{-1}$ and $+40\pm 9$ mV, respectively with anatase as the dominant phase. However, the phase changed to rutile at the annealing temperature of 800°C with the crystallite size, particle size, surface area and zeta potential becoming 142

nm, 145 ± 60 nm, $7.5\text{ m}^2\text{ g}^{-1}$ and -26 ± 8 mV respectively. In addition to that, the zeta potential of the titania nanoparticles at 25 nm size was affected by changing the pH of the suspension, at low pH, the zeta potential was +40 mV giving high stability and fully dispersed particles while the nanoparticles flocculated in the basic medium with a zeta potential of -25 mV, with the isoelectric point of titania nanoparticles being pH 6.7. Changing the pH of the solution for titania nanoparticles caused an irreversible process as it was not possible to convert the aggregated titania nanoparticles from microscale to nanoscale.

Chapter four describes the investigation into the nanotoxicity of the titania nanoparticles (TiO_2NPs) at various hydrodynamic diameters and crystallite size on *C. reinhardtii* microalgae and *S. cerevisiae* (yeast) upon illumination with UV and visible light. The cell viability was assessed for a range of nanoparticle concentrations and incubation times. It was found that uncoated TiO_2NPs affect the *C. reinhardtii* cell viability at a much lower particle concentrations than for yeast. It was also observed that the TiO_2NPs toxicity increased upon illumination with UV light compared to dark conditions due to the oxidative stress of the reactive oxygen species produced. It was also found that TiO_2NPs nanotoxicity increased upon illumination with visible light which indicated that the nanoparticles might also interfere with the microalgae photosynthetic system leading to decreased chlorophyll content upon exposure to TiO_2NPs . The results showed that the larger the hydrodynamic diameter of the TiO_2NPs the lower their nanotoxicity, with anatase TiO_2NPs generally being more toxic than rutile TiO_2NPs . A range of polyelectrolyte-coated TiO_2NPs were also prepared using the layer by-layer method and their nanotoxicity on yeast and microalgae was studied. It was found that the toxicity of the coated TiO_2NPs alternates with their surface charge. TiO_2NPs coated with cationic polyelectrolyte as an outer layer exhibited much higher nanotoxicity than the ones with an outer layer of anionic polyelectrolyte. TEM images of sectioned microalgae and yeast cells exposed to different polyelectrolyte-coated TiO_2NPs confirmed the formation of a significant build-up of nanoparticles on the cell surface for bare and cationic polyelectrolyte-coated TiO_2NPs . The effect came from the increased adhesion of cationic nanoparticles to the cell walls. Significantly, coating the TiO_2NPs with anionic polyelectrolyte as an outer layer led to a reduced adhesion and much lower nanotoxicity due to electrostatic repulsion with the cell walls.

Chapter five describes the development and characterisation of berberine-loaded and chlorhexidine-loaded polyacrylic acid based microgels. The procedure for loading the

Carbopol microgels with both berberine and chlorhexidine was developed using a swelling-deswelling cycle dependent on pH. The result of this protocol was a colloidal suspension of collapsed microgel particles loaded with fixed percentage of the antimicrobial agents, berberine and chlorhexidine, respectively. The initial microgel particle concentration, as well as the initial concentrations of berberine and chlorhexidine, were optimized to allow for maximum encapsulation efficiency of the loaded reagent in the microgel while maintaining the colloidal stability of the Carbopol microgel suspension. It was determined that 0.15 wt% berberine and 0.1% chlorhexidine could be successfully incubated with 0.1 wt% Carbopol microgel while the pH was varied from 8 to 5.5 with a measurable increase of the collapsed microgel due to electrostatic conjugation of these cationic antimicrobial agents with the carboxylic groups of the microgel.

While for berberine, only 10% encapsulation efficiency was achieved, for chlorhexidine over 90% encapsulation efficiency was obtained without significant impact on the colloidal stability of the microgel. The zeta potential of the loaded microgels remained negative in the range of -35 mV - -40 mV with very moderate increase of the collapsed (and loaded) microgel particle size. The release of berberine and chlorhexidine from these microgel materials was studied and sustained release from the formulations was demonstrated upon dilution over the period of up to 6 hours. The berberine- and chlorhexidine-loaded microgel particles were then further coated with cationic polyelectrolytes, PAH and PDAC. This carried out to increase the adhesion of these antimicrobial particles to the cell membranes. These studies showed a reversal of the zeta-potential of the PDAC coated microgels after their loading with berberine and chlorhexidine, respectively.

In chapter six, the antimicrobial activity of both berberine and chlorhexidine loaded Carbopol microgel was studied upon incubation with algae, yeast and *E.coli*. It was noticed that an increase in the antimicrobial activity of berberine and chlorhexidine Carbopol microgel occurred after 6 hours incubation time for algae and after 24 hours for *E.coli* while there was no pronounced antimicrobial action for yeast in comparison with the antimicrobial activity of free berberine or chlorhexidine. This was due to the repulsion forces between the anionic microgel and the anionic cell membrane which did not allow the encapsulated berberine or chlorhexidine to be released and diffuse into the cytoplasm causing cell death. In addition to that, the fully anionic charged Carbopol microgel did not allow berberine and chlorhexidine to be released easily at pH 5.5 while the percentage of release increased with pH up to 7.5.

The antimicrobial activity of cationic PDAC coated berberine and chlorhexidine loaded-Carbopol microgel was also studied for algae, yeast and *E.coli*. It was found that cationic PDAC on its own had an acute toxic effect on algae, yeast and *E.coli* while the toxicity of cationic PDAC reduced upon coating Carbopol microgel with cationic PDAC. Algae and *E.coli* stayed viable up to 0.0045 wt. % and 0.009 wt. % of PDAC coated Carbopol microgel, respectively. Yeast was resistance to the PDAC coated carbopol for a wide range of concentrations of PDAC coated Carbopol microgel up to 0.018 wt. %. This was due to the different thicknesses of the cell membrane. The Carbopol microgels with encapsulated berberine and chlorhexidine were then coated with cationic PDAC to form PDAC coated particles. The PDAC coated berberine or chlorhexidine loaded carbopol microgel were then incubated with each of algae, yeast, and *E.coli*. The coating appeared to increase the antimicrobial actions against algae, yeast and *E.coli* for short incubation times. The increase in the antimicrobial activity was attributed to the electrostatic interaction between the cationic PDAC coated berberine or chlorhexidine loaded carbopol microgel and the anionic cell membrane allowing diffusion of berberine or chlorhexidine easily through cell membrane causing cell death. TEM images showed aggregation of these cationic PDAC coated berberine or chlorhexidine loaded carbopol microgel on the surface of the cell membrane.

Chapter seven describes the development of new microfluidics device for cell trapping to achieve a microscreening cell based assay. The idea involved trapping the cells in a micro chamber and then passing over suspensions of the nanomaterials and monitoring the effect. Three design of microfluidic chips were studied with different designs, channel dimensions (depth and width) cell trapping techniques and materials. Initially chemical adhesion was investigated to adhere cells into micro chamber of the microfluidics device using poly-l-lysine but the cells detached from the surface of microchip because of shear stress forces. Synthesized magnetic yeast cells which were then investigated for trapping other cells into the micro chamber of the chip but the back pressures were too high when liquids were flowed through the system. Magnetic glass beads were then studied to trap the cells, these were synthesized by coating anionic glass beads with cationic and anionic polyelectrolytes such as PAH and PSS, however, they had a low magnetic response towards the magnet. Synthesized magnetic beads were then synthesized using a PDMS based ferrofluid but again a low magnetic response was obtained towards the magnet. Synthesis by flow focusing microfluidics was the tried to generate mono dispersed magnetic beads where SDS with water

was the continuous phase and a styrene based ferrofluid was the dispersed phase but the magnetic beads were unstable and they need to be optimized. The continuous phase was then changed to use Hitenol BC20 a polymerisable surfactant, to form hydrophobic magnetic beads and a mixing serpentine was added to the chip design to give the generated magnetic beads time to be stabilise. Despite these changes the magnetic beads stayed unstable and therefore an emulsification method was used to fabricate poly dispersed magnetic beads which produced 20 μ m to 50 μ m magnetic beads. These beads were successfully utilized for trapping cells into the micro chamber of the chip device. A new microfluidic device was designed with suitable channel dimensions which allowed the magnetic beads to move freely inside the micro chamber of the device. These beads were placed into the micro chamber could be controlled using the neodymium magnet easily move the beads.

Dedication

To the soul of my dear father who passed away during my PhD study,

To my mother with love,

To my beloved and supportive wife Rawafid,

To my children who are my future..... Ruba, Hawraa and Hussein.

I dedicate this work

Mohammed
December 2015

Acknowledgements

Firstly, I would like to express my profound thankfulness to my supervisors Professor Gillian M Greenway and Professor Vesselin N Paunov for the continuous support of my PhD study and related research and for their patience, motivation, advice, direction and encouragement throughout this research. Their guidance helped me in all the time of research and writing up this thesis.

Secondly, my gratitude also goes to labmates Dr. Anupam Das, Dr. Hamza Alshehri and Benjamin Thompson for the inspiring discussions, and for all the fun we have had in the last three years. Also I thank Ann Lowry (TEM technician) and Tony Sinclair (SEM technician) for the help during training and pretreatment and measurement of nanomaterials and cells samples.

Thirdly, I would also like to thank my wife, my parents and to my brothers and sister for the help and support throughout writing this thesis and my life in general. I am grateful to all members in physical chemistry and analytical chemistry research groups and my friends in the department of chemistry for their valuable help.

Last but not least, my special thanks also go to the Iraqi Government/The Higher Committee for Education Development in Iraq (HCED-Iraq), The University of Babylon / Iraq, The Green University of Qasim / Iraq for supporting me all financially.

Mohammed
December 2015

Publications, Presentations and Certificates

1. Al-Awady, Mohammed J., Gillian M. Greenway, and Vesselin N. Paunov. "Nanotoxicity of polyelectrolyte-functionalized titania nanoparticles towards microalgae and yeast: role of the particle concentration, size and surface charge." *RSC Advances* 5.46 (2015): 37044-37059.
2. The First Poster Presentation in the PhD Postgraduate Conference at the University of Hull on 22nd July 2014. The poster entitled "Micro Screening System for Investigating the Toxicity of Nanoparticles on Individual Cells".
3. Poster presentation in PhD colloquia 2014 which was held in the department of chemistry at the University of Hull. The poster entitled "Micro Screening System for Investigating the Toxicity of Nanoparticles on Individual Cells".
4. Poster Presentation in the Fourth International on Multifunctional Hybrid, and Nanomaterials, Sitges, Barcelona, Spain on 9th – 13th March 2015. The poster entitled "Nanotoxicity of polyelectrolyte-functionalized titania nanoparticles towards microalgae and yeast: role of the particle concentration, size and surface charge".
5. Oral presentation in PhD colloquia 2015 which was held in the department of chemistry at the University of Hull. The talk entitled "Nanotoxicity of polyelectrolyte-functionalized titania nanoparticles towards microalgae and yeast: role of the particle concentration, size and surface charge".
6. Oral Presentation in the 29th Conference of the European Colloid and Interface Society (ECIS) which was held in Bordeaux, France on 6th – 11th September 2015. The talk entitled "Nanotoxicity of polyelectrolyte-functionalized titania nanoparticles towards microalgae and yeast: role of the particle concentration, size and surface charge".
7. Postgraduate Diploma in Research Training (PGDip) from the University of Hull as I studied chemistry related modules and communication and research skills and collected 120 credits.

Table of Contents

ABSTRACT	I
DEDICATION	VI
ACKNOWLEDGEMENTS	VII
PUBLICATIONS, PRESENTATIONS AND CERTIFICATES	VIII
TABLE OF CONTENTS	IX
LIST OF FIGURES	XV
LIST OF TABLES	XXXIV
ABBREVIATIONS	XXXV
1 CHAPTER ONE: INTRODUCTION AND LITERATURE REVIEW	1
1.1 NANOMATERIALS	1
1.2 OCCURRENCE OF NANOPARTICLES (NPs).....	4
1.3 PHYSICOCHEMICAL PROPERTIES OF NANOMATERIALS	5
1.4 METHODS FOR THE SYNTHESIS OF TITANIA NANOPARTICLES	11
1.4.1 Sol-Gel Method.....	11
1.4.2 Sol Method.....	11
1.4.3 Hydrothermal Method.....	12
1.4.4 Solvothermal method	12
1.5 CHARACTERIZATION OF TiO ₂ NANOPARTICLES.....	12
1.5.1 Dynamic Light Scattering.....	12
1.5.2 X-Ray Diffraction (XRD).....	13
1.5.3 Zeta Potential	15
1.5.4 UV-Visible Spectroscopy	17
1.5.5 Fourier Transform- Infrared Spectroscopy.....	18
1.5.6 BET Surface Area Measurement	19
1.5.7 Scanning Electron Microscope	21
1.5.8 Transmission Electron Microscope	22
1.6 FUNCTIONALIZATION OF NANOMATERIALS	23
1.7 GENERAL APPLICATIONS OF NANOMATERIALS	27
1.8 TOXICOLOGICAL IMPACTS OF NANOMATERIALS	28
1.9 TOXICITY OF TiO ₂ NANOPARTICLE.....	31
1.10 INTRACELLULAR PENETRATION OF NANOPARTICLES	35
1.11 NANOMATERIALS FOR DRUG DELIVERY	39
1.12 MICROGEL AS A NANOCARRIER.....	40
1.13 DESIGN OF NANOCARRIERS AS A DRUG DELIVERY SYSTEM.....	40
	IX

1. 13.1	Biocompatibility and degradability.....	40
1. 13.2	Swelling behavior.....	40
1. 13.3	High encapsulation stability.....	41
1. 13.4	Controlled and sustained drug release.....	42
1. 13.5	Response to stimuli.....	43
1.13.6	Targeting.....	43
1. 14	CARBOPOL AQUA SF1 POLYMER.....	46
1. 15	BERBERINE.....	48
1. 16	CHLORHEXIDINE.....	51
1. 17	MICROFLUIDIC DEVICES: AN INTRODUCTION.....	57
1. 18	MATERIALS FOR FABRICATING MICROFLUIDIC DEVICES.....	58
1. 18.1	Silica and Glass.....	58
1. 18.2	Elastomers.....	59
1. 19	FABRICATION OF MICROFLUIDIC DEVICES.....	60
1. 19.1	Photolithography.....	60
1. 19.2	Soft Lithography.....	61
1. 20	MICROFLUIDIC CHIPS SEALING.....	64
1. 21	DROPLET BASED MICROFLUIDICS.....	64
1.21.1	T-Junction.....	65
1.21.2	Flow Focusing Microfluidics.....	66
1.21.3	Coaxial Microfluidics.....	67
1. 22	SOME METHODS FOR SYNTHESIS OF MAGNETIC POLYMER BEADS.....	68
1. 23	HIGH THROUGHPUT CELL BASED SCREENING.....	70
1. 24	MICROFLUIDIC DEVICES CELL BASED ASSAY.....	71
1.22.1	Surface Contact Cell Immobilization.....	72
1.22.2	Contact-Free Cell Immobilization.....	73
1. 25	SUMMARY OF TRAPPING METHODS.....	76
1. 26	MICROFLUIDIC BASED CYTOTOXICITY MICRO SCREENING.....	76
1. 27	OBJECTIVES OF THE RESEARCH.....	81
	BIBLIOGRAPHY.....	83
2	CHAPTER TWO: EXPERIMENTAL SECTION.....	94
2.1	MATERIALS.....	94
2.1.1	Purified Water.....	94
2.1.2	General Chemicals Reagents.....	94
2.1.3	Polyelectrolytes.....	96
2.1.4	Fluorescein Diacetate (FDA).....	97
2.1.5	BacTiter-Glo Microbial Cell Viability Assay.....	97
2.1.6	Culture Medium for C.reinhardtii cc-124 strain Growth.....	99
2.1.7	Growth of Baker's yeast (Saccharomyces cerevisiae).....	100
2.1.8	Growth of Escherichia Coli (E.coli).....	100
2.2	INSTRUMENTATION.....	101

2.2.1	Synthesis of Titanium Nanoparticles	102
2.2.2	Zeta Potential Measurement	103
2.2.3	Exposure of TiO ₂ NPs to <i>C. Reinhardtii</i> Cells.....	103
2.2.4	Determination of the chlorophyll content of <i>C. reinhardtii</i>	105
2.2.5	Exposure of TiO ₂ NPs to Yeast Cells	105
2.2.6	Layer by Layer Polyelectrolytes coating of Titania Nanoparticles	106
2.2.7	TEM images of Cells	107
2.2.8	TEM Protocol for Nanomaterials	107
2.2.9	SEM Protocol for Cells.....	107
2.2.10	Swelling Study of Carbopol Aqua SF1	108
2.2.11	Cytotoxicity Effect of Carbopol Aqua SF1.....	108
2.2.12	Antimicrobial activity of Free Berberine or Chlorhexidine.....	109
2.2.13	Encapsulation of Berberine into Carbopol Aqua SF1	109
2.2.14	Encapsulation of Chlorhexidine into Carbopol Aqua SF1.....	110
2.2.15	Antimicrobial Activity of Encapsulated Active Material with <i>C.Reinhardtii</i> 110	
2.2.16	Antimicrobial Activity of Encapsulated Active material with Yeast.....	111
2.2.17	Antimicrobial Activity of Encapsulated Active Material with <i>E.coli</i>	111
2.2.18	Measurement of Encapsulation Efficiency	111
2.2.19	% Drug Release.....	112
2.2.20	Functionalization of Carbopol Aqua SF1	112
2.2.21	Functionalization of Encapsulated Berberine with PDAC	113
2.2.22	Functionalization of Encapsulated Chlorhexidine with PDAC	113
2.2.23	Cytotoxic Effect of PDAC on Algae, Yeast and <i>E.coli</i>	113
2.2.24	Cytotoxic Effect of PDAC Coated Carbopol Aqua SF1 on Algae, Yeast and <i>E.coli</i> 113	
2.2.25	Antimicrobial Activity of PDAC Coated BLC	114
2.2.26	Antimicrobial Activity of PDAC Coated CLC	114
2.2.27	Chemical Adhesion of <i>C.reinhardtii</i>	115
2.2.28	Synthesis of Magnetized Glass Beads	115
2.2.29	Synthesis of Magnetized Yeast Cells.....	116
2.2.30	Synthesis of Magnetized PDMS Beads in Wet Agar Layer	116
2.2.31	Synthesis of Magnetic Micro Beads	117
2.3	CHIP FABRICATION.....	118
2.3.1	Fabrication of Microfluidic Flow Focusing Chip.....	118
2.3.2	Fabrication of Microfluidic Cell Trapping Chip.....	119

3 CHAPTER THREE: SYNTHESIS, CHARACTERIZATION AND FUNCTIONALIZATION OF TITANIA NANOPARTICLES:AN INTRODUCTION **122**

3.1	SYNTHESIS OF TITANIA NANOPARTICLES	122
3.1.1	Effect of the amount of Titanium Isopropoxide Precursor	124

3.1.2	Effect of Reaction pH on particle size	126
3.1.3	Effect of Temperature on the Titanium Dioxide Particle Size	127
3.2	CHARACTERIZATION OF TITANIA NANOPARTICLES	128
3.2.1	The Absorption of UV-Vis Spectroscopy of Titania Nanoparticles	129
3.2.2	Calcination of Synthesized Titania Nanoparticle	129
3.2.3	Transmission Electron Microscope Images of Titania NPs.....	132
3.2.4	Fourier Transform Infrared Spectroscopy (FTIR)	133
3.2.5	Thermogravimetric Analysis (TGA)	134
3.2.6	Surface Area Measurement.....	135
3.2.7	Measurement of Zeta Potential of Titania Nanoparticles	136
3.3	FUNCTIONALIZATION OF TITANIA NANOPARTICLES	138
3.3.1	The Effect of Addition of Titania Nanoparticles	139
3.3.2	Effect of Ionic Strength.....	141
3.3.3	Effect of Molar Mass of Polyelectrolyte.....	142
3.3.4	Zeta Potential of Bare and Coated Titania NPs	143
	BIBLIOGRAPHY	145
4	CHAPTER FOUR: NANOTOXICITY OF TITANIA NANOPARTICLES.....	146
4.1	TOXICITY OF TiO ₂ NPs ON <i>C.REINHARDTII</i> IN UV/VISIBLE LIGHT	146
4.2	CHLOROPHYLL CONTENT OF <i>C. REINHARDTII</i> AFTER EXPOSURE TO TiO ₂ NPs.....	150
4.3	TOXICITY EFFECT OF TiO ₂ NPs ON YEAST IN VISIBLE/UV LIGHT.....	157
4.4	EFFECT OF THE TiO ₂ NPs SIZE ON MICROALGAE AND YEAST CELL VIABILITY	166
4.5	NANOTOXICITY OF POLYELECTROLYTE-COATED TiO ₂ NPs ON <i>C. REINHARDTII</i> ...	168
4.6	NANOTOXICITY OF POLYELECTROLYTE-COATED TiO ₂ NPs ON YEAST	172
	CONCLUSION	176
	BIBLIOGRAPHY	178
5	CHAPTER FIVE: CHARACTERIZATION AND FUNCTIONALIZATION OF FORMULATED NANOCARRIERS: AN INTRODUCTION.....	179
5.1	PARTICLE SIZE AND ZETA POTENTIAL OF CARBOPOL AQUA SF1	179
5.2	SWELLING BEHAVIOR OF CARBOPOL AQUA SF1	183
5.3	ENCAPSULATION OF BERBERINE INTO CARBOPOL AQUA SF1 MICROGEL.....	191
5.4	CHARACTERIZATION OF BERBERINE-LOADED CARBOPOL AQUA SF1	193
5.4.1	Effect of Carbopol Concentration on Berberine Encapsulation	193
5.4.2	Effect of the Berberine Concentration on the Carbopol Stability.....	194
5.4.3	Determination of the Berberine-Loaded Carbopol Microgel Particle Size	195
5.4.4	UV-Visible Spectrophotometry of Berberine-Loaded Carbopol.....	199
5.4.5	FTIR Spectrometry of Berberine Loaded Carbopol	201
5.4.6	Thermogravimetric Analysis of Berberine Loaded Carbopol	203
5.4.7	Elemental Analysis of Berberine-Loaded Carbopol Aqua SF1	205
5.4.8	Berberine Encapsulation Efficiency and Loading Content.....	206
5.4.9	Berberine Release Studies	208

5.5	ENCAPSULATION OF CHLORHEXIDINE INTO CARBOPOL AQUA SF1 MICROGEL.....	210
5.6	CHARACTERIZATION OF CHLORHEXIDINE-LOADED CARBOPOL	212
5.6.1	Effect of the Carbopol Concentration on the Chlorhexidine Microencapsulation 212	
5.6.2	Effect of the Chlorhexidine Concentration on the Carbopol Stability.....	214
5.6.3	Measurement of the Particle Hydrodynamic Diameter and Zeta Potential	216
5.6.4	UV-Vis Spectroscopy of Carbopol, CHX and CHX-Loaded Carbopol	219
5.6.5	FTIR Spectroscopy of Carbopol, CHX, and CHX-Loaded Carbopol	221
5.6.6	Thermogravimetry Analysis of Chlorhexidine-Loaded Carbopol.....	223
5.6.7	Elementary Analysis of CHX and BRB Loaded Carbopol.....	225
5.6.8	Encapsulation Efficiency and Drug Loading Content	226
5.6.9	Chlorhexidine Release Kinetics.....	228
5.7	FUNCTIONALIZATION OF CARBOPOL AND ENCAPSULATED CARBOPOL	230
5.7.1	Effect of PAH Concentration on Carbopol Coating.....	234
5.7.2	Effect of the PDAC Concentration on the Carbopol Coating.....	235
5.7.3	Cationic Functionalization of Antimicrobial-loaded Carbopol Microgel.....	236
	BIBLIOGRAPHY	239
6	CHAPTER SIX: ANTIMICROBIAL FORMULATED IN NANOCARRIERS: AN INTRODUCTION.....	240
6.1	CYTOTOXICITY ASSAY OF CARBOPOL AQUA SF1 MICROGEL	240
6.2	TEM IMAGE OF CELLS INCUBATED WITH CARBOPOL MICROGEL.....	243
6.3	ANTIMICROBIAL ACTIVITY OF BERBERINE-LOADED CARBOPOL (BLC).....	245
6.3.1	Antimicrobial Activity of Berberine Loaded Carbopol (BLC) on Algae.....	246
6.3.2	Antimicrobial Activity of Berberine-Loaded Carbopol (BLC) on Yeast.....	252
6.3.3	Antimicrobial Activity of Berberine-Loaded Carbopol (BLC) on E.coli.....	257
6.4	ANTIMICROBIAL ACTIVITY OF CHLORHEXIDINE-LOADED CARBOPOL (CLC)	261
6.4.1	Antimicrobial Activity of CHX-Loaded Carbopol (CLC) on microalgae.....	261
6.4.2	Antimicrobial Activity of Chlorhexidine-Loaded Carbopol (CLC) on Yeast.	265
6.4.3	Antimicrobial Activity of CHX-Loaded Carbopol (CLC) on E.coli.....	269
6.5	ANTIMICROBIAL ACTIVITY OF PDAC-COATED ENCAPSULATED CARBOPOL.....	272
6.5.1	Cytotoxic Effect of PDAC on Microalgae, Yeast and E.coli	273
6.5.2	Cytotoxic Effect of PDAC-Coated Carbopol on Algae, Yeast and E.coli	276
6.5.3	Antimicrobial Activity of PDAC-coated BLC on Microalgae	279
6.5.4	Antimicrobial Activity of PDAC coated BLC on Yeast.....	285
6.5.5	Antimicrobial Activity of PDAC Coated BLC on E.coli	289
6.5.6	Antimicrobial Activity of PDAC-coated CLC on Microalgae	293
6.5.7	Antimicrobial Activity of PDAC-coated CLC on Yeast	297
6.5.8	Antimicrobial Activity of PDAC Coated CLC on E.coli	301
7	CHAPTER SEVEN: MICROFLUIDIC CELL BASED ASSAY: AN INTRODUCTION.....	307

7.1.	CELL ADHESION USING POLY-L-LYSINE	307
7.2	MICROFLUIDIC CELL TRAPPING	314
7.3	FABRICATION OF MAGNETIC MICROBEADS	318
7.3.1	Magnetic Glass Beads.....	318
7.3.2	Magnetic Yeast Cells	323
7.3.3	PDMS stabilized oleic acid coated magnetic nanoparticles	327
7.3.4	Flow Focusing Microfluidic Device	332
7.3.5	Flow focusing Microfluidic with Serpentine	339
7.3.6	Fabrication of Magnetized Micro Beads by Emulsification.....	344
7.4	MAGNETIC GATE KEEPERS IN MICROCHIP	346
8.	CHAPTER EIGHT: CONCLUSIONS AND FUTURE WORKS.....	355
8.1	CONCLUSIONS	355
8.2	FUTURE WORKS	358

List of Figures

FIGURE 1.1: EXAMPLES OF NANOCARRIERS FOR DRUG DELIVERY AND BIOMEDICAL IMAGING. ⁵	1
FIGURE 1.2: STRUCTURES OF SOME NATURAL AND MANUFACTURED NANOPARTICLES. ³⁸	5
FIGURE 1.3: SIMPLIFIED TiO ₂ BANDGAP STRUCTURE AND SCHEMATIC FORMATION OF FREE RADICAL COMPOUNDS.	7
FIGURE 1.4: THE AGGLOMERATION AND AGGREGATION OF PARTICLES CONFIGURATION IN NANOPOWDERS AND LIQUID NANOPARTICLE DISPERSIONS. ⁵⁶	8
FIGURE 1.5:: DLVO SCHEME OF DISPERSIONS STABILITY FOR THE ATTRACTIVE VAN DER WAALS AND AND REPULSIVE ELECTROSTATIC DOUBLE-LAYER FORCES TOGETHER DETERMINING THE TOTAL INTERACTION POTENTIAL BETWEEN TWO CHARGED SURFACES IN AQUEOUS ELECTROLYTE SOLUTIONS AT DIFFERENT SURFACE CHARGE DENSITIES Σ OR POTENTIALS Ψ_0 . ⁵⁹	10
FIGURE 1.6: DIAGRAM OF DYNAMIC LIGHT SCATTERING INSTRUMENT. ⁷⁸	13
FIGURE 1.7: PARTICLE SIZE DISTRIBUTION OF TITANIUM DIOXIDE NANOPARTICLE AT 166 NM (TP _S) AND 596 NM (TP _L). ⁷⁹	13
FIGURE 1.8: BRAGG DIFFRACTION REPRESENTED BY INTERACTION BETWEEN X-RAYS AND A CRYSTALLINE SAMPLE. ⁸⁰	14
FIGURE 1.9: X-RAY DIFFRACTION PATTERNS TITANIUM DIOXIDE NANOPARTICLES AT DIFFERENT CALCINATION TEMPERATURE FROM 100°C TO 800°C, PROVIDING DIFFERENT CRYSTALLITE SIZES. ⁸²	15
FIGURE 1.10: THE SCHEMATIC REPRESENTATION OF ZETA POTENTIAL WHICH SHOWING THE DISTRIBUTION OF IONS AROUND THE CHARGED PARTICLE. ⁸⁴	16
FIGURE 1.11: THE IMPACT OF IONIC STRENGTH ON THE ZETA POTENTIAL AND THE HYDRODYNAMIC SIZE OF TiO ₂ DISPERSIONS. ⁵⁶	17
FIGURE 1.12: THE SCHEMATIC DIAGRAM OF DOUBLE BEAM SPECTROPHOTOMETER SETUP. ⁸⁷	18
FIGURE 1.13: A SCHEMATIC DIAGRAM OF FTIR SETUP. ⁸⁷	19
FIGURE 1.14: BET PLOT FOR THE MEASUREMENT OF SURFACE AREA OF SOLID ADSORBENT THROUGH PHYSICAL ADSORPTION OF GAS MOLECULES ON A SOLID SAMPLE.	21
FIGURE 1.15: THE SCHEMATIC DIAGRAM OF THE SEM SETUP. ⁹¹	22
FIGURE 1.16: A SCHEMATIC DIAGRAM OF A TEM SETUP. ⁹¹	23
FIGURE 1.17: (A) SCHEME OF THE FILM DEPOSITION PROCESS. STEPS 1 AND 3 DENOTE THE ADSORPTION OF A CATIONIC AND ANIONIC POLYELECTROLYTES, RESPECTIVELY, AND STEPS 2 AND 4 ARE WASHING STEPS (B) ADSORPTION STEPS FOR THE FORMATION OF THIN FILM, STARTING WITH A POSITIVELY CHARGED SUBSTRATE WHICH FIRSTLY WAS COATED WITH POLYANIONS AND THEN POLYCATIONS (C) CHEMICAL STRUCTURES OF ANIONIC AND CATIONIC POLYELECTROLYTES, THE SODIUM SALT OF POLY(STYRENE SULFONATE) AND POLY(ALLYLAMINE HYDROCHLORIDE). ¹⁰³	26
FIGURE 1.18: PATHWAYS OF AN IN VIVO AND IN VITRO NANOPARTICLES EXPOSURE AND RELATED DISEASES AS SUGGESTED BY EPIDEMIOLOGICAL STUDIES. ³	30
FIGURE 1.19: A SCHEME OF NANOMATERIALS FUNCTIONALIZATION FOR INTERNALIZATION WHEREBY NANOMATERIALS ASSEMBLED WITH VARIOUS MATERIALS THAT HAVE DIFFERENT CHEMICAL AND PHYSICAL PROPERTIES. ¹⁶¹	36
FIGURE 1.20: INTRACELLULAR TRANSPORT OF NANOPARTICLES. AFTER INTERNALIZATION VIA ONE OR MORE OF THE ENDOCYTIC PATHWAYS, NANOPARTICLES ARE TRAFFICKED ALONG THE ENDOLYSOSOMAL NETWORK WITHIN VESICLES WITH THE HELP OF MOTOR PROTEINS AND CYTOSKELETAL STRUCTURES. VESICLES CAN TRANSPORT THEIR CONTENTS INTO SORTING ENDOSOMES, OR EXCRETE/RECYCLE THEM BACK TO THE CELL SURFACE BY FUSING WITH THE PLASMA MEMBRANE. ALTERNATIVELY, ENDOSOMES CAN MATURE INTO LYSOSOMES VIA LUMINAL ACIDIFICATION AND RECRUITMENT OF DEGRADATIVE ENZYMES. ENDOCYTIC RECYCLING COMPARTMENT (ERC), ENDOPLASTIC RETICULUM (ER), MICROTUBULE-ORGANISING CENTRE (MTOC) AND MULTIVESICULAR BODIES (MVB) ¹⁶¹	37

FIGURE 1.21: THE POSSIBLE MECHANISM OF TiO ₂ NANOPARTICLES - INDUCED GENOTOXICITY AND CYTOTOXICITY, WHEREBY THESE ROS INDUCED EITHER LIPID PEROXIDATION, CAUSING LDH RELEASING, OR INHIBITION OF GLUTATHIONE PEROXIDASE OR DNA DAMAGE. LACTATE DEHYDROGENASE (LDH); REDUCED GLUTATHIONE (GSH); LIPID PEROXIDATION (LPO).....	38
FIGURE 1.22: UNTARGETED AND TARGETED DRUG DELIVERY. ¹⁶⁹	39
FIGURE 1.23: OFF –TARGET TOXICITY OF UNSTABLE LEAKY DELIVERY CARRIERS. ¹⁷⁹	41
FIGURE 1.24: THE CONCEPT OF PASSIVE TARGETING THROUGH THE EPR EFFECT AND ACTIVE TARGETING THROUGH LIGAND DISPLAY. ^{179, 190}	44
FIGURE 1.25: THE CHEMICAL STRUCTURE OF CARBOPOL AQUA SF1 (POLY ACRYLIC ACID)	46
FIGURE 1.26: THE CHEMICAL STRUCTURE OF BERBERINE.	48
FIGURE 1.27: THE CHEMICAL STRUCTURE OF CHLORHEXIDINE DIGLUCONATE.....	52
FIGURE 1.28: MINIATURIZATION AND INTEGRATION OF LABORATORY PROCESSES ONTO A MICROCHIP DEVICE. THIS FIGURE WAS ADOPTED WITH A PERMISSION FROM AUTHOR. ²⁵⁶	57
FIGURE 1.29: SIMPLIFIED MICROFABRICATION PROCESS FOR RAPID PROTOTYPING OF MICROFLUIDIC CHIPS ON SODA-LIME GLASS SUBSTRATES. ²⁶⁰	61
FIGURE 1.30: ORGANOMETALLIC CROSSLINKING REACTION BETWEEN OLIGOMER BASE AND CURING AGENT TO PRODUCE PDMS.	62
FIGURE 1.31: SCHEMATIC OF TYPICAL DEVICE FABRICATION USING PHOTOLITHOGRAPHY FOR STRUCTURING AND PDMS AS A DEVICE MATERIAL. ²⁸⁴	63
FIGURE 1.32: ILLUSTRATION OF THE PDMS REPLICATION PROCESS.	64
FIGURE 1.33: (A) A SCHEMATIC DIAGRAM OF RECTANGULAR CHANNELS OF THE MICROFLUIDIC T-JUNCTION DROPLET GENERATION. (B) A TWO DIMENSIONAL FLOW FOCUSING DROPLET GENERATION IN THE TOP VIEW. ²⁹⁴	66
FIGURE 1.34: (A) SIDE VIEW OF FLOW FOCUSING MICROFLUIDIC SETUP FOR THE TWO-PHASE FLOW. THE CHANNEL HEIGHT IS 75 MM. (B) TOP VIEW OF FLOW FOCUSING GEOMETRY OF MICROFLUIDICS CHIP. ²⁹⁷ ...	67
FIGURE 1.35: (A) SCHEMATIC FOR COAXIAL MICROFLUIDICS FOR GENERATING DROPLETS ²⁹⁸ (B) .(B) DROPLET GENERATION AT LOW FLOW RATES. (C) DROPLET GENERATION UPON INCREASING FLOW RATES. (D) INDIVIDUAL MONODISPERSED DROPLET PRODUCED BY MICRO CAPILLARY DEVICE. ^{298, 299}	68
FIGURE 1.36: WATER IN OIL IN WATER DOUBLE EMULSION DROPLET GENERATION OF MAGNETIC BEADS USING COAXIAL MICROFLUIDIC DEVICE. ⁽³⁰⁶⁾	70
FIGURE 1.37: THE SCHEMATIC CONFIGURATION OF THE 96-WELL MICROPLATE CYTOTOXICITY SCREENING METHOD. ³⁰⁸	71
FIGURE 1.38: CELL IMMOBILIZATION METHODS IN THE MICROCHAMBER OF MICROFLUIDIC CHIP. ³¹⁶	72
FIGURE 1.39: HYDRODYNAMIC SINGLE CELL TRAPPING ARRAY AS ILLUSTRATED BY DI CARLO ET AL. ³²⁰	73
FIGURE 1.40: DIELECTROPHORETIC (DEP) SEPARATION CAN BE A) POSITIVE (pDEP) OR B) NEGATIVE (nDEP) WHICH INFLUENCES WHERE CELLS ARE LOCATED WITHIN A FIELD. C) DEP HAS BEEN USED IN MICROFLUIDIC SYSTEMS IN A VARIETY OF ARRANGEMENTS. ³²²	74
FIGURE 1.41: THE LEFT IMAGE ILLUSTRATES A PARTICLE SUSPENSION PASSING OVER THE TRANSDUCER WHERE THE PARTICLES ARE MOVED AT A RATE DETERMINED BY THEIR ACOUSTIC PROPERTIES TOWARD THE CENTER OF THE SEPARATION CHANNEL. BECAUSE OF THE LAMINAR FLOW ALMOST NO MIXING HAPPENS. THE RIGHT IMAGE REPRESENTS THE FRACTIONATION OF THE SEPARATED PARTICLES THROUGH FIVE CONSECUTIVE OUTLETS/FRACTIONS AT THE END OF THE SEPARATION CHANNEL. SINCE THE SEPARATION IS SYMMETRICAL ALONG THE CENTER OF THE CHANNEL; EIGHT OF THE FRACTIONATION OUTLET CHANNELS ARE PAIRWISE CONNECTED. ³²⁵	75
FIGURE 1.42: (A) FUNDAMENTAL SCHEME OF THE GLASS SUBSTRATE, (B AND C) SIZE OF THE MICROCHANNEL AND CHAMBER AND (D) PICTURE OF THE MICROFLUIDIC CELL CHIP. ³³²	77
FIGURE 1.43: (A) SCHEMATIC OF THE MICROFLUIDIC ARRAY FOR PARALLEL CELL CYTOTOXICITY SCREENING. (B) CELL LOADING SIMULATION IN ONE CHAMBER. ³³³	78

FIGURE 1.44: CHIP DESIGN AND CELL CULTURE. (A) SCHEMATIC ILLUSTRATION OF THE MICROFLUIDIC CHANNELS WITH CELL CULTURE CHAMBERS. (B) A CELL CULTURE CHAMBER WITH A C-SHAPED DAM. (C) HEK293 CELLS CULTURED IN A CELL CULTURE CHAMBER. ³³⁴	79
FIGURE 1.45: MICROSCREENING CYTOTOXICITY ASSAY (A) PDMS GLASS MICRO SCREENING SYSTEM. TWO PARALLEL SYSTEMS ARE USED, ONE TO TEST AN UNKNOWN SAMPLE AND THE SECOND WITH A REFERENCE. THE MAGNETS WERE PLACED ABOVE THE CHAMBERS TO RETAIN THE MAGNETIC YEAST. (B) A SCHEME SHOWING THE POSITION OF THE MAGNET ON THE TOP OF THE CHAMBERS. (C) DETECTION OF CYTOTOXICITY MICRO SCREENING OF GFP YEAST. ³²⁷	80
FIGURE 2.1: THE CHEMICAL FORMULAS OF POLY (ALLYLAMINE HYDROCHLORIDE) (PAH), POLY (SODIUM-4-STYRENESOLFONATE) (PSS), POLYETHYLENEIMINE, AND POLY(DIALLYLDIMETHYLAMMONIUM CHLORIDE)	96
FIGURE 2.2: THE HYDROLYSIS OF FLUORESCIN DIACETATE USING INTRACELLULAR ESTERASE ENZYME.....	97
FIGURE 2.3: THE LUCIFERASE REACTION. MONO-OXYGENATION OF LUCIFERIN IS CATALYZED BY LUCIFERASE IN THE PRESENCE OF Mg^{2+} , ATP AND MOLECULAR OXYGEN.	98
FIGURE 2.4: OPTICAL MICROSCOPIC IMAGE OF CONTROL SAMPLE OF <i>C. REINHARDTII</i> AT PH 4. (A) BRIGHT FIELD AND (B) FLUORESCENT FILTER.....	104
FIGURE 2.5: OPTICAL MICROSCOPIC IMAGES OF CONTROL SAMPLE OF YEAST CELLS AT PH 4. (A) BRIGHT FIELD. (B) FLUORESCENT FILTER.	106
FIGURE 2.6: THE DROPLET GENERATION MICROFLUIDIC CHIP USING FLOW FOCUSING TECHNIQUE. (A) NORMAL FLOW FOCUSING MICROCHIP AND (B) FLOW FOCUSING MICROCHIP WITH SERPENTINE MIXING CHANNELS	119
FIGURE 2.7: MICROFLUIDIC SCHEME FOR TRAPPING CELLS INTO MICROCHAMBER. THE TWO INLETS ARE USED FOR PASSING CELLS, TOXIN, AND FDA SOLUTION, THE MICROCHAMBER IS FOR TRAPPING CELLS USING MAGNETIC BEADS THROUGH CONTROLLING WITH VERY STRONG MAGNET AND THE OUTLET IS FOR FLUSHING OUT CELLS AND CHEMICALS OFF CHIP.	120
FIGURE 3.1: THE AVERAGE SIZE DISTRIBUTION OF WATER DISPERSED TITANIUM DIOXIDE NPs (PH 4) THAT SYNTHESIZED BY HYDROLYSIS AND CONDENSATION OF TITANIUM ISOPROPOXIDE AT ACIDIC MEDIUM FOR 20 HOURS AT 70°C.	123
FIGURE 3.2: X-RAY DIFFRACTION PATTERN OF ANATASE TiO_2 NPs WHICH WAS PREPARED BY HYDROLYSIS AT PH 2 FOLLOWED BY CONDENSATION OF TITANIUM ISOPROPOXIDE AT 70°C FOR 20 HOUR.....	124
FIGURE 3.3: THE VARIATION OF THE NPs SIZE WITH THE AMOUNT OF PRECURSOR (TITANIUM ISOPROPOXIDE) IN WHICH THE SAMPLES ARE SYNTHESIZED BY HYDROLYSIS AND CONDENSATION OF TITANIUM ISOPROPOXIDE IN WATER AT PH 2.	125
FIGURE 3.4: X-RAY DIFFRACTION PATTERNS OF TITANIUM DIOXIDE NANOPARTICLES SYNTHESIZED FROM THE HYDROLYSIS OF (A) 1.0 ML, (B) 3.0 ML, (C) 5.0 ML, AND (D) 7.0 ML OF TITANIUM ISOPROPOXIDE IN ACIDIC MEDIUM AND CONDENSATION AT 70°C FOR 20 HOUR.....	126
FIGURE 3.5: THE VARIATION OF PARTICLE SIZE OF TITANIUM DIOXIDE WITH PH OF THE REACTION SOLUTION USING 5.0 ML OF TITANIUM ISOPROPOXIDE, 15.0 ML OF ISOPROPANOL AND 250 ML OF MILLI-Q WATER AFTER HEATING AT 70°C FOR 20 HOURS.....	127
FIGURE 3.6: THE EFFECT OF TEMPERATURE ON PARTICLE SIZE FOR TITANIA NANOPARTICLES PREPARED BY USING 5.0 ML OF TITANIUM ISOPROPOXIDE, 15.0 ML OF ISOPROPANOL AND 250.0 ML OF MILLI-Q DISTILLED WATER ADJUSTED TO PH 2.0 WITH 0.1 N HNO_3 OR 0.1 N NH_4OH	128
FIGURE 3.7: FIGURE 18: UV-VISIBLE ABSORPTION SPECTRUM OF 5 NM ANATASE TITANIA NANOPARTICLES SHOWING BAND GAP ENERGY 3.5 eV IN COMPARISON WITH 3.2 eV OF BULK TiO_2 . DOTTED LINE THAT CROSSES THE X-AXIS REPRESENT THE ABSORPTION EDGE.....	129
FIGURE 3.8: POWDER X-RAY DIFFRACTION PATTERNS OF PREPARED TiO_2 NANOPARTICLE AT VARIOUS CALCINATION TEMPERATURES (A) 200°C, (B) 300°C, (C) 400°C, (D) 500°C, AND (E) 600°C, SHOWING THE FORMATION OF DIFFERENT SIZES OF ANATASE TiO_2 WITH SHARPER PEAKS AS THE TEMPERATURE IS INCREASED FROM 200°C TO 600°C (A, B, C, AND D). HOWEVER, WITH (E), THE XRD PEAKS OF ANATASE	

TiO ₂ ARE VERY SHARP (CRYSTALLITE SIZE 28 NM AND 38 NM FOR ANATASE AND RUTILE, RESPECTIVELY) WHILE AT 800 °C, RUTILE TiO ₂ NANOPARTICLES ARE DOMINANT WITH 142 NM CRYSTALLITE SIZE.....	131
FIGURE 3.9: TEM PHOTOGRAPHS OF SYNTHESIZED TITANIA NANOPARTICLES AT (A) AS PREPARED TiO ₂ AT 100 °C WHICH SHOWN CRYSTALLITE SIZE LESS THAN 10 NM, (B) UNIFORMED SIZE ANATASE TITANIA NANOPARTICLES AT 400 °C, (C) TiO ₂ NANOPARTICLES AT 600 °C AND (D) LARGE SIZED RUTILE TITANIA NANOPARTICLES AT 800 °C.....	132
FIGURE 3.10: FOURIER TRANSFORM INFRARED SPECTROSCOPY (FTIR) SPECTRUM OF ANNEALED TITANIA NANOPARTICLES AT 100, 400, 600 AND 800°C.....	133
FIGURE 3.11: THERMAL GRAVIMETRIC ANALYSIS (TGA) GRAPH OF 5 NM ANATASE TITANIA NANOPARTICLES. SHOWING THREE STEPS OF THERMAL DEGRADATION: THE STEP 1 REPRESENTS DEHYDRATION, STEP 2 REFERS TO ORGANIC COMPOUND DEGRADATION AND THE STEP 3 IS THE PHASE TRANSFORMATION FROM ANATASE TO RUTILE TITANIA NANOPARTICLES.	134
FIGURE 3.12: THE VARIATION THE ZETA POTENTIAL AND THE PARTICLE DIAMETER OF DISPERSED ANATASE TiO ₂ NPS IN AN AQUEOUS SOLUTION OF 20 mM NaCl AS FUNCTION OF pH ADJUSTED BY ADDITION OF 1 M HCl OR 1 M NaOH. THE TRIANGLES SHOW THE EFFECT OF pH ON THE AVERAGE PARTICLE HYDRODYNAMIC DIAMETER.	136
FIGURE 3.13: THE AGGREGATION PROFILE OF TiO ₂ NANOPARTICLES AT pH 2-9 BY USING MILLI-Q WATER AS A SOLVENT AND SAMPLES WERE DISPERSED AT 30% OF THE MAXIMUM POWER OF THE SONIFIER FOR 5 MINUTES. pH OF THE SOLUTION WAS ADJUSTED BY ADDITION OF HCl OR NaOH. THIS PROFILE ALSO REPRESENTS THE EFFECT OF pH ON THE AVERAGE PARTICLE DIAMETER.	137
FIGURE 3.14: THE VARIATION THE ZETA POTENTIAL AND THE PARTICLE DIAMETER OF DISPERSED RUTILE TiO ₂ NPS IN AN AQUEOUS SOLUTION OF 1 mM OF NaCl AS A FUNCTION OF pH WHICH WAS ADJUSTED BY ADDITION OF SMALL AMOUNT OF AQUEOUS SOLUTIONS OF 1M HCl OR 1M NaOH. THE SQUARE SYMBOLS SHOW THE EFFECT OF pH ON THE AVERAGE PARTICLE HYDRODYNAMIC DIAMETER WHILE THE CIRCLE SYMBOLS REPRESENT THE PARTICLE ZETA POTENTIAL VS. pH.....	138
FIGURE 3.15: THE SCHEMATIC FUNCTIONALIZATION OF TITANIA NANOPARTICLES WITH ANIONIC AND CATIONIC POLYELECTROLYTES. THE PSS AND PAH REPRESENT POLYSTYRENE SULFONATES AND POLY(ALLYLAMINE HYDROCHLORIDE), RESPECTIVELY.....	139
FIGURE 3.16: THE EFFECT OF ADDITION OF BARE OR COATED TITANIA NANOPARTICLES TO THE ANIONIC OR CATIONIC POLYELECTROLYTES ON THE AVERAGE PARTICLE DIAMETER OF COATED TITANIA NANOPARTICLES. IT WAS USED THREE METHODS OF ADDITION, DIRECT ADDITION, DROPWISE ADDITION AND DROPWISE ADDITION WITH ULTRASONIC ENERGY. IT WAS FOUND THAT THE DROP BY DROP ADDITION WITH ULTRA-SONICATION IS THE FAVORABLE METHOD WITH AVERAGE PARTICLE DIAMETER 80 NM.....	140
FIGURE 3.17: THE EFFECT OF THE SOLUTION IONIC STRENGTH ON THE PARTICLE SIZE DISTRIBUTION OF TiO ₂ NPS COATED WITH ANIONIC AND CATIONIC POLYELECTROLYTES. DIFFERENT CONCENTRATIONS (1, 5, 20, 50 mM) OF SODIUM CHLORIDE SOLUTION WERE USED TO DISSOLVE THE POLYELECTROLYTES. DROPWISE ADDITION WITH ULTRA-SONICATION WAS USED FOR THE ADDITION OF THE DIFFERENT IONIC STRENGTH DISSOLVED POLYELECTROLYTES TO THE COLLOIDAL PARTICLES OF TITANIA.....	141
FIGURE 3.18: THE EFFECT OF THE MOLAR MASS OF ANIONIC OR CATIONIC POLYELECTROLYTES ON THE AVERAGE PARTICLE DIAMETER OF THE COATED TITANIA NANOPARTICLES AS A FUNCTION OF NUMBER OF DEPOSITED LAYERS OF POLYELECTROLYTES OF DIFFERENT MOLAR MASS. 70 kDa AND 10 kDa POLYSTYRENE SULFONATES AND 56 kDa AND 15 kDa POLY(ALLYLAMINE HYDROCHLORIDE) WERE USED IN 1 mM OF SODIUM CHLORIDE SOLUTION WITH DROPWISE ADDITION WITH ULTRA-SONICATION METHOD.	142
FIGURE 3.19: THE ZETA-POTENTIAL OF BARE AND MULTI-LAYER COATED TiO ₂ NPS AS A FUNCTION OF NUMBERS OF DEPOSITED LAYERS OF ANIONIC AND CATIONIC POLYELECTROLYTES. 10 kDa OF POLYSTYRENE SULFONATES AND 15 kDa OF POLY(ALLYLAMINE HYDROCHLORIDE) AS POLYELECTROLYTES FOR COATING TITANIA NANOPARTICLES WERE USED WITH 1 mM SODIUM CHLORIDE SOLUTION WITH DROPWISE ADDITION WITH ULTRA-SONICATION.	143

- FIGURE 4.1: THE EMISSION SPECTRUM OF THE VISIBLE LIGHT SOURCE WHICH WAS USED FOR IRRADIATING *C.REINHARDTII* IN THE PRESENCE OF TiO_2NPs AT VARIOUS EXPOSURE TIME WHICH WAS MEASURED BY USB4000-UV-VIS DETECTOR (TOSHIBA TCD1304AP LINEAR CCD ARRAY, USA).146
- FIGURE 4.2: LHS AXIS: THE ABSORBANCE SPECTRUM OF THE SODA GLASS TUBES USED FOR THE INCUBATION OF THE CELL WITH TiO_2NPs IN UV LIGHT. RHS AXIS: THE EMISSION SPECTRUM OF THE UV LAMP WHICH REFERS TO THAT THE MAXIMUM EMISSION OCCURS AT 365 NM WHICH WAS MEASURED BY USB4000-UV-VIS DETECTOR (TOSHIBA TCD1304AP LINEAR CCD ARRAY, USA). THIS UV LIGHT SOURCE WAS USED TO IRRADIATE *C.REINHARDTII* AND YEAST IN THE PRESENCE OF TiO_2NPs147
- FIGURE 4.3: THE VIABILITY OF *C.REINHARDTII* CELLS INCUBATED WITH SOLUTIONS OF DIFFERENT CONCENTRATIONS OF TiO_2NPs ($1\text{-}500\ \mu\text{G ML}^{-1}$) AT PH 4 IN DARK CONDITIONS AND IN VISIBLE LIGHT AT 0 H, 2 H, 4 H AND 6 H EXPOSURE TIMES AS COMPARED WITH THE CONTROL SAMPLE AT ROOM TEMPERATURE. THE CELL SUSPENSIONS WERE FREE FROM CULTURE MEDIA UPON INCUBATION WITH SOLUTIONS OF TITANIA NPs CONCENTRATIONS TO AVOID INTERACTION BETWEEN TiO_2 NPs WITH CULTURE MEDIA COMPONENTS.148
- FIGURE 4.4: THE 50X BRIGHT FIELD MICROSCOPIC IMAGE OF (B) AGGREGATED *C.REINHARDTII* AT HIGH CONCENTRATION OF TiO_2NPs AGAINST CONTROL SAMPLE (A).....149
- FIGURE 4.5: COMPARISON OF THE *C.REINHARDTII* CELL VIABILITY AS A FUNCTION OF THE TiO_2NPs CONCENTRATIONS IN DARK CONDITIONS AND IN UV LIGHT AT 0H, 2H, 4H, AND 6 HOURS OF INCUBATION TIMES IN COMPARISON WITH CONTROL SAMPLE OF MICROALGAE.150
- FIGURE 4.6: THE EFFECT OF THE TiO_2NPs CONCENTRATION ON THE CHLOROPHYLL CONTENT OF GREEN ALGAE *C.REINHARDTII* IN DARK CONDITIONS AND UNDER VISIBLE LIGHT AFTER 0H, 2H, 4H, AND 6 H EXPOSURE TIME. THE TOTAL CHLOROPHYLL CONTENT (A, B) WAS EXTRACTED FROM ALGAL CELLS USING 80 % AQUEOUS ACETONE SOLUTION, THEN MIXED FOR A MINUTES, CENTRIFUGED FOR 5 MINUTES WITH 13,000 RPM. THE SOLUTION PRODUCED WAS SCANNED OVER A WIDE RANGE OF WAVELENGTHS FROM 200 NM TO 700 NM. THE CHLOROPHYLL A AND B CONCENTRATIONS WERE MEASURED AT MAXIMUM WAVELENGTHS 645 AND 663 NM, RESPECTIVELY.....151
- FIGURE 4.7: THE EFFECT OF THE TiO_2NPs CONCENTRATION ON THE CHLOROPHYLL CONTENT OF GREEN ALGAE *C.REINHARDTII* IN DARK CONDITIONS AND UNDER UV LIGHT AFTER 0H, 2H, 4H, AND 6 H EXPOSURE TIME. THE TOTAL CHLOROPHYLL CONTENT (A, B) WAS EXTRACTED FROM ALGAL CELLS USING 80 % AQUEOUS ACETONE SOLUTION, THEN MIXED FOR A MINUTES, CENTRIFUGED FOR 5 MINUTES WITH 13,000 RPM. THE SOLUTION PRODUCED WAS SCANNED OVER A WIDE RANGE OF WAVELENGTHS FROM 200 NM TO 700 NM. THE CHLOROPHYLL A AND B CONCENTRATIONS WERE MEASURED AT MAXIMUM WAVELENGTHS 645 AND 663 NM, RESPECTIVELY.152
- FIGURE 4.8: OPTICAL IMAGES OF *C.REINHARDTII* SAMPLES AFTER 0, 2, 4 AND 6 HOURS OF ILLUMINATION WITH UV LIGHT IN THE PRESENCE OF TiO_2NPs AT THE SAME CONCENTRATION RANGE ($0\text{-}500\ \text{MG L}^{-1}$) AS IN FIGURE 6 AND 7. THE LHS TEST TUBES ON ALL FOUR IMAGES IN FIGURE 8 REPRESENT THE CONTROL SAMPLE OF MICROALGAE WITHOUT TiO_2NPs153
- FIGURE 4.9: TEM IMAGES OF MICROTOME-SECTIONED SAMPLES OF *C.REINHARDTII* CELLS AFTER BEING INCUBATED WITH 0, 100, AND $500\ \mu\text{G ML}^{-1}$ TiO_2NPs AND IRRADIATED FOR 6 HOURS WITH VISIBLE LIGHT. IMAGE (A) REPRESENTS THE CONTROL SAMPLE OF THE CELLS WITHOUT TiO_2NPs ; IMAGE (B) CORRESPONDS TO MICROALGAE INCUBATED WITH $100\ \mu\text{G ML}^{-1}$ TiO_2NPs ; IMAGES (C) AND (D) SHOW THE MICROSTRUCTURE OF A MICROALGAE CELL WALL AFTER INCUBATION WITH $500\ \mu\text{G ML}^{-1}$ TiO_2NPs . INTERNALIZATION OF TITANIA NANOPARTICLES INSIDE THE ALGAL CELLS IS NOT SEEN EVEN AT A $500\ \mu\text{G ML}^{-1}$ CONCENTRATION AS DISPLAYED IN FIGURE 10. THE DATA INDICATE THE ABSENCE OF TI IN THE CELL INTERIOR BUT SHOW ITS PRESENCE ON THE CELL OUTER MEMBRANE.154
- FIGURE 4.10: EDX DIAGRAM OF THE *C.REINHARDTII* ALGAE CELL AT 750 PPM: (A) CELL INTERIOR MEMBRANE AND (B) CELL OUTER MEMBRANE REGIONS; (C) WHOLE CELL. THIS DEMONSTRATES THE LACK OF INTERNALIZED TiO_2NPs IN *C.REINHARDTII* EVEN AT NPs CONCENTRATION 750 PPM.156
- FIGURE 4.11: THE VIABILITY OF BAKER'S YEAST AT DIFFERENT CONCENTRATIONS OF TITANIA NANOPARTICLES AGAINST CONTROL SAMPLE AT DARK CONDITION AND VISIBLE LIGHT CONDITION WHICH SHOWS A TOXIC EFFECT OF TITANIA NANOPARTICLES IN VISIBLE LIGHT IN COMPARISON WITH THE DARK CONDITIONS. THIS

EXPERIMENT WAS CONDUCTED THROUGH PIPETTING 1 MILLILITER OF SAMPLES, CENTRIFUGED, INCUBATED WITH ONE DROP OF FDA SOLUTION FOR 10 MINUTES, AND CENTRIFUGED TWICE , THEN MEASURED THEIR VIABILITY USING AUTOMATIC CELL COUNTER.....	158
FIGURE 4.12: BRIGHT FIELD MICROSCOPE IMAGE OF (B) AGGREGATED YEAST CELLS AFTER INCUBATION WITH TITANIA NANOPARTICLES ($5000 \mu\text{G.ML}^{-1}$) IN THE PRESENCE OF VISIBLE LIGHT AGAINST CONTROL SAMPLE (A).	159
FIGURE 4.13: THE PERCENTAGE OF VIABLE YEAST CELLS AFTER INCUBATION WITH TiO_2 NPs OF DIFFERENT CONCENTRATION IN THE PRESENCE OF UV LIGHT AND IN DARK CONDITIONS AT EXPOSURE TIMES VARYING FROM 0 H TO 24 H. THE DATA SHOW HIGHER TOXIC EFFECT OF THE TiO_2 NPs IN UV LIGHT THAN IN DARK CONDITIONS WHICH CAN BE ATTRIBUTED TO THE PRODUCTION OF REACTIVE OXYGEN SPECIES IN THE PRESENCE OF ATMOSPHERIC OXYGEN.....	161
FIGURE 4.14: TEM IMAGES OF <i>S. CEREVISIAE</i> SECTIONED AFTER 24 HOURS OF IRRADIATION WITH UV LIGHT AND INCUBATION IN (A) MILLI-Q WATER AND (B) $5000 \mu\text{G mL}^{-1}$ TiO_2 NPs. (C) HIGH RESOLUTION TEM IMAGE OF THE OUTER AND INNER CELL WALL OF THE YEAST CELL TREATED AS IN (B) WHICH SHOWS THE ATTACHMENT OF TiO_2 NPs TO THE OUTER CELL SURFACE AND INDICATES THEIR INTERNALISATION INSIDE THE CELL.....	163
FIGURE 4.15: EDX DIAGRAM OF YEAST CELL AT 1000 PPM: (A) CELL INTERIOR MEMBRANE AND (B) CELL OUTER MEMBRANE REGIONS; (C) THE CELL CENTRE. THE DATA INDICATE THE PRESENCE OF TiO_2 NPs BOTH ON THE OUTER AND THE INNER PART OF THE CELL MEMBRANE. THIS CONFIRMS THE INTERNALISED TiO_2 NPs IN YEAST AT THIS NPs CONCENTRATION.	165
FIGURE 4.16:(A) THE CELL VIABILITY OF <i>C.REINHARDTII</i> INCUBATED WITH TiO_2 NPs OF DIFFERENT AVERAGE PARTICLE SIZES (25 NM, 35 NM, 50 NM AND 145 NM) AND TOTAL PARTICLE CONCENTRATION OF $250 \mu\text{G mL}^{-1}$ IN DARK CONDITIONS AND IN UV LIGHT FOR 6 HOURS. (B) THE CELL VIABILITY OF <i>S. CEREVISIAE</i> INCUBATED WITH TiO_2 NPs OF DIFFERENT AVERAGE PARTICLE SIZES (THE SAME AS IN (A)) BUT AT TOTAL PARTICLE CONCENTRATION OF $2500 \mu\text{G mL}^{-1}$ IN DARK CONDITIONS AND IN UV LIGHT FOR 24 HOURS. ...	167
FIGURE 4.17: THE EFFECT OF ANATASE TiO_2 NPs COATED WITH DIFFERENT NUMBER OF LAYERS OF ANIONIC (PSS) AND CATIONIC (PAH) POLYELECTROLYTES ON THE VIABILITY OF <i>C.REINHARDTII</i> MICROALGAE AT DIFFERENT PARTICLE CONCENTRATIONS (0, 100 AND $500 \mu\text{G mL}^{-1}$). THE CELLS WERE INCUBATED WITH THE TiO_2 NPs FOR AT 0 H, 3 H AND 6 H EXPOSURE TIMES IN DARK CONDITIONS (A-D) AND IN UV LIGHT (E-H), RESPECTIVELY. THE CYTOTOXIC EFFECT ON THE MICROALGAE CELLS WAS ASSESSED FOR: (A, E) BARE TiO_2 NPs; (B, F) TiO_2 NPs/PSS; (C, G) TiO_2 NPs/PSS/PAH AND (D, H) TiO_2 NPs/PSS/PAH/PSS AT DIFFERENT NANOPARTICLE CONCENTRATIONS AND EXPOSURE TIMES.....	169
FIGURE 4.18: TEM IMAGES OF MICROTOME-SECTIONED <i>C.REINHARDTII</i> MICROALGAE CELLS AFTER BEING INCUBATED FOR 6 HOURS WITH POLYELECTROLYTE-COATED TiO_2 NPs WHILE ILLUMINATED WITH UV LIGHT. THE TiO_2 NPs HAVE BEEN MODIFIED BY DEPOSITION OF DIFFERENT NUMBER LAYERS OF ANIONIC (PSS) AND CATIONIC (PAH) POLYELECTROLYTES. (A) THE CONTROL SAMPLE OF THE MICROALGAE WITHOUT TiO_2 NPs. THE MICROALGAE AFTER BEING INCUBATED WITH (B) TiO_2 NPs/PSS; (C) TiO_2 NPs/PSS/PAH AND (D) TiO_2 NPs/PSS/PAH/PSS.....	171
FIGURE 4.19: THE CELL VIABILITY OF YEAST UPON INCUBATION OF BARE AND POLYELECTROLYTE-COATED ANATASE TiO_2 NPs OF DIFFERENT PARTICLE CONCENTRATIONS (0, 1000, AND $2500 \mu\text{G mL}^{-1}$) IN DARK CONDITIONS (A-D) AND IN UV LIGHT (E-H) AT 0 H, 6 H, 12 H AND 24 H EXPOSURE TIMES. THE YEAST CELLS WERE INCUBATED WITH: (A, E) BARE TiO_2 NPs; (B, F) TiO_2 NPs/PSS; (C, G) TiO_2 NPs/PSS/PAH AND (D, H) TiO_2 NPs/PSS/PAH/PSS.....	173
FIGURE 4.20: TEM IMAGES OF MICROTOME SECTIONED YEAST CELLS AFTER BEING INCUBATED FOR 24 HOURS UNDER UV LIGHT WITH TiO_2 NPs COATED WITH DIFFERENT NUMBER OF POLYELECTROLYTE LAYERS: (A) CONTROL SAMPLE WITHOUT TiO_2 NPs. (B) YEAST CELL INCUBATED WITH TiO_2 NPs/PSS. (C) YEAST CELLS INCUBATED WITH TiO_2 NPs/PSS/PAH. (D) YEAST CELLS INCUBATED WITH TiO_2 NPs/PSS/PAH/PSS.....	175
FIGURE 5.1: PROPOSED SCHEMATICS OF CROSS LINKED NETWORK OF THE CARBOPOL MICROGEL PARTICLES IN COLLAPSED STATE (AT LOW PH).....	180

FIGURE 5.2: THE AVERAGE PARTICLE DIAMETER OF 0.05 WT% CARBOPOL AQUA SF1 PREPARED FROM 30 WT% STOCK SOLUTION (AS SUPPLIED BY THE MANUFACTURER) AT pH 5.	180
FIGURE 5.3: THE ZETA POTENTIAL OF 0.05 WT. % CARBOPOL AQUA SF1 AT pH 5.5 PREPARED FROM 30 WT. % STOCK SOLUTION (AS SUPPLIED BY THE MANUFACTURER).	181
FIGURE 5.4: THE TEM IMAGE OF CARBOPOL AQUA SF1 PARTICLES AFTER DRYING THE SUSPENSION. THE IMAGE WAS TAKEN AFTER PRETREATMENT OF CARBOPOL SAMPLE WITH THE TEM PROTOCOL FOR NANOMATERIALS DESCRIBED IN CHAPTER 2 TO INCREASE THE IMAGING CONTRAST.....	182
FIGURE 5.5: THE VARIATION OF REFRACTIVE INDEX OF CARBOPOL AQUA SF1 AS A FUNCTION OF CARBOPOL AQUA SF1 CONCENTRATIONS AT ROOM TEMPERATURE USING ABBEY REFRACTOMETER WITH SODIUM LINE AT WAVELENGTH 589 NM.	185
FIGURE 5.6: THE AVERAGE PARTICLE DIAMETER (NM) OF CARBOPOL AQUA SF1 MICROGEL AS A FUNCTION OF THE REFRACTIVE INDEX WHICH WAS MEASURED BY ABBEY REFRACTOMETER WITH 589 NM SODIUM LINE AT ROOM TEMPERATURE. THE MEASUREMENT WAS CONDUCTED USING 0.3 WT% OF CARBOPOL ADJUSTED TO pH 8 BY ADDING SMALL AMOUNT OF 0.25 M SODIUM HYDROXIDE.....	186
FIGURE 5.7: SCHEMATIC FOR THE SWELLING/DESWELLING BEHAVIOR OF CARBOPOL AQUA SF1 IN CASE OF INCREASE AND DECREASE OF pH OF THE SURROUNDING SOLUTION, RESPECTIVELY.	189
FIGURE 5.8: THE AVERAGE PARTICLE DIAMETER OF CARBOPOL AQUA SF1 AS A FUNCTION OF pH. THE SIZE IS CALCULATED USING VARIABLE REFRACTIVE INDEX OF THE PARTICLES IN THE MALVERN MASTERSIZER, ONE IS AT THE COLLAPSED CARBOPOL MICROGEL WHICH IS 1.453 WHILE THE REFRACTIVE INDEX IS 1.336 IN CASE OF FULLY SWOLLEN CARBOPOL AT pH 8. ALIQUOT OF 0.25 M SODIUM HYDROXIDE WAS USED TO ADJUST THE pH. EACH READING WAS REPEATED SIX TIMES.....	190
FIGURE 5.9: THE SCHEMATIC DIAGRAM FOR THE ENCAPSULATION OF BERBERINE INTO CARBOPOL AQUA SF1 DEPENDING ON THE SWELLING AND DESWELLING BEHAVIOR OF THE MICROGEL IN THE BASIC AND ACIDIC MEDIUM, RESPECTIVELY.....	191
FIGURE 5.10: DIGITAL PHOTOGRAPHS OF THE SAMPLES OF BARE CARBOPOL AQUA SF1, BERBERINE, BERBERINE-LOADED CARBOPOL AQUA SF1 AT pH 8 AND BERBERINE-LOADED CARBOPOL AQUA SF1 AT pH 5.5.	192
FIGURE 5.11: AVERAGE PARTICLE DIAMETER OF CARBOPOL CONCENTRATIONS UPON ENCAPSULATION OF DIFFERENT AMOUNTS OF BERBERINE.	193
FIGURE 5.12: THE AVERAGE PARTICLE DIAMETER AND THE ZETA POTENTIAL OF CARBOPOL AQUA SF1 AS A FUNCTION OF BERBERINE CONCENTRATIONS AT pH 5.5 USING 0.1 WT% CARBOPOL AQUA SF1, ACETATE BUFFER SOLUTION (pH 5.5) AND EACH SOLUTION WAS SONICATED FOR 5 MINUTES TO FACILITATE ITS DISPERSING.	195
FIGURE 5.13: THE AVERAGE PARTICLE DIAMETER OF 0.015 WT.% BERBERINE LOADED CARBOPOL AQUA SF1 AT pH 5.5 PRODUCED FROM ADDITION OF ALIQUOT OF BERBERINE SOLUTION TO 0.1 WT% OF CARBOPOL AQUA SF1 MICROGEL AT pH 8 FOLLOWED BY DECREASE OF THE pH TO 5.5 TO FORM BERBERINE-LOADED COLLAPSED CARBOPOL AQUA SF1. THE FINAL SUSPENSION WAS ADJUSTED WITH ACETATE BUFFER SOLUTION SUPPORTING pH 5.5.	196
FIGURE 5.14: ZETA POTENTIAL OF 0.015 WT.% BERBERINE-LOADED CARBOPOL AQUA SF1 AT pH 5.5 ACETATE BUFFER SOLUTION WHICH WAS MEASURED BY MALVERN ZETASIZER NANO ZS MACHINE WITH DIP CELL IMMERSED IN PLASTIC CUVETTE.	197
FIGURE 5.15: TEM IMAGE OF BERBERINE-LOADED COLLAPSED CARBOPOL AQUA SF1 AT pH 5.5 ADJUSTED WITH ACETATE BUFFER SOLUTION. THE ENCAPSULATION WAS CONDUCTED THROUGH ADJUSTING THE MICROGEL AT pH 8, THEN BERBERINE WAS ADDED TO PRODUCE THE SWOLLEN CARBOPOL AQUA SF1 MICROGEL. THE PRODUCED SUSPENSION WAS ADJUSTED TO pH 5.5 TO FORM BERBERINE-LOADED CARBOPOL AQUA SF1 MICROGEL.	198
FIGURE 5.16: THE UV-VISIBLE SPECTRUM OF 0.01 WT. % CARBOPOL (BLUE LINE), 0.025 WT. % BERBERINE (ORANGE LINE) AND BERBERINE-LOADED CARBOPOL (BLACK LINE). ALL SOLUTIONS WERE ADJUSTED TO pH 5.5 USING ACETATE BUFFER SOLUTION. PERKIN ELMER LAMBDA 25 UV-VISIBLE	

SPECTROPHOTOMETER WAS UTILIZED TO MEASURE THE SPECTRUM IN THE WAVELENGTH RANGE FROM 200 NM TO 700 NM.	200
FIGURE 5.17: THE FTIR SPECTRUM OF CARBOPOL AQUA SF1 (A), BERBERINE (B) AND BERBERINE-LOADED CARBOPOL AQUA SF1 (C). EACH SAMPLE WAS DRIED IN THE OVER OVERNIGHT AND MIXED WITH EXCESS AMOUNT OF DRIED KBr PELLETS TO MAKE KBr DISK. THE SAMPLES THEN SCANNED WITH PERKIN ELMER FT-IR SPECTROMETER IN THE RANGE OF WAVELENGTH FROM 400 cm^{-1} TO 4000 cm^{-1}	202
FIGURE 5.18: THE THERMOGRAVIMETRIC ANALYSIS AND THE FIRST DERIVATIVE CURVE OF CARBOPOL (BLUE CURVE), BERBERINE (BLACK CURVE) AND BERBERINE-LOADED CARBOPOL (RED CURVE) WHERE THE MASS IS PLOTTED IN THE Y-AXIS WHILE THE TEMPERATURE ON THE X-AXIS. THIS EXPERIMENT WAS CONDUCTED IN THE AIR ATMOSPHERE WITH A PURGE RATE OF 10 mL/MINUTE AT TEMPERATURE FROM 100 $^{\circ}\text{C}$ TO 900 $^{\circ}\text{C}$	204
FIGURE 5.19: THE ABSORBANCE SPECTRUM OF SERIES OF SOLUTIONS OF BERBERINE (BRB) CONCENTRATIONS MEASURED AT 422 NM WAVELENGTH. THE DILUTED CONCENTRATIONS OF BERBERINE WERE PREPARED FROM 0.2 WT% STOCK SOLUTION OF BERBERINE CHLORIDE.	207
FIGURE 5.20: THE PERCENTAGE OF <i>IN VITRO</i> BERBERINE RELEASE AS A FUNCTION OF TIME WHICH WAS CONDUCTED USING 10 K MWCO DIALYSIS BAG FILLED UP WITH 50 mL OF BERBERINE-LOADED CARBOPOL SUSPENSION. THE WHOLE DIALYSIS BAG WAS DIPPED IN A BEAKER FILLED WITH 500 mL OF EITHER ACETATE BUFFER SOLUTION AT pH 5.5 OR PHOSPHATE BUFFER SALINE AT pH 7.5. IN THIS PROTOCOL, 3 mL OF BERBERINE-LOADED CARBOPOL SUSPENSION WERE MIXED WITH 3 mL OF FRESH BUFFER SOLUTION. THE SAMPLES ABSORBANCE WAS SCANNED IN A RANGE OF WAVELENGTH (200 NM-700 NM) USING PERKIN ELMER UV-VISIBLE SPECTROPHOTOMETER.	209
FIGURE 5.21: THE SCHEMATIC DIAGRAM FOR THE ENCAPSULATION OF CHLORHEXIDINE INTO CARBOPOL AQUA SF1, IN THIS DIAGRAM THE SWELLING AND DE-SWELLING OF CARBOPOL MICROGEL WERE TAKEN PLACE TO INVOLVE CHLORHEXIDINE INTO THE COLLAPSED MICROGEL.	210
FIGURE 5.22: THE PHOTOGRAPHIC IMAGE OF BARE CARBOPOL, CHLORHEXIDINE, CHLORHEXIDINE-LOADED CARBOPOL AT pH 8 AND CHLORHEXIDINE-LOADED CARBOPOL AT pH 5.5.....	211
FIGURE 5.23: THE AVERAGE PARTICLE HYDRODYNAMIC DIAMETER OF CHLORHEXIDINE-LOADED CARBOPOL AS A FUNCTION OF SOLUTION CONCENTRATION OF CHLORHEXIDINE. THE TWO LINES CORRESPOND TO INCUBATION OF TWO DIFFERENT CONCENTRATIONS OF CARBOPOL AQUA SF1 (ONE IS WITH 0.05 WT% (DOTTED) AND 0.1 WT% (DASHED)) WITH SERIES OF SOLUTION OF DIFFERENT CONCENTRATION OF CHLORHEXIDINE. THE ENCAPSULATION PROCESS WAS CONDUCTED BY SWELLING AND DESWELLING OF CARBOPOL AQUA SF1 TO pH 8 AND pH 5.5, RESPECTIVELY.....	213
FIGURE 5.24: THE AVERAGE PARTICLE HYDRODYNAMIC DIAMETER AND THE ZETA POTENTIAL OF CARBOPOL AQUA SF1 MICROHEL PARTICLES AS A FUNCTION OF THE CONCENTRATION OF ADDED CHLORHEXIDINE. THIS LOADING METHOD WAS BASED ON DROP BY DROP ADDITION OF SOLUTIONS OF DIFFERENT CONCENTRATION OF CHLORHEXIDINE SEPARATELY TO FOUR EQUAL AMOUNTS OF 0.1 WT. % CARBOPOL AQUA SF1 AT pH 8, THEN DECREASED pH TO 5.5, CENTRIFUGED THREE TIMES AND FINALLY RE-DISPERSED IN ACETATE BUFFER SOLUTION AT pH 5.5. EACH SOLUTION WAS SONICATED FOR 5 MINUTES TO FACILITATE THE RE-DISPERSING OF THE PARTICLES.	215
FIGURE 5.25: THE AVERAGE PARTICLE DIAMETER OF 0.09 WT.% CHLORHEXIDINE-LOADED SWOLLEN CARBOPOL AT pH 8 WHICH MEASURED USING MALVERN ZETASIZER ZS (UK) AFTER A SPECIFIC AMOUNT CHLORHEXIDINE MIXED WITH A FIXED CONCENTRATION OF CARBOPOL (0.1 WT%).....	216
FIGURE 5.26: THE AVERAGE PARTICLE HYDRODYNAMIC DIAMETER OF 0.09 WT.% CHLORHEXIDINE-LOADED COLLAPSED CARBOPOL RESULTED FROM ADDITION OF ALIQUOT OF CHLORHEXIDINE SOLUTION TO 0.1 WT% OF SWOLLEN CARBOPOL AT pH 5.5 THEN THE pH WAS REDUCED TO FORM CHLORHEXIDINE LOADED COLLAPSED CARBOPOL. THE FINAL SUSPENSION WAS CENTRIFUGED THREE TIMES AND DISPERSED WITH ACETATE BUFFER SOLUTION AT pH 5.5 TO RESIST ANY CHANGE IN pH UPON INCUBATION WITH MICROORGANISMS.....	217
FIGURE 5.27: THE ZETA POTENTIAL OF 0.09 WT.% CHLORHEXIDINE-LOADED COLLAPSED CARBOPOL MICROGEL PRODUCED FROM MIXING SPECIFIC AMOUNT OF CHLORHEXIDINE WITH 0.1 WT% CARBOPOL TO FORM	

PHYSICAL INTERACTED COMPLEX AT pH 8, THEN THE pH DECREASED TO pH 5.5 TO FORM CHLORHEXIDINE-LOADED COLLAPSED CARBOPOL. THE LATTER WAS CENTRIFUGED AND DISPERSED WITH ACETATE BUFFER AT pH 5.5. THE RESULTED SUSPENSION WAS MEASURED BY MALVERN ZETASIZER ZS WITH DIP CELL USING PLASTIC CUVETTE.	217
FIGURE 5.28: TEM IMAGE OF CHLORHEXIDINE-LOADED COLLAPSED CARBOPOL AT pH 5.5 WHICH PRESENTED THE SPHERICAL SHAPE OF THE PRODUCED MICROGEL. THE ENCAPSULATION WAS ACHIEVED THROUGH ADJUSTING CARBOPOL TO pH 8, THEN CHLORHEXIDINE WAS ADDED TO FORM CHLORHEXIDINE LOADED SWOLLEN CARBOPOL. THE FORMED SUSPENSION WAS ADJUSTED TO pH 5.5 TO FORM CHLORHEXIDINE LOADED CARBOPOL MICROGEL. THE TEM SAMPLES WERE PREPARED ACCORDING TO THE PROCEDURE MENTIONED IN CHAPTER 2, SECTION 2.2.7.	218
FIGURE 5.29: THE UV/VIS ABSORBANCE SPECTRUM OF 0.01 WT% CARBOPOL AQUA SF1 (BLUE LINE), 0.007 WT% CHLORHEXIDINE (ORANGE LINE) AND 0.006 WT% CHLORHEXIDINE-LOADED CARBOPOL AQUA SF1 (BLACK LINE). THE MEASUREMENT WAS DONE IN THE RANGE OF WAVELENGTH FROM 200 NM TO 400 NM USING PERKING ELMER LAMBDA 25 UV-VISIBLE SPECTROPHOTOMETER WITH 1 CM PATH LENGTH OF QS CUVETTE.	220
FIGURE 5.30: THE FOURIER TRANSFORM-IR SPECTRUM OF CARBOPOL AQUA SF1 (A), CHLORHEXIDINE (B) AND CHLORHEXIDINE-LOADED CARBOPOL AQUA SF1 (C). THESE MATERIALS WERE DRIED AND MIXED WITH EXCESS AMOUNT OF KBR PELLETS TO PREPARED KBR DISCS FOR EACH OF CARBOPOL MICROGEL, CHLORHEXIDINE AND CHLORHEXIDINE-LOADED CARBOPOL MICROGEL WHICH IN TURN WERE SCANNED INDIVIDUALLY IN RANGE OF WAVE NUMBERS FROM 400 CM ⁻¹ TO 4000 CM ⁻¹ TO MEASURE THEIR FTIR SPECTRUM.	222
FIGURE 5.31: THERMAL GRAVIMETRIC ANALYSIS (TGA) AND DIFFERENTIAL THERMAL ANALYSIS (DTA) OF CHLORHEXIDINE (RED LINE), CARBOPOL AQUA SF1 (BLUE LINE) AND CHLORHEXIDINE-LOADED CARBOPOL MICROGEL (BLACK LINE) WHICH ARE CONDUCTED THROUGH WEIGHING A KNOWN AMOUNT OF EACH SAMPLE AND DRYING, THEN RAN BY THE TGA MACHINE AT A RANGE OF TEMPERATURE FROM 100 °C TO 900 °C AT 10 °C/MINUTE IN AIR ATMOSPHERE WITH PURGE RATE OF 10 mL/MIN.	224
FIGURE 5.32: THE STANDARD CURVE OF SOLUTIONS OF DIFFERENT CONCENTRATIONS OF CHLORHEXIDINE DIGLUCONATE AT WAVELENGTH 254 NM USING PERKING ELMER LAMBDA 25 UV-VISIBLE SPECTROPHOTOMETER. THE SOLUTIONS WERE PREPARED FROM 0.2 WT% STOCK SOLUTION OF CHLORHEXIDINE DIGLUCONATE.	227
FIGURE 5.33: THE PERCENTAGE OF <i>IN VITRO</i> CHLORHEXIDINE RELEASE AS A FUNCTION OF TIME. THE EXPERIMENT WAS CONDUCTED USING 10 K MWCO DIALYSIS BAG FILLED UP WITH 50 mL OF CHLORHEXIDINE LOADED CARBOPOL AQUA SF1 SUSPENSION. THE WHOLE DIALYSIS BAG WAS DIPPED IN A BEAKER FILLED WITH 500 mL OF EITHER ACETATE BUFFER SOLUTION AT pH 5.5 OR PHOSPHATE BUFFER SALINE AT pH 7.5. A 3 mL SAMPLE OF LOADED CARBOPOL MICROGEL WERE PIPETTED FROM EACH BUFFER SOLUTION AND IN THE SAME TIME, A 3 mL OF FRESH BUFFER SOLUTION WAS ALSO ADDED TO THE BEAKER. THE PIPETTED AMOUNT WAS SCANNED IN A RANGE OF WAVELENGTH (200 -700 NM) USING PERKIN ELMER UV-VISIBLE SPECTROPHOTOMETER.	229
FIGURE 5.34: THE AVERAGE PARTICLE DIAMETER OF CATIONIC POLYELECTROLYTE FUNCTIONALIZED CARBOPOL AQUA SF1 MICROGEL VERSUS THE CATEGORY OF CATIONIC POLYELECTROLYTE. THE EXPERIMENT WAS ACHIEVED BY MIXING EXCESS AMOUNT OF EITHER POLY (ALLYLAMINE HYDROCHLORIDE) (PAH), OR BRANCHED POLY (DIALYLDIMETHYLAMMONIUM) CHLORIDE (PDAC) OR POLYETHYLENEIMINE (PEI) WITH 0.1 WT. % CARBOPOL AQUA SF1 MICROGEL, THEN GENTLY STIRRED AND ULTRA-SONICATED FOR A MINUTE.	231
FIGURE 5.35: THE AVERAGE PARTICLE HYDRODYNAMIC DIAMETER (A) AND ZETA POTENTIAL (B) OF PAH-COATED CARBOPOL AQUA SF1 MICROGEL AT pH 5. THIS WAS ACHIEVED THROUGH MIXING EXCESS AMOUNT OF SOLUTION OF THE CATIONIC POLYELECTROLYTE PAH WITH A FIXED CONCENTRATION OF CARBOPOL AQUA SF1 SUSPENSION TO FORM PAH-COATED CARBOPOL AQUA SF1. THE PRODUCED SUSPENSIONS WERE STIRRED, ULTRA-SONICATED AND CENTRIFUGED ONCE AT 10,000 RPM FOR AN HOUR.	232

FIGURE 5.36: THE AVERAGE PARTICLE DIAMETER (A) AND ZETA POTENTIAL (B) OF PAH-COATED CARBOPOL MICROGEL AT PH 5 WHICH WAS CONDUCTED THROUGH STIRRING AND ULTRA-SONICATING OF THE SUSPENSION PRODUCED FROM THE FIRST CENTRIFUGATION AND THEN CENTRIFUGED AGAIN AT 10,000 RPM FOR 1 HOUR.	233
FIGURE 5.37: THE AVERAGE PARTICLE DIAMETER AND ZETA POTENTIAL OF PAH COATED CARBOPOL AQUA SF1 MICROGEL AS A FUNCTION OF PAH CONCENTRATION IN MG.ML ⁻¹ . THE RESULTS WERE ACHIEVED THROUGH MIXING DIFFERENT CONCENTRATIONS OF PAH WITH 0.1 WT. % CONCENTRATION OF CARBOPOL MICROGEL WITH GENTLE STIRRING AND ULTRA-SONICATION FOR A MINUTE.	234
FIGURE 5.38: THE AVERAGE PARTICLE HYDRODYNAMIC DIAMETER AND ZETA POTENTIAL OF PDAC-COATED CARBOPOL AQUA SF1 SUSPENSION AS A FUNCTION OF THE PDAC CONCENTRATION WHICH WERE ACCOMPLISHED THROUGH MIXING SOLUTIONS OF VARIED CONCENTRATION OF PDAC SOLUTIONS WITH 0.1 WT% CARBOPOL MICROGEL, FOLLOWED BY STIRRING AND ULTRA-SONICATION FOR A MINUTE. THE PARTICLE DIAMETER AND ZETA POTENTIAL WERE MEASURED BY MALVERN ZETASIZER NANO ZS.	236
FIGURE 5.39: THE PARTICLE SIZE DISTRIBUTION (A) AND ZETA POTENTIAL (B) OF BERBERINE-LOADED CARBOPOL COATED WITH THE CATIONIC POLYELECTROLYTE PDAC VIA ADDITION OF THE CATIONIC POLYELECTROLYTE TO THE SOLUTION OF BERBERINE-LOADED CARBOPOL, FOLLOWED BY SHAKING OF THE SOLUTION FOR 5 MINUTES.	237
FIGURE 5.40: THE PARTICLE SIZE DISTRIBUTION (A) AND ZETA POTENTIAL (B) OF CHLORHEXIDINE-LOADED CARBOPOL COATED WITH THE CATIONIC POLYELECTROLYTE PDAC VIA ADDITION OF THE CATIONIC POLYELECTROLYTE TO THE SOLUTION OF CHLORHEXIDINE-LOADED CARBOPOL, FOLLOWED BY SHAKING OF THE SOLUTION FOR 5 MINUTES.	238
FIGURE 6.1: THE CHANGE IN CELL VIABILITY OF <i>C.REINHARDTII</i> CELLS INCUBATED IN AQUEOUS SUSPENSIONS OF VARYING CONCENTRATIONS OF CARBOPOL AQUA SF1 MICROGEL PARTICLES. THE EXPERIMENT WAS CONDUCTED AT ROOM TEMPERATURE THROUGH INCUBATION OF CARBOPOL SOLUTIONS WITH CULTURE MEDIA FREE ALGAL CELLS AT PH 5.5 FOR UP TO 6 HOURS. THE CELLS WERE WASHED BY CENTRIFUGATION AND TESTED WITH FDA CELL VIABILITY ASSAY AS DESCRIBED ABOVE.....	241
FIGURE 6.2: THE CYTOTOXIC EFFECT OF CARBOPOL AQUA SF1 ON YEAST CELLS WHEREBY THE CELLS WERE INCUBATED WITH SUSPENSIONS OF DIFFERENT CONCENTRATIONS OF CARBOPOL AQUA SF1 MICROGEL PARTICLES AT PH 5.5 AT ROOM TEMPERATURE UP TO 24 HOURS. THE CELLS WERE WASHED BY CENTRIFUGATION AND TESTED WITH FDA CELL VIABILITY ASSAY AS DESCRIBED ABOVE.	242
FIGURE 6.3: THE CYTOTOXIC EFFECT OF SUSPENSIONS OF DIFFERENT CONCENTRATION OF CARBOPOL AQUA SF1 MICROGEL PARTICLES ON <i>E. COLI</i> CELLS AT DIFFERENT INCUBATION TIMES. THE EXPERIMENT WAS CONDUCTED BY INCUBATION OF THE CELLS WITH SOLUTIONS OF DIFFERENT CONCENTRATIONS OF CARBOPOL AQUA SF1 AT PH 5.5 AT ROOM TEMPERATURE FOR UP TO 24 HOURS. THE ASSAY WAS PERFORMED BY PIPETTING A MILLILITER OF THE SAMPLE, WASHING, CENTRIFUGING AND DISPERSING WITH MILLI-Q WATER. AFTER THAT, 100 μ L OF EACH SAMPLE WAS PLACED IN 96-MICROWELL PLATE AND THEN, 100 μ L LEUCIFERIN REAGENT WAS ADDED TO THE 100 μ L SAMPLE, SHAKED FOR 30 SECONDS, AND INCUBATED FOR 5 MINUTES AT 25 °C. THE RELATIVE LUMINESCENCE INTENSITY WHICH REPRESENTS THE PERCENTAGE OF VIABLE CELLS WAS MEASURED USING A LUMINOMETER.	243
FIGURE 6.4: THE TEM IMAGES OF <i>C. REINHARDTTI</i> CELLS AFTER INCUBATION WITH 0.1 WT% CARBOPOL AQUA SF1 MICROGEL. THE TEM IMAGING WAS CONDUCTED WITH THE SIMILAR WAY AS IT WAS MENTIONED IN SECTION 2.2.7. BRIEFLY, THE CELLS WERE CENTRIFUGED AT 500 RPM, WASHED WITH MILLI-Q WATER, FIXED IN 2 WT% GLUTARALDEHYDE FOR 1 HOUR AT ROOM TEMPERATURE, THEN TREATED WITH 1 WT% OSMIUM TETROXIDE FOR 1 HOUR, FOLLOWED BY TREATMENT WITH 2.5 WT% URANYL ACETATE FOR 1 HOUR AND WASHED WITH SOLUTIONS OF DIFFERENT CONCENTRATIONS OF ETHANOL. AFTER THAT, THE CELL WERE EMBEDDED IN FRESH EPOXY/ARALDITE FOR 48 HOURS AT 60 °C, LEFT AT ROOM TEMPERATURE FOR FURTHER 48 HOURS AND SECTIONED USING AN ULTRA-MICROTOME. THE IMAGES WERE TAKEN BY USING JOEL TEM MACHINE.	244
FIGURE 6.5: THE TEM (A-B) AND SEM (C-D) IMAGES OF YEAST CELLS INCUBATED WITH A SPECIFIC CONCENTRATION OF CARBOPOL AQUA SF1/ MICROGEL AT PH 5.5 FOR 24 HOUR INCUBATION TIME. THE	

- EXPERIMENT WAS CONDUCTED AS DESCRIBED IN SECTION 2.2.7. (A) TEM IMAGE OF THE CONTROL SAMPLE, (B) TEM IMAGE OF THE YEAST CELLS AFTER INCUBATION IN 0.15 WT% CARBOPOL AQUA SF1 FOR 24 HOURS, (C) SEM IMAGE OF THE CONTROL SAMPLE OF YEAST AND (D) SEM IMAGE OF YEAST CELL AFTER INCUBATION IN 0.15 WT% CARBOPOL AQUA SF1 FOR 24 HOURS.245
- FIGURE 6.6: THE VIABILITY OF *C. REINHARDTII* CELLS INCUBATED WITH SOLUTIONS OF DIFFERENT CONCENTRATIONS OF BERBERINE AT DIFFERENT INCUBATION TIMES. THE pH OF THE SOLUTION WAS ADJUSTED WITH ACETATE BUFFER SOLUTION (pH 5.5) TO AVOID ANY CHANGE IN pH UPON INCUBATION. THE INCUBATION WAS CONDUCTED THROUGH MIXING A SOLUTION OF SPECIFIC CONCENTRATION OF BERBERINE WITH A FIXED AMOUNT OF CULTURE MEDIA FREE MICROALGAE CELLS IN A 20 mL GLASS VIAL CAPED WITH COTTON PLUG AND PLACED IN AN INCUBATOR TO AVOID CONTAMINATION. A 1.0 mL OF EACH SAMPLE WAS PIPETTED, CELLS WERE CENTRIFUGED AND WASHED WITH MILLI-Q WATER AND THEIR VIABILITY WAS TESTED USING FDA ASSAY.247
- FIGURE 6.7: THE VIABILITY OF *C. REINHARDTII* CELLS INCUBATED WITH SOLUTIONS OF SERIES OF DIFFERENT OVERALL CONCENTRATION OF BERBERINE LOADED INTO CARBOPOL AQUA SF1 MICROGEL AFTER DIFFERENT INCUBATION TIMES. THE INCUBATION WAS CONDUCTED AT pH 5.5 BY MIXING A SOLUTION OF A SPECIFIC OVERALL CONCENTRATION OF BERBERINE LOADED INTO CARBOPOL MICROGEL WITH A FIXED AMOUNT MICROALGAE CELLS REMOVED FROM THE CULTURE MEDIA IN A 20 mL GLASS VIAL CAPED WITH A COTTON PLUG AND PLACED IN AN INCUBATOR TO AVOID CONTAMINATION. A 1.0 mL OF EACH SAMPLE WAS PIPETTED, WASHED WITH MILLI-Q WATER AND THE VIABILITY WAS TESTED USING FDA ASSAY.249
- FIGURE 6.8: SEM IMAGES OF *C. REINHARDTII* CELLS UPON INCUBATION WITH 0.01 WT% ENCAPSULATED BERBERINE INTO CARBOPOL AQUA SF1 PARTICLES WHEREBY (A) REPRESENTS THE CONTROL SAMPLE AND (B, C, AND D) SHOW THE INCUBATED CELLS WITH 0.01 WT% BERBERINE LOADED CARBOPOL AQUA SF1 FOR 2 HOURS. THESE CELLS WERE PRE-TREATED AFTER INCUBATION AS DESCRIBED IN SECTION 2.2.8.250
- FIGURE 6.9: SCHEMATIC FOR THE RELEASE OF BERBERINE FROM CARBOPOL MICROGEL THROUGH DIRECT DIFFUSION IN THE OUTER CELL MEMBRANE OF CELL AS WELL AS BY THE INTERNALIZATION OF BERBERINE-LOADED CARBOPOL MICROGEL THROUGH THE CELL MEMBRANE FORMING ENDOSOME OF BERBERINE LOADED MICROGEL PARTICLE BY ENDOCYTOSIS WHEREBY BERBERINE MOLECULES CAN BE FURTHER RELEASED INSIDE THE CELL'S CYTOPLASM.251
- FIGURE 6.10: THE VIABILITY OF BAKER'S YEAST CELLS INCUBATED WITH SERIES OF SOLUTIONS OF DIFFERENT CONCENTRATIONS OF FREE BERBERINE AT pH 5.5 FROM 0 HOURS TO 6 HOURS. THE EXPERIMENT WAS CONDUCTED BY MIXING YEAST CELLS REMOVED FROM THE CULTURE MEDIA WITH SOLUTIONS OF BERBERINE CONCENTRATIONS FROM 0.01 WT% TO 0.15 WT% IN A 20 mL GLASS VIAL WITH GENTLE STIRRING. THE CELL VIABILITY WAS MEASURED BY USING FDA ASSAY WHEREBY, 1 mL OF SAMPLE WAS PIPETTED, WASHED AND ONE DROP OF FDA ACETONE SOLUTION WAS ADDED AND STIRRED FOR 10 MINUTES, CENTRIFUGED AND DISPERSED IN PBS BUFFER SOLUTION. A 20 μ L OF THE SAMPLE WAS PLACED IN A CHIP OF MEASUREMENT TO DETERMINE THE VIABILITY OF CELLS.253
- FIGURE 6.11: THE VIABILITY OF YEAST CELLS INCUBATED WITH SERIES OF AVERAGE ENCAPSULATED BERBERINE CONCENTRATIONS AT pH 5.5 FROM 0 HOUR TO 6 HOURS INCUBATION TIMES. THE EXPERIMENT WAS CONDUCTED BY MIXING CULTURE MEDIA FREE YEAST CELLS WITH SOLUTIONS OF OVERALL CONCENTRATION OF ENCAPSULATED BERBERINE FROM 0.001 WT% TO 0.015 WT% IN A 20 mL GLASS VIAL WITH GENTLE STIRRING. THE VIABILITY WAS MEASURED BY USING FDA VIABILITY ASSAY WHEREBY, 1 mL OF SAMPLE WAS PIPETTED, WASHED AND ONE DROP OF FDA ACETONE SOLUTION WAS ADDED AND STIRRED FOR 10 MINUTES, CENTRIFUGED AND DISPERSED IN PBS BUFFER SOLUTION. A 20 μ L OF THE SAMPLE WAS PLACED IN THE CELL COUNTER CHIP FOR MEASUREMENT TO DETERMINE THE VIABILITY OF CELLS.254
- FIGURE 6.12: TEM IMAGES OF CULTURE MEDIA FREE YEAST CELLS THAT HAVE BEEN INCUBATED WITH SOLUTIONS OF DIFFERENT CONCENTRATIONS OF BERBERINE: (A) CONTROL SAMPLE WITHOUT BERBERINE, (B) 0.15 WT% BERBERINE, AND (C AND D) 0.001 WT. % AND 0.015 WT. % OF OVERALL ENCAPSULATED BERBERINE INTO CARBOPOL AQUA SF1 MICROGEL, RESPECTIVELY. THE TEM IMAGES DID NOT APPEAR TO

- SHOW SIGNIFICANT DIFFERENCE IN COMPARISON WITH THE CONTROL IN CASE OF USING BOTH FREE OR ENCAPSULATED BERBERINE. THE TEM SAMPLES WERE FIRST TREATED WITH GLUTARALDEHYDE FOR 2 HOURS AND WASHED WITH A BUFFER SOLUTION (pH 7.4) THREE TIMES, THEN STAINED WITH URANYL ACETATE AND WASHED WITH AQUEOUS SOLUTIONS OF DIFFERENT CONCENTRATIONS OF ETHANOL AS EXPLAINED IN DETAILS IN THE EXPERIMENTAL SECTION (CHAPTER 2).255
- FIGURE 6.13: SEM IMAGES OF YEAST CELLS INCUBATED FOR 6 AND 24 HOURS WITH SOLUTIONS OF FREE AND MICROGEL-ENCAPSULATED BERBERINE, RESPECTIVELY. (A) CONTROL SAMPLE OF YEAST CELLS; (B) YEAST CELLS INCUBATED WITH 0.15 WT% FREE BERBERINE, (C) YEAST CELLS INCUBATED WITH 0.001 WT% MICROGEL-ENCAPSULATED BERBERINE, AND (D, E, AND F) YEAST CELLS INCUBATED WITH 0.015 WT. % OF MICROGEL-ENCAPSULATED BERBERINE. HERE THE OVERALL BERBERINE CONCENTRATION IN THE MICROGEL FORMULATION IS QUOTED. THE CELLS WERE PRE-TREATED WITH GLUTARALDEHYDE FOR TWO HOURS AND WASHED WITH BUFFER SOLUTION (pH 7.4) FOR THREE TIMES, DRIED AND THEN GOLD-SPUTTERED TO INCREASE THE IMAGING CONTRAST.256
- FIGURE 6.14: THE RELATIVE LUMINESCENCE INTENSITIES OF VIABILITY OF *E. COLI* CELLS AS A FUNCTION OF BERBERINE CONCENTRATIONS FOR 2 HOURS INCUBATION TIME. THIS EXPERIMENT WAS PERFORMED THROUGH PIPETTING 1 mL OF EACH SAMPLE WAS CENTRIFUGED THrice TO GET RID OF THE EXCESS AMOUNT OF BERBERINE, THEN DISPERSED IN MILLI-Q WATER. AFTER THAT, 100 μ L OF THE SAMPLE WAS MIXED WITH 100 μ L OF LUCIFERASE REAGENT IN 96 MICROWELL PLATE FOR 30 SECONDS, INCUBATED FOR 5 MINUTES AT 25 $^{\circ}$ C, AND THE RELATIVE LUMINESCENCE WAS MEASURED BY USING A LUMINOMETER. 258
- FIGURE 6.15: THE RELATIVE LUMINESCENCE INTENSITIES OF VIABILITY OF *E. COLI* CELLS AS A FUNCTION OF OVERALL CONCENTRATION OF ENCAPSULATED BERBERINE LOADED INTO CARBOPOL AQUA SF1 MICROGEL FOR DIFFERENT INCUBATION TIMES. THIS EXPERIMENT WAS PERFORMED THROUGH PIPETTING 1 mL OF EACH SAMPLE, CENTRIFUGED THrice TO GET RID OF THE EXCESS AMOUNT OF BERBERINE, THEN DISPERSED IN MILLI Q WATER. AFTER THAT, 100 μ L OF THE SAMPLE WAS MIXED WITH 100 μ L OF LUCIFERASE REAGENT IN 96 MICROWELL PLATE FOR 30 SECONDS, INCUBATED FOR 5 MINUTES AT 25 $^{\circ}$ C, AND THE LUMINESCENCE INTENSITY WAS MEASURED BY USING LUMINOMETER.....259
- FIGURE 6.16: SEM IMAGES FOR *E. COLI* CELLS INCUBATED WITH A SUSPENSION OF 0.01 WT% BERBERINE-LOADED CARBOPOL AQUA SF1 MICROGEL. (A) CONTROL SAMPLE AND (B, C, D, E, AND F) REPRESENT *E. COLI* CELLS INCUBATED WITH 0.01 WT% BERBERINE-LOADED CARBOPOL AQUA SF1 MICROGEL AT ROOM TEMPERATURE FOR 24 HOURS INCUBATION TIME.260
- FIGURE 6.17: THE VIABILITY OF *C. REINHARDTII* CELLS INCUBATED WITH SOLUTIONS OF VARIED CONCENTRATIONS OF FREE CHLORHEXIDINE AT DIFFERENT INCUBATION TIMES. THE INCUBATION WAS CONDUCTED THROUGH MIXING A SOLUTION OF SPECIFIC CONCENTRATION OF CHLORHEXIDINE WITH A FIXED AMOUNT OF MICROALGAE CELLS REMOVE FROM THE CULTURE MEDIA IN A 20 mL GLASS VIAL CAPED WITH COTTON AND PLACED IN AN INCUBATOR. 1.0 mL OF EACH SAMPLE WAS PIPETTED, WASHED WITH MILLI-Q WATER AND THE CELL VIABILITY WAS TESTED USING FDA ASSAY.262
- FIGURE 6.18: THE VIABILITY OF *C. REINHARDTII* CELLS INCUBATED WITH SOLUTIONS OF DIFFERENT OVERALL CONCENTRATIONS OF ENCAPSULATED CHLORHEXIDINE INTO CARBOPOL AQUA SF1 MICROGEL AFTER DIFFERENT INCUBATION TIMES. THE INCUBATION WAS CONDUCTED AT pH 5.5 BY MIXING AN ALIQUOT OF SPECIFIC OVERALL CONCENTRATION OF CHLORHEXIDINE-LOADED CARBOPOL AQUA SF1 MICROGEL WITH A FIXED AMOUNT OF CULTURE MEDIA FREE MICROALGAE CELLS IN A 20 mL GLASS VIAL CAPED WITH COTTON AND PLACED IN AN INCUBATOR. A 1.0 ML OF EACH SAMPLE WAS PIPETTED, WASHED WITH MILLI-Q WATER AND THE VIABILITY WAS TESTED USING FDA ASSAY.263
- FIGURE 6.19: SEM IMAGES OF *C. REINHARDTII* CELLS. (A) CONTROL SAMPLE OF *E. COLI*. (B) *E. COLI* CELLS INCUBATED WITH 0.09 WT% CHLORHEXIDINE-LOADED CARBOPOL AQUA SF1 FOR TWO HOURS. THE SAMPLES WERE PRE-TREATED FOR SEM USING THE PROCEDURE DESCRIBED IN SECTION 2.2.8.264
- FIGURE 6.20: THE VIABILITY OF YEAST CELLS INCUBATED WITH SERIES OF SOLUTIONS OF FREE CHLORHEXIDINE WITH DIFFERENT CONCENTRATIONS AT pH 5.5 AFTER INCUBATION FROM 0 TO 1 HOURS. THE EXPERIMENT WAS CONDUCTED BY MIXING THE YEAST CELLS (REMOVED FROM THE MEDIA) WITH SOLUTIONS OF CHLORHEXIDINE CONCENTRATIONS FROM 0.001 WT% TO 0.05 WT% IN A 20 mL GLASS VIAL WITH GENTLE

STIRRING. THE CELL VIABILITY WAS MEASURED BY USING FDA VIABILITY ASSAY WHEREBY, 1 ML OF SAMPLE WAS PIPETTED, WASHED AND ONE DROP OF FDA ACETONE SOLUTION WAS ADDED AND STIRRED FOR 10 MINUTES AND CENTRIFUGED AND DISPERSED WITH PBS SOLUTION. A 20 μ L OF THE SAMPLE WAS PLACED IN A CELL COUNTING CHIP TO DETERMINE THE CELL VIABILITY.	266
FIGURE 6.21: THE VIABILITY OF YEAST CELLS INCUBATED WITH SERIES OF AVERAGE ENCAPSULATED CHLORHEXIDINE CONCENTRATIONS AT PH 5.5 FROM 0 HOUR TO 24 HOURS INCUBATION TIMES. THE EXPERIMENT WAS ACHIEVED THROUGH MIXING CULTURE MEDIA FREE YEAST CELLS WITH SOLUTIONS OF OVERALL ENCAPSULATED CHLORHEXIDINE CONCENTRATIONS FROM 0.001 WT% TO 0.05 WT%.	267
FIGURE 6.22: SEM IMAGES OF YEAST CELLS. (A) CONTROL SAMPLE OF YEAST CELLS AND (B, C, D, E AND F) YEAST CELLS AFTER INCUBATION IN SOLUTION OF 0.045 WT% CHLORHEXIDINE-LOADED CARBOPOL AQUA SF1 MICROGEL WITH YEAST CELLS FOR 24 HOURS INCUBATION TIME AT ROOM TEMPERATURE. THE CELLS WERE PRE-TREATED FOR SEM USING THE PROCEDURE DESCRIBED IN SECTION 2.2.8.	268
FIGURE 6.23: THE RELATIVE LUMINESCENCE INTENSITIES (A MEASURE OF THE VIABILITY) OF <i>E. COLI</i> CELLS AS A FUNCTION OF THE FREE CHLORHEXIDINE CONCENTRATION FOR UP TO 4 HOURS INCUBATION TIME. THIS EXPERIMENT WAS PERFORMED THROUGH PIPETTING 1 ML OF EACH SAMPLE, CENTRIFUGED THRICE TO GET RID OF THE EXCESS AMOUNT OF CHLORHEXIDINE AND THEN DISPERSED IN MILLI-Q WATER. AFTER THAT, 100 μ L OF THE SAMPLE WAS MIXED WITH 100 μ L OF LUCIFERASE REAGENT IN 96 MICRO-WELL PLATE FOR 30 SECONDS, INCUBATED FOR 5 MINUTES AT 25 $^{\circ}$ C, AND THE LUMINESCENCE WAS MEASURED BY USING A LUMINOMETER.	270
FIGURE 6.24: THE RELATIVE LUMINESCENCE INTENSITIES OF VIABILITY OF <i>E. COLI</i> CELLS AS A FUNCTION OF THE OVERALL CONCENTRATION OF CHLORHEXIDINE-LOADED INTO CARBOPOL AQUA SF1 MICROGEL FOR UP TO 24 HOURS INCUBATION TIME. THIS EXPERIMENT WAS PERFORMED AT THE SAME CONDITIONS AS THE ONE WITH FREE CHLORHEXIDINE (FIGURE 6.23).	271
FIGURE 6.25: SEM IMAGES OF <i>E. COLI</i> CELLS. (A) CONTROL SAMPLE OF <i>E. COLI</i> CELLS. (B, C, AND D) <i>E. COLI</i> CELLS INCUBATED WITH 0.045 WT% CHLORHEXIDINE-LOADED IN CARBOPOL AQUA SF1 MICROGEL. THE CELLS WERE PRE-TREATED WITH THE PROCEDURE DESCRIBED IN SECTION 2.2.8.	272
FIGURE 6.26: THE CYTOTOXIC EFFECT OF SOLUTIONS OF DIFFERENT PDAC CONCENTRATION ON MICROALGAE CELLS (<i>C. REINHARDTII</i>) FOR 1 HOUR INCUBATION TIME AT ROOM TEMPERATURE. PDAC SOLUTIONS OF DIFFERENT CONCENTRATIONS WERE INCUBATED WITH A FIXED AMOUNT OF MICROALGAE CELLS.	274
FIGURE 6.27: THE CYTOTOXIC EFFECT OF SOLUTIONS OF DIFFERENT PDAC CONCENTRATION ON YEAST CELLS FOR UP TO 1 HOUR INCUBATION TIME AT ROOM TEMPERATURE. A FIXED AMOUNT OF YEAST CELLS WAS INCUBATED WITH A SOLUTION OF DIFFERENT PDAC CONCENTRATIONS	275
FIGURE 6.28: THE CYTOTOXIC EFFECT OF SOLUTIONS OF DIFFERENT PDAC CONCENTRATION ON <i>E. COLI</i> CELLS FOR UP TO 1 HOUR INCUBATION TIME AT ROOM TEMPERATURE. SOLUTIONS OF DIFFERENT PDAC CONCENTRATIONS WERE INCUBATED WITH A FIXED AMOUNT OF <i>E. COLI</i> CELLS.	276
FIGURE 6.29: THE CYTOTOXIC EFFECT OF PDAC-COATED CARBOPOL AQUA SF1 MICROGEL UPON INCUBATION WITH MICROALGAE CELLS FOR 2 HOURS AT ROOM TEMPERATURE. THE MEASUREMENT WAS CONDUCTED THROUGH PIPETTING 1 ML OF EACH SAMPLE, CENTRIFUGED TWICE, INCUBATED WITH 1 DROP OF FDA SOLUTION FOR 10 MINUTES AND THEN CENTRIFUGED AND RE-DISPERSED WITH PBS SOLUTION (PH 7.4). AFTER THAT, THE CELL VIABILITY WAS MEASURED BY AUTOMATIC CELL COUNTER.	277
FIGURE 6.30: THE CYTOTOXIC EFFECT OF PDAC-COATED CARBOPOL MICROGEL UPON INCUBATION WITH YEAST CELLS FOR UP TO 6 HOURS AT ROOM TEMPERATURE. THE MEASUREMENT WAS CONDUCTED THROUGH PIPETTING 1 ML OF EACH SAMPLE, CENTRIFUGED TWICE, INCUBATED WITH FDA SOLUTION FOR 10 MINUTES AND THEN CENTRIFUGED AND DISPERSED WITH PBS SOLUTION (PH 7.4). AFTER THAT, THE CELL VIABILITY WAS MEASURED BY AUTOMATIC CELL COUNTER.	278
FIGURE 6.31: THE CYTOTOXIC EFFECT OF PDAC COATED CARBOPOL AQUA SF1 MICROGEL UPON INCUBATION WITH <i>E. COLI</i> CELLS FOR 2 HOURS AT ROOM TEMPERATURE. THE MEASUREMENT WAS CARRIED OUT THROUGH PIPETTING 1 ML OF EACH SAMPLE, CENTRIFUGED TWICE, AFTER THAT 100 μ L OF EACH CELL SAMPLE WAS PLACED IN A 96-MICROPLATE WELLS AND ADDED 100 μ L OF LUMINESCENCE REAGENT. THE	

96 MICROPLATE WELLS WERE SHAKEN FOR 30 SECONDS, INCUBATED FOR 5 MINUTES AND THE INTENSITY WAS MEASURED BY LUMINOMETER.....	279
FIGURE 6.32: THE VIABILITY OF <i>C.REINHARDTII</i> MICROALGAE CELLS UPON INCUBATION WITH SOLUTIONS OF DIFFERENT CONCENTRATIONS OF PDAC-COATED BERBERINE-LOADED CARBOPOL AQUA SF1 MICROGEL. THE SOLUTIONS WERE PREPARED DEPENDING ON DILUTION FROM STOCK SOLUTION WITH THE CONCENTRATION 0.009 WT% PDAC-0.0075 WT%-0.075 WT% BERBERINE-CARBOPOL AQUA SF1 COMPLEX. THE MEASUREMENT WAS CONDUCTED THROUGH PIPETTING 1 ML OF EACH SAMPLE, CENTRIFUGED TWICE, INCUBATED WITH A DROP OF FDA SOLUTION IN ACETONE FOR 10 MINUTES, AND THEN CENTRIFUGED AND DISPERSED WITH PBS SOLUTION (PH 7.4). AFTER THAT, THE CELL VIABILITY WAS MEASURED BY AUTOMATIC CELL COUNTER.	281
FIGURE 6.33: THE VIABILITY OF <i>C.REINHARDTII</i> MICROALGAE CELLS UPON INCUBATION WITH 0.0045 WT% PDAC, 0.0045 WT% PDAC-COATED CARBOPOL, 0.0375 WT% BERBERINE, 0.00375 WT% CARBOPOL-ENCAPSULATED BERBERINE, AND 0.0045 WT. % PDAC-COATED 0.00375 WT% BERBERINE-LOADED CARBOPOL AQUA SF1 MICROGEL COMPLEX. THE MEASUREMENT WAS CONDUCTED THROUGH PIPETTING 1 ML OF EACH SAMPLE, CENTRIFUGED TWICE, INCUBATED WITH 1 DROP OF FDA SOLUTION IN ACETONE FOR 10 MINUTES AND THEN CENTRIFUGED AND DISPERSED WITH PBS SOLUTION (PH 7.4). AFTER THAT, THE VIABILITY WAS MEASURED BY AN AUTOMATIC CELL COUNTER.....	282
FIGURE 6.34: SEM IMAGES OF <i>C.REINHARDTII</i> MICROALGAE CELLS. (A) CONTROL SAMPLE OF THE MICROALGAE CELLS. (B, C, AND D) <i>C.REINHARDTII</i> CELLS INCUBATED WITH 0.0045 WT. % PDAC COATED 0.00375 WT% BERBERINE-LOADED CARBOPOL AQUA SF1 MICROGEL COMPLEX AFTER ONE HOUR INCUBATION TIME AT ROOM TEMPERATURE. THE EXPERIMENT WAS CONDUCTED THROUGH INCUBATION A SUSPENSION OF MICROALGAE CELLS WITH SOLUTION OF PDAC-COATED 0.00375 WT% BERBERINE-LOADED CARBOPOL AQUA SF1 PARTICLES. THE CELLS WERE PRE-TREATED FOR SEM USING THE PROCEDURE DESCRIBED IN SECTION 2.2.8.....	283
FIGURE 6.35: SCHEMATIC DIAGRAM FOR THE ELECTROSTATIC INTERACTION BETWEEN PDAC-COATED BERBERINE-LOADED CARBOPOL AQUA SF1 PARTICLES AND THE ANIONIC CELL MEMBRANE OF MICROALGAE CELLS.	284
FIGURE 6.36: THE VIABILITY OF YEAST CELLS UPON INCUBATION WITH SOLUTIONS OF DIFFERENT CONCENTRATIONS OF PDAC-COATED BERBERINE-LOADED CARBOPOL MICROGEL. THESE SUSPENSIONS WERE PREPARED BY DILUTION FROM A STOCK SOLUTION WITH THE CONCENTRATION 0.009 WT% PDAC-0.0075 WT% BERBERINE -0.075 WT% CARBOPOL AQUA SF1 COMPLEX.	286
FIGURE 6.37: THE VIABILITY OF YEAST CELLS UPON INCUBATION WITH 0.009 WT% PDAC, 0.009 WT% PDAC-COATED CARBOPOL AQUA SF1, 0.0075 WT% BERBERINE, 0.0075 WT% ENCAPSULATED BERBERINE, AND 0.009 WT% PDAC-COATED 0.0075 WT% BERBERINE-LOADED CARBOPOL AQUA SF1 MICROGEL COMPLEX.....	287
FIGURE 6.38: SEM IMAGES OF YEAST CELLS. (A) CONTROL SAMPLE OF YEAST CELL AND (B, C, D, AND E) YEAST CELLS THAT INCUBATED WITH 0.009 WT% PDAC-COATED 0.0075 WT% BERBERINE-LOADED CARBOPOL AQUA SF1 MICROGEL COMPLEX AFTER TWO HOURS OF INCUBATION. THE SEM SAMPLES WERE PRETREATED WITH THE PROCEDURE DESCRIBED IN SECTION 2.2.8.	288
FIGURE 6.39: THE ANTIMICROBIAL ACTIVITY OF SUSPENSIONS OF DIFFERENT CONCENTRATIONS OF PDAC-COATED BERBERINE-LOADED CARBOPOL AQUA SF1 (PDAC COATED BLC) AGAINST <i>E.COLI</i> CELLS. THE SOLUTIONS WERE PREPARED FROM THE STOCK SOLUTION (0.011 WT% PDAC-COATED 0.0075 WT% BERBERINE-LOADED 0.05 WT% CARBOPOL AQUA SF1 COMPLEX.	290
FIGURE 6.40: THE ANTIMICROBIAL ACTIVITY OF 0.0088 WT% PDAC-COATED 0.006 WT% BERBERINE-LOADED CARBOPOL TOWARDS <i>E.COLI</i> CELLS AS A FUNCTION OF BOTH THE ANTIMICROBIAL ACTIVITY OF FREE AND CARBOPOL-ENCAPSULATED BERBERINE AND THE CYTOTOXIC EFFECT OF UNCOATED AND PDAC-COATED PARTICLES. THE INCUBATION WAS ALSO PERFORMED THROUGH INCUBATION EACH CONCENTRATION WITH A FIXED AMOUNT OF <i>E.COLI</i> CELLS AFTER THEIR REMOVAL FROM THE CULTURE MEDIA.	291

FIGURE 6.41: SEM IMAGES OF <i>E. COLI</i> CELLS. (A) CONTROL SAMPLE OF <i>E. COLI</i> AND (B, C, AND D) INCUBATION OF <i>E. COLI</i> CELLS WITH SOLUTION OF 0.0088 WT% PDAC COATED 0.006 WT% BERBERINE-LOADED CARBOPOL SUSPENSION.	292
FIGURE 6.42: THE VIABILITY OF MICROALGAE CELLS VERSUS SOLUTION OF SEVERAL DIFFERENT CONCENTRATIONS OF PDAC-COATED CHLORHEXIDINE LOADED CARBOPOL MICROGEL WHICH HAVE BEEN PREPARED FROM THE STOCK SOLUTION 0.0045 WT% PDAC – 0.045 WT% CHLORHEXIDINE – 0.05 WT% CARBOPOL DISPERSION.	294
FIGURE 6.43: THE COMPARISON BETWEEN THE ANTIMICROBIAL ACTIVITY OF 0.0045 WT% PDAC-0.0225 WT% CHLORHEXIDINE-CARBOPOL MICROGEL, THE CARBOPOL-ENCAPSULATED CHLORHEXIDINE (0.0225 WT%), 0.025 WT% CHLORHEXIDINE AND THE CYTOTOXIC EFFECT OF FREE 0.0045 WT% PDAC AND 0.0045 WT% PDAC-COATED CARBOPOL AQUA SF1 AGAINST THE CONTROL SAMPLE OF ALGAL CELLS.	295
FIGURE 6.44: SEM IMAGES OF <i>C. REINHARDTII</i> CELLS. (A) CONTROL SAMPLE AND (B, C, D, AND E) SAMPLES AFTER INCUBATION IN A SUSPENSION OF 0.0045 WT% PDAC-0.0225 WT% CHLORHEXIDINE-CARBOPOL AQUA SF1 COMPLEX SUSPENSION WITH <i>C. REINHARDTII</i> CELLS FOR ONE HOUR.	296
FIGURE 6.45: THE VIABILITY OF YEAST CELLS VERSUS SUSPENSIONS OF SEVERAL CONCENTRATIONS OF PDAC-COATED CHLORHEXIDINE-LOADED CARBOPOL PREPARED FROM A STOCK SOLUTION 0.0045 WT% PDAC – COATED PARTICLES OF 0.045 WT% CHLORHEXIDINE – LOADED IN 0.05 WT. % CARBOPOL AQUA SF1 MICROGEL.	298
FIGURE 6.46: THE COMPARISON BETWEEN THE ANTIMICROBIAL ACTIVITY AGAINST YEAST OF 0.009 WT% PDAC-0.045 WT% CHLORHEXIDINE-CARBOPOL MICROGEL PARTICLES, THE CARBOPOL-ENCAPSULATED CHLORHEXIDINE (OF OVERALL CONCENTRATION 0.045 WT. %), 0.05 WT% CHLORHEXIDINE AND THE CYTOTOXIC EFFECT OF FREE 0.009 WT. % PDAC AND 0.009 WT. % PDAC-COATED CARBOPOL AGAINST THE CONTROL SAMPLE.....	299
FIGURE 6.47: SEM IMAGES OF YEAST CELLS: (A) CONTROL SAMPLE OF YEAST CELL AND (B, C, D, AND E) REPRESENT THE RESULT OF THE INCUBATION OF YEAST CELLS IN SUSPENSION AND 0.009 WT% PDAC-0.045 WT% CHLORHEXIDINE-LOADED CARBOPOL MICROGEL PARTICLES AFTER 2 HOURS.....	300
FIGURE 6.48: THE RELATIVE LUMINESCENCE INTENSITY OF <i>E. COLI</i> INCUBATED WITH SUSPENSIONS OF VARIOUS CONCENTRATIONS OF PDAC-COATED CHLORHEXIDINE-LOADED CARBOPOL FOR UP TO TWO HOURS OF INCUBATION. THE DILUTED CONCENTRATIONS WERE PREPARED FROM THE STOCK SOLUTION (0.011 WT% PDAC-COATED 0.0075 WT% CHLORHEXIDINE-LOADED 0.05 WT% CARBOPOL. THE INCUBATION WAS CONDUCTED THROUGH INCUBATION EACH CONCENTRATION WITH A FIXED AMOUNT OF CULTURE MEDIA FREE <i>E. COLI</i> CELLS.	301
FIGURE 6.49: THE ANTIMICROBIAL ACTIVITY OF 0.0055 WT% PDAC-COATED 0.0225 WT% CHLORHEXIDINE-LOADED CARBOPOL MICROGEL TOWARDS <i>E. COLI</i> AS A FUNCTION OF THE ANTIMICROBIAL ACTIVITY OF THE FREE AND CARBOPOL-ENCAPSULATED CHLORHEXIDINE. WE ALSO COMPARE WITH CYTOTOXIC EFFECT OF UNCOATED AND COATED CHX.	303
6.50: SEM IMAGES OF <i>E. COLI</i> CELLS. (A) CONTROL SAMPLE OF <i>E. COLI</i> AND (B, C, D, E, AND F) REPRESENT THE INCUBATION OF <i>E. COLI</i> CELLS WITH A SUSPENSION OF 0.0055 WT% PDAC COATED 0.0225 WT% CHLORHEXIDINE-LOADED CARBOPOL FOR 2 HOURS AT ROOM TEMPERATURE. THE CELLS WERE PRE-TREATED WITH THE PROCEDURE DESCRIBED IN SECTION 2.2.8.	304
FIGURE 6.51: THE SCHEMATIC OF THE ELECTROSTATIC INTERACTION BETWEEN PDAC-COATED CHLORHEXIDINE-LOADED CARBOPOL MICROGEL PARTICLES AND THE OUTER CELL MEMBRANE OF <i>E. COLI</i> CELLS IN WHICH THE CHLORHEXIDINE MOLECULES ARE DELIVERED LOCALLY AT HIGH CONCENTRATIONS ON THE CELL MEMBRANE OF <i>E. COLI</i> CELLS.	305
FIGURE 7.1: A) SCHEMATIC OF A MICROFLUIDIC CHIP; B) PHOTOGRAPHIC IMAGE OF THE MICROFLUIDIC CHIP-CELL BASED ASSAY FOR TRAPPING CELLS INTO A MICRO CHAMBER.....	308
FIGURE 7.2: THE SCHEMATIC FOR THE IONIC BONDING BETWEEN POLY-L-LYSINE AND BOTH OF GLASS CHIP AND CELL.	309

- FIGURE 7.3: (A) A SCHEMATIC FLOWGRAM OF THE MICROFLUIDICS GLASS CHIP WHERE THE MICRO CHAMBER IS EXAMINED UNDER MICROSCOPE. (B) THE EXPERIMENTAL SETUP OF ALGAL CELLS TRAPPING ON THE MICRO CHAMBER OF THE MICROCHIP DEVICE USING POLY-L-LYSINE.....310
- FIGURE 7.4: BRIGHT FIELD MICROSCOPIC IMAGES OF ALGAL CELLS TRAPPED IN THE MICRO CHAMBER OF THE MICROFLUIDIC CHIP USING POLY-L-LYSINE AS AN ADHESANT AGENT. (A) TRAPPED CELLS IN THE OUTLET OF THE MICRO CHAMBER, (B) TRAPPED CELLS IN THE CENTRE OF THE MICRO CHAMBER, (C) TRAPPED CELLS IN THE INLET OF THE MICRO CHAMBER, (D) ON-CHIP TRAPPED CELLS AT 10X MAGNIFICATION, (E) ON-CHIP TRAPPED CELLS AT 20X MAGNIFICATION, AND (F) ON-CHIP TRAPPED CELLS AT 50X MAGNIFICATION.311
- FIGURE 7.5: THE VIABILITY OF ON-CHIP TRAPPED CELLS USING CHEMICAL ADHESION THROUGH THE INTERACTION BETWEEN CELLS AND GLASS CHIP ADHERED POLY-L-LYSINE. THE VIABILITY WAS MEASURED BY INCUBATING CELLS WITH FDA SOLUTION FOR 10 MINUTES. WHITE ARROWS REFER TO THE DETACHMENT OF CELLS FROM THE SURFACE OF THE MICROCHAMBER DUE TO THE WEAK INTERACTION WHERE THE EFFECT OF FLOW RATE IS DOMINANT CAUSING SHEAR STRESS ON THE INTERACTION BETWEEN ADHERED CELLS AND THE SURFACE.313
- FIGURE 7.6: THE SCHEMATIC DIAGRAM OF MICROFLUIDIC CELL TRAPPING BY GATE KEEPERS (MAGNETIC MICROBEADS) WHICH ARE USED FOR INVESTIGATING THE CYTOTOXIC EFFECT OF NANOPARTICLES OR ANTIMICROBIAL ASSAY UPON INCUBATION WITH CELLS INTO THE MICRO CHAMBER FOR PERIODS OF INCUBATION TIME. (A) PLACING MAGNETIC BEADS INTO MICRO CHAMBER. (B) ATTRACTION OF MAGNETIC BEADS BY MAGNET (C) PASSING AND TRAPPING THE CELLS INTO MICRO CHAMBER (D) FLUSHING OUT CELLS UPON MOVING THE MAGNET TO THE SIDE.....315
- FIGURE 7.7: THE MICROFLUIDIC CHIP DESIGN WHICH GENERATES CONCENTRATION GRADIENTS BY PUMPING STOCK SOLUTION OF A REAGENT FROM INLET 1 AND WATER FROM INLET 2 WITH DILUTION OCCURRING IN THE BRANCHED CHANNELS. THIS DESIGN WAS FABRICATED AS MENTIONED IN CHAPTER 2, SECTION OF CHIP FABRICATION316
- FIGURE 7.8: THE MICROFLUIDIC CHIP FOR HIGH THROUGHPUT MICRO SCREENING CELL BASED ASSAY. (A) THE WHOLE MICROFLUIDICS CHIP WITH CONCENTRATION GRADIENT GENERATOR. (B) THE BRANCHED POINT FOR CONCENTRATION GRADIENT GENERATOR (CGG), (C) THE MICRO CHAMBERS FOR TRAPPING CELLS AND (D) THE CROSS CHANNELS BETWEEN CONCENTRATION GRADIENT GENERATOR (CGG) AND THE MICRO CHAMBERS.317
- FIGURE 7.9: THE PHOTOGRAPHIC PROFILE OF BLACK PRECIPITATE OF MAGNETIC NANOPARTICLES DISPERSED IN MILLI Q WATER (A) AND PARTICLES ATTRACTED BY MAGNET (B). THE MAGNETIC PARTICLES WERE PREPARED BY MIXING FERROUS AND FERRIC IONS AND AMMONIA SOLUTION WAS ADDED DROP WISE TO FORM IRON OXIDE NANOPARTICLES.....318
- FIGURE 7.10: THE AVERAGE PARTICLE DIAMETER (A) AND ZETA POTENTIAL (B) OF MAGNETIC IRON OXIDE NANOPARTICLES PREPARED FROM MIXING FERRIC AND FERROUS SOLUTIONS IN THE BASIC MEDIUM.319
- FIGURE 7.11 : THE ZETA POTENTIAL OF PAH COATED MAGNETIC IRON OXIDE NANOPARTICLES WHICH WERE ACHIEVED THROUGH A SPECIFIC AMOUNT OF IRON OXIDE NANOPARTICLES SOLUTION WITH EXCESS AMOUNT OF CATIONIC POLYELECTROLYTE. THE EXCESS AMOUNT OF POLYELECTROLYTES WAS REMOVED FROM THE SOLUTION BY SEPARATION WITH MAGNET.320
- FIGURE 7.12: THE SCHEMATIC DIAGRAM FOR THE FUNCTIONALIZATION OF GLASS BEADS WITH MAGNETIC NANOPARTICLES IN WHICH THE FUNCTIONALIZATION WAS ACHIEVED USING CATION AND ANIONIC POLYELECTROLYTE SUCH AS POLY (ALLYLAMINE HYDROCHLORIDE) AND POLY(STYRENE-4-SOLFONATE SODIUM).321
- FIGURE 7.13: BRIGHT FIELD IMAGES OF MAGNETIC NANOPARTICLES COATED GLASS BEADS WHEREBY (A) REPRESENTS MAGNETIC GLASS BEADS WITHOUT ANY EXTERNAL OPERATOR AND (B) DENOTES TO THE MAGNETIC GLASS BEADS UNDER THE CONTROL OF MAGNET322
- FIGURE 7.14: SCHEMATIC DIAGRAM FOR THE MAGNETIZATION OF YEAST CELLS USING MAGNETIC NANOPARTICLES THAT PREVIOUSLY COATED WITH CATIONIC POLYELECTROLYTE (PAH) TO FORM PAH COATED Fe_3O_4 NANOPARTICLES WITH STIRRING FOR 20 MINUTES. THE MAGNETIC NANOPARTICLES WERE

PREPARED FROM PRECIPITATION OF FERROUS AND FERRIC IONS IN THE BASIC MEDIUM OF AMMONIA SOLUTION, THEN HEATED UP TO 80°C FOR AN HOUR TO GET SUPERPARAMAGNETIC NANOPARTICLES WHICH THEN SEPARATED BY APPROACHING NEODYMIUM MAGNET.....	324
FIGURE 7.15: THE BRIGHT FIELD MICROSCOPIC IMAGES OF (A) NORMAL YEAST CELLS AND (B) YEAST CELLS THAT MAGNETIZED USING POLY (ALLYLAMINE HYDROCHLORIDE) COATED MAGNETIC NANOPARTICLES WHICH IN TURN FUNCTIONALIZED YEAST CELLS TO FORM MAGNETIC YEAST CELLS.....	325
FIGURE 7.16: (A) EXPERIMENTAL SETUP OF TRAPPING MAGNETIZED YEAST CELLS INTO THE MICRO CHAMBERS OF THE MICRO DEVICE USING NEODYMIUM MAGNETIC ON TOP OF THE MICRO CHAMBERS. THIS EXPERIMENT WAS ACHIEVED BY PUMPING THE CELLS USING SYRINGE PUMP FROM INLET 1 AND INLET 2 AT FLOW RATE 25 $\mu\text{L}\cdot\text{MIN}^{-1}$ AND TRAPPING CELLS IN THE MICRO CHAMBERS FOLLOWING THAT FLUSHING OUT TRAPPED CELLS TO THE OUTLET UPON REMOVAL THE MAGNET FROM THE CHIP, (B) A BRIGHT FIELD MICROSCOPIC IMAGE OF THE MICRO CHAMBERS BEFORE THE TRAPPING PROCESS, AND (C) A MICROSCOPIC IMAGE OF TRAPPED CELLS INTO THE MICRO CHAMBERS OF THE CHIP AFTER TRAPPING UPON PLACING THE MAGNET OF THE TOP OF THE CHAMBERS.....	326
FIGURE 7.17: THE SCHEMATIC OF SYNTHESIS OF PDMS STABILIZED OLEIC ACID COATED MAGNETIC NANOPARTICLES WHICH WERE SYNTHESIZED USING OLEIC ACID COATED MAGNETIC NANOPARTICLES AND THEN DISPERSED IN LOW DENSITY SILICONE OIL AND MIXED WITH PDMS TO FORM HYDROPHOBIC MAGNETIC NANOPARTICLES.	328
FIGURE 7.18: (A) SCHEME OF THE SYNTHESIS OF SOLIDIFIED MAGNETIC PDMS MICRO BEADS IN A PLASTIC PETRI DISH IN WHICH THE UPPER LAYER INCLUDES 1 WT. % OF BOTH XANTHAN GUM AND SODIUM DODECYL SULPHATE (SDS) AND THE LOWER LAYER IS SOLIDIFIED AGAR. (B) PHOTOGRAPHIC IMAGE OF POLYMERISED MAGNETIC PDMS MICRO BEADS ON THE TOP LAYER OF PETRI DISH.	329
FIGURE 7.19: THE BRIGHT FIELD MICROSCOPIC IMAGES OF SOLIDIFIED MAGNETIC PDMS MICRO BEADS WHICH WERE PREPARED FROM GENERATION OF DROPLET OF PDMS STABILISED OLEIC ACID COATED MAGNETIC NANOPARTICLES USING GLASS MICROSYRINGE IN THE PRESENCE OF MIXTURE OF XANTHAN GUM AND THE SURFACTANT SDS, AND THEN THESE DROPLETS WERE THERMALLY POLYMERISED TO FORM SOLIDIFIED MAGNETIC PDMS MICRO BEADS. THE SCALE BAR IS 200 μM	330
FIGURE 7.20: ON-CHIP MICROFLUIDIC INTERACTION BETWEEN MAGNETIC PDMS MICRO BEADS AND THE NEODYMIUM MAGNET. (A-C) REPRESENT THE RESPONSE OF THE MAGNETIC BEADS UPON APPROACHING THE MAGNET WHEREBY THEY SHOWED WEAK MAGNETIC RESPONSE AND (D) REPRESENTS THE HORIZONTAL FLAT SURFACE OF THE MICROFLUIDIC CHIP SHOWING PART OF THE MAGNETIC BEADS ON THE TOP OF THE CHIP.	331
FIGURE 7.21: (A) THE SCHEMATIC DIAGRAM FOR THE SYNTHESIS OF STYRENE BASED FERROFLUID WHICH WAS SYNTHESIZED FROM MIXING THE PRECURSORS FERROUS AND FERRIC IONS IN BASIC MEDIUM OF AMMONIA WHICH THEN DISPERSED IN STYRENE. (B) A PHOTOGRAPHIC IMAGE OF MICROFLUIDIC FLOW FOCUSING USED FOR THE GENERATION OF MAGNETIC MICROBEADS. (C) THE FLOW GRAM OF COMPONENTS OF CONTINUOUS AND DISPERSED PHASE IN THE FLOW FOCUSING MICROCHIP.	332
FIGURE 7.22: THE DROPLET GENERATION USING MICROFLUIDIC FLOW FOCUSING TECHNIQUE DEPENDING ON PUMPING SODIUM DODECYL SULPHATE ON BOTH SIDES OF THE INLET1 AT FLOW RATE 5 $\mu\text{L}\cdot\text{MIN}^{-1}$ AND STYRENE BASED FERROFLUID IN THE CENTRE OF THE CHIP (INLET 2) WITH FLOW RATE 1 $\mu\text{L}\cdot\text{MIN}^{-1}$ AND THE DROPLETS WERE GENERATED IN THE CROSS JUNCTION AREA TO BE COLLECTED IN A GLASS TUBE FROM THE OUTLET OF THE CHIP.....	334
FIGURE 7.23: (A) PROFILE FOR THE FLOW GRAM OF SDS AS A CONTINUOUS PHASE AND STYRENE BASED FERROFLUID IN THE MICROFLUIDIC FLOW FOCUSING TECHNIQUE FOR GENERATING DROPLET. (B) THE CHANNEL DIMENSIONS OF THE CHIP WHICH EXPLAINED THAT THE WIDTH IS 100 μM AND THE DEPTH IS μM . (C) PHOTOGRAPHIC IMAGE OF THE EXPERIMENTAL SETUP FOR THE GENERATION OF MAGNETIC DROPLETS USING MICROFLUIDIC FLOW FOCUSING.	335
FIGURE 7.24: THE EFFECT OF SURFACTANT (SDS) ON THE SIZE OF THE DROPLET GENERATED FROM MICROFLUIDIC FLOW FOCUSING TECHNIQUE. (A) 0.035 M SDS (B) 0.052 M SDS, (C) 0.07 M SDS, (D) 0.07 M SDS, (E) 0.14 M SDS AND (F) 0.17M SDS.....	336

- FIGURE 7.25: EFFECT OF FLOW RATE OF CONTINUOUS PHASE OF SODIUM DODECYL SULPHATE (SDS) ON THE SIZE OF MAGNETIZED DROPLET USING FLOW FOCUSING MICROFLUIDIC TECHNIQUE WHILE THE DISPERSED PHASE (STYRENE BASED FERROFLUID) BEING KEPT AT 0.1 $\mu\text{L}/\text{MIN}$. (A) 1 $\mu\text{L}/\text{MIN}$, (B) 2 $\mu\text{L}/\text{MIN}$, (C) 3 $\mu\text{L}/\text{MIN}$, (D) 4 $\mu\text{L}/\text{MIN}$, AND E AND F REPRESENT THE FLOW GRAM AND DROPLET GENERATED AT FLOW RATE OF SDS AT 5 $\mu\text{L}/\text{MIN}$338
- FIGURE 7.26: THE EXPERIMENTAL SETUP FOR THE THERMAL POLYMERIZATION OF GENERATED MAGNETIZED DROPLETS FROM THE SYSTEM DISPERSED PHASE (STYRENE BASED FERROFLUID) AND THE CONTINUOUS PHASE SDS SOLUTION USING MICROFLUIDIC FLOW FOCUSING TECHNIQUE AT 70°C FOR THREE HOURS. 339
- FIGURE 7.27: THE MICROFLUIDIC FLOW FOCUSING WITH SERPENTINE MIXING PART FOR THE GENERATION OF MAGNETIZED DROPLETS. (A) FLOW GRAM OF FLOW FOCUSING TECHNIQUE WITH SERPENTINE, (B) PHOTOGRAPHIC IMAGE OF THE DEVELOPED MICROCHIP FOR FLOW FOCUSING TECHNIQUE. (C) FLOW FOCUSING CROSS JUNCTION, (D) MIXING COIL 1 AND (E) SERPENTINE MIXING COIL 2.340
- FIGURE 7.28: THE DROPLET GENERATION USING FLOW FOCUSING TECHNIQUE WITH SERPENTINE MIXING PART. (A) DROPLET GENERATION IN THE CROSS JUNCTION, (B) THE GENERATED DROPLETS IN THE MIXING COIL 1, (C) THE GENERATED MAGNETIZED DROPLET BEFORE ENTERING THE SERPENTINE PART, AND (D) THE GENERATED DROPLET IN THE SERPENTINE PART AS ACTUALLY SEEN IN THE MICROSCOPE.341
- FIGURE 7.29: THE EFFECT OF HITENOL BC20 ON THE SIZE OF THE MAGNETIZED DROPLET GENERATED FROM THE SYSTEM THAT CONSISTS OF HITENOL AS A CONTINUOUS PHASE AND STYRENE BASED FERROFLUID AS A DISPERSED PHASE. (A) 1 WT. % HITENOL BC20, (B) 2 WT. % HITENOL BC20, (C) 3 WT. % HITENOL BC20, AND 4 WT. % HITENOL BC20.342
- FIGURE 7.30: THE EFFECT OF FLOW RATE OF THE DISPERSED PHASE OF STYRENE BASED FERROFLUID ON THE SIZE OF THE GENERATED MAGNETIZED MICRO BEADS AT FIXED FLOW RATE OF CONTINUOUS PHASE OF HITENOL BC20. (A) 0.1 $\mu\text{L MIN}^{-1}$, (B) 0.5 $\mu\text{L MIN}^{-1}$, 0.75 $\mu\text{L MIN}^{-1}$, AND (D) 1 $\mu\text{L MIN}^{-1}$344
- FIGURE 7.31: THE SCHEMATIC DIAGRAM FOR THE MANUAL SYNTHESIS OF MAGNETIZED MICRO BEADS USING THE PRECURSOR'S FERROUS AND FERRIC IONS IN THE BASIC MEDIUM OF AMMONIA TO FORM MAGNETIC NANOPARTICLES WHICH IN TURN FUNCTIONALIZED WITH OLIC ACID AND DISPERSED IN STYRENE TO FORM STYRENE BASED FERROFLUID. THE LATTER THEN HOMOGENIZED WITH EQUAL AMOUNT OF 2% HITENOL BC20 TO FOR OIL IN WATER EMULSION USING PIPETTE. AFTER THAT, THE EMULSION WAS ADDED TO WARMED AGAROSE AND COOLED DOWN TO ROOM TEMPERATURE, WHICH THEN HEATED UP TO 70°C FOR THREE HOURS TO POLYMERISE THE BEADS.345
- FIGURE 7.32: THE GENERATION OF MAGNETIC MICRO BEADS FROM THE EMULSIFICATION OF THE SYSTEM HITENOL BC20 AS A CONTINUOUS PHASE AND STYRENE BASED FERROFLUID AS A DISPERSED PHASE AND THERMALLY POLYMERISED USING THERMAL INITIATOR. (A) THE PREPARED OIL IN WATER MAGNETIZED DROPLETS, (B) THE PARALLEL CHAINS OF MAGNETIZED MICRO BEADS BEFORE THERMAL POLYMERIZATION AND (C AND D) THE FABRICATED MAGNETIC MICRO BEADS AFTER THERMAL POLYMERIZATION.346
- FIGURE 7.33: THE PDMS/GLASS MICROFLUIDIC CELL BASED ASSAY FOR TRAPPING CELLS USING MAGNETIC MICRO BEADS AS GATE KEEPERS INTO THE MICRO CHAMBER OF THE MICROCHIP. (A) MICROFLUIDICS CHIP CELL TRAPPING WITH 100 μM IN DEPTH, (B) MICROFLUIDICS CHIP CELL TRAPPING WITH 150 μM IN DEPTH, (C) MICROFLUIDICS GLASS CHIP CELL TRAPPING WITH 100 μM IN DEPTH AS A LOWER PLATE BONDED WITH PDMS USING CHIP HOLDER WHERE ALL TUBING HOLES WERE ACHIEVED BY PUNCH DEVICE AND THE TUBING WAS 1.6 MM PTFE. (D) PDMS/GLASS MICROFLUIDIC CHIP BONDED WITH CHIP HOLDER AND MAGNETIC MICRO BEADS ARE IN THE MICRO CHAMBER OF THE CHIP347
- FIGURE 7.34: MICROFLUIDICS CHIP DESIGN THAT MADE OF PMMA POLYMER FROM A CAD FILE DESIGNED BY COMPUTER SOFTWARE THAT CONSTRUCTED BY CNC MACHINE TO FORM THREE DIMENSION MICRO CHANNELS. (A) THE CAD FILE OF THE CHIP DESIGN. (B) THE MASTER DESIGN MADE OF PMMA POLYMER BY CNC MACHINE. (C) THE MASTER DESIGN PLACED IN RECTANGULAR BLOCK WHICH CAN BE USED FOR MAKING REPLICA THAT MADE OF PDMS (D) THE MICRO CHAMBER OF THE MASTER PMMA DESIGN. (E) THE MICRO CHANNELS OF THE MASTER PMMA POLYMER DESIGN.349

FIGURE 7.35: GLASS/PDMS MICROFLUIDICS CELL TRAPPING CHIP. (A) THE MICROFLUIDICS CHIP WHICH CONSISTS OF PDMS PLATE WITH MICRO CHANNELS AND GLASS PLATE WITH HOLES. (B) OXYGEN PLASMA BONDED GLASS/PDMS MICROFLUIDICS CHIP.351

FIGURE 7.36: GLASS / PDMS MICROFLUIDIC CHIP FOR CELL BASED ASSAY WHICH WAS CONDUCTED THROUGH BONDING GLASS TO PDMS USING PLASMA CLEANER AND MAGNETIC BEADS PLACED INSIDE THE MICRO CHAMBER. (A) GLASS/PDMS MICROFLUIDICS CHIP WITH MAGNETIC BEADS ATTRACTED BY NEODYMIUM MAGNET. (B) THE EXPERIMENTAL SETUP OF THE MICROFLUIDIC GLASS BEADS TRAPPING INTO THE MICRO CHAMBERS. (C) PHOTOGRAPHIC IMAGE OF THE SIDE OF THE GLASS/PDMS MICROCHIP WITH THE MAGNET ON TOP. (D) PHOTOGRAPHIC IMAGE OF THE TOP OF GLASS/PDMS MICROCHIP WITH THE MAGNET ON TOP OF THE GLASS PLATE TRAPPING MAGNETIC BEADS INSIDE THE MICRO CHAMBER.352

FIGURE 7.37: BRIGHT FIELD MICROSCOPIC IMAGES OF THE MICRO CHAMBER OF GLASS / PDMS MICROFLUIDIC CHIP WHERE MAGNETIC BEADS ARE INSIDE THE MICRO CHAMBER AND ATTRACTED BY NEODYMIUM MAGNET UPON APPROACHING THE MAGNET FROM THE MICRO BEADS. (A) MAGNETIC BEADS UPON APPROACHING THE MAGNET FROM THE UPPER SIDE OF THE CHIP. (B) MAGNETIC BEADS UPON APPROACHING THE MAGNET FROM THE DOWN SIDE OF THE CHIP. (C) MAGNETIC BEADS UPON APPROACHING THE MAGNET FROM THE RIGHT HAND SIDE OF THE CHIP. (D) MAGNETIC BEADS UPON APPROACHING THE MAGNET FROM THE LEFT HAND SIDE OF THE CHIP.353

List of Tables

TABLE 2.1: CHEMICALS FOR THE SYNTHESIS AND CHARACTERIZATION OF NANOMATERIALS	94
TABLE 2.2: PREPARATION PROTOCOL OF CULTURE MEDIA O FOR GROWING <i>C. REINHARDTII</i> . ^{5,6}	99
TABLE 2.3: GENERAL EQUIPMENT.....	102
TABLE 3.1: THE EFFECT OF THE ANNEALING TEMPERATURE DURING THE TiO ₂ NPS SYNTHESIS ON THE CRYSTALLITE DOMAIN SIZE AND THE BET SURFACE AREA OF TITANIA. THE HYDRODYNAMIC DIAMETERS AND ZETA POTENTIAL OF THE TiO ₂ NPS AFTER DISPERSING EACH SAMPLE IN MILLI-Q WATER AT PH 4 BY SONICATION AT THE SAME CONDITIONS ARE ALSO REPORTED.	135
TABLE 4.1: THE ELEMENTARY ANALYSIS OF CARBOPOL AND BERBERINE LOADED CARBOPOL AFTER CENTRIFUGATION AND DRYING OF ONLY CARBOPOL AND BERBERINE-LOADED INTO CARBOPOL.	205
TABLE 4.2: THE ENCAPSULATION EFFICIENCY AND THE PERCENTAGE OF BERBERINE LOADING CONTENT OF 0.15 WT. % BERBERINE (BRB) INTO 0.1 WT. % OF CARBOPOL MICROGEL.....	206
TABLE 4.3: THE ELEMENTARY ANALYSIS OF CARBOPOL AQUA SF1 AND THE ENCAPSULATED CHLORHEXIDINE (CHX) INTO CARBOPOL AQUA SF1 MICROGEL THROUGH CENTRIFUGING AND DRYING THE EACH SAMPLE IN AIR AT ROOM TEMPERATURE.	225
TABLE 4.4: THE ENCAPSULATION EFFICIENCY AND CHLORHEXIDINE LOADING CONTENT FOR THE ENCAPSULATION OF 0.1 WT% CHLORHEXIDINE IN 0.1 WT% CARBOPOL AQUA SF1.	226

Abbreviations

NPs	Nanoparticles
NMs	Nanomaterials
CMC	Critical Micelle Concentration
ROS	Reactive Oxygen Species
QDs	Quantum Dots
VB	Valence Band
CB	Conduction Band
XRD	X-Ray Diffraction
DLS	Dynamic Light Scattering
UV	Ultraviolet
DNA	Deoxyribonucleic Acid
TAP	Tris-Acetate-Phosphate
EDTA	Ethylenediaminetetraacetic Acid
Tris	Tris(hydroxymethyl)-aminomethane
PAH	Poly(allylamine hydrochloride)
PSS	Poly(sodium-4-styrenesulfonate)
PDAC	Poly(diallyldimethylammonium chloride)
PEI	Polyethyleneimine
LBL	Layer By Layer
BLC	Berberine Loaded Carbopol
CLC	Chlorhexidine Loaded Carbopol

1 Chapter One: Introduction and Literature Review

1.1 Nanomaterials

Nanotechnology can be defined as the science which deals with nanoscale objects. Such objects are described as materials with at least one dimension less than approximately 100 nanometer in range ($1\text{nm}=10^{-9}\text{m}$).^{1,2} These might be materials with one dimension such as nanofilms, two dimensions like nanowires and nanotubes, or three dimension for example nanoparticles.² The chemical and physical properties of nanomaterials (NMs) are considerably different from those of atoms, molecules, and bulk materials.¹ Nanoparticles can be amorphous or crystalline structure but differ from the ordinary solid state of matter because of their large surface area, quantum size effects and high chemical activity. They can be used as a carrier for liquid droplets or gases³ and have many applications in different areas of life for example, in medicine for diagnosis and therapy, in environmental remediation as biosensors and agents, in production and storage of energy, catalysis and agriculture.⁴ There are many types of nanomaterials as shown in Figure 1.1

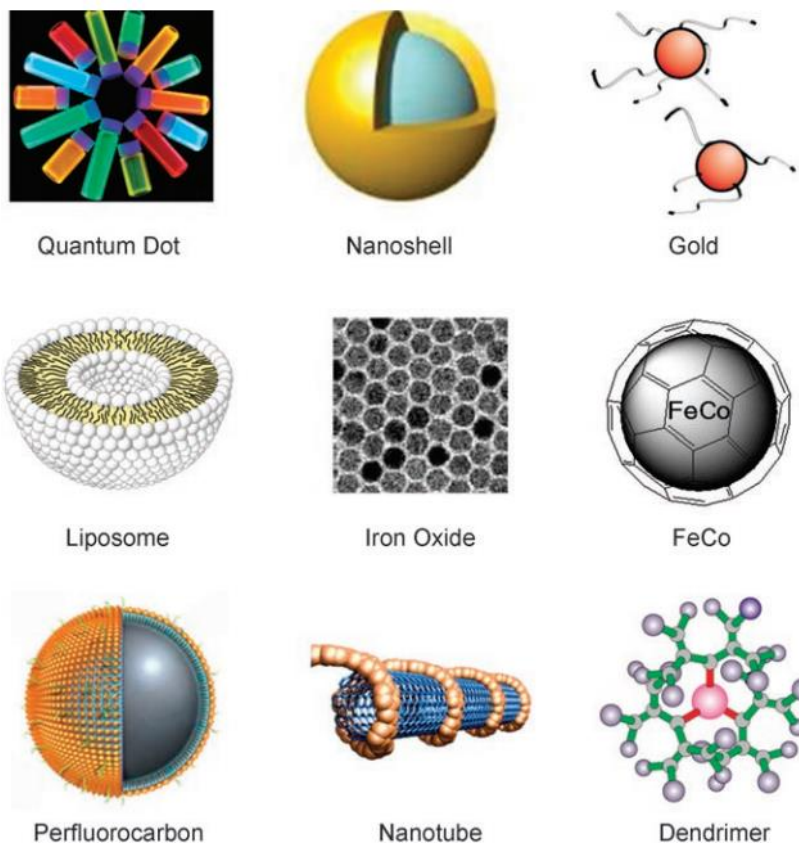


Figure 1.1: Examples of nanocarriers for drug delivery and biomedical imaging.⁵

Liposomes are tiny synthetic vesicles of spherical shape consisting of a lipid shell surrounding a core containing a therapeutic molecule or gene which are biocompatible and nontoxic. To allow clinical use they are produced from the natural nontoxic phospholipids and cholesterol.⁶ They are mainly valuable as gene therapy devices because of their capability to pass through lipid bilayers and cell membranes.^{7, 8} for example Zhang *et al.* showed the use of liposomes as a targeted therapy for the human insulin receptor through PEGylated (treated with polyethylene glycol) liposomes linked to a monoclonal antibody.⁹

Polymeric micelles can be used as an alternative to liposomes. They are synthesized from copolymers which consist of both hydrophilic and hydrophobic monomer units. The synthesis process occurs through spontaneous assembly when the concentrations of the copolymers are above critical micelle concentration (CMC). They are nanosize their surface chemistry is easily manipulated, they have core functionalities, and are easy to produce. This makes them suitable as vehicles for encapsulation, and delivery of water insoluble agents.¹⁰ The micelles have a solid-like inner core, which helps as a powerful nanocontainer of hydrophobic compounds for solubilization of chemotherapeutics, such as docetaxel (DOC).¹¹

Dendrimers are artificial macromolecules with tree-like structures in which the atoms are put together in many branches and subbranches radiating out from a central core.¹² Unique interfacial and functional properties are offered by these highly branched architectures because of their empty internal cavities and surface functional groups.¹³ For example, Choi *et al.* have prepared generation 5 polyamidoamine (G5 PAMAM) dendrimers conjugated to fluorescein and folic acid. They in turn were linked together using complementary DNA oligonucleotides to produce clustered nanoparticles for targeting cancer cells. *In vitro* studies indicated a specific binding taking place between the DNA-linked dendrimer clusters and KB cells demonstrating that they could be used as imaging agents and therapeutics for cancer therapy.¹⁴

Carbon nanotubes are cylinders of graphite sheets with a particle diameter in the order of nanometers.¹⁵ They can be divided into two general groups according to their structure: single-walled carbon nanotubes (SWCNTs) with a single cylindrical carbon wall and multiwalled carbon nanotubes (MWCNTs) with multiple walls—cylinders nested

within other cylinders.¹⁶ They can be functionalized to be taken up by cancerous cells through tumor-specific ligands and antibody, like folic acid and monoclonal antibody.¹⁷

Inorganic nanoparticles can be defined as either metallic in composition or particles of metal oxide having at least one dimension in the nanometer range. These nanostructures reveal significantly novel and distinct chemical, physical, and biological properties, and functionality due to their nanosize.^{1, 18} Gold nanoparticles for example can be readily functionalized with probe molecules such as antibodies, enzymes, nucleotides, etc. These active elements are crucial in biosensor assays, drug and gene delivery systems, laser confocal microscopy diagnostic tools, and other biomaterial-based imaging systems.¹⁹ Song *et al.* reported that amine groups functionalized mesoporous silica SBA-15 materials act as drug matrixes. Ibuprofen (IBU) and bovine serum albumin (BSA) were loaded onto the unmodified and functionalized SBA-15. The % drug release of ibuprofen from the functionalized SBA-15 particles was found to be effectively controlled as compared to that from pure SBA-15 suggesting that functional groups are needed on the surface of SBA-15 for well controlled drug delivery.²⁰ Although inorganic nanoparticles are attracting great attention in the field of nanomedicine, their effects such as long-term tissue damage, toxicity, immunogenicity, carcinogenesis, and inflammation need to be studied.²¹

Polymeric nanoparticles (NPs) are composed of biodegradable or biostable polymers and copolymers with less than 1000 nm in size. The drug molecules can be encapsulated within the particle, physically adsorbed on the surface, or chemically associated to the surface of the particle.²²⁻²⁴ Poly(D,L-Lactic-co-Glycolic Acid) (PLGA) and Poly(D,L-Lactic Acid) (PLA) polymers nanoparticles are being explored as a nonviral gene delivery system because of their sustained-release features, biocompatibility, biodegradability, and ability to protect DNA from degradation in endolysosomes.²⁵ PLGA formulated nanoparticles demonstrated superior gene transfection than those formulated using PLA polymer in breast cancer (MCF-7) and prostate cancer cell lines (PC-3), due to the higher DNA release compared to PLA nanoparticles.²⁶

The work described in this thesis focuses on using inorganic nanoparticles as a toxic material and organic based microgel as a drug delivery nanocarrier in terms of properties, stimuli responsive, drug loading and release and targeting.

1.2 Occurrence of Nanoparticles (NPs)

Nanoparticles have been in existence from the beginning of earth's history. For instance, nanoparticles have been found in glacial ice cores 10,000 years old.²⁷ Natural materials have therefore definitely existed in the environment at nanoscale, for example as colloids in freshwater (colloids particle dimensions vary between 1 nm and 10 μm),²⁸ as atmospheric volcanic dusts and ashes²⁹ and as particles with a nm scale from soil erosion.³⁰ There are many mechanisms for creating naturally occurring nanoparticles which can be either geological or biological. Geological mechanisms depend on weathering, authigenesis / neoformation (in soils), and volcanic activity. These geological paths produce inorganic NPs whereas, biological mechanism usually manufacture organic nanomolecules, in spite of the fact that some organisms have the ability to create mineral grains in cells.³¹ It could be debated that as nanoparticles have been in the environment, living organisms should have adapted to their presence.³² Anthropogenic activity has however generated nanoscale contaminants such as air-borne particles from car exhaust gases³³ and from the erosion of car tyres.³⁴

Engineered nanoparticles (manufactured nanoparticles) appear in many forms which include nanoclusters (1-10 nm), nanopowders (less than 100 nm) and nanocrystals (less than 100 nm). These nanoparticles (and natural NPs) usually show novel chemical and physical properties that are substantially different from the bulk materials of the same component because of their small particle sizes and large surface area.³⁵ These properties make them very enticing for economic and health development; therefore, they can be found in cosmetics, clothes, electronics, biomedicine, aerospace and computer industry.³⁶ These nanoparticles can, however, have toxic effects on the environment for example, carbon fullerene NPs (C60 particles),³⁵ titanium dioxide NPs and Zinc Oxide NPs³⁷. Figure 1.2 shows some typical structures of nanoparticles.

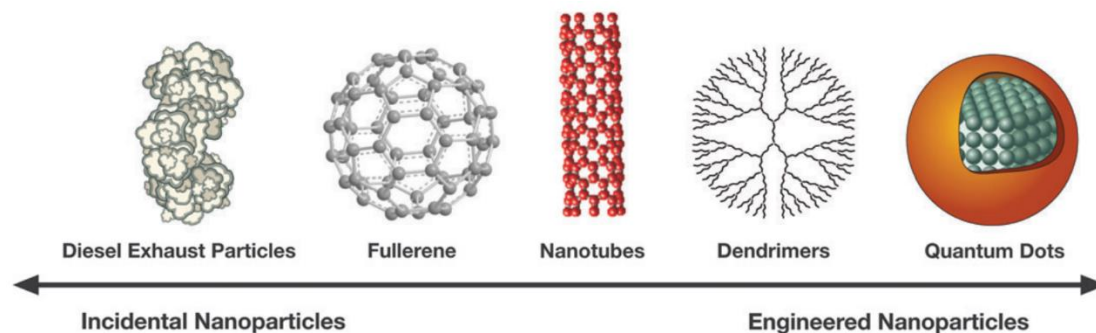


Figure 1.2: Structures of some natural and manufactured nanoparticles.³⁸

1.3 Physicochemical Properties of Nanomaterials

The physical and chemical properties of nano-sized particles are completely different from bulk materials of the same chemical component, due to their large surface area, tiny sizes and reactivity, leading to potential toxic effects.¹⁸ For instance for reasons discussed later, copper oxide (CuO) nanoparticles are 50-fold more toxic than bulk CuO particles towards crustaceans,³⁷ algae,³⁹ protozoa⁴⁰ and yeast.⁴¹ On the other hand, TiO₂ and Al₂O₃ NPs are approximately twice as toxic as their bulk preparations towards nematodes.⁴² Likewise, the activity of nanoparticles changes as the shape of the particles changes, leading to variation in their toxicity. Silver nanoparticles for example, have been shown antibacterial effect depending on their shape.⁴³

The chemical composition of the particle surface has significant effects on nanoparticles. Most metal nanoparticles have toxic effects by increasing the level of reactive oxygen species in free cell system due to the photocatalytic effect of the metal nanoparticles. It is expected that the surface modification of nanoparticles can reduce their toxicity by surface coating.^{44, 45} Free radicals produced by many toxic nanoparticles *in vivo*, may cause an oxidative stress, which leads to inflammation, cell destruction, and genotoxicity.⁴⁶ Furthermore, the surface charge of the nanoparticle dispersions plays an dramatic role in the effective toxicity because the hydrodynamic diameter of the nanoparticles changes with the change in the ionic strength and the pH according to DLVO theory which is responsible on the stability of colloidal system.⁴⁷ For example, the toxic effect of iron oxide nanoparticles on microorganisms (Baker's yeast and *E.Coli*) has been shown to change with pH. At pH 4 the viability rate of *E.Coli* was 1% while there was a

less pronounced effects on *S. Cerevisiae* because of the different electrostatic interaction between these microorganisms and the iron oxide nanoparticles. At pH 10, *S. Cerevisiae* had 20% survival rate, however for *E.Coli* nearly 99% of the cells survived suggesting that there is a stronger repulsion between *E.Coli* and the nanoparticles which means that there is no adsorption of NPs.⁴⁸ Nanoparticles of small grain size might be able to migrate easily between biological compartments, causing harmful effect on living organisms.⁴⁷

Titanium dioxide (titania) is widely used for pigmentary purposes, with 70% of its production capacity used in paints, plastics, inks, foods, and toothpastes. Nano-grade titania can be used in cosmetics and skin care products, such as sunscreens to block UV light, as well as in catalysts. There are three crystalline phases of TiO₂: anatase, rutile and brookite with the anatase phase having a higher photocatalytic activity than rutile and brookite.⁴⁹ Titania nanoparticles are commonly found in aggregate form⁵⁰ and the aggregation, size and shape of TiO₂ nanoparticle,⁵¹ are important parameters in understanding prospective cytotoxicity.⁵⁰

Dunford *et al.*, (1997) have reported that nanosized (20–50 nm) TiO₂ has been commonly accepted to be a safe sunscreen as it is able to reflect and scatter ultraviolet UVB and UVA in sunlight but TiO₂ absorption of incident UV light is about 70%; therefore, in aqueous environments this is going to lead to the formation of hydroxyl radicals. The crystalline TiO₂ forms, *anatase* and *rutile*, are semiconductors with gap energies of about 3.23 and 3.06 eV, respectively. Figure 1.3 portrays the valance and conduction bandgap of titanium dioxide. Light at or under these wavelengths holds enough energy to stimulate electrons from the valence band (VB) to the conduction band (CB), producing single electrons (e⁻) and positively charged holes (h⁺) as carriers. Electrons and holes often recombine rapidly whereas they can also transfer to the particle surface, where they react with adsorbed species: (i) electrons react with oxygen and (ii) holes with hydroxyl ions or water to form superoxide and hydroxyl radicals.⁵²

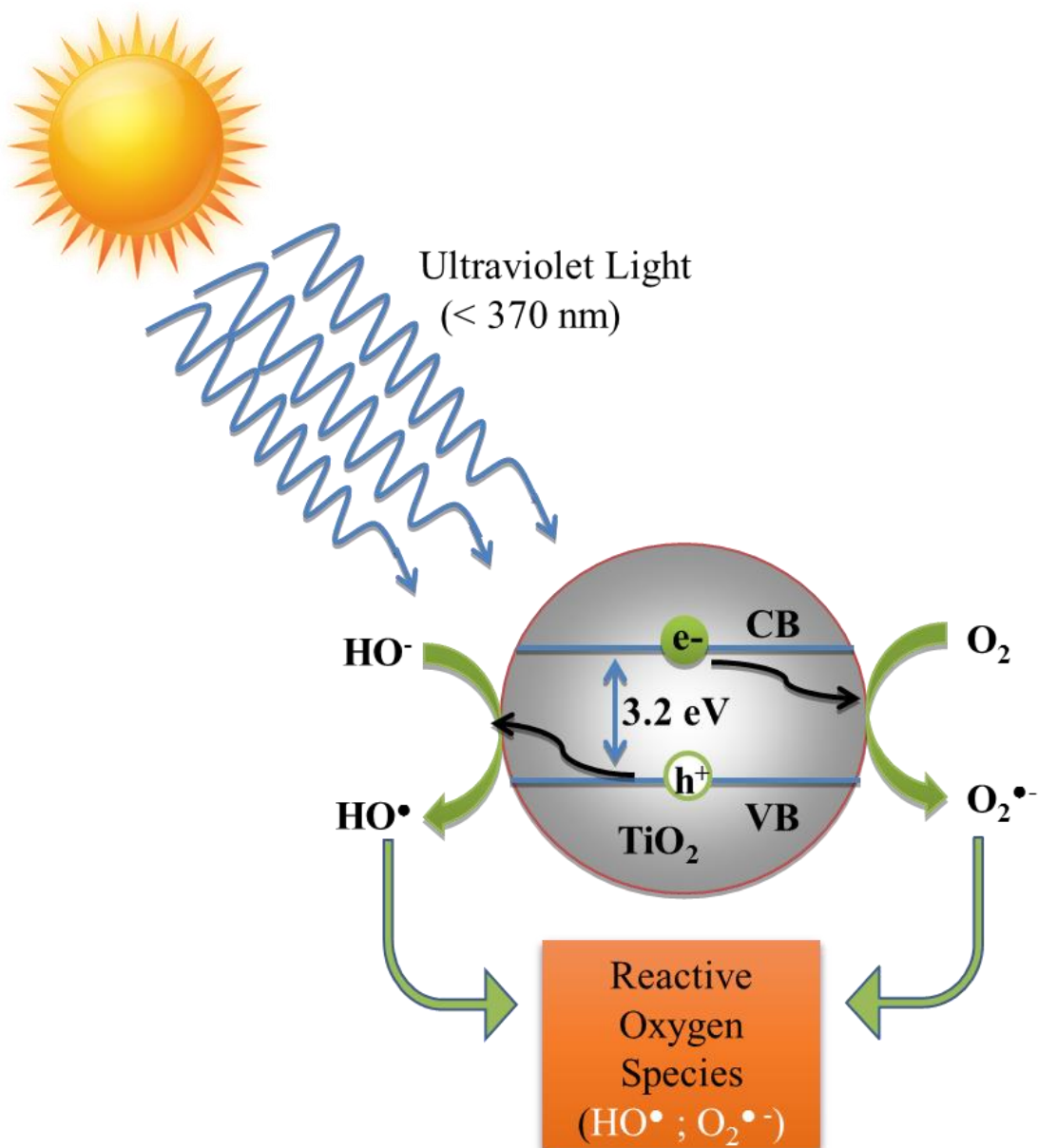


Figure 1.3: Simplified TiO₂ bandgap structure and schematic formation of free radical compounds.

TiO₂ is widely employed as a photocatalyst which can be only excited by ultraviolet light which is 3% - 5% of solar radiation. It is however possible to extend the optical response of TiO₂ to the visible light region by modifying the TiO₂. Noble metal deposition, for example silver or gold, has been used which enable metal photosensitization of titania by electron injection into the conduction band, where the diffusion of the electron in the conduction band is usually faster while hole-migration takes place typically by charge

jumping from neighbour sites. Those electron and holes that are not instantly destroyed can migrate to the surface of the particle and there, they are available for reaction with chemical species such as hydroxide, oxygen and water.^{53, 54}

Agglomeration and aggregation of nanoparticles have a significant impact on sample preparation for toxicological studies. Warheit *et al.* (2004) have shown that utilizing unstable and agglomerated nanoparticle dispersions in an *in vitro* or *in vivo* experiment lead to inaccurate assessment of nanoparticle toxicity.⁵⁵ Therefore, it is vital to know whether these particles are in an agglomerated (weak attraction between primary particles) or aggregated (strong attraction between primary particles) state, as this implies different toxicological effects.⁵⁶ Figure 1.4 describes the effect of agglomeration and aggregation on particles in dry and liquid dispersion states.

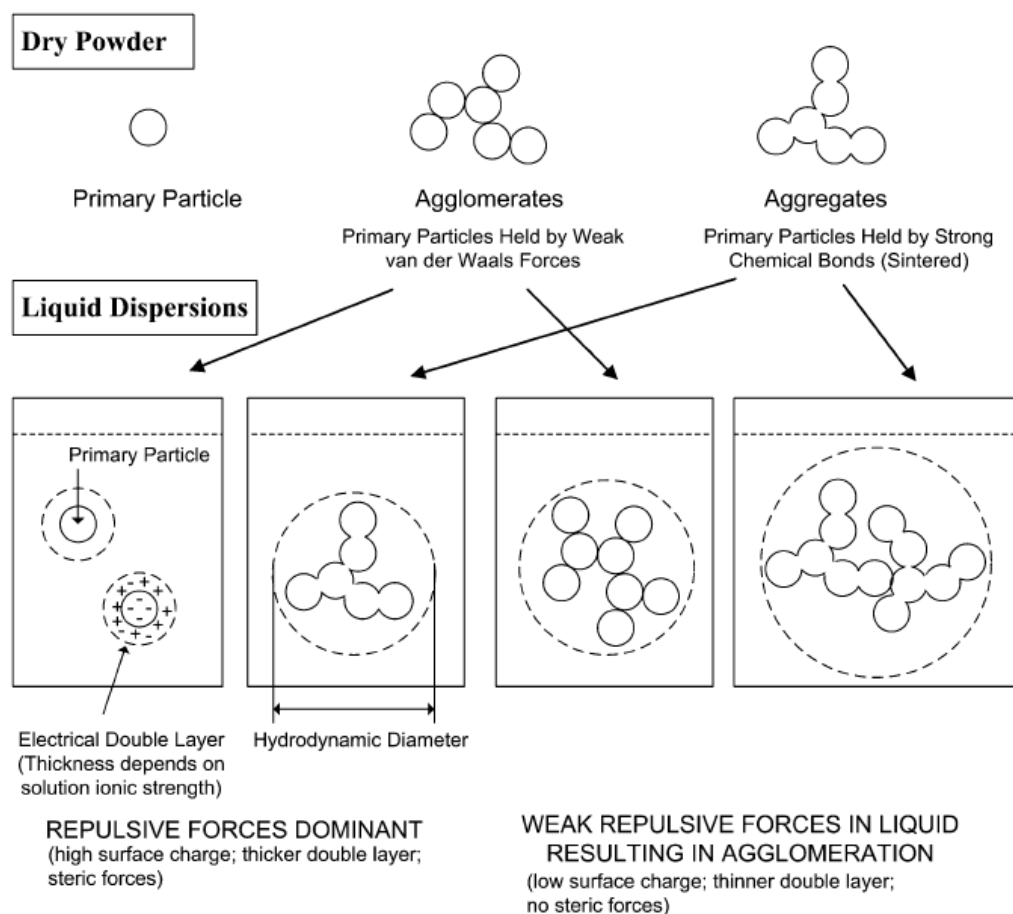


Figure 1.4: The agglomeration and aggregation of particles configuration in nanopowders and liquid nanoparticle dispersions.⁵⁶

The Derjaguin-Landau-Verwey-Overbeek (DLVO) theory is usually used to explain the stability of nanoparticle dispersions and their ability to agglomerate or aggregate. Figure 1.5 shows the relationship between the interaction energy and normalized distance. Factors that could affect this are electrostatic double layers, steric, and van der Waals forces between particles. The nanoparticle stability is affected by ionic strength and pH which in turn have a huge impact on the particle size and surface charge. In DLVO theory, the attraction between particles is considered to be due to the van der Waals force, while the electrical double layer interaction surrounding each particle is the electrostatic repulsive force. At low ionic strength or high surface charge densities (σ), the particles suspensions are stable as the double layer repulsion dominates. However, at high ionic strength or small surface charge densities (σ), the interaction is dominated by the attractive van der Waals force which means fast agglomeration. At intermediate values, particles are into the second minimum where slow agglomeration occurs. After that the critical coagulation

concentration (CCC) takes place as shown in Figure 1.5 whereby particles stay in the second minimum with fast agglomeration.^{57, 58}

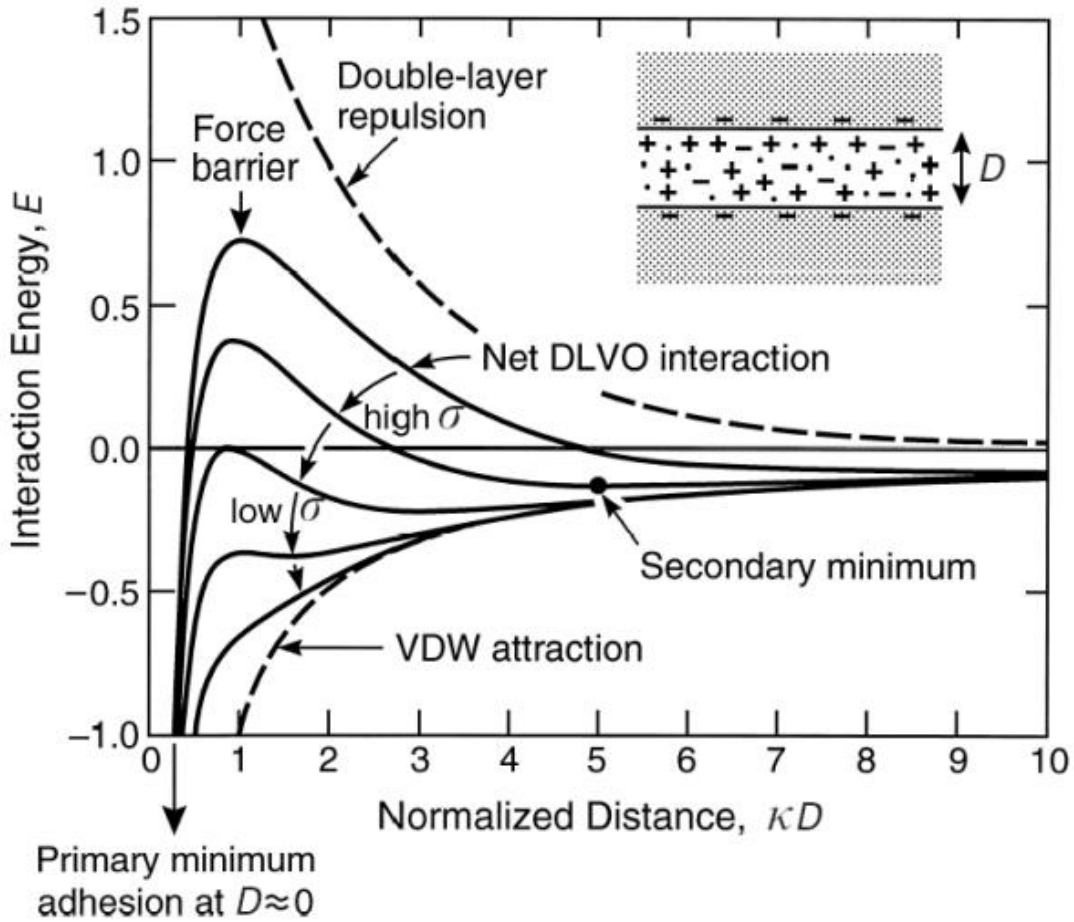


Figure 1.5:: DLVO scheme of dispersions stability for the attractive van der Waals and and repulsive electrostatic double-layer forces together determining the total interaction potential between two charged surfaces in aqueous electrolyte solutions at different surface charge densities σ or potentials Ψ_0 .⁵⁹

With reference to drug delivery, the synthesis of nanocarrier typically results in spherical particles with diameter from 20 to 200 nm, which can be examined by dynamic light scattering and electron microscopy methods.^{60, 61} The chemically controlled size and surface properties of nanocarrier can be used to limit the rate of clearance by phagocytic cells and to enable either passive or active cell targeting. In order to traverse capillaries and penetrate tissues through either paracellular or transcellular pathways, nanocarriers must be small enough⁶² to avoid rapid renal exclusion and uptake by the reticuloendothelial system.⁶³ Surface charge determines the stability of the formulation and the particles

tendency to accumulate in the blood stream or interact with the membrane.⁶⁴ The zeta potential is commonly used to measure the surface charge, a large zeta potential signifies a larger surface charge and it is also an index for particle stability.⁶⁵ In charged particles, the zeta potential increases due to more repulsive forces, leading to stable particles.⁶⁶ For stable nanosuspension the particles must have a minimum of ± 30 zeta potential.⁶⁷

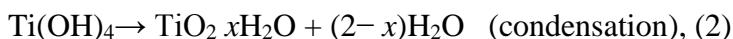
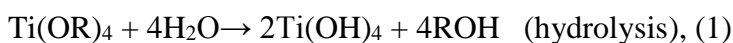
There is a wide range of nanomaterials investigated in this work, based on two types of nanoparticles. TiO₂NPs were chosen because they are highly photocatalyst which meant that they could have toxic effect and microgel type particles were chosen for drug delivery as they were thought to be nontoxic.

1.4 Methods for the Synthesis of Titania Nanoparticles

TiO₂ has been produced on a massive scale because of its industrial, technological and commercial importance. The current global production of titanium dioxide is 5000 ton a year.⁶⁸ There are many methods that can be used for synthesizing TiO₂ nanoparticles. Here are some of them:

1.4.1 Sol-Gel Method

The sol-gel method is a useful technique used in the fabrication of various ceramic materials. A colloidal suspension, or a sol, results from the hydrolysis and polymerization reactions of the titanium precursors, which are usually inorganic metal salts or metal organic compounds such as titanium alkoxides.⁶⁹ This method usually uses low temperatures and creates very fine particles however the chemicals are quite expensive and the synthesized nanoparticles contain hydrocarbon impurities from metal precursors.⁷⁰



1.4.2 Sol Method

The sol method refers to nonhydrolytic sol-gel processes and generally includes reactions between titanium tetrachloride and a variety of different oxygen donor molecules, e.g., a metal alkoxide or an organic ether. This method uses high temperatures for

calcination, needs expensive chemicals, and also has hydrocarbon impurities. However, this method can be used for producing nanoscale materials.⁷¹

1. 4.3 Hydrothermal Method

Hydrothermal synthesis normally occurs in steel pressure vessels under controlled temperature and/or pressure with the reaction in aqueous solutions. Nano-TiO₂ colloids preparation can be efficiently carried out through the hydrolysis and peptization of titanium alkoxides in aqueous media, followed by hydrothermal treatment.⁷² The main advantages of this method are that the reaction kinetics are significantly increased with a slight increase in temperature, new metastable products can be produced, normally single crystals are achieved and there is low contamination because of the closed system conditions and recycled reagents. However, the disadvantage is slow kinetics at any given temperature.⁷³

1. 4.4 Solvothermal method

The solvothermal method is similar to the hydrothermal method but the solvent used is nonaqueous, and the temperature can be raised much higher than that in hydrothermal method.⁷⁴ This method was used for the synthesis of mesoporous core/shell titania nanospheres using a water-ethanol mixture as a solvent from TiCl₃ as a titanium precursor.⁷⁵ The pros and cons are similar to hydrothermal process.

1. 5 Characterization of TiO₂ Nanoparticles

Many techniques have been used for studying the surface charge, size distribution, and morphology of Titania nanoparticles which are as follows:

1.5.1 Dynamic Light Scattering

This method is used to measure particle size distribution. A schematic for dynamic light scattering is shown in Figure 1.6. Dynamic Light Scattering depends on irradiating the sample with a monochromatic beam of laser light which is scattered into a detector located at an angle (θ) relating to the transmitted light, which allows the measurement of the size distribution of suspended particles.⁷⁶ The particle size can be measured using Stokes-Einstein equation.

$$D_h = \frac{kT}{3\pi\eta Dt} \dots \dots \dots (1)$$

where D_h is the hydrodynamic diameter, D_t is the translational diffusion coefficient, k is Boltzmann's constant, T is thermodynamic temperature, and η is dynamic viscosity.⁷⁷

Figure 1.7 shows a typical particle size distribution of a TiO_2 nanoparticle sample.

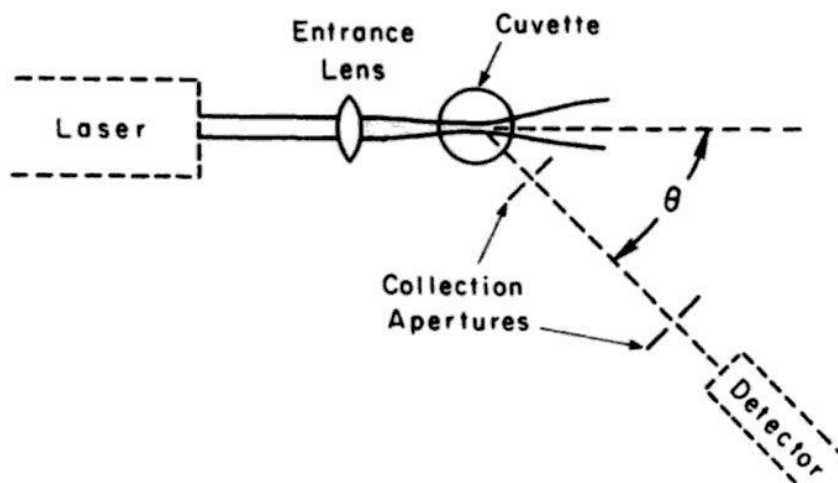


Figure 1.6: Diagram of Dynamic Light Scattering instrument.⁷⁸

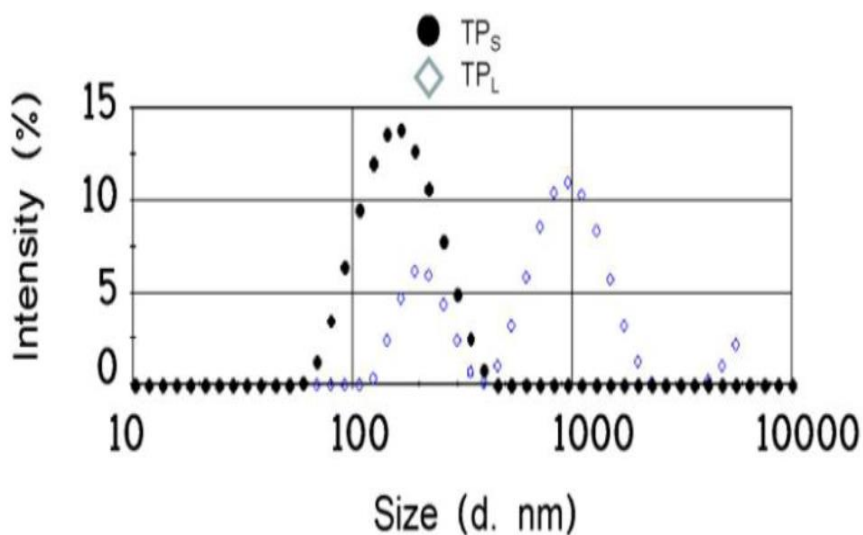


Figure 1.7: Particle size distribution of titanium dioxide nanoparticle at 166 nm (TP_S) and 596 nm (TP_L).⁷⁹

1.5.2 X-Ray Diffraction (XRD)

XRD is a crucial technique for determining the crystalline structure and estimating the crystal particle size according to the Scherrer equation. X-ray diffraction depends on the constructive interference of monochromatic X-rays and a crystalline sample. Figure 1.8

shows the Bragg's angle diffraction. The primary domain size of the crystallites is given by the equation:

$$D = \frac{K\lambda}{\beta \cos \theta} \dots\dots\dots (2)$$

where K is a dimensionless shape constant taken as 0.94 (varied according to the shape obtained) , 2θ is the diffraction angle, λ is the wavelength of the X-ray radiation (Monochromatic CuK_α wavelength = 0.15406 nm), and β is the Full Width at Half-Maximum (FWHM) of the diffraction peak.^{80, 81} Figure 1.9 represents the XRD patterns for TiO_2 nanoparticles at different crystallite sizes. It was observed that the particle size increases as the temperature is raised from 100°C to 800°C whereby from 100 – 600°C, the amount of anatase TiO_2 decreases and the percentage of rutile TiO_2 starts to increase from 600°C.⁸²

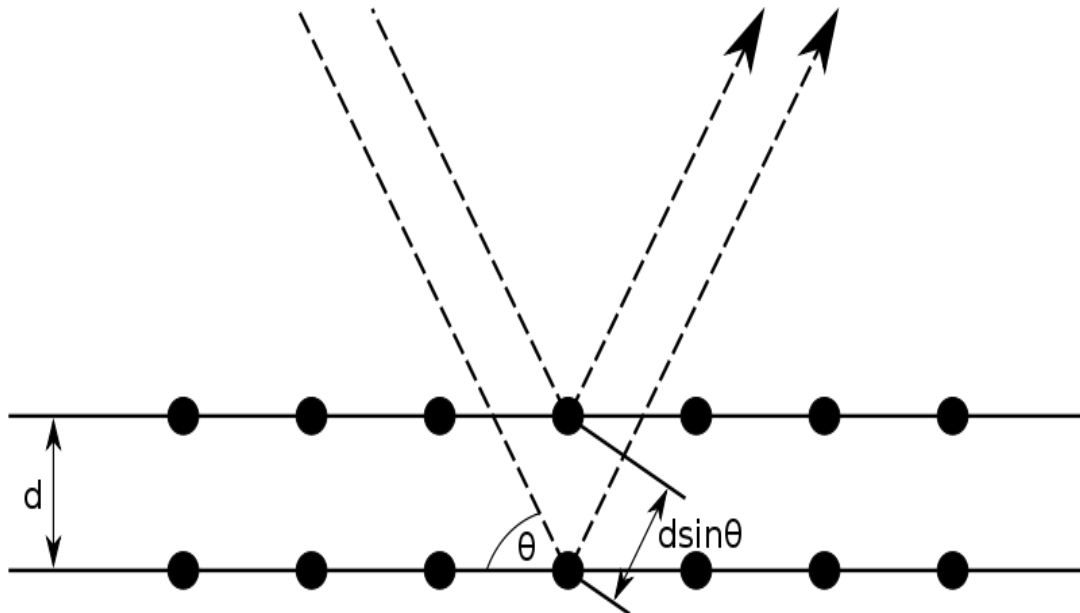


Figure 1.8: Bragg diffraction represented by interaction between X-rays and a crystalline sample.⁸⁰

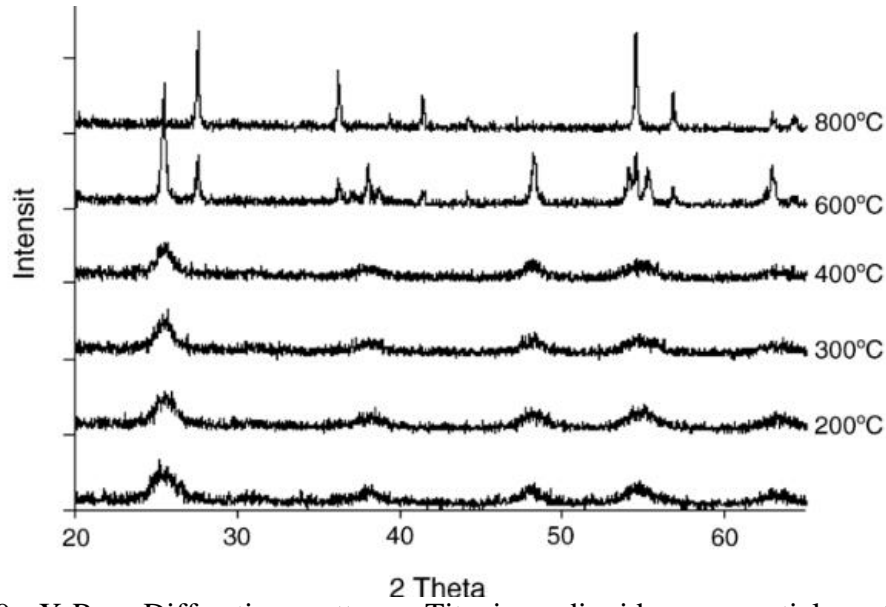


Figure 1.9: X-Ray Diffraction patterns Titanium dioxide nanoparticles at different calcination temperature from 100°C to 800°C, providing different crystallite sizes.⁸²

1.5.3 Zeta Potential

When particles are placed in an aqueous medium, an electrical double layer is made around them with one layer consisted of ions strongly adsorbed on the surface of the particles (Stern layer). The other layer is encompassed of ions less tightly adsorbed (diffuse layer), as showed in Figure 1.10. The zeta potential (ζ) can be defined as the average potential (ψ) in the electrical double layer at the shear zone between a mobile charged particles and the immobile liquid phase in which a particle is suspended.⁸³ The potential difference is called the zeta potential and it is measured at the border of the diffuse layer; therefore, the zeta-potential is a measurement of the quantity of charge existing on the particle surface relative to the bulk of the dispersing media.⁸⁴ The zeta potential can be determined using Henry's equation through measuring the electrophoretic mobility of a particle.

$$UE = \frac{2\varepsilon z f(Ka)}{3\eta} \dots \dots \dots (3)$$

where UE is the electrophoretic mobility, ε is the dielectric constant, z is the zeta potential, $f(Ka)$ is Henry's function, and η is the viscosity. Henry's function generally has value of either 1.5 or 1.0.⁸⁵

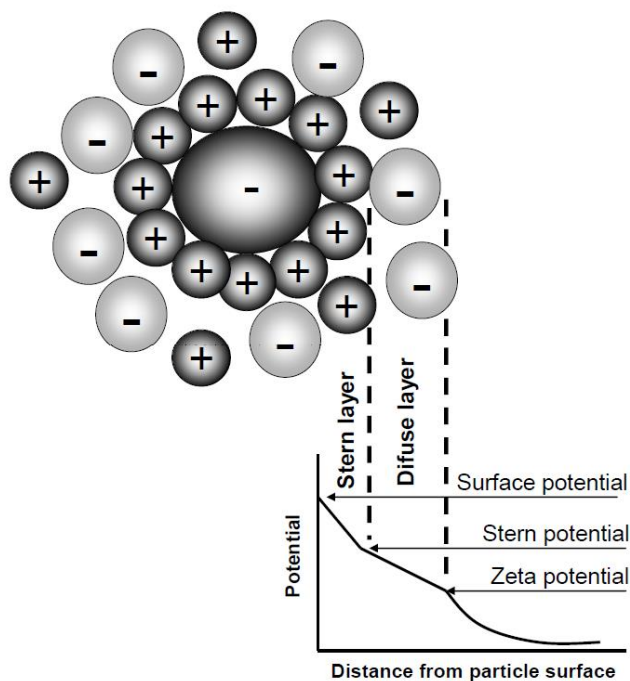


Figure 1.10: The schematic representation of zeta potential which showing the distribution of ions around the charged particle.⁸⁴

The particles surface charge (zeta potential) and subsequently the particle size can be changed by varying the pH of solution due to the change the ionic strength causing agglomeration. For TiO₂ NPs dispersed in water, at low pH such particles have a positive surface charge and, conversely, at high pH, a negative surface charge. The isoelectric point is the intermediate pH at with a particle has zero net surface charge. The zeta potential and average particle size of typical TiO₂ dispersions as a function of pH with ionic strength are shown in Figure 1.11. The higher the zeta potential, the more predominant over van der Waals forces is the electrostatic repulsion between the electric double layers, resulting in a lower agglomeration and a lower viscosity value. The zero value of the zeta potential, the isoelectric point, indicates the pH at which the particles tend to form flocculates.^{84, 86}

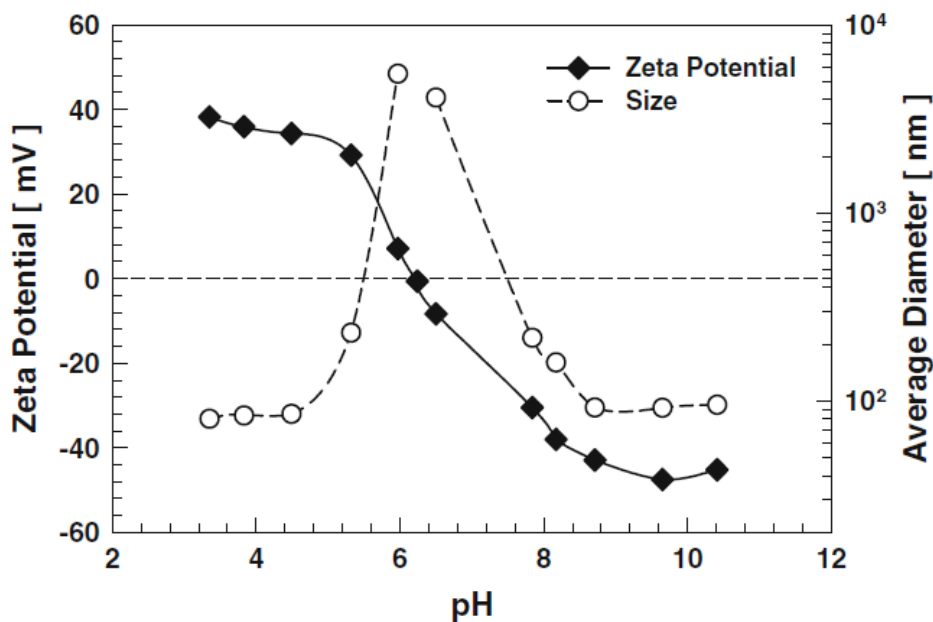


Figure 1.11: The impact of ionic strength on the zeta potential and the hydrodynamic size of TiO_2 dispersions.⁵⁶

1.5.4 UV-Visible Spectroscopy

Ultraviolet and visible molecular absorption spectroscopy is widely used for the quantitative determination of a large number of inorganic, organic, and biological species. The molecular absorption spectroscopy based on electromagnetic radiation of liquid solution in the wavelength region of 190 to 800 nm to measure of the transmittance T or the absorbance A of solutions contained in transparent cells having a path length of b centimeters. The concentration of an analyte is linearly associated to absorbance as given by Beer's law:

$$A = -\log T = \log \frac{I_0}{I} = \epsilon bc$$

Where Incident light intensity, I_0 , Transmitted light intensity, I , Absorbance, A Transmittance, T , Path length, b , Concentration of absorber, c , Absorptivity, a , Molar absorptivity, ϵ

Many spectrophotometers are depended on a double-beam design. Figure 1.12 demonstrates a double-beam- instrument in which two beams are shaped in space by a V-shape mirror called a *beamsplitter*. One beam traverses the reference solution to a detector,

and the second simultaneously passes through the sample to a second, matched detector. Both of outputs are amplified, and their ratio (or the logarithm of their ratio) is determined electronically or by a computer and displayed by the readout device.⁸⁷

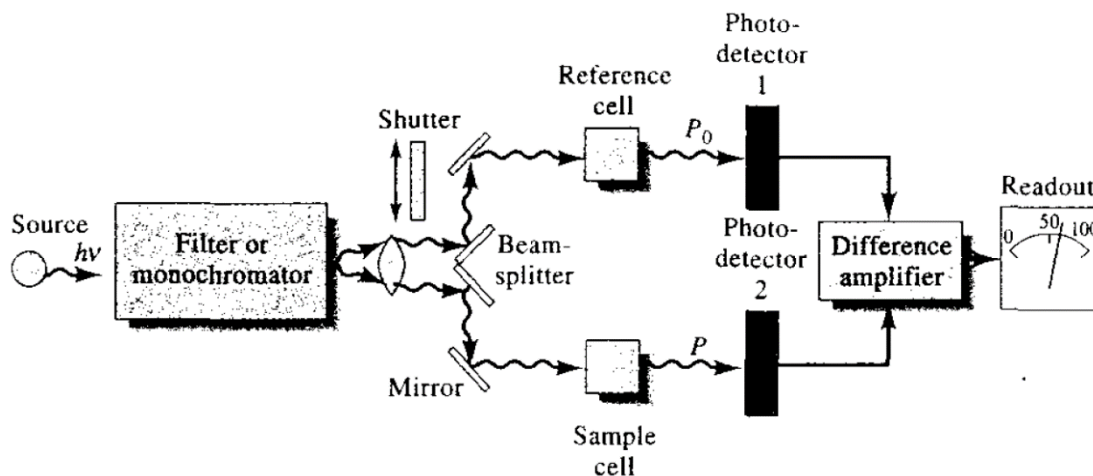


Figure 1.12: The schematic diagram of double beam spectrophotometer setup.⁸⁷

1.5.5 Fourier Transform- Infrared Spectroscopy

Fourier Transform Infra-red Spectroscopy (FTIR) is a sensitive technique mainly for identifying organic chemicals and some inorganics owing to the variety of functional groups, side chains and cross-links involved, all of which will have characteristic vibrational frequencies in the infra-red range. Examples include paints, adhesives, resins, polymers, coatings and drugs. It is also valuable tool in isolating and characterizing organic contamination. FTIR based on the point that the most molecules absorb light in the infra-red region of the electromagnetic spectrum. This absorption matches precisely to the bonds existing in the molecule. The frequency range are measured as wave numbers typically over the range $4000 - 600 \text{ cm}^{-1}$.⁸⁷

Figure 1.13 shows the FTIR analysis which can be conducted in the one arm through, the IR source radiation passes through the beam splitter to the fixed mirror, then back to the beam splitter, and through the sample to the IR transducer. While in the other arm, the IR source light traverses to the beam splitter, is reflected to the movable mirror, and travels back through the beam splitter to the sample and to the transducer. When the two beams

meet again at the beam splitter, they can interfere with each other if the phase difference (path difference) is appropriate. A signal versus mirror displacement plot represents the interferogram. The interferogram has information about all the frequencies present. The spectrum, intensity versus wavenumber, is the Fourier Transform of the interferogram.⁸⁷

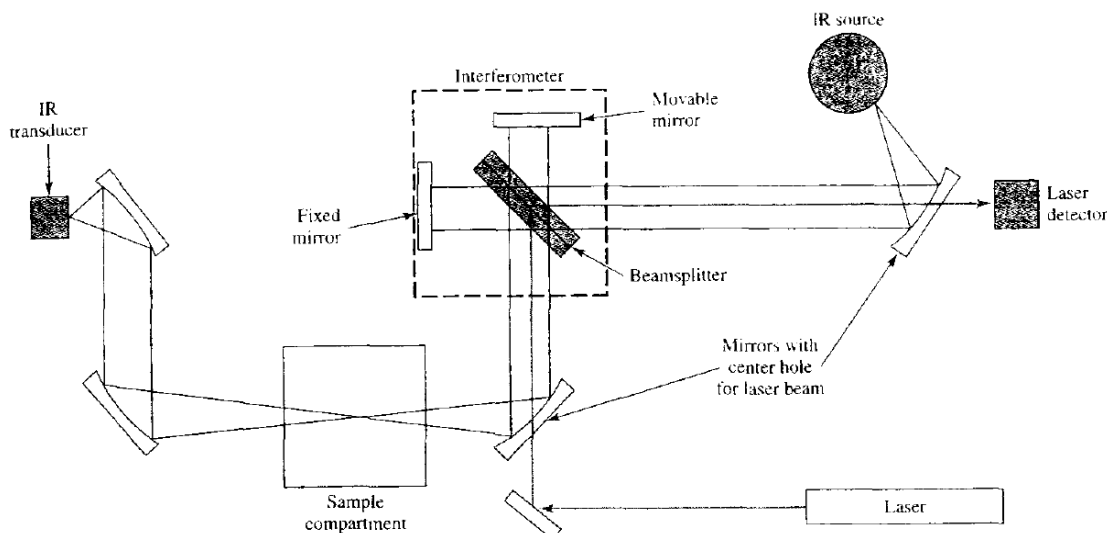


Figure 1.13: A schematic diagram of FTIR setup.⁸⁷

1.5.6 BET Surface Area Measurement

Brunauer–Emmett–Teller (BET) theory aims to explain the physical adsorption of gas molecules on a solid surface and acts as the basis for an important analysis technique for the measurement of the specific surface area of a material. The BET depends on multilayer adsorption of gases (like nitrogen, argon, carbon dioxide, etc.) as adsorbates to determine the surface area of adsorbent. An Adsorption Isotherm is achieved by quantifying the amount of gas adsorbed through a wide range of relative pressures at a constant temperature (typically liquid N₂, 77K). Contrastingly, desorption Isotherms are accomplished by measuring gas removed as pressure is reduced. BET derived the BET equation:⁸⁸

$$\frac{p}{v(p_0 - p)} = \frac{1}{v_m c} + \frac{c - 1}{v_m c} \left(\frac{p}{p_0} \right) \dots \dots \dots (5)$$

where P and P_0 are the equilibrium and the saturation pressure of adsorbates at the temperature of adsorption, v is the adsorbed gas amount, and v_m is the monolayer adsorbed gas amount. c is the BET constant,

$$c = e^{\left[\frac{E_{ads} - E_{cond}}{RT}\right]} \dots \dots \dots (6)$$

$$E_{ads} \gg E_{cond}$$

where E_{ads} is the heat of adsorption for the first layer, and E_{cond} is that for the second and higher layers and is equal to the heat of condensation.

Equation (5) can be plotted as a straight line with $1/v[(p_0/p) - 1]$ on the y-axis and $\phi = p/p_0$ on the x-axis according to experimental results as shown in Figure 1.14. This plot is called a *BET plot*. The value of the slope A and the y-intercept I of the line are utilized to measure the monolayer adsorbed gas amount v_m and the BET constant c . The following equations can be used:

$$v_m = \frac{1}{A + I}$$

$$c = 1 + \frac{A}{I}$$

The total Surface area (S_{Total}) and BET surface area (S_{BET}) can then be derived:

$$S_{Total} = \frac{v_m N A_{cs}}{M}$$

$$S_{BET} = \frac{S_{Total}}{a}$$

Where N = Avogadro's number (6.023×10^{23}), M = Molecular mass of adsorbate, A_{cs} = Adsorbate cross sectional area (16.2 \AA for Nitrogen) and a the weight of the solid adsorbent.⁸⁸

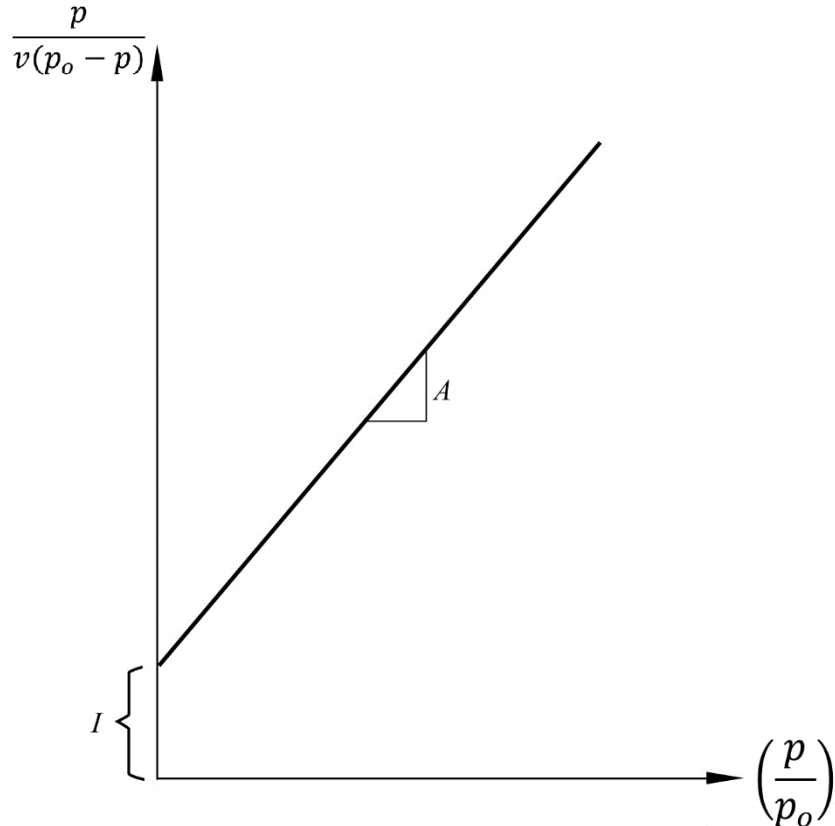


Figure 1.14: BET plot for the measurement of surface area of solid adsorbent through physical adsorption of gas molecules on a solid sample.

1.5.7 Scanning Electron Microscope

A Scanning Electron Microscope (SEM) is a microscope that utilizes electrons, instead of light, to make a magnified image. It can be used to detect the topography, composition and crystallographic information at a variety of materials such as minerals, artifacts, microorganisms, and manufactured materials. Figure 1.15 shows a schematic setup of SEM machine. It can be seen the figure that electrons are generated at the top of the microscope by a metallic filament which referred to as the electron gun. The emitted electrons are then formed into a beam and accelerated down the column toward the specimen. The beam is further focused and directed by electromagnetic lenses as it moves down the column. When the beam reaches the specimen, electrons are knocked loose from the surface of the specimen. These electrons are referred to as secondary electrons. These electrons are “seen” by a detector that amplifies the signal and sends it to a monitor. The

electron beam scans back and forth across the sample building up an image from the number of electrons emitted from each spot on the sample.^{89, 90}

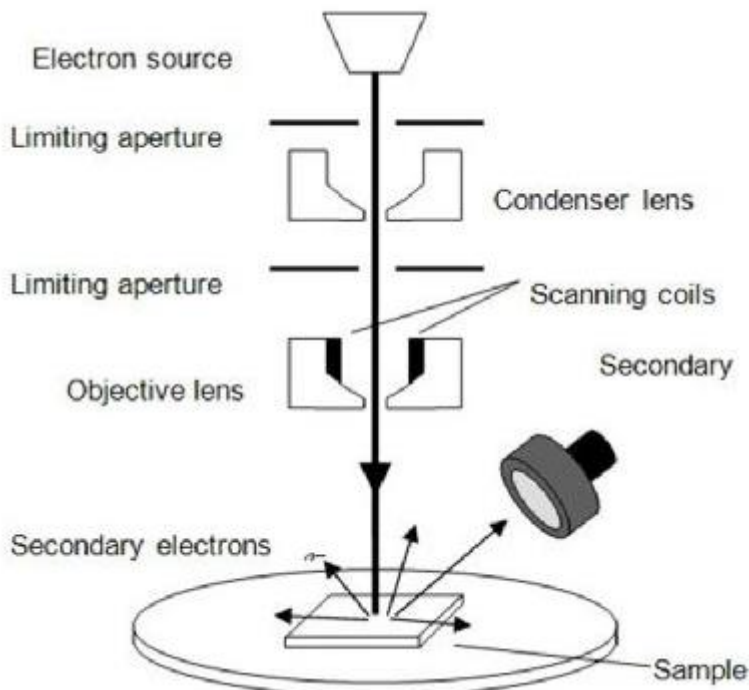


Figure 1.15: The schematic diagram of the SEM setup.⁹¹

1.5.8 Transmission Electron Microscope

TEM is a powerful technique to reveal information about morphology, crystallography, particle size distribution, and elemental composition. It is able to provide atomic-resolution lattice images and giving chemical information for a wide variety of materials such as metals, minerals, ceramics, semiconductors, and polymers. Because the unique physical and chemical properties of nanomaterials not only depend on their composition, but also on their structures, TEM offers a means for characterizing and understanding such structures. TEM is unique as it can be used to focus on a single nanoparticle in a sample, and directly identify and quantify its chemical and electronic structure.⁹²

Figure 1.16 describes that as the electron beam travels through the sample, only certain parts of it are transmitted, creating an amplitude contrast image. The image traverses through a magnifying lens and is then projected onto a phosphor screen or a charge coupled device (CCD), which permits for quantitative data processing. Information may also be obtained from backscattered and secondary electrons, as well as emitted photons.⁹¹

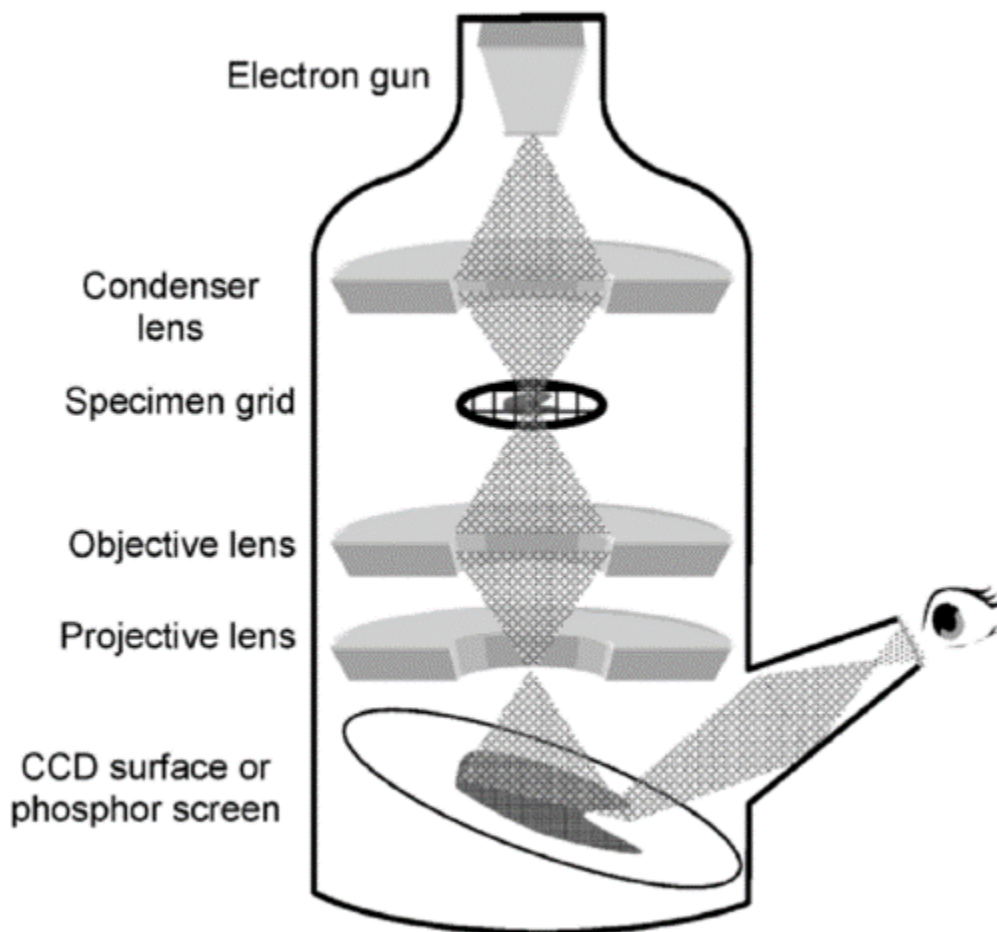


Figure 1.16: A schematic diagram of a TEM setup.⁹¹

1.6 Functionalization of Nanomaterials

The surface of nanoparticles can be functionalized to change their properties and interactions with ligands. Nanomaterials can be functionalized with hydroxyl groups which can react with carboxyl groups of organic or inorganic molecules, whether they are produced in aqueous or nonhydrolytic solutions, through its oxygen atom or with various silane groups through -O-Si bond such as surface modification of hydrophobic

superparamagnetic iron oxide nanoparticles (SPIONs) to be hydrophilic through covalent bonding (Fe-S) with bi-functional 3-mercaptopropionic acid and then, carboxyl group was esterified with dextran for biocompatibility which is important in the clinical applications.⁹³

Amine and oxysilane are other common functional groups that are useful for the functionalization of nanoparticles, which can possibly have a wide biological applications.⁹⁴ Semiconducting nanoparticles for example quantum dots (QDs), Pt, Ag and Au can be useful for targeted drug delivery systems through their surface modification with mercapto groups using thiolate polymers.⁹⁵ Surface molecules might be essential to graft and activate the surface for extra modification with other chemical or bioactive molecules. Silane coupling agents are materials with dual functional groups, one for the surface binding to the nanoparticles and the other for starting additional chemical reactions.⁹⁶ Physical adsorption for example using electrostatic interactions⁹⁷ and Van der Waals interactions⁹⁸ are also considered to be useful methods for the functionalization of nanoparticles because of the good stability, hydrophilicity in suspensions, simple synthetic conditions at room temperature but they tend to be weak. Human Serum Albumin (HAS) was used as a probe for physical adsorption of protein to some nanoparticles for biodistribution.⁹⁹

Self-assembly is a method which has the ability to make multidimensional assemblies of nanomaterials.¹⁰⁰ The main forces that control self-assembly are electrostatic interactions, surface tension, capillary forces, hydrophobic interactions dipole-dipole interaction, Van der Waals forces and bio-specific recognition.¹⁰¹ Electrostatic interaction is the driving force for layer-by-layer (LbL) self-assembly of polyelectrolyte shells. This method allows the deposition of many chemicals onto various nanomaterials.¹⁰² The shell thickness can be controlled by consecutively depositing oppositely charged polyelectrolytes or nanomaterials on the surface through mainly electrostatic interactions.¹⁰³ Polyelectrolytes (PEs) are cationic or anionic polymers with charged or chargeable monomer repeat units, whereby in polar solvents such as water, these ion pairs are able to dissociate, producing the charges on the surface of the polymer while the counter ions are released in solution. If they involve permanent charges and fully dissociate in water, they are referred to as strong PEs. Whereas, weak PEs are strongly dependent on

pH.¹⁰⁴ For example, the surface of 35 nm gold nanoparticles was coated with up to eight layers of polyelectrolytes using electrostatic interaction.¹⁰⁵ The method has also been used for the manufacturing ultra-thin films with desirable properties for corrosion control through cationic and anionic polyelectrolyte multilayers coating of stainless steel wires.¹⁰⁶ Figure 1.17 depicts multilayer structures composed of a positively charged substrate adsorbing a polyanion and a polycation consecutively.¹⁰³

More precisely, anionic titanium(IV) bis(ammonium lactate)dihydroxide (TALH) as a titania precursor can be electrostatically assembled with cationic polyelectrolyte poly(allylamine hydrochloride) (PAH), allowing the formation of multilayers, and moreover, negatively charged Pt nanoparticles can be easily inserted within (TALH/PAH) multilayers using the same LBL process to produce titania nanocomposite.^{107, 108} Amphoteric crystalline titania nanoparticles with polyelectrolytes were used to manufacture a dye-sensitized solar cell through assembling polyion/TiO₂ nanocomposite multilayered films by the electrostatic layer-by-layer deposition technique using two weak polyelectrolytes, poly(allylamine hydrochloride) and poly-(acrylic acid), and two strong polyelectrolytes, poly(dimethyldiallylammonium chloride) (PDAC) and poly-(sodium 4-styrenesulfonate).¹⁰⁹

Martin *et al.* used wet layer by layer self-assembly to fabricate rectifying junctions on metal nanowires from nanoparticles (TiO₂/ZnO)/polymers thin films.¹¹⁰ Metal-ion-(Ag, Co, Ni and Pd) doped titania nanocatalysts exhibited photo catalytic activity towards Rhodamine B in the presence of visible light upon deposition on glass slides by the LbL self-assembly technique using a poly(styrene sulfonate sodium salt) (PSS) and poly(allylamine hydrochloride) (PAH) polyelectrolyte system. This technique of metal doped titania nanoparticles thin film gave robust adhesion properties with high stability and the same efficiency for up to five reusable cycles.¹¹¹ Stable and super-hydrophilic titanium dioxide nanoparticle thin films have also displayed biocompatibility and suitability for successful cell culturing and attachment to human dermal fibroblast through layer by layer coating of substrates for example glass, poly(methyl methacrylate) (PMMA) and poly(dimethyl siloxane) (PDMS) with poly(styrene sulfonate) to form films with various thicknesses.¹¹² The polyelectrolytes coated photocatalyst titania was also proficiently utilized for coating polyester textiles and producing solar light antibacterial

textiles. This was achieved through layer by layer assembly coating of cationic polyethylenimine (PEI) with negatively charged titania particles dispersions and polyanionic poly(styrene sulfonate) (PSS) with positively-charged TiO_2 particles.¹¹³

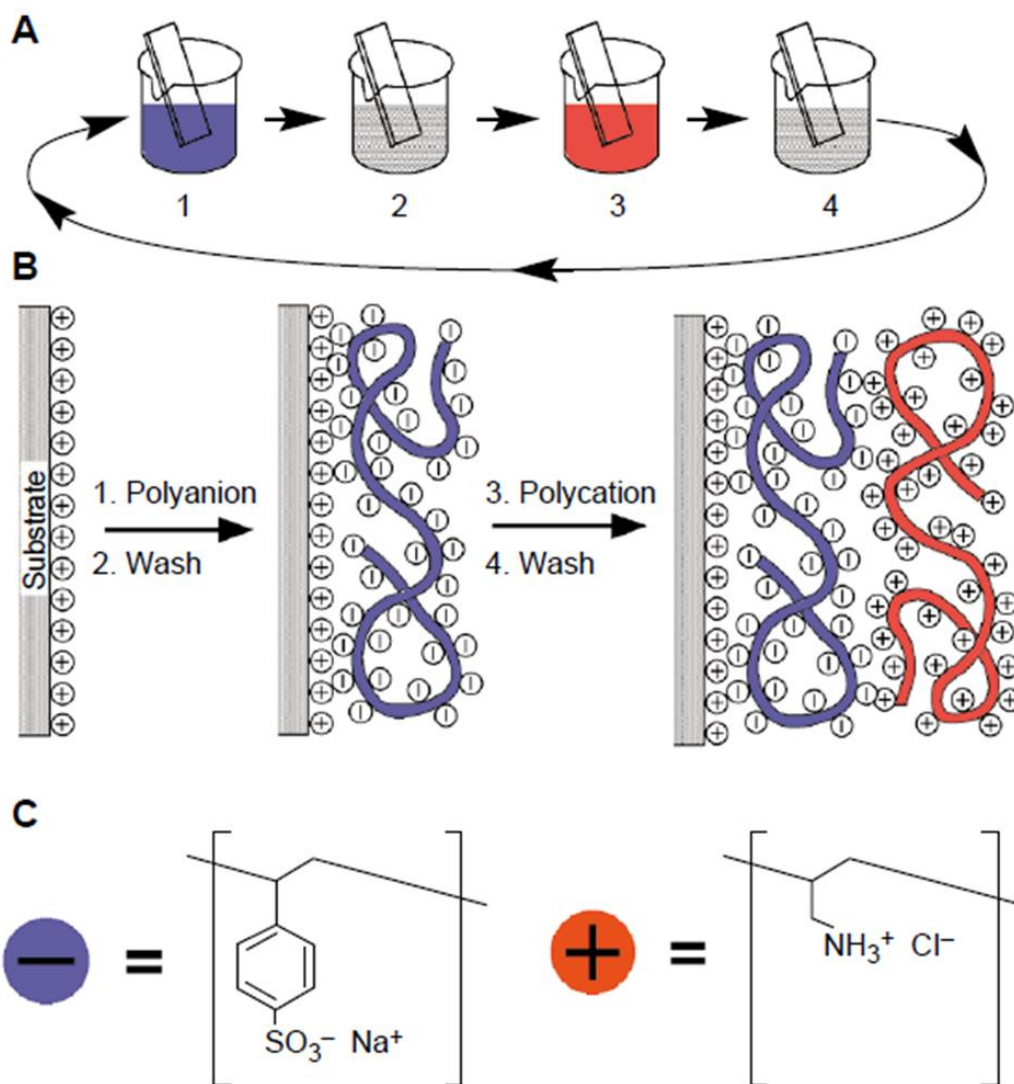


Figure 1.17: (A) Scheme of the film deposition process. Steps 1 and 3 denote the adsorption of a cationic and anionic polyelectrolytes, respectively, and steps 2 and 4 are washing steps (B) Adsorption steps for the formation of thin film, starting with a positively charged substrate which firstly was coated with polyanions and then polycations (C) Chemical structures of anionic and cationic polyelectrolytes, the sodium salt of poly(styrene sulfonate) and poly(allylamine hydrochloride).¹⁰³

Nanosized hollow spheres or capsules can also be formed using layer by layer self-assembly from core-shell structures using templating methods.¹¹⁴ The polyelectrolytes and nanoparticles functionalized nanoparticles were accomplished with polymerization and silanization methods. Hollow capsules can be produced upon removal of the templates *via* calcination or etching, these can then be used as transporters for drug delivery.^{115, 116} The most frequently used cation-anion polyelectrolyte pairs include poly(styrene sulfonate) (PSS) and poly(diallyldimethylammonium chloride) (PDADMAC)^{105, 117}, PSS and poly(allylamine hydrochloride) (PAH)^{114, 116}, PSS and poly(diallyldimethyl-ammonium) (PDDA) or poly(pyrrole) and poly(N-methylpyrrole).^{118, 119} Successive coating of nanoparticles and polyelectrolytes can be useful to assemble different nanomaterials.^{115, 120}

1.7 General Applications of Nanomaterials

In nano-cosmetics and sunscreen lotions for example, the nanosized materials have unique chemical and physical properties that improve the product. The titania (and ZnO) present in the cosmetics are considered to be safe physical sunscreens according to US Federal Register, 43FR38206, 25 August 1978 as they have the ability to reflect and scatter both UVB and UVA, the major cause of skin cancer.⁵² Nanomaterials can also be used as self-cleaning materials in the case of the deposition of dust or the growth of microorganisms (bacteria and algae) on the surface of buildings. Buildings are functionalized with a layer of the photocatalyst which causes chemical damage to the organic particles adsorbed on the surface of the photocatalyst, making the surface superhydrophilic which in turn repels dirt and microorganisms.¹²¹

In agriculture, pesticides are used as formulations for a specific target in the field. However, these pesticides are toxic and cumulative in the environment and their presence might cause a serious problem for living beings. Therefore, nanomaterials have a great role in the protection of plant, pathogen detection, and as a smart nanosensor to detect pesticide residue for example, titania nanoparticles have the ability to photodegrade the pesticides through photooxidation.^{122, 123} Nanotechnology also shows the ability to remove pollutants and germs from contaminated water efficiently through using nanoparticles, nano membrane and nano powder. These pollutants are either heavy metals or organic and inorganic nutrients or microorganisms. The efficiency of nanomaterials for wastewater

treatment is attributed to its high surface area.¹²⁴ titania nanoparticles were used for the degradation of wastewater pollutants depending on its photocatalysis. The photocatalysis process of titania nanoparticles were conducted using suspension and immobilization reaction systems.¹²⁵

Nanostructured materials have also played an effective role in enhancing the efficiency of solar cells, lithium ion batteries, super capacitors, and hydrogen storage methods due to their unique optical and electronic properties in terms of providing a large surface area to improve the electrochemical reaction or molecular adsorption taking place at the solid–liquid or solid–gas interface. They also create optical effects that increase the optical absorption in solar cells. Moreover, the crystallinity and porosity of nanomaterials increase the transportation of ions and electrons and electrolyte diffusion in order to ensure highly efficient electrochemical process, and achieving more efficient energy conversion and storage.¹²⁶ Nanomaterials are used in medicine to deliver conventional drugs, recombinant proteins, vaccines and more recently nucleotides using nano drug delivery devices where these devices are targeted directly to the cell or tissue where they release their loading in a controlled way.¹²⁷ Poly(lactic-co-glycolic acid) (PLGA) for example, was used in biomedical applications because of its biocompatibility and biodegradation and also for its surface properties.¹²⁸ Nanomaterials can be used for biosensing as the transduction element, magnetic particles, gold nanoparticles, and quantum dots have been immobilised with bioreceptor units, increasing the sensitivity and lowering the limit of detection.¹²⁹ In biomedical imaging, Fe₂O₃ nanoparticles have been used as a contrasting agent in Magnetic Resonance Imaging (MRI) because of their magnetic properties upon applying magnetic field. This unique property can be beneficial to diagnose many diseases.¹³⁰

1. 8 Toxicological Impacts of Nanomaterials

In recent years, due to the huge growth in the production of engineered nanomaterials, many studies have shown the effect of these nanomaterials on the environment. Nanoparticles used commercially in cosmetics and sunscreens (TiO₂, Fe₂O₃, and ZnO), fillers of dental fillings (SiO₂), in systems of water filtration and catalysis, and in photovoltaic cells (CdS, CdSe, ZnS) are released in to the environment.¹³¹ However, there

is an increasing debate about release these very tiny particles and the risks related to exposure as well as their side effects.³⁶ Toxicological studies of nanoparticles on human cells *in vivo* are still limited and most of the knowledge on nanomaterials toxicity comes from mammalian studies where rats, mice, guinea pigs have been exposed to carbon nanotubes, nano sized TiO₂, nano sized cadmium selenide particles, and metal oxides particles, causing lung damage.^{32, 132, 133} It is well-known that not only bacteria, viruses and parasites are a major cause of diseases, but very small inorganic particles may cause health related problems as they have the ability to penetrate through the cellular membranes of living organisms. For example, asbestos fibres are known to asbestosis, which leads to lung cancer.^{3, 134, 135} while long term inhalation of silica powder can cause silicosis.¹³⁶

In the human body, three significant organs are exposed to the environment: the skin, lungs and the digestive tract. These organs have ability to protect the body from harmful agents. Similarly, they can transmit nutrients, water and oxygen. The skin acts as a barrier against toxic materials (with the exception of for example, oxygen for the retina and UV rays for vitamin D synthesis).^{3, 36, 137, 138} Nanoscale particles can penetrate through some organs for instance, the lungs, intestine, and skin. Some of these particles can enter into the deepest layers of skin depending on size and surface area. Nanomaterials which enter into the human body *via* the mouth may cause inflammatory effects or cancer and other diseases.^{36, 138} Figure 1.18 shows how nanoparticles exposure can be associated with diseases *in vivo* and *in vitro*. Contrastingly, there are some toxic nanoparticles that can be beneficial to fight diseases and can be used as a medical treatment for instance, targeting and damaging only cancerous cells.³⁶

In drug delivery system, nanocarriers themselves should be free from toxicity, biocompatible, and biodegradable with non-toxic degradation products that can be readily cleared from the body.¹³⁹ A non-toxic delivery vehicle can be designed through selecting either nontoxic materials to start with or materials that can be metabolized into non-toxic components before any damage can be achieved in the body. For instance, acrylate- and methacrylate-based polymeric systems can be easily metabolized into small molecule alcohols and reasonably non-toxic poly-methacrylic acid and poly-acrylic acid components.^{140, 141} In such systems toxicity of the carrier could be dominated mainly by its hydrolyzed small molecule components. Nanovehicles may exert side effects due to a

massive surface/mass ratio that might adversely change both the degradation rate and reactive capacity of the nanocarrier's surface. Moreover, its interactions with cells – surface activation, uptake, intracellular degradation or deposition, all of which may abnormally activate, damage or kill the cells taking up the carriers.¹³⁹ Nanotoxicology has therefore developed as a new branch of toxicology which deals with the health side effects that can be caused by nanomaterials.¹⁴²

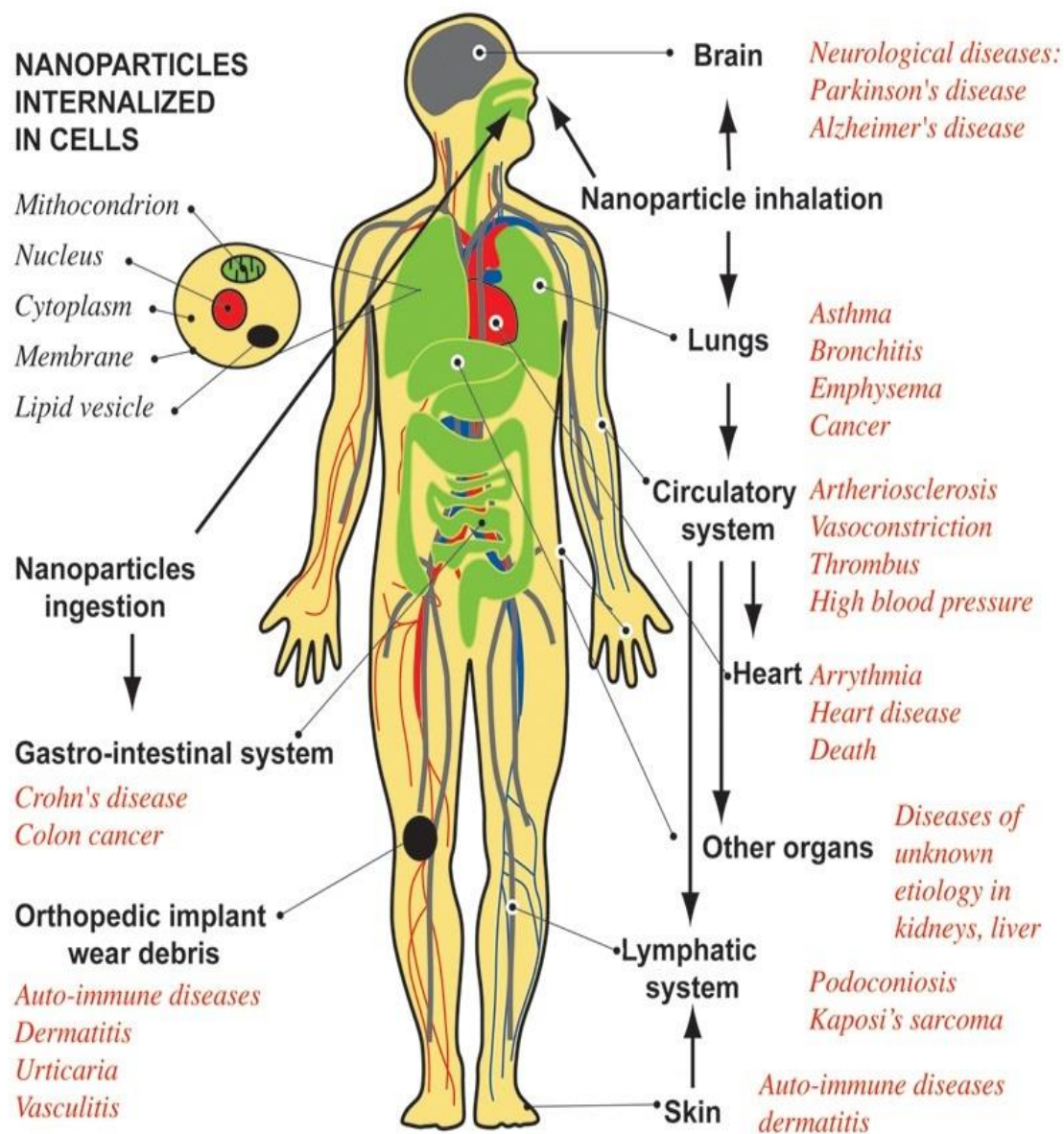


Figure 1.18: Pathways of an in vivo and in vitro nanoparticles exposure and related diseases as suggested by epidemiological studies.³

1.9 Toxicity of TiO₂ Nanoparticle

Titanium dioxide (titania) is usually used, essentially for pigmentary purposes, with 70% of its production capacity used in paints, plastics, inks, foods, and toothpastes. Nano-grade titania can be used in cosmetics and skin care products, such as sunscreens to block UV light, as well as in catalysts. There are three crystalline phases of TiO₂: anatase, rutile and brookite whereby it is normally known that anatase phase has higher photocatalytic activity than rutile and brookite.⁴⁹ Titania nanoparticles are commonly found in aggregate form⁵⁰ and the aggregation, size and shape of TiO₂ nanoparticle,⁵¹ are important parameters in understanding prospective cytotoxicity.⁵⁰

Dunford *et al.*, (1997) reported that nanosized (20–50 nm) TiO₂ has been commonly accepted to be a safe sunscreen as it is able to reflect and scatter ultraviolet UVB and UVA in sunlight but TiO₂ absorption of incident UV light is about 70%; therefore, in aqueous environments this is going to lead to the formation of hydroxyl radicals. Hence, photo-oxidations may elucidate the illuminated TiO₂ toxicity and it is probable effects on DNA. Dunford *et al.*, studied *in vivo* commercial 20 - 25 nm TiO₂ samples with different ratios of anatase/rutile (some samples also contained ZnO) after that DNA illumination. The study revealed that DNA in human cells was damaged by illumination in the presence of TiO₂.⁵²

Federici *et al.*, studied the toxicological effect of titania nanoparticles on rainbow trout by exposing them to different concentrations of TiO₂ NPs for up to 14 days and the results demonstrated that TiO₂ NPs exposure resulted in some physiological effects.¹⁴³ Lovern and Klaper exposed *D.magna* to either to filtered (30 nm) or unfiltered (100 and 500 nm) TiO₂ NPs for 48 h as an acute toxicity test. In the case of filtered TiO₂ NPs, *D. magna* presented rising mortality with increasing concentration (100% mortality at 10 mg l⁻¹), while only 9% mortality resulted from 0–500 mg l⁻¹ of the unfiltered TiO₂. Thus, the toxicity effect depended on the type of dispersion of TiO₂ NPs.¹⁴⁴ Titania, ZnO and CuO NPs have been revealed to have toxic effects and have the ability to inhibit the growth of microalgae *P. subcapitata* in visible light due to the generation of free radicals.³⁹ It was also found that ZnO and CuO have a toxic influence on crustaceans *D.magna*, *T. platyurus* and the bacteria *V. fischeri* but in that study TiO₂ NPs were not found to be toxic. Thus,

the nanoparticle toxicity depends on the particle morphology and size, test organism species, and synthetic method.³⁷

Hu *et al.* exposed the earthworm *E. fetida* in soil to various concentrations of titania and ZnO NPs for 7 days to evaluate their toxicity. It was discovered that these NPs were able to substantially damage the earthworms when doses were higher than 1.0 g kg⁻¹, affecting the mitochondria, DNA and cellulose enzyme activity.¹⁴⁵ Kasemet *et al.* studied the toxic effect of nano-grade ZnO, CuO, and TiO₂ to *S.cerevisiae*—an unicellular eukaryotic organism for a 24 hour exposure time. No toxicity was seen from nano sized and bulk TiO₂ even at 20000 mg/l and both, nano and bulk ZnO were of equivalent toxicity, whereas, nano CuO was about 60-fold more toxic than bulk CuO.⁴¹ The ecotoxic effects of TiO₂, SiO₂ and ZnO towards Gram-positive *Bacillus subtilis* and Gram-negative *E.coli* was investigated. This study proved that these three nanomaterials were harmful to variable degrees, with antibacterial activity rising with the concentration of particles. In the same way, the antibacterial effect of these nanomaterials usually increased from SiO₂ to TiO₂ to ZnO under both dark and light conditions demonstrating that mechanisms additional to ROS generation were responsible for growth inhibition.¹⁴⁶ Similarly, Reeves *et al.* demonstrated for fish cells *in vitro* that hydroxyl radicals were generated by TiO₂ nanoparticles in the absence of ultraviolet light.¹⁴⁷

Aquatic species can be used for monitoring of water quality and hazard assessment of wastewaters as they respond in a predictable manner to the presence of most types of contaminants.¹⁴⁸ Hund-Rinke and Simon studied the effect of two illuminated photocatalytic TiO₂ nanoparticles (mainly *anatase*, 25 nm and 100 nm) to the green algae *D. subspicatus* and the daphnid *D.magna*, respectively. The results indicated that there was growth inhibition for the green algae. However, no toxic influence was detected with the *D. magna*.¹⁴⁹ Rincon and Pulgarin found an antibacterial effect of illuminated photocatalytic TiO₂ on pure culture of *E.coli* (K12). It was noticed that a rise of *E.coli* concentration was detected after bacteria illumination without TiO₂. However, the reduction of bacteria continued in the dark, and no regrowth was perceived within the next 60 hour in the presence of TiO₂ (photocatalysis).¹⁵⁰ Kim and Lee¹⁵¹ have shown a toxicological effect of TiO₂ NPs which might include the production of hydroxyl radicals

because of visible light generating extracellular reactive oxygen species (ROS) that may have ability to damage cell membranes.

Jing *et al.* studied the toxicities of four oxide nanoparticles (Al_2O_3 , SiO_2 , ZnO , and TiO_2) to microalgae *Chlorella sp.* and it was observed that nanoparticles of Al_2O_3 , SiO_2 , and TiO_2 (DJ3, rutile) had no substantial toxicity, while nano- ZnO (20 mg L^{-1}) and nano- TiO_2 (HR3, anatase) (30 mg L^{-1}) significantly inhibited the growth of algae with an exposure time of 6 day. Moreover, nanoscale particles demonstrated higher toxicity than that of bulk materials.¹⁵² The ecological effect of TiO_2 nanoparticles was assessed on two microalgae (*Scenedesmus sp.* and *Chlorella sp.*) which already isolated from the environment after 72 h EC_{50} exposure time. The study demonstrated the inhibitory influence of titania nanoparticles on both of the species (16.12 mg/L for *Chlorella sp.*; 21.2 mg/L for *Scenedesmus sp.*). bulk TiO_2 material also shown toxicity but lesser than nanotitania particles.¹⁵³

Three different species of freshwater algae (*S. quadricauda*, *C. moewusii*, and *C. vulgaris*) were exposed to series of TiO_2 nanoparticle concentrations to elucidate their effects on growth and metabolism of three green algae in terms of growth rates, production, and respiration. Population growth rate decreased from 11 to 27%, depending on the species. In addition, TiO_2 NPs impact on their metabolism depending on different algae.¹⁵⁴ Wang *et al.* evaluated the toxic effect of two economically important nanomaterials, titanium dioxide (TiO_2) and Quantum Dots (QDs) on unicellular green algae *C. reinhardtii* in terms of inhibition growth, oxidative stress and gene expression. The results proved that growth rate was inhibited during the first two to three days in the case of both of TiO_2 and Quantum Dots (QDs). Additionally, lipid peroxidation took place after 6 h exposure to TiO_2 and QDs.¹⁵⁵

Photosynthesis and growth inhibition has been studied through exposing nano- TiO_2 to unicellular green algae. It was found that titania nanoparticles inhibited growth rate and photosynthetic efficiency. Chlorophyll a content was not affected but chlorophyll b and carotenoid increased. It was also noticed that *C. reinhardtii* cells were damaged with increasing concentrations of TiO_2 . Lee and An¹⁵⁶ studied ecotoxic effects of zinc oxide nanoparticles and titanium dioxide nanoparticles to the green algae *P. subcapitata* under visible, UVA, and UVB irradiation conditions. Algal growth was detected to be inhibited

as the nanoparticle concentration increased, and ZnO NPs caused destabilization of the cell membranes. The growth rate of *P. subcapitata* decreased with increasing TiO₂ NPs concentration up to 72 h under all irradiation, similarly to ZnO nanoparticles which was attributed to the photo catalytic activity of TiO₂ induced by the visible light as well as UV light.

Hartmann *et al.* investigated the ecotoxicity of three different sizes of titanium dioxide (TiO₂) particles (primary particles sizes: 10, 30, and 300 nm) to the freshwater green alga *P.subcapitata* using a cold light fluorescent tube emitting light in the visible spectrum. It was consistently found that, out of three types of commercially available TiO₂ particles, the smallest TiO₂ nanoparticles type (primary particle size <10 nm) resulted in higher inhibition at lower concentrations than the two other particle types (30 and 300 nm). The mechanisms for all three types are believed to comprise of more than generation of reactive oxygen species and possible mechanisms include adhesion of TiO₂ to algal cells and physical disruption of the cell membranes.¹⁵⁷ Hong and Otaki¹⁵⁸ studied the relationship of photosynthesis and photocatalytic inhibition by TiO₂ of algal growth (*Chroococcus* sp.) by an ATP assay under ultraviolet (UV) and fluorescent light (FL) irradiations. The adverse effects on *Chroococcus* sp. growth in the TiO₂+FL+UV were higher than those in the TiO₂+UV. The difference is attributed to oxygen generated by *Chroococcus* sp. under FL irradiation.

Dalai *et al.* found that TiO₂ nanoparticle (NPs) at low concentrations ($\leq 1 \mu\text{g mL}^{-1}$), in a freshwater bacterial isolate, *B. licheniformis*, under light (UV-illuminated) and dark (non-illuminated) conditions showed a decrease in the bacterial cell viability. The difference in reduction of cell viability under light (20.7%) and dark conditions (21.3%) was statistically non-significant at $1 \mu\text{g mL}^{-1}$ concentration and 2 h exposure time. The fluorescence microscopy of the NP incubated cells ($1.0 \mu\text{g mL}^{-1}$, 2 h) under light and dark conditions exhibited a mixture of live and dead cells. A significant dose dependent increase in intracellular ROS generation compared to control was noted. The reactive oxygen species level after 2 h of incubation was considerably higher under light conditions ($7.4 \pm 0.13\%$) as compared to dark conditions ($4.35 \pm 0.12\%$). The LDH analyses confirmed a statistically significant increase in membrane permeability under dark conditions compared to the light conditions. The dominant cytotoxicity mechanism under light conditions was

found to be ROS generation, whereas, NP attachment to the cell membrane leading to membrane damage significantly contributed in dark conditions.¹⁵⁹

1. 10 Intracellular Penetration of Nanoparticles

Nanoparticles of different compositions can be assembled with different physical and chemical properties and functionalized with a myriad of ligands for biological targeting as shown in figure 1.19. Nanoparticles may be internalized in cells either by directly interacting with membrane-embedded receptors or indirectly by associating with the lipid bilayer on cell membrane. In the first approach, nanoparticles are functionalized with ligands that bind to receptors on the cell with high affinity and specificity. Ligands can be selected or engineered to target receptors on healthy and diseased cells. Internalization of the resulting receptor–ligand complexes then leads to receptor-mediated endocytosis of the nanoparticles.¹⁶⁰ Alternatively, nanoparticles can interact with the membrane via hydrophobic and electrostatic interactions and be taken into the cell through pinocytosis, a form of fluid-phase uptake where cell takes in the local extracellular environment by invaginating and pinching off pieces of the plasma membrane into vesicles containing the extracellular fluid.¹⁶¹

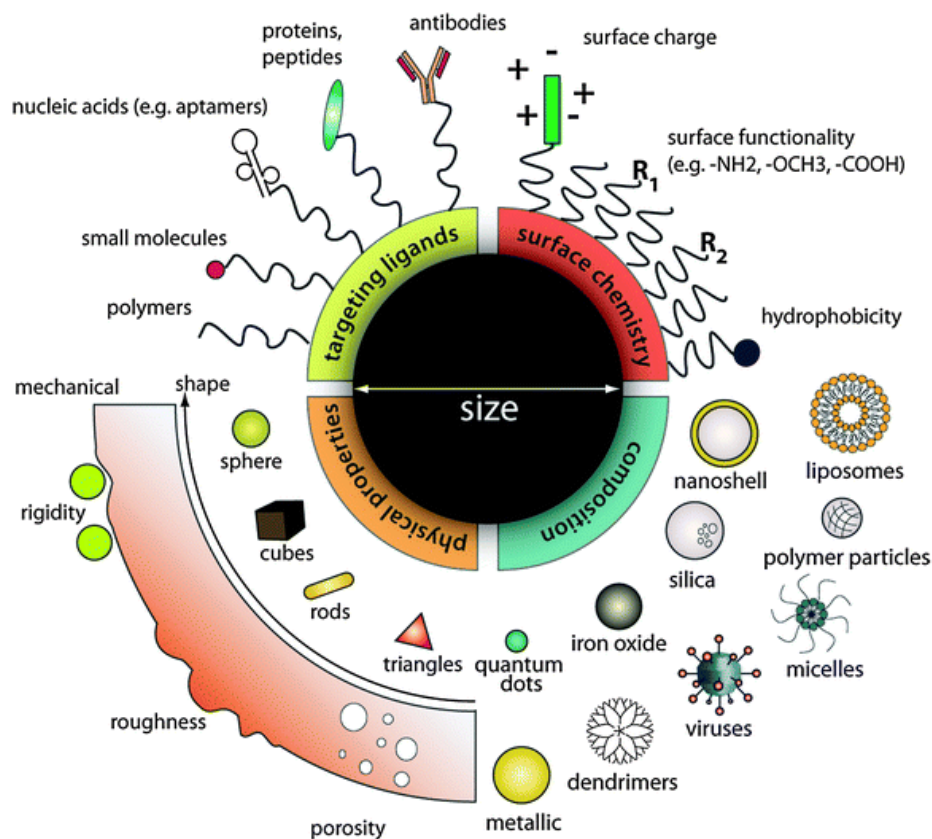


Figure 1.19: A scheme of nanomaterials functionalization for internalization whereby nanomaterials assembled with various materials that have different chemical and physical properties.¹⁶¹

For a specialized set of cells, namely macrophages, monocytes and neutrophils, nanoparticles can also be internalized via phagocytosis due to the interaction between the nanoparticles and cell membrane components.¹⁶² Nanoparticles can also internalize by endocytosis which means transportation of nanoparticles into cells within vesicles and, depending on the mode of internalization, can either be recycled and exocytose out of the cell or trafficked to organelles including the lysosomes, Golgi, and mitochondria. Endosomal trafficking is a complex intracellular process involving motor proteins that shuttle vesicles along microtubules within the cell. During this process, vesicles are sorted, fused or dissociated, as well as mature into endosomes and lysosomes (see figure 1.20).¹⁶³

Once released from the endosomal compartments, nanoparticles must travel through the cytoplasm to bind with their intracellular targets. The cytoplasm is crowded with cytoskeletal structures, proteins, nutrients and small molecules. Diffusion mobility of the nanoparticle within the cytoplasm depends on its size and interactions with these biological

entities. Binding to intracellular components may significantly retard the mobility of small particles while the geometry becomes important in the movement of larger nanoparticles.¹⁶⁴

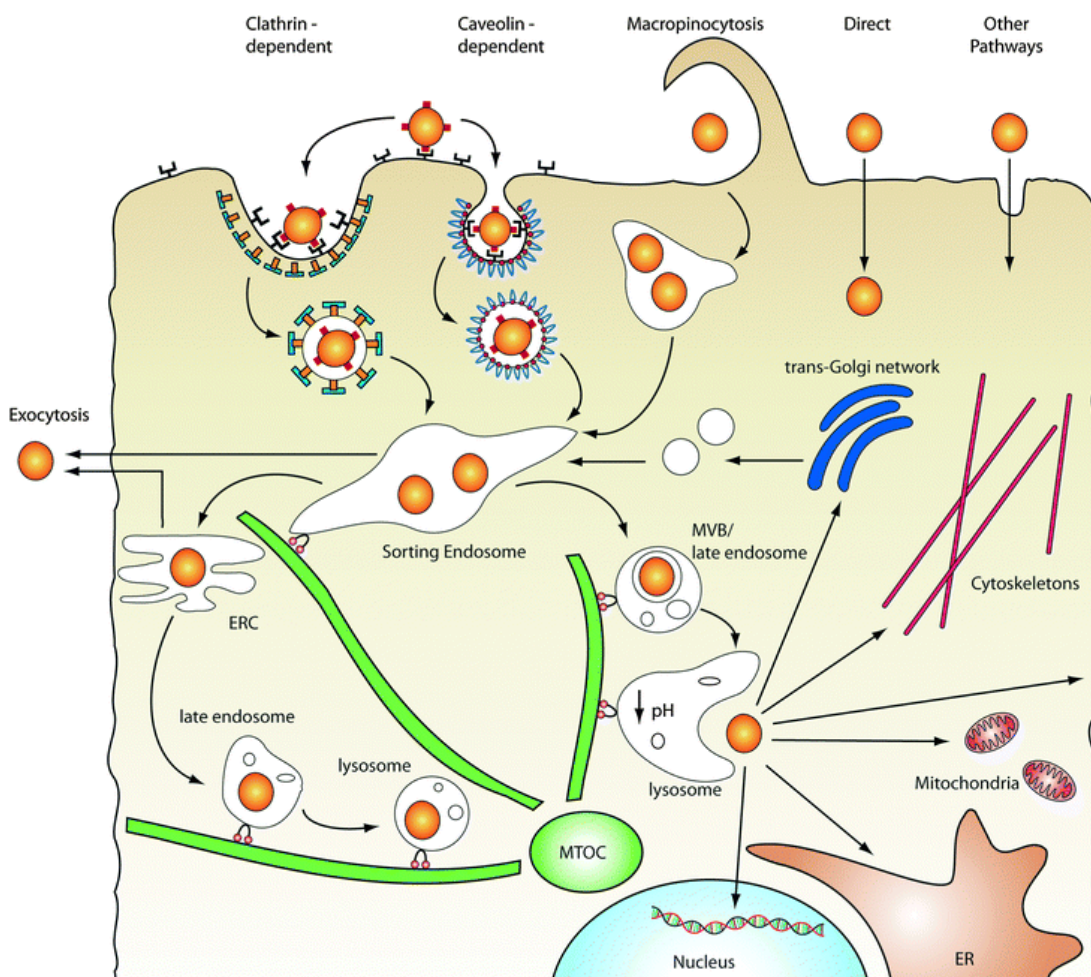


Figure 1.20: Intracellular transport of nanoparticles. After internalization via one or more of the endocytic pathways, nanoparticles are trafficked along the endolysosomal network within vesicles with the help of motor proteins and cytoskeletal structures. Vesicles can transport their contents into sorting endosomes, or excrete/recycle them back to the cell surface by fusing with the plasma membrane. Alternatively, endosomes can mature into lysosomes via luminal acidification and recruitment of degradative enzymes. Endocytic Recycling Compartment (ERC), Endoplasmic Reticulum (ER), Microtubule-organising centre (MTOC) and Multivesicular bodies (MVB)¹⁶¹

As illustrated in figure 1.21 when TiO₂ nanoparticles are internalized into cells, they can induce significant oxidative stress resulting in DNA damage and cell death. Based on these observations a hypothetical mechanism for cellular toxicity could be through the generation

of $\text{OH}\cdot$, O_2^- , and H_2O_2 in cells leading to oxidation of polyunsaturated phospholipids. The lipid peroxidation reaction subsequently causes DNA damage, GSH depletion, and disruption of membrane morphology and the electron transport chain, which leads to cell death.¹⁶⁵

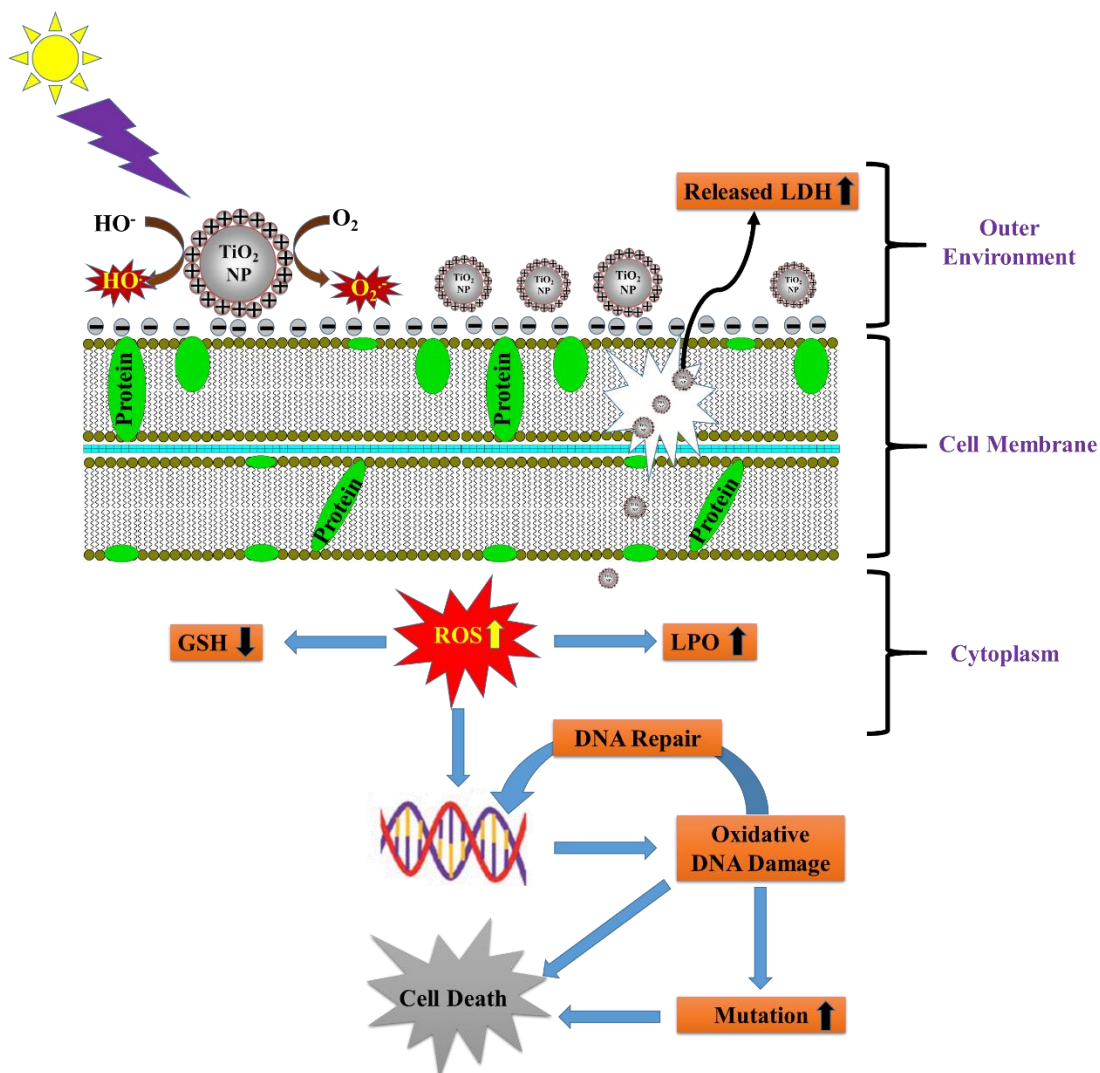


Figure 1.21: The possible mechanism of TiO_2 nanoparticles - induced genotoxicity and cytotoxicity, whereby these ROS induced either lipid peroxidation, causing LDH releasing, or inhibition of glutathione peroxidase or DNA damage. Lactate Dehydrogenase (LDH); Reduced Glutathione (GSH); Lipid Peroxidation (LPO).

1.11 Nanomaterials for Drug Delivery

In the treatment of diseases, drugs are often injected directly into the blood stream. However, only a minor portion of injected drugs deliver to, and act in, the diseased tissue site.¹⁶⁶ Drug delivery is a developing field focused on targeting drugs or genes to a desirable group of cells as shown in figure 1.22. The goal of this targeted delivery is to transmit proper amounts of drugs to the desirable sites (such as diseased tissues, tumors, etc.) using nanocarriers while reducing unwanted side effects of the drugs on other tissues.¹⁶⁷ The nanomaterials for drug delivery must be biocompatible, nontoxic, biodegradable and nonimmunogenic. The most common drug delivery nanocarriers include liposomes, polymeric micelles and dendrimers, artificial DNA structures, and biodegradable scaffolds.¹⁶⁸

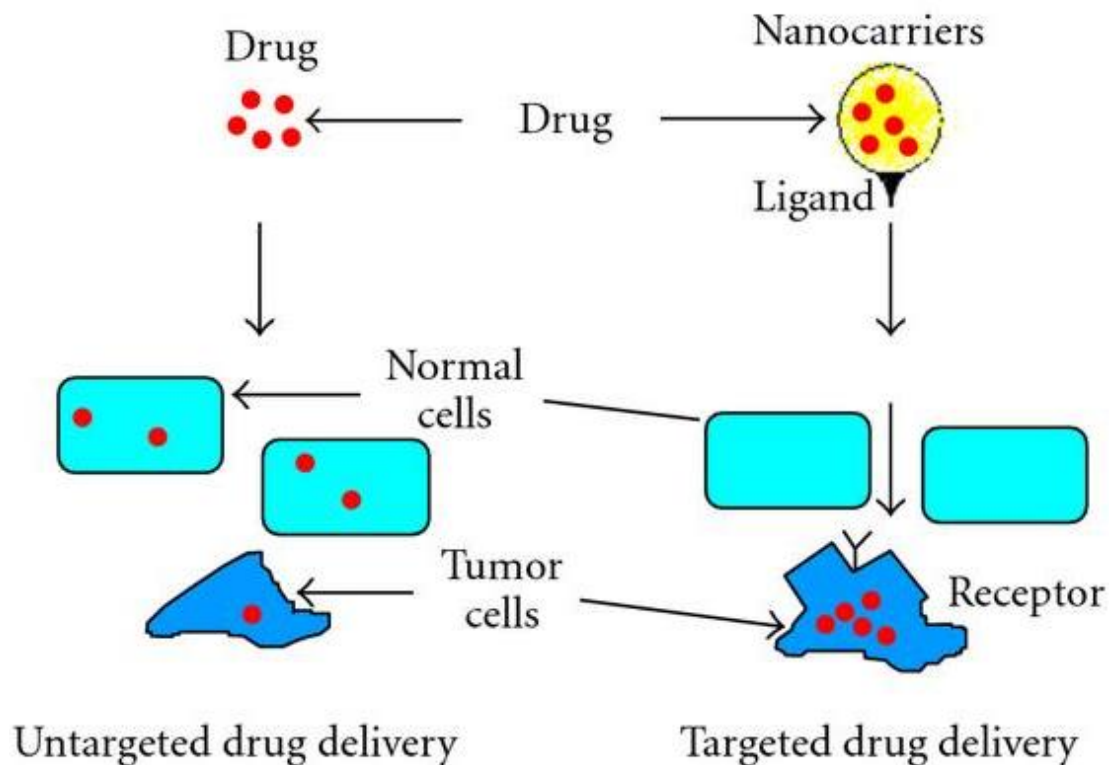


Figure 1.22: Untargeted and targeted drug delivery.¹⁶⁹

1. 12 Microgel as a Nanocarrier

Microgels are cross-linked polymeric particles. When the microgels size is in submicrometer range, they are known as nanogels.¹⁷⁰ Microgels are produced by physically or chemically cross-linking polymer networks that swell in an aqueous solvent. This swelling occurs due to the absorption of water facilitated by the presence of hydrophilic groups such as ether, sulphate, hydroxyl and carboxyl groups which are present in polymer chains.¹⁷¹ Cross-linked bifunctional networks of a polyion and a nonionic polymer (cross-linked polyethyleneimine (PEI) and poly (ethylene glycol) (PEG) or PEG-*cl*-PEI) as microgels were utilized for delivery of polynucleotides.¹⁷²

1. 13 Design of Nanocarriers as a Drug Delivery System

1. 13.1 Biocompatibility and degradability

Good biocompatibility is vital for any nanomaterials used for therapeutic reasons so that the nanocarriers do not evoke any harmful biological responses at the molecular, cellular or organ levels when utilized.¹⁷³ Biocompatibility is usually measured using cell toxicity and cell viability assays which have shown an absence of cytotoxic effects for many different nanocarriers formulations. It is also vital for clearing nanocarriers from the body into non-toxic degradation products of adequately small size and of chemical composition that do not provoke any adverse responses such as allergy, blood clot formation, or induce disease states such as cancer.^{174, 175}

1. 13.2 Swelling behavior

Nano and microgels swelling are organized by multiple factors in aqueous environments, including: (i) the cross-linking concentration. At high ionic strengths, the swelling of cationic nanocarrier gels has been shown to be dependent mainly on the cross-linker concentration, while at low ionic strengths nanocarrier gel swelling is based on both the cross-linker and the charge concentration;¹⁷⁶ and (ii) environmental factors such as temperature, pH and ionic strength. Core-shell nanocarrier gels consisting of cross-linked poly(ethylene glycol)-b-poly(methacrylic acid) (PEG-b-PMA) became swollen with increasing pH due to ionization of carboxylic groups within the PMA.¹⁷⁷ Alternatively,

PEG-cl-PEI nanogels collapsed when the pH was increased from 8.5 to 10, as a result of deprotonation of amino groups within the PEI.¹⁷⁸

1. 13.3 High encapsulation stability

Drug molecules loaded into nanocarriers must be retained, and not be transported out or leak prematurely while circulating in the body in order to deliver maximum therapeutic effects and lowest toxicity or side effects. Cross linking of the polymer constituents within the nanocarrier can be used to control drug encapsulation and drug release.¹³⁹ Therefore, upon designing a drug delivery vehicle, the encapsulation stability is an important feature that needs to be addressed. Accidental leakage can result in the supply of drug molecules to healthy cells leaving a nearly empty nanocarrier upon arrival at the disease site, as illustrated in figure 1.23.¹⁷⁹

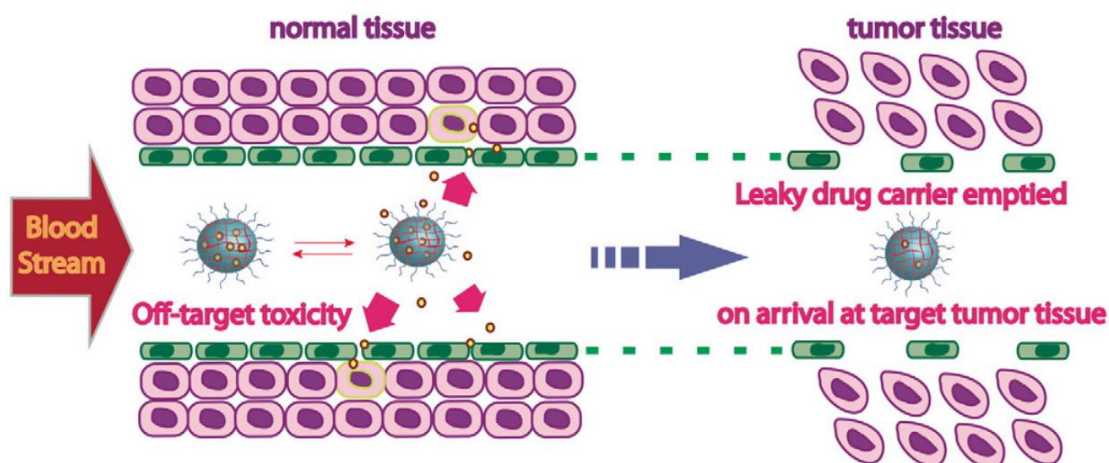


Figure 1.23: Off –target toxicity of unstable leaky delivery carriers.¹⁷⁹

Drug loading into nanocarrier can be accomplished using a variety of strategies. These include:

- (i) Covalent conjugation of biological agents, which is achievable either during or following nanocarrier synthesis. Copolymerization of modified enzymes with acrylamide was conducted in both inverse microemulsion¹⁸⁰ and dilute aqueous solutions¹⁸¹ to produce nanosized hydrogels.

- (ii) Physical entrapment of compounds within nanocarrier. This approach was used to incorporate proteins into cholesterol-modified pullulan nanogels¹⁸² and siRNA into hyaluronic acid or HA nanogels.¹⁸³ Amphiphilic cross-linked nanogels whose formulation is based on PEG and pluronic F127 were utilized to load and release doxorubicin drug.¹⁸⁴
- (iii) Passive/diffusion-based drug loading. Dextran-lysozyme nanogels have been used for loading silver nanoparticles^{60, 185} and dexamethasone⁶¹ separately by diffusion alone, through incubation of nanogels in excess drug or nanoparticle solution on a shaker.

1. 13.4 Controlled and sustained drug release

Drug transport should happen at the targeted site, thereby producing both therapeutic efficacy and lessened side effects. Drug loading necessarily needs to be high to accomplish therapeutic goals.¹³⁹ Encapsulation of a delivery system is regularly stated in terms of its percent drug loading capacity i.e. the weight percent of the drug loaded per unit weight of the delivery vehicle. However, it is notable that percent loading is simply the thermodynamic distribution coefficient of the drug molecule between the interior of the nanocarrier and the bulk solvent (aqueous phase).¹⁷⁹

Drug release from nanocarriers occurs by multiple mechanisms. The diffusional release of dexamethasone from dextran lysozyme nanogels was sufficient to improve the development of pulmonary inflammation in a murine model of lung injury,⁶¹ whereas silver nanoparticle exposure from the same nanogel inhibits bacterial growth.⁶⁰ *In vitro* diffusional doxorubicin release from amphiphilic cross-linked nanogels was sustained for up to one week.¹⁸⁴

Nanocarriers can also release drugs when the nanocarrier structure is biological or chemical degradable. For examples, the release of doxorubicin from pH-sensitive drug-loaded nanogels was considerably enhanced at lower pH values, which led to increased drug uptake by lung carcinoma cells under a slightly acidic pH condition.¹⁸⁶ Moreover, nanogels were developed to release compounds in response to other environmental cues. Disulphide cross-linked POEOMA nanogels biodegrade and release cargo upon exposure to glutathione tripeptide, which is commonly found in cells.¹⁸⁷

1.13.5 Response to stimuli

Stimuli responsive nanocarriers must retain high drug encapsulation stability while injected in the blood stream. The drug should release readily in response to the proper stimulus upon arrival to the targeting site.¹³⁹ This can be accomplished by combining chemical moieties into the design that make the carrier responsive to stimuli applicable to the disease being targeted. There are two types of stimuli: chemical and physical that can be engineered into delivery systems. When covalent bonds occur between drug and the delivery carrier, a chemical response is required to cleave the linking bond between the carrier and the drug. This chemical response could be triggered by an enzymatic reaction, a reaction with biological chemicals, redox, changes in pH, or even by an external stimulus such as light. However, if the encapsulated drug is trapped through a physical or supramolecular interactions, the delivery carrier could be either engineered to release the drug because of a chemical response, as shown above, or a physical change in the structure of the vehicle, such as swelling triggered by temperature, pH, etc.¹⁷⁹

1.13.6 Targeting

One of the most recognized benefits of utilizing nanoparticles as drug carriers is to enable targeted delivery to the desirable sites of intervention – organs, tissues, cells and their compartments, pathological formations such as thrombi, etc. Delivery to these sites is impeded by clearance from the bloodstream via “non-specific” uptake in tissues including the vascular system (i.e., binding to endothelial and blood cells), reticuloendothelial system (RES, including the liver, spleen and lymphatic nodes) and excretory organs including kidneys, lungs, and the bile tract.^{187, 188} Site-specific delivery of nanocarriers can be achieved either by coupling to their surface affinity ligands, binding to target determinants, or using responsiveness to local factors as explained in section 1.13.5, or via “passive” targeting approaches including extravasation in the pathological sites and retention in the microvasculature.¹³⁹

1.13.6.1 Passive targeting

In some cases, nanocarriers “passively” gather at desired sites. Nanoparticles typically exhibit circulation times that can be systematically varied and if desirable, extended to allow for the sufficient time of blood perfusion to deliver the cargo to a target site. In

addition, the increased retention of nanoparticles within the blood pool, due to their inability to diffuse across continuous (i.e., non-fenestrated) endothelium, is often associated with a reduction in off-target toxicity.¹⁸⁹ Currently, it is purported that most pre-clinical and all FDA-approved nanoparticles for oncologic purposes passively accumulate at their target site (pathophysiological targeting) as a consequence of enhanced permeability and retention (EPR) effects as illustrated in figure 1.24.¹⁹⁰

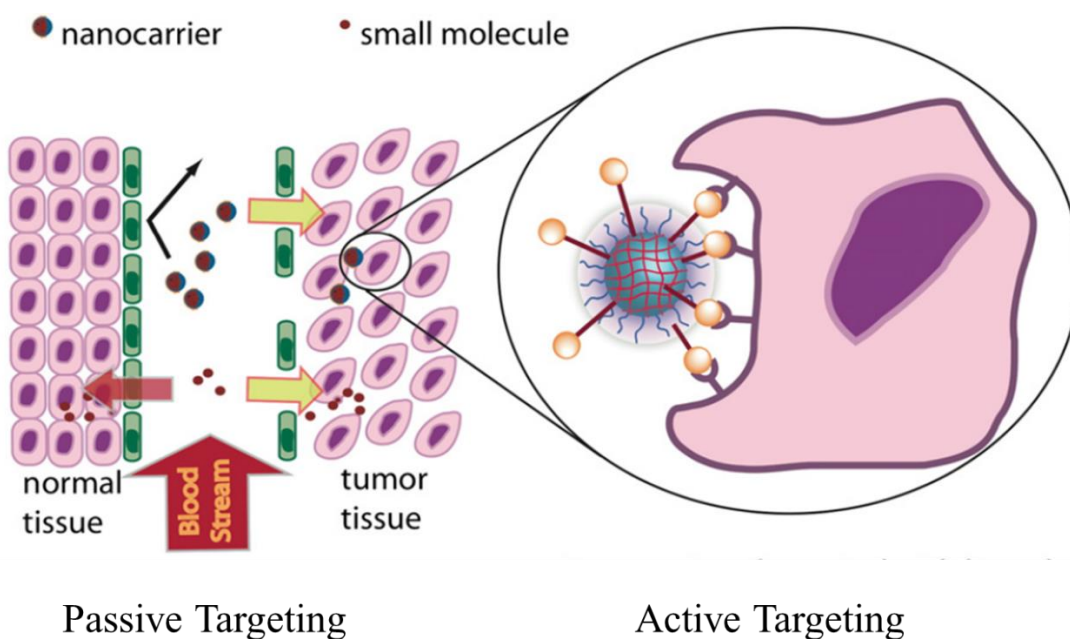


Figure 1.24: The concept of passive targeting through the EPR effect and active targeting through ligand display.^{179, 190}

The EPR stems from the abnormal increase in vascular permeability that arises during the pathogenesis of a wide range of diseases including inflammation and solid tumors, allowing nanoparticles to deposit in the extracellular space. In some cases, such as in cancer, nanoparticle retention may be heightened due to impaired lymphatic drainage. The EPR effect is highly variable between diseases, organs, and even within a single pathological site. For example, EPR is not commonly observed in gastric and pancreatic cancer,¹⁹¹ and in most tumors at least some of the vasculature remains intact. In contrast, some regions may be extremely permeable, allowing submicron nanoparticles to penetrate

into the interstitium.¹⁹² Although passive targeting continues to be the primary mechanism by which most new nanoparticle formulations reach their target site, there has been a general movement towards the use of active targeting to complement EPR.

1.13.6.2 Active targeting

“Active targeting” mediated by affinity ligands coupled to a carrier is a more precise and universal approach. It uses ligands that bind to molecules present or enriched in a cell, tissue, or pathological structure of interest (target determinants). Antibodies, their fragments and recombinant polypeptides including single chain antigen binding fragments (scFv), nutrients, hormones, mediators, receptor ligands, peptides, aptamers, and nucleic acids have been explored as targeting ligands as shown in figure 1.14.^{63, 193-196} Recently, lipid derivatives such as choline group containing molecules have also shown significant promise for active targeting.^{197, 198}

Target determinants must meet numerous criteria in order to be useful for drug delivery. First of all, they must run binding or anchoring of carriers. For this purpose, determinant molecules should exist at the site of interest in sufficient surface density on the target cell, tissue or structure accessible to allow anchoring of ligand-directed carriers. Secondly, binding to the target determinants have to not cause side effects that may hinder or defeat the purpose of the intended medical intervention. Third, anchoring to the target determinants should favor subsequent addressing to the sub-cellular compartments where the drug cargo is supposed to serve.¹³⁹ The foreseen advantages of active targeting include higher specificity, higher accumulation of nanoparticles at the target site and an increase in the intracellular penetration of nanoparticles, all of which probably lead to an improved therapeutic index. however it is usually known that actively targeting vascular biomarkers can refine the accumulation and specificity of nanoparticles at a disease site.¹⁹⁹

In this work, Carbopol Aqua SF1 as a derivative of polyacrylic acid polymer was used to encapsulate individually two antimicrobial agents (berberine and chlorhexidine). Stability of carbopol microgel, biocompatibility and biodegradation, the encapsulation efficiency, controlled drug release, and toxicity were investigated. The reason for choosing Carbopol Aqua SF1 is because this material is not toxic and biodegradable and it needs to be discovered as a nanocarrier in drug delivery system. the encapsulated medicines were then incubated with algae, yeast and E.coli to improve and control the antimicrobial actions

of these medicines where berberine has low antimicrobial action²⁰⁰ while chlorhexidine has high antimicrobial action which causes some side effects,²⁰¹ therefore, they need to be encapsulated to control the amount of medicine released.

1. 14 Carbopol Aqua SF1 Polymer

Carbopol compounds have plenty of applications in the industry, medicine, and cosmetics due to the biocompatibility, and with no side effects upon biodegradation. Carbopol Aqua SF-1 polymer is a lightly cross-linked and highly hydrophilic acrylic polymer as shown in Figure 1.25 dispersion considered to provide suspending, stabilizing, and thickening properties to a diversity of surfactant-based personal cleansing products. It is milky, white liquid with a low acrylic odor, comprising 30% active polymer in water that is simply pumped, poured and diluted into aqueous formulations. Having a low viscosity it is easily and quickly combined, providing significant suspending and stabilizing properties to formulations with insoluble and difficult-to-stabilize ingredients, such as silicones. It is also capable of thickening shampoo, body wash and other cleansing formulations to their ideal viscosity and offering highly favorable flow characteristics and allowing the formulation of highly transparent shampoos and body washes at neutral pH. The polymer is highly active in surfactant based formulations over a wide pH range from 3.5 to 10 or higher. Furthermore, it is compatible with almost all commercial nonionic, anionic and amphoteric surfactants in addition to a wide array of popular additives and conditioning agents, such as cationic polymers.²⁰²

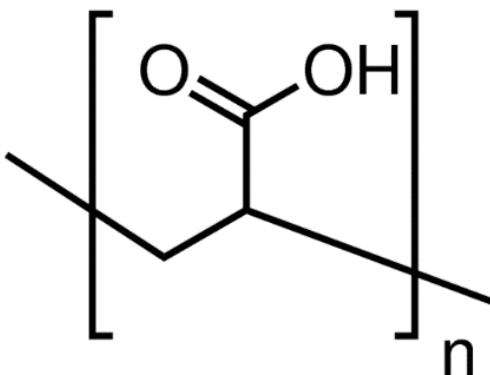


Figure 1.25: The chemical structure of Carbopol Aqua SF1 (Poly Acrylic Acid)

As purchased, the majority of the polymer's carboxyl functionality is in the protonated form; the polymer molecules are coiled and impart moderately little suspension and viscosity to the liquid. Upon neutralization, the molecules ionize and expand because of charge repulsion of the anionic carboxylate and this provides suspending and thickening properties. This mechanism is known as "hydrodynamic" thickening. In hydrodynamic thickening theory, it is the physical packing of the polymer molecules (and possibly other formula ingredients) that effects the suspending ability and viscosity. This "space-filling" mechanism is different from the associative thickening mechanism attributed to hydrophobically modified polymers. Therefore, it is well used in the 2-in-1 conditioning shampoos. Additionally, in terms of toxicity the carbopol Aqua SF1 polymer does not exhibit any toxicity towards animal organs and some microorganisms.²⁰²

Ocular drug delivery systems require muco/bioadhesive polymers which elongate the residence time at the site of drug absorption. They ensure optimal contact between the formulation and the absorbing surface to enhance the bioavailability of topical administration.^{203, 204} Carbopol resins, have been widely used for the ocular drug delivery systems due to their excellent mucoadhesive property.²⁰³ Tang *et al.* (2005) synthesized superporous hydrogel composites (SPHCs) based on aqueous carbopol solution. Carbopol 934P and 974P are able to swell quickly in water as a result of the crosslinking bond in the structure and adhere to the intestinal mucus due to the functional groups (COOH) to form hydrogen bridges to interpenetrate the mucus layer. *In vitro* study of the bioadhesive force observed that the SPHCs adhered to the intestinal mucosal more rapidly and displayed higher mucoadhesion as compared to superporous hydrogel (SPH).²⁰⁵ Silver nanoparticles were formulated with Carbopol 980 NF polymer to evaluate its wound healing efficacy on rat model *via* visual observation, transepidermal water loss and histology of skin. It was proved that AgNPs-based gel presented superior wound healing efficacy as compared to marketed formulations and silver ions.²⁰⁶ Lin and Sung (2000) showed that the carbopol/pluronic solution had an improved capability of holding drug compared to the carbopol or pluronic solutions alone. The results demonstrated that the carbopol/pluronic mixture can be utilized as an *in situ* gelling carrier to improve the ocular bioavailability.²⁰⁷

A mucoadhesive ophthalmic drug delivery system comprising puerarin based on Pluronic P407/P188 and Carbopol 1342 have demonstrated that combining either 0.1% or

0.2% Carbopol 1342 into Pluronic P407/P188 solution would significantly refine the mucoadhesive force. The combined solutions had better drug retaining than poloxamer analogs or carbopol alone. It also appears that ocular bioavailability can be increased more readily by using the in situ gelling and mucoadhesive vehicle. Therefore, the combined systems can be used as the ocular in situ gelling and mucoadhesive vehicles to enhance bioavailability.²⁰⁸

1.15 Berberine

Berberine (Fig. 1.26) is a bright yellow isoquinoline quaternary alkaloid (or a 5,6-dihydrodibenzo[a,g] quinolizinium derivative) extracted from many kinds of medicinal plants such as *Hydrastis canadensis*, *Berberis aristata*, *Coptis chinensis*, *Coptis rhizome*, *Coptis japonica*, *Phellodendron amurense*, *Phellodendron Chinese schneid*.²⁰⁹ The alkaloid has brought wide attention as a therapeutics against a number of diseases including hyperlipidemia, diabetes, metabolic syndrome, polycystic ovary syndrome, obesity, fatty liver disease, coronary artery disease.²¹⁰

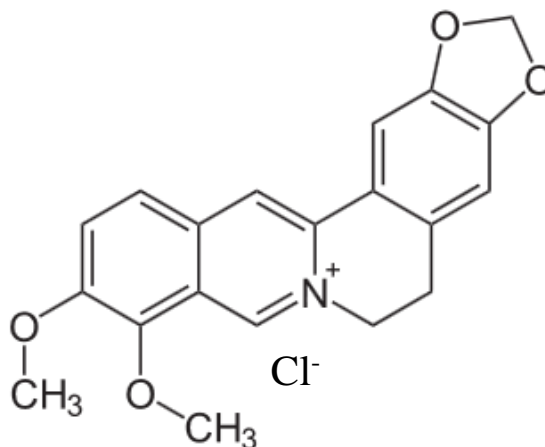


Figure 1.26: The chemical structure of berberine.

Berberine has a definite potential as drug in a wide spectrum of clinical applications. Berberine shows a broad array of pharmacological effects, being effective against gastroenteritis, abdominal pain and diarrhea, and having antimicrobial, antidiabetic and anti-inflammatory properties.^{209, 211, 212} Berberine employs antimicrobial effects being a NorA substrate able of gathering in bacterial cells and of binding both single and double-stranded DNA, thus causing bacterial death by DNA damage.²⁰⁰

It has a weak activity against Gram-negative bacteria²⁰⁰, and is more powerful against Gram-positive bacteria, such as *Mycobacterium tuberculosis* and MRSA (Methicillin-Resistant *S.aureus*), by the multi drug resistant (MDR) pump NorA inhibition.^{200, 213, 214} It also shows antifungal activity on *Aspergillus*, *Penicillium*, *Candida*, and *Cryptococcus*.^{209, 212} Berberine has anti-inflammatory activity by inhibiting the production of tumor necrosis factor- α (TNF- α), interleukin-6 (IL-6) and monocyte chemoattractant protein 1 (MCP-1). Moreover, it affects prostaglandin E2 (PGE2) production and exudate production, and down-regulates the expression of COX-2, matrix metalloproteinase (MMP)-2 and -9 (MMP-9) through mitogen-activated protein kinase (MAPK) and NF- κ B signaling pathways.²¹⁵

Berberine has been encapsulated in nanoparticles to form (Berberine Chloride-O-Hexadecyl-Dextran NPs) (BC-HDD NPs). Upon incubation with glucose stressed hepatocytes, a decrease in ROS generation, oxidative stress, caspase activation, prevention of depolarisation of mitochondria, and lipid peroxidation was detected in BC-HDD NPs treated cells in comparison with bulk berberine.²¹⁶ Tsai *et al* (1999) merged berberine into a chitosan hydrogel to design a transdermal delivery system for the treatment of cutaneous leishmaniasis. The results showed that only trace amounts of berberine passed through the rat skin; therefore, they used some surfactants such as Tween 80 to increase the loading of berberine in the skin.²¹⁷

Chang *et al.* (2011) have developed a novel nanocarrier with a heparin shell for berberine delivery to treat *H. pylori*. *In vitro* analysis of drug release from the nanovehicle designated that the system was able to control berberine release in a simulated gastrointestinal dissolution medium, and that the berberine was able to localize specifically to intercellular spaces or in the cell cytoplasm, the site of *H. pylori* infection. The prepared berberine/heparin/chitosan nanoparticles were capable of increasing the values of *H. pylori* growth inhibition, compared with berberine alone in solution.²¹⁸ Lin *et al.* (2014) used berberine-loaded fucose-chitosan/heparin nanoparticles to obtain an enhanced suppressive effect when they interact with *H.pylori* and effectively reduce gastric inflammation in an *H. pylori*-infected animal study.²¹⁹

Berberine has been shown to be a potent anti-diabetic agent but this efficacy can hardly be achieved using conventional oral dosage forms. To refine oral bioavailability and

anti-diabetic efficacy of berberine (BER), a new anhydrous reverse micelle (ARMs) delivery system was successfully prepared for berberine. *In vivo* measurements on diabetic mice confirmed that BER-loaded ARMs reduced the blood glucose by 57% of encapsulated berberine in comparison with 22% blood glucose level upon intravenous injection of berberine solution. Berberine loaded ARMs could remarkably enhance drug oral bioavailability and thereby anti-diabetic efficacy.²²⁰

Berberine hydrochloride (BH) has been shown to have promising anticancer efficacies through a solid lipid nanoparticle (SLN)-based delivery system. Berberine-loaded SLNs showed high drug encapsulation efficiency and drug-loading, and the release of berberine from the SLNs was significantly slower than free berberine. The *in vitro* study indicated that berberine-loaded SLNs more considerably inhibited cell proliferation on MCF-7, HepG 2, and A549 cancer cells. Berberine-loaded SLNs also enhanced the antitumor efficacies of BH on MCF-7 cancer cells.²²¹ Berberine has also revealed anticancer activity against human hepatic carcinoma in a murine xenograft model in a liposomal berberine formulation using a thin film hydration /extrusion method. This method showed a high encapsulation efficiency with higher growth inhibition of HEpG2 cells that of berberine alone. Moreover, *in vivo* studies confirmed that the liposome efficiently decreased the berberine elimination rate in both plasma and tissue, and liposomal berberine effectively reduced the size and weight of tumors as compared with the untreated tumor control.²²²

PLGA (polylactide glycolic acid) nanoparticles were prepared using an emulsification method. Berberine was loaded onto PLGA nanoparticles by single emulsion as well as multiple emulsion solvent evaporation techniques. *In vitro* drug release analysis demonstrated that acidic pH of 5.5 was more suitable for berberine release than pH 7.4.²²³ Yeast cells of *S.cerevisiae* were utilized for encapsulating berberine as novel carriers for the food and drug industries. Analytical methods proved that berberine was encapsulated in the yeast cells. The results confirmed that *S.cerevisiae* could be an efficient and safe carrier for active materials.²²⁴ Likewise, berberine hydrochloride was encapsulated into alginate microspheres via an emulsification/gelation method. Those drug-loaded microspheres were further trapped into carboxymethyl chitosan (CMC) hydrogel to form a new drug-delivery system (DDS). The results revealed that the swelling ratio has a

minimum at around pH 3.0 and a maximum within a pH range 8–10. DDSs composed of alginate microspheres and CMC decreased the burst effect of the alginate microspheres.²²⁵

Berberine-loaded chitosan/ fucoidan-taurine nanoparticles were developed and served as an epithelial protective material to prevent redistribution of TJ protein caused by bacterial endotoxin (LPS). The pH-responsive nanoparticles were stable at pH 2.0 but became unstable when the pH increased to 7.4. The release rate of berberine from the nanoparticle was slow in simulated gastric fluid (SGF) but fast in simulated intestinal fluid (SIF). These findings suggested that the berberine-loaded nanoparticle is a potential carrier for site-specific delivery of berberine to the intestine for the inhibition of impaired intestinal barrier function.²²⁶ Hydrogel composites also were prepared using a cross linking method with variable amounts of gellan gum and polyvinyl alcohol loaded with berberine and its functionalization to gold nanoparticles. It was clear that this addition system produced a composite which considers the most suitable drug delivery system for berberine, due to all characteristics (higher encapsulation efficiency) of the matrix structure, creating a promising drug delivery system for delivery hydrophilic drugs.²²⁷

1.16 Chlorhexidine

Caries and periodontal disease are the most widespread oral diseases in humans which are related with dental plaque. The removal of dental plaque is a crucial component in the prevention and treatment of such diseases. The use of mechanical agents is a simple and economical method that was validated in the control of gingivitis.²²⁸ However, the efficiency of this method is affected by the individual's manual dexterity and motivation. Therefore, there is a great attention to the use of antimicrobial agents to replace or to be adjuncts to the mechanical methods. Chlorhexidine (CHX) is one of the most effective antimicrobial agents for dental plaque control.^{229,230} 10 ml of 0.2% chlorhexidine gluconate solution can be used for rinsing for 60 s twice a day in the absence of normal tooth cleaning, leading to inhibit plaque regrowth and the increase of gingivitis.²³¹ Chlorhexidine gluconate (CHX), a cationic bisbiguanide and a strong base is more stable in the form of its salts. The original salts were chlorhexidine acetate and hydrochloride, which are relatively sparingly soluble in water. Therefore, they have been swapped by chlorhexidine digluconate. CHX belongs to the polybiguanide antibacterial family, consisting of two

symmetric 4-chlorophenyl rings and two biguanide groups linked by a central hexamethylene chain (Fig. 1.27). CHX digluconate salt is easily soluble in water.^{232, 233} It is one of the most frequently used chemotherapeutic agents against oral diseases. This is because of its wide spectrum of activity against yeasts, Gram positive, and Gram negative bacteria as well as many anaerobic pathogens.²³⁴ The mechanism of action is due to its cationic nature which links to anionic compounds on the bacterial surface such as phosphate groups of teichoic acid in Gram positive and lipopolysaccharide in Gram negative bacteria and disrupts bacterial integrity.²³⁵ This leads to leakage of the cell constituents and eventually cell death.²³⁶

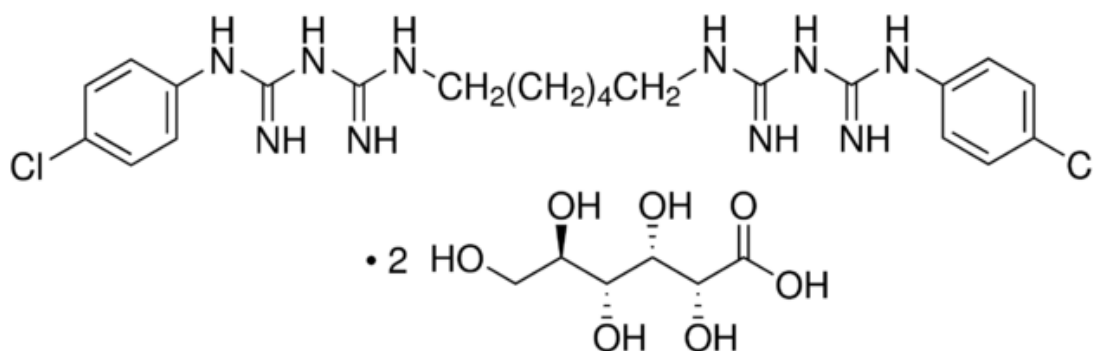


Figure 1.27: The chemical structure of chlorhexidine digluconate.

The substantial effects of chlorhexidine on plaque and gingivitis were attributed to the decline of pellicle formation and attachment of bacteria on the tooth surface.²³⁷ However, prolonged usage of chlorhexidine carries with it numerous side effects such as disturbances in taste sensation, teeth staining, and increased dental accumulation.^{201, 238} Another important subject is the release mechanism, to improve the effectiveness of chlorhexidine it is more desirable to release it slowly over a prolonged period of time, this ensures a greater reduction of microorganisms (longer exposure time). A recent and practical release system is the combination of microfibrillated cellulose (MFC) and β -cyclodextrin (β CD) that produces a large dosage of chlorhexidine gluconate over a prolonged period of time, MFC is known for its burst action whilst β CD is a slow releasing drug delivery agent.²³⁹ It might be beneficial to see a mixed composition of chlorhexidine with possibly calcium hydroxide or fluoride and the incorporated MFC/ β CD mechanism.

It is important to be aware of other interactions between the cationic biguanides such as chlorhexidine and other antimicrobial actives such as titanium oxide where the chlorhexidine binds more favorably with anatase rather than rutile.²⁴⁰ It is also possible to use mesoporous nanoparticles combined with nano-chlorhexidine; exposing 50 mg of mesoporous silica nanoparticles to 4 ml of 50 mg of chlorhexidine dissolved in 5ml ethanol produces a nanoparticle chlorhexidine release system that effectively targets planktonic and biofilm modes of oral pathogens.²⁴¹ An implantable, anti-microbial delivery device for the treatment of periodontal disease was prepared by single emulsion/ solvent evaporation technique according to the association complex of microparticles of poly (dl-lactic-co-glycolic acid) (PLGA) containing chlorhexidine (CHX) free base, chlorhexidine digluconate (Chx-Dg) with methylated- β -cyclodextrin (MBCD) and hydroxypropyl- β -cyclodextrin (HPBCD). It was observed that complexation of the poorly water soluble CHX with the more hydrophilic HPBCD resulted in 62% higher encapsulation efficiency and longer duration of sustained release over a 2-week period than complexation with the more lipophilic MBCD. However, the more water-soluble derivative of chlorhexidine, CHX-Dg incorporated with the more lipophilic MBCD enhanced encapsulation efficiency by 12% and prolonged its release as compared with both the free CHX-Dg and its complex with HPBCD. Biologically it is proved that the chlorhexidine released from PLGA chips is active against bacterial population that is relevant in periodontitis (*P. gingivalis* and *B. forsythus*) and a healthy inhibition zone is maintained in agar plate assay over a period of at least a 1-week.²⁴²

A thermosensitive hydrogel system was prepared from an inclusion complex between β -cyclodextrin and chlorhexidine, then the latter was merged into the chitosan. Then, the human bone morphogenetic protein-2 (rhBMP-2) was added to the hydrogel simultaneously. The *in vitro* drug release demonstrated that the rate release of both chlorhexidine and rhBMP-2 from hydrogel become slower with continuous release up to a month.²⁴³ A drug delivery system consisting of (meth) acrylic microparticles containing chlorhexidine digluconate was prepared by the non-aqueous emulsion/solvent evaporation method. The particles were micrometer-sized, heat-stable and amorphous/non-crystalline formulations with drug-loading efficiencies higher than 90%. Drug-loaded (meth) acrylic microparticles as compacted tablets provided a significant decrease of dissolution rate of

chlorhexidine digluconate. Therefore, these formulations are possible carriers for controlled release of chlorhexidine digluconate and can be used in additional innovative skin and oral products proposed for a long-lasting antiseptic effect.²⁴⁴

Chlorhexidine-loaded polyurethane was prepared as a material suitable for the fabrication of devices which are able to resist microbial contamination. *In vitro* release of chlorhexidine diacetate and digluconate from orthodontic chains loaded with 10% or 20% (w/w) chlorhexidine salt was sustained for 42 days. The drug diffusion through the polyurethane was found to depend not only on chlorhexidine loading, but also on the chlorhexidine salt. The antibacterial activity of 0.2% (w/w) chlorhexidine diacetate-loaded orthodontic chain was successfully examined towards *Staphylococcus epidermidis* via agar diffusion test. Thus, the chlorhexidine salt-loaded chains could provide an advanced approach in the prevention of oral infections related to the use of orthodontic devices.²⁴⁵

Therapeutic activity of locally applied drugs depends on both the pharmaceutical system which enables the release of the molecule and the thermodynamic activity of the active molecule as well as the vasoconstrictive activity of vessels plays a vital role. The release of chlorhexidine was assessed according to the use of methylcellulose (MC) and poly (acrylic acid) (Carbopol 934P NF) (PA) polymeric carriers at temperatures in the range between 22°C and 42°C as well as the temperature of 32°C as the reference surface body temperature. The released drug increases with the temperature after 10 h and is higher in the case of the MC system: the greatest difference detected between the MC-CHX preparations was about 35 %, whereas for PA-CHX, the difference was only 0.5 % of the initial amount of the drug in the donor compartment. This study is important for patients with various surface body temperature conditions, who needed to receive local biocides applied on skin or into the oral cavity.²⁴⁶

Chlorhexidine base loaded PCL nanocapsules, prepared by interfacial polymer deposition /solvent displacement yields relatively monodisperse particle size and stable positively charged nanocapsules with good encapsulation efficiency.²⁴⁷ The study described a sustained release of chlorhexidine base from PCL nanocapsules by mediating a more direct and prolonged contact between the nanocapsules and bacteria, skin surface, and skin follicles and provided a prolonged *ex vivo* topical antimicrobial activity against *Staphylococcus epidermidis*.²⁴⁷ Wound treatment needs molecules that both improve

healing and control infection. Hence, Poly (lactic-co-glycolic acid) (PLGA) microspheres based drug delivery system was prepared by a double emulsion process. This system simultaneously transports platelet-derived growth factor (PDGF)-BB, a hydrophilic protein known to stimulate wound healing, and chlorhexidine (CHX), an antimicrobial agent for infection treatment. CHX encapsulation efficiency was $19.6 \pm 0.8\%$ and $28.9 \pm 1.5\%$ for PLGA 50:50 and 85:15 (w:o) ratio, respectively. This can improve healing and decrease bacteria levels in an infected wound model.²⁴⁸ Fini *et al.* were investigated the *in vitro/ex vivo* buccal release of chlorhexidine salt (CHX) from nine mucoadhesive aqueous gels in addition to their physicochemical and mucoadhesive properties. The mucoadhesive/gel forming materials were carboxymethyl- (CMC), hydroxypropylmethyl- (HPMC) and hydroxypropyl- (HPC) cellulose, alone (3% w/w) Orin binary mixtures (5% w/w); gels. The results proved that combination of HPMC or HPC with CMC revealed slower drug release as compared with each of the individual polymers. All the systems proved suitable for CHX buccal delivery in terms of prolonged release and reduced transmucosal permeation.²⁴⁹

Enterococcus faecalis is a major cause of bacterial persistence root canal infections. These bacteria attacks dentinal tubule size which is slightly small between 1-3 μ m producing difficulty drug penetrations to remove root canal. Silica microcapsules with 2% chlorhexidine active compound coated with sodium alginate and chitosan (<1 μ m in size), were able to get in and act in dentinal tubules of teeth root canal and also 2% chlorhexidine has the possibility to be released from silica-chitosan-sodium alginate microcapsules at pH condition 6.5 better than normal pH condition at 7.4, so the 2% chlorhexidine microencapsulation has the power to be used as a better root canal drug.²⁵⁰ Nanocomposite biocompatible hydrogels (NCHG) were used as local drug delivery devices for curing periodontal infections. The composite consists of the following components: nanoparticles (NPs), matrix gel, and chlorhexidine (CHX) as antibacterial drug. The NPs were obtained by free radical initiated copolymerization of the monomers, 2-hydroxyethyl methacrylate (HEMA) and polyethylene glycol dimethacrylate (PEGDMA), in aqueous solution. NCHGs were obtained by mixing NPs, monomers, and drug in an aqueous solution then crosslinked by photopolymerization. Studies discovered that on average 60% of the loaded drug was released. The fastest release was noticed over a 24 h

period for matrix gels with low crosslinking density. For NCHGs, the release period exceeded 48 h.²⁵⁰ Novel antimicrobial nanoparticles (NPs) were developed based on a hexametaphosphate salt of chlorhexidine (CHX). These were synthesized by simultaneous reaction between aqueous solutions of CHX digluconate and sodium hexametaphosphate, under room temperature and pressure. The reaction resulted in a stable colloid composed of extremely negatively charged NPs (-50 mV), of size 20–160 nm. The NPs adhered quickly to samples of glass, titanium, and an elastomeric wound dressing, in a dose-dependent manner. The functionalized materials showed a slow release of soluble CHX over a period of at least 50 days. The NP colloid is effective against methicillin-resistant *S.aureus* (MRSA) and *P.aeruginosa* in both planktonic and biofilm conditions.²⁵¹

1. 17 Microfluidic Devices: An Introduction

Microfluidics (Fig. 1.28) is the science and technology of systems that uses channels with dimensions of tens to hundreds of micrometres to use or control small (10^{-9} to 10^{-18} litres) amounts of fluids.²⁵² Some unique phenomena emerge at such scale. For instance, reactions are completed in a shorter amount of time as the travel distances of mass and heat are relatively small; the flows are laminar because of low Reynolds number in microfluidic channels; capillary effects becomes dominant due to large surface-to-volume ratios.^{253, 254} In the microscale, the surface properties of the device material are greatly amplified, which can either realize unique functions or lead to problems that would not be encountered at macroscale;²⁵⁵ the materials largely determine the function of the devices. Reynold number²⁵³ can be used for the characterization of flow of a fluid through a microfluidic channel, defines as

$$Re = \frac{\text{Inertial Force}}{\text{Viscous Force}} = \frac{L\rho V_{avg}}{\eta}$$

where L is the channel length scale, η is the viscosity, r is the fluid density, and $V_{average}$ is the average velocity of the flow. For various micro channels, L is equal to $4A/P$ where A is the cross sectional area of the channel and P is the wetted perimeter of the channel.

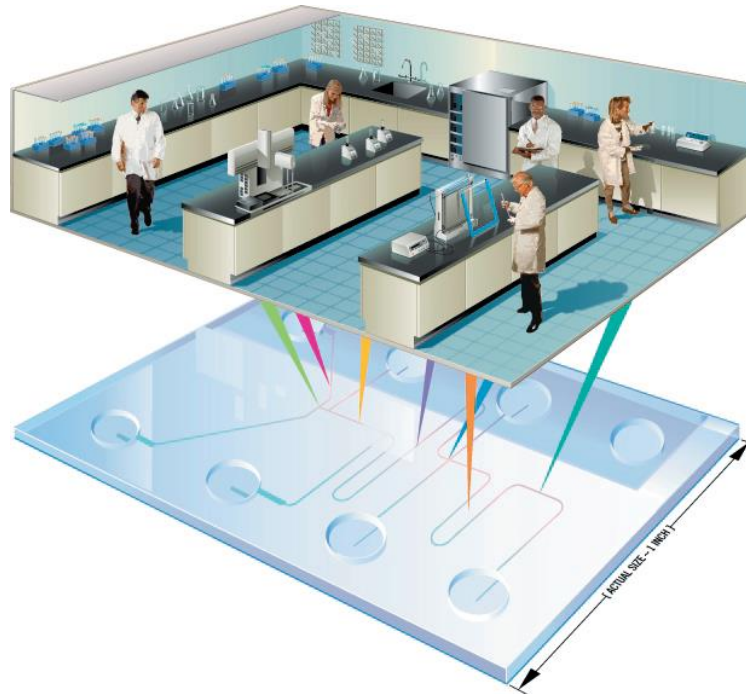


Figure 1.28: Miniaturization and integration of laboratory processes onto a microchip device. This figure was adopted with a permission from author.²⁵⁶

Microfluidic systems have interdisciplinary applications in a wide range of areas: molecular analysis, molecular biology, microelectronics, clinical diagnostics, and drug development.²⁵⁷

There are many substantial advantages resulting from the miniaturization of devices for use in these areas, including low cost of manufacturing, easiness to use, and disposal; short time of analysis; decreased consumption of reagents and analytes; reduced production of potentially harmful by-products; high separation efficiency with high resolution and sensitivity; decreased weight and volume; decreased requirements for power; and increased portability.^{257, 258} The design and development of a functional microfluidic device must also take into account the type of material used to fabricate the device. The material should be compatible with sensitive methods of detection, enable easy interfacing with the user, and allow integration of functional components. The material should also be inexpensive, and compatible with micrometer-scale features and microfabrication methods, if the devices are aimed for large-scale application.²⁵⁹

1. 18 Materials for Fabricating Microfluidic Devices

1. 18.1 Silica and Glass

Silica and glass devices are normally processed with standard photolithography.²⁶⁰ Glass is electrically insulating and optically translucent; as an amorphous material, etched glass channels have curved sidewalls unless etching by special techniques.²⁶¹ In contrast, silicon is opaque and vertical channel sidewalls are created in crystalline silicon. Due to its resistance to organic solvents, ease in metal depositing, high thermoconductivity, and stable electroosmotic mobility, glass is frequently utilized in numerous chemical applications.²⁶² The main application of glass chips is capillary electrophoresis.²⁶³ Characteristic applications include on-chip reactions,²⁶⁴ droplet formation,²⁶⁵ and solvent extraction and *in situ* fabrication.²⁶⁶

The hardness of glass also poses limits to its application in microfluidics. One problem is the high cost of fabrication: finally, the bonding of such chips is difficult (high temperature, high pressure and super clean environment are normally required [263]). Furthermore, glass or silicon is not gas permeable and their chips with etched channels and chambers cannot be used for long-term cell culture.²⁶²

1. 18.2 Elastomers

Elastomers comprise of cross-linked polymer chains that are generally entangled; when external force is applied, they can stretch or compress, and return to the original shape when the external force is withdrawn. The most common elastomer used in microfluidics is polydimethylsiloxane (PDMS).²⁶²

A significant advantage of PDMS is its ease and cheap microfabrication.²⁶⁷ Liquid PDMS prepolymer is cured thermally at moderate temperatures (40-70°C) and the PDMS can be cast from photoresist templates to obtain nanoscale resolution devices, which are easier and cheaper to make than glass templates;²⁶⁸ PDMS chip can be reversibly and conformally bonded to another piece of PDMS, glass, or other substrates by simply making contact.²⁶⁷ Oxygen plasma oxidation of PDMS surface is also suitable to irreversibly bond PDMS to PDMS, glass, or silicon or using a thin layer of PDMS as glue.²⁶⁷ Multilayer channel structures were fabricated by stacking several PDMS layers with through holes to connect different layers.²⁶⁹

Another advantage of PDMS originates from its high elasticity. Quake *et al.* developed an integrated valve depending on two layers of microchannels,²⁷⁰ allowing high-density integration of valves (1×10^6 valves/cm²) with picoliter to femtoliter dead volumes, and realized parallel and complicated on-chip manipulation.^{271, 272} In contrast to glass, silicon, and other hard materials (e.g. poly(methyl methacrylate) (PMMA) and polycarbonate (PC)), PDMS is gas permeable (which is crucial for long-term cell culture in sealed microchannels); also its surface is compatible for cell culture. In comparison with macroscale culture, the microchip also provides a well-controllable microenvironment. For example, gradients and oscillations as well as complicated media changing schemes can be easily accomplished.²⁷³ It is worth observing that cell behaviors on plain PDMS can be different from those on rigid substrate or on textured or modified PDMS.^{274, 275} Because of these traits, PDMS devices are widely used in bio-related research, primarily, cell culture, cell screening, and biochemical assays.^{274, 276, 277} The ability of handling picoliter to femtoliter volume makes it superior in single-cell analysis.^{272, 278}

PDMS also has notable limitations despite its popularity.²⁷⁹ At the molecular level, PDMS is a porous matrix of Si-O backbones covered with alkyl groups. This structure permits permeation of gases, which helps cell culture; however, it also leads to some major

difficulties: the incapability to support certain quantitative experiments and the incompatibility with organic solvents due to three effects; the adsorption of biomolecules onto channel walls, the absorption of small hydrophobic molecules into channel walls, and the change in concentration of solution by water evaporation through channel wall (this property has been exploited for protein crystallization).²⁸⁰

1. 19 Fabrication of Microfluidic Devices

1. 19.1 Photolithography

Lithography is the most significant technique for fabricating microscale structures. Depending on the nature of energy beam, lithography techniques can be further divided into photolithography, electron lithography, X-ray lithography, and ion lithography.²⁸¹ Photolithography technique is the most applicable technique for the fabrication of microfluidic devices. The patterning process with photolithography is limited to two-dimensional, lateral structures. This technique utilizes a photosensitive emulsion layer called resist, which transfers a preferred pattern from a transparent mask to the substrate. The mask is a transparent glass plate with chromium metal patterns on it. For relatively large structures of microfluidic applications, a mask patterned on a plastic transparency film by high-resolution image setter is a choice for cheap and fast prototyping. Photolithography consists of three process steps: *Positioning process*: Lateral positioning of the mask and the substrate, which is treated with a resist, regulating the distance between mask and substrate. *Exposure process*: Optical or X-ray exposure of the resist layer, transferring patterns to the photoresist layer by changing properties of exposed area. *Development process*: Dissolution (for negative resist) or etching (for positive resist) of the resist pattern in a developer solution.²⁸²

The fast prototyping of photolithography starts by using a computer-aided design (CAD) program to make a design for a channel. The CAD file is then printed onto a transparency film with a high-resolution image setter; the transparency acts as a photomask in contact photolithography. A thin layer of photoresist (fig. 1.29) is applied to the wafer and exposed to an ultraviolet exposure, which transfers the micropattern on a transparency mask to the photoresist layer; the photoresist is developed to create a mask for etching;

after microchannels are made, the photoresist is removed and the channels are bonded with a flat substrate, for example, through a fusion bonding process.²⁶⁰

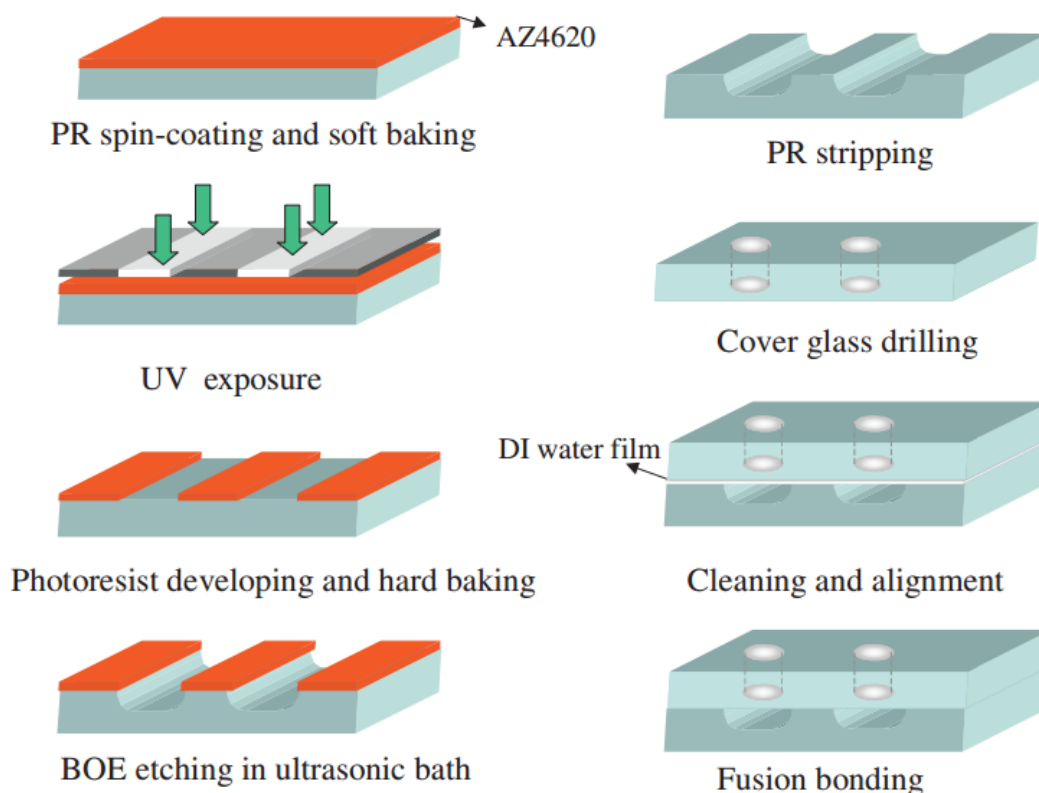


Figure 1.29: Simplified microfabrication process for rapid prototyping of microfluidic chips on soda-lime glass substrates.²⁶⁰

1. 19.2 Soft Lithography

Soft lithography is a useful methodology for fabricating microfluidic devices. It is particularly useful as a non-photolithographic technique for replicating pattern and allows fast prototyping of devices. The method includes replication of a structure on a master in a soft elastomer (PDMS). The process can be performed in ambient laboratory conditions; therefore, it does not require costly cleanroom facilities to fabricate features in the size range of 20–100 μm (this size range is microfluidics based bioanalysis).^{267, 283}

Soft lithography starts with the production of a PDMS replica of a master (or mold). The PDMS used is supplied in two components, a base and a curing agent. Silicon hydride groups existed in the curing agent react with vinyl groups present in the base to form a cross-linked, elastomeric solid as illustrated in Figure 1.30. To produce a replica, two parts

(typically at 10:1 (v/v) base: curing agent) are mixed together, poured the liquid pre-polymer over the master, and cured at 70°C for 1 h. The liquid PDMS pre-polymer conforms and replicates the features of the master up to 10's of nm. The low surface free energy and elasticity of PDMS allow it to peel off from masters without damaging the master or itself. The master is the limiting factor in the production of PDMS replicas. A common method begins with a high-resolution transparency as a photomask for generation of the master by photolithography (Figure 1.31).²⁸³

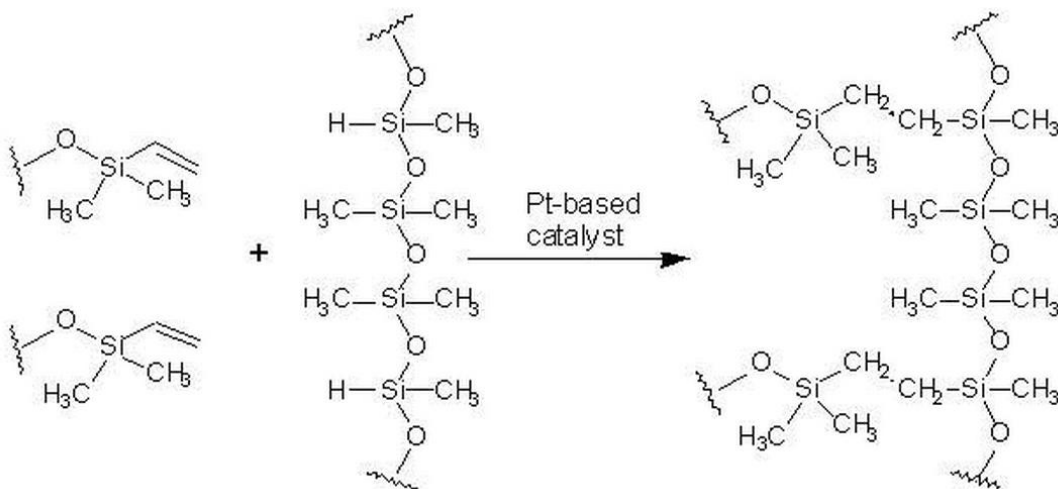


Figure 1.30: Organometallic crosslinking reaction between oligomer base and curing agent to produce PDMS.

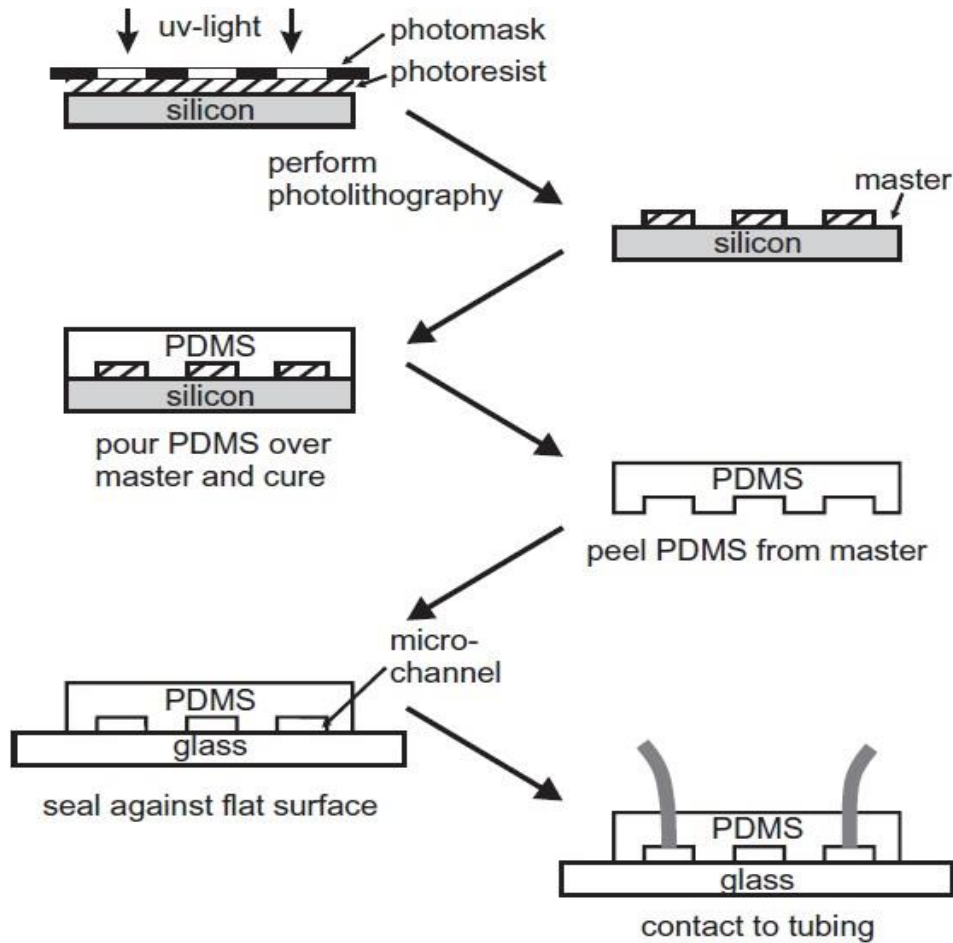


Figure 1.31: Schematic of typical device fabrication using photolithography for structuring and PDMS as a device material.²⁸⁴

PDMS replica can also be fabricated by micromoulding technique which duplicates microstructures on polymer substrates. A molding template is manufactured by either patterning negative photoresist, e.g., SU-8, on silicon wafer for precise microstructures (i.e. $<50\ \mu\text{m}$) or direct micromachining PMMA substrate for larger microstructures (i.e. $>50\ \mu\text{m}$). Then a PDMS mixture is applied over the molding template, cured, and peeled off from the template as shown in figure 1.32. The preferred microstructures providing high aspect ratios can be obtained in the PDMS substrate.²⁸⁵

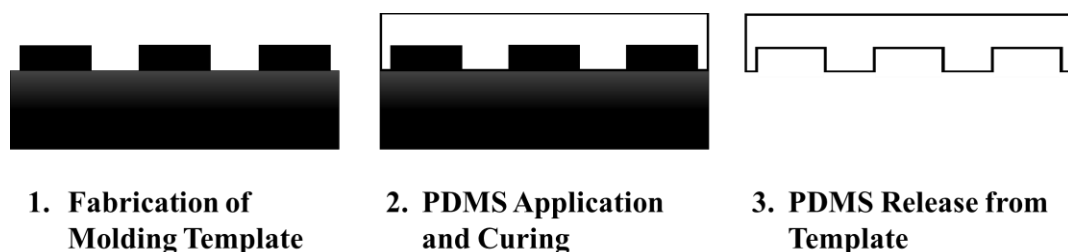


Figure 1.32: Illustration of the PDMS replication process.

1. 20 Microfluidic Chips Sealing

PDMS can reversibly or irreversibly seal to itself, or to other surfaces without distortion of the channels. Sealing of PDMS channels is significantly easier than that for glass, silicon, or thermoplastics because high temperatures, pressures, and high voltages are not required.²⁶⁷ A reversible seal provided by van der Waals contact is closely sealed but cannot resist pressures higher than ~ 5 psi.²⁶⁷ Adhesive tapes-silicone or cellophanes also seal the PDMS channels reversibly.²⁸⁶ Cellophane tape offers only a temporary seal; silicone tape makes a greatly robust seal and is waterproof.

PDMS channels can also be irreversibly sealed to PDMS, glass, silicon, polystyrene, polyethylene, or silicon nitride by oxidizing using a plasma which generates silanol groups on PDMS, and $-OH$ -containing functional groups on the other materials; these polar groups produce covalent $-O-Si-O$ -bonds with oxidized PDMS when these surfaces are got into contact.²⁸⁷ Another way to irreversibly seal two PDMS slabs includes adding an excess of the monomer to one slab and an excess of the curing agent to the other. When the two slabs are cured together, an irreversible seal, indistinguishable from the bulk properties of PDMS, forms.²⁷⁰

1. 21 Droplet Based Microfluidics

Droplet-based microfluidics includes the generation and manipulation of discrete droplets inside microdevices.²⁸⁸ Highly monodisperse droplets can be produced from this method from nanoscale to microscale diameter range, with flow rate up to twenty thousand per second.²⁸⁹ Heat and mass transfer times and diffusion distances are shorter, enabling faster reaction times owing to high surface area to volume ratios at the microscale. Independent control of each droplet can be achieved through droplet-based microfluidics, hence

generating microreactors that can be discretely transported, mixed, and investigated.²⁹⁰ Droplet-based microfluidic devices are compatible with many chemical and biological reagents and able to perform a variety of “digital fluidic” operations that can be rendered programmable and reconfigurable. This platform has dimensional scaling benefits that have enabled controlled and rapid mixing of fluids in the droplet reactors, resulting in decreased reaction times. This, coupled with the precise generation and repeatability of droplet operations, has made the droplet-based microfluidic system a potent high throughput platform for biomedical research and applications, directly synthesis of particles and encapsulate many biological entities for biomedicine and biotechnology applications.²⁹¹ Researchers have developed a variety of different droplet formation techniques. T-junction, flow-focusing and coaxial microfluidics are three methods that based on channel geometry to control the generation of droplets.

1.21.1 T-Junction

In the configuration of T-junction microchip, the inlet channel accommodating the dispersed phase perpendicularly intersects the main channel which holds the continuous phase.²⁹² An interface at the junction is formed from the two phases, and as fluid flow carry on, the tip of the dispersed phase enters the main channel. The shear forces produced by the continuous phase and the subsequent pressure gradient cause the head of the dispersed phase to elongate into the main channel until the neck of the dispersed phase thins and finally breaks the stream into a droplet (Fig. 1.33). The droplet sizes can be modified by changing the fluid flow rates, the channel widths, or by altering the relative viscosity between the two phases.²⁹³

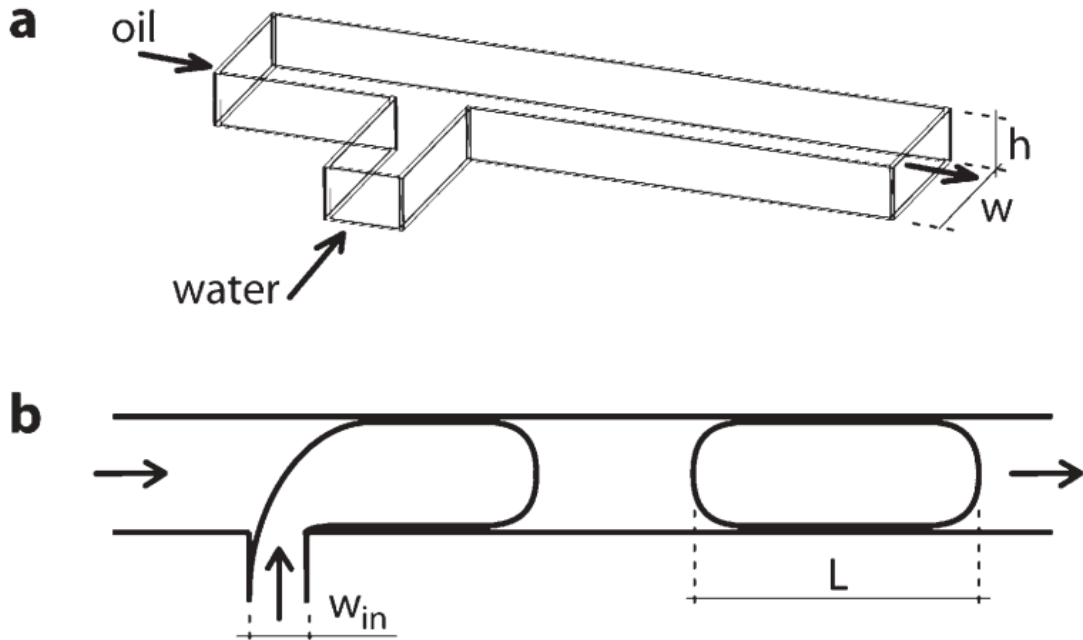


Figure 1.33: (a) A schematic diagram of rectangular channels of the microfluidic T-junction droplet generation. (b) A two dimensional flow focusing droplet generation in the top view.²⁹⁴

1.21.2 Flow Focusing Microfluidics

In the configuration of flow-focusing, the dispersed and continuous phases are forced through a narrow region in the microfluidic device.²⁹⁵ The design works symmetric shearing by the continuous phase on the dispersed phase which capable of more controlling and stable generation of droplets. An extension of flow-focusing is shear-focusing, which aims to create a singular point of highest shear, which occurs at the narrowest region of the nozzle.²⁹⁶ This singular point confirms that the break-off of droplets from the fluid stream happens constantly at that point thus forming uniform droplets as shown in Figure 1.34. The sizes of the droplets can decreased by increasing flow rates of the continuous phase and an increase in oil flow rates also rises the droplet generation frequency.

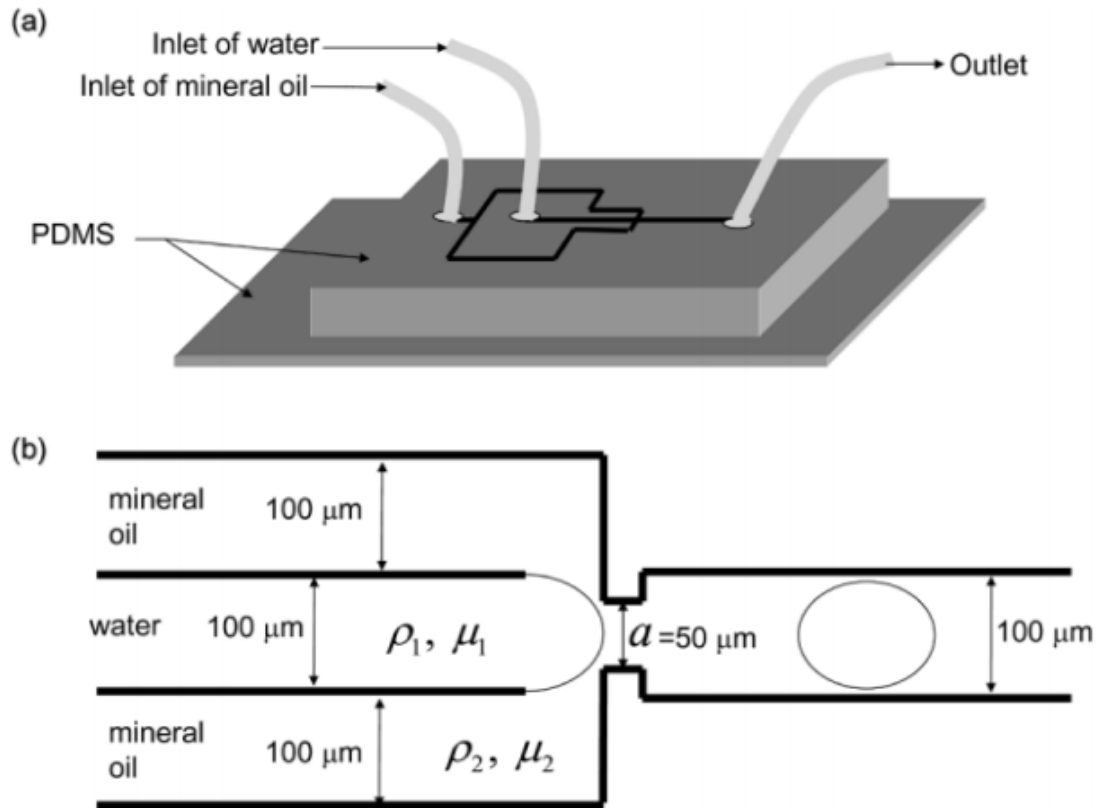


Figure 1.34: (a) side view of flow focusing Microfluidic setup for the two-phase flow. The channel height is 75 μm . (b) Top view of flow focusing geometry of microfluidics chip.²⁹⁷

1.21.3 Coaxial Microfluidics

Coaxial alignment of the two capillaries is ensured by selecting the capillaries such that the outer diameter of the circular capillary is the similar as the inner dimensions of the square capillary. Coaxial geometry happens when one fluid flows inside the circular capillary whereas the other fluid flows through the square capillary in the same direction, resulting in a coaxial flow of the two fluids (Fig. 1.35a). A dipping process occurs forming individual monodispersed drops at low flow rates of fluids (Fig. 1.35b and 1.35d). However, upon increasing the flow rate of either fluid beyond a certain critical limit, producing jet process, a long stream of the inner fluid with drops forming downstream (Fig. 1.35c).^{298, 299}

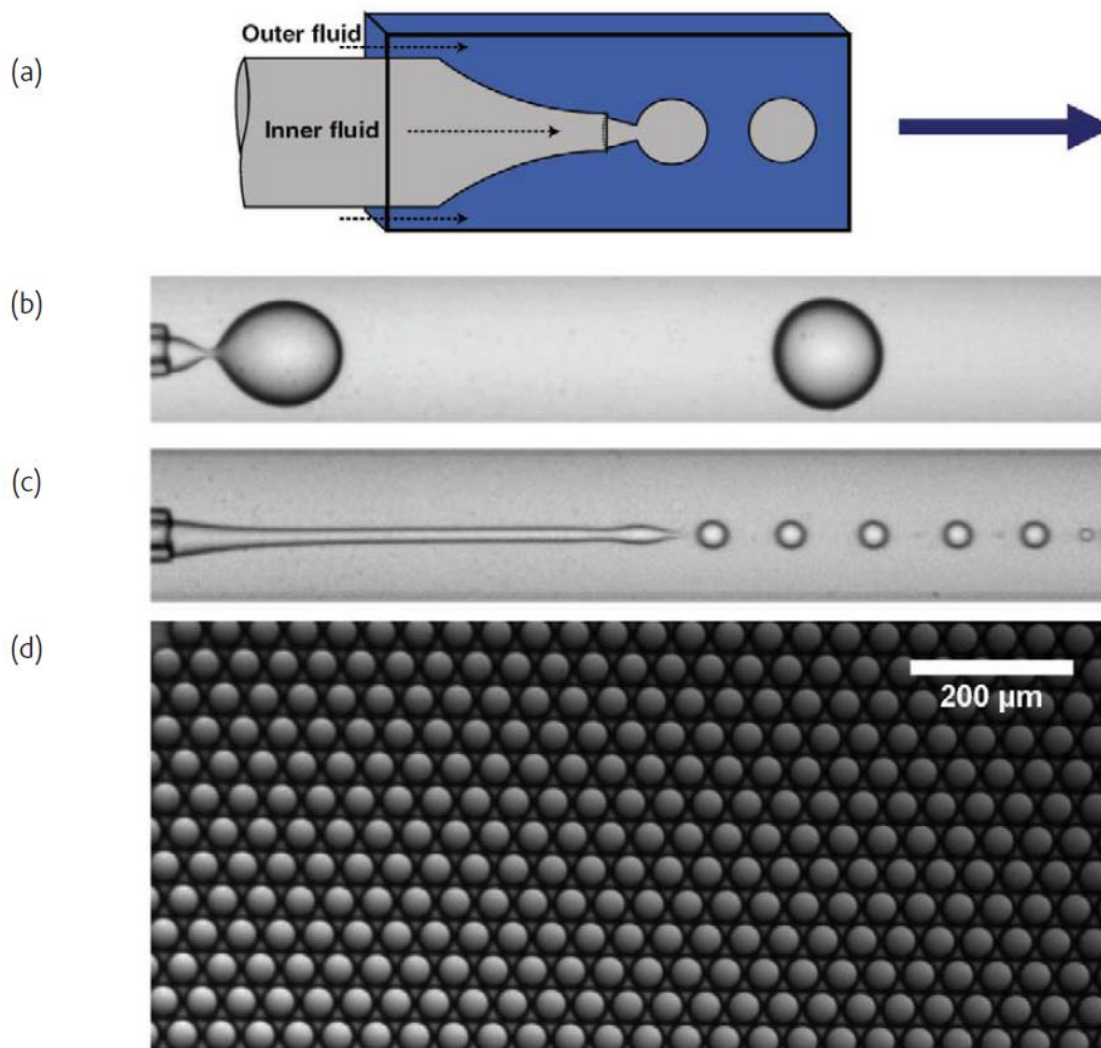


Figure 1.35: (a) Schematic for coaxial microfluidics for generating droplets²⁹⁸ (b) Droplet generation at low flow rates. (c) Droplet generation upon increasing flow rates. (d) Individual monodispersed droplet produced by micro capillary device.^{298, 299}

1. 22 Some Methods for Synthesis of Magnetic Polymer Beads

Magnetic polymer beads are consisted of magnetic nano- or microparticles encapsulated in a polymer matrix. The beads size can differ from hundred nanometers to few millimeters. The synthesis of magnetic polymer beads can be achieved by three common ways. Either, the magnetic particles are synthesized inside polymer matrix or one polymer is created in the presence of magnetic particles or the beads are synthesized from pre-formed polymer

and magnetic particles.³⁰⁰ magnetic nanoparticles of magnetite Fe_3O_4 and maghemite $\gamma\text{-Fe}_2\text{O}_3$ are usually synthesized by the alkaline coprecipitation of ferric and ferrous salts.³⁰¹ Superparamagnetic nanocomposite particles were prepared containing functional groups for adsorption application. The polymer solution contains two different particles: magnetite (14 nm) and polymer ion exchanger (150 nm). The evaluation of the protein binding capacity of the composite material displays excellent values, which are comparable to other ion exchange resins.³⁰² It was also synthesized magnetic nanoparticles that functionalized with oleic acid to decrease its agglomeration. However, for biological application the amount of free oleic acid needs to be reduced to minimize the cytotoxicity of the formulation. the efficacy of magnetic particles – oleic acid for improved killing of tumor cells has been confirmed in mice fibrosarcoma tumor cells signifying their suitability for hyperthermia application.³⁰³ Magnetic nanoparticles were utilised to synthesize novel nanocomposites which sustain both magnetic properties of nanoparticles and self-assembly of amorphous block copolymer matrix. Therefore, to increase both the dispersion and the affinity of iron oxide magnetic nanoparticles, they were modified with one of the blocks of polystyrene-*b*-polybutadiene-*b*-polystyrene block copolymer using atomic transfer radical polymerization.³⁰⁴ Magnetically anisotropic microparticles were fabricated depend on oleic acid coated magnetite nanoparticles (OCMNs) dispersed within the oil drops of a polymerisable oil-in-water emulsion. This was accomplished by polymerising the oil drops after gelling the continuous aqueous phase in the presence of an external magnetic field. Magnetic Janus particles were produced with anisotropic optical and magnetic properties. These magnetic particles have strong magnetic response upon exposed to magnetic field.³⁰⁵ Another technique was used for fabricating monodisperse magnetic macroporous polymer beads using coaxial microfluidic. Water-in-oil high internal phase emulsion (HIPE) is synthesized by emulsifying aqueous iron ions solution in an oil phase containing monomers. The HIPE is pumped into a coaxial droplet based microfluidic device to synthesize monodisperse (water-in-oil)-in-water double emulsion droplets as shown in Figure 1.36. The prepared magnetic beads appeared uniform size, porosity, superparamagnetic behavior and identical distribution of Fe_3O_4 in polymer matrix.³⁰⁶

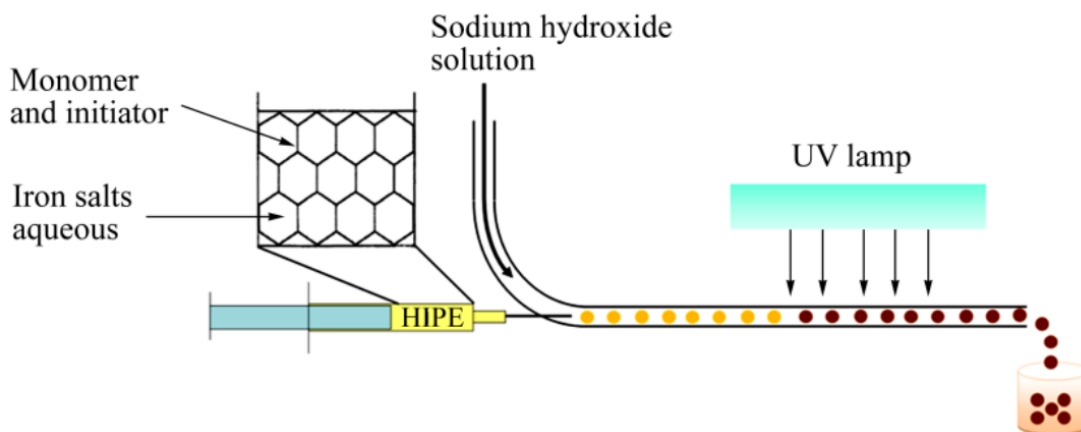


Figure 1.36: Water in oil in water double emulsion droplet generation of magnetic beads using coaxial microfluidic device.⁽³⁰⁶⁾

1.23 High Throughput Cell Based Screening

High-throughput cell-based screening platforms have stimulated great interest in the pharmaceutical industry for enhanced high-throughput cell-based screening platforms as well as for use in pre-clinical trials.³⁰⁷ The present method of high throughput cell based screening uses a 96-well microplate for a study of cell growth with different concentrations of toxin. The 96-well microplate screening method allows for a quite fast screening of the cytotoxicity of the toxins with adequate number of wells for statistical significance. The overall protocol for the 96-well screening method based on seeding cells in each of the 96 wells. Then, different concentrations of toxin prepared in culture media are individually distributed into the 96 wells in order to make gradient concentrations of toxin alongside the 96-well plate length as shown in Figure 1.37. Eight repeat measurements of varied concentrations of toxin are allowed for a screening by microplate well. The 96-well plate containing cells and toxin-added culturing media is located in an incubator and the cells are continuously cultured for different incubation times, exposed to the toxin. The cells in the 96 plates are screened with cell viability assay if they are viable or dead after a specific incubation time. The relative intensity of stained cells in each well is measured using either an absorbance or a fluorescence or a luminescence measurement. The cytotoxicity of the toxin can be then determined by comparing the relatively intensities of viable cells as a function of time with respect to different concentrations of toxin.^{308, 309}

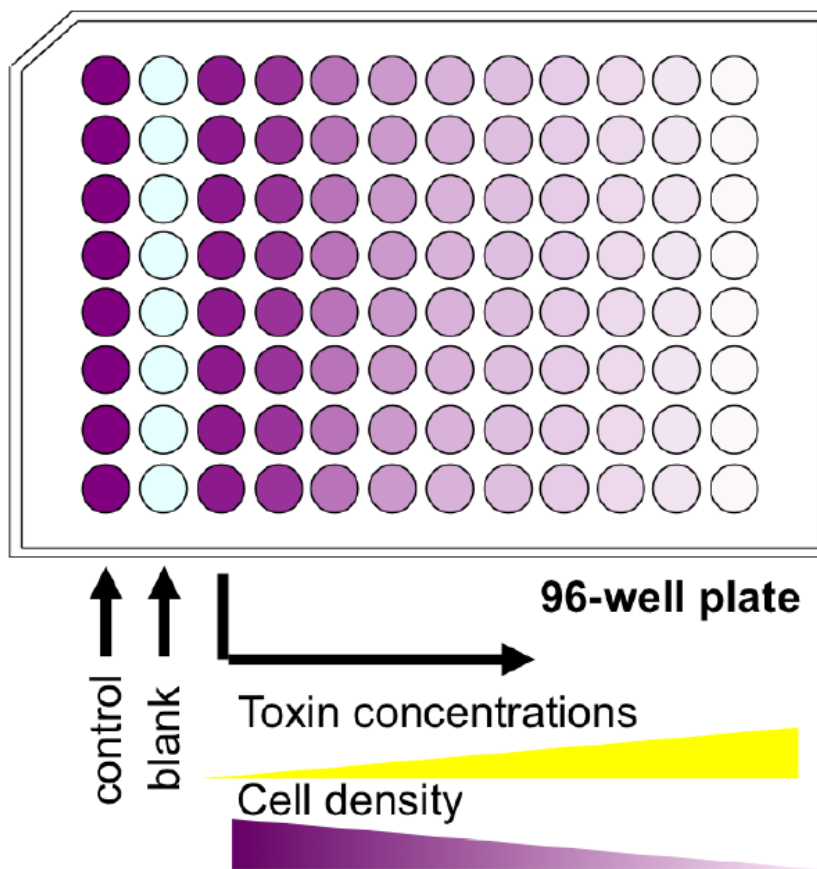


Figure 1.37: The schematic configuration of the 96-well microplate cytotoxicity screening method.³⁰⁸

1.24 Microfluidic Devices Cell Based Assay

Microfluidic devices have been investigated for cell based assay³¹⁰ Microfluidic systems were studied for trapping cells with the aim of reducing the well volumes in a standard micro titre plate from tens of microlitres to the nano- or picolitre scale to speed up the process.³¹¹ The benefits of the use of microfluidics in cell biology typically demonstrate small footprint, low reagent consumption increased fluid control, capability to deal with the cellular length scale, approximating the physiologic culture environment, enhanced culture efficiency, low fluorescence background, and batch production of high-throughput arrays.^{312,313} Microfluidic conditions for example, transport limitations, surface chemistry effect, and shear forces, might create unique environments for cells comparing with larger volumes assays.³¹⁴

A practical microfluidic cell array ideally requires regular cell immobilization and distribution in each chamber. Small perturbation to fluid flow can considerably agitate cell

positions in microculture chambers with nanolitre volumes.³¹⁵ To address this challenge, several groups developed a number of microfluidic techniques to confine cells in defined positions, including cell immobilization on a surface and contact-free cell immobilization techniques. Figure 1.38 shows a variety of cell-immobilization methods which can be classified as contactless cell trapping or as cell immobilization on a surface. Cell encapsulation is regarded as being situated in between³¹⁶

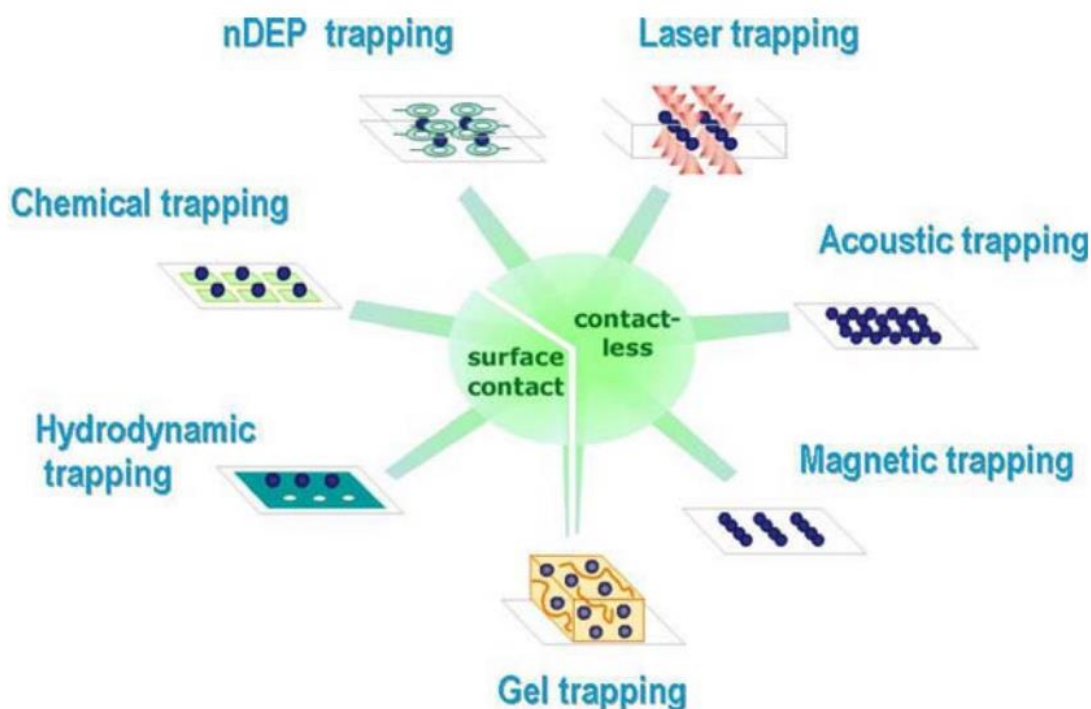


Figure 1.38: Cell immobilization methods in the microchamber of microfluidic chip.³¹⁶

1.22.1 Surface Contact Cell Immobilization

1.22.1.1 Chemical Trapping

Cell adhesion and culture on plane substrate is a common approach on the macro scale. A two-dimensional ordered immobilization array on micro patterned surfaces allows easy analysis and signal assignment, because a specific cell is fixed and labelled by its position. Additionally, cell and substance consumption are strongly reduced. Such cell-array platforms are used as biosensors, for example in drug screening.³¹⁷ Disadvantages of

surface immobilization methods are not applicable to non-adherent cells and deposition is often irreversible.³¹⁸

1.22.1.2 Hydrodynamic trapping

The most common way of realizing cell or particle trapping functions in microfluidic systems is to create mechanical obstacles or barriers in a main transport channel; these separate the object from the fluid which can still move through the device. Vertical walls topographies are designated where particles are immobilized, the height of obstacles are smaller than that of the channel, or pores are produced in the channel bottom or the side walls.³¹⁹ Hydrodynamic trapping is used in drug screening or tissue engineering and is fast compared with chemical trapping. A drawback is that precision in particle deposition is difficult to achieve with obstacle sites staying empty or aggregates being trapped instead of single cells.³¹⁶ Figure 1.39 depicts hydrodynamic cell trapping using microwells.³²⁰

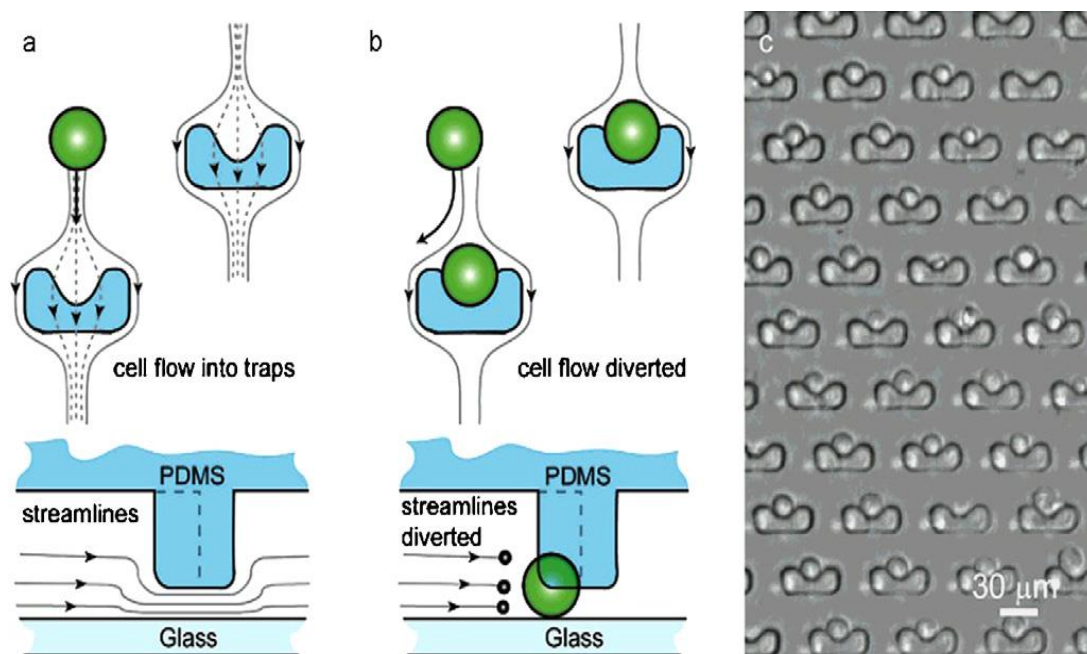


Figure 1.39: Hydrodynamic single cell trapping array as illustrated by Di Carlo et al.³²⁰

1.22.2 Contact-Free Cell Immobilization

1.22.2.1 Dielectrophoretic Trapping

Dielectrophoresis is the movement of a dielectric object due to forces generated by a non-uniform electric field. Depending on the differences between the permittivity and

conductivity of the particle and the liquid medium, which vary as a function of the frequency of the applied field, the particle is either attracted toward the higher field (Positive Dielectrophoresis, pDEP) or repelled from it (negative Dielectrophoresis, nDEP) as described in Figure 1.40. A drawback of dielectrophoresis is the existence of a strong AC field, which cause localised Joule heating, and the setup of a transmembrane voltage.^{316, 321}

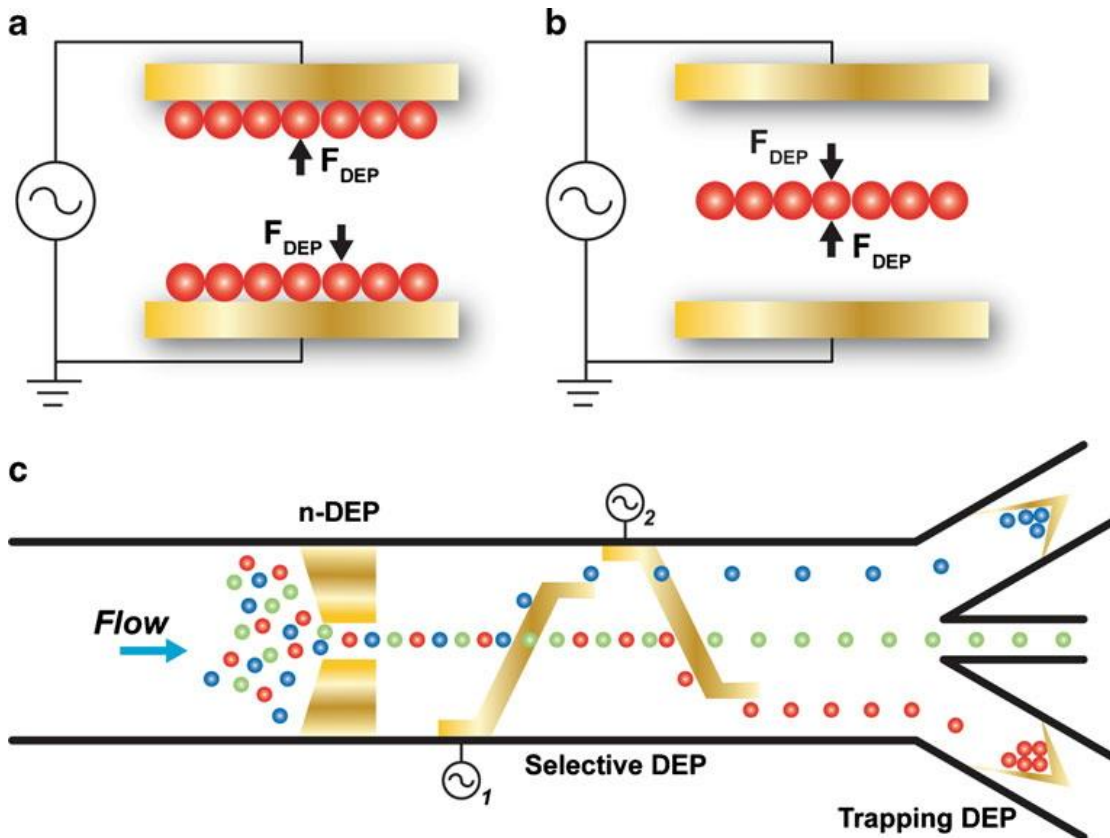


Figure 1.40: Dielectrophoretic (DEP) separation can be a) positive (pDEP) or b) negative (nDEP) which influences where cells are located within a field. c) DEP has been used in microfluidic systems in a variety of arrangements.³²²

1.22.2.2 Laser Trapping

Particles to be trapped by the laser must be transparent, non-absorbing at the trapping wavelength, and have a refractive index different from that of the surrounding medium to be appropriate for laser trapping. In optical trapping, a tightly focused laser beam is used to trap and manipulate particles and cells with very high precision. In the optical trap two forces are on a particle or cell- the scattering force, which orientates the particle away from the light source by radiation pressure, and the gradient force, which attracts the particle

into the centre of the trap. The balance between these forces is critical to obtain a stable trap.³²³ Ashkin and Dziedzic³²³ studied trapping of single tobacco mosaic viruses and *Escherichia coli* bacteria with no apparent problems then.

1.22.2.3 Acoustic Trapping

In acoustic trapping, a standing acoustic wave field is produced by one or more ultrasonic transducer integrated on the chip. Different densities and sound speeds of particle and fluid and scales linearly with particles in an exposed volume are addressed instantaneously and accumulated in either the nodes or anti-nodes of the periodic wave pattern.³¹⁶ A relatively simple and frequently applied configuration is the confinement of free-floating objects in thin parallel lines of anti-nodes in which the objects can move freely within a line as described in figure 1.41. This configuration can be used to move particles, hold them in a flow, or for particle concentration, agglomeration, and separation.³²⁴

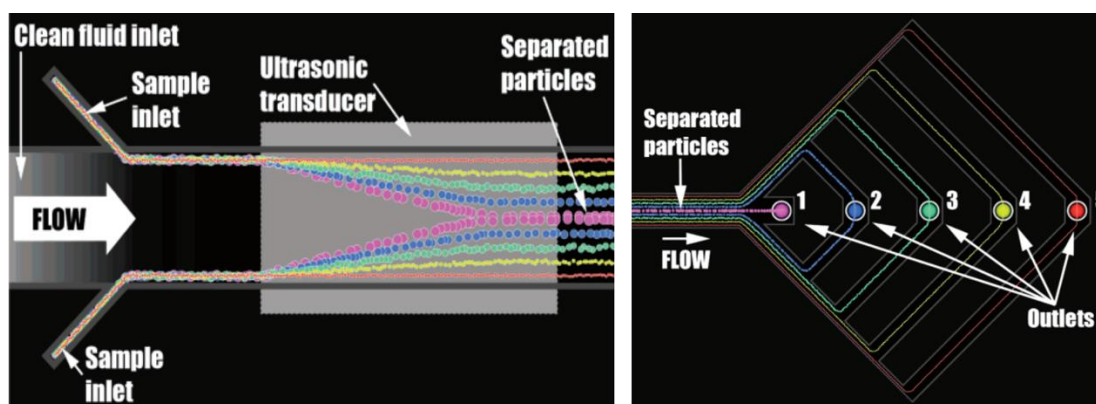


Figure 1.41: The left image illustrates a particle suspension passing over the transducer where the particles are moved at a rate determined by their acoustic properties toward the center of the separation channel. Because of the laminar flow almost no mixing happens. The right image represents the fractionation of the separated particles through five consecutive outlets/fractions at the end of the separation channel. Since the separation is symmetrical along the center of the channel; eight of the fractionation outlet channels are pairwise connected.³²⁵

1.22.2.4 Magnetic Trapping

A recently developed method allows periodic spatial arrangement of cells based on diamagnetic cell response in a modulated magnetic field. The advantage of this technique is that it is applicable to any diamagnetic particle, as long as its magnetic susceptibility is

different from that of the medium, eliminating the need for cell labeling with ferromagnetic beads.³²⁶ An approach to magnetic trapping was conducted by functionalizing particles or cells with magnetic nanoparticles and trapping them within the microchamber of a microfluidic chip using permanent magnet. This type of magnetic trapping is applicable in cytotoxicity assay and drug discovery.³²⁷

1.25 Summary of Trapping Methods

The performance of all trapping methods is very similar in terms of the force exerted, the minimum particle size manipulated, biocompatibility, and applicability. However, the possible drawback of these technique is that cells are permanently exposed to weak electric and magnetic fields or mechanical forces, to slightly increase temperature or cell membrane damage because of functionalization with magnetic nanoparticles, these might be affecting the viability of cells in case of microscreening assays.

1.26 Microfluidic based Cytotoxicity Micro Screening

As discussed in 1.23, cell toxicity test have a crucial role to play in early-stage drug screening. They could offer more extensive functional information than biochemical assays and lower cost and shorter period than animal tests.³²⁸ Currently, new technologies, such as microfluidics and chip-based technology are being merged with traditional cell culture and detection techniques to developed new opportunities in toxicity testing.³²⁹ Koh and Pishko have succeeded in designing a three-dimensional (3D) culture of cells through hydrogel encapsulation of mammalian cells and the cytotoxicity test of toxins. Cytotoxicity assays proved that small molecular mass toxins such as sodium azide could easily diffuse into the hydrogel microstructures and damage the encapsulated cells, which resulted in reduced viability.³³⁰ Sung and Shuler devised a microfluidic chip composed of a concentration gradient generator and a cavity array to study the liver toxicity of multiple medications. The results showed good correlation with *in vivo* drug test results.³³¹ Wang *et al.* (2008) developed a novel microfluidic chip composed of a 6 x 6 array of cell culture microchambers for Hep-G2 cell culture and parallel drug cytotoxicity assay of artemisinin as depicted in figure 1.42. Viable cells stained with green fluorescence, was used for the on-chip detection and quantification of cells. Results showed that Hep-G2 cells were

successfully cultured in the microchip for over 72 h. Moreover, artemisinin (ART) could inhibit the activity of Hep-G2 cells, which based on the dose of ART and action time.³³²

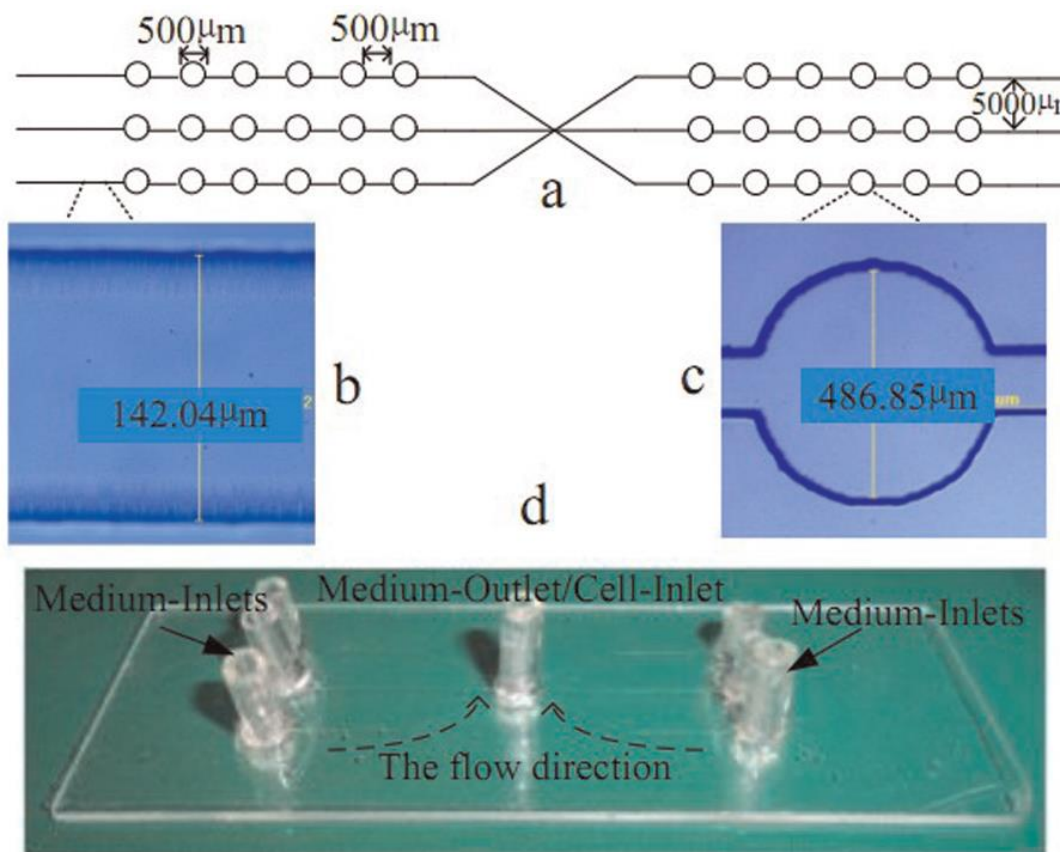


Figure 1.42: (a) Fundamental scheme of the glass substrate, (b and c) size of the microchannel and chamber and (d) picture of the microfluidic cell chip.³³²

A PDMS microfluidic array with micro cell sieves was developed to fabricate a multiple mammalian cell lines array for high throughput cell cytotoxicity screening. The microfluidic array was used for seeding multiple mammalian cell lines in chambers and detecting the cell viabilities after cells were exposed to different toxins using fluorescence microscope as shown in figure 1.43. The densities achieved were much higher than existing multi-well plate technologies.³³³

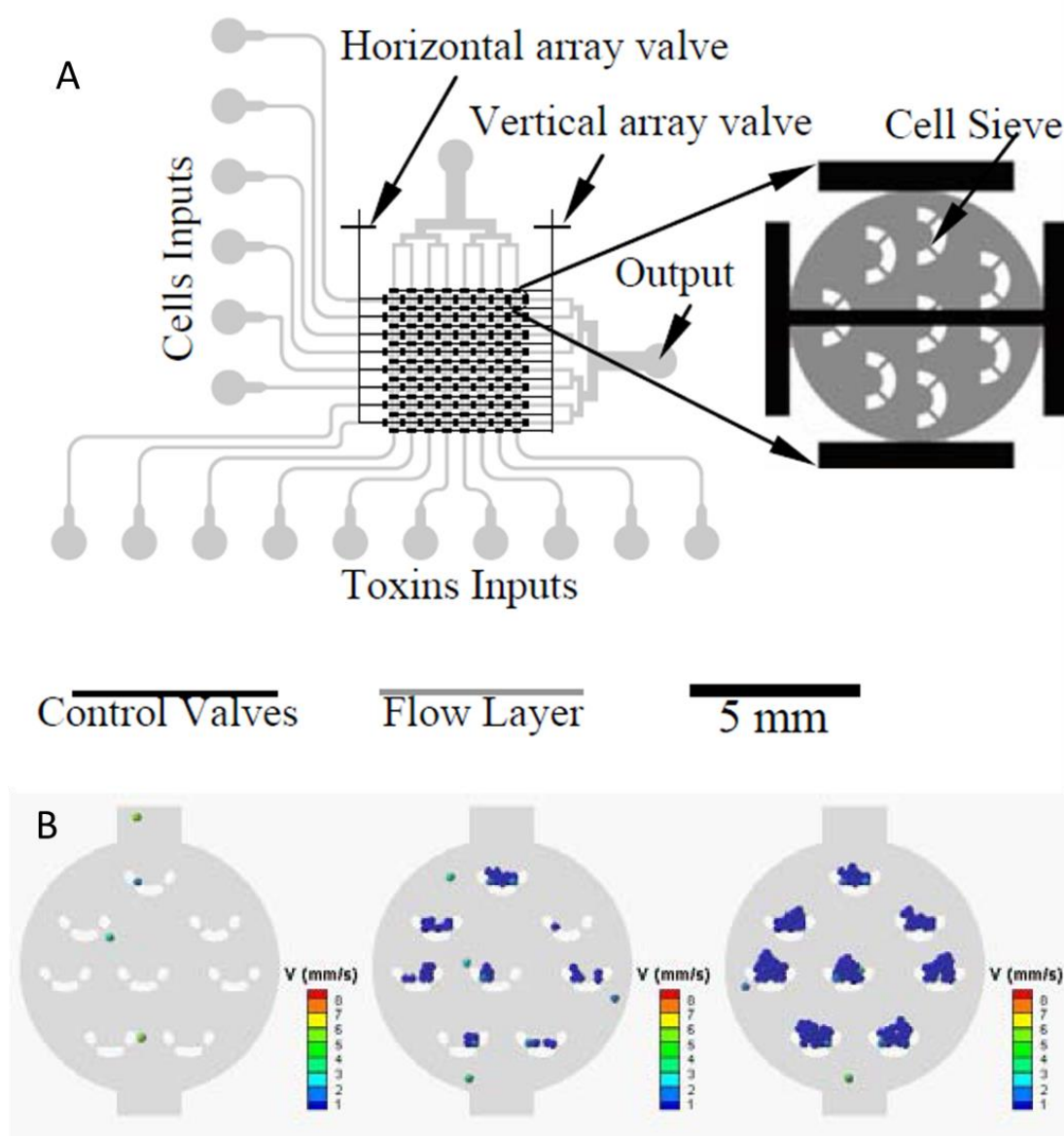


Figure 1.43: (A) Schematic of the microfluidic array for parallel cell cytotoxicity Screening. (B) Cell loading simulation in one chamber.³³³

Zheng, Xiannuo, *et al.* (2012) investigated the cytotoxicity of cadmium-containing QDs based on using a newly developed cell-based high-throughput assay-microfluidic chip as described in figure 1.44. It simultaneously measured QD-induced multiple cellular events such as cell morphology, viability, proliferation, and QD uptake in HEK293 cells. The satisfactory results showed that microfluidic chips can be a valuable tool in nanoparticle toxicity assessment.³³⁴

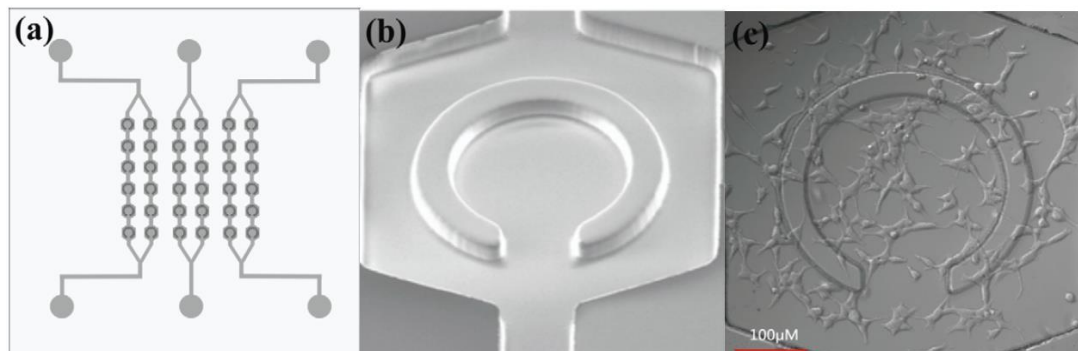


Figure 1.44: Chip design and cell culture. (a) Schematic illustration of the microfluidic channels with cell culture chambers. (b) A cell culture chamber with a C-shaped dam. (c) HEK293 cells cultured in a cell culture chamber.³³⁴

In addition to that, a new high throughput microfluidic cell based assay was developed based on magnetic functionalization of genetically modified yeast (GFP) and holding them into microchambers of microchip. The cells were magnetized using biocompatible positively charged PAH-stabilized magnetic nanoparticles with diameters around 15 nm. Gradient mixing was utilized to simultaneously expose yeast to a range of concentrations of toxins, and the effective fluorescence emitted from the produced GFP was measured. The magnetically enhanced retention of the yeast cells, with their facile subsequent removal and reloading, allowed for very convenient and rapid toxicity screening of a wide range of chemicals. Figure 1.45 describes an assay method to use viable, genetically modified green fluorescent protein (GFP) reporter yeast that was magnetized with PAH-stabilized 15 nm magnetic nanoparticles and held within a microfluidic device, and also gradient concentration generator on a chip was used to simultaneously incubate yeast to different concentrations of toxins.

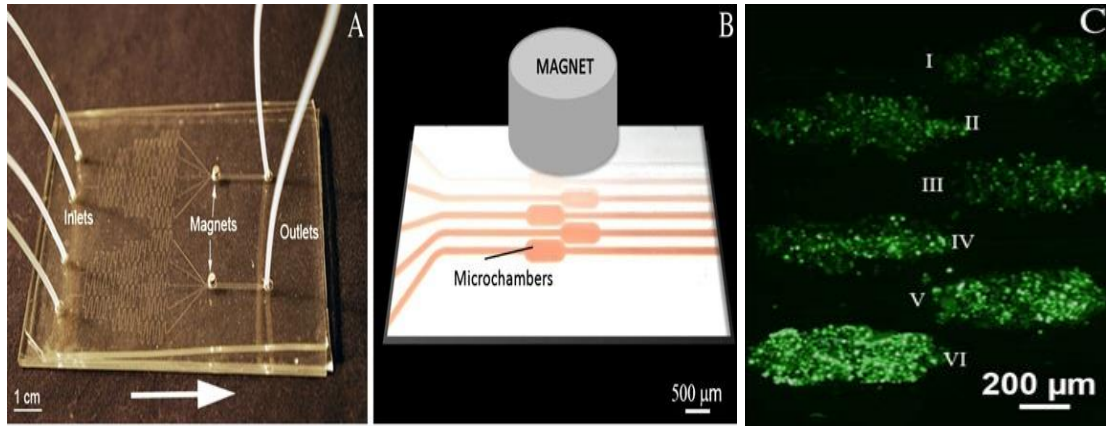


Figure 1.45: Microscreening cytotoxicity assay (A) PDMS glass micro screening system. Two parallel systems are used, one to test an unknown sample and the second with a reference. The magnets were placed above the chambers to retain the magnetic yeast. (B) A scheme showing the position of the magnet on the top of the chambers. (C) Detection of Cytotoxicity Micro Screening of GFP Yeast.³²⁷

1. 27 Objectives of the Research

The purpose of this research is to examine two different nanomaterials:

Firstly, titania nanoparticles as it has toxicological impact on baker's yeast and *C.Reinhardtii* green algae since they are considered to be an ecological marker. The objectives were conducted through:

1. Synthesize different particle sizes of titanium dioxide nanoparticles by sol-gel method taking into consideration investigating the chemical and physical parameters of the method and then the prepared titania nanoparticles are to be calcinated at wide ranges of temperatures (200°C – 800°C) to prepare different crystallite sizes.
2. Study the effect pH and ionic strength on size and surface charge of TiO₂ nanoparticles.
3. Coat titania nanoparticles by layer by layer technique using anionic and cationic polyelectrolyte such as poly allylamine hydrochloride and poly styrene sulfonate sodium to prepare multicoated titania nanoparticles. The varied concentrations of bare and multicoated titania nanoparticles are to be incubated with microorganisms for examples baker's yeast (Eukaryotic Cell) and *C.reinhardtii* (Aquatic Microorganism) in dark conditions and in the presence of visible and UV light. The toxic effects of bare and multicoated titania nanoparticles are measured at different exposure times.

Secondly, polyacrylic acid based microgel as a nanocarrier for drug delivery to increase the antimicrobial action with high encapsulation efficiency and controlled drug release using two medicines berberine and chlorhexidine. The aims are to:

1. Study the chemical and physical properties of Carbopol Aqua SF1 in terms of refractive index, particle size distribution and zeta potential in case of swelling and deswelling using pH stimuli.
2. Encapsulate berberine and chlorhexidine into Carbopol Aqua SF1 using swelling-deswelling technique and then to investigate the antimicrobial activity of encapsulated berberine and chlorhexidine upon incubation with algae, yeast and E.coli at different incubation time in comparison with the antimicrobial action for unencapsulated berberine and chlorhexidine at the same conditions.

3. Coat berberine or chlorhexidine loaded Carbopol Aqua SF1 with cationic polyelectrolyte (PDAC) to form PDAC coated berberine loaded carbopol microgel or PDAC coated chlorhexidine loaded carbopol microgel. The coated encapsulated berberine or chlorhexidine allowing electrostatic interaction between cationic coated encapsulated carbopol microgel and anionic cell membrane of microorganisms.

Finally, develop a novel microfluidic cell trapping micro device for testing the nanotoxicity of titania nanoparticles or the antimicrobial action of encapsulated medicines into carbopol microgel. The cell trapping microchip can be achieved through using magnetic beads which trapped into the outlet of the microchamber of microchip for trapping cells into the microchip.

Bibliography

1. C. N. R. Rao and A. C. Müller, K Anthony in *The Chemistry of Nanomaterials: Synthesis, Properties and Applications*, eds. C. N. R. Rao and A. C. Müller, K Anthony Wiley. com, Editon edn., 2006, vol. 1, pp. 1-11.
2. R. Handy, F. Kammer, J. Lead, M. Hassellöv, R. Owen and M. Crane, *Ecotoxicology*, 2008, **17**, 287-314.
3. C. Buzea, I. Pacheco and K. Robbie, *Biointerphases*, 2007, **2**, MR17-MR71.
4. E. Casals, E. Gonzalez and V. F. Puentes, *Journal of Physics D: Applied Physics*, 2012, **45**, 443001.
5. W. Cai and X. Chen, *Small*, 2007, **3**, 1840-1854.
6. S. K. Sahoo and V. Labhasetwar, *Drug Discovery Today*, 2003, **8**, 1112-1120.
7. S. L. Hart, *Current Drug Delivery*, 2005, **2**, 423-428.
8. K. Ewert, H. M. Evans, A. Ahmad, N. L. Slack, A. J. Lin, A. Martin-Herranz and C. R. Safinya, *Advances in genetics*, 2005, **53**, 119-155.
9. Y. Zhang, F. Schlachetzki, J. Y. Li, R. J. Boado and W. M. Pardridge, *Mol Vis*, 2003, **9**, 465-472.
10. N. Wiradharma, Y. Zhang, S. Venkataraman, J. L. Hedrick and Y. Y. Yang, *Nano Today*, 2009, **4**, 302-317.
11. B. Liu, M. Yang, R. Li, Y. Ding, X. Qian, L. Yu and X. Jiang, *European Journal of Pharmaceutics and Biopharmaceutics*, 2008, **69**, 527-534.
12. W. Yang, Y. Cheng, T. Xu, X. Wang and L.-p. Wen, *European Journal of Medicinal Chemistry*, 2009, **44**, 862-868.
13. S. Svenson and D. A. Tomalia, *Advanced Drug Delivery Reviews*, 2005, **57**, 2106-2129.
14. Y. Choi, T. Thomas, A. Kotlyar, M. T. Islam and J. R. Baker, *Chemistry & biology*, 2005, **12**, 35-43.
15. A. Shvedova, E. Kisin, D. Porter, P. Schulte, V. Kagan, B. Fadeel and V. Castranova, *Pharmacology & Therapeutics*, 2009, **121**, 192-204.
16. L. Lacerda, A. Bianco, M. Prato and K. Kostarelos, *Advanced Drug Delivery Reviews*, 2006, **58**, 1460-1470.
17. X. Zhang, L. Meng, Q. Lu, Z. Fei and P. J. Dyson, *Biomaterials*, 2009, **30**, 6041-6047.
18. A. Nel, T. Xia, L. Mädler and N. Li, *Science*, 2006, **311**, 622-627.
19. C. Loo, L. Hirsch, M.-H. Lee, E. Chang, J. West, N. Halas and R. Drezek, *Opt. Lett.*, 2005, **30**, 1012-1014.
20. S. W. Song, K. Hidajat and S. Kawi, *Langmuir*, 2005, **21**, 9568-9575.
21. H.-C. Huang, S. Barua, G. Sharma, S. K. Dey and K. Rege, *Journal of Controlled Release*, 2011, **155**, 344-357.
22. Y.-C. Kuo and H.-H. Chen, *International Journal of Pharmaceutics*, 2006, **327**, 160-169.
23. S. Parveen, R. Misra and S. K. Sahoo, *Nanomedicine: Nanotechnology, Biology and Medicine*, 2012, **8**, 147-166.
24. A. Zensi, D. Begley, C. Pontikis, C. Legros, L. Mihoreanu, S. Wagner, C. Büchel, H. von Briesen and J. Kreuter, *Journal of Controlled Release*, 2009, **137**, 78-86.
25. J. Panyam and V. Labhasetwar, *Advanced Drug Delivery Reviews*, 2003, **55**, 329-347.
26. S. Prabha and V. Labhasetwar, *Pharmaceutical Research*, 2004, **21**, 354-364.
27. L. Murr, E. Esquivel, J. Bang, G. De La Rosa and J. Gardea-Torresdey, *Water Research*, 2004, **38**, 4282-4296.
28. J. R. Lead and K. J. Wilkinson, *Environmental Chemistry*, 2006, **3**, 159-171.
29. M. Ammann, H. Burtscher and H. Siegmann, *Journal of Aerosol Science*, 1990, **21**, S275-S278.

30. S. Hasegawa, S. Wakamatsu, T. Ohara, Y. Itano, K. Saitoh, M. Hayasaki and S. Kobayashi, *Atmospheric Environment*, 2007, **41**, 717-729.
31. R. D. Handy, R. Owen and E. Valsami-Jones, *Ecotoxicology*, 2008, **17**, 315-325.
32. R. D. Handy and B. J. Shaw, *Health, Risk & Society*, 2007, **9**, 125-144.
33. D. Imhof, E. Weingartner, C. Ordóñez, R. Gehrig, M. Hill, B. Buchmann and U. Baltensperger, *Environmental Science & Technology*, 2005, **39**, 8341-8350.
34. A. Dahl, A. Gharibi, E. Swietlicki, A. Gudmundsson, M. Bohgard, A. Ljungman, G. Blomqvist and M. Gustafsson, *Atmospheric Environment*, 2006, **40**, 1314-1323.
35. P. G. Barlow, K. Donaldson, J. MacCallum, A. Clouter and V. Stone, *Toxicology Letters*, 2005, **155**, 397-401.
36. C. Medina, M. Santos-Martinez, A. Radomski, O. Corrigan and M. Radomski, *British Journal of Pharmacology*, 2007, **150**, 552-558.
37. M. Heinlaan, A. Ivask, I. Blinova, H.-C. Dubourguier and A. Kahru, *Chemosphere*, 2008, **71**, 1308-1316.
38. S. T. Stern and S. E. McNeil, *Toxicological Sciences*, 2008, **101**, 4-21.
39. V. Aruoja, H.-C. Dubourguier, K. Kasemets and A. Kahru, *Science of the Total Environment*, 2009, **407**, 1461-1468.
40. M. Mortimer, K. Kasemets and A. Kahru, *Toxicology*, 2010, **269**, 182-189.
41. K. Kasemets, A. Ivask, H.-C. Dubourguier and A. Kahru, *Toxicology In Vitro*, 2009, **23**, 1116-1122.
42. H. Wang, R. L. Wick and B. Xing, *Environmental Pollution*, 2009, **157**, 1171-1177.
43. S. Pal, Y. K. Tak and J. M. Song, *Applied and Environmental Microbiology*, 2007, **73**, 1712-1720.
44. S. Singh, T. Shi, R. Duffin, C. Albrecht, D. van Berlo, D. Höhr, B. Fubini, G. Martra, I. Fenoglio and P. J. Borm, *Toxicology and Applied Pharmacology*, 2007, **222**, 141-151.
45. J. Ai, E. Biazar, M. Jafarpour, M. Montazeri, A. Majdi, S. Aminifard, M. Zafari, H. R. Akbari and H. G. Rad, *International Journal of Nanomedicine*, 2011, **6**, 1117.
46. S. Hussain, S. Boland, A. Baeza-Squiban, R. Hamel, L. C. Thomassen, J. A. Martens, M. A. Billon-Galland, J. Fleury-Feith, F. Moisan and J.-C. Pairon, *Toxicology*, 2009, **260**, 142-149.
47. A. Hoshino, K. Fujioka, T. Oku, M. Suga, Y. F. Sasaki, T. Ohta, M. Yasuhara, K. Suzuki and K. Yamamoto, *Nano Letters*, 2004, **4**, 2163-2169.
48. H. Schwegmann, A. J. Feitz and F. H. Frimmel, *Journal of Colloid and Interface Science*, 2010, **347**, 43-48.
49. A. Ranga Rao and V. Dutta, *Solar Energy Materials and Solar Cells*, 2007, **91**, 1075-1080.
50. P. Baveye and M. Laba, *Environmental Health Perspectives*, 2008, **116**, A152.
51. K. M. Waters, L. M. Masiello, R. C. Zangar, B. J. Tarasevich, N. J. Karin, R. D. Quesenberry, S. Bandyopadhyay, J. G. Teeguarden, J. G. Pounds and B. D. Thrall, *Toxicological Sciences*, 2009, **107**, 553-569.
52. R. Dunford, A. Salinaro, L. Cai, N. Serpone, S. Horikoshi, H. Hidaka and J. Knowland, *FEBS Letters*, 1997, **418**, 87-90.
53. A. Primo, A. Corma and H. García, *Physical Chemistry Chemical Physics*, 2011, **13**, 886-910.
54. Y. WEN and H. DING, *Chinese Journal of Catalysis*, 2011, **32**, 36-45.
55. D. B. Warheit, B. Laurence, K. L. Reed, D. Roach, G. Reynolds and T. Webb, *Toxicological Sciences*, 2004, **77**, 117-125.
56. J. Jiang, G. Oberdörster and P. Biswas, *Journal of Nanoparticle Research*, 2009, **11**, 77-89.
57. B. Derjaguin, *Acta Physicochim. USSR*, 1941, **14**, 633-662.
58. E. J. W. Verwey, *The Journal of Physical and Colloid Chemistry*, 1947, **51**, 631-636.

59. J. N. Israelachvili, *Intermolecular and Surface Forces: 3rd ed.*; Elsevier: San Diego, CA, USA, P.674, 2011.
60. M. C. C. Ferrer, S. Dastgheyb, N. J. Hickok, D. M. Eckmann and R. J. Composto, *Acta Biomaterialia*, 2014, **10**, 2105-2111.
61. M. C. C. Ferrer, V. V. Shuvaev, B. J. Zern, R. J. Composto, V. R. Muzykantov and D. M. Eckmann, *PLoS One*, 2014, **9**, e102329.
62. C. Gonçalves, P. Pereira and M. Gama, *Materials*, 2010, **3**, 1420-1460.
63. M. M. Yallapu, M. K. Reddy and V. Labhasetwar, eds., *Biomedical Applications of Nanotechnology*, John Wiley & Sons, 2007.
64. Y. Matsumura and H. Maeda, *Cancer Research*, 1986, **46**, 6387-6392.
65. L. Brannon-Peppas and J. O. Blanchette, *Advanced Drug Delivery Reviews*, 2012, **64**, 206-212.
66. S. M. Moghimi, A. C. Hunter and J. C. Murray, *The FASEB Journal*, 2005, **19**, 311-330.
67. R. Müller, C. Jacobs and O. Kayser, *Advanced Drug Delivery Reviews*, 2001, **47**, 3-19.
68. N. C. Mueller and B. Nowack, *Environmental Science & Technology*, 2008, **42**, 4447-4453.
69. Y. Bessekhoud, D. Robert and J. V. Weber, *Journal of Photochemistry and Photobiology A: Chemistry*, 2003, **157**, 47-53.
70. C. B. Carter and M. G. Norton, in *Ceramic Materials*, Springer, Editon edn., 2007, pp. 400-411.
71. J. Tang, F. Redl, Y. Zhu, T. Siegrist, L. E. Brus and M. L. Steigerwald, *Nano Letters*, 2005, **5**, 543-548.
72. S. Mahata, S. S. Mahato, M. M. Nandi and B. Mondal, *AIP Conference Proceedings*, 2012, **1461**, 225-228.
73. S. Komarneni, *Current Science-Bangalore-*, 2003, **85**, 1730-1734.
74. X. Wang, J. Zhuang, Q. Peng and Y. Li, *Nature*, 2005, **437**, 121-124.
75. B. Xue, T. Sun, F. Mao, L.-C. Sun, W. Yang, Z.-D. Xu and X. Zhang, *Materials Research Bulletin*, 2011, **46**, 1524-1529.
76. B. Berne and R. Pecora, *Mineola, NY: Dover Publications*.
77. J. T. Edward, *Journal of Chemical Education*, 1970, **47**, 261.
78. R. Pecora, *Dynamic light scattering: applications of photon correlation spectroscopy*, Springer, 1985.
79. J. Okuda-Shimazaki, S. Takaku, K. Kanehira, S. Sonezaki and A. Taniguchi, *International Journal of Molecular Sciences*, 2010, **11**, 2383-2392.
80. A. L. Patterson, *Physical Review*, 1939, **56**, 978-982.
81. G. Oskam, A. Nellore, R. L. Penn and P. C. Searson, *The Journal of Physical Chemistry B*, 2003, **107**, 1734-1738.
82. S. Mahshid, M. S. Ghamsari, M. Askari, N. Afshar and S. Lahuti, *Semicond Phys Quantum Electron Optoelectron*, 2006, **9**, 65-68.
83. W. Chesworth, *Encyclopedia of soil science*, Springer, 2008.
84. S. Ramanathan, K. P. K. Kumar, P. K. De and S. Banerjee, *Bull Mater Sci*, 2005, **28**, 109-114.
85. R. J. Hunter, R. H. Ottewill and R. L. Rowell, *Zeta Potential in Colloid Science: Principles and Applications*, Elsevier Science, 2013.
86. M. Kosmulski, *Advances in Colloid and Interface Science*, 2002, **99**, 255-264.
87. D. A. Skoog, F. J. Holler and S. R. Crouch, *Instrumental analysis*, Cengage Learning India, 2007.
88. S. Brunauer, P. H. Emmett and E. Teller, *Journal of the American chemical society*, 1938, **60**, 309-319.
89. S. J. B. Reed, *Electron microprobe analysis and scanning electron microscopy in geology*, Cambridge University Press, 2005.

90. J. Bindell, in *Encyclopedia of Materials Characterization: Surfaces, Interfaces, Thin Films* eds. C. R. Brundle, C. A. Evans and S. Wilson, Gulf Professional Publishing, Editon edn., 1992.
91. K. Kalantar-zadeh and B. Fry, *Nanotechnology-enabled sensors*, Springer Science & Business Media, 2007.
92. L. A. Bendersky and F. W. Gayle, *Journal of Research of the National Institute of Standards and Technology*, 2001, **106**, 997.
93. W. Kyoungja and J. Hong, *Magnetics, IEEE Transactions on*, 2005, **41**, 4137-4139.
94. R. Shen, P. H. Camargo, Y. Xia and H. Yang, *Langmuir*, 2008, **24**, 11189-11195.
95. J. M. Bergen, H. A. von Recum, T. T. Goodman, A. P. Massey and S. H. Pun, *Macromolecular Bioscience*, 2006, **6**, 506-516.
96. L. M. Liz-Marzán, M. Giersig and P. Mulvaney, *Langmuir*, 1996, **12**, 4329-4335.
97. A. M. De Campos, A. Sánchez, R. Gref, P. Calvo, M. Alonso, amp, x and J. a, *European Journal of Pharmaceutical Sciences*, 2003, **20**, 73-81.
98. D. Jian-Fang and J. Ji-Sen, *Journal of Inorganic Materials*, 2007, **22**, 859-863.
99. T. I. Armstrong, M. C. Daves and L. Dium, *Journal of Drug Targeting*, 1997, **4**, 389-398.
100. D. E. Bergbreiter, *Angewandte Chemie International Edition*, 1999, **38**, 2870-2872.
101. F. Caruso, M. Spasova, V. Salgueiriño-Maceira and L. Liz-Marzán, *Advanced Materials*, 2001, **13**, 1090-1094.
102. F. Caruso, E. Donath and H. Möhwald, *The Journal of Physical Chemistry B*, 1998, **102**, 2011-2016.
103. G. Decher, *Science*, 1997, **277**, 1232-1237.
104. A. Ciferri, *Chemistry-A European Journal*, 2010, **16**, 10930-10945.
105. D. I. Gittins and F. Caruso, *Advanced Materials*, 2000, **12**, 1947-1949.
106. T. R. Farhat and J. B. Schlenoff, *Electrochemical and Solid-State Letters*, 2002, **5**, B13-B15.
107. C. Lee, I. Kim, H. Shin, S. Kim and J. Cho, *Nanotechnology*, 2010, **21**, 185704.
108. R. A. Caruso, A. Susha and F. Caruso, *Chemistry of Materials*, 2001, **13**, 400-409.
109. J.-A. He, R. Mosurkal, L. A. Samuelson, L. Li and J. Kumar, *Langmuir*, 2003, **19**, 2169-2174.
110. N. I. Kovtyukhova, B. R. Martin, J. K. Mbindyo, P. A. Smith, B. Razavi, T. S. Mayer and T. E. Mallouk, *The Journal of Physical Chemistry B*, 2001, **105**, 8762-8769.
111. M. M. Mahlambi, A. K. Mishra, S. B. Mishra, A. M. Raichur, B. B. Mamba and R. W. Krause, *Journal of Nanomaterials*, 2012, **2012**, 1.
112. D. S. Kommireddy, A. A. Patel, T. G. Shutava, D. K. Mills and Y. M. Lvov, *Journal of Nanoscience and Nanotechnology*, 2005, **5**, 1081-1087.
113. G. Carré, L. Garnier, J. Moeller-Siegert, J.-P. Gies, V. Keller, P. André and N. Keller, *RSC Advances*, 2015, **5**, 38859-38867.
114. Y. Wang, A. S. Angelatos and F. Caruso, *Chemistry of Materials*, 2008, **20**, 848-858.
115. F. Caruso, *Chemistry – A European Journal*, 2000, **6**, 413-419.
116. Y. Wang, V. Bansal, A. N. Zelikin and F. Caruso, *Nano Letters*, 2008, **8**, 1741-1745.
117. F. Caruso and H. Möhwald, *Langmuir*, 1999, **15**, 8276-8281.
118. A. B. Artyukhin, O. Bakajin, P. Stroeve and A. Noy, *Langmuir*, 2004, **20**, 1442-1448.
119. T. Cassagneau and F. Caruso, *Journal of the American Chemical Society*, 2002, **124**, 8172-8180.
120. F. Caruso, R. A. Caruso and H. Möhwald, *Science*, 1998, **282**, 1111-1114.
121. I. P. Parkin and R. G. Palgrave, *Journal of Materials Chemistry*, 2005, **15**, 1689-1695.
122. J. Santhanalakshmi, R. Komalavalli and P. Venkatesan, *Nanoscience and Nanotechnology*, 2012, **2**, 8-12.
123. K. Dai, T. Peng, H. Chen, R. Zhang and Y. Zhang, *Environmental Science & Technology*, 2008, **42**, 1505-1510.
124. D. K. Tiwari, J. Behari and P. Sen, 2008.

125. N. M. Mahmoodi and M. Arami, *Journal of Photochemistry and Photobiology B: Biology*, 2009, **94**, 20-24.
126. Q. Zhang, E. Uchaker, S. L. Candelaria and G. Cao, *Chemical Society Reviews*, 2013, **42**, 3127-3171.
127. O. Kayser, A. Lemke and N. Hernandez-Trejo, *Current Pharmaceutical Biotechnology*, 2005, **6**, 3-5.
128. F. Danhier, E. Ansorena, J. M. Silva, R. Coco, A. Le Breton and V. Préat, *Journal of Controlled Release*, 2012, **161**, 505-522.
129. M. Holzinger, A. Le Goff and S. Cosnier, *Frontiers in Chemistry*, 2014, **2**.
130. Y.-w. Jun, J.-H. Lee and J. Cheon, *Angewandte Chemie International Edition*, 2008, **47**, 5122-5135.
131. C. S. Kumar, *Nanomaterials: Toxicity, Health and Environmental issues*, Wiley-VCH Weinheim, 2006.
132. C.-W. Lam, J. T. James, R. McCluskey and R. L. Hunter, *Toxicological Sciences*, 2004, **77**, 126-134.
133. S. Takenaka, E. Karg, W. G. Kreyling, B. Lentner, H. Schulz, A. Ziesenis, P. Schramel and J. Heyder, *Inhalation Toxicology*, 2004, **16**, 83-92.
134. E. Casals, S. Vázquez-Campos, N. G. Bastús and V. Puentes, *TrAC Trends in Analytical Chemistry*, 2008, **27**, 672-683.
135. N. Künzli, M. Jerrett, W. J. Mack, B. Beckerman, L. Labree, F. Gillil, D. Thomas, J. Peters and H. N. Hodis, *Environ Health Perspect* 2005, **113**, 201-206.
136. C. Pelucchi, E. Pira, G. Piolatto, M. Coggiola, P. Carta and C. La Vecchia, *Annals of Oncology*, 2006, **17**, 1039-1050.
137. M. Geiser and W. G. Kreyling, *Part Fibre Toxicol*, 2010, **7**, 1-17.
138. P. Revell, *Nanotech Perceptions*, 2006, **2**, 283-298.
139. D. Eckmann, R. Composto, A. Tsourkas and V. Muzykantov, *Journal of Materials Chemistry B*, 2014, **2**, 8085-8097.
140. N. A. Peppas and R. Langer, *Science*, 1994, **263**, 1715-1720.
141. R. Langer and D. A. Tirrell, *Nature*, 2004, **428**, 487-492.
142. K. Donaldson, V. Stone, C. Tran, W. Kreyling and P. J. Borm, *Occupational and Environmental Medicine*, 2004, **61**, 727-728.
143. G. Federici, B. J. Shaw and R. D. Handy, *Aquatic Toxicology*, 2007, **84**, 415-430.
144. S. B. Lovern and R. Klaper, *Environmental Toxicology and Chemistry*, 2006, **25**, 1132-1137.
145. C. Hu, M. Li, Y. Cui, D. Li, J. Chen and L. Yang, *Soil Biology and Biochemistry*, 2010, **42**, 586-591.
146. L. K. Adams, D. Y. Lyon and P. J. Alvarez, *Water Research*, 2006, **40**, 3527-3532.
147. J. F. Reeves, S. J. Davies, N. J. F. Dodd and A. N. Jha, *Mutation Research/Fundamental and Molecular Mechanisms of Mutagenesis*, 2008, **640**, 113-122.
148. A. Baun, N. Hartmann, K. Grieger and K. O. Kusk, *Ecotoxicology*, 2008, **17**, 387-395.
149. K. Hund-Rinke and M. Simon, *Environmental Science and Pollution Research*, 2006, **13**, 225-232.
150. A.-G. Rincón and C. Pulgarin, *Applied Catalysis B: Environmental*, 2004, **49**, 99-112.
151. S.-C. Kim and D.-K. Lee, *Microchemical Journal*, 2005, **80**, 227-232.
152. J. Ji, Z. Long and D. Lin, *Chemical Engineering Journal*, 2011, **170**, 525-530.
153. I. M. Sadiq, S. Dalai, N. Chandrasekaran and A. Mukherjee, *Ecotoxicology and Environmental Safety*, 2011, **74**, 1180-1187.
154. B. J. Cardinale, R. Bier and C. Kwan, *Journal of Nanoparticle Research*, 2012, **14**, 1-8.
155. J. Wang, X. Zhang, Y. Chen, M. Sommerfeld and Q. Hu, *Chemosphere*, 2008, **73**, 1121-1128.
156. W.-M. Lee and Y.-J. An, *Chemosphere*, 2013, **91**, 536-544.

157. N. B. Hartmann, F. Von der Kammer, T. Hofmann, M. Baalousha, S. Ottofuelling and A. Baun, *Toxicology*, 2010, **269**, 190-197.
158. J. Hong and M. Otaki, *Journal of Bioscience and Bioengineering*, 2006, **101**, 185-189.
159. S. Dalai, S. Pakrashi, R. S. S. Kumar, N. Chandrasekaran and A. Mukherjee, *Toxicology Research*, 2012, **1**, 116-130.
160. S. D. Conner and S. L. Schmid, *Nature*, 2003, **422**, 37-44.
161. L. Y. T. Chou, K. Ming and W. C. W. Chan, *Chemical Society Reviews*, 2011, **40**, 233-245.
162. L. M. Stuart and R. A. B. Ezekowitz, *Immunity*, 2005, **22**, 539-550.
163. L. M. Bareford and P. W. Swaan, *Advanced Drug Delivery Reviews*, 2007, **59**, 748-758.
164. A. S. Verkman, *Trends in Biochemical Sciences*, 2002, **27**, 27-33.
165. A. Kumar, A. K. Pandey, S. S. Singh, R. Shanker and A. Dhawan, *Free Radical Biology and Medicine*, 2011, **51**, 1872-1881.
166. P. S. Ayyaswamy, V. Muzykantov, D. M. Eckmann and R. Radhakrishnan, *Journal of Nanotechnology in Engineering and Medicine*, 2013, **4**, 011001.
167. P. A. Tran, L. Zhang and T. J. Webster, *Advanced Drug Delivery Reviews*, 2009, **61**, 1097-1114.
168. K. S. Soppimath, T. M. Aminabhavi, A. R. Kulkarni and W. E. Rudzinski, *Journal of Controlled Release*, 2001, **70**, 1-20.
169. T. Tanaka, S. Shiramoto, M. Miyashita, Y. Fujishima and Y. Kaneo, *International Journal of Pharmaceutics*, 2004, **277**, 39-61.
170. N. B. Graham and A. Cameron, *Pure and Applied chemistry*, 1998, **70**, 1271-1275.
171. N. A. Peppas, Y. Huang, M. Torres-Lugo, J. H. Ward and J. Zhang, *Annual Review of Biomedical Engineering*, 2000, **2**, 9-29.
172. A. Kabanov and S. Vinogradov, in *Multifunctional Pharmaceutical Nanocarriers*, ed. V. Torchilin, Springer New York, Editon edn., 2008, vol. 4, pp. 67-80.
173. S. Liu, R. Maheshwari and K. L. Kiick, *Macromolecules*, 2009, **42**, 3-13.
174. W. Shen, Y. Chang, G. Liu, H. Wang, A. Cao and Z. An, *Macromolecules*, 2011, **44**, 2524-2530.
175. H. Urakami, J. Hentschel, K. Seetho, H. Zeng, K. Chawla and Z. Guan, *Biomacromolecules*, 2013, **14**, 3682-3688.
176. K. McAllister, P. Sazani, M. Adam, M. J. Cho, M. Rubinstein, R. J. Samulski and J. M. DeSimone, *Journal of the American Chemical Society*, 2002, **124**, 15198-15207.
177. S. Bontha, A. V. Kabanov and T. K. Bronich, *Journal of Controlled Release*, 2006, **114**, 163-174.
178. T. K. Bronich, S. V. Vinogradov and A. V. Kabanov, *Nano Letters*, 2001, **1**, 535-540.
179. R. T. Chacko, J. Ventura, J. Zhuang and S. Thayumanavan, *Advanced Drug Delivery Reviews*, 2012, **64**, 836-851.
180. Y. L. KHMELNITSKY, I. N. NEVEROVA, A. V. GEDROVICH, V. A. POLYAKOV, A. V. LEVASHOV and K. MARTINEK, *European Journal of Biochemistry*, 1992, **210**, 751-757.
181. M. Yan, J. Ge, Z. Liu and P. Ouyang, *Journal of the American chemical Society*, 2006, **128**, 11008-11009.
182. K. Akiyoshi, Y. Sasaki and J. Sunamoto, *Bioconjugate Chemistry*, 1999, **10**, 321-324.
183. S. H. Lee, S. H. Choi, S. H. Kim and T. G. Park, *Journal of Controlled Release*, 2008, **125**, 25-32.
184. D. Missirlis, R. Kawamura, N. Tirelli and J. A. Hubbell, *European Journal of Pharmaceutical Sciences*, 2006, **29**, 120-129.
185. M. C. C. Ferrer, R. C. Ferrier Jr, D. M. Eckmann and R. J. Composto, *Journal of Nanoparticle Research*, 2013, **15**, 1-7.

186. N. M. Oh, K. T. Oh, H. J. Baik, B. R. Lee, A. H. Lee, Y. S. Youn and E. S. Lee, *Colloids and Surfaces B: Biointerfaces*, 2010, **78**, 120-126.
187. J. K. Oh, R. Drumright, D. J. Siegwart and K. Matyjaszewski, *Progress in Polymer Science*, 2008, **33**, 448-477.
188. S. E. Gratton, P. D. Pohlhaus, J. Lee, J. Guo, M. J. Cho and J. M. DeSimone, *Journal of Controlled Release*, 2007, **121**, 10-18.
189. M. O'Brien, N. Wigler, M. Inbar, R. Rosso, E. Grischke, A. Santoro, R. Catane, D. Kieback, P. Tomczak and S. Ackland, *Annals of oncology*, 2004, **15**, 440-449.
190. H. Maeda, H. Nakamura and J. Fang, *Advanced Drug Delivery Reviews*, 2013, **65**, 71-79.
191. M. R. Kano, Y. Bae, C. Iwata, Y. Morishita, M. Yashiro, M. Oka, T. Fujii, A. Komuro, K. Kiyono and M. Kaminishi, *Proceedings of the National Academy of Sciences*, 2007, **104**, 3460-3465.
192. V. P. Torchilin, *European Journal of Pharmaceutical Sciences*, 2000, **11**, S81-S91.
193. R. A. Petros and J. M. DeSimone, *Nature Reviews Drug Discovery*, 2010, **9**, 615-627.
194. G. S. Kwon, M. Yokoyama, T. Okano, Y. Sakurai and K. Kataoka, *Pharmaceutical research*, 1993, **10**, 970-974.
195. D. Neradovic, C. Van Nostrum and W. Hennink, *Macromolecules*, 2001, **34**, 7589-7591.
196. Q. Ma, E. E. Remsen, T. Kowalewski and K. L. Wooley, *Journal of the American Chemical Society*, 2001, **123**, 4627-4628.
197. K. Glunde, Z. M. Bhujwalla and S. M. Ronen, *Nature Reviews Cancer*, 2011, **11**, 835-848.
198. W. Zhou, J. Shao, Q. Jin, Q. Wei, J. Tang and J. Ji, *Chem. Commun.*, 2010, **46**, 1479-1481.
199. Z. Cheng, A. Al Zaki, J. Z. Hui, V. R. Muzykantov and A. Tsourkas, *Science*, 2012, **338**, 903-910.
200. J. M. Boberek, J. Stach and L. Good, *PloS one*, 2010, **5**, e13745.
201. O. Türkoğlu, S. Becerik, G. Emingil, N. Kütükçüler, H. Baylas and G. Atilla, *Inflammation Research*, 2009, **58**, 277-283.
202. C. A. Lubrizol, *Noveon Consumer Specialties, Technical Data Sheet*, 2007, **294**.
203. J. R. Robinson and G. M. Mlynek, *Advanced Drug Delivery Reviews*, 1995, **16**, 45-50.
204. A. Ludwig, *Advanced Drug Delivery Reviews*, 2005, **57**, 1595-1639.
205. C. Tang, C. Yin, Y. Pei, M. Zhang and L. Wu, *European Polymer Journal*, 2005, **41**, 557-562.
206. A. Kaler, A. K. Mittal, M. Katariya, H. Harde, A. K. Agrawal, S. Jain and U. C. Banerjee, *Journal of Nanoparticle Research*, 2014, **16**, 1-10.
207. H.-R. Lin and K. Sung, *Journal of Controlled Release*, 2000, **69**, 379-388.
208. H. Qi, W. Chen, C. Huang, L. Li, C. Chen, W. Li and C. Wu, *International Journal of Pharmaceutics*, 2007, **337**, 178-187.
209. M. Imanshahidi and H. Hosseinzadeh, *Phytotherapy research*, 2008, **22**, 999-1012.
210. G. A. Cordell, M. L. Quinn-Beattie and N. R. Farnsworth, *Phytotherapy Research*, 2001, **15**, 183-205.
211. S. Kulkarni and A. Dhir, *Phytotherapy Research*, 2010, **24**, 317-324.
212. P. R. Vuddanda, S. Chakraborty and S. Singh, *Expert Opinion on Investigational Drugs*, 2010, **19**, 1297-1307.
213. K. A. Ettefagh, J. T. Burns, H. A. Junio, G. W. Kaatz and N. B. Cech, *Planta medica*, 2011, **77**, 835.
214. S. Samosorn, B. Tanwirat, N. Muhamad, G. Casadei, D. Tomkiewicz, K. Lewis, A. Suksamrarn, T. Prammananan, K. C. Gornall and J. L. Beck, *Bioorganic & medicinal chemistry*, 2009, **17**, 3866-3872.
215. A. Rempis, F. Bea, H. J. Greten, A. Buttler, H. Wang, Q. Zhou, M. R. Preusch, R. Enk, R. Eehalt and H. Katus, *Mediators of inflammation*, 2010, **2010**.
216. R. Kapoor, S. Singh, M. Tripathi, P. Bhatnagar, P. Kakkar and K. C. Gupta, *PloS One*, 2014, **9**.

217. C. J. Tsai, L. R. Hsu, J. Y. Fang and H. H. Lin, *Biol Pharm Bull*, 1999, **22**, 397-401.
218. C.-H. Chang, W.-Y. Huang, C.-H. Lai, Y.-M. Hsu, Y.-H. Yao, T.-Y. Chen, J.-Y. Wu, S.-F. Peng and Y.-H. Lin, *Acta biomaterialia*, 2011, **7**, 593-603.
219. Y.-H. Lin, J.-H. Lin, S.-C. Chou, S.-J. Chang, C.-C. Chung, Y.-S. Chen and C.-H. Chang, *Nanomedicine*, 2014, **10**, 57-71.
220. T. Wang, N. Wang, H. Song, X. Xi, J. Wang, A. Hao and T. Li, *European Journal of Pharmaceutical Sciences*, 2011, **44**, 127-135.
221. L. Wang, H. Li, S. Wang, R. Liu, Z. Wu, C. Wang, Y. Wang and M. Chen, *AAPS PharmSciTech*, 2014, **15**, 834-844.
222. Y.-C. Lin, J.-Y. Kuo, C.-C. Hsu, W.-C. Tsai, W.-C. Li, M.-C. Yu and H.-W. Wen, *International Journal of Pharmaceutics*, 2013, **441**, 381-388.
223. M. Khemani, M. Sharon and M. Sharon, *International Scholarly Research Notices*, 2012, **2012**.
224. R. Salari, B. S. F. Bazzaz, O. Rajabi and Z. Khashyarmanesh, *DARU Journal of Pharmaceutical Sciences*, 2013, **21**, 73.
225. A. M. Zhu, J. Hua Chen, Q. L. Liu and Y. L. Jiang, *Journal of Applied Polymer Science*, 2011, **120**, 2374-2380.
226. S.-J. Wu, T.-M. Don, C.-W. Lin and F.-L. Mi, *Marine Drugs*, 2014, **12**, 5677-5697.
227. C. R. Souza, H. R. Oliveira, W. M. Pinheiro, L. S. Biswaro, R. B. Azevedo, A. J. Gomes and C. N. Lunardi, *Journal of Biomaterials and Nanobiotechnology*, 2015, **6**, 53.
228. M. Beltrami, M. Bickel and P. Baehni, *Journal of Clinical Periodontology*, 1987, **14**, 161-164.
229. M. Bral and C. Brownstein, *Dental Clinics of North America*, 1988, **32**, 217-241.
230. N. Lang and M. C. Brex, *Journal of Periodontal Research*, 1986, **21**, 74-89.
231. H. Løe and C. Rindom Schiøtt, *Journal of Periodontal Research*, 1970, **5**, 79-83.
232. D. Foulkes, *Journal of Periodontal Research*, 1973, **8**, 55-60.
233. G. Greenstein, C. Berman and R. Jaffin, *Journal of Periodontology*, 1986, **57**, 370-377.
234. M. P. Young, D. H. Carter, H. V. Worthington, J. F. McCord, M. Korachi and D. B. Drucker, *Clinical oral implants research*, 2002, **13**, 20-29.
235. C. Estrela, R. G. Ribeiro, C. R. Estrela, J. D. Pécora and M. D. Sousa-Neto, *Brazilian Dental Journal*, 2003, **14**, 58-62.
236. J. F. Siqueira, I. N. Rôças, S. S. Paiva, T. Guimarães-Pinto, K. M. Magalhães and K. C. Lima, *Oral Surgery, Oral Medicine, Oral Pathology, Oral Radiology, and Endodontology*, 2007, **104**, 122-130.
237. J. Fiorellini and D. Paquette, *Current Opinion in Dentistry*, 1992, **2**, 63-79.
238. L. C. McCoy, C. J. Wehler, S. E. Rich, R. I. Garcia, D. R. Miller and J. A. Jones, *The Journal of the American Dental Association*, 2008, **139**, 178-183.
239. N. Lavoine, N. Tabary, I. Desloges, B. Martel and J. Bras, *Colloids and Surfaces B: Biointerfaces*, 2014, **121**, 196-205.
240. M. E. Barbour, D. J. O'Sullivan and D. C. Jagger, *Colloids and Surfaces A: Physicochemical and Engineering Aspects*, 2007, **307**, 116-120.
241. C. J. Seneviratne, K. C.-F. Leung, C.-H. Wong, S.-F. Lee, X. Li, P. C. Leung, C. B. San Lau, E. Wat and L. Jin, *PloS One*, 2014, **9**, e103234.
242. I. C. Yue, J. Poff, M. a. E. Cortés, R. D. Sinisterra, C. B. Faris, P. Hildgen, R. Langer and V. P. Shastri, *Biomaterials*, 2004, **25**, 3743-3750.
243. W. R. Ma Zhi-Wei, WU Zhi-Fen, Chen Dong, Zhang Bang-Le, He Wei, Wang Xiao-Juang, Liu Qing, Xu Jie and Zhu Hao *Chinese Journal of Biotechnology*, 2007, **23**, 1049-1054.
244. S. M. Reinke, M. C. RASTELLI, R. Garcia, L. A. Esmerino, J. P. De Paula, F. A. Dos Santos and P. V. Farago, *Lat. Am. J. Pharm*, 2014, **33**, 47-55.
245. K. Padois, V. Bertholle, F. Pirot, T. T. N. Hyunh, A. Rossi, P. Colombo, F. Falson and F. Sonvico, *AAPS PharmSciTech*, 2012, **13**, 1446-1450.

246. W. Musial, V. Kokol and B. Voncina, *Chemical Papers*, 2010, **64**, 346-353.
247. H. Lboutounne, J.-F. Chaulet, C. Ploton, F. Falson and F. Pirot, *Journal of Controlled Release*, 2002, **82**, 319-334.
248. B. Jiang, G. Zhang and E. M. Brey, *Acta biomaterialia*, 2013, **9**, 4976-4984.
249. A. Fini, V. Bergamante and G. C. Ceschel, *Pharmaceutics*, 2011, **3**, 665-679.
250. N. Denny and S. P. Bambang, *Solids and Structures*, 2013, **2**, 9-15.
251. M. E. Barbour, S. E. Maddocks, N. J. Wood and A. M. Collins, *International Journal of Nanomedicine*, 2013, **8**, 3507.
252. A. Manz, D. J. Harrison, E. M. Verpoorte, J. C. Fettinger, A. Paulus, H. Lüdi and H. M. Widmer, *Journal of Chromatography A*, 1992, **593**, 253-258.
253. T. M. Squires and S. R. Quake, *Reviews of Modern Physics*, 2005, **77**, 977.
254. D. Janasek, J. Franzke and A. Manz, *Nature*, 2006, **442**, 374-380.
255. J. Atencia and D. J. Beebe, *Nature*, 2005, **437**, 648-655.
256. A. W. Chow, *AIChE Journal*, 2002, **48**, 1590-1595.
257. G. M. Whitesides, *Nature*, 2006, **442**, 368-373.
258. S. K. Tang and G. M. Whitesides., in *Optofluidics: fundamentals, devices, and applications*, eds. Y. Fainman, L. Lee, D. Psaltis and C. Yang, McGraw-Hill New York:, Editon edn., 2010.
259. A. D. Stroock and G. M. Whitesides, *Electrophoresis*, 2002, **23**, 3461-3473.
260. C.-H. Lin, G.-B. Lee, Y.-H. Lin and G.-L. Chang, *Journal of Micromechanics and Microengineering*, 2001, **11**, 726.
261. X. Mu, Q. Liang, P. Hu, K. Ren, Y. Wang and G. Luo, *Lab Chip*, 2009, **9**, 1994-1996.
262. K. Ren, J. Zhou and H. Wu, *Accounts of chemical research*, 2013, **46**, 2396-2406.
263. A. T. Woolley and R. A. Mathies, *Proceedings of the National Academy of Sciences*, 1994, **91**, 11348-11352.
264. B. K. Yen, A. Günther, M. A. Schmidt, K. F. Jensen and M. G. Bawendi, *Angewandte Chemie*, 2005, **117**, 5583-5587.
265. S. Marre and K. F. Jensen, *Chemical Society Reviews*, 2010, **39**, 1183-1202.
266. P. J. Kenis, R. F. Ismagilov, S. Takayama, G. M. Whitesides, S. Li and H. S. White, *Accounts of chemical research*, 2000, **33**, 841-847.
267. J. R. Anderson, D. T. Chiu, H. Wu, O. J. Schueller and G. M. Whitesides, *Electrophoresis*, 2000, **21**, 27-40.
268. Y. Xia and G. M. Whitesides, *Annual Review of Materials Science*, 1998, **28**, 153-184.
269. H. Wu, T. W. Odom, D. T. Chiu and G. M. Whitesides, *Journal of the American Chemical Society*, 2003, **125**, 554-559.
270. M. A. Unger, H.-P. Chou, T. Thorsen, A. Scherer and S. R. Quake, *Science*, 2000, **288**, 113-116.
271. F. K. Balagaddé, L. You, C. L. Hansen, F. H. Arnold and S. R. Quake, *Science*, 2005, **309**, 137-140.
272. B. Huang, H. Wu, D. Bhaya, A. Grossman, S. Granier, B. K. Kobilka and R. N. Zare, *Science*, 2007, **315**, 81-84.
273. C. J. Kastrup, M. K. Runyon, E. M. Lucchetta, J. M. Price and R. F. Ismagilov, *Accounts of chemical research*, 2008, **41**, 549-558.
274. A. Khademhosseini, R. Langer, J. Borenstein and J. P. Vacanti, *Proceedings of the National Academy of Sciences of the United States of America*, 2006, **103**, 2480-2487.
275. K. Ren and R. N. Zare, *ACS Nano*, 2012, **6**, 4314-4318.
276. X. Mu, W. Zheng, J. Sun, W. Zhang and X. Jiang, *Small*, 2013, **9**, 9-21.
277. J. El-Ali, P. K. Sorger and K. F. Jensen, *Nature*, 2006, **442**, 403-411.
278. D. Ryan, K. Ren and H. Wu, *Biomicrofluidics*, 2011, **5**, 021501.
279. R. Mukhopadhyay, *Analytical chemistry*, 2007, **79**, 3248-3253.

280. J.-u. Shim, G. Cristobal, D. R. Link, T. Thorsen, Y. Jia, K. Piattelli and S. Fraden, *Journal of the American Chemical Society*, 2007, **129**, 8825-8835.
281. M. Bowden, L. Thompson and C. Willson, *Washington: ACS*, 1994.
282. N.-T. Nguyen and S. T. Wereley, *Fundamentals and applications of microfluidics: Fabrication Techniques for Microfluidics (Chapter 3)*, Artech House, 2002.
283. D. C. Duffy, J. C. McDonald, O. J. A. Schueller and G. M. Whitesides, *Analytical Chemistry*, 1998, **70**, 4974-4984.
284. R. Seemann, M. Brinkmann, T. Pfohl and S. Herminghaus, *Reports on Progress in Physics*, 2012, **75**, 016601.
285. K. F. Lei, in *Microfluidics in Detection Science: Lab-on-a-chip Technologies*, eds. H. L. Fatima and O. F. Henry, The Royal Society of Chemistry, Editon edn., 2015, pp. 1-28.
286. J. C. McDonald, M. L. Chabinyc, S. J. Metallo, J. R. Anderson, A. D. Stroock and G. M. Whitesides, *Analytical chemistry*, 2002, **74**, 1537-1545.
287. M. J. Owen and P. J. Smith, *Journal of Adhesion Science and Technology*, 1994, **8**, 1063-1075.
288. K. Jensen and A. Lee, Royal Soc Chemistry Thomas Graham House, Science Park, Milton Rd, Cambridge CB4 0WF, CAMBS, ENGLAND, Editon edn., 2004.
289. I. Kobayashi, K. Uemura and M. Nakajima, *Colloids and Surfaces A: Physicochemical and Engineering Aspects*, 2007, **296**, 285-289.
290. R. B. Fair, *Microfluidics and Nanofluidics*, 2007, **3**, 245-281.
291. S.-Y. Teh, R. Lin, L.-H. Hung and A. P. Lee, *Lab on a Chip*, 2008, **8**, 198-220.
292. T. Nisisako, T. Torii and T. Higuchi, *Lab on a Chip*, 2002, **2**, 24-26.
293. Z. T. Cygan, J. T. Cabral, K. L. Beers and E. J. Amis, *Langmuir*, 2005, **21**, 3629-3634.
294. P. Garstecki, M. J. Fuerstman, H. A. Stone and G. M. Whitesides, *Lab on a Chip*, 2006, **6**, 437-446.
295. C. Zhou, P. Yue and J. J. Feng, *Physics of Fluids (1994-present)*, 2006, **18**, 092105.
296. Y.-C. Tan, V. Cristini and A. P. Lee, *Sensors and Actuators B: Chemical*, 2006, **114**, 350-356.
297. T. Ward, M. Faivre, M. Abkarian and H. A. Stone, *Electrophoresis*, 2005, **26**, 3716-3724.
298. A. Utada, L.-Y. Chu, A. Fernandez-Nieves, D. Link, C. Holtze and D. Weitz, *Mrs Bulletin*, 2007, **32**, 702-708.
299. A. S. Utada, A. Fernandez-Nieves, H. A. Stone and D. A. Weitz, *Physical Review Letters*, 2007, **99**, 094502.
300. O. Philippova, A. Barabanova, V. Molchanov and A. Khokhlov, *European polymer journal*, 2011, **47**, 542-559.
301. P. Berger, N. B. Adelman, K. J. Beckman, D. J. Campbell, A. B. Ellis and G. C. Lisensky, *Journal of Chemical Education*, 1999, **76**, 943.
302. T. Banert and U. Peuker, *Chemical Engineering Communications*, 2007, **194**, 707-719.
303. N. V. Jadhav, A. I. Prasad, A. Kumar, R. Mishra, S. Dhara, K. Babu, C. Prajapat, N. Misra, R. Ningthoujam and B. Pandey, *Colloids and Surfaces B: Biointerfaces*, 2013, **108**, 158-168.
304. I. García, A. Tercjak, L. Rueda and I. Mondragon, *Macromolecules*, 2008, **41**, 9295-9298.
305. A. K. Dyab, M. Ozmen, M. Ersoz and V. N. Paunov, *Journal of Materials Chemistry*, 2009, **19**, 3475-3481.
306. W.-c. Wang, C. Peng, K. Shi and Y.-x. Pan, *Chinese Journal of Polymer Science*, 2014, **32**, 1639-1645.
307. S. A. Sundberg, *Current opinion in biotechnology*, 2000, **11**, 47-53.
308. M. Plewa, Y. Kargalioglu, D. Vankerck, R. Minear and E. Wagner, *Water Science & Technology*, 2000, **42**, 109-116.
309. M. J. Plewa, J. E. Simmons, S. D. Richardson and E. D. Wagner, *Environmental and Molecular Mutagenesis*, 2010, **51**, 871-878.

310. P. S. Dittrich and A. Manz, *Nature Reviews Drug Discovery*, 2006, **5**, 210-218.
311. A. R. Wheeler, W. R. Throdsset, R. J. Whelan, A. M. Leach, R. N. Zare, Y. H. Liao, K. Farrell, I. D. Manger and A. Daridon, *Analytical Chemistry*, 2003, **75**, 3581-3586.
312. T. H. Park and M. L. Shuler, *Biotechnology Progress*, 2003, **19**, 243-253.
313. Z. Wang, M.-C. Kim, M. Marquez and T. Thorsen, *Lab on a Chip*, 2007, **7**, 740-745.
314. G. M. Walker, H. C. Zeringue and D. J. Beebe, *Lab on a Chip*, 2004, **4**, 91-97.
315. P. J. Lee, N. Ghorashian, T. A. Gaige and P. J. Hung, *Journal of the Association for Laboratory Automation*, 2007, **12**, 363-367.
316. R. Johann, *Anal Bioanal Chem*, 2006, **385**, 408-412.
317. D. Juncker, H. Schmid and E. Delamarche, *Nat Mater*, 2005, **4**, 622-628.
318. D. G. Anderson, S. Levenberg and R. Langer, *Nat Biotech*, 2004, **22**, 863-866.
319. A. Khademhosseini, J. Yeh, G. Eng, J. Karp, H. Kaji, J. Borenstein, O. C. Farokhzad and R. Langer, *Lab on a Chip*, 2005, **5**, 1380-1386.
320. D. Di Carlo, L. Y. Wu and L. P. Lee, *Lab on a Chip*, 2006, **6**, 1445-1449.
321. J. Voldman, M. L. Gray, M. Toner and M. A. Schmidt, *Analytical Chemistry*, 2002, **74**, 3984-3990.
322. D. R. Gossett, W. M. Weaver, A. J. Mach, S. C. Hur, H. T. K. Tse, W. Lee, H. Amini and D. Di Carlo, *Anal Bioanal Chem*, 2010, **397**, 3249-3267.
323. A. Ashkin and J. Dziedzic, *Science*, 1987, **235**, 1517-1520.
324. M. Wiklund, P. Spégel, S. Nilsson and H. M. Hertz, *Ultrasonics*, 2003, **41**, 329-333.
325. F. Petersson, L. Åberg, A.-M. Swärd-Nilsson and T. Laurell, *Analytical chemistry*, 2007, **79**, 5117-5123.
326. T. Kimura, Y. Sato, F. Kimura, M. Iwasaka and S. Ueno, *Langmuir*, 2004, **21**, 830-832.
327. J. García-Alonso, R. Fakhrullin, V. Paunov, Z. Shen, J. Hardege, N. Pamme, S. Haswell and G. Greenway, *Anal Bioanal Chem*, 2011, **400**, 1009-1013.
328. G. E. Croston, *Trends in Biotechnology*, 2002, **20**, 110-115.
329. A. Tirella, M. Marano, F. Vozzi and A. Ahluwalia, *Toxicology in vitro*, 2008, **22**, 1957-1964.
330. W.-G. Koh and M. V. Pishko, *Anal Bioanal Chem*, 2006, **385**, 1389-1397.
331. J. H. Sung and M. L. Shuler, *Lab on a Chip*, 2009, **9**, 1385-1394.
332. Y. Wang, Y. Xu, Z. Zhou, W. Li, C. Dong, H. Liu and L. Zhao, *Proceedings of the Institution of Mechanical Engineers, Part N: Journal of Nanoengineering and Nanosystems*, 2014, 1740349913487900.
333. Z. Wang, M.-C. Kim and T. Thorsen, *Information Technology and Applications in Biomedicine*, 2008. ITAB 2008. International Conference on, 2008.
334. X. Zheng, J. Tian, L. Weng, L. Wu, Q. Jin, J. Zhao and L. Wang, *Nanotechnology*, 2012, **23**, 055102.

2 Chapter Two: Experimental Section

2.1 Materials

2.1.1 Purified Water

High purity water was essential for this work. It was purified by reverse osmosis and ion exchange using Milli-Q water system (Millipore, UK). Its surface tension was 71.9 mN m⁻¹ at 25°C, with measured resistivity less than 18 m Ω/cm.

2.1.2 General Chemicals Reagents

Many chemicals were used for the preparation of titania nanoparticles, formulated nanocarriers and fabrication and application of microfluidic devices as micro screening assay. Table 1 tabulates the chemicals.

Table 2.1: Chemicals for the synthesis and characterization of nanomaterials

Material	Purity	Supplier
Sodium Chloride	99.5%	Fisher, UK
Sodium Hydroxide	99.6%	Fisher, UK
Hydrochloric Acid	37%	Fisher, UK
Nitric Acid	68%	PROLABO, UK
Ammonia Solution	33%	Prime, UK
Ethanol	Absolute	Fisher, UK
Acetone	Absolute	Fisher, UK
Titanium Isopropoxide	97%	Sigma Aldrich, UK
Isopropanol Alcohol	99%	Merck, UK
Acetic acid	≥99.7%	Fisher, UK
Sodium Acetate	>99%	Aldrich, UK
Carbopol aqua SF1	30%	Lubrizol, USA
Berberine Chloride	-	Fluka, UK
Chlorhexidine digluconate	20% (V/V)	Sigma Aldrich, UK

Table 2.1: Continued

Material	Purity	Supplier
Anhydrous Ferric Chloride	97%	Fisher, UK
Ferrous Chloride	98%	Sigma-Aldrich, UK
Ammonia	33%	BDH, UK
Oleic Acid	99%	Sigma-Aldrich, UK
Styrene	99.5%	Sigma-Aldrich, UK
1 1-azobis(cyclohexanecarbonitrile)	98%	Sigma-Aldrich, UK
Hitenol BC20	-	DAI-ICHI KOGYO, Japan
Agarose	High Purity	Sigma-Aldrich, UK
(3-Aminopropyl)triethoxysilane	99%	Sigma-Aldrich, UK
Poly-L-Lysine	0.01%	Sigma, UK
Glutaraldehyde solution	25%	Sigma-Aldrich, UK
Poly (Dimethylsiloxane) SYLGARD® 184 Silicone Elastomer Kit	10:1 (Curing agent: Base)	Dow Corning, USA
Glass beads with acid- washed/silanized	75 µm size	SUPELCO, UK

2.1.3 Polyelectrolytes

Anionic and cationic polyelectrolytes were used for layer by layer coating of titania nanoparticles to obtain negatively or positively surface charged titania nanoparticles as well as obtaining cationic polyelectrolyte coated Carbopol Aqua SF1. For examples, poly (allylamine hydrochloride) (PAH) (Sigma Aldrich, UK) as a cationic polyelectrolyte with different molecular weight (15 kDa and 56 kDa), Poly (sodium-4-styrenesulfonate) (PSS) (Sigma Aldrich, UK) as an anionic polyelectrolytes with two molecular masses (10 kDa and 70 kDa), branched poly(ethyleneimine) (PEI) (Sigma Aldrich, UK), and poly(diallyldimethylammonium chloride) (PDAC) (Sigma Aldrich, UK). Figure 2.1 shows the chemical structures of PAH, PSS, PEI and PDAC.

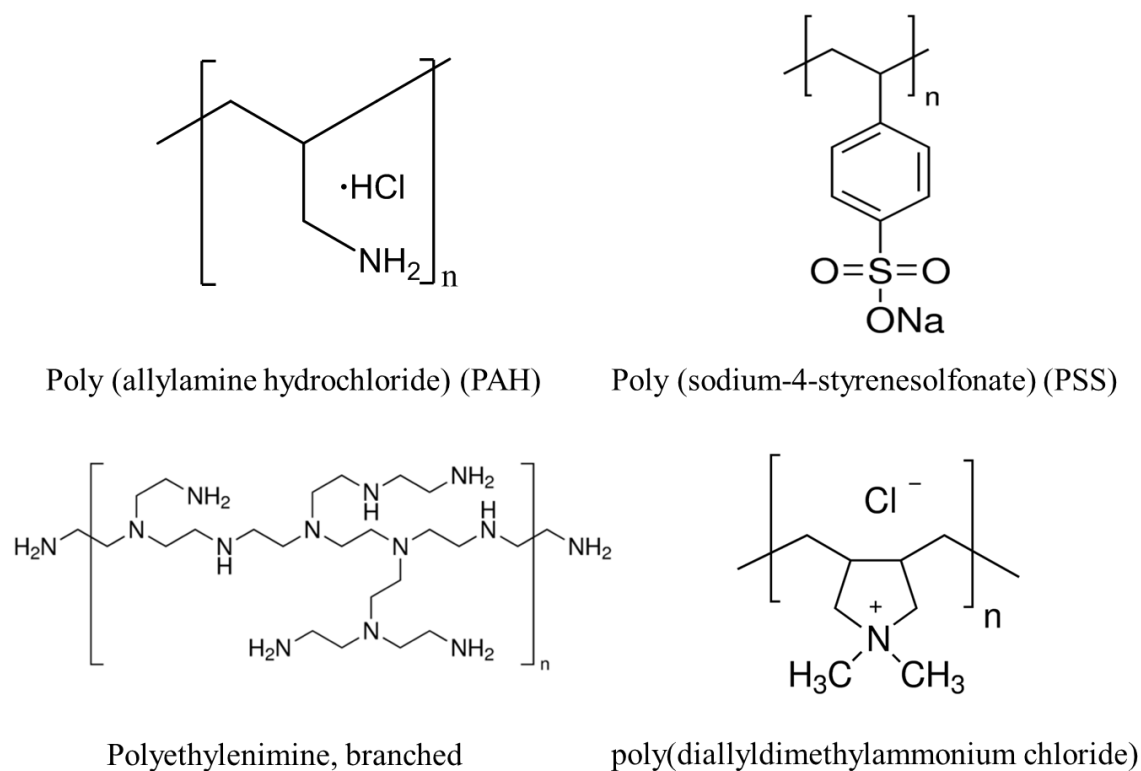


Figure 2.1: The chemical formulas of poly (allylamine hydrochloride) (PAH), Poly (sodium-4-styrenesulfonate) (PSS), polyethylenimine, and poly(diallyldimethylammonium chloride)

2.1.4 Fluorescein Diacetate (FDA)

Fluorescein diacetate (FDA) (Sigma Aldrich, UK) is an acetylated derivative of the green fluorescent dye fluorescein. The attachment of acetyl groups on the xanthenone group confers the ability to passively diffuse through a phospholipid bilayer. When FDA is in the cytoplasm, non-specific esterases de-acetylate the FDA molecule to convert it to fluorescein as shown in figure 2.2. FDA is a simple assay which is sensitive and rapid for determining microbial activity by measuring the number of viable cells according to the membrane integrity.^{1,2} FDA staining solution is prepared by dissolving 5 mg of FDA in 1 ml of acetone.³

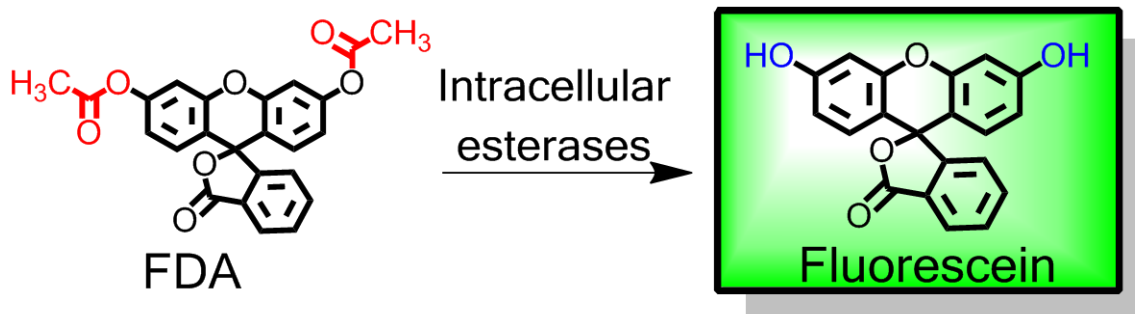


Figure 2.2: The hydrolysis of fluorescein diacetate using intracellular esterase enzyme.

2.1.5 BacTiter-Glo Microbial Cell Viability Assay

The BacTiter-Glo Microbial Cell Viability Assay is a homogenous luminescence-based assay for measuring the number of viable cells, depending on quantity of ATP presented in viable cells. The chemistry of this reaction is based on the properties of a thermostable luciferase and a proprietary formulation for extracting ATP from bacteria. The assay protocol is achieved through the addition of the BacTiter-Glo reagent directly to the sample, and subsequent measurement of luminescence. The luminescent signal generated is proportional to the amount of ATP which is considered as an indicator of the viability of cells. The luminescence nature of the assay depends on the type of bacteria to allow signal measurement.⁴ Figure 2.3 shows the luminescence reaction between the reagent and ATP in the presence of molecular oxygen.

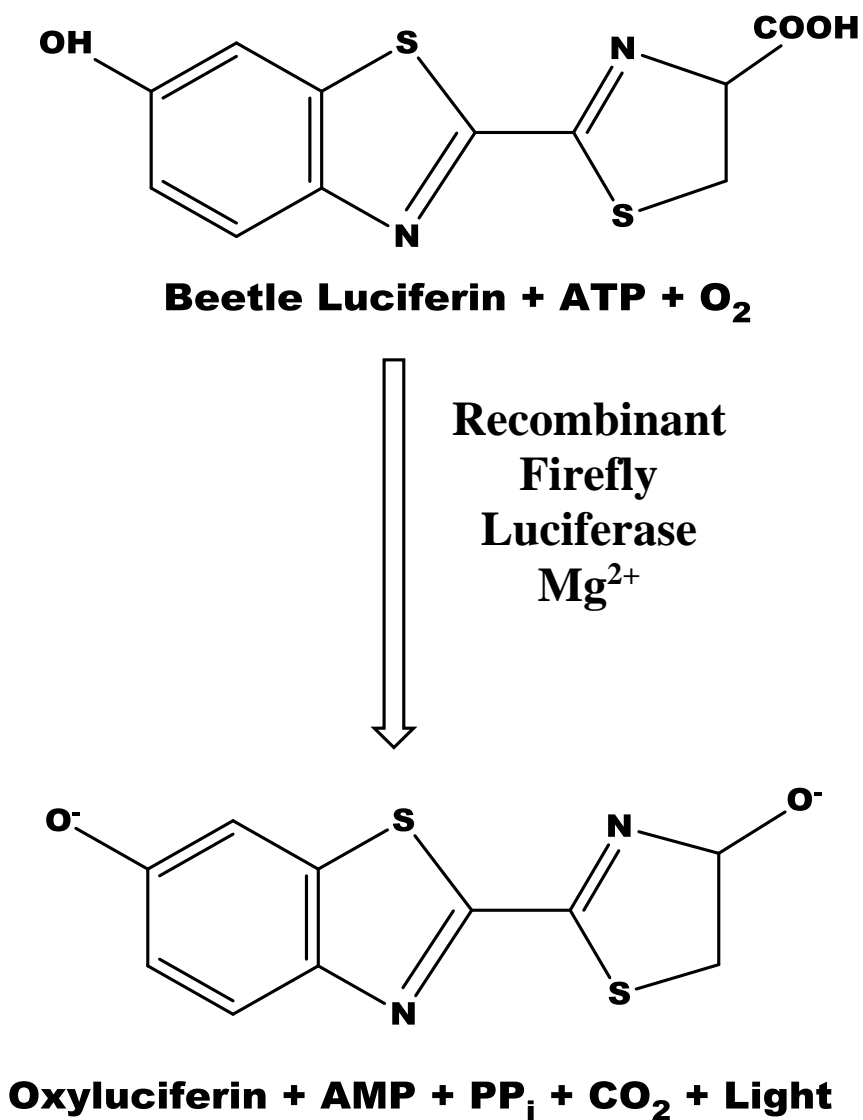


Figure 2.3: The luciferase reaction. Mono-oxygenation of luciferin is catalyzed by luciferase in the presence of Mg²⁺, ATP and molecular oxygen.

2.1.6 Culture Medium for *C.reinhardtii* cc-124 strain Growth

C. reinhardtii was supplied by Velev's group from North Carolina State University, USA. This algae culture was grown in Tris-Acetate-Phosphate (TAP) culture medium. The chemicals for the culture media (all materials provided by Sigma-Aldrich, UK) are tabulated in Table 2.2 as follows:

Table 2.2: Preparation protocol of culture media o for growing *C.reinhardtii*.^{5, 6}

1. TAP salts	NH ₄ Cl	15.0 g
	MgSO ₄ .7H ₂ O	4.0 g
	CaCl ₂ .2H ₂ O	2.0 g
Samples were dilute to 1L by Milli-Q Water		
2. Phosphate Solution	K ₂ HPO ₄	28.8 g
	KH ₂ PO ₄	14.4 g
Samples were dilute with Milli-Q Water to 100.0 ml		

3. Hutner's Trace Elements Solution. (For 1 litre final mix, each compound was dissolved in the volume of water indicated. The EDTA was dissolved in boiling water, and the FeSO ₄ solution was prepared last to avoid oxidation).	Salt	Weight (g)	Volume (ml)
	EDTA disodium salt	50 g	250 ml
	ZnSO ₄ . 7 H ₂ O	22 g	100 ml
	H ₃ BO ₃	11.4 g	200 ml
	MnCl ₂ . 4 H ₂ O	5.06 g	50 ml
	CoCl ₂ . 6 H ₂ O	1.61 g	50 ml
	CuSO ₄ . 5 H ₂ O	1.57 g	50 ml
	(NH ₄) ₆ Mo ₇ O ₂₄ . 4 H ₂ O	1.10 g	50 ml
	FeSO ₄ . 7 H ₂ O	4.99 g	50 ml
The solution was diluted to 1.0 litre and left for two weeks, in which the color changed from green to purple. It was stored in the refrigerator.			

The final culture media was produced by mixing the following:

Culture Media for <i>C.Reinhardtii</i>	Tris	2.42 g
	TAP salts	25.0 ml
	Phosphate Buffer Solution	0.375 ml
	Hutner's Trace Solution	1.0 ml
	Glacial Acetic Acid	1.0 ml
The solution produced diluted to 1.0 litre with Milli-Q Water, then autoclaved for an hour at 1.5 bar at 125°C. Cells are then cultured in this culture media for three days according to the optimum conditions given below.		

The following optimal conditions were needed to cultivate *C.Reinhardtii*:

1. Purified water.
2. light Intensity 100 W/M²
3. Temperature 30 °C
4. Light cycle 24 h ON
5. Salinity (pH 8.2 – 8.7 Max 7-9)

2.1.7 Growth of Baker's yeast (*Saccharomyces cerevisiae*)

Baker's yeast was purchased from Sigma Aldrich, UK. It is prepared using yeast extract, peptone, and dextrose (YPD medium)⁷ which is a complex medium for routine growth of yeast. It is prepared from 2 g peptone, 1g yeast extract and 2 g glucose in 100 ml Milli-Q water. These components are autoclaved for an hour at 1.5 bar at 125°C. Then, to culture yeast cells, 0.01 g of dried yeast is dispersed in the autoclaved culture media and incubated for 24 hour at 30°C.

2.1.8 Growth of Escherichia Coli (E.coli)

Non-pathogenic E.coli was supplied from Rotchell's group in the school of Biological, Biomedical and Environmental Science at the University of Hull, UK. E.coli was grown up using Luria-Bertani medium (LB medium)⁸ which can be prepared from 1

g tryptone, 0.5 g yeast extract and 0.5 g sodium chloride in 100 ml Milli-Q water. Then, these components were autoclaved for one hour at 1.5 bar at 125°C. Once the culture media was at room temperature, a few microlitres of stock suspension of E.coli was dispersed in the autoclaved culture media next to the Bunsen burner. The cultured E.coli is incubated with shaking at 25°C for 48 hour.

2.2 Instrumentation

A digital sonifier (Branson LTD) was used for dispersing TiO₂ nanoparticles samples with 30% amplitude for 5 minutes at 1.0 sec ON/1.0 sec OFF pulse time. The microscopy examination was achieved by using Olympus (Olympus BX51) and was used for obtaining transmitted and fluorescence images with different objective lenses (4x, 10x, 20x, 40x, 50x, and 100x) *via* digital camera system DP70. A Zetasizer nano ZL (Malvern, UK) was used for measuring the nanoparticles size distribution and the zeta potential of titanium dioxide nanoparticles, whereas a Mastersizer Model 2000 (Malvern, UK) was used for measuring titania particles at microscale. A Siemens D5000 X-Ray Diffractometer with 0.15418 nm wavelength (CuK α radiation) was used for the measurement of crystallite size of TiO₂ nanoparticles at different temperatures. A Perkin-Elmer UV-Vis Spectrophotometer, USA (Model Bio Lambda 25) with UV Winlab software was used to measure the absorbance of chlorophyll a and b in *Chlamydomonas R.* at 646 nm and 663 nm, respectively and additionally, the absorbance spectrum of titania nanoparticles. FT-IR spectrums were recorded at room temperature with a Perkin-Elmer FT-IR spectrometer-spectrum RX1. The FT-IR spectrometer was connected to a computer loaded with an IR Data Manager (IRDM) program. The samples were pressed into discs using spectroscopically pure KBr. A Mettler Toledo TGA/DSC1 with Star^c software system analyzer to characterize Titania nanoparticles sample over a wide temperature range. A Micromeritics instrument (USA) was used for measuring surface area of titania nanoparticles by the BET method. A Nexcelom Cellometer Auto X4 Fluorescence (fluorescence optics module XB-535-401, Excitation 475 nm /Emission 535 nm) assisted automated cell counter (purchased from Bioscience, USA) connected to a computer with Cellometer software was used to measure total, live, and dead cells, concentration, % viability and cell size. Table 2.3 shows the general equipment used to obtain results. Transmission electron microscopy (TEM) images were obtained from a JEM 2011 (JEOL,

Japan) running at 200 KV. A USB4000-UV-VIS detector (Toshiba TCD1304AP Linear CCD array, USA) was used to measure the emission spectrums of visible and UV lamp.

Table 2.3: General equipment

Instrument	Provider and Model
Centrifuge	Thermo Biofuge Primo, UK
Mini-Centrifuge	Eppendorff mini spin plus, UK
pH-meter	Fisher Brand Hydrous 300, UK
Micropipettes	Eppendorff, UK
Shaker	IKA MS 3 Basic, UK
Vortex Mixer	Stuart, UK
Hotplate with Magnetic Stirrer	IKA C-MAG HS7, UK
Rotary Evaporator	Heidolph, Germany
Muffle Furnace	Carbolite, UK
Balance	Precisa 125 ASC, UK
Homogenizer	IKA Ultra-Turrex, UK

2.2.1 Synthesis of Titanium Nanoparticles

The hydrolysis reaction of titanium tetraisopropoxide (TTIP) used for the synthesis of TiO₂NPs was a modified version of that described by Mahshid *et al.*⁹ as described in the introduction. There are two steps in the synthesis of TiO₂NPs using the sol-gel method. In the first step, titanium isopropoxide was hydrolysed with excess of water made in an acidic medium (pH 2) by using nitric acid as a peptizing agent to convert the produced precipitate to colloid particles of titanium hydroxide. Briefly, 1M HNO₃ was added drop-wise to 250 ml of purified water to adjust the pH to 2 followed by the addition of 15 ml aliquot of isopropanol. Then, 5.0 ml of TTIP was added drop-wise to the solution with vigorous stirring which led to formation of a white turbid dispersion due to the TTIP hydrolysis. The second step includes the condensation of the resulted suspension of Ti(OH)₄ which was conducted through heating for 20 hours at 70 °C. This yielded a yellow-white precipitate which was filtered, washed with ethanol and dried under vacuum (Gallenkamp vacuum

oven) at 100 °C for 2 hours. For the preparation of TiO₂NPs of different crystallite size, the titania produced was further annealed at different temperatures ranging from 100 °C to 800 °C for 2 hours. The crystallite sizes of the prepared titania in solid state were characterised using X-ray diffraction (XRD), transmission electron microscopy (TEM) and surface area measurements (BET). Aqueous dispersions of the TiO₂NPs were then prepared by dispersing 4 mg of each titania sample in 10 ml aliquots of 20 mM aqueous solution of NaCl at pH 4 by using a digital sonicator (Branson Ltd.) at 40% of the maximum power for 10 minutes at 1 sec ON/1 sec OFF pulse time and followed by filtration through a syringe filter of pore size 0.22 µm. The characterization of the TiO₂NPs size distribution and zeta potential in aqueous solutions was carried out using a Zetasizer Nano ZL (Malvern, UK). For testing the pH effect on the particle hydrodynamic diameter and zeta potential the pH was adjusted from 2 to 9 using 1 M HCl or 1 M NaOH.

2.2.2 Zeta Potential Measurement

0.0278 g of TiO₂ nanoparticles were dissolved in 100 ml of each of 0.0, 5.0, 10.0 and 20 mM of ultrapure sodium chloride aqueous solution (provided by Riedel De Haen) and dispersed using the ultrasonic probe at 30% amplitude for 5 minutes at 1.0 sec ON/1.0 sec OFF pulse time. Then, each sample was used for preparing various pH solutions ranging from 2 to 9 (0.1 M HCl or NaOH was used for adjusting the medium). The samples were used for measuring zeta potential by use of Malvern Zetasizer Nano ZL.

2.2.3 Exposure of TiO₂NPs to *C. Reinhardtii* Cells

A 100 ml aliquot of 5×10^6 cells ml⁻¹ *C.reinhardtii* was centrifuged from the culture media, washed three times and re-dispersed with 50 ml Milli-Q water. 5 ml aliquots of 1×10^7 cells ml⁻¹ suspension of the washed *C.reinhardtii* microalgae cells were then incubated with a series of 5 ml aliquots of aqueous dispersions of TiO₂NPs of a range of total particle concentrations (50-500 µg ml⁻¹). The pH of the dispersions was adjusted to 4 and then the samples were split in three parts which were illuminated for fixed periods of 0, 2, 4 and 6 hours with UV light or visible light, or kept in dark conditions, respectively. A control sample of the microalgae was also treated under the same conditions without exposure to TiO₂NPs (see fig. 2.4). Then, 1 ml aliquots of the suspended cells were taken

from each treated sample, centrifuged for 4 minutes at 3000 rpm and washed with Milli-Q water to remove the excess of TiO₂NPs. The cells were re-suspended in 1 ml of Milli-Q water, incubated with one drop of FDA solution in acetone for 10 minutes and then washed three times with Milli-Q water by centrifugation at 4000 rpm for 3 minutes. The cell viability was examined by using Olympus BX51 fluorescence microscope fitted with a DP70 digital camera and FITC fluorescence filter set. The bulk of the cell viability measurements were carried out using the automatic cell counter.. The same procedure was used to test the effect of polyelectrolyte-functionalized TiO₂NPs on the viability of *C.reinhardtii* cells as a proxy for aquatic microorganisms. *C.reinhardtii* cells were incubated with three different concentrations of TiO₂NPs/PSS (0.0, 100, and 500 µg ml⁻¹) which were incubated for 6 hours in dark conditions or illuminated with UV light. Analogous experiments were conducted with TiO₂NPs/PSS/PAH and TiO₂NPs/PSS/PAH/PSS polyelectrolyte coated particles at temperature 31 ± 2 °C.

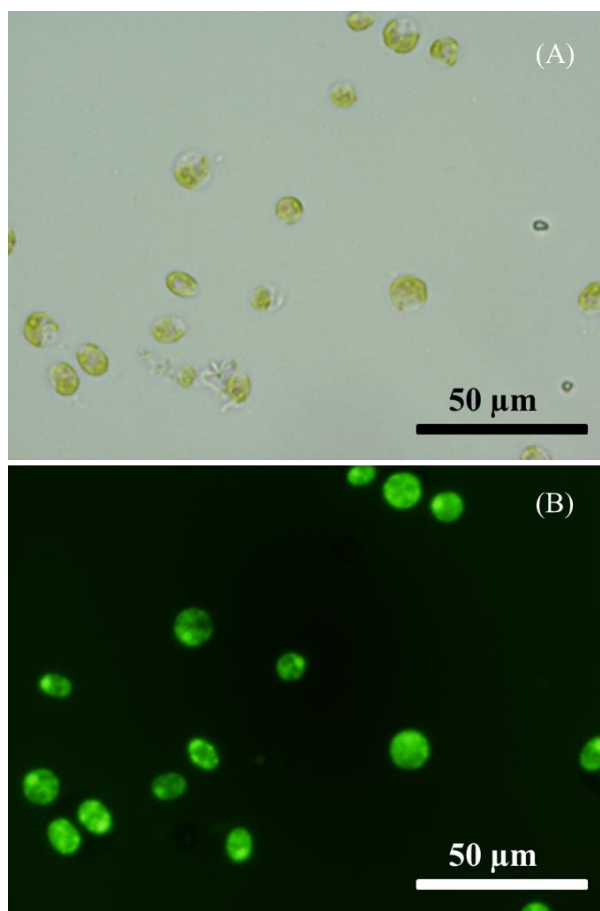


Figure 2.4: Optical microscopic image of control sample of *C.reinhardtii* at pH 4. (A) Bright field and (B) Fluorescent filter.

2.2.4 Determination of the chlorophyll content of *C. reinhardtii*

The protocol used for the determination of the total chlorophyll content of *C. reinhardtii* was adapted from Hartmut.¹⁰ An aliquot of 2.4 ml acetone was added to 0.6 ml of the *C. reinhardtii* samples which had been exposed TiO₂NPs at different particle concentration (50 – 500 µg ml⁻¹) in the presence of UV or visible light or in dark conditions. The chlorophyll content of the microalgae was extracted for 1 minute by using vortex mixer followed by centrifugation for 5 minutes at 13000 rpm. The absorbance of the supernatant was measured at 646 nm and 663 nm for the determination of chlorophyll a and chlorophyll b, respectively, by UV-Vis Spectrophotometer.

2.2.5 Exposure of TiO₂NPs to Yeast Cells

A 20 ml of the dispersion of baker's yeast was washed by centrifugation with Milli-Q water three times and then re-dispersed in 40 ml Milli-Q water. 5 ml aliquots of this cell dispersion were incubated with 5 ml TiO₂NPs aqueous suspension to obtain different total particle concentrations (250, 500, 1000, 2500 and 5000 µg ml⁻¹). The yeast samples were then exposed separately for 0, 3, 6, 12, 18 and 24 hours to visible light or UV light from the top in open glass tubes. The glass tubes were transparent to UV/vis light above 310 nm (as shown in figure 4.2 in chapter 4). The same experiments were also repeated in dark conditions. An aliquot of the yeast cells suspension was incubated with three concentrations (0, 1000, and 2500 µg ml⁻¹) of TiO₂NPs coated with PSS (M.W. 10kDa) and PAH (M.W. 15kDa). The samples were incubated at different times (0.0 h, 6 h, 12 h and 24 h) in dark conditions or illuminated with UV light. After each experiment, 1 ml of each yeast suspension sample was washed, re-suspended in 1 ml Milli-Q water and incubated with a drop of FDA solution in acetone (0.5 mg ml⁻¹) for 20 minutes. The samples were then washed with Milli-Q water, centrifuged three times at 3000 rpm for 4 minutes and the cell viability was examined by fluorescence microscopy and an automatic cell counter.

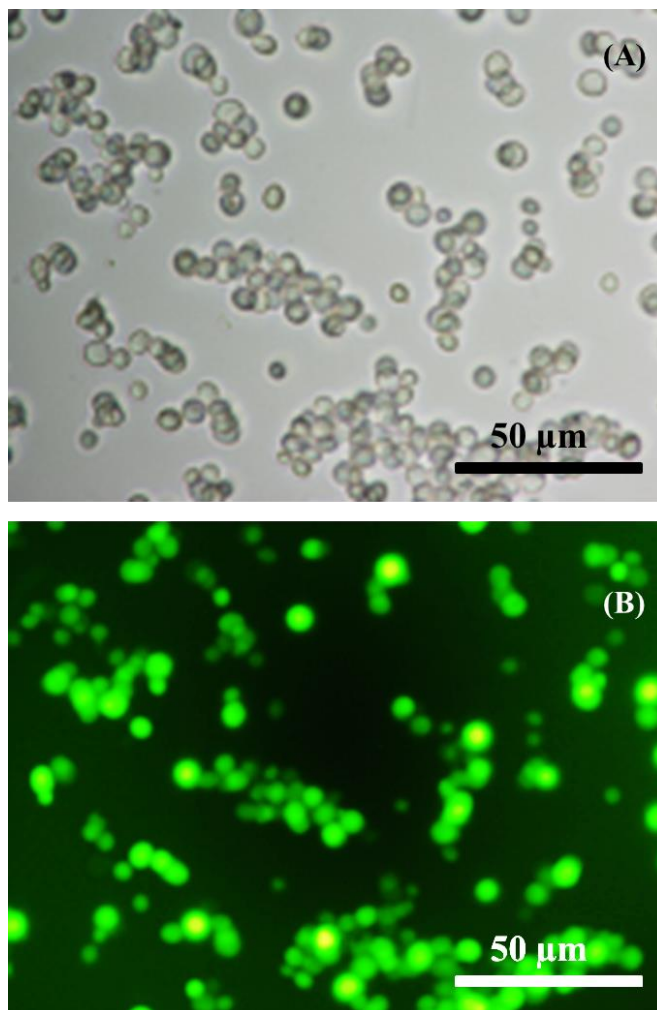


Figure 2.5: Optical microscopic images of control sample of yeast cells at pH 4. (A) Bright field. (B) Fluorescent filter.

2.2.6 Layer by Layer Polyelectrolytes coating of Titania Nanoparticles

Polyelectrolyte-coated TiO_2 NPs were prepared using only titania synthesised and annealed at $100\text{ }^\circ\text{C}$ as described in section 2.2.1. 10 ml aliquot of $1500\text{ }\mu\text{g ml}^{-1}$ TiO_2 NPs dispersion in Milli-Q water was added drop-wise to an equal amount of 10 mg ml^{-1} of solution of PSS (M.W. $\sim 70\text{kDa}$) dissolved in 1 mM NaCl solution. After shaking for 20 minutes, the particles were washed three times by centrifugation for one hour at 8000 rpm to remove the excess of PSS and were finally redispersed in 10 ml of Milli-Q water. The PSS-coated TiO_2 NPs were then mixed drop-wise with 10 ml of 10 mg ml^{-1} PAH (M.W. 15 kDa) dissolved in 1mM NaCl solution, shaken for 20 minutes and centrifuged again three

times at 8000 rpm for 1 hour to yield TiO₂NPs/PSS/PAH. For further coating with PSS, the latter was mixed drop-wise with an equal volume of 10 ml of 10 mg ml⁻¹ PSS while sonicated, then shaken for 20 min, centrifuged and dispersed in Milli-Q water to produce TiO₂NP/PSS/PAH/PSS. Furthermore, we used PSS and PAH of various molar masses (10 kDa and 70 kDa for PSS and 15 kDa and 56 kDa for PAH) to examine their effect on the size of the coated TiO₂NPs. After each polyelectrolyte coat, the TiO₂NPs were characterised by the Zetasizer to check their zeta potential and the particle aggregation.

2.2.7 TEM images of Cells

The cell morphology of *C.reinhardtii* or yeast or *E.coli* cells after incubation with nanomaterials were examined with TEM using the following protocol. The cells studied were centrifuged from nanomaterial suspension at 500 rpm, washed with Milli-Q water and fixed in 2 wt% glutaraldehyde for 1 hour at room temperature followed by treatment with 1 wt% osmium tetroxide for 1 hour. The cells were then treated for 1 h with 2.5 % uranyl acetate and washed with solutions of ethanol of increasing concentration. After standard dehydration, the cell were embedded in fresh epoxy/Araldite for 48 hours at 60 °C, left at room temperature for 48 hours at room temperature and sectioned using the ultramicrotome. The sectioned samples were then imaged with a JEOL 2010 Transmission Electron Microscope (TEM) (Japan) operating at 80 kV and the images were captured with a Gatan US4000 digital camera. A lanthanum hexaboride (LaB6) crystal was used as the electron source.

2.2.8 TEM Protocol for Nanomaterials

Titania nanoparticles or Carbopol Aqua SF1 particles was negatively stained for TEM in order to generate contrast in the TEM image. A few drops of the sample were transferred to carbon coated copper grids and allowed to settle for one minute. Then, this grid was covered with a drop of 1% aqueous uranyl acetate. The excess liquid was wicked off with filter paper and the grids allowed to air dry.

2.2.9 SEM Protocol for Cells

The cells are entirely rinsed of any growth media off the cells using PBS, adhered to Aclar film, fixed in 2.5% glutaraldehyde in 0.1M cacodylate buffer pH 7.2 for 2 hours at

room temperature, rinsed in three changes of cacodylate buffer, post fixed in 1% osmium tetroxide in cacodylate buffer for one hour, rinsed in cacodylate buffer, dehydrated in serial ethanols up to 100% and dried using liquid carbon dioxide in a critical point dryer.

2.2.10 Swelling Study of Carbopol Aqua SF1

A 0.3 wt. % w/w of Carbopol Aqua SF1 was prepared by weighing 1.5 g in 500 ml volumetric flask which completed up to the mark with purified water. 40 ml of the stock solution was added into each sample tube of eight 50 ml centrifuge tubes. The 40 ml of each centrifuge tube was adjusted to have a range of solution from pH 5 to pH 12 (0.1 M NaOH and 0.1 M HCl were used to adjust the medium). Then the particle size distribution was measured with Mastersizer 2000 MS (1000 rpm, Malvern Instruments, UK) for each pH solution at a fixed refractive index 1.453. The machine was washed three times using Milli Q water after each measurement. Then the samples were diluted to the right laser obscuration levels using the Milli-Q water.

2.2.11 Cytotoxicity Effect of Carbopol Aqua SF1

A 0.3 wt. % stock solution of Carbopol Aqua SF1 was prepared by weighing 0.3 g of Carbopol Aqua SF1 in 100 ml volumetric flask and diluting to the mark with milli-Q water. The pH of the solution was adjusted to 5.5 using acetate buffer solution. 5 ml aliquots of suspension of the washed cells were then incubated with a series of 5 ml aliquots of aqueous dispersions of Carbopol Aqua SF1 solutions at a range of concentrations (0.01-0.15 wt. %) at different incubation times. The control sample was treated in the same way without exposing to Carbopol Aqua SF1 solution. Then, 1 ml aliquots of the suspended cells were taken from each treated sample, centrifuged for 4 minutes at 3000 rpm and washed with Milli-Q water to remove the excess of Carbopol Aqua SF1 suspension. The cells were re-suspended in 1 ml of Milli-Q water, incubated with one drop of FDA solution in acetone for 10 minutes and then washed three times with Milli-Q water by centrifugation at 4000 rpm for 3 minutes. The cell viability was examined by using automatic cell counter with respect to algae and yeast while fluorescence spectroscopy was utilized to measure the relative fluorescence unit for E.coli.

2.2.12 Antimicrobial activity of Free Berberine or Chlorhexidine

A 0.2 wt. % stock solution of either berberine or chlorhexidine was prepared by weighing 0.2 g of berberine or chlorhexidine and making up to the mark to a 100 ml volumetric flask. 5 ml aliquots suspensions of the washed cells were then incubated with 5 ml of a series of concentrations (0.005-0.15 wt. %) of either berberine or chlorhexidine (prepared and diluted with autoclaved Milli-Q water from 0.2 wt. % stock solution) at various incubation times. The control sample was incubated under the same conditions but without the active material. After that, 1 ml aliquots of the suspended cells were taken from each treated sample with time, centrifuged for 4 minutes at 3000 rpm and washed with Milli-Q water to remove Carbopol Aqua Sf1 suspension. The cells were re-suspended in 1 ml of Milli-Q water, incubated with one drop of FDA solution in acetone for 10 minutes and then washed three times with Milli-Q water by centrifugation at 4000 rpm for 3 minutes. The cell viability was examined by using automatic cell counter with respect to algae and yeast while fluorescence spectroscopy was utilized to measure the relative fluorescence unit for E.coli.

2.2.13 Encapsulation of Berberine into Carbopol Aqua SF1

A 0.1 wt. % Carbopol Aqua SF1 concentration was prepared by weighing 0.1 g of stock solution and dispersed in a 20 ml Milli-Q water, then adjusted to pH 8 using 2 drops of 0.25 M NaOH. 75 ml of 0.2 wt. % of berberine chloride was added to carbopol solution to prepare 0.15 wt. % berberine in 0.1 wt. % carbopol solution. The resulted solution was stirred for half an hour and the pH of the solution were decreased to pH 5.5 using 2 drops of 0.25 M HCl with stirring. After that the solution was centrifuged for 30 minutes at 8500 rpm. The supernatant was taken to measure the encapsulation efficiency of berberine in carbopol and the precipitates were washed twice in Milli Q water. Afterwards, the precipitate was dispersed in Milli Q water and the pH of the solutions was increased to pH 8 using 2 drops of 0.25 NaOH solution. The resulting solution was stirred overnight to make sure all aggregated Carbopol solution to be swelled at pH 8 and then the pH of the solution was decreased to pH 5 using acetate buffer solution. The total volume of berberine loaded Carbopol Aqua SF1 suspension was kept at 100 ml.

2.2.14 Encapsulation of Chlorhexidine into Carbopol Aqua SF1

A 0.1 wt. % solution of Carbopol Aqua SF1 concentration were prepared by weighing 0.1 g of stock solution and dispersed in a 75 ml Milli-Q water, then adjusted to pH 8 using 3 drops of 0.25 M NaOH. Aliquot of 0.1 wt. % of chlorhexidine digluconate was added dropwise to Carbopol Aqua SF1 solution to prepare 0.1 wt. % chlorhexidine in 0.1 wt. % carbopol solution. The pH of the resulting solution were decreased to pH 5.5 using 3 drops of 0.25 M HCl with stirring. After that the solution was centrifuged for 30 minutes at 8500 rpm. The supernatant was taken to measure the encapsulation efficiency of chlorhexidine in carbopol and the precipitates were washed twice in Milli Q water. Afterwards, the precipitate was dispersed in Milli Q water and the pH of the solutions was increased to pH 8 using 3 drops of 0.25 NaOH solution. The resulted solution was stirred over night to make sure all aggregated carbopol solution to be swelled at pH 8 and then the pH of the solution was decreased to pH 5 using acetate buffer solution. The total volume of chlorhexidine loaded Carbopol Aqua SF1 suspension should be kept at 100 ml.

2.2.15 Antimicrobial Activity of Encapsulated Active Material with *C.reinhardtii*

A 100 ml aliquot of 5×10^6 cells ml⁻¹ *C.reinhardtii* was centrifuged from the culture media, washed three times and re-dispersed with 50 ml Milli-Q water. 5 ml aliquots of 1×10^7 cells ml⁻¹ suspension of the washed *C.reinhardtii* microalgae cells were then incubated with a series of 5 ml aliquots of different equivalent concentrations of 0.15 wt. % berberine or 0.1 wt. % chlorhexidine loaded 0.1 wt.% carbopol solution (0.01, 0.025, 0.05, 0.075, and 0.1 wt. %). The cell viability was measured at different incubation times up to 6 hours. Then, 1 ml aliquots of the suspended cells were taken from each treated sample, centrifuged for 4 minutes at 3000 rpm and washed with Milli-Q water to remove the free and encapsulated drug. The cells were re-suspended in 1 ml of Milli-Q water, incubated with one drop of FDA solution in acetone for 10 minutes and then washed three times with Milli-Q water by centrifugation at 4000 rpm for 3 minutes. The cell viability was examined by using Olympus BX51 fluorescence microscope fitted with a DP70 digital camera and FITC fluorescence filter set. The bulk of the cell viability measurements were carried out using an automatic cell counter.

2.2.16 Antimicrobial Activity of Encapsulated Active material with Yeast

20 ml of the dispersion of baker's yeast cultured in YPD medium was washed by centrifugation with Milli-Q water three times and then re-dispersed in 40 ml Milli-Q water. 5 ml aliquots of this cell dispersion were incubated with 5 ml of different equivalent concentrations of 0.15 wt. % berberine or 0.1 wt. % chlorhexidine loaded 0.1 wt. % Carbopol Aqua SF1 solution to obtain different total particle concentrations of each encapsulated drug. The cell viability was measured at different incubation times up to 24 hours. After each incubation, 1 ml of each yeast suspension sample was washed, re-suspended in 1 ml Milli-Q water and incubated with a drop of FDA solution in acetone (0.5 mg mL⁻¹) for 15 minutes. The samples were then washed with Milli-Q water, centrifuged three times at 3000 rpm for 4 minutes and the cell viability was examined by fluorescence microscopy and an automatic cell counter.

2.2.17 Antimicrobial Activity of Encapsulated Active Material with *E.coli*

50 ml of dispersed *E.coli* cells cultured in LB medium was washed, centrifuged three times with autoclaved milli-Q water for 3 minutes at 5000 rpm and redispersed with 50 ml Milli Q water in 50 ml red centrifuge tube. The relative luminescence unit for the culture media free cells was found to be 140 a.u. 5 ml aliquots of this cell dispersion were incubated with 5 mL of different equivalent concentrations of 0.15 wt. % berberine or 0.1 wt. % chlorhexidine loaded 0.1 wt. % carbopol solution to obtain different total particle concentrations of each encapsulated drug. After each incubation, 1 ml of each *E.coli* suspension sample was washed, re-suspended in 1 ml Milli-Q water. Then 100 µl of culture media free *E.coli* cells was incubated with 100 µl of BacTiter-Glo Microbial cell viability reagent in white opaque 96-well microplate solid flat bottom. The relative luminescence intensity was measured as a function of incubation time to find out the cell viability upon incubation with different concentration of encapsulated drug.

2.2.18 Measurement of Encapsulation Efficiency

The supernatant produced from the encapsulation of drug into Carbopol Aqua SF1 was taken and the absorbance was measured at either 252 nm for chlorhexidine or 430 nm for berberine using UV-Visible spectrophotometer. Calibration curves of each drug were created by preparing different concentrations of the drug and measuring the absorbance of

each concentration. Then, a graph was plotted for the absorbance as a function of the concentration of the drug. The linear regression equation was used to calculate the unknown concentration of the unencapsulated drug. The encapsulation efficiency of the active material loaded Carbopol Aqua SF1 was calculated by

$$\text{Encapsulation Efficiency (\%)} = \frac{[\text{Total Drug} - \text{Unencapsulated Drug}]}{[\text{Total Drug}]} \times 100$$

$$\text{Drug Loading Content (\%)} = \frac{[\text{Total Drug} - \text{Unencapsulated Drug}]}{[\text{Total Drug} - \text{Unencapsulated Drug} + \text{Carbopol amount}]} \times 100$$

2.2.19 % Drug Release

A 50 ml of average encapsulated active material (Berberine or Chlorhexidine) loaded 0.1 wt. % carbopol was added into a dialysis bag (10K MWCO). Then, the bag was placed into 500 ml beaker which has already being filled with 500 ml of acetate buffer solution (pH 5.5) (1M: 1M Acetic acid: Sodium Acetate) and capped with an aluminum foil. The bag was stirred gently with an orbital shaker at room temperature. After that, the drug release was measured in a range of wavelength from 400 nm to 200 nm using UV-Visible spectrophotometer of buffer solution in the micro centrifuge tube against water sample as a blank. The measurements were taken at 15, 30, 60, 120, 180, 240, 300, 360 and 1440 minutes. All release experiments were carried out in triplicate. The percentage of cumulative drug release can be calculated by

$$\% \text{ In Vitro Drug Release} = \frac{MR}{ML} \times 100$$

where MR is the amount of drug released from the Carbopol Aqua SF1 at time t and ML is the amount of drug loaded in Carbopol Aqua SF1.

2.2.20 Functionalization of Carbopol Aqua SF1

Varied concentrations of polyallylamine hydrochloride (PAH) (0.5 mg ml^{-1} – 2 mg ml^{-1}) and Poly(diallyldimethylammonium chloride) solution (PDAC) (0.01 mg ml^{-1} - 0.1 mg ml^{-1}) were mixed separately with a fixed concentration of Carbopol Aqua SF1 (0.1 wt. %) at

pH adjusted to 4.75-5 using acetate buffer solution whereby the final volume was 10 ml. Then the zeta potential measurement was conducted for each sample to find out the optimum concentration of both cationic polyelectrolyte and Carbopol Aqua SF1 which in turn give stable suspension.

2.2.21 Functionalization of Encapsulated Berberine with PDAC

A 1100 μ l of 0.2 wt. % poly(diallyldimethylammonium chloride) solution was rapidly added to suspension of 10 ml of 0.015 wt. % berberine loaded 0.1 wt. % Carbopol Aqua SF1 (Already prepared in section 2.2.12) with vigorous shaking and then the volume was diluted to 20 ml to form PDAC coated 0.0075 wt. % berberine loaded 0.05 wt.% Carbopol Aqua SF1 (PDAC coated BLC). The resulting solution was utilized as a stock solution to study the antimicrobial activity with algae, yeast and E.coli.

2.2.22 Functionalization of Encapsulated Chlorhexidine with PDAC

A 1150 μ l of 0.2 wt. % poly(diallyldimethylammonium chloride) solution was rapidly added to suspension of 10 ml of 0.09 wt. % chlorhexidine loaded 0.1 wt. % Carbopol Aqua SF1 (Already prepared in section 2.2.13) with vigorous shaking and then the volume was diluted to 20 ml to form PDAC coated 0.045 wt. % chlorhexidine loaded 0.05 wt. % Carbopol Aqua SF1 (PDAC coated CLC). The resulting solution was utilized as a stock solution to study the antimicrobial activity of PDAC coated CLC individually with each of algae, yeast and E.coli.

2.2.23 Cytotoxic Effect of PDAC on Algae, Yeast and E.coli

A series of concentrations of poly(diallyldimethylammonium chloride) solution (0.0045 wt. % - 0.05 wt. %) were incubated separately with 5 ml volumes of each microorganisms (algae, yeast and *E.coli*) and the cell viability was measured at different incubation time using the same procedure mentioned in sections 2.2.14, 2.2.15, and 2.2.16, respectively.

2.2.24 Cytotoxic Effect of PDAC Coated Carbopol Aqua SF1 on Algae, Yeast and E.coli

5 ml aliquots of each concentration of PDAC coated Carbopol Aqua SF1 suspension (0.0018 wt. % to 0.018 wt. %) were incubated individually with 5 ml volume of each cell,

algae, yeast and *E.coli*. Then the viability was measured using the same procedure mentioned in sections 2.2.14, 2.2.15, and 2.2.16, respectively.

2.2.25 Antimicrobial Activity of PDAC Coated BLC

A 50 ml aliquot of each cell (Algae, Yeast and *E.coli*) was centrifuged from the culture media, washed three times and re-dispersed with 5 ml autoclaved purified water. 250 µl aliquots of the washed cells were then incubated with 5 ml of series concentrations of stock solution of PDAC coated 0.0075 wt. % berberine loaded 0.05 wt.% Carbopol Aqua SF1 (PDAC coated BLC) whereby the cell viability was measured according to the procedures mentioned in sections 2.2.14, 2.2.15, and 2.2.16, respectively. For algae, the series concentrations were ranged from 0.0018 wt. % PDAC coated 0.0015 wt. % berberine loaded Carbopol Aqua SF1 suspension to 0.0045 wt. % PDAC coated 0.00375 wt. % berberine loaded Carbopol Aqua SF1 microgel complex while for yeast were from 0.0018 wt. % PDAC coated 0.0015 wt. % berberine loaded Carbopol Aqua SF1 to 0.009 wt. % PDAC coated 0.0075 wt. % berberine loaded Carbopol Aqua SF1 and for *E.coli* was from 0.0022 wt. % PDAC coated 0.0015 wt. % berberine loaded Carbopol Aqua SF1 to 0.0088 wt. % PDAC coated 0.006 wt. % berberine loaded Carbopol Aqua SF1.

2.2.26 Antimicrobial Activity of PDAC Coated CLC

The same procedure as mentioned in Section 2.2.24 was followed to study the antimicrobial activities of PDAC coated chlorhexidine loaded Carbopol Aqua SF1 against each of algae, yeast and *E.coli* cells. The stock solution used was 0.0045 wt. % PDAC coated 0.045 wt. % chlorhexidine loaded 0.05 wt. % Carbopol Aqua SF1 (PDAC coated CLC). In this experiment, the series of concentrations of stock solution incubated with algal cells ranged from 0.0018 wt. % PDAC coated 0.009 wt. % chlorhexidine loaded Carbopol Aqua SF1 microgel, to 0.0045 % PDAC coated 0.0225 wt. % chlorhexidine loaded Carbopol Aqua SF1 microgel. For yeast, from 0.0018 wt. % PDAC coated 0.009 wt. % chlorhexidine loaded Carbopol Aqua SF1 microgel to 0.009 % PDAC coated 0.045wt. % chlorhexidine loaded Carbopol Aqua SF1 microgel was used and for *E.coli* cells, 0.0022 wt. % PDAC coated 0.009 wt. % chlorhexidine loaded Carbopol Aqua SF1 microgel to 0.0055 % PDAC coated 0.0225 wt. % chlorhexidine loaded Carbopol Aqua SF1 microgel was used.

2.2.27 Chemical Adhesion of *C.reinhardtii*

1.5 μl of poly L lysine (50 ml of sterile tissue culture grade water to 5 mg of poly-lysine) was added to the surface of sterile micro chamber and incubated for 24 h. Now, the glass chip was bonded with PDMS chip by chip holder and tubing where the coated glass/PDMS chip washed with Phosphate Buffered Saline (PBS, pH 7.4). Then, the algae cell suspension was pumped immediately at flow rate $10 \mu\text{l}\cdot\text{min}^{-1}$ for 30 minutes and the pumping was stopped for 30 minutes to allow cells to adhere to the poly-L-lysine adhered to the surface of glass chip. After that, the chip was washed with PBS buffer solution (pH7.4) to remove unbounded cells, then FDA solution was pumped for 15 minutes and stopped for 10 minutes to check the viability of cells. The viability of cells was determined using fluorescence microscope at FITC position with different magnifications.

2.2.28 Synthesis of Magnetized Glass Beads

Magnetic nanoparticles were synthesized according to procedure published by Berger *et al.*¹¹ Briefly, 1 ml of 2M FeCl_2 solution and 4 ml of 1M FeCl_3 solution (Both of salts were dissolved in 2.0 M of Hydrochloric acid) were mixed vigorously together. Then a magnetic stirring bar was placed in the flask and began stirring vigorously. 50 ml of 0.7 M aqueous NH_3 solution was added dropwise by pipette or burette into the flask. The slow rate of addition is critical, and a burette is a convenient means of slowing the addition rate. Magnetite, a black precipitate, was formed immediately. Stir throughout the addition of the ammonia solution. After that the precipitate to settle without stirring (5–10 min), the dark, and sludge like solid at the bottom of the beaker was iron oxide magnetic nanoparticles. Afterwards, the precipitate was washed three times until the solution gives pH 6.5-7. Then magnetic particles were heated up to 80°C for one hour. After that, the solution was incubated at room temperature and washed three times with Milli Q water. The synthesized iron oxide nanoparticles was coated with cationic polyelectrolyte (polyallylamine hydrochloride) to convert the surface charge of magnetic particles to positive charge by dispersing small amount of magnetic nanoparticles with 10 mg/ml of PAH for 20 minutes with ultrasonic probe to form PAH coated magnetic nanoparticles.

On the other hand, layer by layer coating was conducted for glass beads with $75 \mu\text{m}$ with cationic and anionic polyelectrolyte. The first step included surface activation of glass

beads with piranha solution and washed many times. The activated glass beads were first coated with 10 mg.ml^{-1} PAH cationic polyelectrolyte and washed with purified water three times, then further coated with 10 mg. ml^{-1} PSS anionic polyelectrolyte to generate PSS-PAH-glass beads. After that the PSS-PAH-glass beads suspension were mixed with equal volume of PAH coated magnetic nanoparticles for 20 minutes and ultra-sonication for 5 minutes to form PAH-magnetic nanoparticles coated PSS-PAH-Glass beads (Magnetized magnetic beads). The final suspension was tested their magnetic response using high performance neodymium magnet.

2.2.29 Synthesis of Magnetized Yeast Cells

The same procedure for the synthesis of magnetic nanoparticles mentioned in section 2.2.28 was utilized which involves synthesis of PAH coated magnetic nanoparticles.¹² These PAH coated magnetic nanoparticles were added dropwise with vigorous stirring to equal volume of yeast cells suspension at flow rate $250 \mu\text{l.min}^{-1}$. Then, the magnetized yeast cells were washed three times with purified water to get rid of the excess amount of cationic polyelectrolyte (PAH). These magnetized yeast cells were further used for trapping cells in the micro chambers of microchip.

2.2.30 Synthesis of Magnetized PDMS Beads in Wet Agar Layer

The same procedure as described in section 2.2.28 was used with some modifications. The synthesized magnetic nanoparticles were heated up to 1 hour at 80°C and then 1 ml of oleic acid was added with continuing heating for 1 more hour with drastic stirring. A black precipitate was formed in the bottom of 100 ml beaker trapped on the magnet. The suspension was cooled to room temperature. The precipitated particles were washed five times with water and ethanol, separated by magnetic decantation and dried in an oven at 80°C . The obtained oleic acid coated magnetic nanoparticles could be easily dispersed in low density silicone fluid (CP20) using ultrasound to form oil-based ferrofluids. PDMS was prepared by weighing 9 g of pre-polymer and 1 g curing agent and mixing vigorously for couple of minutes till many bubbles appear. The PDMS was then centrifuged for three minutes at 3000 rpm to remove bubbles. After that, a 20% oil based ferrofluid suspension was dispersed with 80% PDMS to form PDMS dispersed OAMNPs. On the other side,

0.75 gm agar was dissolved in Milli-Q water and heated up 80°C for a period of time to dissolve agar completely. Then the agar solution was poured off Petri dish and left to solidify. Then, 1% xanthan gum and 1% sodium dodecyl sulphate (SDS) were dissolved in water and poured on the top layer of solidified agar. A 50 µl glass syringe was filled with PDMS dispersed oleic acid coated magnetic nanoparticles (OCMNs) and then the needle of glass syringe immersed and wiped manually in the interface of wet agar layer. Then the petri dish was placed in an oven with 40°C for 24 hours to allow magnetized PDMS beads to solidify.

2.2.31 Synthesis of Magnetic Micro Beads

Magnetite (Fe_3O_4) nanoparticles were prepared by coprecipitation of Fe^{3+} and Fe^{2+} (2:1 molar ratio) with ammonia solution.¹³ Briefly, 0.1 M of FeCl_3 (anhydrous, 97%, Fisher) and 0.05 M $\text{FeCl}_2 \cdot 4\text{H}_2\text{O}$ (98%, BDH) were dissolved in 40.0 ml of Milli-Q water. The solution was heated and stirred at 80 °C for 1 hour. Then 12.0 ml of NH_4OH (33% w/w, BDH) and 1.0 ml oleic acid (99%, Sigma Aldrich) were added rapidly. At the same temperature, the produced suspension was vigorously stirred for 1 hour and then cooled to room temperature. The precipitated particles were washed five times with water and ethanol, separated by magnetic decantation and dried in an oven at 80 °C. The obtained OCMNs were easily dispersed in styrene (99.5%, Sigma Aldrich) using ultrasound probe to form oil-based ferrofluids for 10 minute at 30 % amplitude. The thermal initiator 1,1-Azobis(cyclohexanecarbonitrile) (Vazo) was added for thermal polymerisation. The oil in water emulsion we prepared by mixing 20% of oil based magnetic nanoparticles with 80% of 5% Hitenol BC20 (Dai-Ichi Kogyo Seiyaku, Japan) and homogenised manually. Afterwards, the resulting emulsion was mixed equally with 2% hot agarose, and cooling them under tap water, then heating them up to 72.5 degree for 3.5 hours. After that, the produced particles was heated up to 88 degree to melt agarose and washing magnetic particles with the same temperature many times to get solidified magnetic particles.

2.3 Chip Fabrication

2.3.1 Fabrication of Microfluidic Flow Focusing Chip

A flow focusing microfluidic device was utilized as a chip for generating different sizes of droplets according to the flow rate of the dispersed and continuous phases. The channel design was drawn in AutoCAD program and sent to Photo Tools LTD (UK) for the photomask production. The photomask was put on top of the photoresist coated borosilicate glass (30 mm length x 60 mm width) and exposed to UV light for 60 second. Then, the chip was developed, chrome etched, and wet etched with a mixture of nitric acid and hydrofluoric acid. The depth of the channel depended on times, as the time increased, the channel becomes deeper. The channel dimension was 50 μm channel width and 100 μm channel depth. Then, fluidic access holes at the end of each channel were drilled using a drill press. The etched chip was then irreversibly sealed under pressure to another glass chip at temperature 640 $^{\circ}\text{C}$, held for 6-8 hours. Figure 2.4 shows the flow focusing microfluidic devices that was used for the generation of magnetic beads. It can be seen in Figure 2.4A that styrene based oleic acid coated magnetic nanoparticles were placed in the centre of the flow focusing chip which represents the dispersed phase at flow rate 1 $\mu\text{l}\cdot\text{min}^{-1}$ while on both sides of flow focusing microchip were the surfactant (sodium dodecyl sulphate or Hitenol BC20) dispersed in purified water as a continuous phase at flow rate 5 $\mu\text{l}\cdot\text{min}^{-1}$. It can also be seen in Figure 2.4B that the same continuous and dispersed phases as mentioned in Figure 2.4A were used while a further serpentine mixing channels were added to increase the stability of generated droplets.

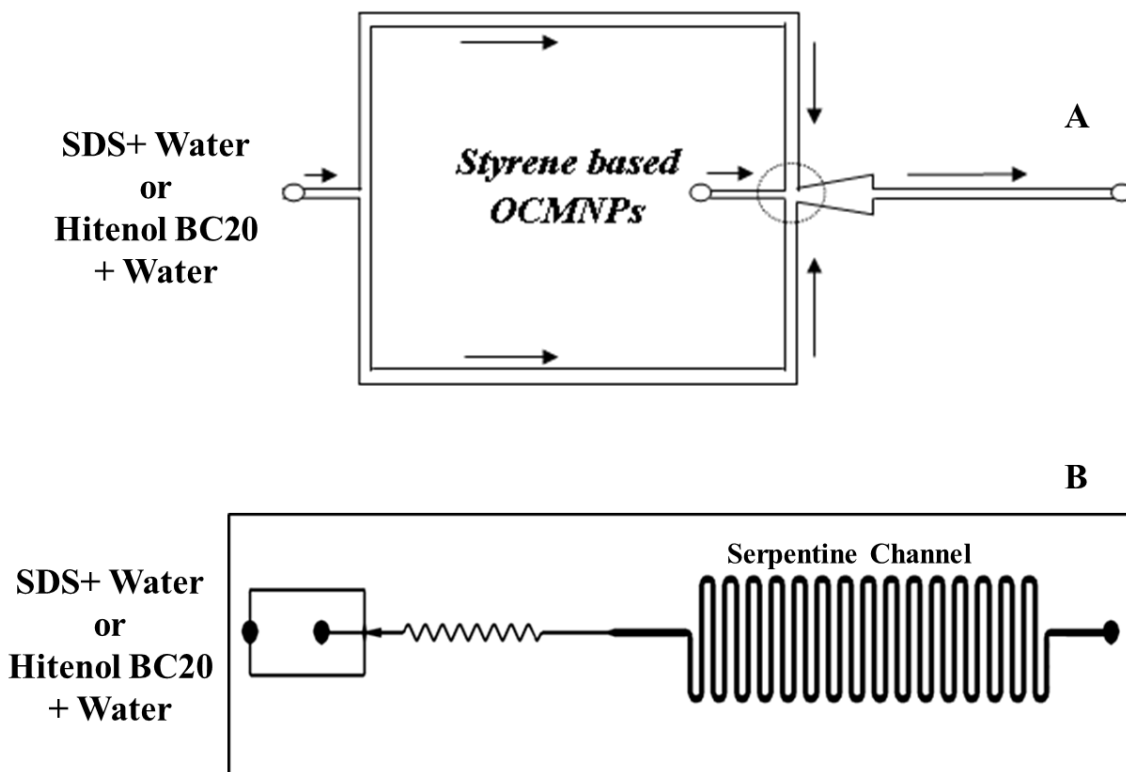


Figure 2.6: The droplet generation microfluidic chip using flow focusing technique. (A) Normal flow focusing microchip and (B) Flow focusing microchip with serpentine mixing channels

2.3.2 Fabrication of Microfluidic Cell Trapping Chip

The microfluidic cell based array (bottom plate) was fabricated by using photolithography technology as described previously. The fabricated chip was 30 mm length x 30 mm width with 50 μm channel width and 100 μm channel depth. It also consisted of two inlets, one inlet for passing a specific concentration of titania nanoparticles, the second inlet to inject cells and from the two inlets the fluorescein diacetate (FDA) solution is utilised to measure the viability of the cells after incubation with titania nanoparticles at different exposure times. The second part of the chip was the microchambers where the cells were trapped by magnetic beads and finally, the outlet which represents the waste as shown in figure 2.5.

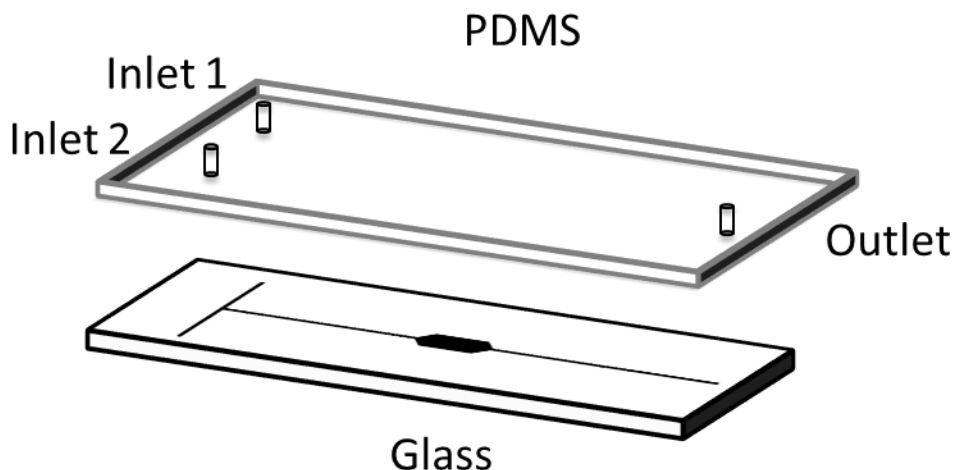


Figure 2.7: Microfluidic scheme for trapping cells into microchamber. The two inlets are used for passing cells, toxin, and FDA solution, the microchamber is for trapping cells using magnetic beads through controlling with very strong magnet and the outlet is for flushing out cells and chemicals off chip.

The upper plate (PDMS) (Sylgard 184, Dow Corning, Midland, MI) was prepared with a 10:1 ratio between the PDMS and the curing agents. The mould was degassed in a vacuum chamber for 10 min before curing in a 70°C oven for 4 h. The devices were then cut by a razor blade and the fluidic connection ports were punched using an 18-gauge flat-tip needle. The device was then irreversibly bonded to glass plate after oxygen plasma treatment (Plasma Therm Etcher, 50 W, 2 torr, 60 sec) for the face up of the glass (bottom plate) and PDMS (top plate), then PDMS/glass microfluidic devices was heated up to 80°C for an hour to strengthen the bonding between PDMS and glass.

Bibliography

1. G. G. Guilbault and D. N. Kramer, *Analytical Chemistry*, 1964, **36**, 409-412.
2. J. Schnürer and T. Rosswall, *Applied and environmental microbiology*, 1982, **43**, 1256-1261.
3. *Cold Spring Harbor Protocols*, 2008, **2008**, pdb.rec11277.
4. *Promega UK Ltd, Technical Bulletin: BacTiter-Glo Microbial Cell Viability Assay. Instructions for use of products G8230, G8231, G8232, G8233, Part# TB337.*
5. D. S. Gorman and R. Levine, *Proceedings of the National Academy of Sciences of the United States of America*, 1965, **54**, 1665.
6. S. Hutner, L. Provasoli, A. Schatz and C. Haskins, *Proceedings of the American Philosophical Society*, 1950, **94**, 152-170.
7. *Cold Spring Harbor Protocols*, 2006, **2006**, pdb.rec8194.
8. *Cold Spring Harbor Protocols*, 2009, **2009**, pdb.rec11945.
9. S. Mahshid, M. S. Ghamsari, M. Askari, N. Afshar and S. Lahuti, *Semicond Phys Quantum Electron Optoelectron*, 2006, **9**, 65-68.
10. K. Hartmut, *Analysis (Peach, K. & Tracey, MV, eds.)*, 1983, **4**, 142-196.
11. P. Berger, N. B. Adelman, K. J. Beckman, D. J. Campbell, A. B. Ellis and G. C. Lisensky, *Journal of Chemical Education*, 1999, **76**, 943.
12. R. F. Fakhrullin, J. Garcia-Alonso and V. N. Paunov, *Soft Matter*, 2010, **6**, 391-397.
13. A. K. F. Dyab, M. Ozmen, M. Ersoz and V. N. Paunov, *Journal of Materials Chemistry*, 2009, **19**, 3475-3481.

3 Chapter Three: Synthesis, characterization and functionalization of titania nanoparticles: An Introduction

Titania nanoparticles play vital role in many applications involving industrial, pharmaceutical and electronics¹ due to their unique physical and chemical properties such as quantum effect, particle size, and surface area where they have potential toxic effect upon releasing to the environment.² Therefore, in this chapter, titania nanoparticles were synthesized and characterized to study their behavior upon incubation with some microorganisms as well as functionalization of titania nanoparticles with anionic and cationic polyelectrolytes to study the effect of surface charge on microorganisms.

3.1 Synthesis of Titania Nanoparticles

The hydrolysis reaction which was used for the synthesis of titanium dioxide nanoparticles involved titanium isopropoxide as a precursor and isopropanol and Milli-Q water as a solvent. There are two steps in the synthesis of TiO₂NPs using the sol-gel method: Firstly, the hydrolysis of titanium isopropoxide with excess water to give a fast reaction in acidic medium (pH 2) by using nitric acid as a peptizing agent to convert the produced precipitate to colloidal particles. Secondly, condensation of the resulting suspended solution for 20 hours at 70 °C. A yellow-white precipitate formed from this procedure. The overall chemical reactions can be schematically denoted by



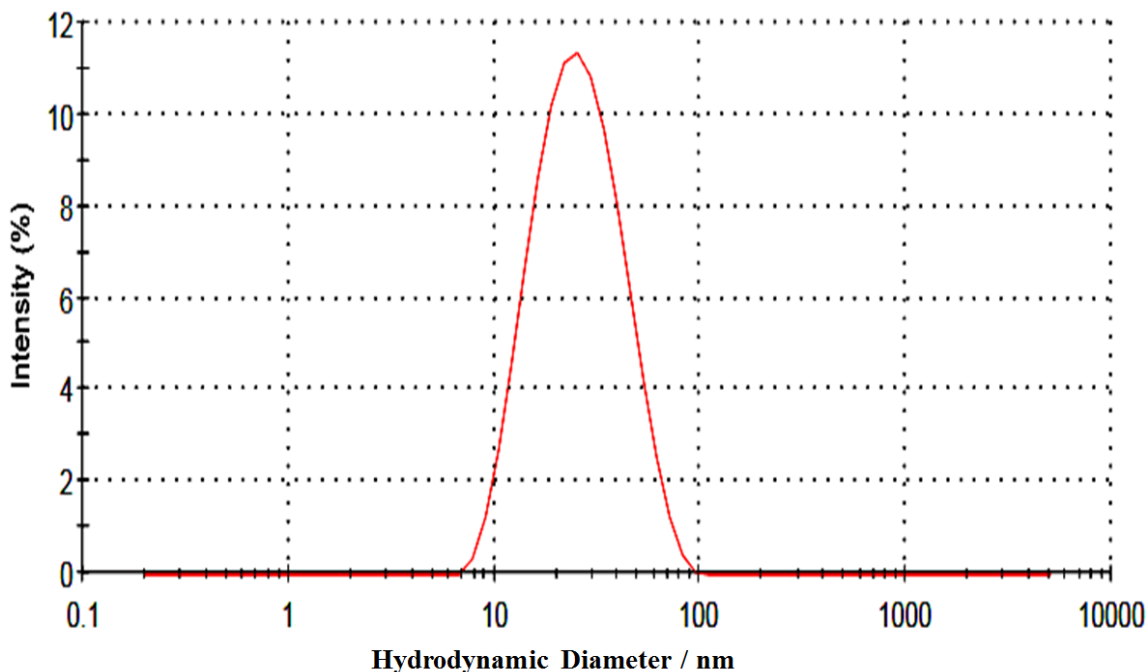


Figure 3.1: The average size distribution of water dispersed titanium dioxide NPs (pH 4) that synthesized by hydrolysis and condensation of titanium isopropoxide at acidic medium for 20 hours at 70°C.

The characterization of TiO₂ nanoparticles was achieved by taking a small portion of precipitate and dispersing in Milli-Q water as described in section 2.2.1 in Chapter 2. The average particle diameter of the dispersed sample was measured using dynamic light scattering. Figure 3.1 illustrates the size distribution of TiO₂ NPs which dispersed in Milli-Q water (pH 4) at 30% amplitude for 5 minutes. The average particle diameter of titania nanoparticles was measured to be 25 nm ranging from 5 nm to 45 nm.

X-Ray Powder Diffraction was used to measure the TiO₂ nanoparticle crystalline size by using the Scherrer function³ and to study the morphology of the synthesized crystalline titanium nanoparticles. Equation (2) from section 1.5.2 was used to calculate the crystallite size of the titania nanoparticles. The *anatase* TiO₂ nanoparticle was found to be 5 nm which agreed with that obtained in the literature.³ Figure 3.2 shows the x-ray diffraction pattern of the TiO₂ NPs sample.

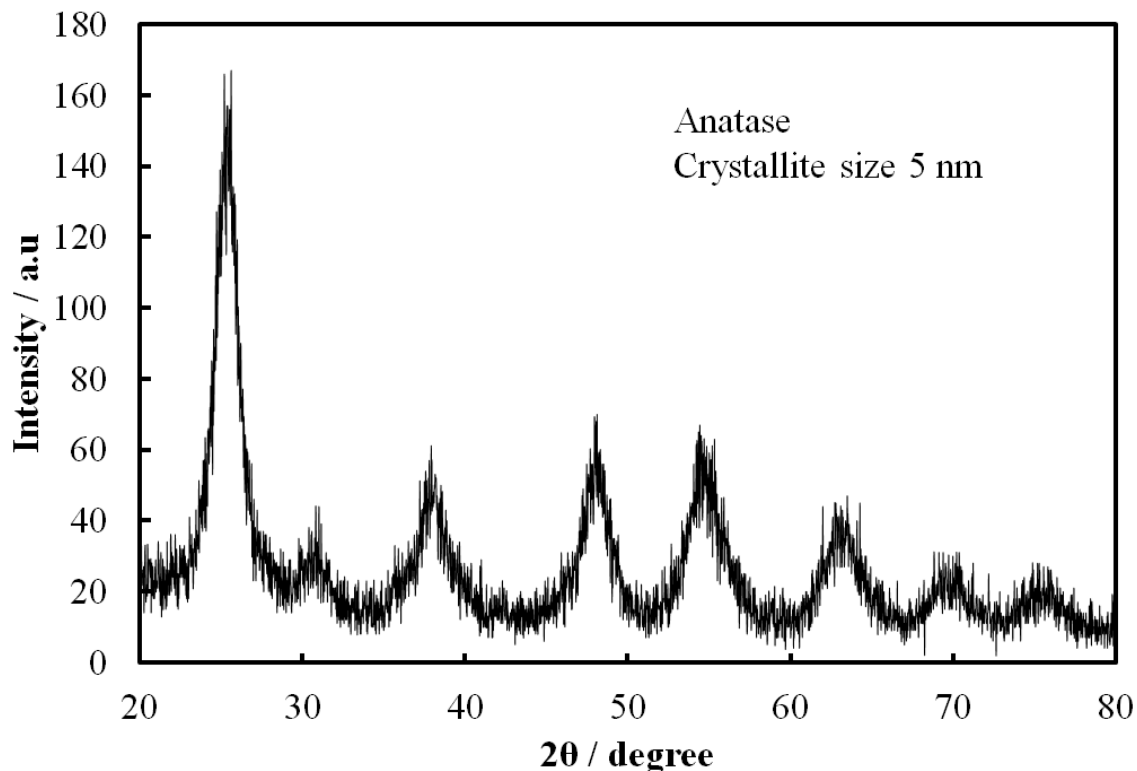


Figure 3.2: X-Ray Diffraction pattern of anatase TiO₂ NPs which was prepared by hydrolysis at pH 2 followed by condensation of titanium isopropoxide at 70°C for 20 hour.

To optimize the synthesis of titania nanoparticles, parameters such as temperature, pH and the volume of the precursor were investigated.

3.1.1 Effect of the amount of Titanium Isopropoxide Precursor

Series of aliquots (1.0, 3.0, 5.0 and 7.0 ml) of titanium isopropoxide as a precursor were utilized to synthesize titania nanoparticles to investigate the effect of volume of the precursor as described in Section 2.2.1 in chapter 2. Four different precipitates were produced and the particle size of each sample was measured three times by the Zetasizer. Figure 3.3 shows the effect of TiO₂ precursor on the particle size indicating that the TiO₂ particle size did not appear a significant increase as the amount of precursor increased, referring to that grain size of titania nanoparticles does not depend on the amount of precursor. Figure 3.4 also shows the X-Ray diffractions patterns of TiO₂ NPs samples that synthesized with different volumes of precursor. It could be seen that the crystallite sizes

obtained from the XRD measurements of TiO_2 samples were approximately 4-6 nm illustrating that there was no significant difference between crystallite sizes of synthetic samples. Thus, it was shown that changing the amount of precursor did not affect significantly the crystallite size.

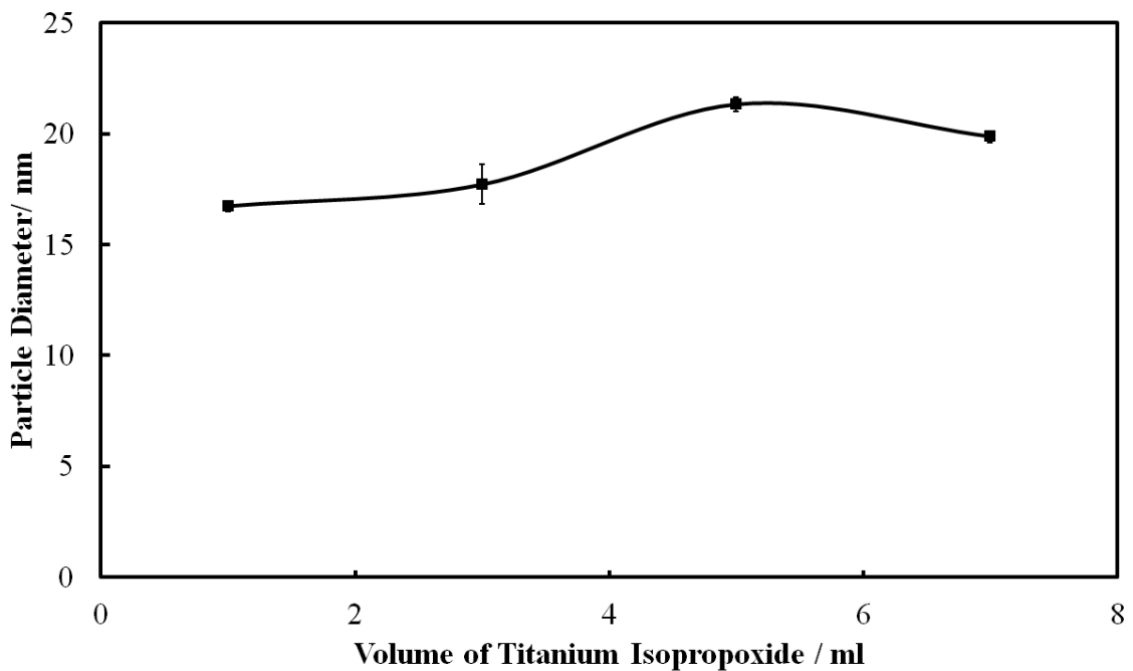


Figure 3.3: The variation of the NPs size with the amount of precursor (titanium isopropoxide) in which the samples are synthesized by hydrolysis and condensation of titanium isopropoxide in water at pH 2.

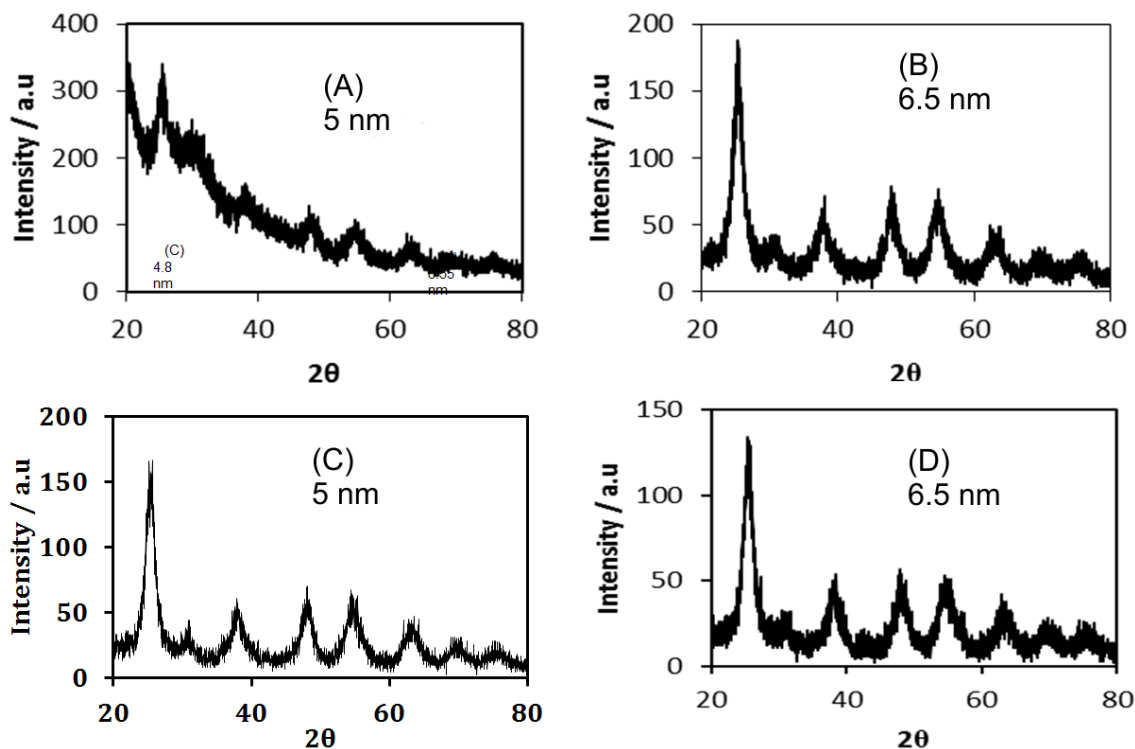


Figure 3.4: X-Ray diffraction patterns of titanium dioxide nanoparticles synthesized from the hydrolysis of (A) 1.0 ml, (B) 3.0 ml, (C) 5.0 ml, and (D) 7.0 ml of titanium isopropoxide in acidic medium and condensation at 70°C for 20 hour.

3.1.2 Effect of Reaction pH on particle size

A range of pH values (2.0, 3.0, 4.0, 5.0 and 6.0) were used for preparation of the titania nanoparticles (0.1M HNO₃ or 0.1M NH₄OH used to adjust the pH) using the procedure mentioned in Section 2.2.1. Each of the above solutions was prepared by using Milli-Q distilled water in 250 ml volumetric flask. Figure 3.5 depicts the effect of pH of the reaction on particle size at constant conditions in terms of sample and reagent volumes, temperature and reaction time. It can be seen that at very strong acidic medium (pH 1-2), the titania nanoparticles will produce homogenous suspension, while they aggregate heavily at pH values higher than 2 whereby the particle sizes become in the microscale; therefore, pH 1-2 is the best value to prepare titania nanoparticles.

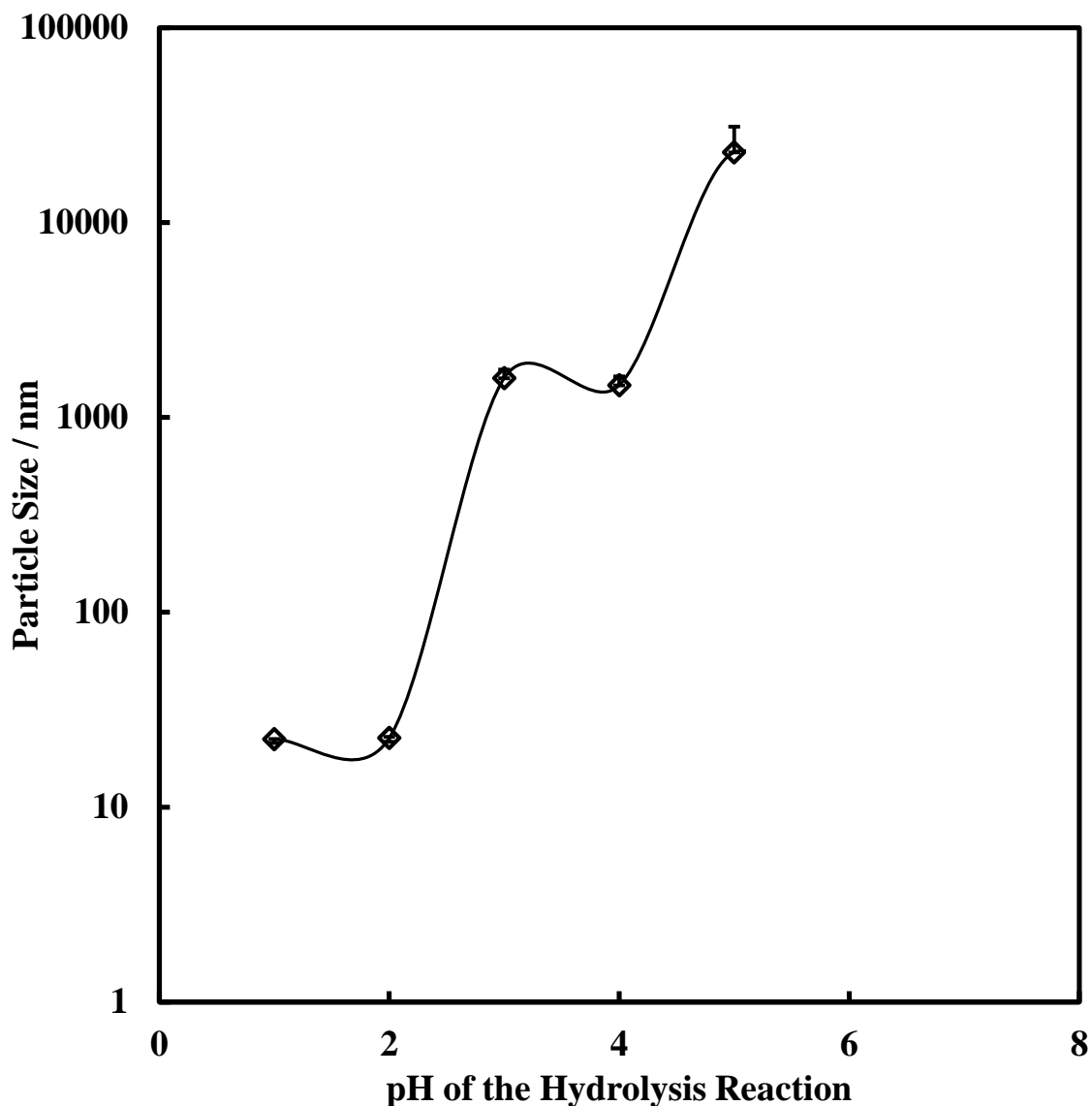


Figure 3.5: The variation of particle size of titanium dioxide with pH of the reaction solution using 5.0 ml of titanium isopropoxide, 15.0 ml of isopropanol and 250 ml of Milli-Q water after heating at 70°C for 20 hours.

3.1.3 Effect of Temperature on the Titanium Dioxide Particle Size

The same procedure for the synthesis of titania nanoparticles as stated in Section 2.2.1 was utilized in this experiment except it was carried out at different reaction temperature. Figure 3.6 shows the effect of temperature of the reaction mixture on the particle size of titanium dioxide for 20 hours. It was found that with high temperature (50-85°C), a nano-sized

titania nanoparticles was produced, however, micro particles were generated at low temperature; therefore, 50-85°C was the optimum temperature range for the preparation of TiO₂ nanoparticles. Thus, the temperature has an important role in the fabrication of titania nanoparticles, preventing aggregation.

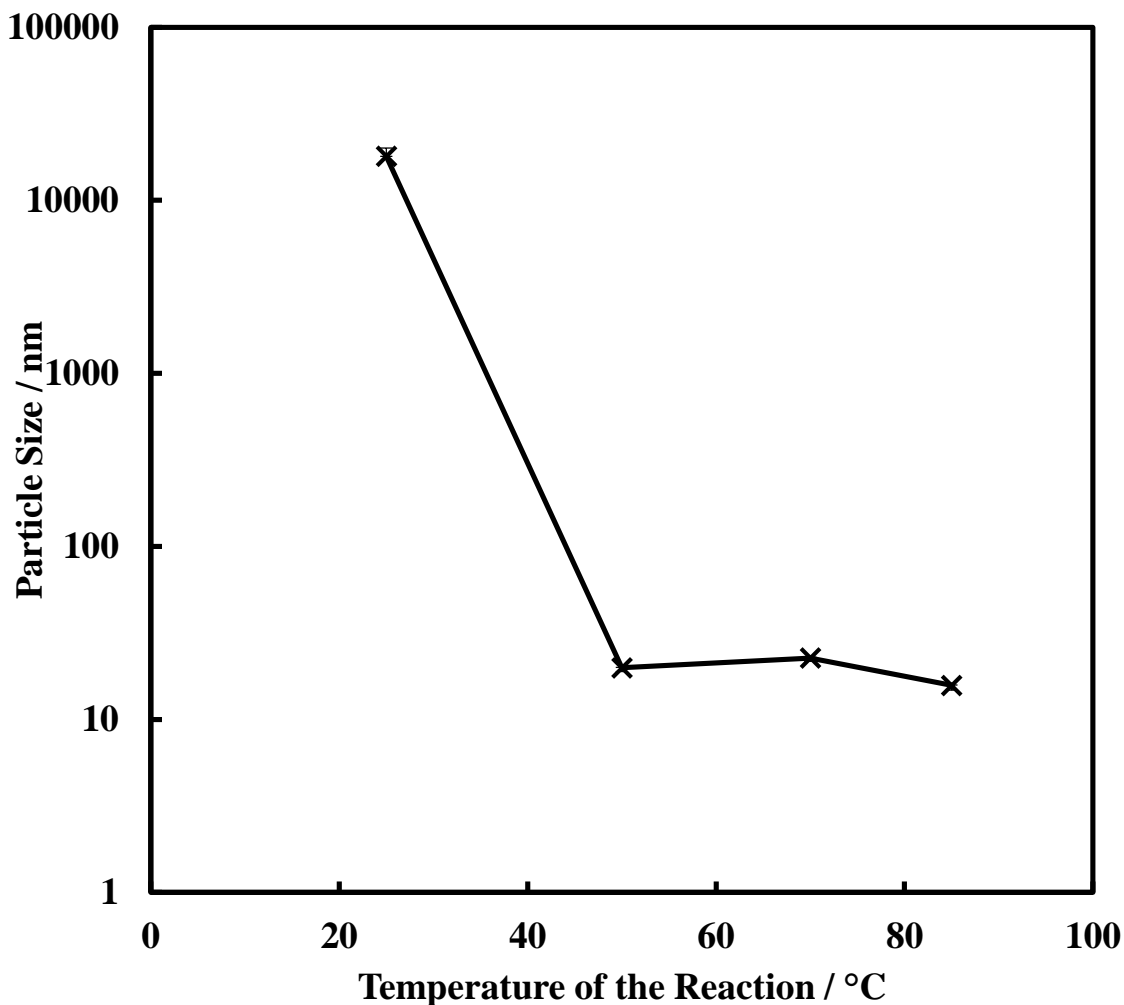


Figure 3.6: The effect of temperature on particle size for titania nanoparticles prepared by using 5.0 ml of titanium isopropoxide, 15.0 ml of isopropanol and 250.0 ml of Milli-Q distilled water adjusted to pH 2.0 with 0.1 N HNO₃ or 0.1 N NH₄OH.

3.2 Characterization of Titania Nanoparticles

Because of the environmental, industrial and technological importance of the titania nanoparticles, the physical and chemical parameters of synthesized TiO₂ nanoparticles were studied.

3.2.1 The Absorption of UV-Vis Spectroscopy of Titania Nanoparticles

A solution of 5.0 nm anatase water dispersed titania nanoparticles was measured by UV-Visible spectrophotometry between 200 nm to 700 nm. It can be clearly seen in figure 3.7 that the 5.0 nm titania nanoparticles has an absorption edge at 375 nm (dotted line) that lies in the near UV range with a band gap energy 3.5 eV, which is larger than the value of 3.2 eV for the bulk TiO₂.⁴ The band gap of a semiconductor depends on particle size,⁵ when the particle size is smaller, the band gap will be bigger. The band gap energy⁶ was calculated using the following equation:

$$\text{Band Gap Energy} \quad E = \frac{hc}{\lambda} \quad \text{Equation (2)}$$

where h is the Planks constant, 6.626×10^{-34} J s, c is the speed of light, 3.0×10^8 m/s and λ is the wavelength (nm).

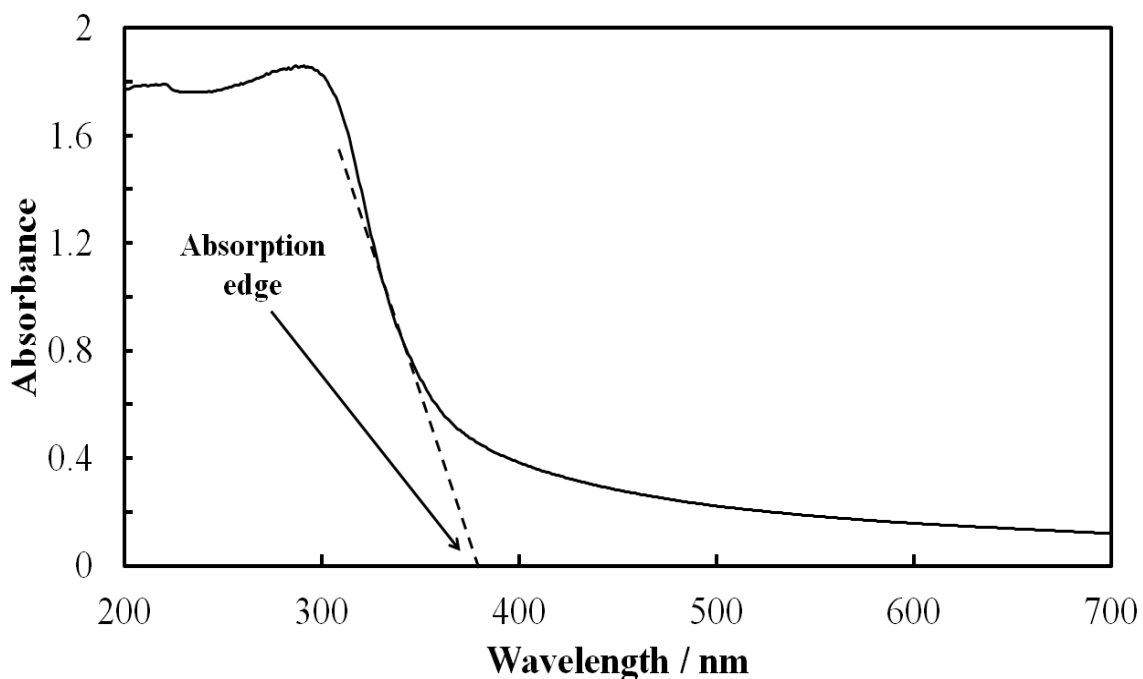


Figure 3.7: Figure 18: UV-Visible absorption spectrum of 5 nm anatase titania nanoparticles showing band gap energy 3.5 eV in comparison with 3.2 eV of bulk TiO₂. Dotted line that crosses the x-axis represent the absorption edge.

3.2.2 Calcination of Synthesized Titania Nanoparticle

Once synthesized titanium dioxide nanoparticles were annealed at different temperatures (200°C - 800°C) using the muffle furnace to find out the effect of temperature on the crystallite size of nanoparticles. Figure 3.8 shows the powder X-ray diffraction patterns of

the calcinated TiO₂ nanoparticles. It can be seen that the crystallite size of anatase TiO₂ become larger and the XRD bands ($2\theta = \sim 25^\circ$) are sharper as the calcination temperature increased resulting in crystallite sizes of the TiO₂ with 6, 6.5, 7 and 12 nm for 200°C, 300°C, 400°C, and 500°C respectively. Additionally, up to 600°C, the anatase and rutile TiO₂ nanoparticles XRD patterns were together appeared with 28 nm and 38 nm, respectively. However, Above 600°C, rutile TiO₂ peaks ($2\theta = \sim 27^\circ$) started to appear as illustrated in figure 3.8(E) and anatase TiO₂ peak was disappeared at 800°C and rutile TiO₂ become dominant (Fig. 3.8(F)). The above results are in agreement with analogous results previously reported in the literature.⁷

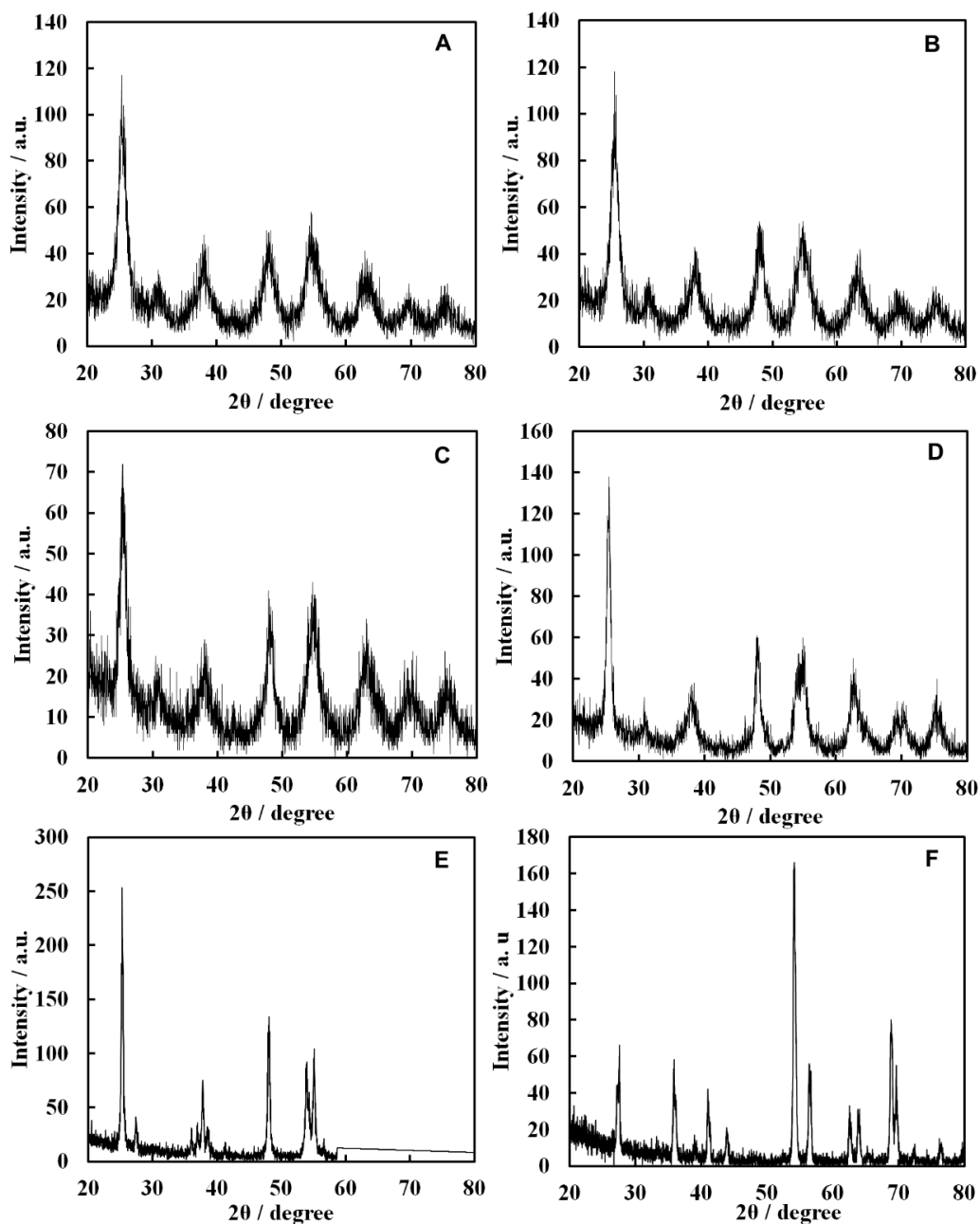


Figure 3.8: Powder X-Ray diffraction patterns of prepared TiO_2 nanoparticle at various calcination temperatures (A) 200°C, (B) 300°C, (C) 400°C, (D) 500°C, and (E) 600°C, showing the formation of different sizes of anatase TiO_2 with sharper peaks as the temperature is increased from 200°C to 600°C (A, B, C, and D). However, with (E), the XRD peaks of anatase TiO_2 are very sharp (crystallite size 28 nm and 38 nm for anatase and rutile, respectively) while at 800 °C, rutile TiO_2 nanoparticles are dominant with 142 nm crystallite size.

3.2.3 Transmission Electron Microscope Images of Titania NPs

The TEM images in figure 3.9 were taken for different sizes titania nanoparticles which were annealed at 100, 400, 600 and 800 °C, respectively. It can be seen in figure 3.9(A) that the TiO₂ nanoparticles prepared are crystalline particles and they are roughly spherical with a diameter of less than 10 nm, which agrees with the crystallite size calculated from XRD patterns. It can also be noticed that the monodispersed titania nanoparticles at high resolution TEM image which refers to anatase grain (Figure 3.9B). However, for Figure 3.9 (C) and (D) a significant difference is seen in terms of morphology and particle size due to the fact that calcination temperature affects the morphology of titania nanoparticles and increases the crystallite size and decreases the surface area. These results are in line with that in the literature.⁸

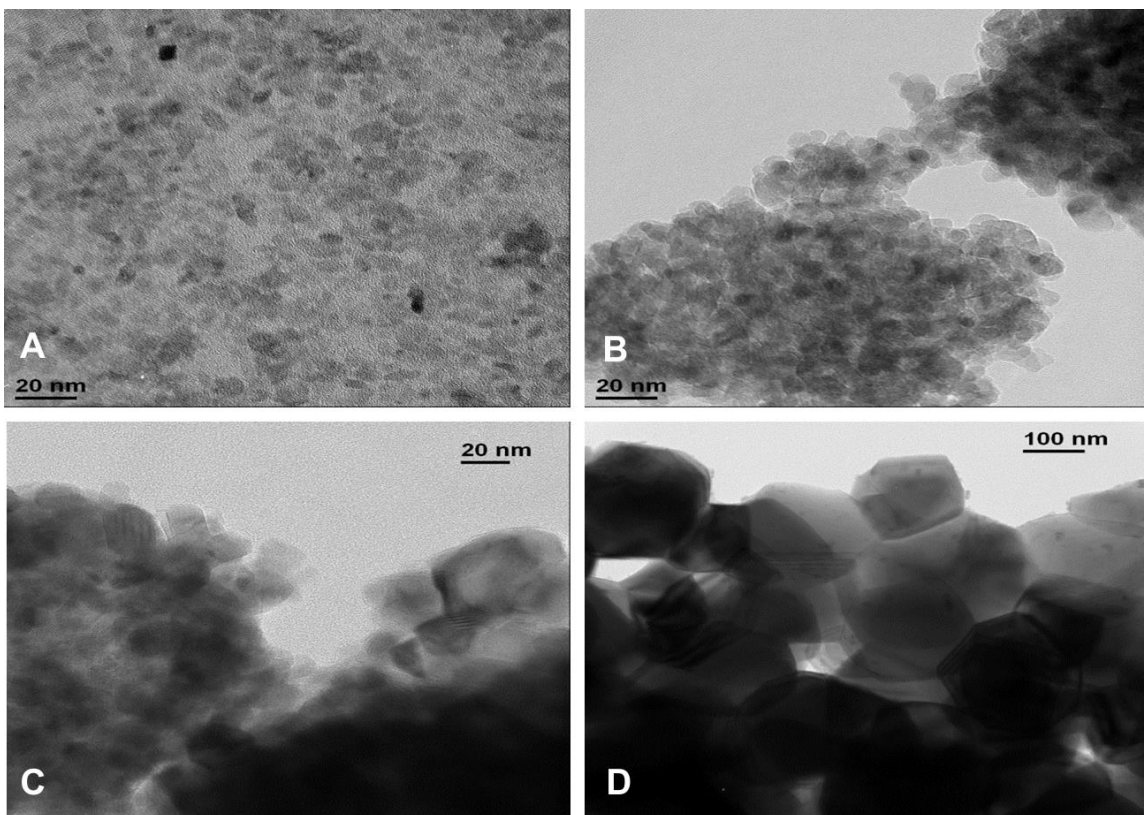


Figure 3.9: TEM photographs of synthesized titania nanoparticles at (A) as prepared TiO₂ at 100 °C which shown crystallite size less than 10 nm, (B) uniformed size anatase Titania nanoparticles at 400 °C, (C) TiO₂ Nanoparticles at 600 °C and (D) large sized rutile titania nanoparticles at 800 °C.

3.2.4 Fourier Transform Infrared Spectroscopy (FTIR)

A Fourier Transform Infrared Spectroscopy (FTIR) spectrum was obtained for the annealed TiO₂ samples at 100, 400, 600 and 800 °C in the range 500-4000 cm⁻¹. Figure 3.10 shows very strong peaks at 500 cm⁻¹ - 650 cm⁻¹ which related to Ti-O bonding in anatase morphology.^{9, 10} Moreover, the band observed at 1623 cm⁻¹ was recognized to be stretching and vibration of the Ti-O-Ti group. Peaks at 1100 cm⁻¹, 3317 cm⁻¹ and 3352 cm⁻¹ correspond to stretching of absorbed water and hydroxyl group vibration⁹. However, at 600 °C the peak 1100 cm⁻¹ vanished which might be attributed to dehydration. Peaks at 2900-3000 cm⁻¹, refer to C-H stretching vibrations but these peaks disappeared at high temperature, which means all organic compounds were removed from the samples after the calcination. . The sharp and intensive peak at 1385 cm⁻¹ is due to the presence of nitrates, which were added as HNO₃, during the acidification of the solution in the sol-gel synthesis as a peptizing agent.

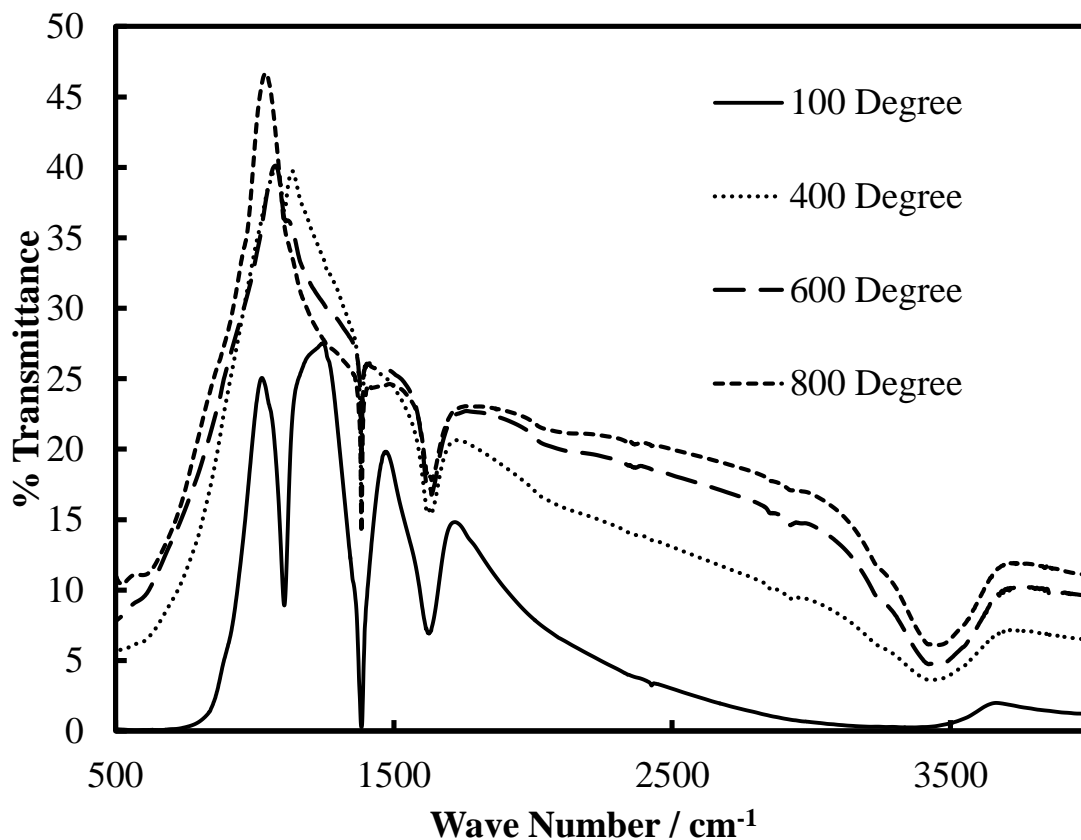


Figure 3.10: Fourier Transform Infrared Spectroscopy (FTIR) spectrum of annealed titania nanoparticles at 100, 400, 600 and 800°C.

3.2.5 Thermogravimetric Analysis (TGA)

The TGA graph for 20.1950 mg of 5 nm anatase titania nanoparticles is shown in Figure 3.11 illustrating that the weight loss has happened in three steps. The first weight loss shows an endothermic peak at 100 °C to 180 °C due to the removal of absorbed water from the surface of sample. The second thermal degradation is from 180 °C to 325 °C because of the dehydration and combustion of organic species for example, residues of the precursor (titanium isopropoxide).¹¹ The third degradation from 325 °C to 600 °C might be attributed to the phase transition¹² corresponding with results of XRD patterns and FTIR spectrum. Above 600 °C, 84% of sample remained representing the thermal stability of the sample.

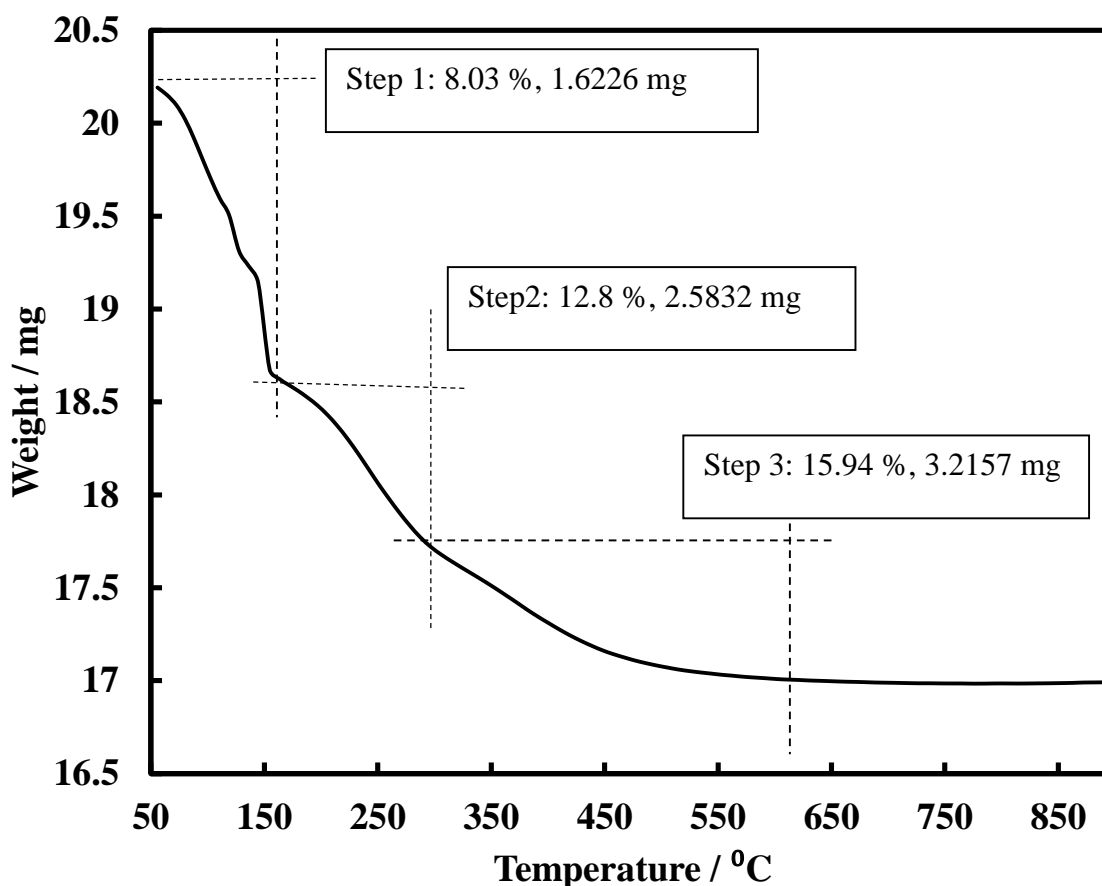


Figure 3.11: Thermal Gravimetric Analysis (TGA) graph of 5 nm anatase titania nanoparticles. showing three steps of thermal degradation: the Step 1 represents dehydration, Step 2 refers to organic compound degradation and the Step 3 is the phase transformation from anatase to rutile titania nanoparticles.

3.2.6 Surface Area Measurement

Surface area measurements of titania nanoparticles at different temperatures were carried out by nitrogen adsorption at 77K using the BET method. Table 1 shows the surface area of titania nanoparticles at different annealing temperatures. It can be clearly seen in table 1 that the smaller the crystallite sizes the larger the surface area. It can also be seen that the surface area decreased as the temperature of annealing increased from 163 $\text{m}^2\cdot\text{g}^{-1}$ for 5 nm anatase TiO_2 nanoparticles at 100°C to 7.5 $\text{m}^2\cdot\text{g}^{-1}$ for 142 nm rutile TiO_2 at 800°C annealing temperature. The increase of the temperature up to 800°C led to the phase transformation from anatase to the more stable rutile TiO_2 . These results are compatible with the reported research.¹³ It can be seen in the table that hydrodynamic diameter of titania nanoparticles increased as the temperatures increased. It should be noted that the average particle diameter was bigger than that of the crystallite size owing to the formation of clusters of nanoparticles in the liquid dispersion which was different from that of dry powder of titania nanoparticles. The zeta potential was also measured for each calcinated sample of titania nanoparticles and it can be observed from the table that at 100°C, the zeta potential was +40 mV which means it was highly stable whereas, at high temperature, the titania nanoparticles are rutile and it is negatively charged (-26 mV).

Table 3.1: The effect of the annealing temperature during the TiO_2 NPs synthesis on the crystallite domain size and the BET surface area of titania. The hydrodynamic diameters and zeta potential of the TiO_2 NPs after dispersing each sample in Milli-Q water at pH 4 by sonication at the same conditions are also reported.

Calcination temperature / °C	Average crystallite size /nm		BET surface area / $\text{m}^2 \text{g}^{-1}$	Hydrodynamic diameter /nm	Zeta potential / mV
	Anatase	Rutile			
100	5	-	163	25 ± 20	40 ± 9
200	6	-	152	25 ± 20	36 ± 10
300	6.5	-	139	27 ± 20	32 ± 6
400	7	-	90	35 ± 25	31 ± 7
500	12	-	46	40 ± 25	3 ± 10
600	28	38	9	50 ± 25	3 ± 10
800	-	142	7.5	145 ± 60	-26 ± 8

3.2.7 Measurement of Zeta Potential of Titania Nanoparticles

A series of various concentrations of sodium chloride were prepared in Milli-Q water and then added to equal amounts of 25 nm-sized titanium nanoparticles. Each solution was dispersed at 30% maximal power for 5 minutes and adjusted to different pH values from 2–9. The zeta potential of the NPs was then measured to find out the effect of pH on the surface charge of nanoparticle. Dilute hydrochloric acid or sodium hydroxide was used to adjust the pH of each solution. Figure 3.12 shows the effect of pH on the average particle diameter and zeta potential of the dispersed titania nanoparticles in the medium. The surface charge of nanoparticles decreased gradually from a positive charge at low pH to negative at high pH, where the isoelectric point was approximately 6.8.

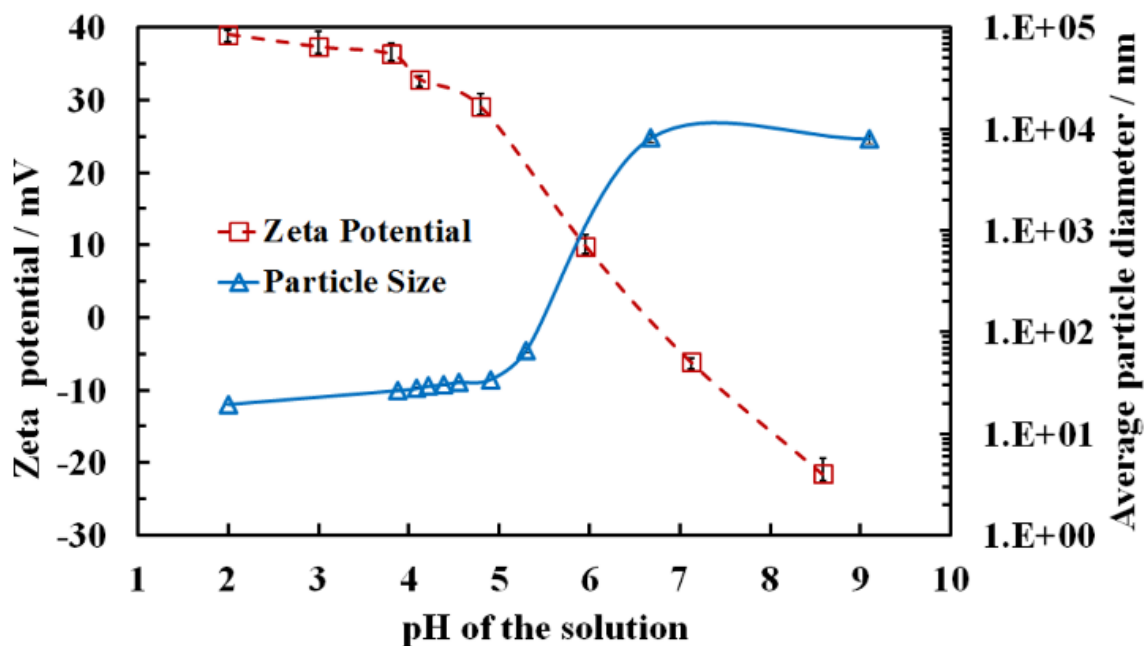


Figure 3.12: The variation the zeta potential and the particle diameter of dispersed anatase TiO₂NPs in an aqueous solution of 20 mM NaCl as function of pH adjusted by addition of 1 M HCl or 1 M NaOH. The triangles show the effect of pH on the average particle hydrodynamic diameter.

It was also found that in acidic medium, the solution was clear but as the pH increases above 5, the particles start to aggregate (Fig. 3.12) as the particle surface charge and the corresponding electrostatic repulsion are not strong enough to prevent their partial coagulation. However, there were unable to redisperse the aggregated TiO₂NPs by subsequent lowering the pH of the aggregated particles dispersion below 5. This indicates that the TiO₂NPs aggregation is irreversible, possibly due to covalent bond formation among TiO₂NPs within the aggregates. Figure 3.13 shows how the nanoparticle dispersion changed with pH values.

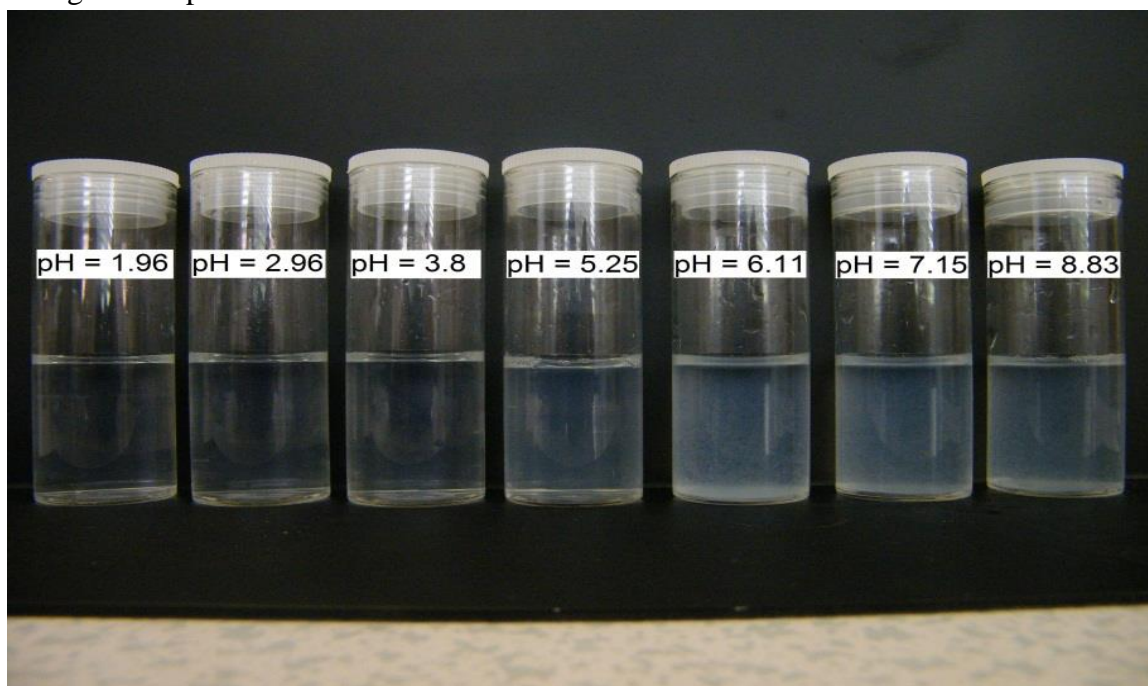


Figure 3.13: The aggregation profile of TiO₂ nanoparticles at pH 2-9 by using Milli-Q water as a solvent and samples were dispersed at 30% of the maximum power of the sonifier for 5 minutes. pH of the solution was adjusted by addition of HCl or NaOH. This profile also represents the effect of pH on the average particle diameter.

Figure 3.14 gives the dependence of the average particle diameter and zeta potential as a function of the solution pH for rutile TiO₂NPs, produced by annealing at 800 °C which was prepared in Milli Q water, sonicated for 5 minutes at 40% of maximum power and filtered using filter syringe 0.2 μm. One sees that rutile NPs have not only different particle size but also different surface properties from anatase NPs in which is also reflected in their nanotoxicity. It can also be observed in figure 3.14 that the zeta potential of rutile titania nanoparticles are negatively charged at pH 4.

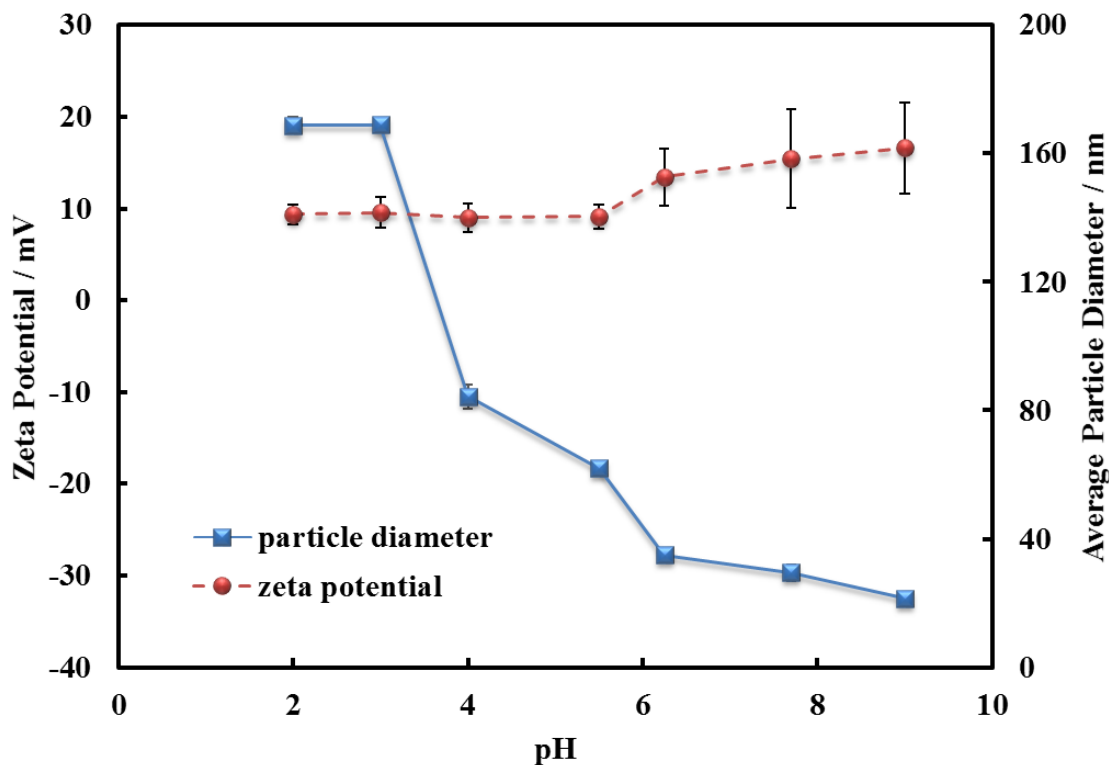


Figure 3.14: The variation the zeta potential and the particle diameter of dispersed rutile TiO_2NPs in an aqueous solution of 1 mM of NaCl as a function of pH which was adjusted by addition of small amount of aqueous solutions of 1M HCl or 1M NaOH. The square symbols show the effect of pH on the average particle hydrodynamic diameter while the circle symbols represent the particle zeta potential vs. pH.

3.3 Functionalization of Titania Nanoparticles

Once the titania nanoparticles were prepared, optimized and characterized, they can be functionalized using a Layer-by-Layer assembly technique. It was used to coat 25 nm anatase TiO_2NPs with alternating layers of anionic (PSS) and cationic (PAH) polyelectrolytes using the protocols described in section 2.2.6. Since the anatase TiO_2NPs were cationic below pH 6.5 the first layer used was PSS, an anionic polyelectrolyte that formed negatively charged $\text{TiO}_2\text{NPs}/\text{PSS}$. Further coating with PAH gave positively charged $\text{TiO}_2\text{NPs}/\text{PSS}/\text{PAH}$. Finally, by using an extra coating of PSS, anionic $\text{TiO}_2\text{NPs}/\text{PSS}/\text{PAH}/\text{PSS}$ particles as stated in figure 3.15. The coating was affected by many parameters such as the addition of titania nanoparticles, the ionic strength and the molar mass of the polyelectrolyte (which can cause partial aggregation).

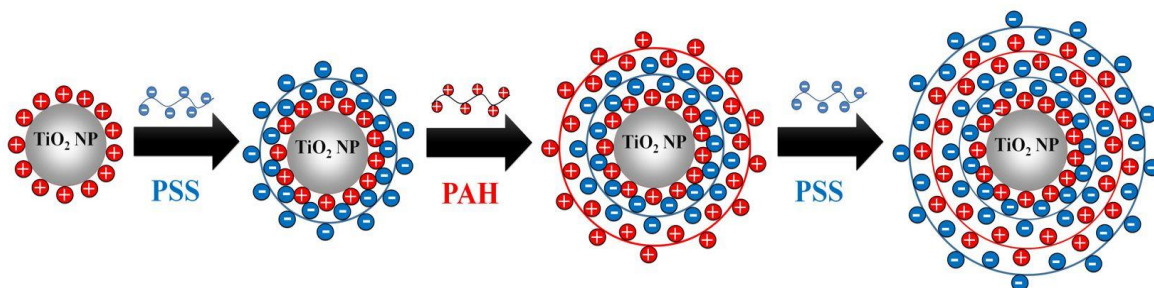


Figure 3.15: The schematic functionalization of titania nanoparticles with anionic and cationic polyelectrolytes. The PSS and PAH represent Polystyrene Sulfonates and Poly(allylamine hydrochloride), respectively.

3.3.1 The Effect of Addition of Titania Nanoparticles

It was investigated the effect of using different methods to add titania nanoparticles to polyelectrolyte (anionic or cationic) including direct addition, drop by drop and dropwise addition with ultra-sonication. Figure 3.16 shows how changes the method of addition of the nanoparticles to the polyelectrolyte can affect the average particle diameter of titania nanoparticles. It can be seen in figure 16 that dropwise addition with drastic shaking appeared to cause aggregation, with particle diameters being greater than 200 nm whereas, in case of direct addition of titania nanoparticles to the polyelectrolyte obtained a particle diameter with 120 nm. However, dropwise addition with ultra-sonication was found to be the best addition method whereby the particle diameter was up to 80 nm. The reason for this is that ultrasonic energy plays an important role in dispersing the clustered nanoparticles upon using excess amount of either anionic or cationic polyelectrolytes, allowing interaction with aggregated nanoparticles to provide a good stability of the colloidal particles. Therefore, this method gave good stability of cationic or anionic polyelectrolytes coated titania nanoparticles.

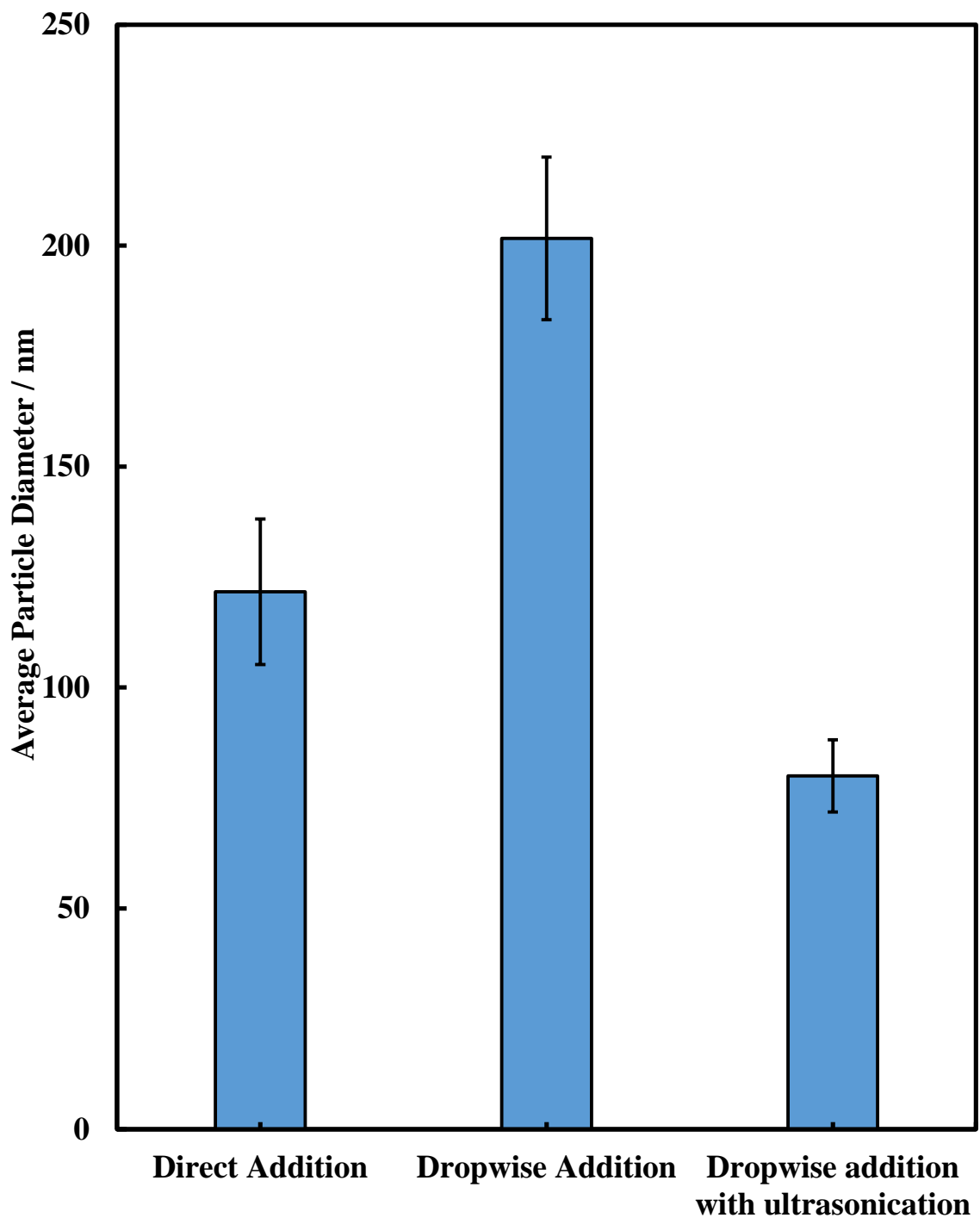


Figure 3.16: The effect of addition of bare or coated titania nanoparticles to the anionic or cationic polyelectrolytes on the average particle diameter of coated titania nanoparticles. It was used three methods of addition, direct addition, dropwise addition and dropwise addition with ultrasonic energy. It was found that the drop by drop addition with ultrasonication is the favorable method with average particle diameter 80 nm.

3.3.2 Effect of Ionic Strength

The average particle size after each polyelectrolyte coating was examined at several different ionic strengths. Figure 3.17 shows the effect of the ionic strength on the size of the TiO₂NPs coated with anionic and cationic polyelectrolytes. Note that the particle hydrodynamic diameter increased with an increase in NaCl concentration. This is largely due to the partial coagulation of the polyelectrolyte-coated TiO₂NPs, during the coating stages due to the diminished electrostatic repulsion at higher salt concentrations. The optimal concentration of NaCl solution, where the coated TiO₂NPs are still nano-sized, was found to be 1 mM.

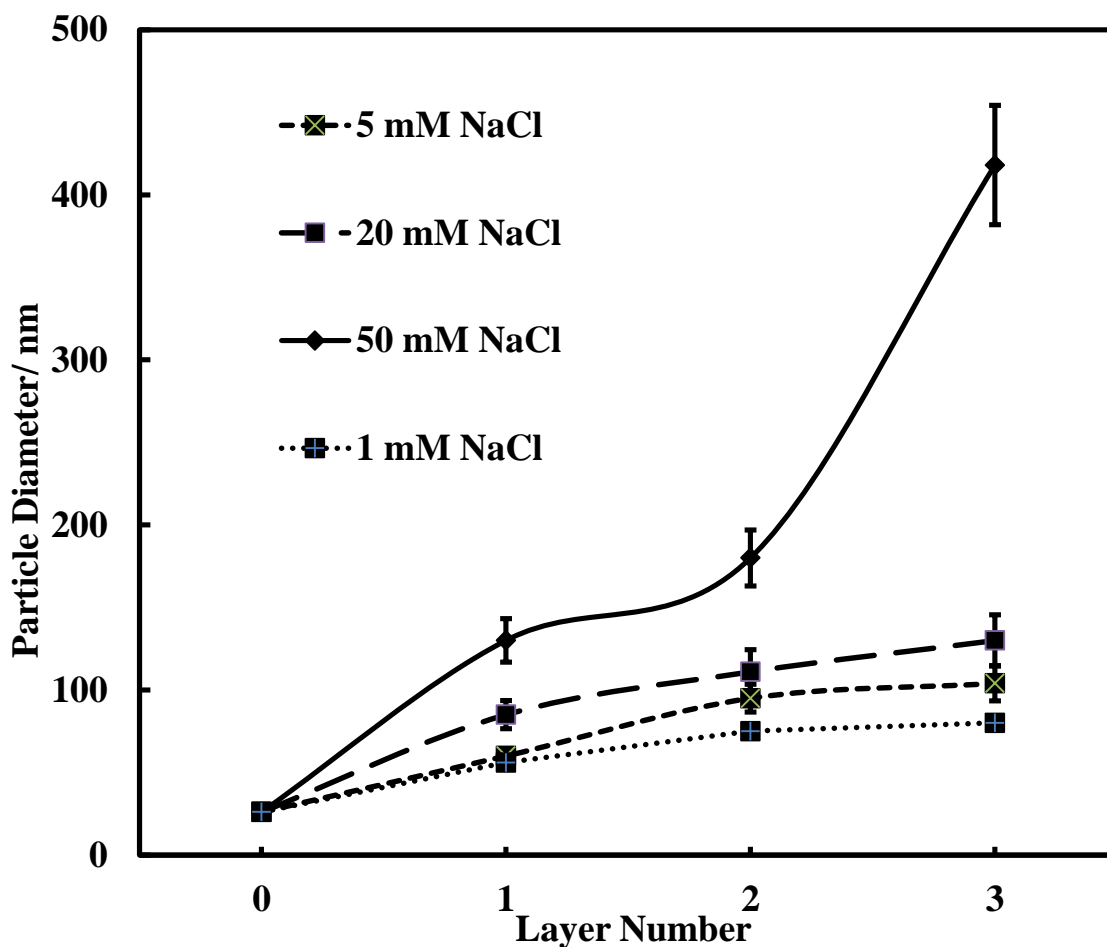


Figure 3.17: The effect of the solution ionic strength on the particle size distribution of TiO₂NPs coated with anionic and cationic polyelectrolytes. Different concentrations (1, 5, 20, 50 mM) of sodium chloride solution were used to dissolve the polyelectrolytes. Dropwise addition with ultra-sonication was used for the addition of the different ionic strength dissolved polyelectrolytes to the colloidal particles of titania.

3.3.3 Effect of Molar Mass of Polyelectrolyte

Layer-by-Layer coating was also carried out using two batches of PSS and PAH with different molar. Figure 3.18 shows that the lower the molar mass of the polyelectrolyte, the smaller the hydrodynamic diameter of the polyelectrolyte coated TiO₂NPs; therefore, 10 kDa PSS and 15 kDa PAH were chosen for coating titania NPs.

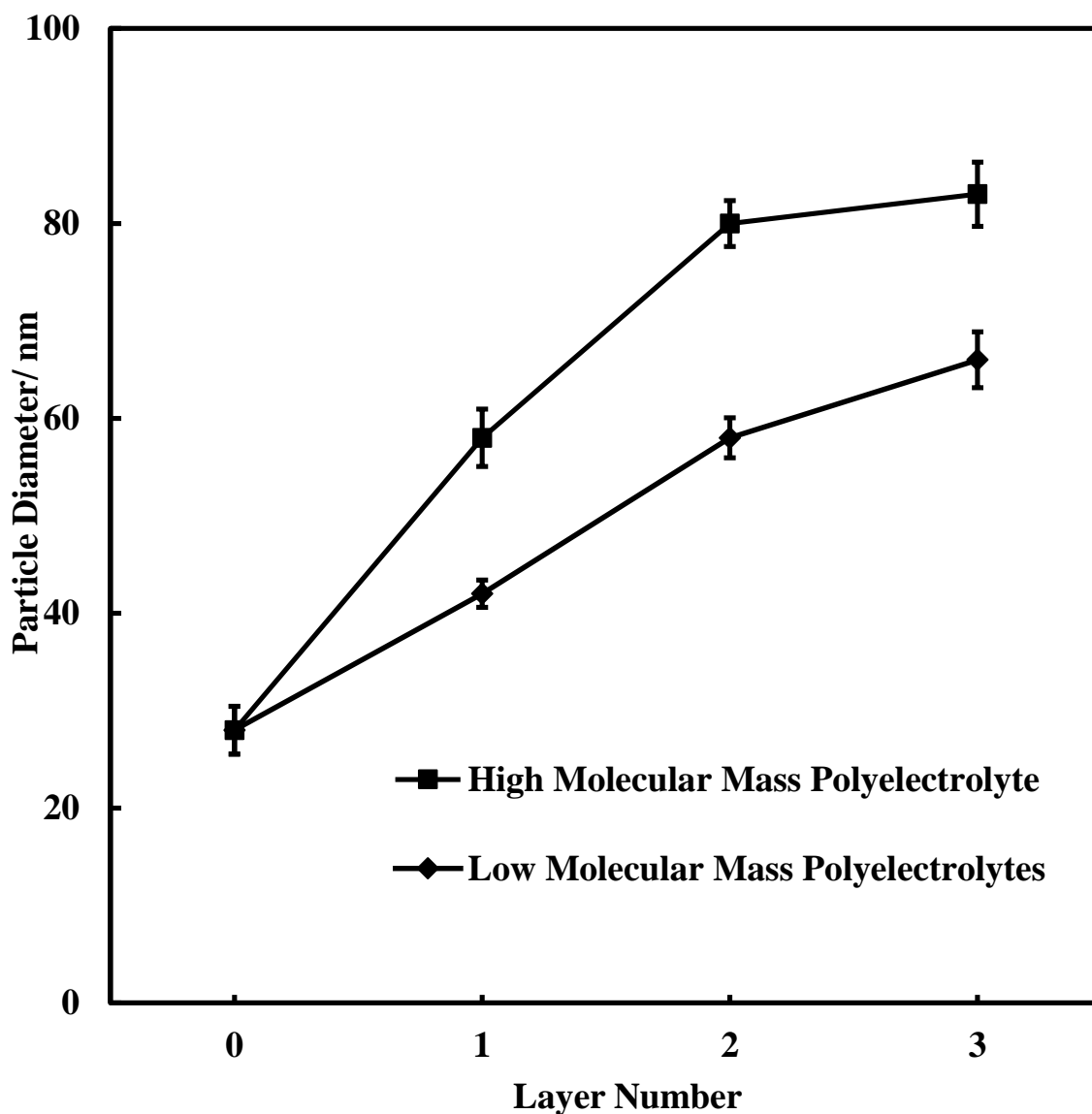


Figure 3.18: The effect of the molar mass of anionic or cationic polyelectrolytes on the average particle diameter of the coated titania nanoparticles as a function of number of deposited layers of polyelectrolytes of different molar mass. 70 kDa and 10 kDa Polystyrene Sulfonates and 56 kDa and 15 kDa Poly(allylamine hydrochloride) were used in 1 mM of sodium chloride solution with dropwise addition with ultra-sonication method.

3.3.4 Zeta Potential of Bare and Coated Titania NPs

The zeta potential of the TiO_2 NPs after each coating with anionic or cationic polyelectrolytes was measured as seen in Figure 3.19. It can be seen that the zeta potential of the polyelectrolyte coated TiO_2 NPs alternates after the coating with the oppositely charged polyelectrolytes, as shown with other studies reported in the literature.¹⁴⁻¹⁶

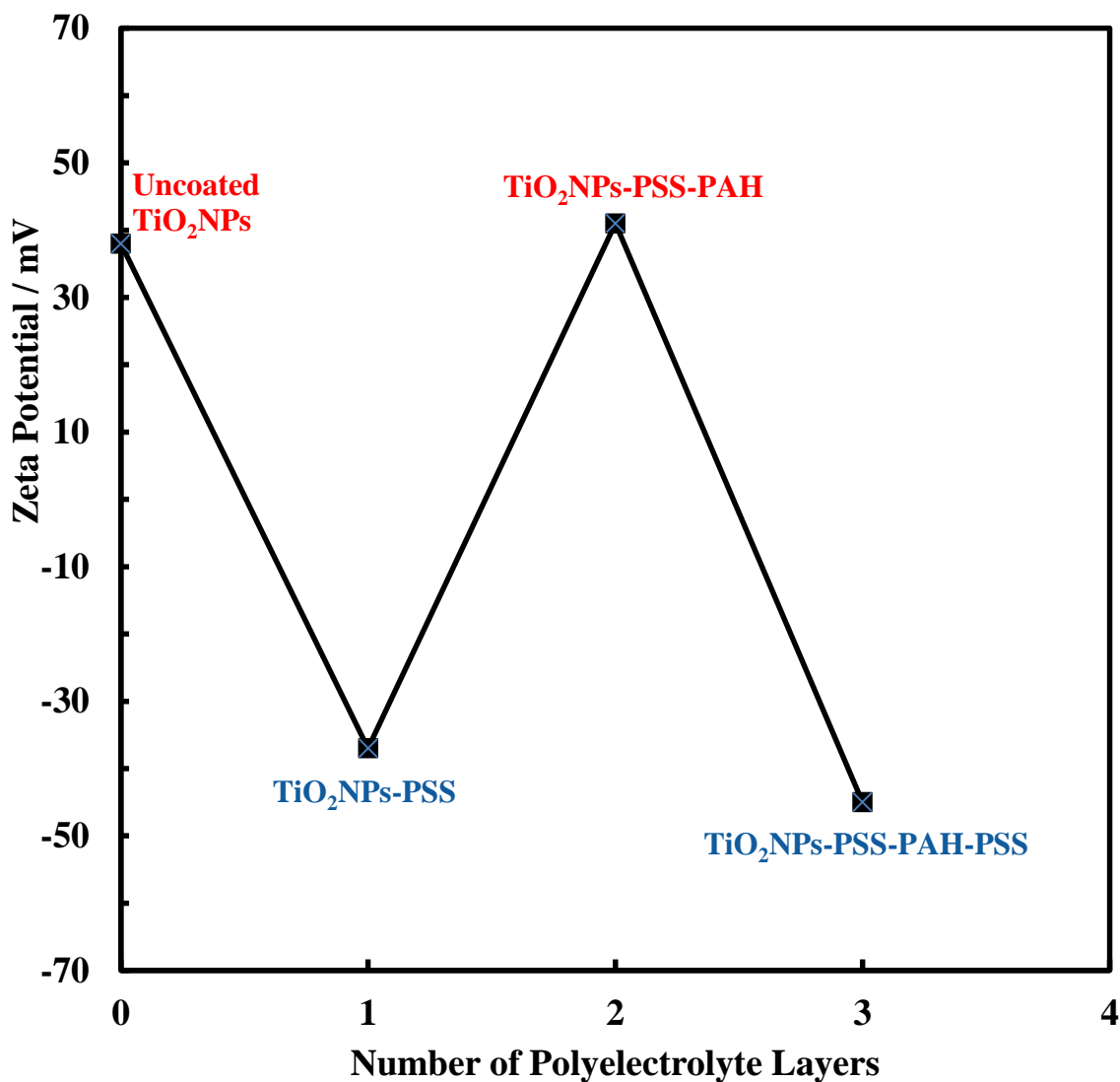


Figure 3.19: The zeta-potential of bare and multi-layer coated TiO_2 NPs as a function of numbers of deposited layers of anionic and cationic polyelectrolytes. 10 kDa of polystyrene Sulfonates and 15 kDa of poly(allylamine hydrochloride) as polyelectrolytes for coating titania nanoparticles were used with 1 mM sodium chloride solution with dropwise addition with ultra-sonication.

It can be concluded that titania nanoparticles were synthesized with crystallite size 5 nm, particle size 25 nm and high surface area $163 \text{ m}^2 \text{ g}^{-1}$. The physical and chemical properties are investigated to be unique. It was also multicoated titania nanoparticles with anionic and cationic polyelectrolyte using layer by layer technique. Here, we will use the prepared coated titania nanoparticles with anionic or cationic polyelectrolytes in the next chapter to be incubated with individual microorganisms such as *C.reinhardtii* and *S.cerevisiae* to study the nanotoxicity effect of coated titania nanoparticles. It also useful to discover the behaviour of these coated nanoparticles upon incubation in dark conditions and in visible and UV lights.

Bibliography

1. M. Guix, C. Carbonell, J. Comenge, L. García-Fernández, A. Alarcón and E. Casals, *Contributions to science*, 2008, **4**, 213-217.
2. A. Nel, T. Xia, L. Mädler and N. Li, *Science*, 2006, **311**, 622-627.
3. A. L. Patterson, *Physical Review*, 1939, **56**, 978-982.
4. C. Dette, M. A. Pérez-Osorio, C. S. Kley, P. Punke, C. E. Patrick, P. Jacobson, F. Giustino, S. J. Jung and K. Kern, *Nano Letters*, 2014, **14**, 6533-6538.
5. K. Madhusudan Reddy, S. V. Manorama and A. Ramachandra Reddy, *Materials Chemistry and Physics*, 2003, **78**, 239-245.
6. C. N. Banwell, *Fundamentals of molecular spectroscopy*, McGraw-Hill, 1983.
7. S. Mahshid, M. S. Ghamsari, M. Askari, N. Afshar and S. Lahuti, *Semicond Phys Quantum Electron Optoelectron*, 2006, **9**, 65-68.
8. N. Wetchakun, B. Incessungvorn, K. Wetchakun and S. Phanichphant, *Materials Letters*, 2012, **82**, 195-198.
9. S. Musić, M. Gotić, M. Ivanda, S. Popović, A. Turković, R. Trojko, A. Sekulić and K. Furić, *Materials Science and Engineering: B*, 1997, **47**, 33-40.
10. M. HEMA, A. Y. ARASI, P. TAMILSELVI and R. ANBARASAN, *Chem Sci Trans.*, 2013, **2**, 239-245.
11. J. Wang, W. Sun, Z. Zhang, Z. Jiang, X. Wang, R. Xu, R. Li and X. Zhang, *Journal of colloid and interface science*, 2008, **320**, 202-209.
12. X. Sun, H. Liu, J. Dong, J. Wei and Y. Zhang, *Catalysis letters*, 2010, **135**, 219-225.
13. S. Mozia, in *Polish Journal of Chemical Technology*, Editon edn., 2008, vol. 10, p. 42.
14. R. F. Fakhrullin, J. García-Alonso and V. N. Paunov, *Soft Matter*, 2010, **6**, 391-397.
15. R. F. Fakhrullin, A. I. Zamaleeva, R. T. Minullina, S. A. Konnova and V. N. Paunov, *Chemical Society Reviews*, 2012, **41**, 4189-4206.
16. J. García-Alonso, R. F. Fakhrullin and V. N. Paunov, *Biosensors and Bioelectronics*, 2010, **25**, 1816-1819.

4 Chapter Four: Nanotoxicity of Titania Nanoparticles

4.1 Toxicity of TiO₂NPs on *C.reinhardtii* in UV/visible light

Experiments were conducted to investigate the effect of TiO₂NPs on *C.reinhardtii* a single-cell green alga. *C.reinhardtii* was incubated with TiO₂NPs whilst being illuminated with visible light, UV light or in dark conditions. The emission spectra of the visible light source and the UV light source are given in Figures 4.1 and 4.2, respectively. It can be seen in Figure 4.1, the emitted light from table lamp which can be used for visible irradiating the incubated cell with titania nanoparticles suspension. However, in Figure 4.2 which represents the UV light emitted from UV lamp at wavelength 365 nm.

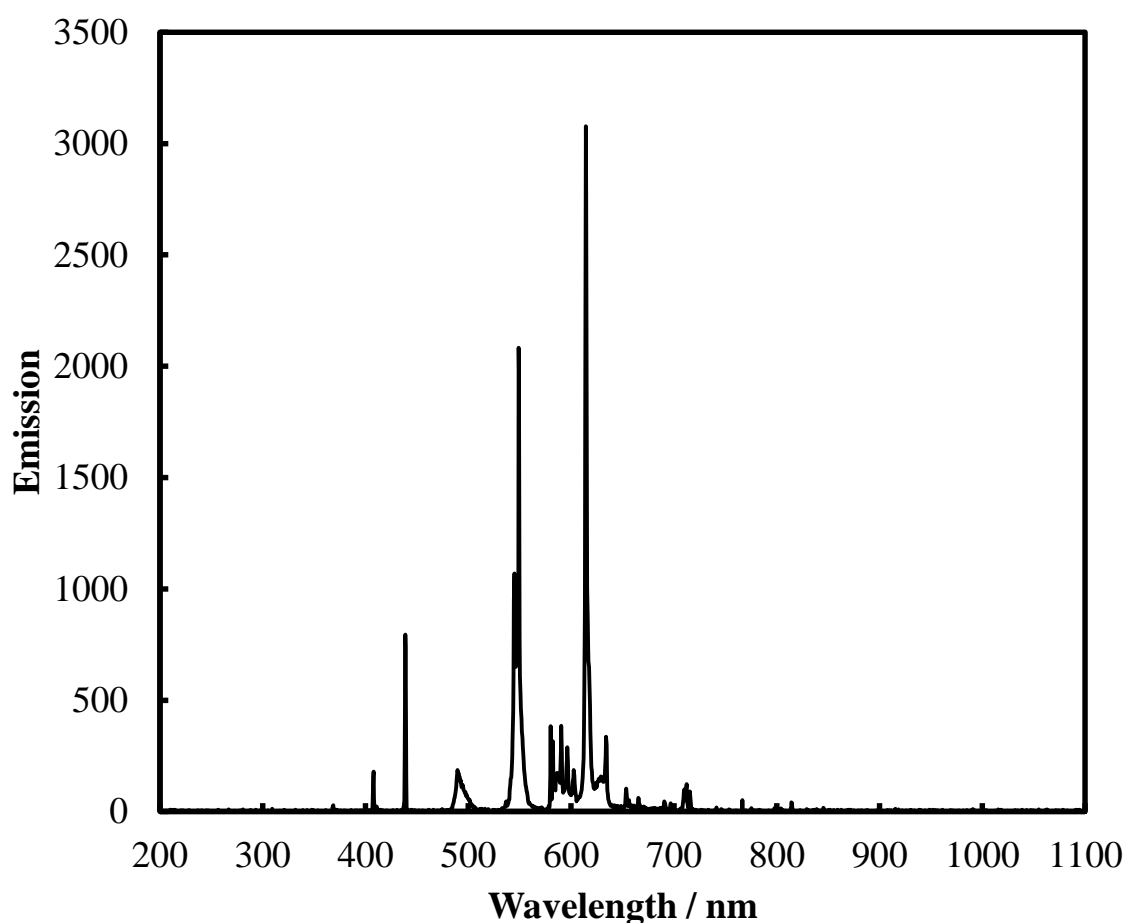


Figure 4.1: The emission spectrum of the visible light source which was used for irradiating *C.reinhardtii* in the presence of TiO₂NPs at various exposure time which was measured by USB4000-UV-VIS detector (Toshiba TCD1304AP Linear CCD array, USA).

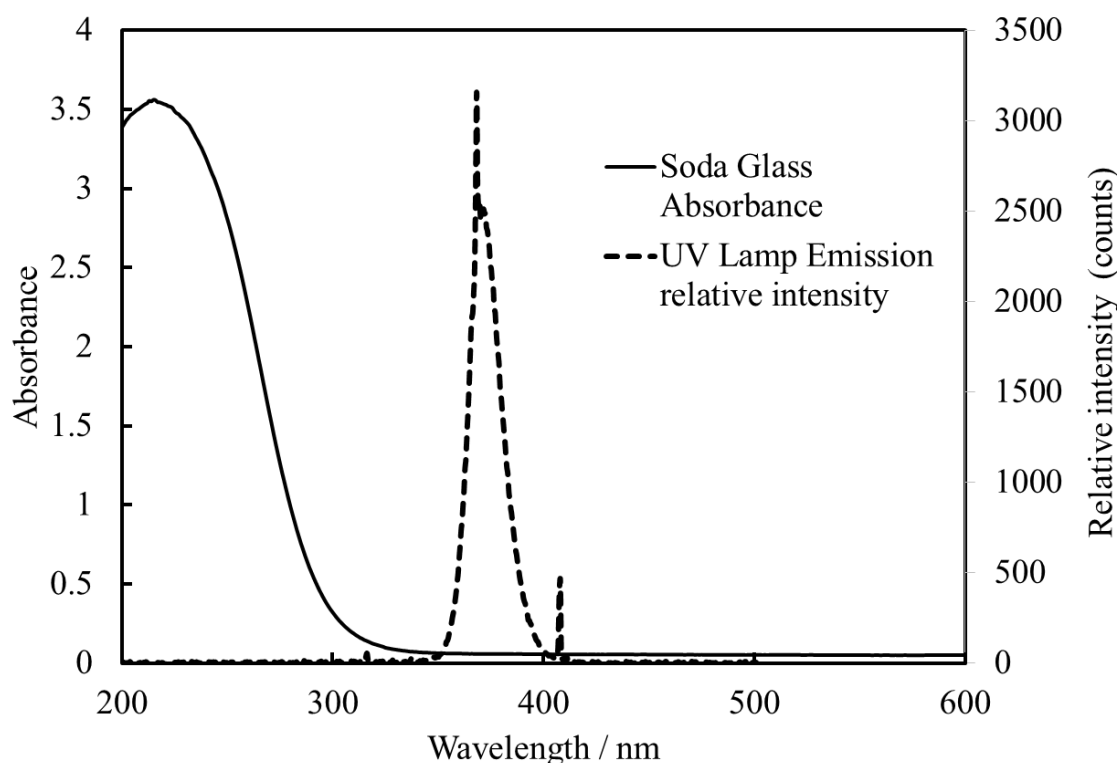


Figure 4.2: LHS axis: The absorbance spectrum of the soda glass tubes used for the incubation of the cell with TiO₂NPs in UV light. RHS axis: The emission spectrum of the UV lamp which refers to that the maximum emission occurs at 365 nm which was measured by USB4000-UV-VIS detector (Toshiba TCD1304AP Linear CCD array, USA). This UV light source was used to irradiate *C.reinhardtii* and yeast in the presence of TiO₂NPs.

It was possible that the TiO₂NPs could interact with the cell growth media. This could affect the cells in two ways: (i) by depleting nutrients from the media and (ii) a protein corona could form around the NPs in solution which would change the way the NPs adhere to the cell membrane. To eliminate the effect of the growth media on the nanoparticles, *C.reinhardtii* cultures were used which had been removed from the growth media and re-dispersed in Milli-Q water. The aqueous suspensions of the microalgae were incubated with aqueous suspensions of TiO₂NPs of various concentrations for several different periods of time. The cell viability was examined immediately after removing the excess TiO₂NPs from the cell suspension.

The comparison of the cell viability of *C.reinhardtii* in dark and visible light conditions is presented in Figure 4.3 at different exposure time up to 6 hours. Note that immediately after incubation (0 hours), the viability of the microalgae gradually decreased with TiO₂NPs concentrations above 100 µg mL⁻¹. After 2-6 hours of incubation in visible light, the cell viability also decreased but at much lower TiO₂NPs

concentrations of 10-250 $\mu\text{g mL}^{-1}$. Above this limit, it was found no viable cells in the samples. Figure 4.4 shows a bright field microscope image of the cells in the presence of high TiO_2NPs concentrations ($>250 \mu\text{g mL}^{-1}$). It can be seen that the cells were highly aggregated while at lower TiO_2NPs concentrations ($50 \mu\text{g mL}^{-1}$) they were fully dispersed. This can be explained by the fact that the positive surface charge of the TiO_2NPs generally has a disruptive effect on the cell membranes. In addition of that, chlorophyll content could release because of the cell membrane disruption which then absorbs on the surface of titania nanoparticles. In the presence of visible light, the absorbed chlorophyll can release one electron which transfers to the conduction band of titania nanoparticle, then generating reactive oxygen species.

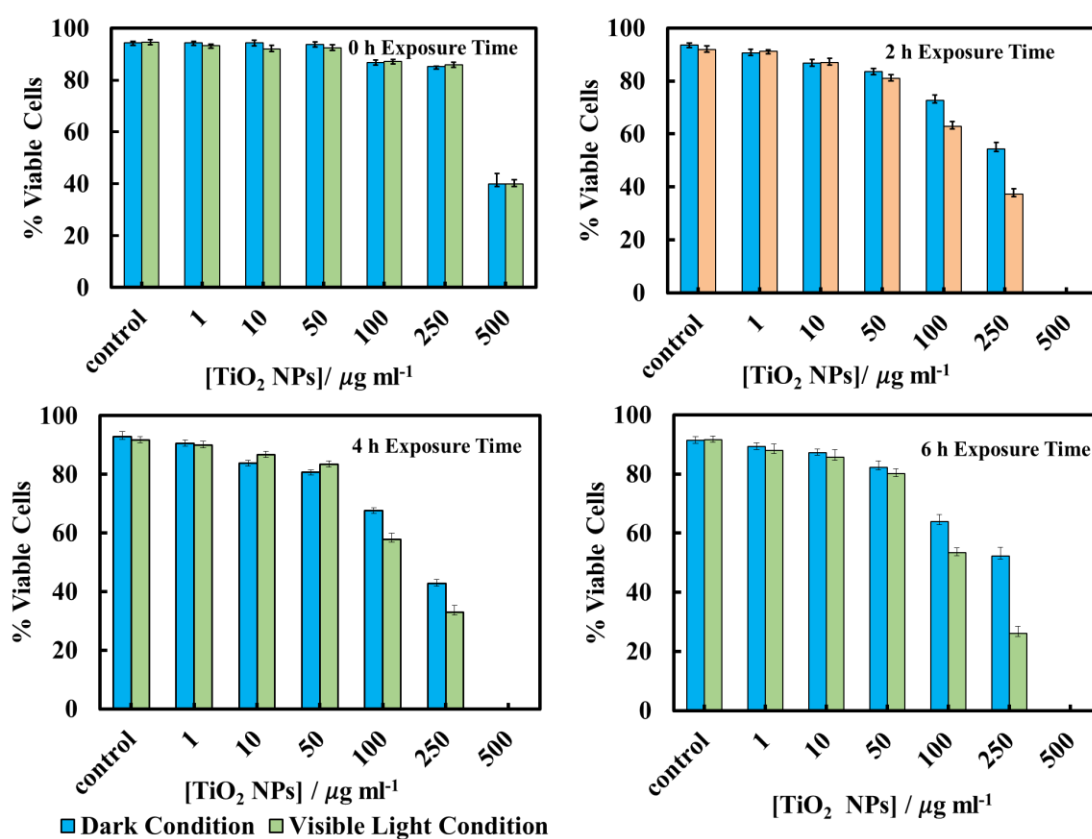


Figure 4.3: The viability of *C. reinhardtii* cells incubated with solutions of different concentrations of TiO_2NPs (1-500 $\mu\text{g mL}^{-1}$) at pH 4 in dark conditions and in visible light at 0 h, 2 h, 4 h and 6 h exposure times as compared with the control sample at room temperature. The cell suspensions were free from culture media upon incubation with solutions of titania NPs concentrations to avoid interaction between TiO_2 NPs with culture media components.

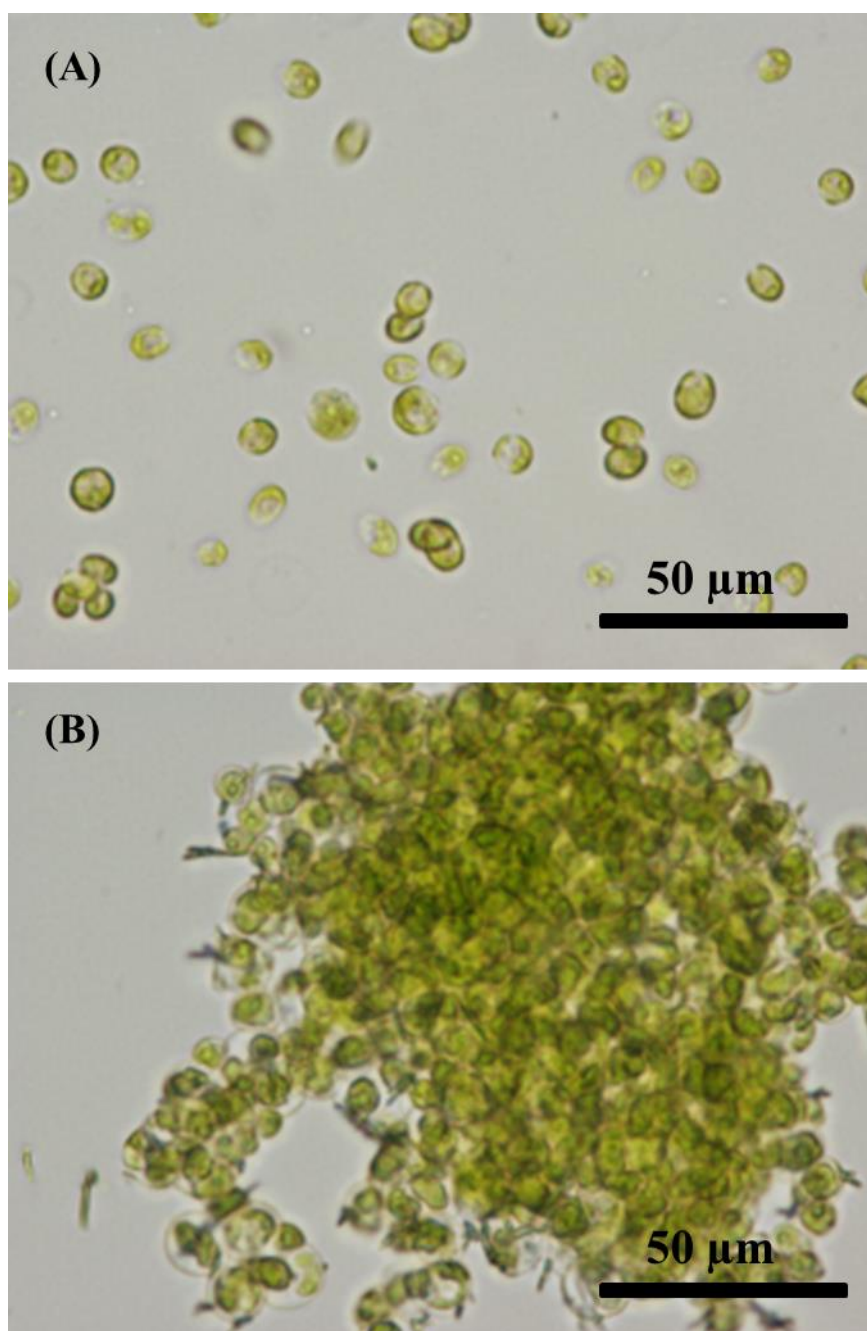


Figure 4.4: The 50x bright field microscopic image of (B) aggregated *C.reinhardtii* at high concentration of TiO_2NPs against control sample (A)

Figure 4.5 shows a comparison of the *C.reinhardtii* cell viability as a function of the TiO_2NPs concentrations in dark conditions and in UV light. At low UV light exposure times there was a pronounced toxic effect for TiO_2NPs concentrations above $250 \mu\text{g mL}^{-1}$. At exposure times above 2 hours, a sharp decrease in the microalgae viability was

observed for TiO₂NPs concentrations from 50-250 µg mL⁻¹. At higher particle concentrations all cells lost their viability. Figure 5 also shows that the toxicity effect of TiO₂NPs on the microalgae irradiated with UV light for 6 hours is definitely higher than that with visible light at the same conditions (Figure 4.4). One would expect that in the presence of UV light and oxygen, the reactive oxygen species produced from the TiO₂NPs would not only oxidise the chlorophyll content in the microalgae, but could also exert oxidative stress to the cell nucleus, mitochondria and other organelles and it is difficult to differentiate between these effects. Figures 4.3 and 4.5 indicate that at low and moderate particle concentrations, the cationic nature of the TiO₂NPs has much more disruptive effect on the cell viability (represented by the data in dark condition) than the additional effects of irradiation by visible and UV light.

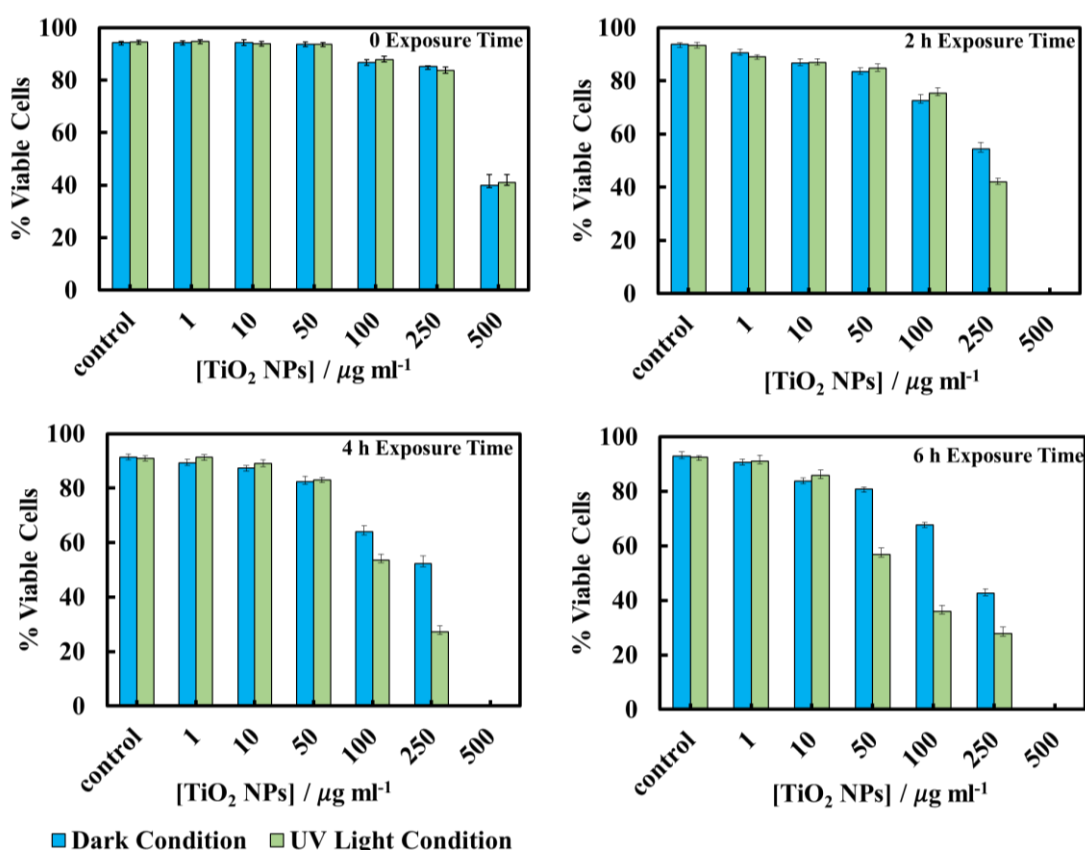


Figure 4.5: Comparison of the *C. reinhardtii* cell viability as a function of the TiO₂NPs concentrations in dark conditions and in UV light at 0h, 2h, 4h, and 6 hours of incubation times in comparison with control sample of microalgae.

4.2 Chlorophyll content of *C. reinhardtii* after exposure to TiO₂NPs

The effect of TiO₂NPs on *C. reinhardtii* was also indirectly evaluated by determining the cells chlorophyll content as a measure of their photosynthetic ability.

Figure 4.6 and figure 4.7 show the total chlorophyll content (chlorophyll a and b) as a function of TiO₂NPs concentration after different exposure times and up to 6 hours in both visible and UV light, respectively. Note that the cells apparently lose part of their chlorophyll content in the presence of TiO₂NPs not only upon exposure to UV light, but also upon irradiation with visible light. Moderate loss of chlorophyll was found even in dark conditions. However, we observed a sharp loss of the cells chlorophyll content upon irradiation with UV light above particle concentration of 50 $\mu\text{g mL}^{-1}$ which is close to the threshold concentration where the cells start to lose their viability, as shown in Figure 4.6 and 4.7. Note that with the UV light source (main peak at 365 nm) used in these experiments, the microalgae cells alone did not lose their viability or discolour over the same period of time.

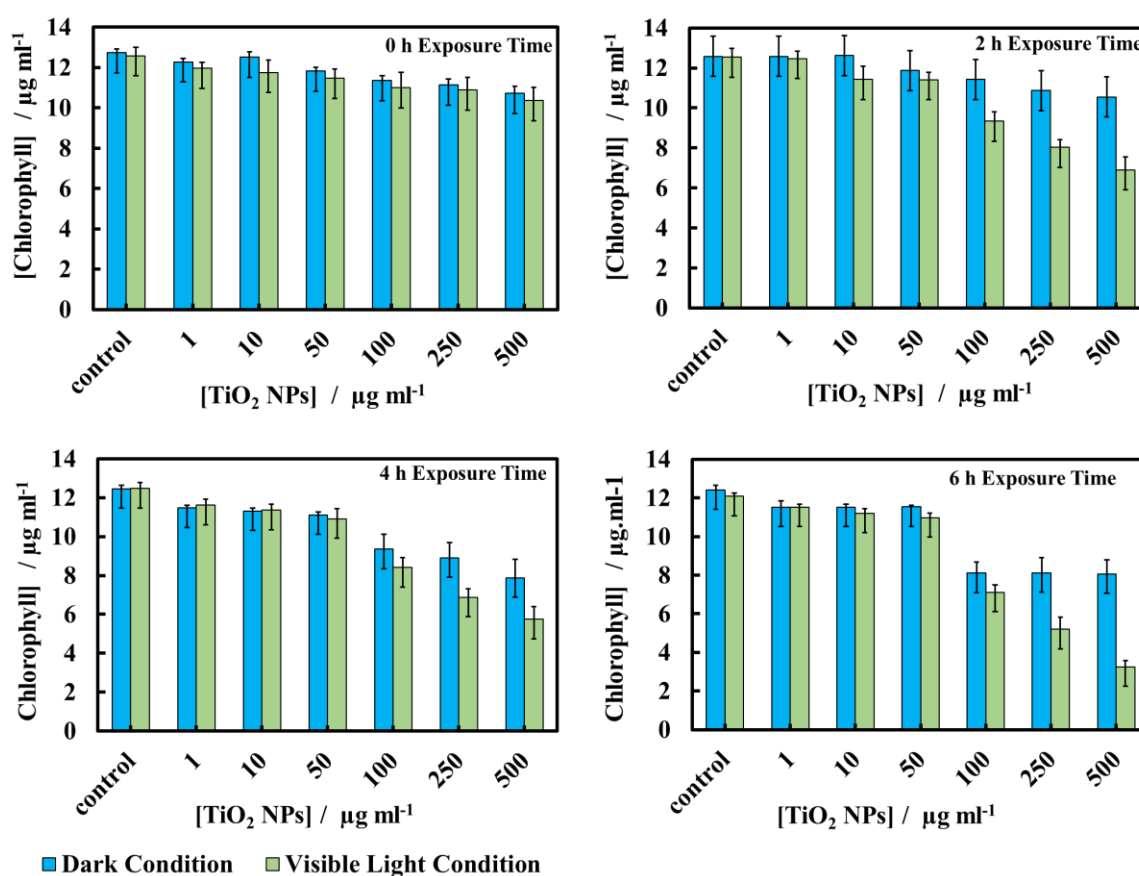


Figure 4.6: The effect of the TiO₂NPs concentration on the chlorophyll content of green algae *C. reinhardtii* in dark conditions and under visible light after 0h, 2h, 4h, and 6 h exposure time. The total chlorophyll content (a, b) was extracted from algal cells using 80 % aqueous acetone solution, then mixed for a minutes, centrifuged for 5 minutes with 13,000 rpm. The solution produced was scanned over a wide range of wavelengths from 200 nm to 700 nm. The chlorophyll a and b concentrations were measured at maximum wavelengths 645 and 663 nm, respectively.

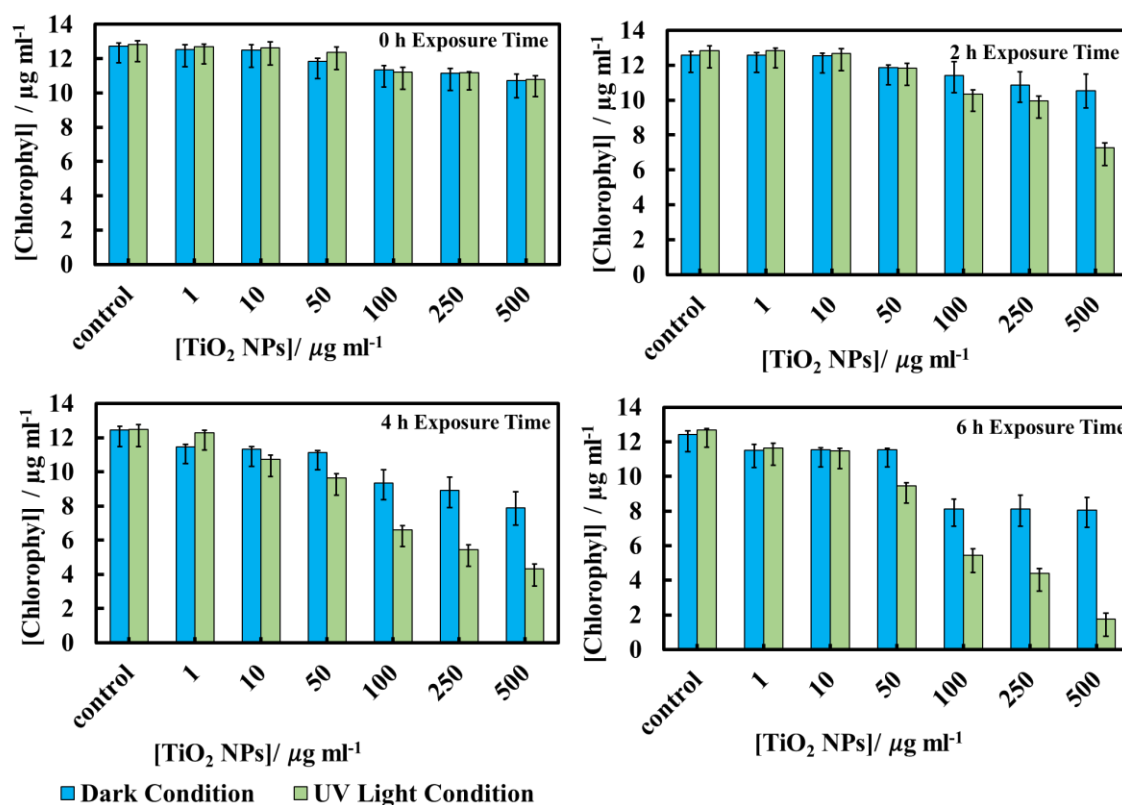


Figure 4.7: The effect of the TiO₂NPs concentration on the chlorophyll content of green algae *C. reinhardtii* in dark conditions and under UV light after 0h, 2h, 4h, and 6 h exposure time. The total chlorophyll content (a, b) was extracted from algal cells using 80 % aqueous acetone solution, then mixed for a minutes, centrifuged for 5 minutes with 13,000 rpm. The solution produced was scanned over a wide range of wavelengths from 200 nm to 700 nm. The chlorophyll a and b concentrations were measured at maximum wavelengths 645 and 663 nm, respectively.

Figure 4.8 shows optical images of the effect of TiO₂NPs on the *C. Reinhardtii* which indicate that for the range of 50-500 µg mL⁻¹ particle concentrations, a distinct discoloration of the cells chloroplasts was observed after 6 hours of exposure to visible light. The decrease of cell chlorophyll content in dark conditions above 100 mg mL⁻¹ TiO₂NPs is surprising as reactive oxygen species would not be expected to be produced in the absence of UV/vis light. Note that the microalgae viability does not correlate 1:1 with their chlorophyll content. The dead cells can temporarily retain some residual amount of chlorophyll in their chloroplasts, although their cell membranes are compromised. This is clearly the case in Figure 4.6 and 4.7 where a small amount of

chlorophyll was extracted from the samples treated with TiO₂NPs at 500 µg/mL, which show 0% viability (Figure 4.3 and 4.5). The complete bleaching of the cells chlorophyll content requires higher TiO₂NPs concentrations and/or longer exposure times to UV light and oxygen.

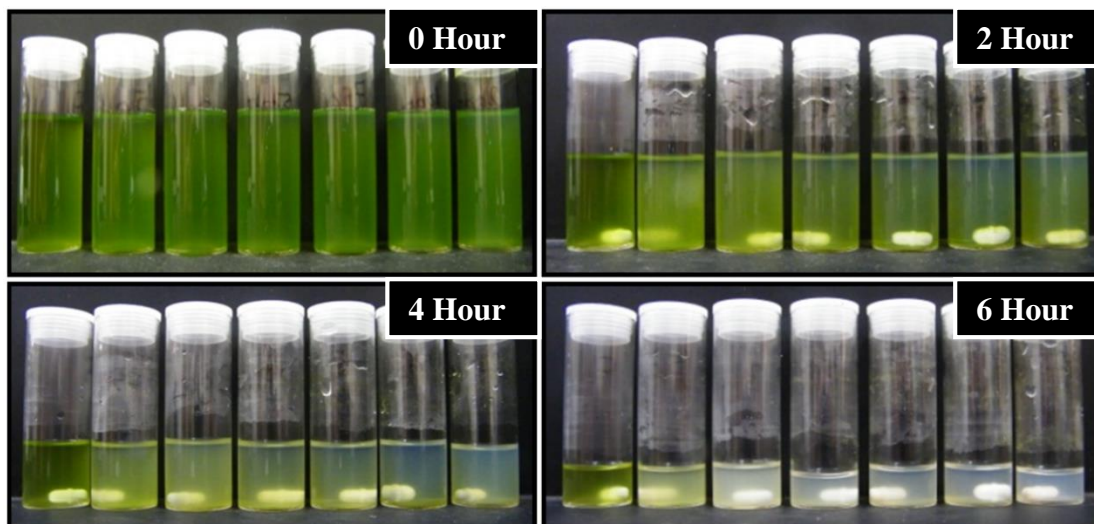


Figure 4.8: Optical images of *C.reinhardtii* samples after 0, 2, 4 and 6 hours of illumination with UV light in the presence of TiO₂NPs at the same concentration range (0-500 mg L⁻¹) as in Figure 6 and 7. The LHS test tubes on all four images in figure 8 represent the control sample of microalgae without TiO₂NPs.

TEM images of the microalgae cells after 6 hours of exposure to TiO₂NPs in visible light were obtained in order to examine the localisation of TiO₂NPs around the cell membrane of *C.reinhardtii*. Figure 4.9 shows TEM images of sections of microalgae cells incubated with TiO₂NPs of different concentrations where it can be seen that the cell membranes have a dense coating of TiO₂NPs and there is a limited penetration of nanoparticles inside the cells even at 100 µg mL⁻¹. In addition, the cells organelles and the inner cell microstructure (Figure 4.9B-D) look very different to the control sample untreated with TiO₂NPs (Figure 4.9A) which indicates that the internalised TiO₂ NPs may interfere with the microalgae photosynthetic pathways even under irradiation with visible light.

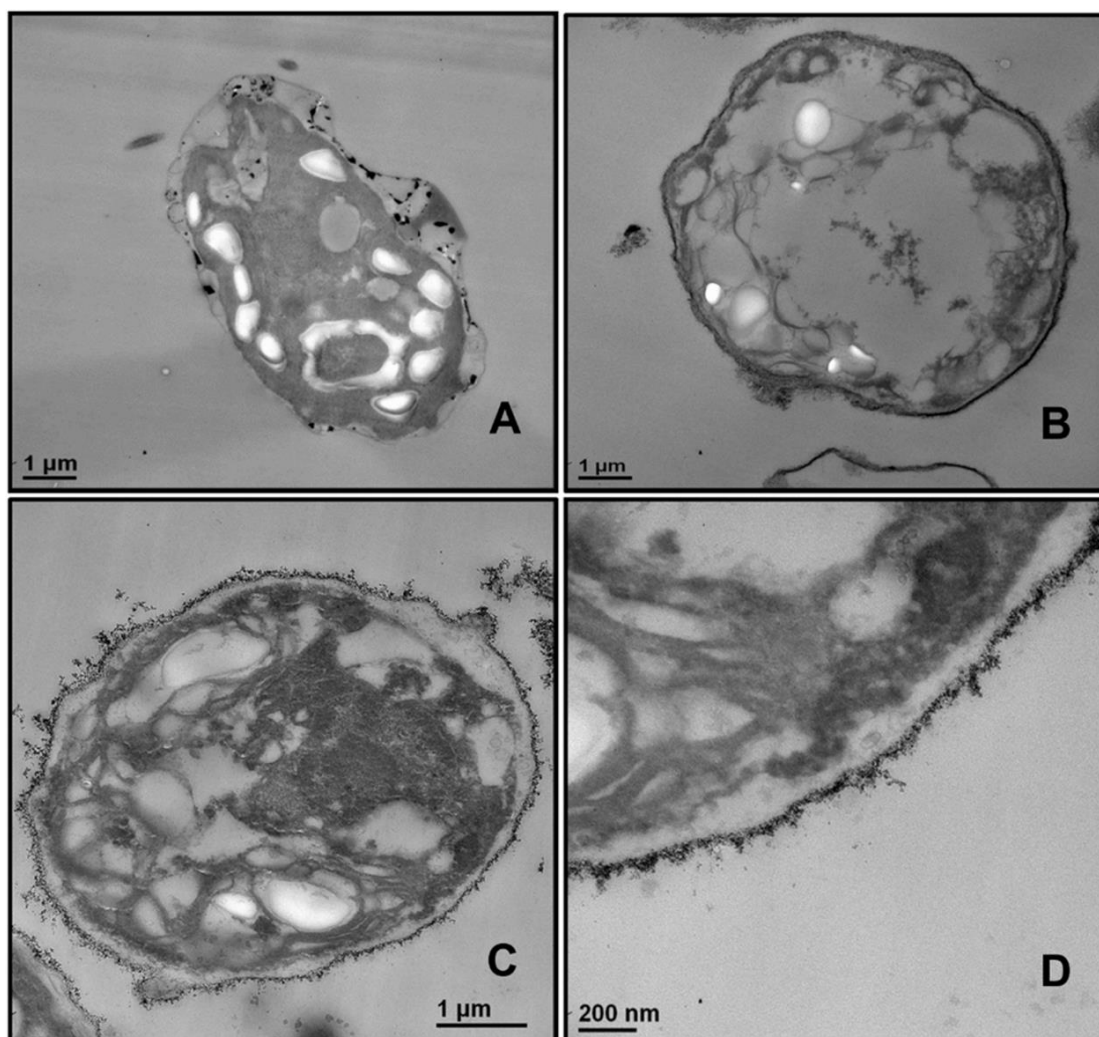


Figure 4.9: TEM images of microtome-sectioned samples of *C. reinhardtii* cells after being incubated with 0, 100, and 500 $\mu\text{g mL}^{-1}$ TiO_2NPs and irradiated for 6 hours with visible light. Image (A) represents the control sample of the cells without TiO_2NPs ; image (B) corresponds to microalgae incubated with 100 $\mu\text{g mL}^{-1}$ TiO_2NPs ; images (C) and (D) show the microstructure of a microalgae cell wall after incubation with 500 $\mu\text{g mL}^{-1}$ TiO_2NPs . Internalization of titania nanoparticles inside the algal cells is not seen even at a 500 $\mu\text{g mL}^{-1}$ concentration as displayed in figure 10. The data indicate the absence of Ti in the cell interior but show its presence on the cell outer membrane.

The possibility of internalisation of the cationic TiO_2NPs in *C. Reinhardtii*¹ was further checked by EDX. Sectioned samples of the microalgae exposed to TiO_2NPs were analysed (Figure 4.10) and this revealed that TiO_2NPs accumulate only at the outer side of the cell membrane without evidence for further penetration in the cell interior. Reactive oxygen species produced by exposure to TiO_2NPs and oxygen in UV/visible light may also interfere with the cell chloroplasts and other vital organelles and disrupt the cell photosynthetic system which corresponds to the higher toxicity. However, since an adverse effect was observed on the microalgae at high TiO_2NPs concentrations in

dark condition, this indicates that another possible mechanism of toxicity may also be in place in addition to the one discussed in the literature.¹ It is envisaged that most of the decrease in the percentage of viable microalgae cells in both visible light and dark conditions is probably due to the cell membrane disruption.

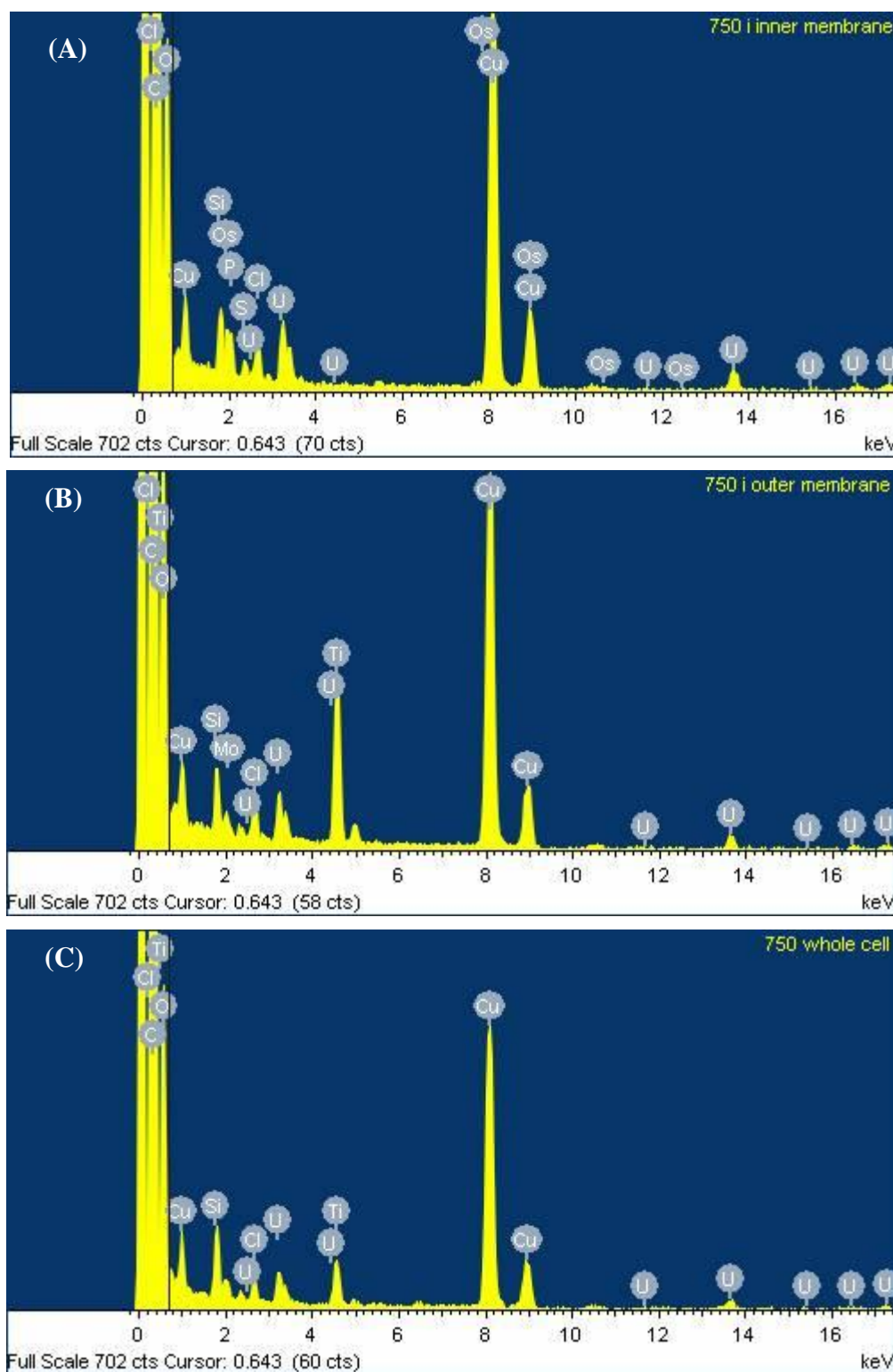


Figure 4.10: EDX diagram of the *C. reinhardtii* algae cell at 750 ppm: (A) cell interior membrane and (B) cell outer membrane regions; (C) whole cell. This demonstrates the lack of internalized TiO₂NPs in *C. reinhardtii* even at NPs concentration 750 ppm.

4.3 Toxicity Effect of TiO₂ NPs on Yeast in Visible/UV Light

Following on from the previous experiments with microalgae we then exposed baker's yeast to TiO₂NPs. As previously the experiments were carried out in the absence of growth media which could have interfered with the evaluation of the interaction between the cells and nanoparticles. The hydrolyzed yeast was incubated with dispersed titanium dioxide nanoparticles solutions (250, 500, 1000, 2500, and 5000 µg ml⁻¹) and exposed separately for 24 hours in dark and in visible light condition (the emission spectrum of visible light as shown in fig. 4.1). After that, an aliquot of each sample was taken to check the percentage of viability by automatic cell counter. Figure 4.11 shows the percentage of viable cells at different exposure time in dark and light (0 h, 3 h, 6 h, 12 h, 18, h, and 24 h).

Figure 4.11 shows that at 0.0 hour exposure time, all cells are viable in dark and in the presence of visible light in line with control sample. When the exposure time of titania nanoparticles interacted yeast increased to 3 hours, no pronounced toxic effect was observed up to 1000 µg ml⁻¹ but there was cytotoxic effect noticed at 2500 and 5000 µg ml⁻¹ in dark and visible light conditions. At 6-18 hour exposure time, the percentage of viability was reduced from 500 – 5000 µg.ml⁻¹ in visible light, while the viability in dark condition was higher than that for visible light for the same concentrations. After 24 hour exposure time, 250 µg ml⁻¹ titania nanoparticles concentration showed no toxic effect in dark and visible light conditions and, the concentrations are higher than 250 µg ml⁻¹, it showed significant inhibition of yeast viability in the presence of visible light in comparison with dark conditions. It was also indicated that yeast cells aggregated at high concentration for both irradiation conditions.

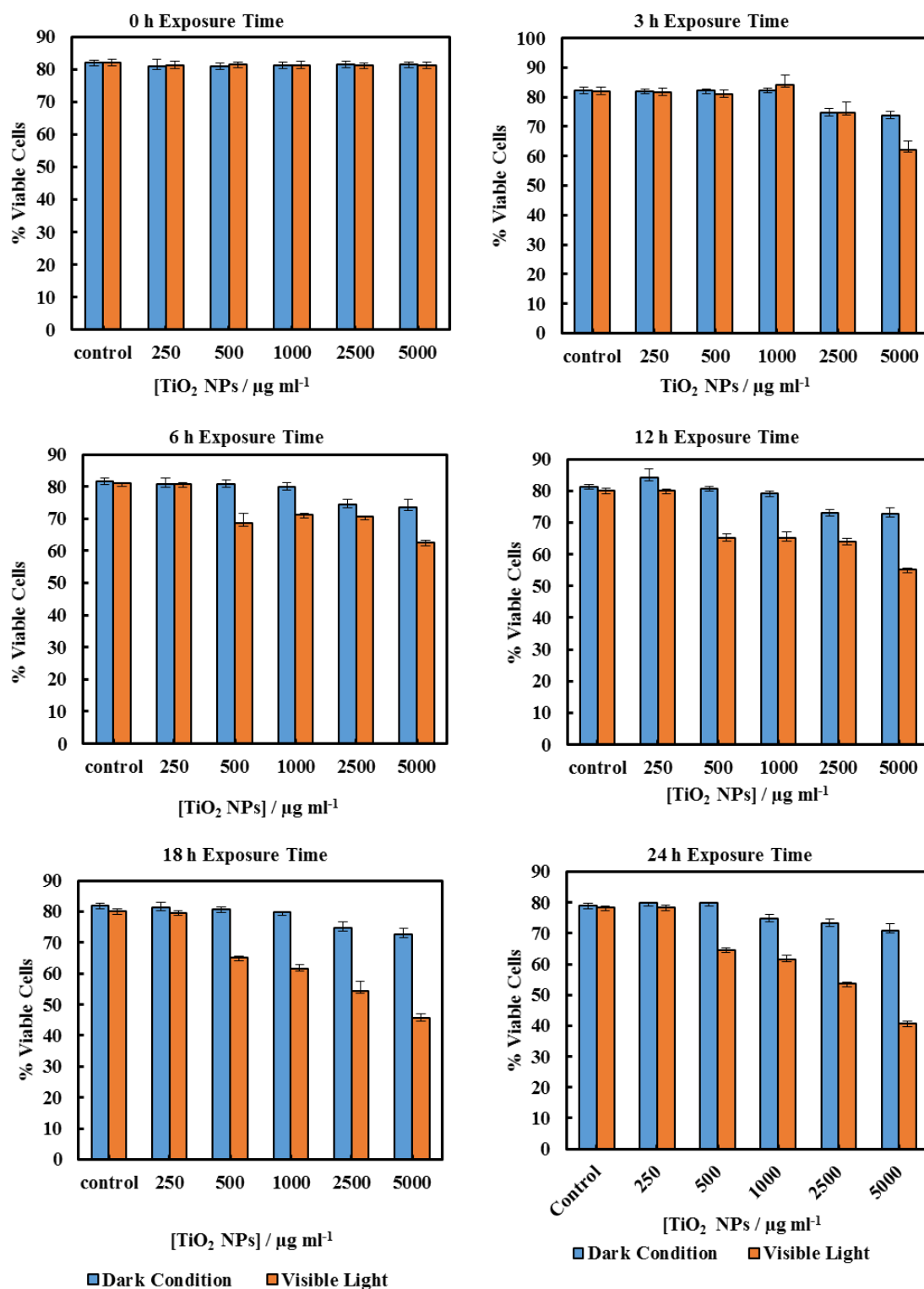


Figure 4.11: The viability of baker's yeast at different concentrations of titania nanoparticles against control sample at dark condition and visible Light condition which shows a toxic effect of titania nanoparticles in visible light in comparison with the dark conditions. This experiment was conducted through pipetting 1 milliliter of samples, centrifuged, incubated with one drop of FDA solution for 10 minutes, and centrifuged twice, then measured their viability using automatic cell counter.

Figure 4.12 shows an optical image of yeast cells after incubation with a $3000 \mu\text{g}\cdot\text{ml}^{-1}$ concentration of titania nanoparticles in the presence of visible light. It can be seen that the cells are aggregated.

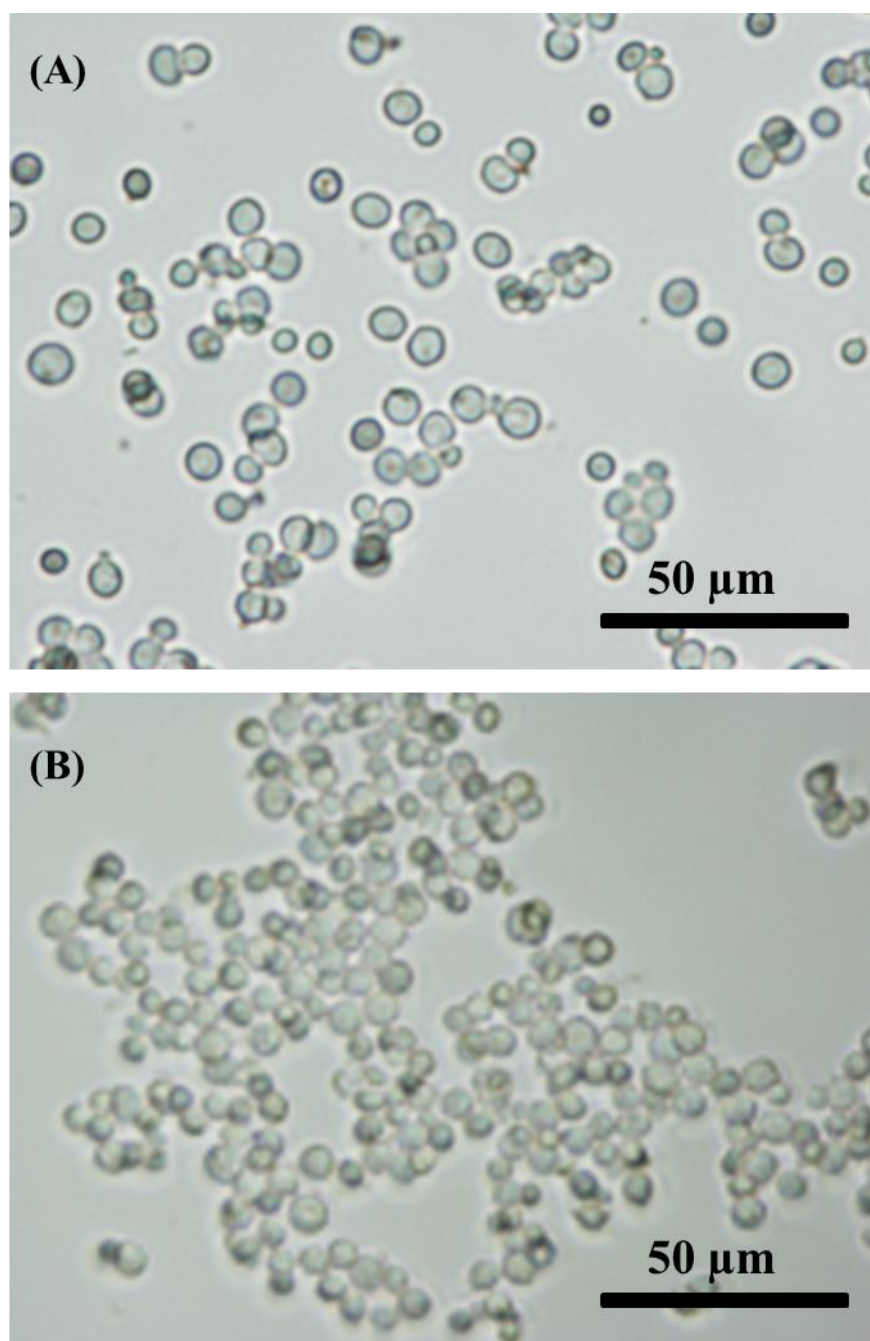


Figure 4.12: Bright field microscope image of (B) aggregated yeast cells after incubation with titania nanoparticles ($5000 \mu\text{g}\cdot\text{ml}^{-1}$) in the presence of visible light against control sample (A).

Samples of yeast cells were also incubated in the presence of UV light with dispersed TiO_2NPs at different particle concentrations for various periods of time for up to 24 hours in dark conditions and in UV light, respectively. It is important to note that the control yeast sample survived without the media for this period of time, i.e. the

effect is not due to the lack of nutrients. The yeast cell viability in each sample was determined as described in section 2.2.5. It was observed that the cells were highly aggregated after incubation with a high TiO₂NPs concentrations, as shown in Figure 4.12 for visible light. This result is similar to clustering of the *C.reinhardtii* cells in the presence of high concentrations of TiO₂NPs which be explained with the positive surface charge of the nanoparticles which hetero-coagulate with the negatively charged cells.

Figure 4.13 shows the cytotoxic effect on yeast of different concentrations of TiO₂NPs (of hydrodynamic diameter 25 nm) upon illumination with UV light (the emission spectrum of UV lamp is as shown in Figure 2) at different exposure time up to 24 hours.

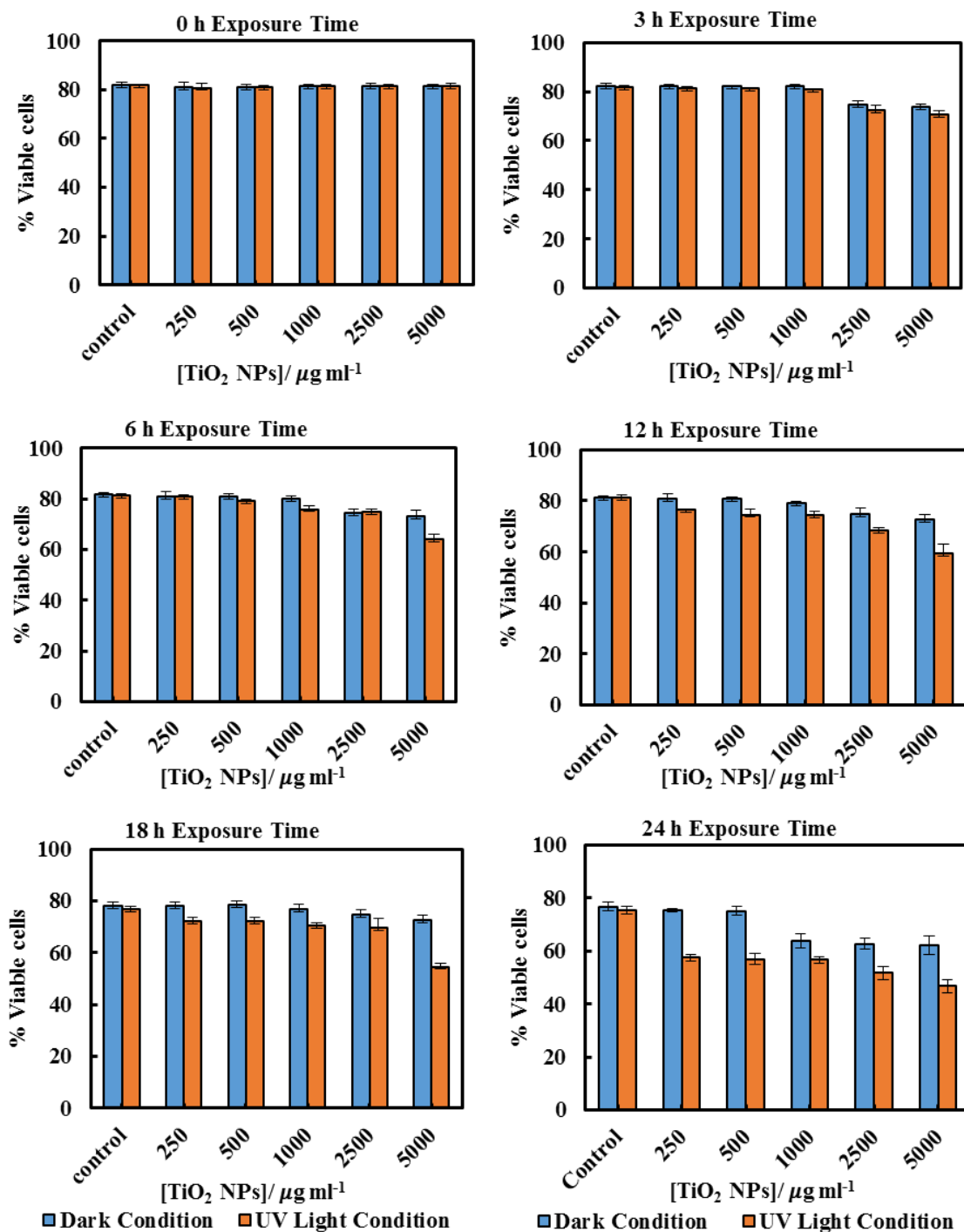


Figure 4.13: The percentage of viable yeast cells after incubation with TiO₂NPs of different concentration in the presence of UV light and in dark conditions at exposure times varying from 0 h to 24 h. The data show higher toxic effect of the TiO₂NPs in UV light than in dark conditions which can be attributed to the production of reactive oxygen species in the presence of atmospheric oxygen.

The figure indicates that the cells are completely unaffected at 0 exposure time which corresponds with the results obtained when the yeast cells were illuminated with visible light for the same period of time. After 3 hour exposure time at higher concentrations of titania nanoparticles ($2500 \mu\text{g ml}^{-1}$ and $5000 \mu\text{g ml}^{-1}$) there was a noticeable drop in the viability of yeast cells, but the effect was less at concentrations from $250 \mu\text{g ml}^{-1}$ – $1000 \mu\text{g ml}^{-1}$ both in dark condition and induced by UV light. After 6 incubation concentrations of 250 – $500 \mu\text{g ml}^{-1}$ titania NPs had no effect, however, at $1000 \mu\text{g ml}^{-1}$ there was a slight drop in the viability under UV light compared to dark condition for the same concentration. For the 12 hour to 18 hour exposure time in UV light there was a considerably lethal effect for concentrations of $250 \mu\text{g ml}^{-1}$ to $5000 \mu\text{g ml}^{-1}$. Contrastingly, in dark condition, there was very little cytotoxic effect for titania NPs concentrations up to $5000 \mu\text{g ml}^{-1}$. After 24 hour exposure time, the percentage of viability significantly declined but remained constant at about 55 % from $250 \mu\text{g ml}^{-1}$ to $2500 \mu\text{g ml}^{-1}$. It was also detected that at $5000 \mu\text{g ml}^{-1}$ titania NPs concentration, a big toxic effect happened about 50% in comparison with control. Moreover, at dark conditions it was perceived that the percentage of viability was seen to be almost identical with other exposure times from 12 hour to 18 hour in the absence of light.

Our results indicated that the TiO_2NPs have a weak effect on the yeast cells viability above 1000mg mL^{-1} in dark conditions. The cytotoxic effect of the TiO_2NPs on microalgae upon illumination with UV light is stronger and can be observed at much lower particle concentrations (above 100mg mL^{-1}). For up to 6 hours of exposure, our data on cell viability agree with the findings of Kasimets *et al.*² who reported that yeast cells are insensitive even to extremely high TiO_2NPs concentrations. However, our cell viability data are acquired in the absence of culture media whose components may also adsorb on the nanoparticles surface and change their interaction with the cells. In order to understand better the differences between the TiO_2NPs effect on microalgae and yeast we used TEM to examine the yeast cells which were incubated with TiO_2NPs for 24 hours and treated similarly to the microalgae as shown in Figure 4.9.

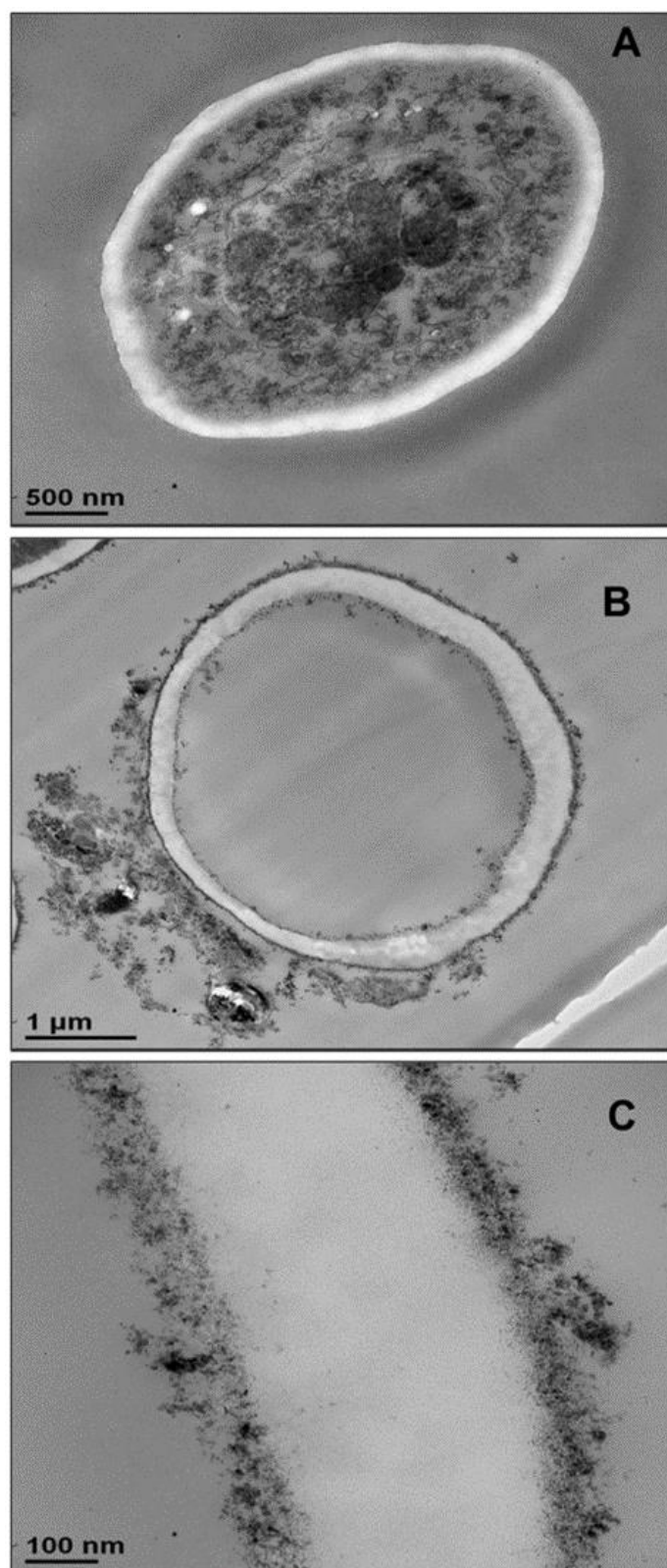


Figure 4.14: TEM images of *S. cerevisiae* sectioned after 24 hours of irradiation with UV light and incubation in (A) Milli-Q water and (B) 5000 µg mL⁻¹ TiO₂NPs. (C) High resolution TEM image of the outer and inner cell wall of the yeast cell treated as in (B) which shows the attachment of TiO₂NPs to the outer cell surface and indicates their internalisation inside the cell.

Figure 4.14B shows the TEM images of microtome-sectioned yeast cells after exposure to UV light and $5000 \mu\text{g mL}^{-1}$ TiO_2NPs for 24 hours compared with the control samples of yeast without exposure to TiO_2NPs (Figure 4.14A). One can see a build-up of TiO_2NPs both on the outer and the inner cell wall which indicates their penetration through the cell wall at high particle concentration (Figure 4.14C). This result was confirmed by performing EDX on sectioned yeast which showed the presence of Ti on both sides of the cell membrane (Figure 4.15).

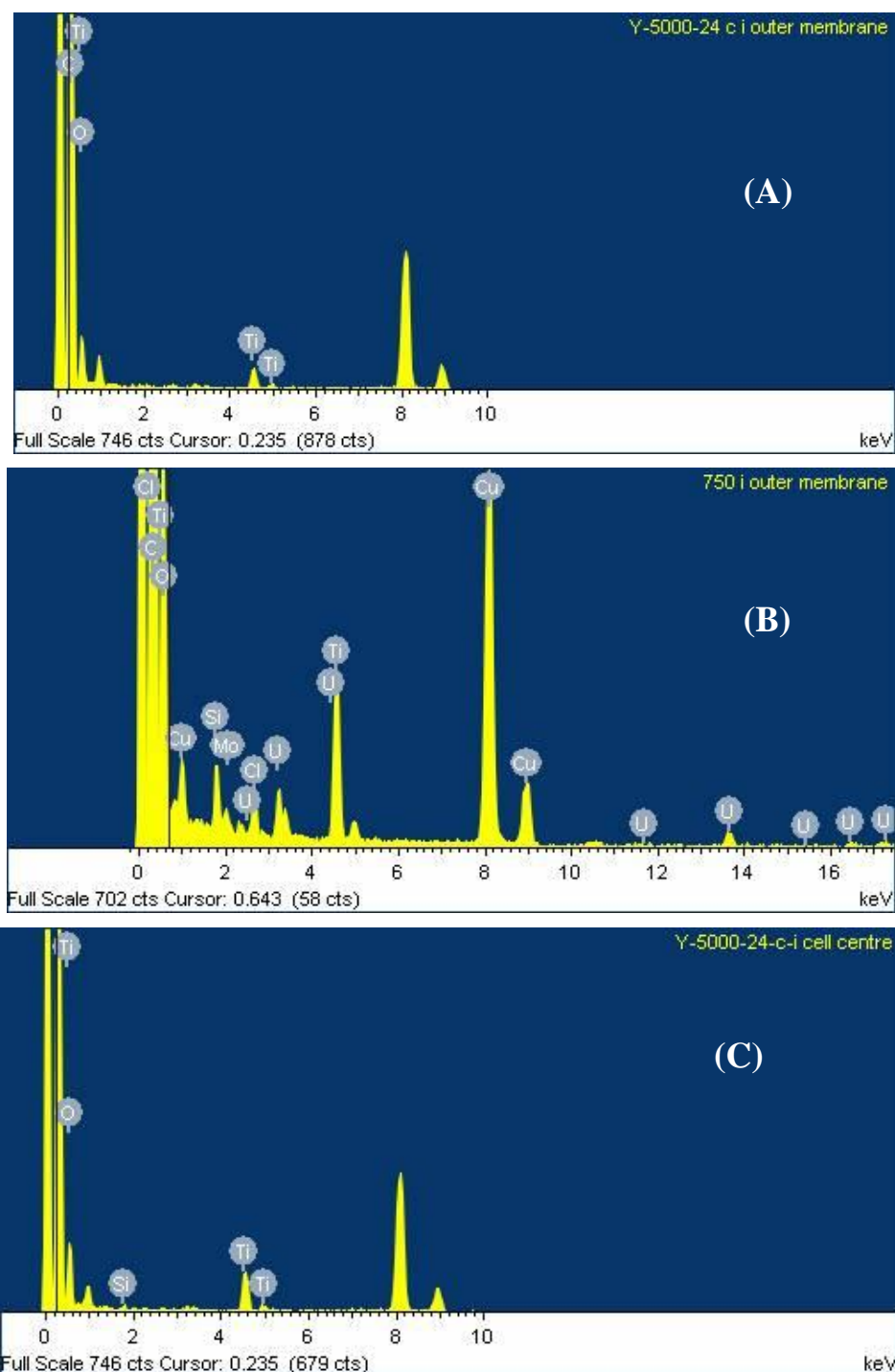


Figure 4.15: EDX diagram of yeast cell at 1000 ppm: (A) cell interior membrane and (B) cell outer membrane regions; (C) the cell centre. The data indicate the presence of TiO₂NPs both on the outer and the inner part of the cell membrane. This confirms the internalised TiO₂NPs in yeast at this NPs concentration.

However, the exposure of yeast to TiO₂NPs in the same concentration range that cause cytotoxicity effect in *C.reinhardtii* (Figure 4.9) did not lead to extensive particle internalisation and cell damage due to the much thicker cell wall of yeast (~200 nm) as

compared to *C.reinhardtii*.

The specific cytotoxicity of TiO₂NPs in UV light probably occurs due to the generation of OH•, O₂⁻, and H₂O₂ in their vicinity as they are deposited on the cell wall which leads to local oxidation of phospholipids into cell membrane. In addition, the internalisation of TiO₂NPs through the damaged cells walls subsequently may cause DNA damage, disruption of vital organelles and the electron transport chain, which leads to the cell death. The cells wall thickness determines the barrier for the TiO₂NPs internalisation and their toxicity threshold.

This study was similar to a recently reported study in the literature² where yeast was incubated with nano-grade ZnO, CuO, and TiO₂ for a 24 hours exposure time. However, no toxicity was seen from nano and bulk TiO₂ even at 20000 mg/l. This study also indicated that the toxicity of metal nanoparticles depended on the particle size and crystal structure³ along with the fact that titania nanoparticles have the ability to generate oxidative stress in visible light.¹ The reported study was however conducted in the presence of growth media and it is known that some the components of the media (e.g. peptones) can interact with metal nanoparticles which could affect results.

4.4 Effect of the TiO₂NPs size on microalgae and yeast cell viability

To study the effect of particle size on cell viability a series of titania samples were produced by thermal annealing at 400 °C , 600 °C and 800 °C, followed by dispersion by sonication in aqueous solution to prepare samples of TiO₂NPs of particle diameters 25 nm, 35 nm, 50 nm and 145 nm. A fixed amount of TiO₂NPs of each sample was incubated with *C.reinhardtii* and *S. cerevisiae* and irradiated with UV light for 6 h and 24 h, respectively. Control samples of the same compositions were kept in dark conditions for the same periods of time. Figure 4.16 shows the effect of TiO₂NPs particle size on their toxicity for *C.reinhardtii* and *S. cerevisiae*.

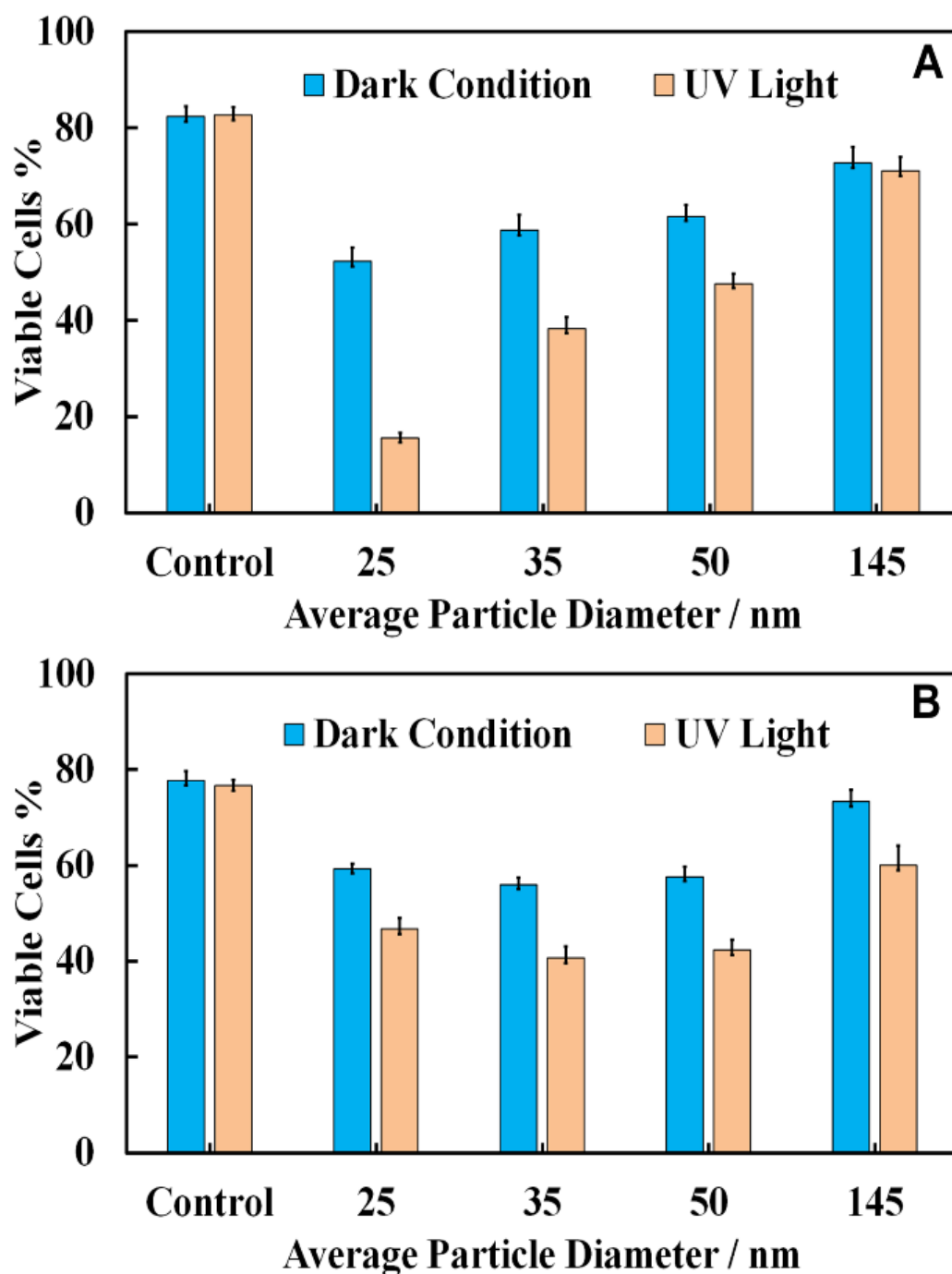


Figure 4.16:(A) The cell viability of *C.reinhardtii* incubated with TiO₂NPs of different average particle sizes (25 nm, 35 nm, 50 nm and 145 nm) and total particle concentration of 250 µg mL⁻¹ in dark conditions and in UV light for 6 hours. (B) The cell viability of *S. cerevisiae* incubated with TiO₂NPs of different average particle sizes (the same as in (A)) but at total particle concentration of 2500 µg mL⁻¹ in dark conditions and in UV light for 24 hours.

The data indicates that the smaller particle sizes had a higher toxic effect on both types of cells at fixed other conditions. The toxicity decreases with increasing particle size for both samples irradiated with UV light and those kept in dark conditions. This effect of particle size can be explained by the packing conditions of the TiO₂NPs which allow more of the smaller nanoparticles to attach to the cell wall as compared to the case of larger nanoparticles. However, the effect is not so pronounced for *S. cerevisiae*.

Note that the toxic effect of the 145 nm TiO₂NPs is much smaller than that of the smaller nanoparticles. This is apparently related to the fact that the 145 nm particles were obtained by dispersing titania annealed at 800°C which corresponds to rutile, while the other three TiO₂NPs samples (25 nm, 35 nm and 50 nm) correspond to anatase form of titania. Since the former has a slightly negative zeta potential at pH 4, this is likely to explain the reduced nanotoxicity of the rutile TiO₂NPs with the lack of electrostatic adhesion with the cells.

It should be noted that the TiO₂NPs samples used in Figure 16 have not only different hydrodynamic diameters but also varying zeta potentials. The reason is that it is practically difficult to vary the particles size at fixed surface potentials as the smallest particle hydrodynamic diameter in solution is limited by the crystallite size of titania, which is controlled by the calcination temperature at the sample preparation stage. For unmodified TiO₂NPs the zeta potential depends on the size of the particle crystallites as well as the degree of aggregation. This is not unusual and is well documented with other materials. Table 1 clearly shows the link between the particle hydrodynamic diameter achieved by sonication in solution and the particle crystallite size. The negative zeta potential for 145 nm TiO₂NPs is because this is a rutile form of titania which has different isoelectric point (IEP) to anatase.

4.5 Nanotoxicity of polyelectrolyte-coated TiO₂NPs on *C. reinhardtii*

Since the adhesion of the TiO₂NPs to the cell membrane is largely driven by electrostatic interactions, we examined the cytotoxicity of TiO₂NPs coated with a varying number of polyelectrolyte layers and compared them with the bare TiO₂NPs. Figure 4.17A and 4.17E represent the cytotoxic effect of bare TiO₂NPs in dark conditions and in UV light while Figures 4.17B and 4.17F give the same effect of TiO₂NPs coated with a single layer of PSS.

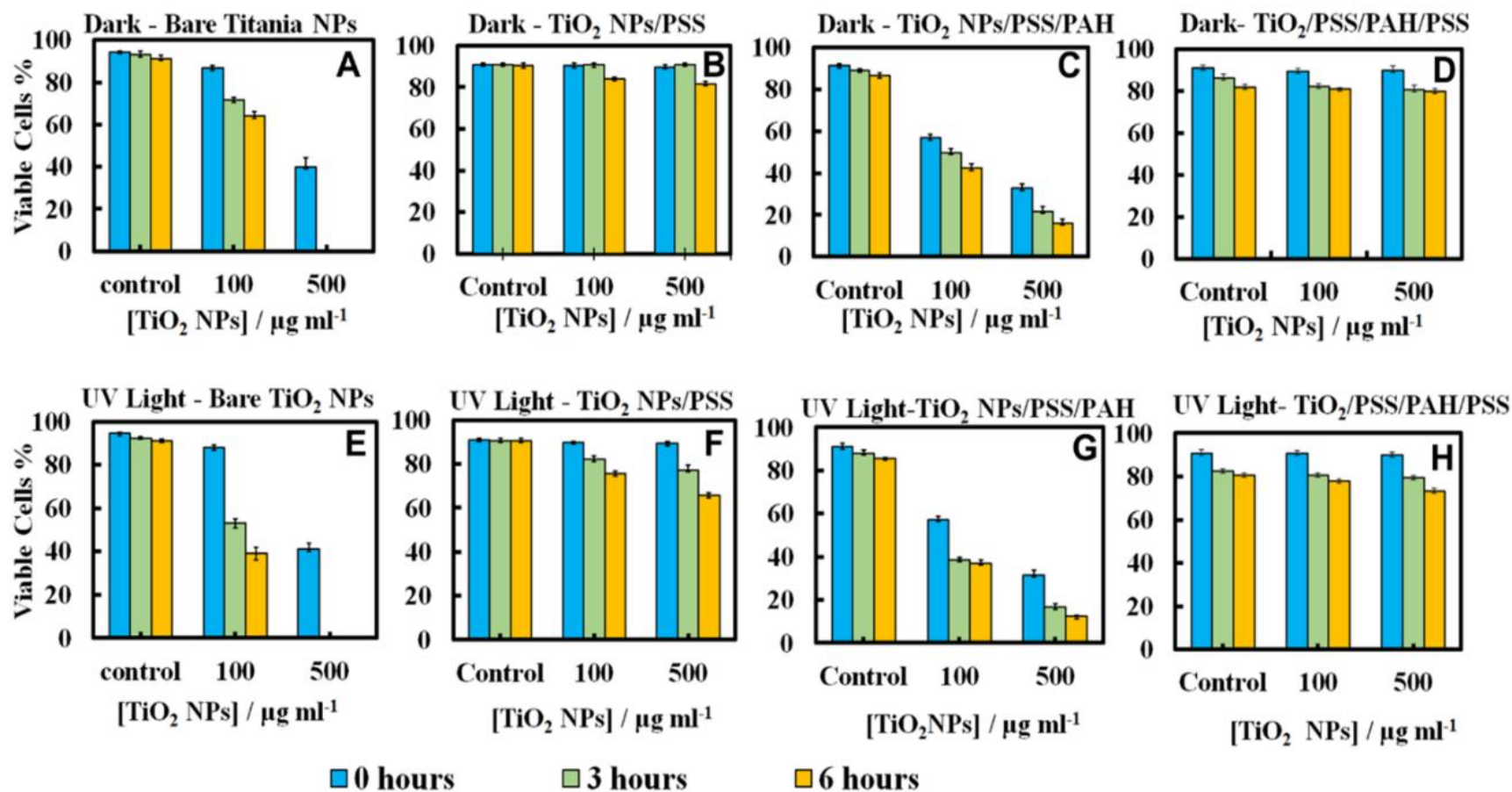


Figure 4.17: The effect of anatase TiO₂NPs coated with different number of layers of anionic (PSS) and cationic (PAH) polyelectrolytes on the viability of *C.reinhardtii* microalgae at different particle concentrations (0, 100 and 500 µg mL⁻¹). The cells were incubated with the TiO₂NPs for at 0 h, 3 h and 6 h exposure times in dark conditions (A-D) and in UV light (E-H), respectively. The cytotoxic effect on the microalgae cells was assessed for: (A, E) bare TiO₂NPs; (B, F) TiO₂NPs/PSS; (C, G) TiO₂NPs/PSS/PAH and (D, H) TiO₂NPs/PSS/PAH/PSS at different nanoparticle concentrations and exposure times.

It should be noted in Figure 4.17 that there is no pronounced toxicity of TiO₂NPs/PSS on the microalgae in dark conditions at this range of particle concentrations irrespectively of the time of exposure. The toxic effect of TiO₂NPs/PSS under UV light is also much lower than the one of the bare TiO₂NPs. The difference between the cell viability in Figures 4.17B and 4.17F is solely due to the photo activity of the titania nanoparticles. One may conclude that the functionalization of the TiO₂NPs with anionic polyelectrolyte reduced its nanotoxicity probably because of the electrostatic repulsion of the coated nanoparticles from the cell surface as both of them have a negative surface charge (see also functionalization of titania nanoparticles in chapter 3).

A very similar effect was observed for TiO₂NPs/PSS/PAH/PSS as shown in Figures 4.17D and 4.17H for these anionic nanoparticles. However in Figure 4.17C and 4.17G where a second coating of the cationic polyelectrolyte PAH is included the viability of the microalgae reduces considerably. In fact it is nearly as toxic to the microalgae as the bare TiO₂NPs. It is interesting that at lower TiO₂NPs/PSS/PAH concentrations (100 mg mL⁻¹) these cationic coated particles are even more toxic than the bare TiO₂NPs irrespectively of the time of exposure in both dark and UV light conditions. However, at higher concentrations, the bare TiO₂NPs exhibit higher toxicity to microalgae than coated TiO₂NPs/PSS/PAH. This pattern of alternating toxicity of the polyelectrolyte coated TiO₂NPs seems to be consistent with their surface charge and the resulting electrostatically driven adhesion to the negatively charged cell wall surface. The cationic nanoparticles (the bare TiO₂NPs and TiO₂NPs/PSS/PAH) have higher nanotoxicity than their anionic versions, TiO₂NPs/PSS and TiO₂NPs/PSS/PAH/PSS.

In order to examine the build-up of TiO₂NPs on the microalgae cell surface we incubated them with the same range of polyelectrolyte-coated TiO₂NPs followed by their removal from the nanoparticle suspension after fixed time of exposure to UV light. The cell samples were sectioned and imaged with TEM as described in the previous section. Figure 4.18 displays TEM images of *C.reinhardtii* for TiO₂NPs coated with different number of anionic (PSS) and cationic (PAH) polyelectrolytes layers after incubation for up to 6 hours in dark conditions and in UV light.

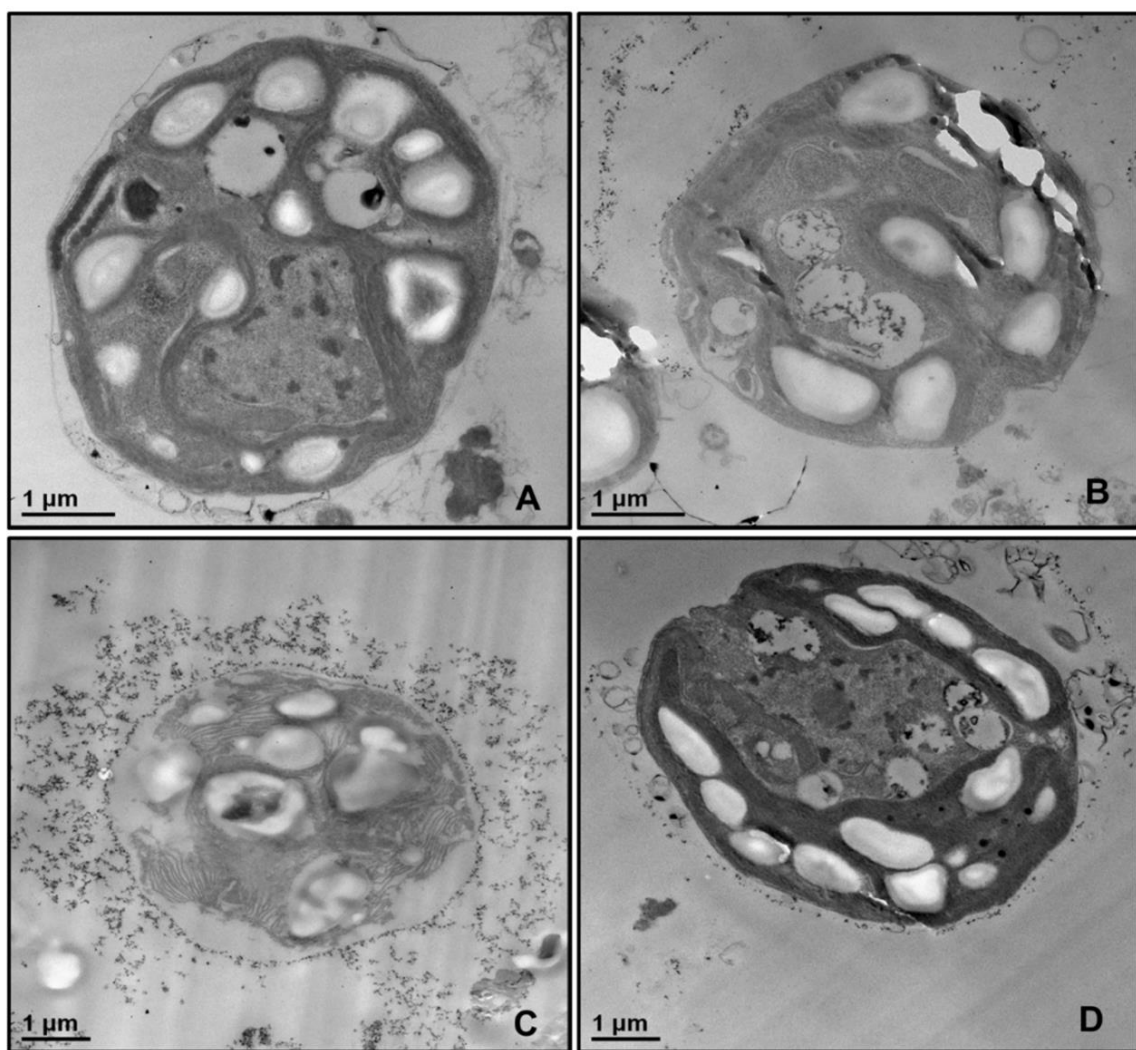


Figure 4.18: TEM images of microtome-sectioned *C.reinhardtii* microalgae cells after being incubated for 6 hours with polyelectrolyte-coated TiO₂NPs while illuminated with UV light. The TiO₂NPs have been modified by deposition of different number layers of anionic (PSS) and cationic (PAH) polyelectrolytes. (A) The control sample of the microalgae without TiO₂NPs. The microalgae after being incubated with (B) TiO₂NPs/PSS; (C) TiO₂NPs/PSS/PAH and (D) TiO₂NPs/PSS/PAH/PSS.

Looking at Figure 4.18 it should be noted that there are very few TiO₂NPs/PSS and TiO₂NPs/PSS/PAH/PSS attached to the cells (Figures 4.18B and 4.18D) while we observe a significant build-up of TiO₂NPs/PSS/PAH on the cell wall (Figure 4.18C). These results are consistent with the nanotoxicity pattern of the polyelectrolyte-coated TiO₂NPs on *C.reinhardtii* displayed in Figure 4.17. One may speculate that the poor attachment of the anionic particles TiO₂NPs/PSS and TiO₂NPs/PSS/PAH/PSS to the cells as confirmed by the TEM images corresponds to less disruption of the cell membranes and to lower oxidative stress in UV light as the ROS are produced around nanoparticles that are in the bulk of the suspension rather than on the cell walls. However, as can be seen in Figures 4.9C and 4.9D for the bare TiO₂NPs and Figure 4.18C for the TiO₂NPs/PSS/PAH, there is an effective hetero-coagulation of the cationic TiO₂NPs on the anionic cell walls which corresponds to much higher local particle concentration which subsequently has a highly disruptive effect on the cell viability (cf. Figures 4.17A, E and 4.17C, G).

4.6 Nanotoxicity of polyelectrolyte-coated TiO₂NPs on yeast

It was also conducted similar tests with yeast cells and polyelectrolyte-coated TiO₂NPs where the cells were removed from their culture media. Figure 4.19 compares the impact of bare and multilayer-coated TiO₂NPs with PSS and PAH polyelectrolytes at different particle concentrations on the yeast cell viability.

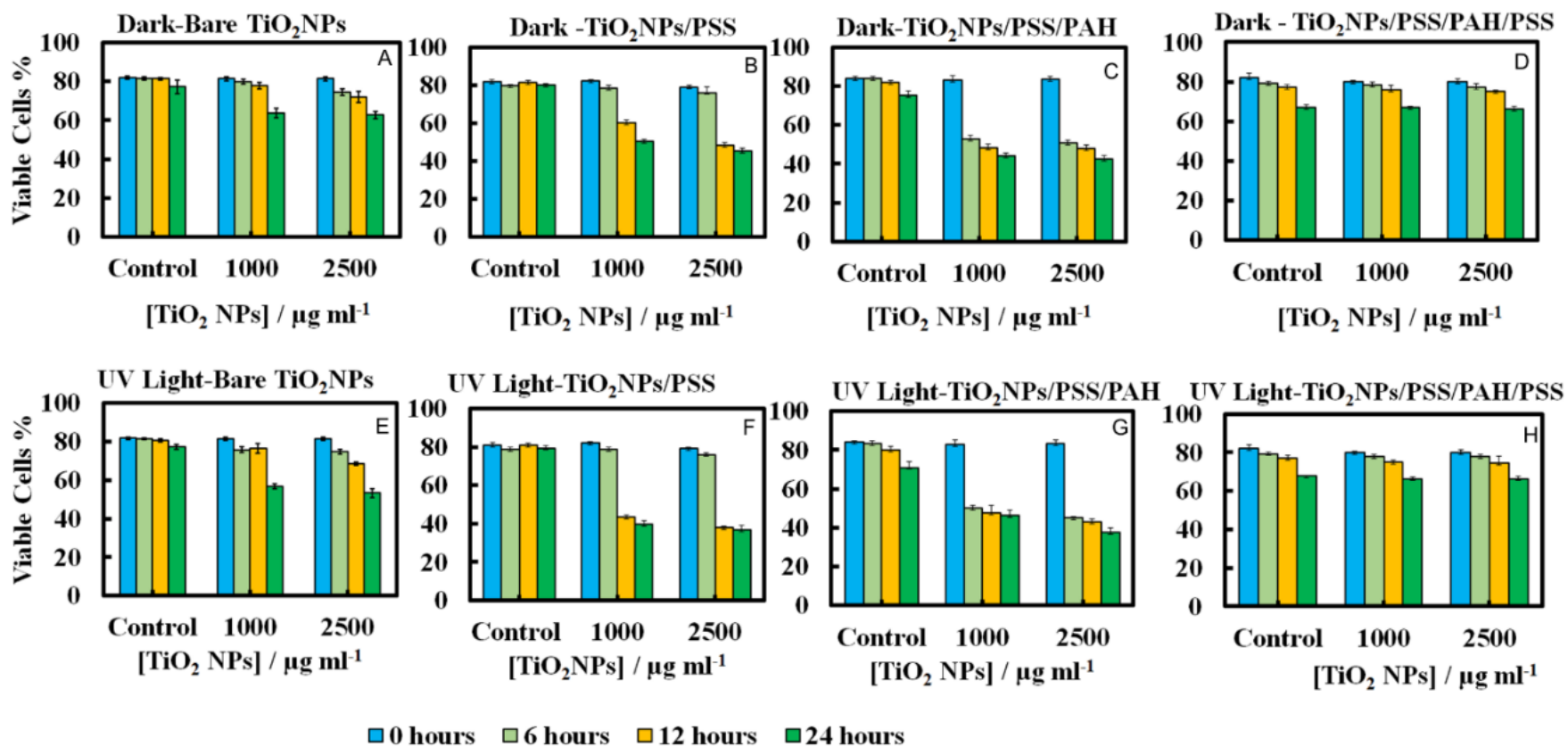


Figure 4.19: The cell viability of yeast upon incubation of bare and polyelectrolyte-coated anatase TiO₂NPs of different particle concentrations (0, 1000, and 2500 µg mL⁻¹) in dark conditions (A-D) and in UV light (E-H) at 0 h, 6 h, 12 h and 24 h exposure times. The yeast cells were incubated with: (A, E) bare TiO₂NPs; (B, F) TiO₂NPs/PSS; (C, G) TiO₂NPs/PSS/PAH and (D, H) TiO₂NPs/PSS/PAH/PSS.

In Figure 4.19 it can be seen that for exposure times up to 6 hours, no measurable change in the yeast cell viability was observed for TiO₂NPs/PSS and TiO₂NPs/PSS/PAH/PSS even at high particle concentrations. Significant difference were also not seen between the samples kept in dark conditions or in UV light at the same particle concentration. However, for longer incubations times, the cationic nanoparticles TiO₂NPs/PSS/PAH showed a significant toxic effect on yeast even at moderate particle concentrations. A strong effect of the bare TiO₂NPs on yeast cells viability was observed upon illumination with UV light at high particle concentrations. It is worth mentioning that no significant toxic effect was detected for bare TiO₂NPs in dark conditions at the same particle concentration range. These results call for some discussion with regard to the possible factors that may contribute to the nanotoxicity of the coated TiO₂NPs on yeast, which differ from their effect on the microalgae cells. Since yeast cells have much thicker cell walls (~200 nm) than microalgae, the data suggests that it takes a much higher nanoparticle concentration to impact the yeast cells viability (see also Figure 4.13). However, upon illumination with UV light, the cell walls are likely to sustain greater damage from the ROS generated in their vicinity which may facilitate further TiO₂NPs internalisation at higher concentrations and exposure times. Upon incubation with the anionic particles, TiO₂NPs/PSS/PAH/PSS, however, we did not observe significant difference between the yeast cells viability both in dark conditions and in UV light for up to 24 hours of exposure except at very high particle concentrations.

The increased toxicity of the TiO₂NPs/PSS (Figure 4.19B) compared to TiO₂NPs/PSS/PAH/PSS (Figure 4.19D) is due to the thicker polyelectrolyte shell of the TiO₂NPs/PSS/PAH/PSS. The ROS generating TiO₂NPs cores are closer to the cell membranes for TiO₂NPs/PSS than for TiO₂NPs/PSS/PAH/PSS. One may conclude that by coating the TiO₂NPs with an outer anionic polyelectrolyte layer their cytotoxicity is greatly reduced for both yeast and microalgae due to the electrostatic repulsion between the cells surface and the nanoparticles. Figure 4.20 shows TEM images of yeast cells incubated with TiO₂NPs coated with polyelectrolyte layer of different surface charge.

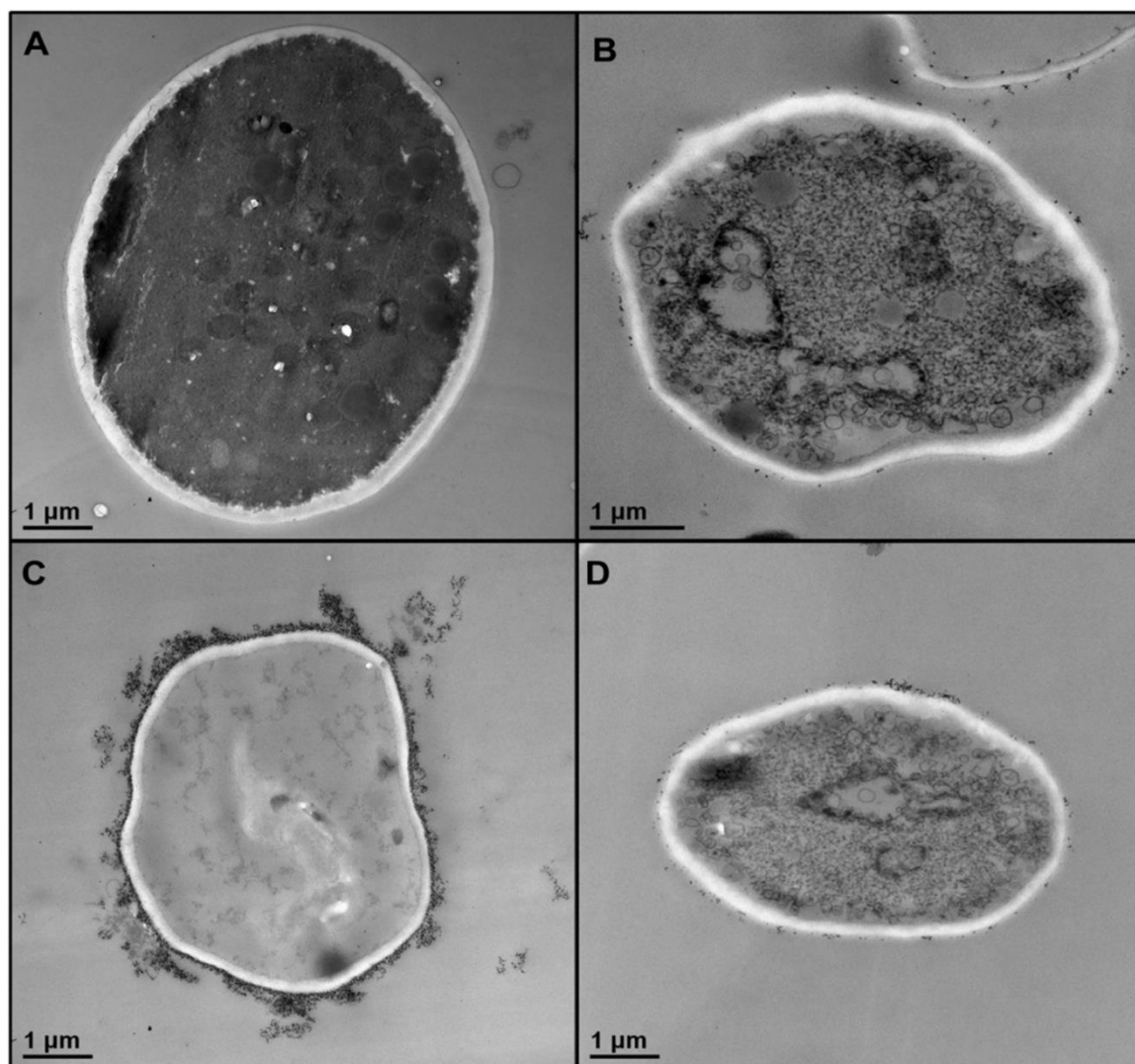


Figure 4.20: TEM images of microtome sectioned yeast cells after being incubated for 24 hours under UV light with TiO_2NPs coated with different number of polyelectrolyte layers: (A) Control sample without TiO_2NPs . (B) Yeast cell incubated with $\text{TiO}_2\text{NPs}/\text{PSS}$. (C) Yeast cells incubated with $\text{TiO}_2\text{NPs}/\text{PSS}/\text{PAH}$. (D) Yeast cells incubated with $\text{TiO}_2\text{NPs}/\text{PSS}/\text{PAH}/\text{PSS}$.

The TEM images in Figures 4.20B and 4.20D supports the hypothesis that the electrostatic repulsion between the negatively charged cell walls and the anionic nanoparticles, $\text{TiO}_2\text{NPs}/\text{PSS}$ and $\text{TiO}_2\text{NPs}/\text{PSS}/\text{PAH}/\text{PSS}$, leads to reduced adhesion onto the cell surface. Figure 4.20C however, shows a much larger build-up of cationic nanoparticles $\text{TiO}_2\text{NPs}/\text{PSS}/\text{PAH}$ which leads to the higher nanotoxicity for yeast both in dark conditions and in UV light. Nano-sized titania can be harmful to the environment as it is a powerful

cell membrane disruptor due to its cationic nature and photo-activity which can make an adverse impact on aquatic organisms especially the ones in the root of the food chain. Our study shows for the first time that coating TiO₂NPs with anionic polyelectrolytes as terminal layer greatly reduces their toxicity on algae and yeast as well as the toxicity threshold concentrations. Our study, as outlined above indicates a way of reducing toxicity of TiO₂NPs by pre-coating them with anionic polymers. An additional improvement, which will be addressed in a follow up publication, would be to use layers of biocompatible anionic polymers to reduce the ecological footprint of such nanomaterials upon their post use release into the environment.

Conclusion

A range of titania nanoparticles of diffuse crystallite size were synthesised and characterised their surface charge and average hydrodynamic diameter in aqueous solutions. We studied the effect of the TiO₂NPs hydrodynamic diameter on their toxicity for *C.reinhardtii* microalgae and yeast. In our nanotoxicity studies we separated the cells from their growth media to avoid any interferences with the TiO₂NPs. The results indicate that smaller TiO₂NPs have higher toxicity than larger ones, with the anatase form of the TiO₂NPs having higher impact on the cell viability than the rutile form. It was found that the bare anatase TiO₂NPs are cationic below pH 6.5 which explains their adhesion to the cell walls of both microalgae and yeast.

Irradiation of the microalgae cells with UV light (peak at 365 nm) had bigger impact on their viability in the presence of TiO₂NPs compared with the same experiments conducted in dark conditions. Surprisingly, illumination with visible light also made the TiO₂NPs more toxic to the microalgae compared to the ones in dark conditions. The experiment showed that TiO₂NPs at concentrations above 50 mg mL⁻¹ noticeably affect the microalgae viability while particle concentrations higher than 250 mg mL⁻¹ led to complete loss of viability. The tests also showed a decrease in the chlorophyll content after prolonged exposure to TiO₂NPs in UV and visible light. This indicated that TiO₂NPs can not only disrupt the cell membranes but also can interfere with the cell chloroplasts. The results with yeast cells showed similar trends but the nanotoxicity concentration threshold TiO₂NPs was about one order of magnitude higher due to the much thicker yeast cells walls.

It was also produced polyelectrolyte-coated TiO₂NPs with up to 4 layers of polyelectrolytes of alternating charge (PSS and PAH) using the layer-by-layer technique. Cell viability tests showed that their nanotoxicity alternates with the particles surface charge and depends on the last coat of polyelectrolytes. Anionic nanoparticles as TiO₂NPs/PSS and TiO₂NPs/PSS/PAH/PSS showed much lower nanotoxicity than the cationic ones, TiO₂NPs/PSS/PAH and bare TiO₂NPs, respectively. This is explained by the poor adhesion of the anionic particles to the cell walls due to their electrostatic repulsion and the amplification of the particle-cell adhesion in the case of cationic TiO₂NPs. These results were checked by TEM images of sectioned microalgae and yeast cells. The results of this study can benefit the understanding the interaction mechanisms of surface modified TiO₂NPs/PSS with living cells and determine the factors which control their nanotoxicity.

Bibliography

1. L. K. Adams, D. Y. Lyon and P. J. Alvarez, *Water research*, 2006, **40**, 3527-3532.
2. K. Kasemets, A. Ivask, H.-C. Dubourguier and A. Kahru, *Toxicology in vitro*, 2009, **23**, 1116-1122.
3. K. Hund-Rinke and M. Simon, *Environmental Science and Pollution Research*, 2006, **13**, 225-232.

5 Chapter Five: Characterization and Functionalization of Formulated Nanocarriers: An Introduction

Recently, nanocarriers have been of great interest across the world due to their potential environmental and medical applications as for delivery systems for active components. In this chapter a polymer, Carbopol Aqua SF1 is used as a microgel for encapsulating two antimicrobial agents, berberine chloride and chlorhexidine digluconate. The unique chemical and physical features of the microgel were investigated, such as particle size distribution, zeta potential and swelling studies at the conditions of its loading with the antimicrobial agents. The factors affecting encapsulation in terms of microgel stability, drug and microgel concentration, the percentage of drug release and its encapsulation efficiency were optimized.

5.1 Particle Size and Zeta Potential of Carbopol Aqua SF1

Carbopol Aqua SF1 is a cloudy white aqueous suspension of a carboxyl groups functionalized cross-linked polyacrylic acid polymer¹ with dendrimers like structure² as shown in Figure 5.1 which represents a schematic for the cross linking network of Carbopol Aqua SF1 but it does not completely similar to carbopol microgel's structure. Aliquots of the suspended Carbopol Aqua SF1 solution were prepared from the stock solution and used to measure the particle size and zeta potential using the Malvern Zetasizer Nano ZS instrument at a refractive index of the collapsed microgel particles of 1.45 at room temperature. Figure 5.2 shows that the average particle diameter of Carbopol Aqua SF1 was found to be approximately 100 nm while the zeta potential is -44 mV which means that the Carbopol Aqua SF1 microgel particles have high stability³ when suspended in MilliQ water at pH 5.5 as shown in Figure 5.3.

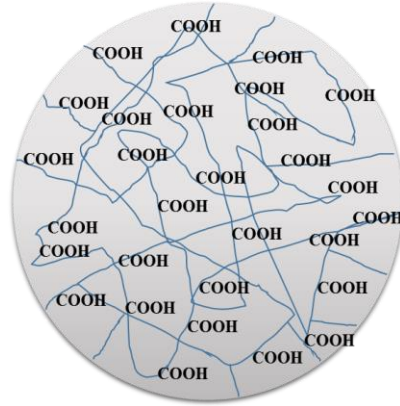


Figure 5.1: Proposed schematics of cross linked network of the Carbopol microgel particles in collapsed state (at low pH).

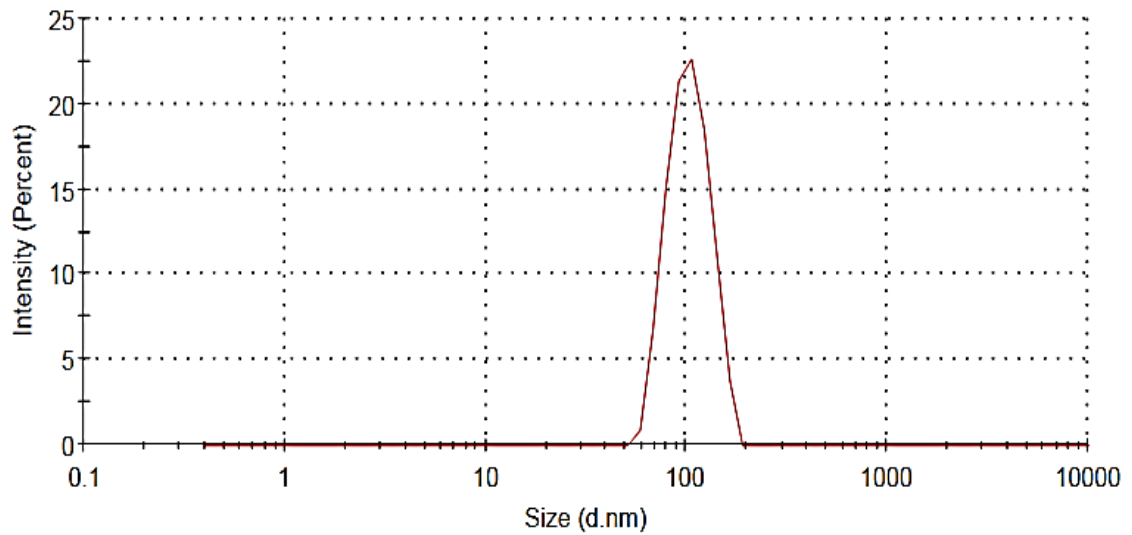


Figure 5.2: The average particle diameter of 0.05 wt% carbopol Aqua SF1 prepared from 30 wt% stock solution (as supplied by the manufacturer) at pH 5.

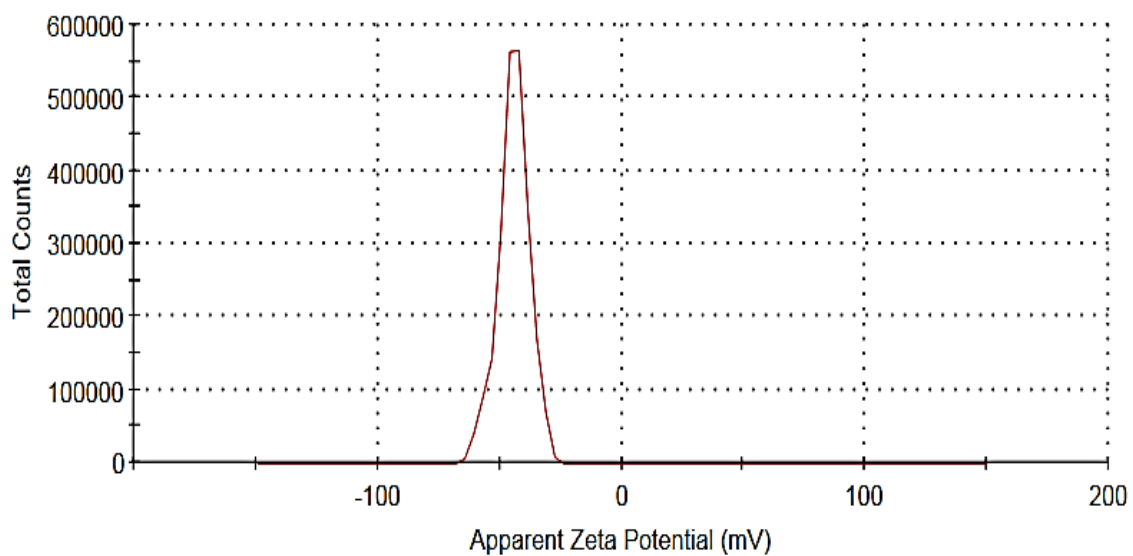


Figure 5.3: The zeta potential of 0.05 wt. % carbopol Aqua SF1 at pH 5.5 prepared from 30 wt. % stock solution (as supplied by the manufacturer).

Figure 5.4 show the TEM image of the dried up suspension of Carbopol Aqua SF1 microgel particles. It can be seen that it contains spherical particles of about $100 \text{ nm} \pm 20$. This is in agreement with the average particle diameter measured by the Zetasizer instrument.

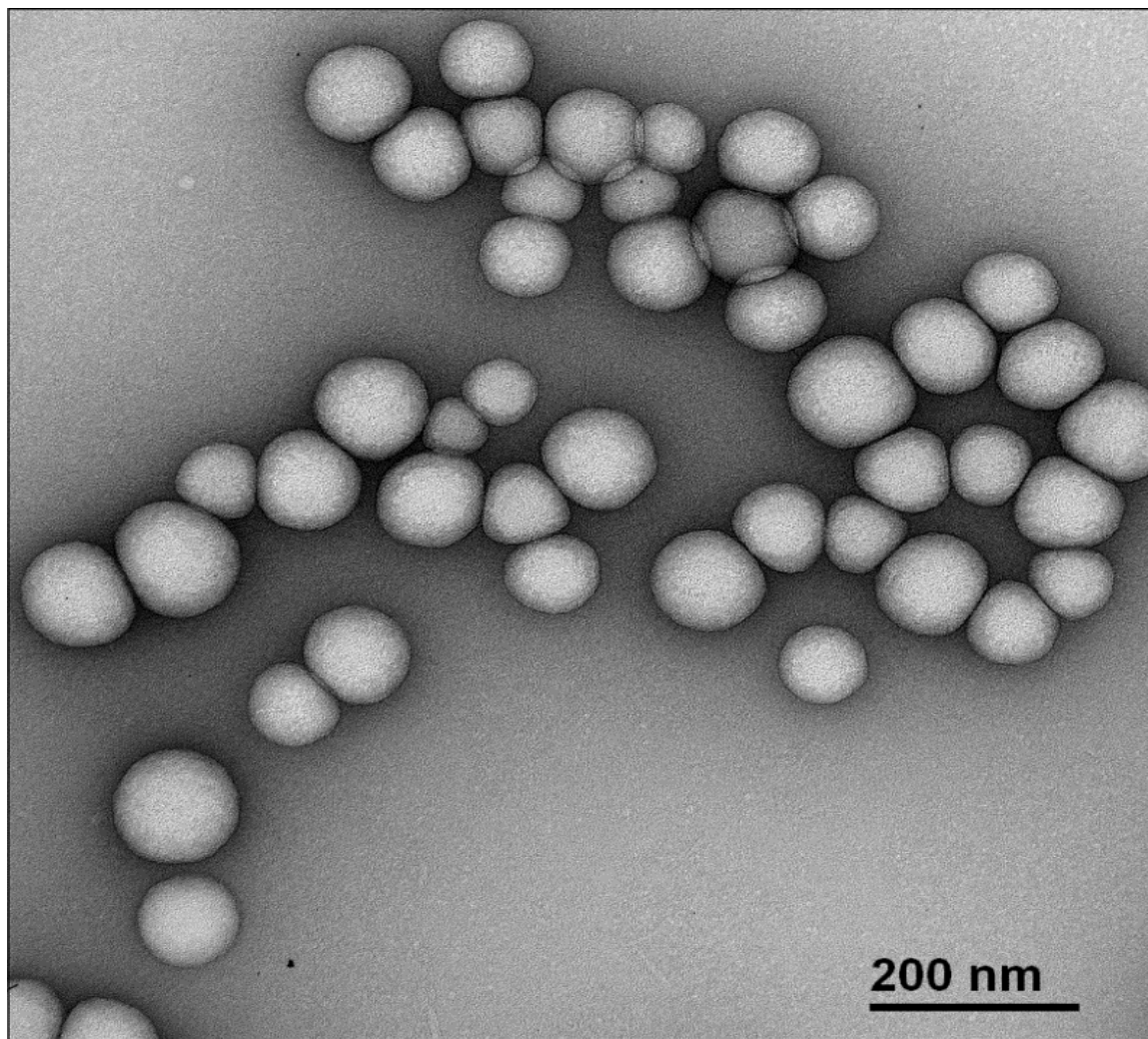


Figure 5.4: The TEM image of Carbopol Aqua SF1 particles after drying the suspension. The image was taken after pretreatment of carbopol sample with the TEM protocol for nanomaterials described in Chapter 2 to increase the imaging contrast.

5.2 Swelling Behavior of Carbopol Aqua SF1

Carbopol Aqua SF1 microgel are known to change their particle size by swelling, depending on the ionic strength and pH of the solution. To quantify this phenomenon aliquots of Carbopol Aqua SF1 were prepared and adjusted in a range of pH from 5 to 12 using small amounts of 0.25 M sodium hydroxide. The average particle diameters of the collapsed and swollen Carbopol Aqua SF1 microgels were determined using Malvern Mastersizer instrument at the refractive indexes of 1.453 and 1.336, respectively. The corrected particle size and refractive index of the swollen microgel particles were calculated by combining the data from the refractometer and the Mastersizer measurements as follows:

At low pH, where the microgel was collapsed, assuming that at this pH the micro gel is pure polyacrylic acid (PAA) then:

$$v_o = \frac{\pi}{6} d_o^3 \dots \dots \dots (1)$$

where

v_o : Volume of the collapsed Carbopol Aqua SF1 particles (at pH 5 for example)

d_o : Diameter of the shrunk Carbopol Aqua SF1 particles (at pH 5 for example)

At high pH the microgel is swollen with water and consequently in one particle of microgel there is both PAA and water. The volume of this particles is then:

$$v = \frac{\pi}{6} d^3 \dots \dots \dots (2)$$

where

v : Volume of swollen Carbopol Aqua SF1 particles at pH 8 for example

d : Diameter of swollen carbopol particles (at pH 8 for example)

Assuming ϕ_a is the volume fraction of PAA in the swollen micro-gel particle and ϕ_w is the volume fraction of water:

$$\phi_a = \frac{v_o}{v} = \left(\frac{d_o}{d}\right)^3 \quad \text{and} \quad \phi_w = 1 - \phi_a = 1 - \left(\frac{d_o}{d}\right)^3 \dots \dots \dots (3)$$

Furthermore if m_a is the mass of PAA in the swollen micro-gel particle, m_w is the mass of water in the swollen micro-gel particle; ρ_w and ρ_a are the mass densities of water and PAA, respectively.

$$m_a = v\phi_a\rho_a \dots \dots \dots (4)$$

$$m_w = v\phi_w\rho_w \dots \dots \dots (5)$$

Finally for the weight percentage of PAA w_a we can write:

$$w_a = \frac{m_a}{m_a + m_w} \times 100 \dots \dots \dots (6)$$

Then, by substituting Eqs (4) and (5) into Eq. (6), the weight percentage of PAA in the swollen micro-gel particle can be calculated to be: $w_a = \frac{100 v\phi_a\rho_a}{v\phi_a\rho_a + v\phi_w\rho_w} =$

$$\frac{100 \phi_a\rho_a}{\phi_a\rho_a + \phi_w\rho_w} \dots \dots \dots (7)$$

After that we substituted Eq. (3) (3) in Eq. (7) to obtain:

$$w_a = \frac{100 d_0^3\rho_a}{d_0^3(\rho_a - \rho_w) + \rho_w d^3} \dots \dots \dots (8)$$

The particle size of the collapsed Carbopol Aqua SF1 microgel particles is $d_0 = 100$ nm which can be obtained from Figure 2, and the mass densities of PAA and water can be taken from the literature^{4,5}, $\rho_w = 1$ g cm⁻³ and $\rho_a = 1.15$ g cm⁻³. The refractive index of the Carbopol Aqua SF1 suspension was measured using Abbey refractometer with 589 nm sodium line at room temperature. The experiment included measurement of the suspension refractive index at different concentrations of carbopol Aqua SF1 as shown in Figure 5. The linear regression equation for the calibration as shown in Figure 5.5 is:

$$n_s = n_w + \alpha w_a \dots \dots \dots (9)$$

Here $n_w = 1.3325$ is the refractive index of water at room temperature and $\alpha = 0.0012$ is the slope of the experimental data plot of the refractive index of the carbopol Aqua SF1 solution, n_s , versus the PAA weight fraction in the suspension, w_a (see Figure 5 for more details).

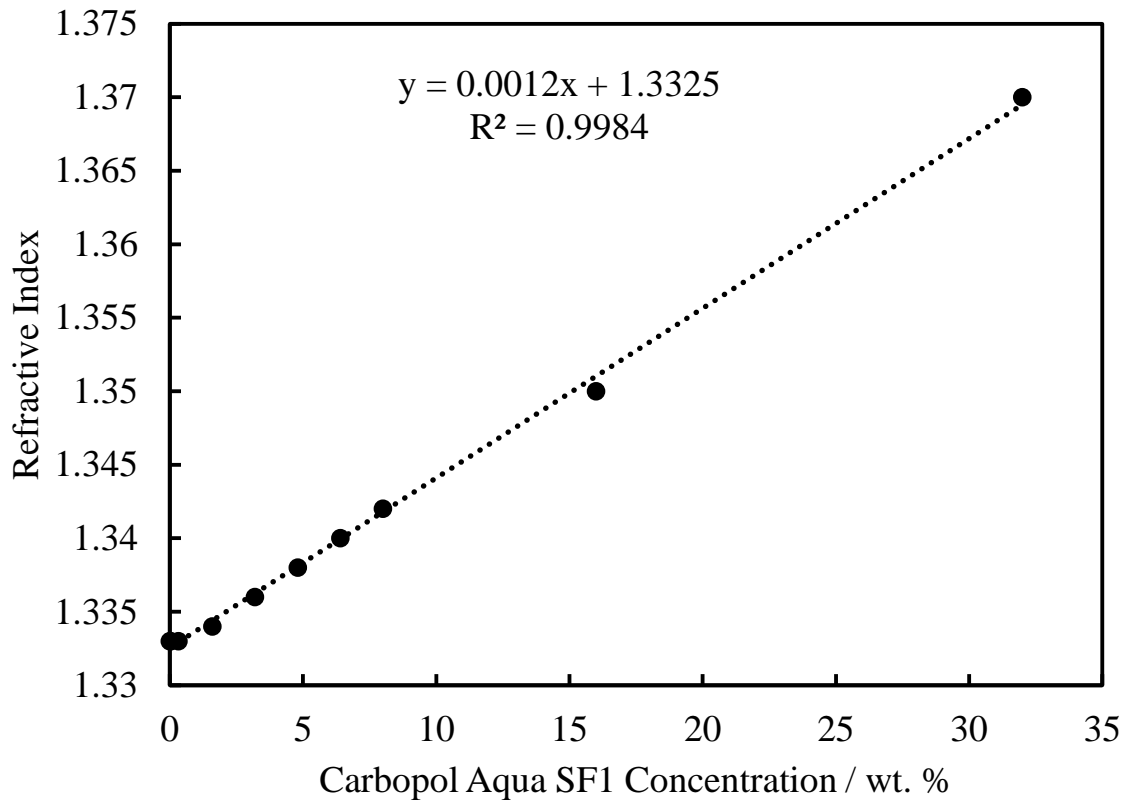


Figure 5.5: The variation of refractive index of Carbopol Aqua SF1 as a function of Carbopol Aqua SF1 concentrations at room temperature using Abbey Refractometer with sodium line at wavelength 589 nm.

Since the microgel particles swell upon changing the pH from 5 to 8 their particle refractive index also changes. Since the refractive index of the swollen microgel particle is unknown, this means that the particles diameter of the swollen microgel are unrealistic if estimated at fixed refractive index of PAA above pH 8. Therefore, the average particle diameter of a specific concentration of Carbopol Aqua SF1 microgel (0.3 wt. %) was determined as a

function of refractive index from Figure 5.6. The linear regression equation for the calibration was:

$$d = d_1 + \beta n_s \dots \dots \dots (10)$$

Where the model parameters $d_1 = 0.6415$ and $\beta = -0.2323$

Are determined by fitting the diameter of the particles versus the refractive index of the suspension.

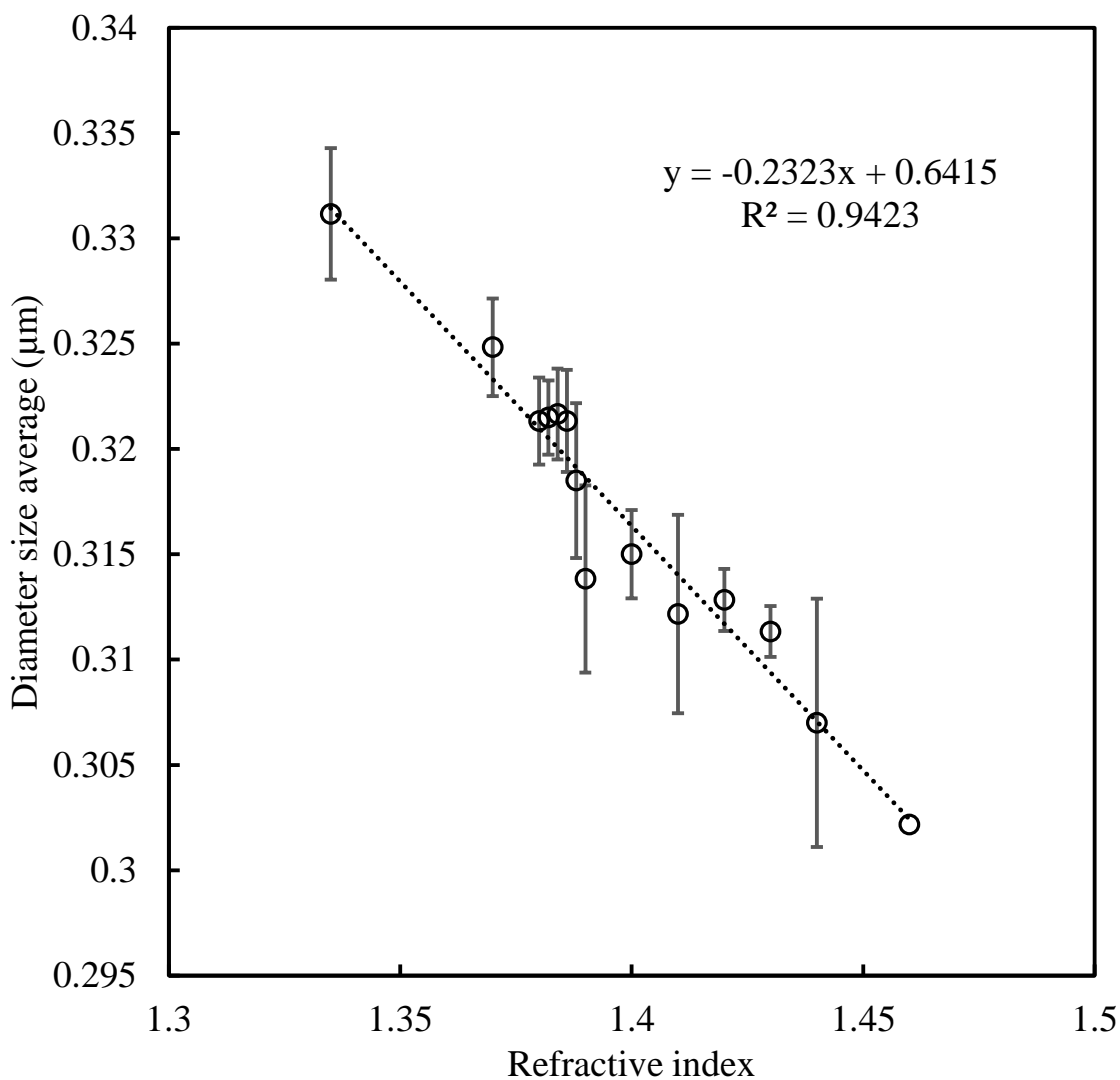


Figure 5.6: The average particle diameter (nm) of carbopol Aqua SF1 microgel as a function of the refractive index which was measured by Abbey Refractometer with 589 nm sodium line at room temperature. The measurement was conducted using 0.3 wt% of carbopol adjusted to pH 8 by adding small amount of 0.25 M sodium hydroxide.

To work out the real size of the swollen microgel particles at pH 8, the particles refractive index (n_p) can be approximated as the dispersion refractive index (n_s) so that the weight fraction of PAA can be calculated.

$$n_p = n_s$$

Hence, equation (9) become,

$$n_p = n_w + \alpha w_a = n_w + \alpha \frac{100 \phi_a \rho_a}{\phi_a (\rho_a - \rho_w) + \rho_w} \dots \dots \dots (11)$$

By substituting equation (11) in equation (10), we obtained

$$d = d_1 + \beta \left(n_w + \alpha \frac{100 \phi_a \rho_a}{\phi_a (\rho_a - \rho_w) + \rho_w} \right) \dots \dots \dots (12)$$

$$\frac{d}{d_0} = \frac{d_1 + \beta \left(n_w + \alpha \frac{100 \phi_a \rho_a}{\phi_a (\rho_a - \rho_w) + \rho_w} \right)}{d_0} \dots \dots \dots (13)$$

From equation (3), we obtain $\phi_a = \left(\frac{d_0}{d}\right)^3$, so $\frac{d}{d_0} = \frac{1}{\phi_a^{1/3}}$

By combining the previous equation with Eq. (13),

$$\frac{1}{\phi_a^{1/3}} = \frac{d_1}{d_0} + \frac{\beta}{d_0} \left(n_w + \alpha \frac{100 \phi_a \rho_a}{\phi_a (\rho_a - \rho_w) + \rho_w} \right) \dots \dots \dots (14)$$

Hence we finally obtain:

$$\phi_a = 0.02592$$

$$d = \frac{d_0}{\phi_a^{1/3}} = \frac{0.1}{\sqrt[3]{0.02592}} = 0.334 \mu m$$

The weight fraction of PAA inside the swollen microgel particles (w_a) is therefore 2.592 % while the rest is water. In addition of that, the refractive index of swollen microgel particles (n_p) is 1.336.

In the above calculations, it was used two different refractive indexes due to the fact that as the Carbopol Aqua SF1 microgel swells, the refractive index changes as the pH increases from 5 to 8. It is therefore important to notice that at low pH (below approximately 7), the microgel particles were collapsed and their refractive index used was 1.453. When the pH increases Carbopol Aqua SF1 dispersion starts to form a gel, the solution became clear and the refractive index changes. In this case the refractive index used in Mastersizer was 1.336. It also seems that in the collapsed form, the Carbopol Aqua SF1 particle contains protonated carboxylic groups and remains collapsed up to pH 7 without any noticeable change. Whereas, as the pH increased above 7, particles swelled leading to the increase in the particle size. The swelling behavior occurred because of the deprotonation of Carbopol Aqua SF1 particles which led to electrostatic repulsion between the dissociated carboxylic groups on the PAA chains. This leads to the partial swelling in the microgel particles and the absorption of enormous amounts of aqueous phase from the surrounding solution. At high microgel concentration at pH higher than 7, this leads to the formation of a highly viscous colorless gel due to the solution being effectively filled in with swollen microgel particles as schematically illustrated in Figure 5.7. This can clearly be seen in in Figure 5.8 where from pH 5 up to pH 7, the average particle diameter is approximately constant at 100 nm. However, as the pH increases, the carbopol starts converting to the colorless gel and the average particle size very steeply increases to more than 300 nm. This behavior of the Carbopol Aqua SF1 microgel is comparable to the other pH responsive hydrogels reported in the literature.⁶

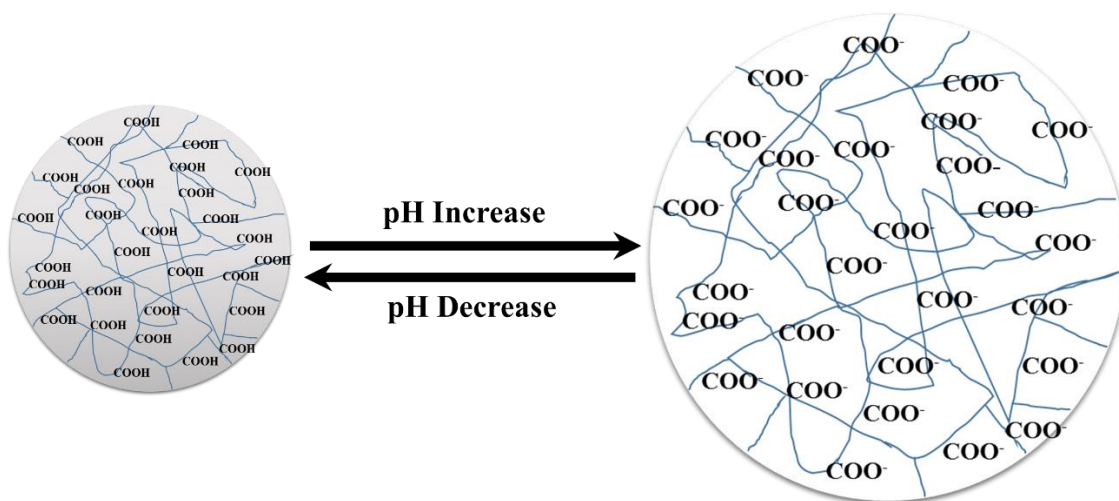


Figure 5.7: Schematic for the swelling/deswelling behavior of carbopol Aqua SF1 in case of increase and decrease of pH of the surrounding solution, respectively.

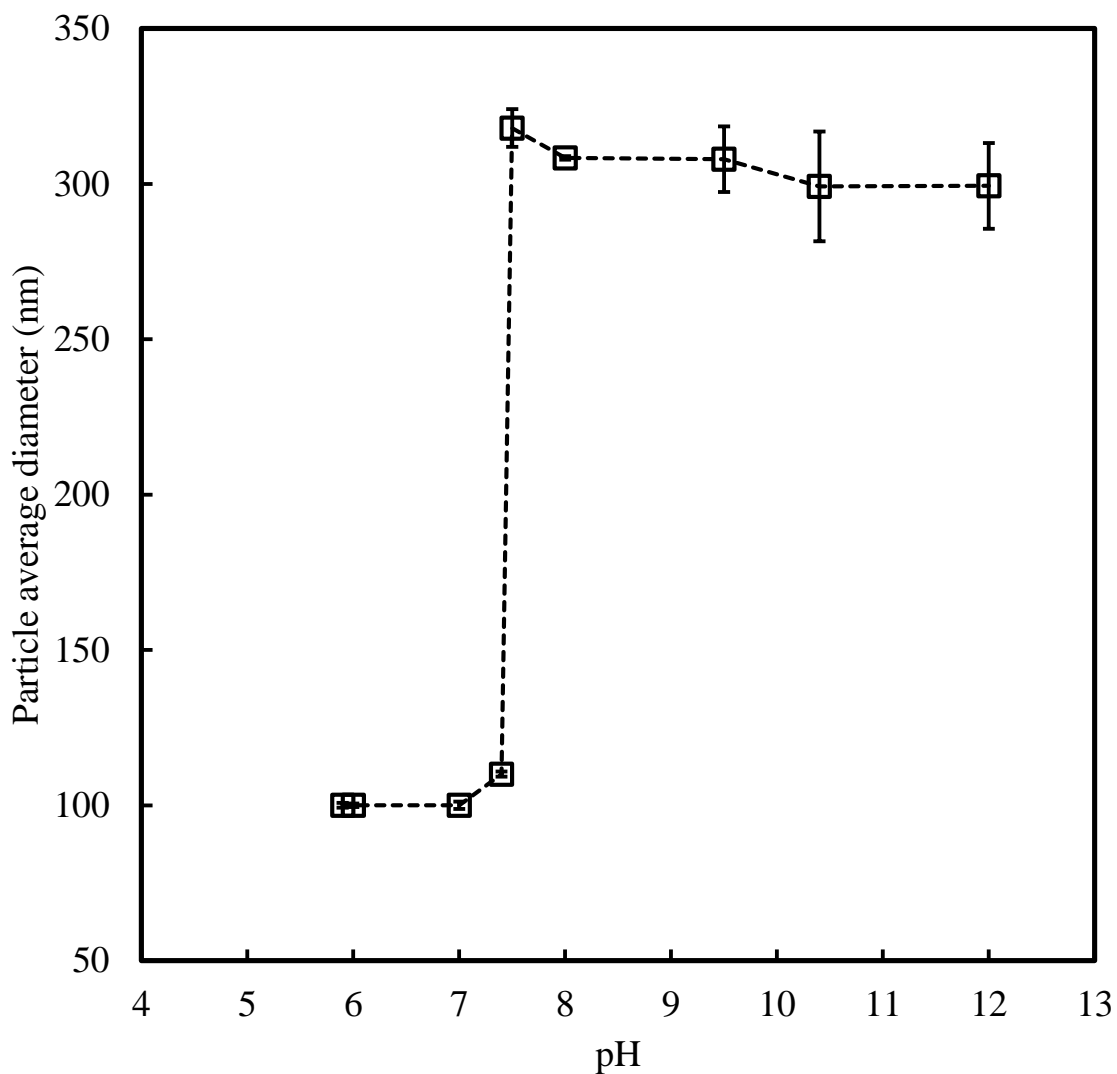


Figure 5.8: The average particle diameter of Carbopol Aqua SF1 as a function of pH. The size is calculated using variable refractive index of the particles in the Malvern Mastersizer, one is at the collapsed carbopol microgel which is 1.453 while the refractive index is 1.336 in case of fully swollen carbopol at pH 8. Aliquot of 0.25 M sodium hydroxide was used to adjust the pH. Each reading was repeated six times.

The swelling / deswelling feature of the Carbopol microgel can be beneficially exploited for the purposes of development of drug delivery systems. This microgel was therefore used to encapsulate antimicrobial agents like berberine chloride and chlorhexidine digluconate with the aim of sustained delivery and slow release of these agent to microbial cells.

5.3 Encapsulation of Berberine into Carbopol Aqua SF1 microgel

To encapsulate berberine, the pH of the Carbopol Aqua SF1 microgel was adjusted from pH 5 to pH 8 to produce the swollen anionic Carbopol Aqua SF1 microgel with a larger particle size. The swollen microgel was then mixed with known aliquots of cationic berberine to form a berberine loaded swollen Carbopol Aqua SF1 complex. The pH of the solution was then decreased to pH 5.5 to collapse the microgel so that the berberine gets encapsulated inside. The schematics shown in Figure 5.9 which explains the encapsulation of berberine into Carbopol Aqua SF1.

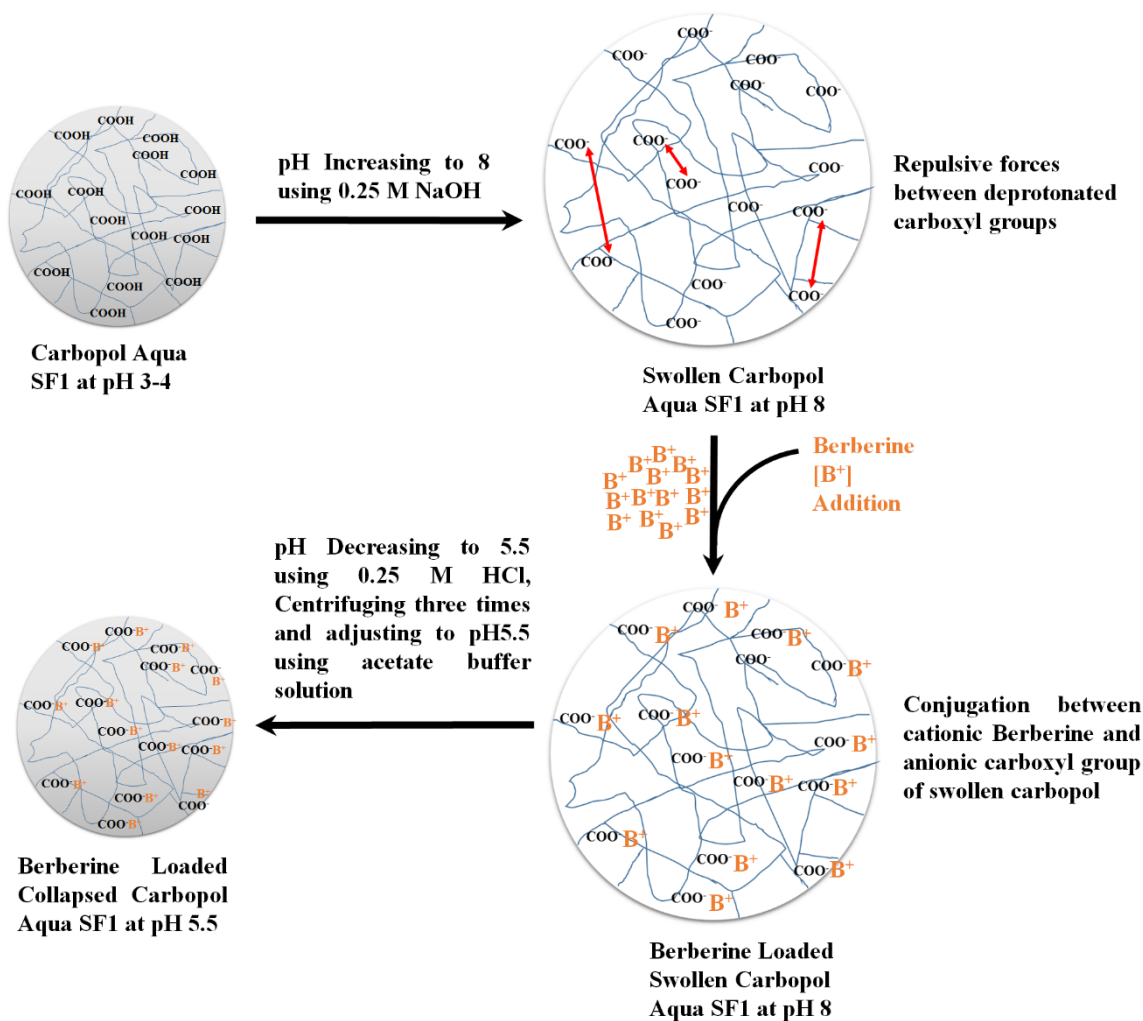


Figure 5.9: The schematic diagram for the encapsulation of Berberine into carbopol Aqua SF1 depending on the swelling and deswelling behavior of the microgel in the basic and acidic medium, respectively.

The interaction between the microgel and berberine are based on electrostatic conjugation with non-covalent bonding to ensure releasing the antimicrobial agent upon incubation of the loaded microgel particles with tested microorganisms. The berberine-loaded Carbopol Aqua SF1 (BLC) suspension was centrifuged three times to remove of the excess berberine which had not been encapsulated and in the last centrifugation step the suspension was adjusted to pH 5.5 with acetate buffer solution (pH 5.5). The benefit behind the addition of acetate buffer solution is to adjust pH to be 5.5 and to ensure the pH is fixed upon incubation with microorganisms. Figure 5.10 shows optical images of the samples of the Carbopol Aqua SF1, berberine, berberine-loaded swollen Carbopol Aqua SF1 at pH 8 and berberine loaded Carbopol Aqua SF1 at pH 5.5.

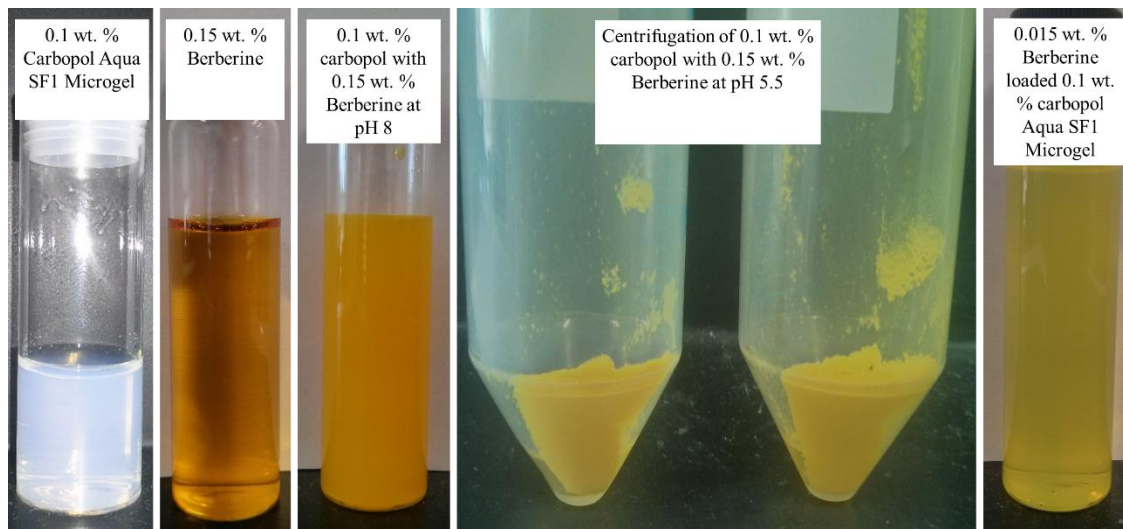


Figure 5.10: Digital photographs of the samples of bare Carbopol Aqua SF1, berberine, berberine-loaded Carbopol Aqua SF1 at pH 8 and berberine-loaded Carbopol Aqua SF1 at pH 5.5.

5.4 Characterization of Berberine-Loaded Carbopol Aqua SF1

5.4.1 Effect of Carbopol Concentration on Berberine Encapsulation

Solutions of different concentrations of berberine were mixed with a dispersion of fixed concentration of Carbopol Aqua SF1, then stirred and its pH was decreased to 5.5, centrifuged and re-dispersed in Milli-Q water. The pH was then increased to pH 8, stirred overnight and then decreased to pH 5.5 with acetate buffer solution. The average particle diameter was measured for the berberine loaded Carbopol Aqua SF1 suspension at a refractive index for Carbopol Aqua SF1 of 1.456 at room temperature. Figure 5.11 shows the effect of the Carbopol Aqua SF1 concentration on the microgel particle size of the berberine-loaded Carbopol Aqua SF1 particles. It can be seen that at 0.10 wt% Carbopol Aqua SF1 the particle size remains low whereas at 0.05 wt% Carbopol Aqua SF1 the particle size increases due to aggregation at high concentrations of berberine.

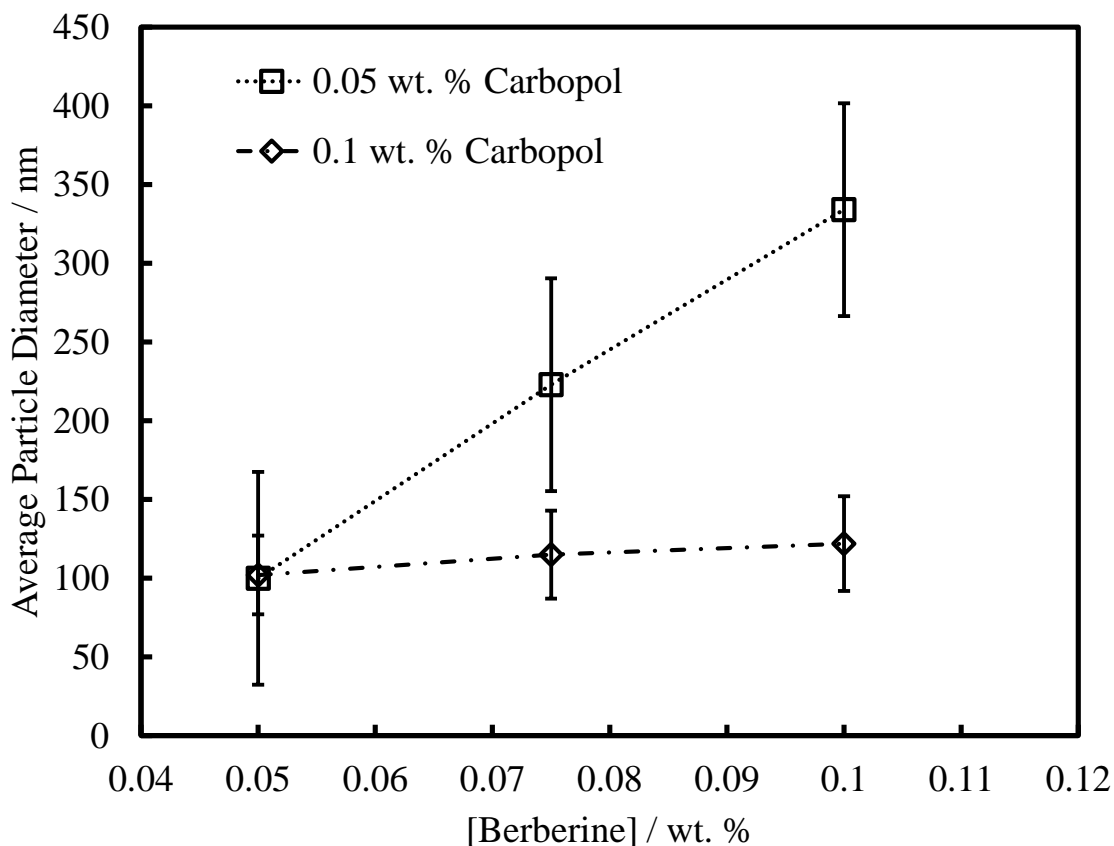


Figure 5.11: Average particle diameter of Carbopol concentrations upon encapsulation of different amounts of berberine.

5.4.2 Effect of the Berberine Concentration on the Carbopol Stability

The effect of the berberine concentration on the colloidal stability of Carbopol Aqua SF1 upon encapsulation of berberine into the Carbopol Aqua SF1 was then studied. Figure 5.12 shows the average microgel particle diameter (purple Line) and their zeta potential (black line) of Carbopol Aqua SF1 as a function of berberine concentration. Please note that the term zeta-potential of a microgel particle is not precisely defined due to the “soft” character of the microgel particle when swollen with the surrounding media. Thus, at pH above 7 the position of the plane of shear is not well defined as the particles can deform as they move electrophoretically and values of the zeta-potential are for indicative purposes only. However, at pH below 7 the microgel particles (including the ones loaded with Berberine) can be treated as solid particles with well-defined zeta potential and plane of shear. As the berberine concentration increases it can be seen that the average particle diameter also increases. Up to 0.15 wt% of berberine, the average particle diameter of Carbopol Aqua SF1 gradually increases but from 0.15 wt% to 0.2 wt%, no change in the particle size was noticed whereby the particle size is around 133 nm. We were not able to increase further the berberine solution concentration due to reaching its solubility limit. It can also be seen in figure 5.4 that zeta potential of Carbopol Aqua SF1 decreases slightly as the berberine concentration rises. At very low concentration of berberine, the zeta potential of Carbopol Aqua SF1 is negative, -44 mV, which means high electrostatic stability of the colloid while it also stays stable at high concentration of berberine where the zeta potential of the microgel at 0.2 wt % is -40 ± 5 mV.

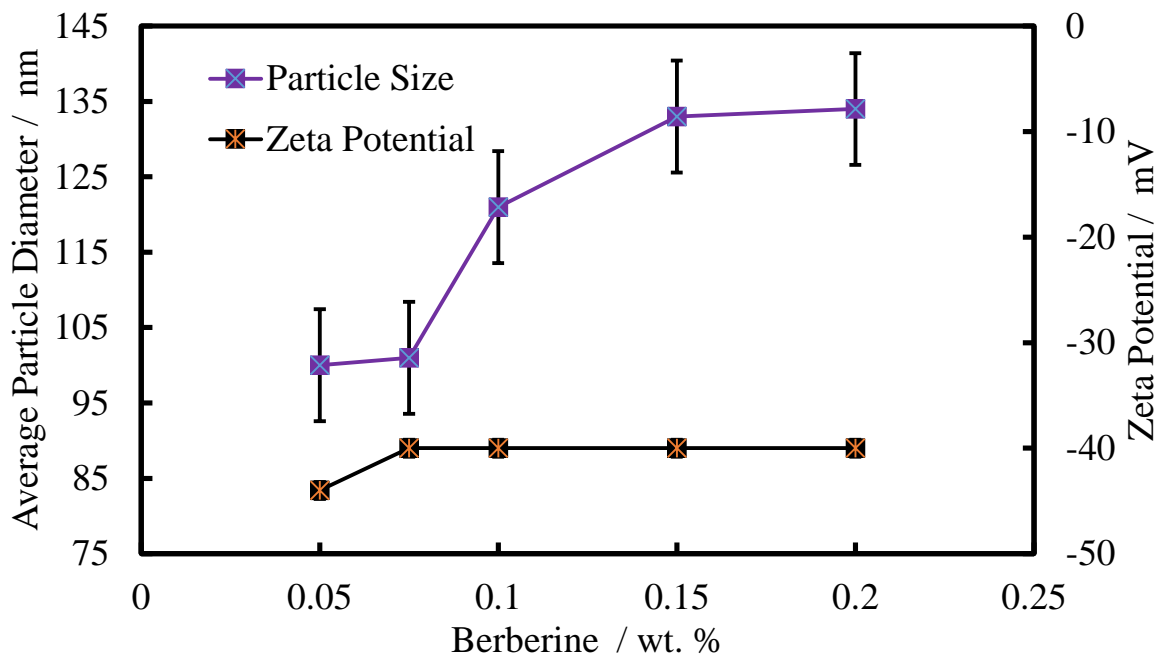


Figure 5.12: The average particle diameter and the zeta potential of Carbopol aqua SF1 as a function of berberine concentrations at pH 5.5 using 0.1 wt% Carbopol Aqua SF1, acetate buffer solution (pH 5.5) and each solution was sonicated for 5 minutes to facilitate its dispersing.

5.4.3 Determination of the Berberine-Loaded Carbopol Microgel Particle Size

The value of average particle diameter of berberine-loaded Carbopol Aqua SF1 was determined using the Malvern Zetasizer instrument and was found to be about 135 nm at pH 5.5 which corresponds to about 35% increase in particle size in comparison with bare carbopol (see figure 2) as shown in figure 5.13. Figure 5.14 shows the zeta potential for the berberine-loaded Carbopol Aqua SF1 suspension and it can be seen that it was -40 mV. This high zeta potential of the berberine-loaded microgel indicates that only a small fraction of COOH-groups on the microgel matrix are bond to the loaded berberine and the COOH groups on the microgel surface can dissociate almost to the same extent as bare carbopol which ensures that the loaded carbopol suspension had high enough colloidal stability due to electrostatic stabilization. The TEM image shown in Figure 5.15 shows that the berberine-loaded Carbopol Aqua SF1 particles which have spherical morphology, although they are slightly larger than these of bare carbopol. The particle size on the image agrees with the results from Malvern Zetasizer (Figure 5.13).

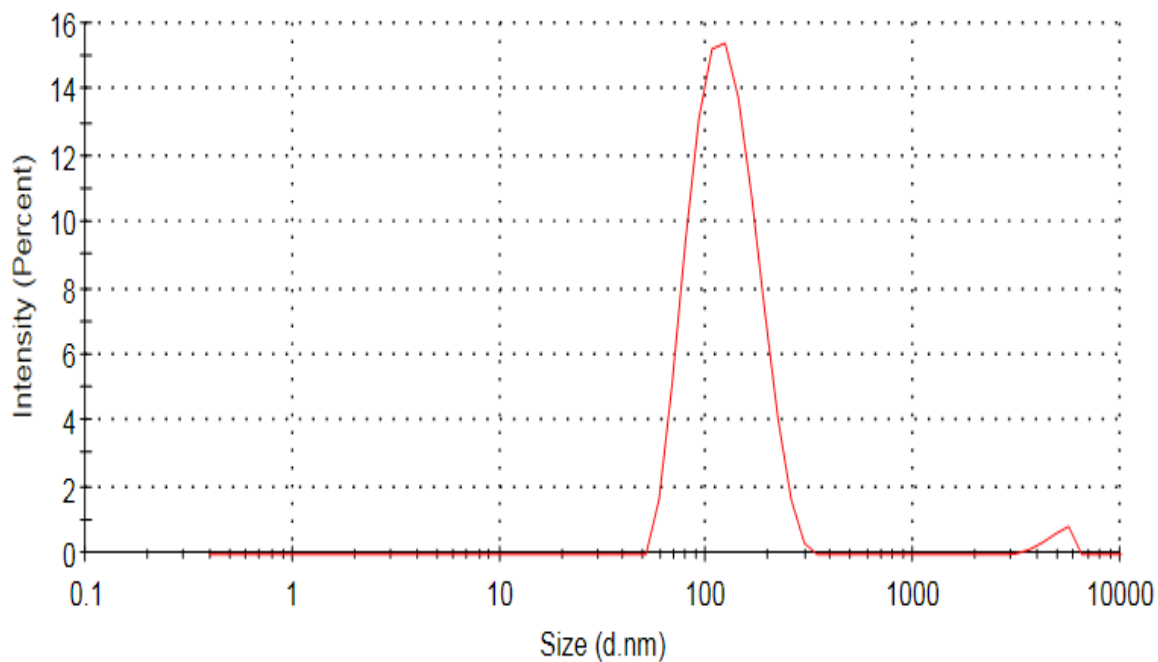


Figure 5.13: The Average particle diameter of 0.015 wt.% berberine loaded Carbopol Aqua SF1 at pH 5.5 produced from addition of aliquot of berberine solution to 0.1 wt% of Carbopol Aqua SF1 Microgel at pH 8 followed by decrease of the pH to 5.5 to form berberine-loaded collapsed Carbopol Aqua SF1. The final suspension was adjusted with acetate buffer solution supporting pH 5.5.

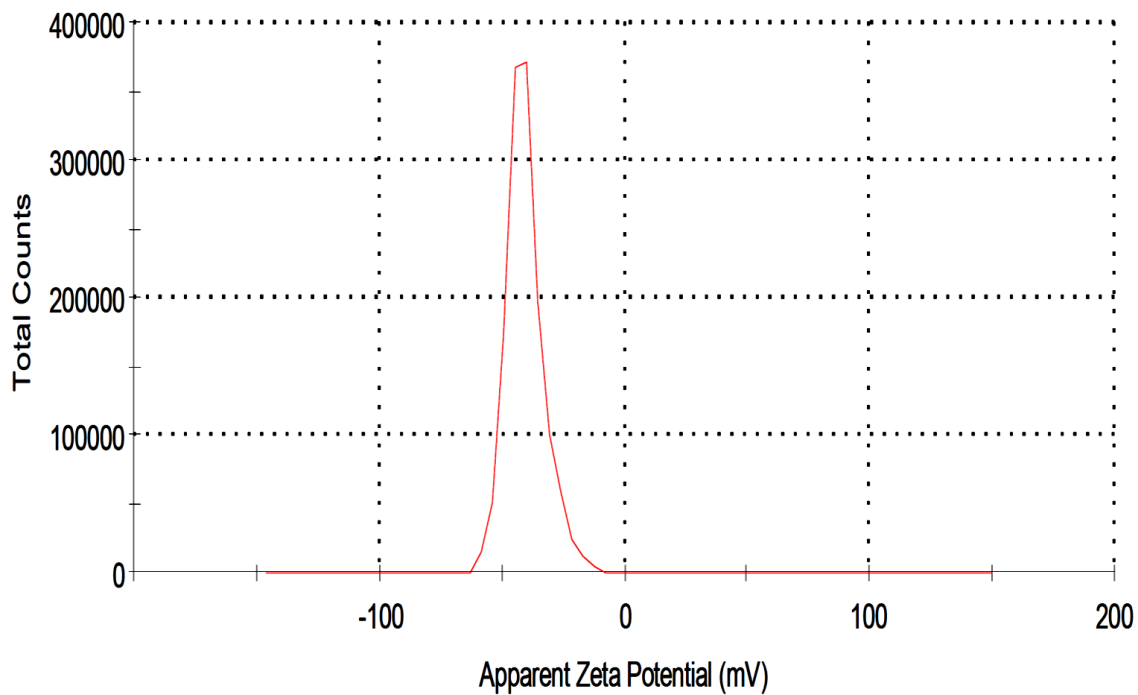


Figure 5.14: Zeta potential of 0.015 wt.% berberine-loaded Carbopol Aqua SF1 at pH 5.5 acetate buffer solution which was measured by Malvern Zetasizer Nano ZS machine with dip cell immersed in plastic cuvette.

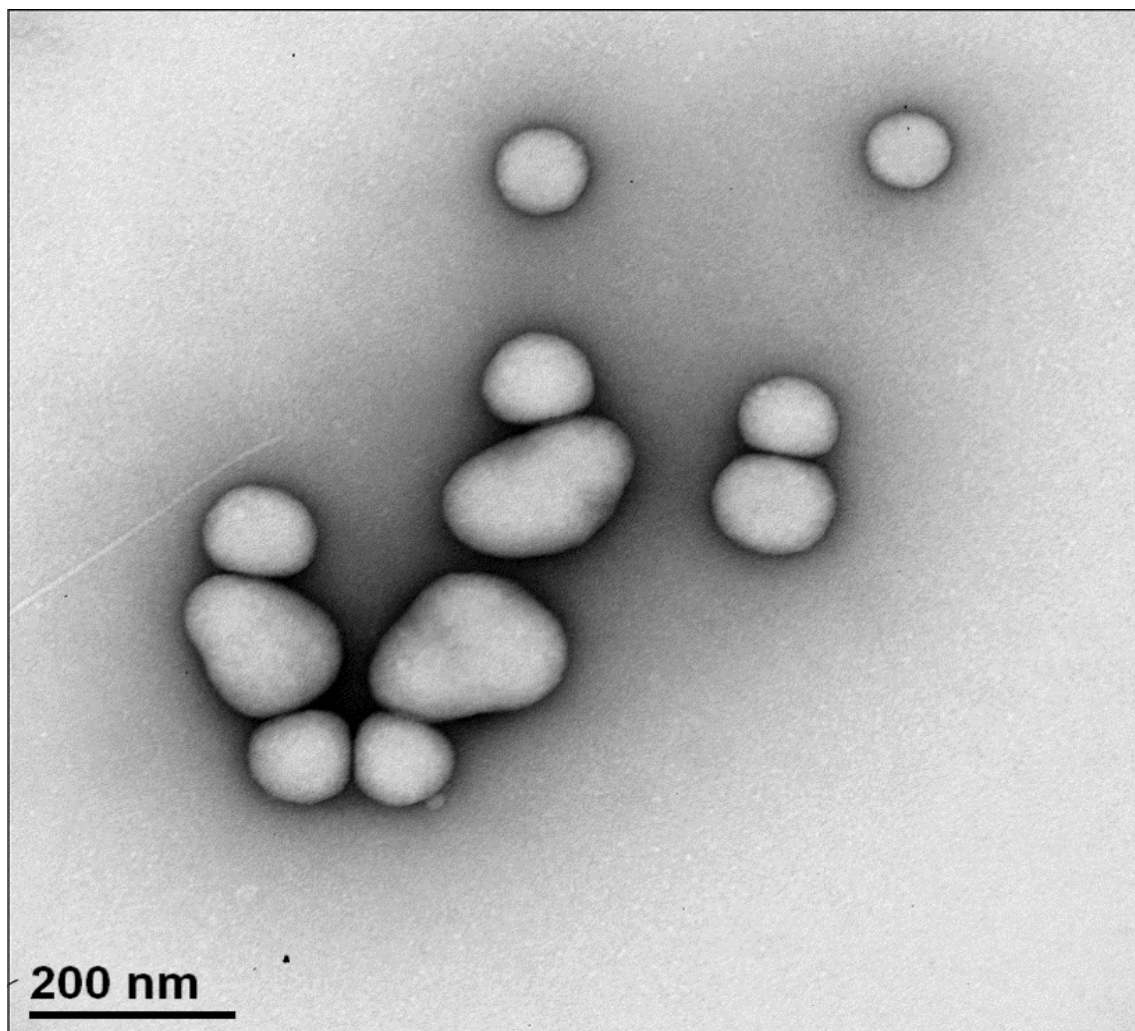


Figure 5.15: TEM image of berberine-loaded collapsed Carbopol Aqua SF1 at pH 5.5 adjusted with acetate buffer solution. The encapsulation was conducted through adjusting the microgel at pH 8, then berberine was added to produce the swollen Carbopol Aqua SF1 microgel. The produced suspension was adjusted to pH 5.5 to form berberine-loaded Carbopol Aqua SF1 microgel.

5.4.4 UV-Visible Spectrophotometry of Berberine-Loaded Carbopol

Carbopol, berberine, and berberine-loaded Carbopol Aqua SF1 were characterized by UV-vis spectrometry to examine the encapsulation of Berberine into Carbopol Aqua SF1 after all the excess berberine had been removed by the centrifugation/washing process which was carried out three times. The UV-visible spectrum of Carbopol Aqua SF1, berberine and berberine-loaded Carbopol Aqua SF1 is given in Figure 5.16. The Carbopol (blue line) absorbed in the UV region around 200 nm with no significant wavelength. The berberine (orange line) however had four absorption peaks, one which was in the visible area with a wavelength around 420 nm and three peaks in the UV region with wavelengths 350 nm, 265 nm and 230 nm respectively. It can be seen that there is no spectral interference between the absorbance of Carbopol Aqua SF1 and berberine. The black line shows the absorbance spectrum for the berberine-loaded Carbopol Aqua SF1 and the spectra for berberine can be clearly seen which showed four peaks similar to those of Berberine. As the all the excess berberine had been removed by the centrifugation process, this provides clear evidence that the cationic berberine is conjugated with the anionic carboxyl group of the Carbopol microgel.

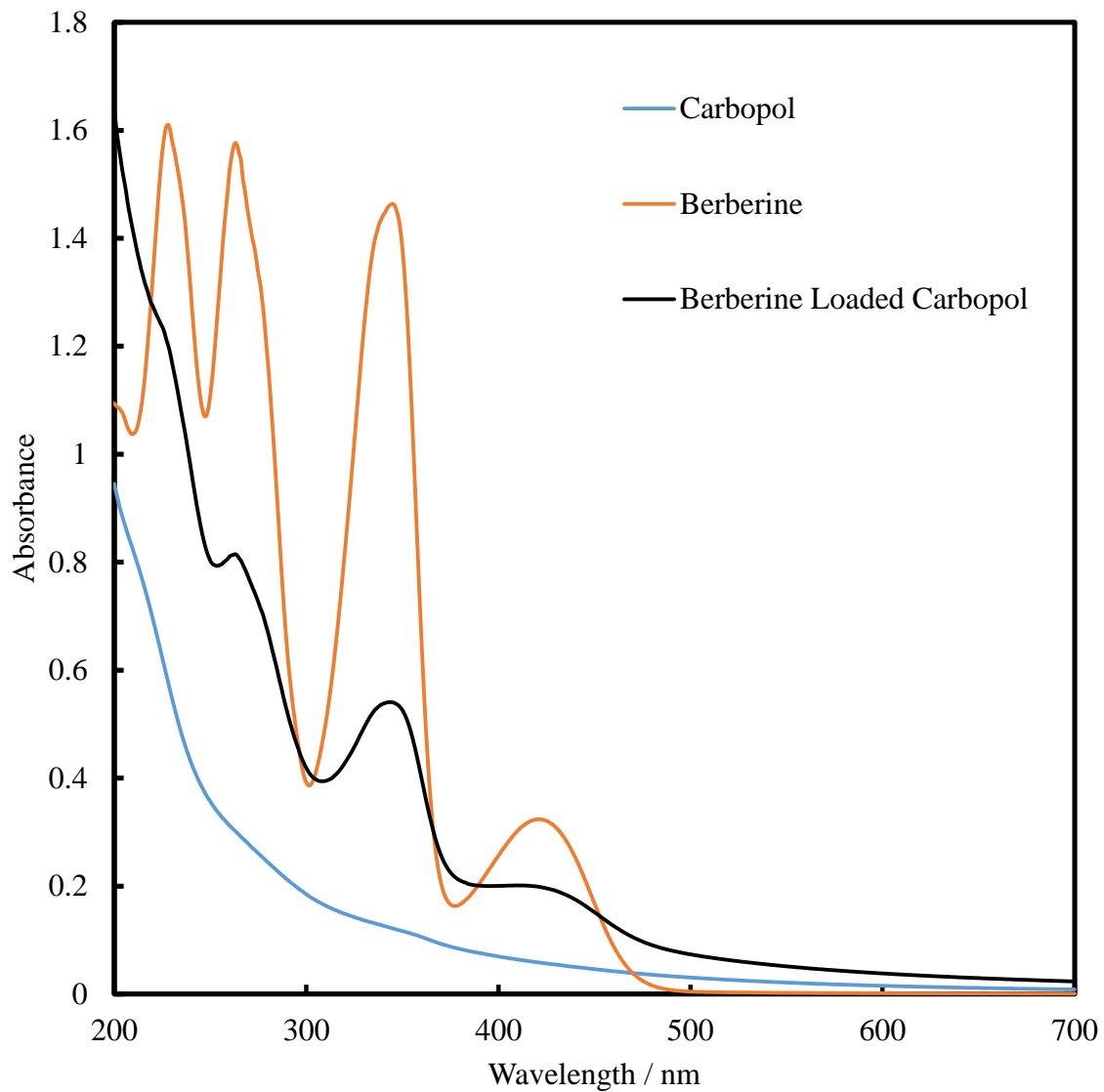


Figure 5.16: The UV-Visible spectrum of 0.01 wt. % carbopol (Blue line), 0.025 wt. % Berberine (Orange line) and berberine-loaded carbopol (Black line). All solutions were adjusted to pH 5.5 using acetate buffer solution. Perkin Elmer Lambda 25 UV-Visible spectrophotometer was utilized to measure the spectrum in the wavelength range from 200 nm to 700 nm.

5.4.5 FTIR Spectrometry of Berberine Loaded Carbopol

Fourier Transform Infra-Red spectroscopy (FTIR) was used to further explore the composition of the loaded carbopol particles. Spectra were obtained for the Carbopol microgel, berberine and berberine-loaded Carbopol microgel in the frequency range from 400 cm^{-1} to 4000 cm^{-1} . In the FTIR spectra of Carbopol microgel as shown in Figure 5.17 A, a characteristic peak was seen in the range $3300\text{--}3500\text{ cm}^{-1}$ due to the stretching vibrations of O-H and intermolecular hydrogen bonding. The strong peak between 2850 and 3000 cm^{-1} was due to the stretching vibration band of the aliphatic C-H bond. The spectra also presented a peak in the range $1670\text{--}1750\text{ cm}^{-1}$ which appointed to a strong vibration band of carbonyl stretching (C=O) while the two variable peaks at $1400\text{--}1490\text{ cm}^{-1}$ were assigned to the stretching vibration band of the carbonyl bond (C-O). The peak appearing from 1000 cm^{-1} to 1300 cm^{-1} was attributed to the coupling between in-plane OH bending and C-O stretching of neighboring carboxyl groups. These explanations of FTIR spectrum of Carbopol Aqua SF1 are in line with the literature^{7, 8}.

For berberine, it can be seen in the figure 5.17B that two weak peaks were noticeable at 2946 cm^{-1} and 2846 cm^{-1} which are assigned to the stretching vibration of the aliphatic C-H group. It was also observed significant bands of berberine at 1636 cm^{-1} , 1602 cm^{-1} and 1505 cm^{-1} and these bands are belonging to heterocyclic amine (C-N), quaternary iminium ion (-C=N-) and the stretching vibration of C=C in the aromatic ring, respectively. However, a peak at 1105 cm^{-1} was prominent which was attributed to the deformation of aromatic ring and the bending vibration in C-H in-plane. In addition of that, the stretching vibration of C-H was presented at 1037 cm^{-1} . The FTIR results of berberine are in line with the literature⁹⁻¹¹

The FTIR spectrum of berberine-loaded Carbopol Aqua SF1 are shown in Figure 5.17C which illustrated some characteristic bands for the encapsulation of berberine into Carbopol Aqua SF1. A broad vibration band at 3460 cm^{-1} was referred to stretching of the O-H bond which was also noticed with the FTIR of Carbopol. Furthermore, it was perceived that a peak at 1700 cm^{-1} is related to the stretching vibration band of carbonyl group (C=O) of the Carbopol (PAA) while another two distinctive peaks were prominent in the berberine-loaded Carbopol at 1653 cm^{-1} and 1600 cm^{-1} for the stretching vibration of C-N and -C=N- bands. These bands were also noticed in the berberine only. Finally, a

significant peak at 1500 cm^{-1} was noted that represents the stretching vibration band of C=C for the aromatic ring.

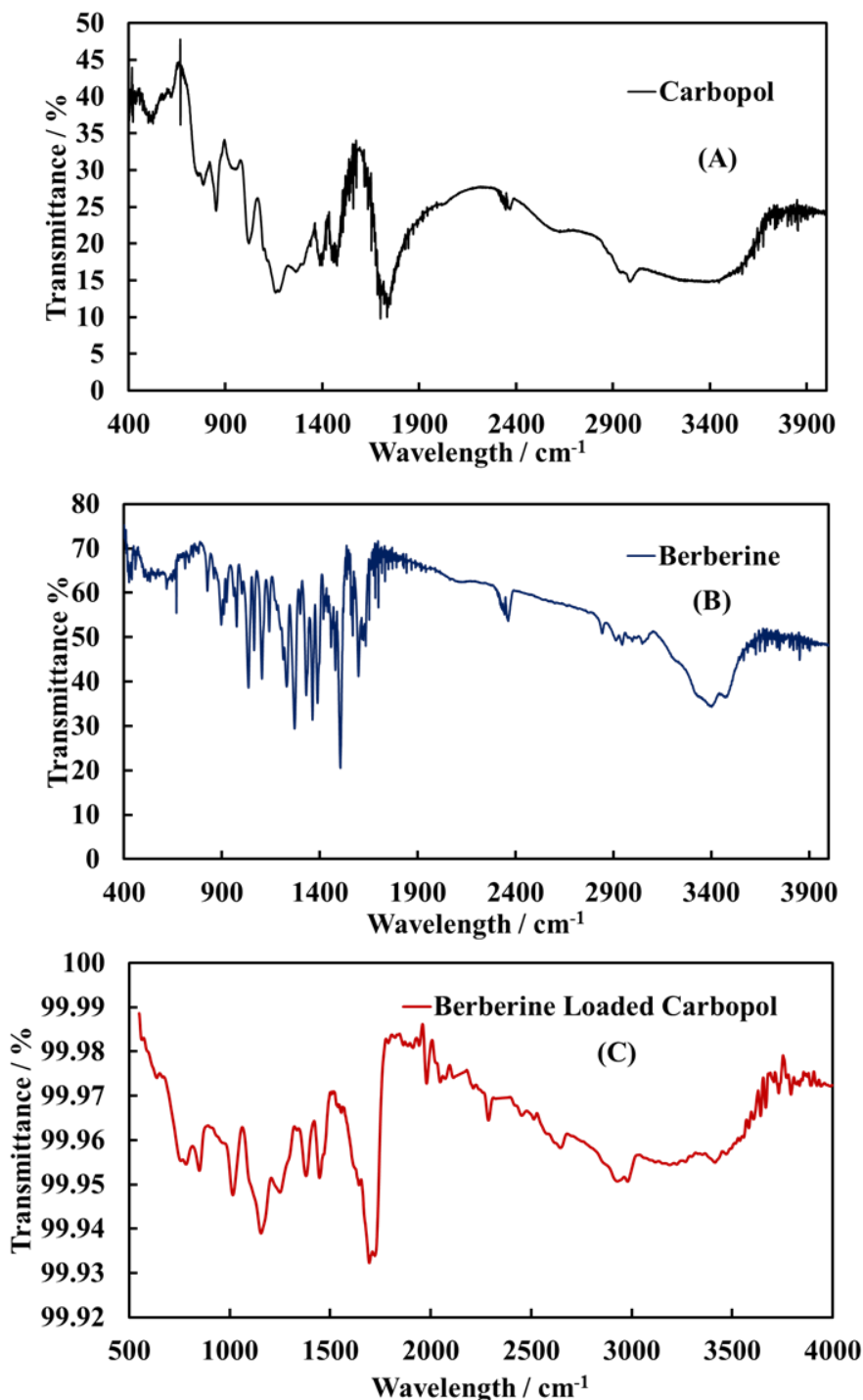


Figure 5.17: The FTIR spectrum of Carbopol Aqua SF1 (A), berberine (B) and berberine-loaded Carbopol Aqua SF1 (C). Each sample was dried in the over overnight and mixed with excess amount of dried KBr pellets to make KBr disk. The samples then scanned with Perkin Elmer FT-IR spectrometer in the range of wavelength from 400 cm^{-1} to 4000 cm^{-1}

5.4.6 Thermogravimetric Analysis of Berberine Loaded Carbopol

The thermal gravimetric analysis was used to study the physical structures of berberine, Carbopol and berberine-loaded Carbopol microgel. The thermal gravimetric analysis can be seen in Figure 5.18 along with the 1st derivative curve (DTA). The materials were heated from 100 °C to 900 °C at 10 °C/minute in air atmosphere with a purge rate of 10 mL/minute. Carbopol (C) (blue curve) lost weight at 400°C which relates to the thermal decomposition of hydrocarbon compounds, no changes were seen over 550°C. The berberine component in Figure 5.18 (black curve) gave an endothermic peak at 150 °C which was attributed to loss of water. After that, upon increasing the temperature little change was seen up to 700°C. The thermal behavior of the berberine loaded carbopol was different to that for the individual compounds (red Curve) The TGA curve showed weight loss at 300 °C, 350 °C and 450 °C.

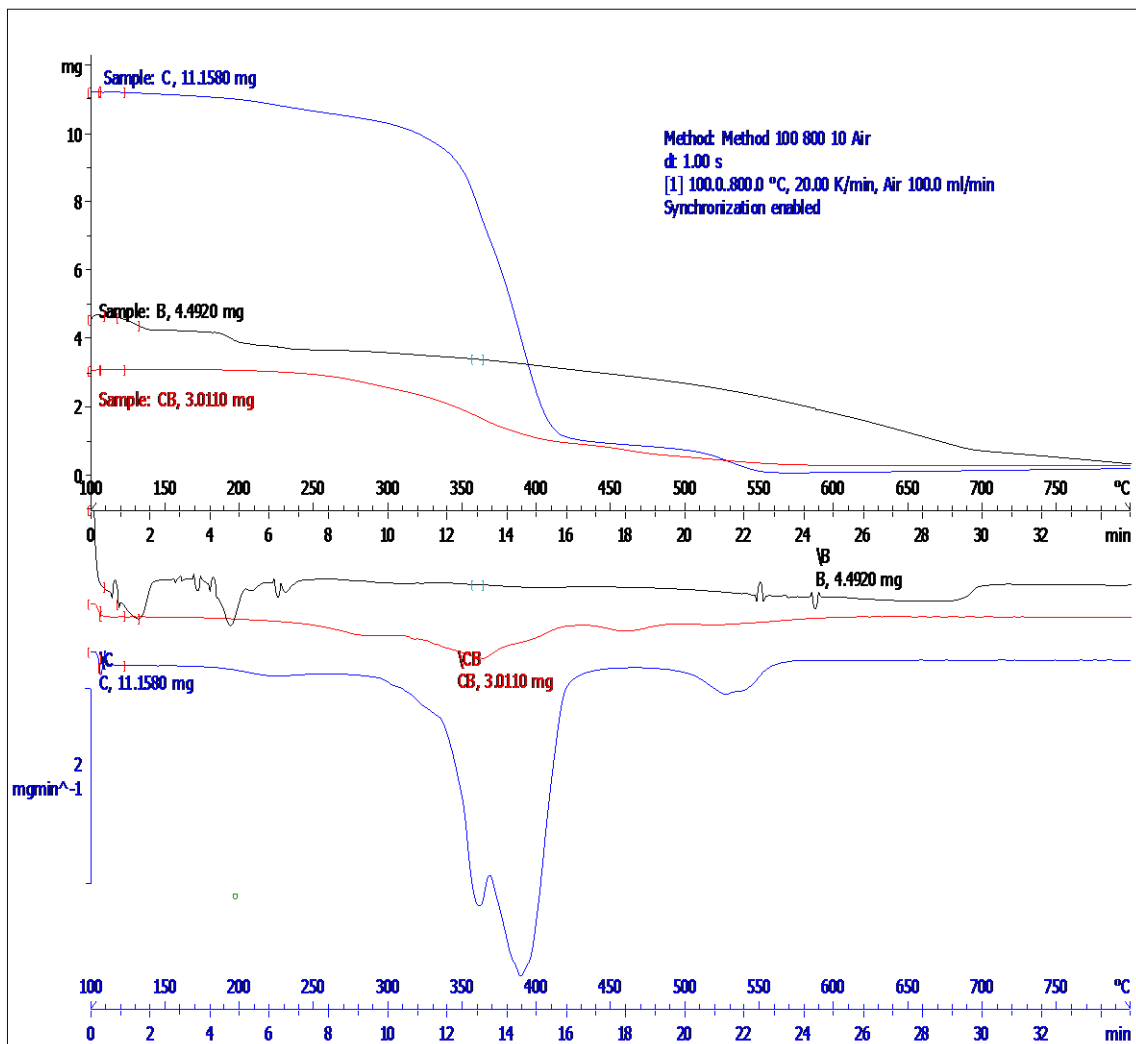


Figure 5.18: The thermogravimetric analysis and the first derivative curve of Carbopol (Blue curve), berberine (Black curve) and berberine-loaded Carbopol (Red curve) where the mass is plotted in the Y-axis while the temperature on the X-axis. This experiment was conducted in the air atmosphere with a purge rate of 10 mL/minute at temperature from 100 $^{\circ}\text{C}$ to 900 $^{\circ}\text{C}$.

5.4.7 Elemental Analysis of Berberine-Loaded Carbopol Aqua SF1

The elemental analysis of Carbopol alone and for the encapsulated berberine was conducted by taking an appropriated amount of 0.15 wt. % berberine-loaded 0.1 wt. % of Carbopol Aqua SF1. This amount was centrifuged, dried and vacuumed overnight at room temperature. The precipitates formed were submitted for elemental analysis. Table 5.1 shows the % value of C, H, and N for Carbopol and berberine-loaded Carbopol. Carbopol contained a higher percentage of carbon in comparison with hydrogen amount but there was no nitrogen in carbopol content which means that Carbopol is typical polyacrylic acid derivative consisting of two main elements, carbon and hydrogen in addition to the oxygen which was not analyzed. However, berberine-loaded Carbopol microgel as expected had carbon, hydrogen and nitrogen demonstrating that the berberine had been encapsulated into the Carbopol particles. Using the percentages of each elements resulted from the elementary analysis, the composition of the loaded particles was determined to contain 12.2 % berberine and 87.8 % carbopol. Therefore, if the dry carbopol is assumed to have the same composition as polyacrylic acid, the mole ratio of the carboxyl group with respect to the loaded berberine is about 33.

Table 5.1: The elementary analysis of Carbopol and Berberine loaded Carbopol after centrifugation and drying of only Carbopol and berberine-loaded into Carbopol.

Results Required	Carbopol %	Berberine-Loaded Carbopol %
C	56.8	54.7
H	5	4
N	0.00	0.51
The % Berberine content in Carbopol		12 %
Mole Ratio (COOH groups / Berberine)		33.5

5.4.8 Berberine Encapsulation Efficiency and Loading Content

The non-encapsulated amount of berberine was measured to determine the encapsulation efficiency and the percentage of the drug loading content from the linear regression equation calculated from the calibration curve of berberine as shown in Figure 5.19. Table 5.2 shows the encapsulation efficiency and the percentage of berberine loading content of the added concentration of berberine. It can be proved that the encapsulation efficiency of berberine into Carbopol microgel is 10 % and this efficiency is low owing to berberine contains one ionisable amino group that can interact electrostatically with each deprotonated carboxyl groups in the Carbopol microgel at pH 5.5. Additionally, the percentage of berberine loading content is 9% which represents the amount of loaded berberine with respect to the amount of dried carbopol microgel (from initial 0.1 wt. % concentration). The following equations were used to calculate the encapsulation efficiency and drug loading content of Berberine (BRB)¹²:

$$\text{Berberine Encapsulation (\%)} = \frac{[w_{\text{BRB}} - w_{\text{U}}]}{w_{\text{BRB}}} \times 100 ,$$

$$\text{Drug Loading Content (\%)} = \frac{[w_{\text{BRB}} - w_{\text{U}}]}{[w_{\text{BRB}} - w_{\text{U}} + w_{\text{C}}]} \times 100 .$$

[Here w_{BRB} is the total amount of Berberine added to the carbopol at pH 8, w_{U} is the non-encapsulated amount of Berberine obtained after the centrifugation and analyzing the supernatant, and w_{C} is the amount of Carbopol used during the whole system which means the concentration of Carbopol microgel in wt. %.

Table 5.2: The encapsulation efficiency and the percentage of berberine loading content of 0.15 wt. % berberine (BRB) into 0.1 wt. % of Carbopol microgel.

Total BRB Concentration wt. %	BRB Non-encapsulated wt. %	BRB Encapsulated wt. %	Encapsulation Efficiency %	Drug Loading Content %
0.15	0.135 ± 0.008	0.015 ± 0.008	10 ± 6	9 ± 5

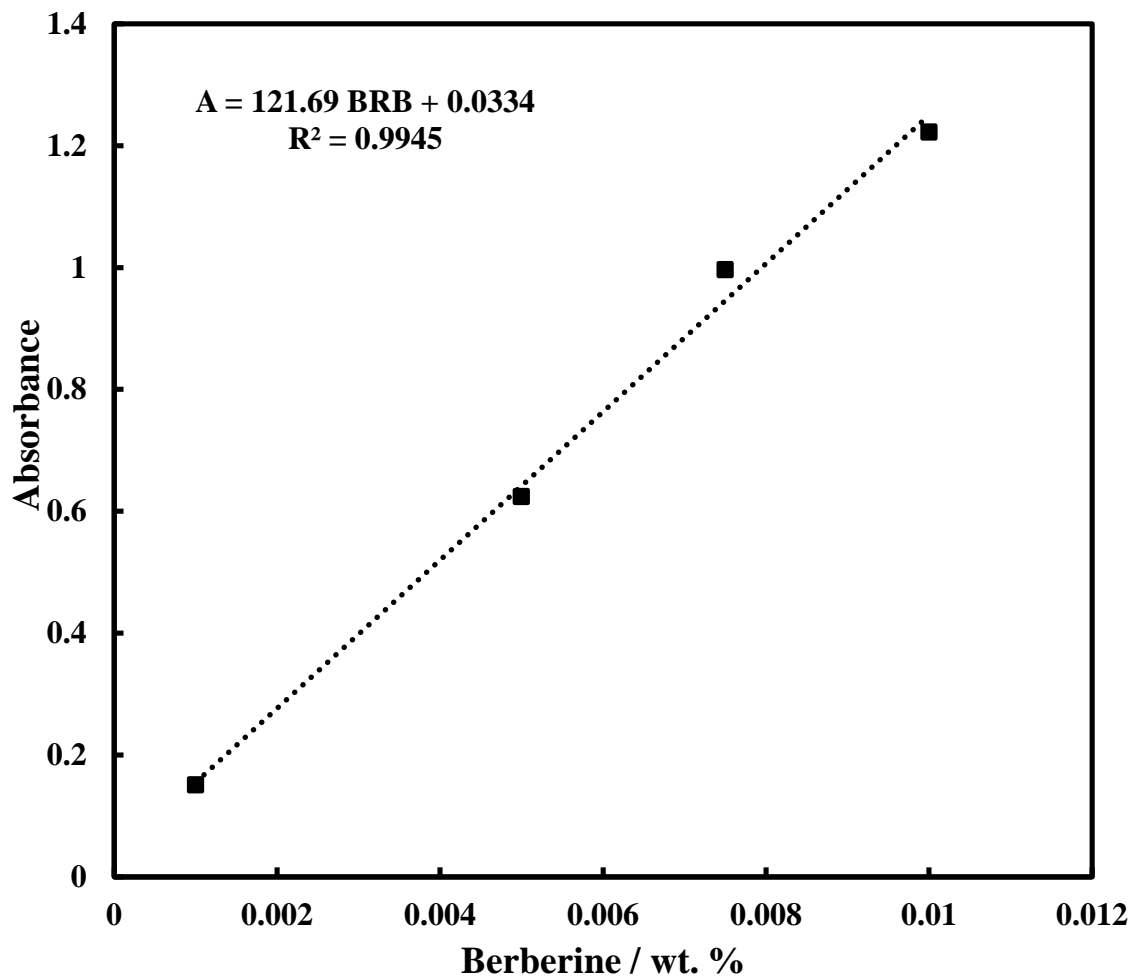


Figure 5.19: The absorbance spectrum of series of solutions of berberine (BRB) concentrations measured at 422 nm wavelength. The diluted concentrations of berberine were prepared from 0.2 wt% stock solution of berberine chloride.

5.4.9 Berberine Release Studies

It was investigated the percentage of *in vitro* berberine release using aliquots of equivalent concentrations of berberine-loaded 0.1 wt% Carbopol. This formulation had already been optimized in terms of the encapsulation stability with particle size and zeta potential of the colloidal microgel was 135 nm and -40 mV at pH 5.5, respectively. The berberine-loaded microgel suspension was placed into a dialysis cassette (10K MWCO, Thermo Fisher, UK) which allowed the berberine released from the microgel to diffuse through its membrane pores. The dialysis device was placed into: (i) a beaker which was already pre-filled with acetate buffer solution (pH 5.5) or (ii) a beaker with a phosphate buffer at pH 7.5 in order to monitor the amount of released berberine at a specific pH. After that, the concentration of the released Berberine *in vitro* was measured using UV-Visible spectrophotometer. All release experiments were carried out in triplicate. The percentage of cumulative drug release was calculated by

$$\% \text{ Drug Release} = \frac{MR}{ML} \times 100$$

where *MR* is the amount of drug released from the Carbopol at time *t* and *ML* is the amount of drug loaded in the Carbopol partricles.

The percentage of cumulative berberine release as a function of time is presented in Figure 5.20. It can be observed that the mechanism of release depends on the pH of the medium. At pH 5.5, approximately 25% of the encapsulated berberine was released in 2 hours and then the 55 % was released after 5 hours. After this the % released levelled off with only a slight increase of 65% after 24 hours. The slow release at pH 5.5 occurred due to the high zeta potential value of the anionic Carbopol microgel at that pH which allowed delay in the release of the cationic berberine moieties out of the microgel. At pH 7.5, there is a more dramatic release of 86 % berberine up to 3 hours and 90% after 24 hours. This due to the decrease in the zeta potential value at pH 7.5 which means the berberine becomes unconjugated from the carboxyl groups of Carbopol. One possible explanation of this result is that at pH 5.5 the berberine is trapped inside the collapsed microgel particles which ensure slower release than at pH 7.5 where the microgel is swollen.

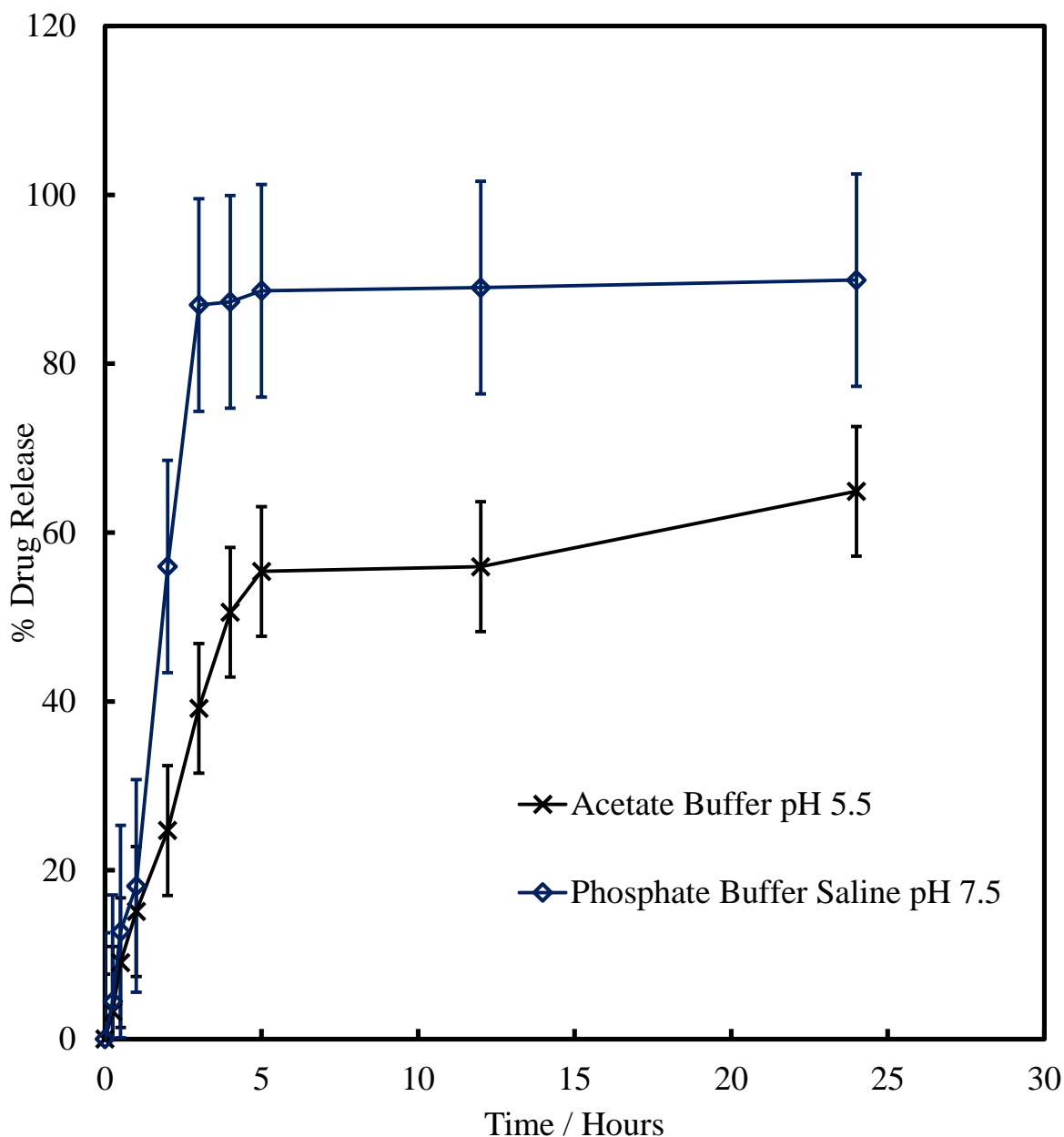


Figure 5.20: The percentage of *in vitro* berberine release as a function of time which was conducted using 10 K MWCO dialysis bag filled up with 50 mL of berberine-loaded Carbopol suspension. The whole dialysis bag was dipped in a beaker filled with 500 mL of either acetate buffer solution at pH 5.5 or phosphate buffer saline at pH 7.5. In this protocol, 3 mL of berberine-loaded carbopol suspension were mixed with 3 mL of fresh buffer solution. The samples absorbance was scanned in a range of wavelength (200 nm-700 nm) using Perkin Elmer UV-Visible Spectrophotometer.

The Carbopol microgel was adjusted to pH 8 to swell the Carbopol Aqua SF1 microgel in a highly anionic form. Chlorhexidine digluconate solution was added drop-wise to the Carbopol microgel to avoid the aggregation which happened if the solution is added in one go. The pH of the solution of chlorhexidine-loaded swollen Carbopol microgel was then decreased to pH 5.5 because at this specific pH, the Carbopol Aqua SF1 has the highest anionic zeta potential as shown in Figure 5.3 which is expected to promote better conjugation between Carbopol and chlorhexidine. The suspension of chlorhexidine-loaded collapsed Carbopol Aqua SF1 was then centrifuged three times to remove the non-encapsulated chlorhexidine. The suspension of collapsed Carbopol microgel was then dispersed in acetate buffer solution (pH 5.5) to prevent any change in pH which could affect the drug release mechanism. The suspension was also ultra-sonicated for 5 minutes to increase and strengthen the conjugation between Carbopol and chlorhexidine where carbopol microgel suffers from aggregation upon incubation with chlorhexidine; therefore, it was ultra-sonicated to break the interaction between the microgel and chlorhexidine. Figure 5.22 illustrates the images of samples of Carbopol Aqua SF1 at pH 5.5, chlorhexidine, chlorhexidine-loaded swollen Carbopol microgel at pH 8 and chlorhexidine-loaded collapsed Carbopol microgel at pH 5.5.

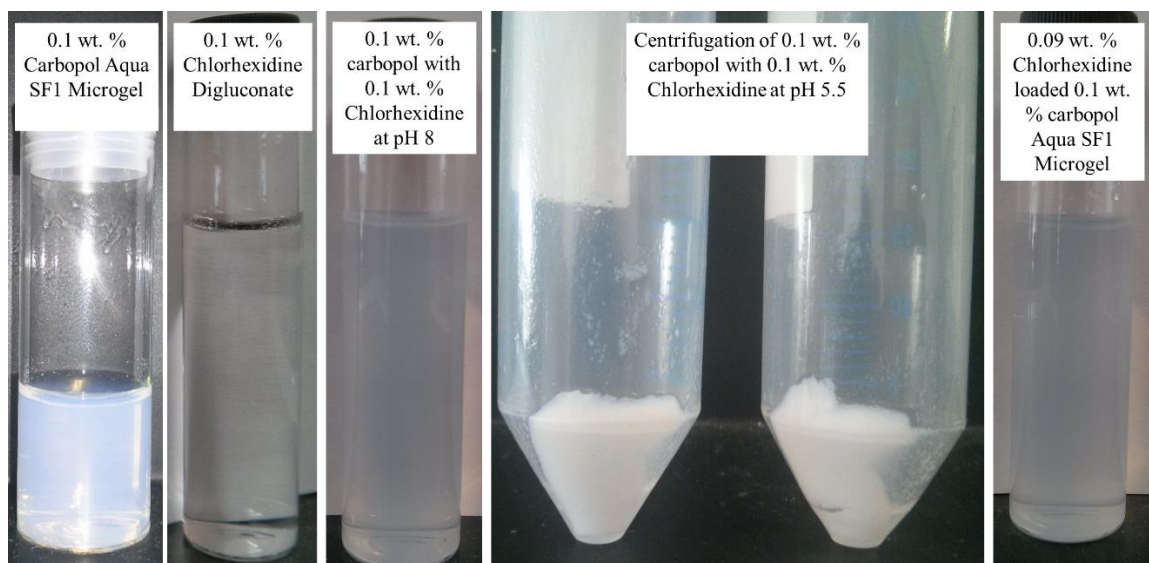


Figure 5.22: The Photographic image of bare carbopol, chlorhexidine, chlorhexidine-loaded Carbopol at pH 8 and chlorhexidine-loaded Carbopol at pH 5.5.

5.6 Characterization of Chlorhexidine-Loaded Carbopol

5.6.1 Effect of the Carbopol Concentration on the Chlorhexidine

Microencapsulation

The effect of the concentration of Carbopol Aqua SF1 on the encapsulation of chlorhexidine was studied by mixing solutions of different concentration of chlorhexidine with a solution of fixed concentration of Carbopol Aqua SF1 (0.05 and 0.1 wt. %). The suspensions produced were then stirred, the pH was decreased to 5.5, and the microgel particles were centrifuged three times and dispersed in a solution of buffer acetate at pH 5.5. The average particle diameter of the chlorhexidine-loaded Carbopol Aqua SF1 suspensions were then measured at the refractive index of Carbopol microgel (1.456) as shown in Figure 5.23. At 0.05 wt% Carbopol Aqua SF1 (dotted curve), the particle size of chlorhexidine-loaded Carbopol Aqua SF1 increased slightly from 110 nm to 134 nm, respectively. For samples with initial concentration of 0.01 wt% chlorhexidine the microgel particle diameter sharply increased to 400 nm. The increase in chlorhexidine concentration caused aggregation of the Carbopol Aqua SF1 microgel because the cationic charges from the chlorhexidine reduced the negative surface charge of the carbopol particles. Thus, 0.05 wt% carbopol would not be suitable for encapsulating higher concentrations of chlorhexidine.

A 0.1 wt% Carbopol Aqua SF1, (see the dotted line in Figure 5.23), the hydrodynamic diameter of Carbopol Aqua SF1 microgel can be seen to increase with the concentration of chlorhexidine. At high concentration of chlorhexidine (0.1 wt. %), the average particle diameter appeared to be 135 nm without any evident particle aggregation. Therefore, we chose 0.1 wt% Carbopol Aqua SF1 as the optimal microgel concentration to encapsulate different concentrations of chlorhexidine. It also indicated that the drop-wise addition of chlorhexidine to Carbopol Aqua SF1 with shaking and ultra-sonication is beneficial to avoid the microgel aggregation upon addition of the chlorhexidine di-gluconate solution.

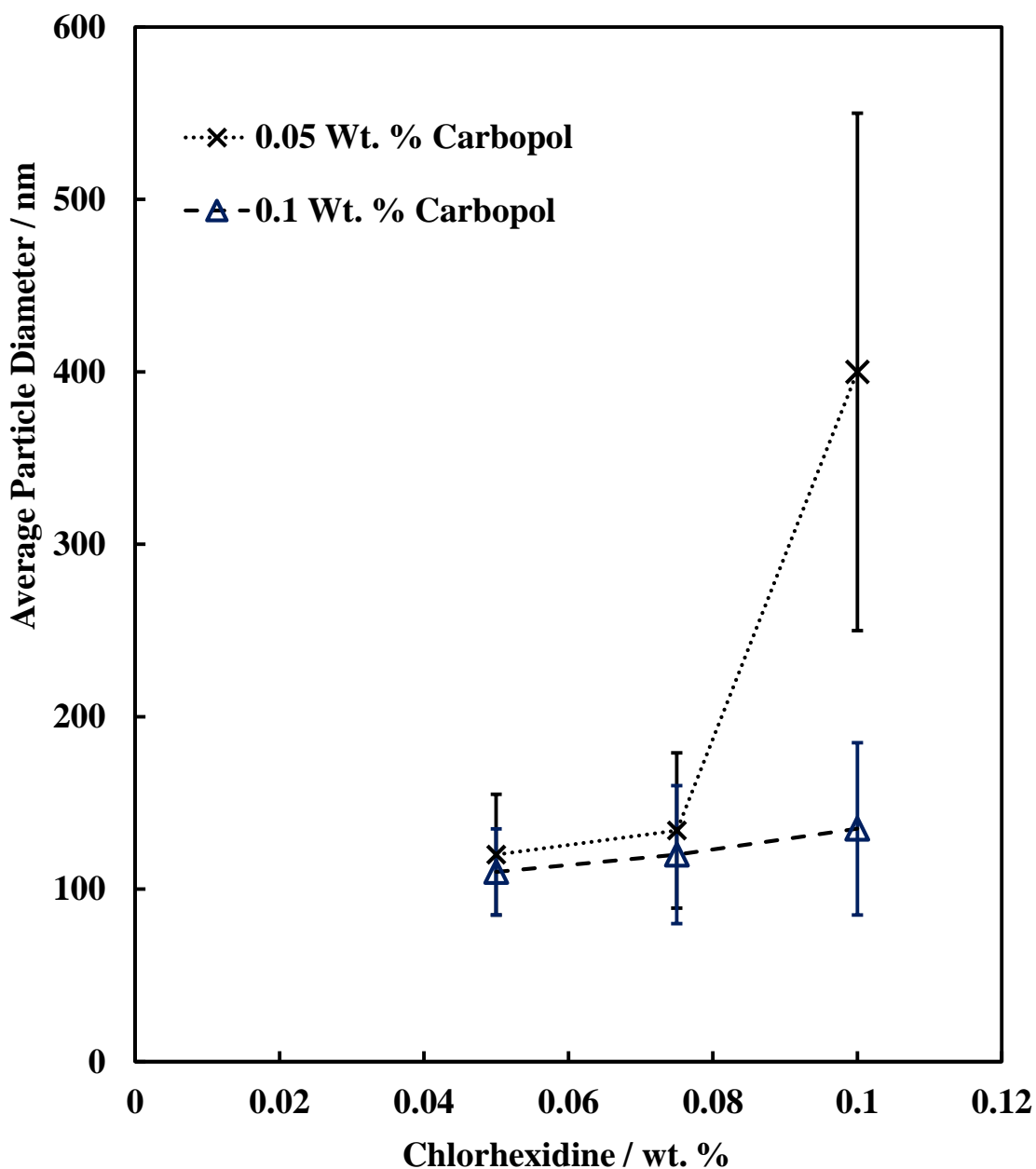


Figure 5.23: The average particle hydrodynamic diameter of chlorhexidine-loaded carbopol as a function of solution concentration of chlorhexidine. The two lines correspond to incubation of two different concentrations of Carbopol Aqua SF1 (one is with 0.05 wt% (Dotted) and 0.1 wt% (Dashed)) with series of solution of different concentration of chlorhexidine. The encapsulation process was conducted by swelling and deswelling of Carbopol Aqua SF1 to pH 8 and pH 5.5, respectively.

5.6.2 Effect of the Chlorhexidine Concentration on the Carbopol Stability

The effect of different concentrations of chlorhexidine on the colloidal stability of the 0.1 wt% Carbopol Aqua SF1 was investigated. Figure 5.24 shows the average particle diameter (blue line) and the zeta potential (black line) of Carbopol Aqua SF1 as a function of the chlorhexidine concentration. This shows that as the chlorhexidine concentration increases, the average particle diameter of Carbopol Aqua SF1 also increases. At 0.05 wt% chlorhexidine (blue line) the average particle diameter of Carbopol Aqua SF1 was 110 nm, then this increased slightly to 120 nm and 135 nm at 0.075 wt% and 0.1 wt% chlorhexidine concentration, respectively. Above 0.1 wt% chlorhexidine (around 0.125 wt%), an aggregation occurred and the hydrodynamic size of chlorhexidine loaded Carbopol Aqua SF1 was found to be 300 nm. Additionally, it can also be seen in Figure 24 (black line) that the zeta potential of Carbopol Aqua SF1 particles decreased as the chlorhexidine concentration increased. At 0.05 wt% concentration of chlorhexidine, the zeta potential of Carbopol Aqua SF1 was -38 mV. This gradually increase until 0.1 wt% chlorhexidine where the zeta potential of the collapsed microgel particles is -35 mV which means the colloid is sufficiently stable. However, above 0.1 wt% of chlorhexidine concentration, the colloid became unstable with a zeta potential of around -15 mV. 0.1 wt% chlorhexidine concentration was therefore selected as the optimum value to be encapsulated with 0.1 wt% Carbopol Aqua SF1 microgel particles. This CHX concentration gave a high colloidal stability and particles with an average particle diameter of 135 nm and zeta potential of -35 mV at pH 5.5.

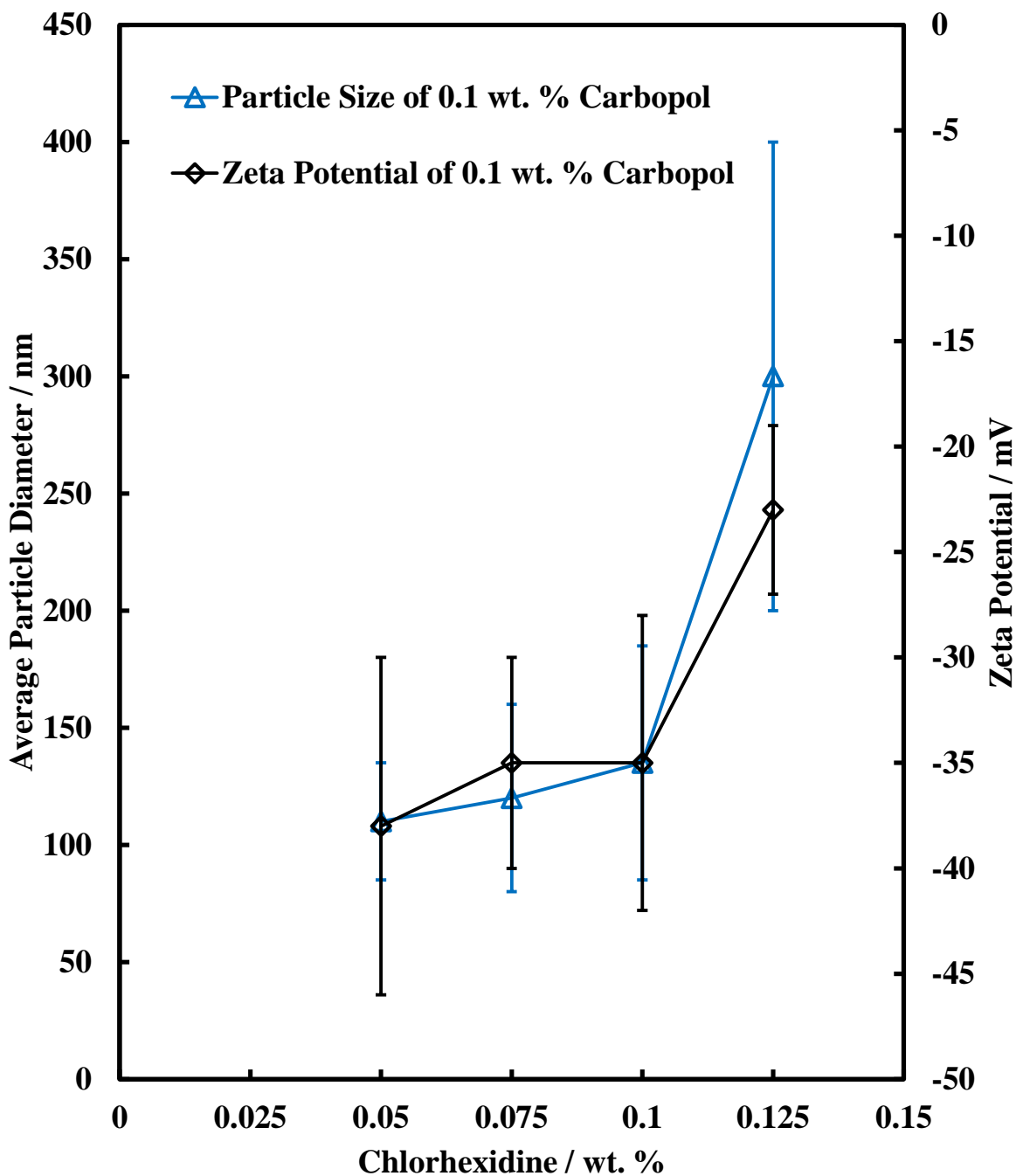


Figure 5.24: The average particle hydrodynamic diameter and the zeta potential of Carbopol aqua SF1 microhel particles as a function of the concentration of added chlorhexidine. This loading method was based on drop by drop addition of solutions of different concentration of chlorhexidine separately to four equal amounts of 0.1 wt. % Carbopol Aqua SF1 at pH 8, then decreased pH to 5.5, centrifuged three times and finally re-dispersed in acetate buffer solution at pH 5.5. Each solution was sonicated for 5 minutes to facilitate the re-dispersing of the particles.

5.6.3 Measurement of the Particle Hydrodynamic Diameter and Zeta Potential

Upon encapsulation of chlorhexidine into the Carbopol Aqua SF1 microgel, the average particle hydrodynamic diameter of chlorhexidine-loaded Carbopol Aqua SF1 was 270 nm at pH 8 because the Carbopol microgel was swollen as shown in Figure 5.25. In comparison, the average particle hydrodynamic diameter and zeta potential of chlorhexidine encapsulated Carbopol Aqua SF1 at pH 5.5 were found to be 135 nm (see fig 5.26) and -40 mV (see Figure 5.27), respectively. The chlorhexidine-loaded Carbopol Aqua SF1 microgel showed an increase in particle size at pH 5.5 in comparison with bare Carbopol Aqua SF1 microgel which partially confirmed that it has encapsulated the chlorhexidine. Additionally, the zeta potential of encapsulated suspension was high giving good colloidal stability. The TEM image of the loaded particles can be seen in Figure 5.28. The particles had spherical morphology with little aggregation and the measured particle size from the TEM images was in good agreement with the results from the Malvern Zetasizer (Figure 5.25).

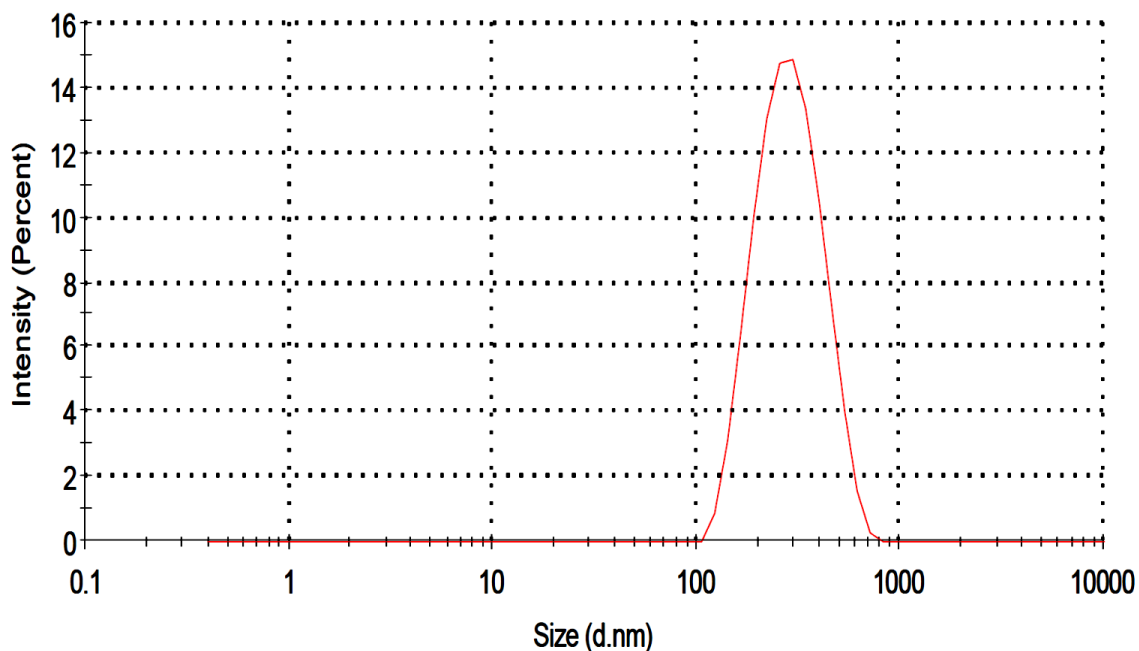


Figure 5.25: The average particle diameter of 0.09 wt.% chlorhexidine-loaded swollen carbopol at pH 8 which measured using Malvern Zetasizer ZS (UK) after a specific amount chlorhexidine mixed with a fixed concentration of carbopol (0.1 wt%).

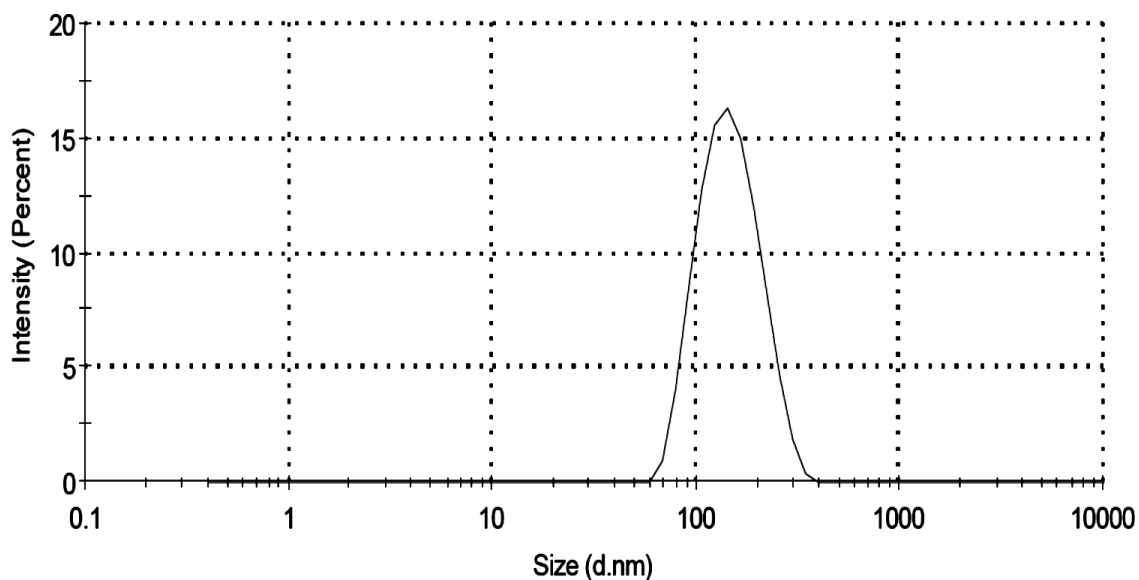


Figure 5.26: The average particle hydrodynamic diameter of 0.09 wt.% chlorhexidine-loaded collapsed carbopol resulted from addition of aliquot of chlorhexidine solution to 0.1 wt% of swollen carbopol at pH 5.5 then the pH was reduced to form chlorhexidine loaded collapsed carbopol. The final suspension was centrifuged three times and dispersed with acetate buffer solution at pH 5.5 to resist any change in pH upon incubation with microorganisms.

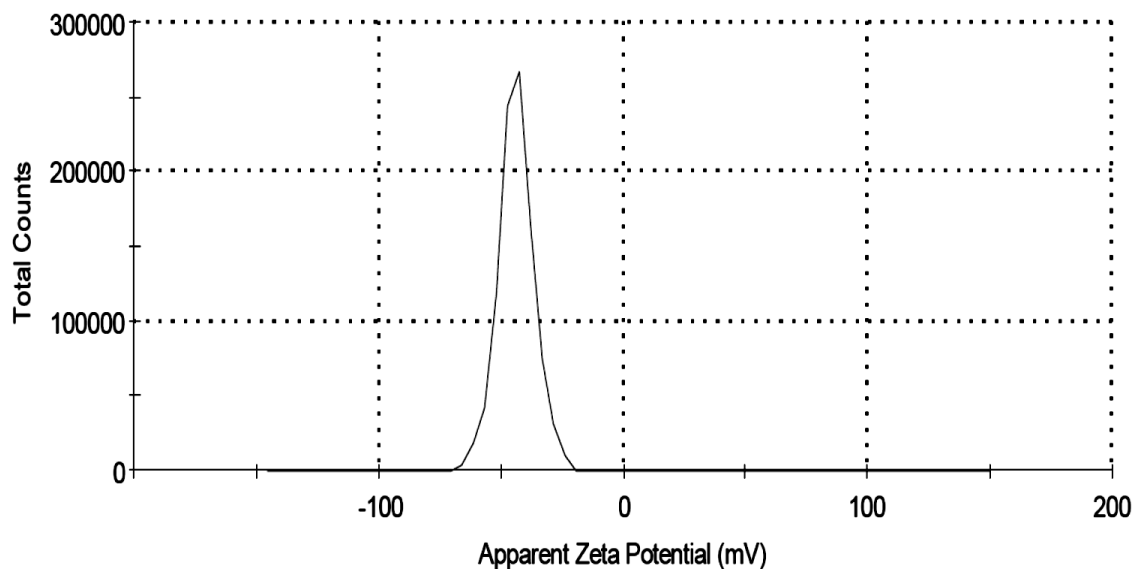


Figure 5.27: The zeta potential of 0.09 wt.% chlorhexidine-loaded collapsed carbopol microgel produced from mixing specific amount of chlorhexidine with 0.1 wt% carbopol to form physical interacted complex at pH 8, then the pH decreased to pH 5.5 to form chlorhexidine-loaded collapsed carbopol. The latter was centrifuged and dispersed with acetate buffer at pH 5.5. The resulted suspension was measured by Malvern Zetasizer ZS with Dip cell using plastic cuvette.

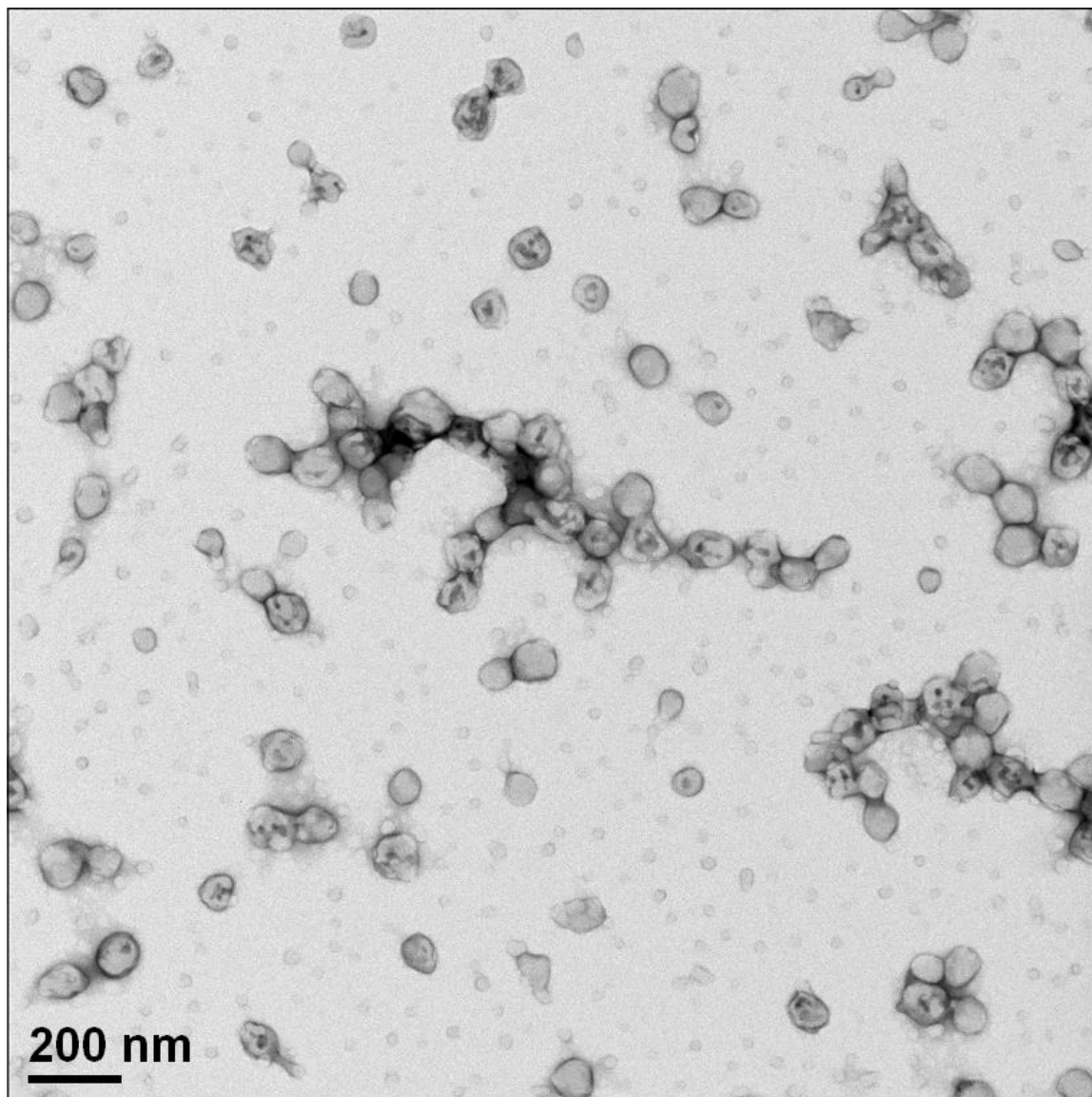


Figure 5.28: TEM image of chlorhexidine-loaded collapsed carbopol at pH 5.5 which presented the spherical shape of the produced microgel. The encapsulation was achieved through adjusting carbopol to pH 8, then chlorhexidine was added to form chlorhexidine loaded swollen carbopol. The formed suspension was adjusted to pH 5.5 to form chlorhexidine loaded carbopol microgel. The TEM samples were prepared according to the procedure mentioned in Chapter 2, Section 2.2.7.

5.6.4 UV-Vis Spectroscopy of Carbopol, CHX and CHX-Loaded Carbopol

UV-Visible spectroscopy to study the absorption spectrum of Carbopol Aqua SF1, chlorhexidine and chlorhexidine loaded Carbopol Aqua SF1 as shown in Figure 5.29. This absorbance spectrum was useful for the characterization of the physical conjugation between Carbopol Aqua SF1 and chlorhexidine. It can be seen from Figure 5.29 (Blue line) that Carbopol Aqua SF1 absorbed in UV region between 250 nm to 200 nm. Chlorhexidine (orange line) also had two broad absorbance peaks in the UV region, one at 254 nm and the other at 233 nm. The chlorhexidine-loaded Carbopol Aqua SF1 (black line) exhibited two substantial peaks in the wavelengths 264 nm and 233 confirming the presence and respectively the conjugation of chlorhexidine into the carbopol particles. There was a shift at 264 nm (compared to 254 nm) which can be attributed to partial scattering of the incident light by Carbopol Aqua SF1 colloid suspension.

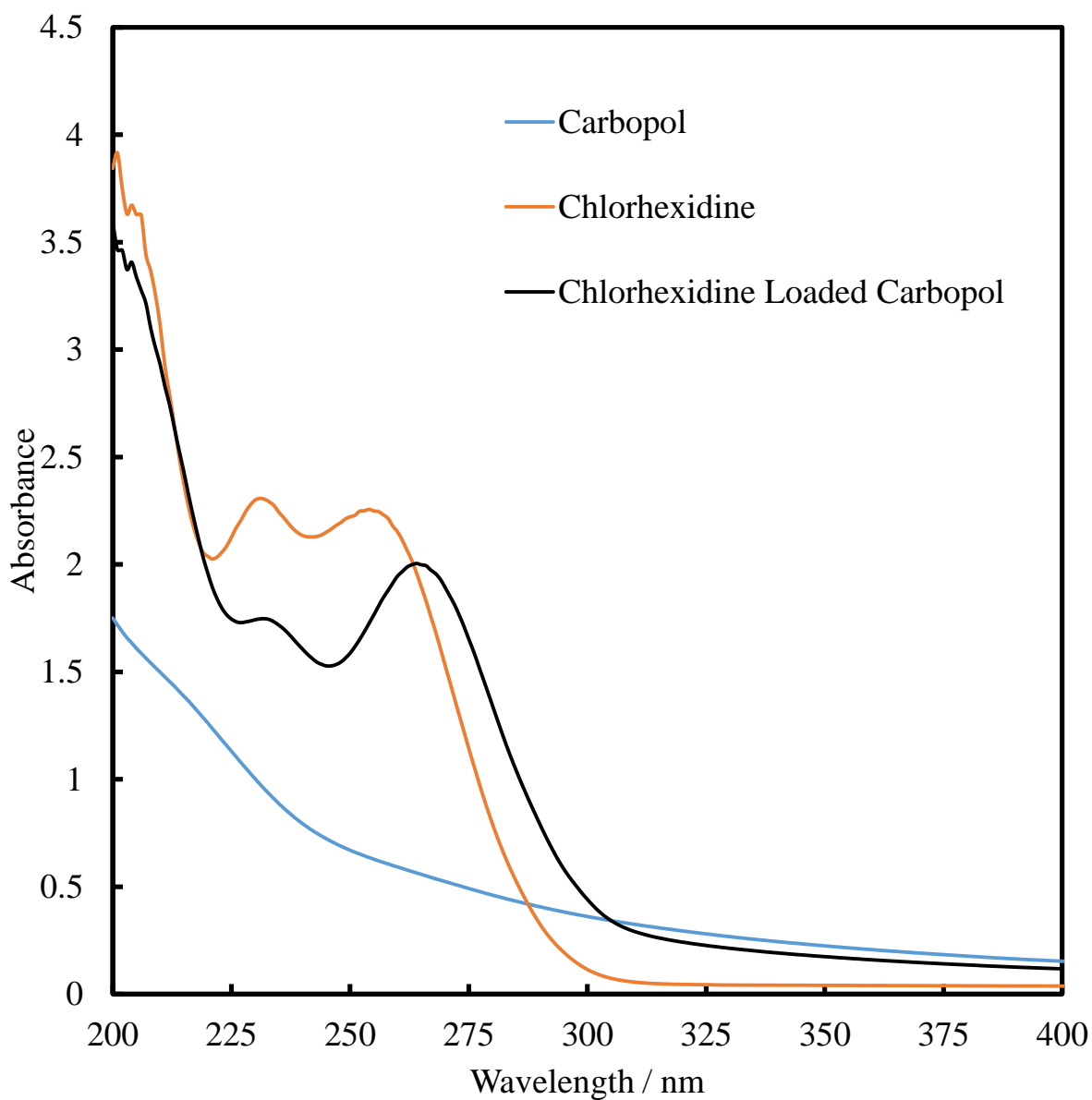


Figure 5.29: The UV/vis absorbance spectrum of 0.01 wt% Carbopol Aqua SF1 (Blue line), 0.007 wt% chlorhexidine (Orange line) and 0.006 wt% chlorhexidine-loaded Carbopol Aqua SF1 (Black line). The measurement was done in the range of wavelength from 200 nm to 400 nm using Perking Elmer Lambda 25 UV-Visible spectrophotometer with 1 cm path length of QS cuvette.

5.6.5 FTIR Spectroscopy of Carbopol, CHX, and CHX-Loaded Carbopol

FT-IR can provide unique information on the conjugation between Carbopol Aqua SF1 and chlorhexidine. The FTIR spectra were obtained for Carbopol, chlorhexidine, chlorhexidine-loaded Carbopol microgel at 400 cm^{-1} to 4000 cm^{-1} (Figure 5.30).

The spectrum for carbopol Aqua SF1 (Figure 5.30A) was discussed in section 5.4.5. The spectrum of chlorhexidine digluconate in Figure 5.30B is characterized by the main stretching vibrations from 3300 cm^{-1} to 3500 cm^{-1} for the N-H group. The bands at 2850 cm^{-1} to 3000 cm^{-1} are stretching vibration bands due to the aliphatic C-H group. Moreover, the peak at 1672 cm^{-1} relates to the stretching vibration band of the aliphatic C=N group which is considered as a characteristic peak of chlorhexidine. There are also peaks at wavenumbers from 1450 cm^{-1} to 1550 cm^{-1} which are assigned to C=C group in the aromatic ring and at 1251 cm^{-1} which relates to the stretching vibration frequency of aliphatic amine (C-N) group. These FTIR results of chlorhexidine are in line with those of the literature.^{13, 14, 15}

Figure 5.30C shows the spectrum of Carbopol Aqua SF1 encapsulated chlorhexidine. The broad absorption band at 3435 cm^{-1} can be allocated to the O-H group for Carbopol microgel while the band at 3364 cm^{-1} for the N-H group for chlorhexidine. The frequencies at 1653 cm^{-1} and 1734 cm^{-1} were noticed as principal characteristic bands for chlorhexidine loaded Carbopol Aqua SF1 because they represent the vibration bands of the aliphatic C=N group for chlorhexidine and the carbonyl group (C=O) for carbopol, respectively. The FTIR spectra therefore confirm that the chlorhexidine was encapsulated into Carbopol Aqua SF1 microgel.

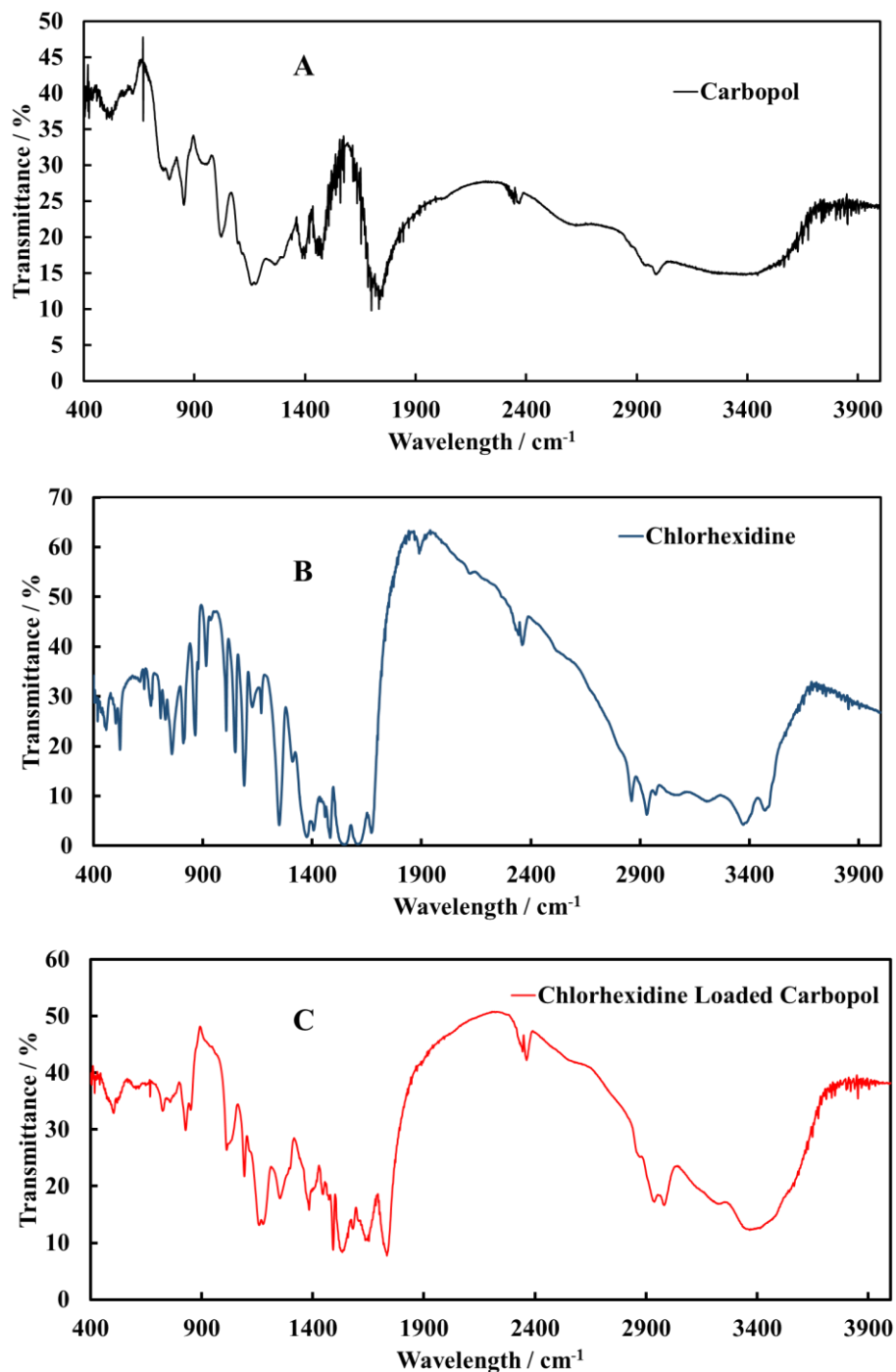


Figure 5.30: The Fourier Transform-IR spectrum of Carbopol Aqua SF1 (A), chlorhexidine (B) and chlorhexidine-loaded Carbopol Aqua SF1 (C). These materials were dried and mixed with excess amount of KBr pellets to prepared KBr discs for each of Carbopol microgel, chlorhexidine and chlorhexidine-loaded Carbopol microgel which in turn were scanned individually in range of wave numbers from 400 cm^{-1} to 4000 cm^{-1} to measure their FTIR spectrum.

5.6.6 Thermogravimetry Analysis of Chlorhexidine-Loaded Carbopol

Figure 5.31 presents data from the thermal gravimetric analysis (TGA) and the differential thermal analysis (DTA) for Carbopol Aqua SF1, chlorhexidine and chlorhexidine-loaded Carbopol Aqua SF1. These materials were heated separately from 100°C to 900°C at 10°C/minute in air atmosphere with a purge rate of 10 mL/minute. The blue line represents the thermal behavior of Carbopol Aqua SF1 as discussed earlier in section 5.4.6.

Figure 5.31 (red line) is for chlorhexidine where an endothermic plateau was obtained at 175°C for both TGA and DTA which relates to the loss of water. Upon increasing the temperature to 450°C, another endothermic peak is seen which relates to the loss of nitrogen and the thermal stability of chlorhexidine was found to be at 650°C. For the chlorhexidine-loaded Carbopol Aqua SF1 (black line) the results were completely different from that of for the individual components. Five endothermic peaks were seen at 225°C for dehydration, 325°C and 375°C for carbon compounds, 425°C for nitrogen molecules and 600°C.

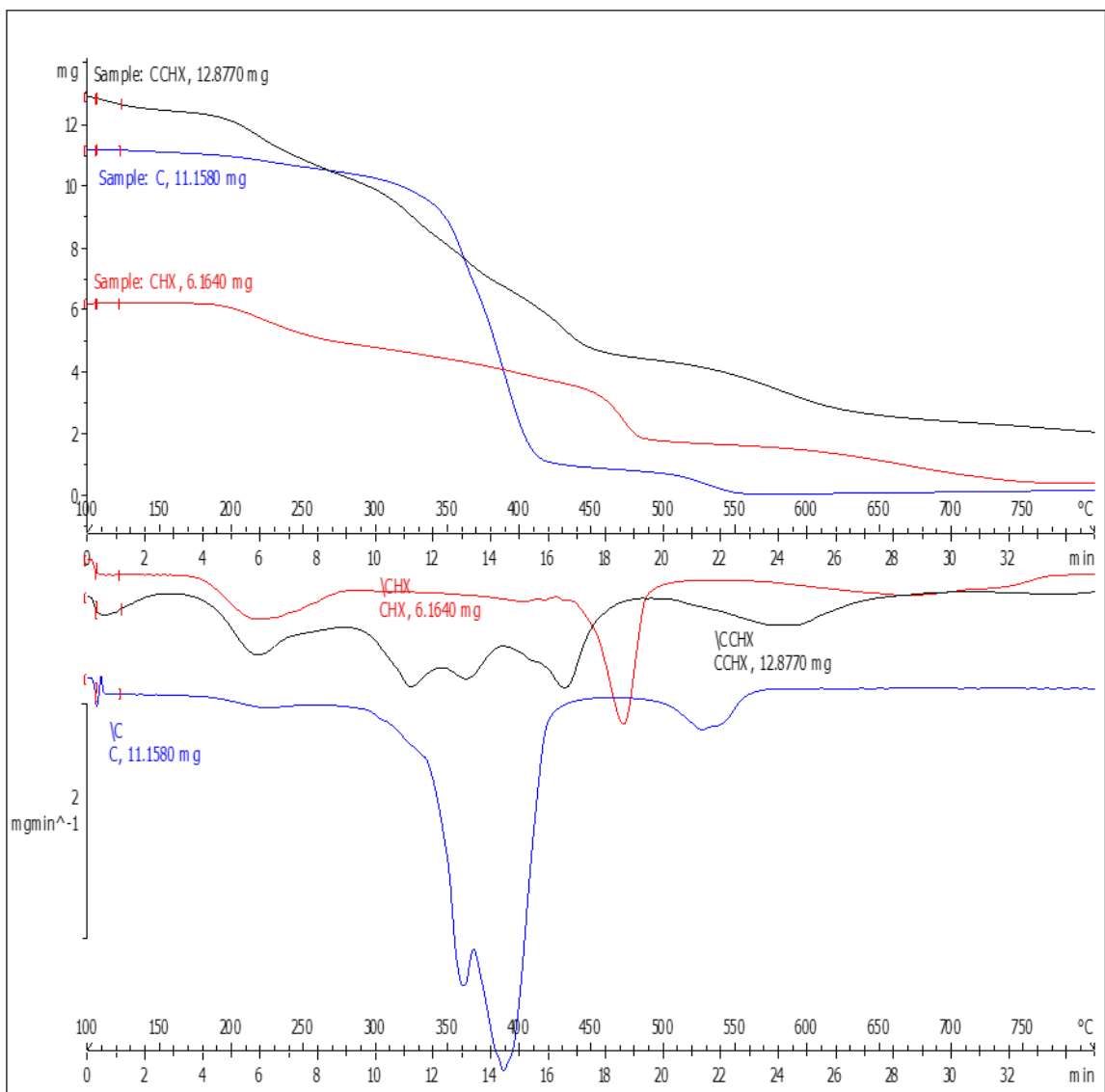


Figure 5.31: Thermal Gravimetric Analysis (TGA) and Differential Thermal Analysis (DTA) of chlorhexidine (red line), Carbopol Aqua SF1 (blue line) and chlorhexidine-loaded Carbopol microgel (black line) which are conducted through weighing a known amount of each sample and drying, then ran by the TGA machine at a range of temperature from 100 °C to 900 °C at 10 °C/minute in air atmosphere with purge rate of 10 mL/min.

5.6.7 Elementary Analysis of CHX and BRB Loaded Carbopol

Table 5.3 shows the % elementary values of C, H, and N for Carbopol Aqua SF1 and chlorhexidine-loaded Carbopol Aqua SF1. It can be seen in Table 5.3 as would be expected, the chlorhexidine-loaded carbopol contained nitrogen in addition to carbon and hydrogen. This amount of nitrogen related to the chlorhexidine and the percentage of nitrogen was much higher than that seen for berberine due to the chemical structure of chlorhexidine (Figure 1.27), which has ten nitrogen atoms as compared to only one in berberine (Figure 1.26). These results confirm that chlorhexidine has been encapsulated into the Carbopol microgel with the percentage of chlorhexidine being 13.2 %. The mole ratio of the carboxyl group of Carbopol Aqua SF1 to chlorhexidine was found to be 50.2 which as expected was much higher than that for berberine due to the higher nitrogen content of chlorhexidine and its higher number of cationic groups. Here we have assumed that the Carbopol chemical composition corresponds to polyacrylic acid.

Table 5.3: The elementary analysis of Carbopol Aqua SF1 and the encapsulated chlorhexidine (CHX) into Carbopol Aqua SF1 microgel through centrifuging and drying the each sample in air at room temperature.

Results Required	Carbopol Aqua SF1 %	CHX Loaded Carbopol Aqua SF1 %
C	56.73	53.59
H	4.99	7.35
N	0.00	3.67
The % drug content in Carbopol Aqua SF1		13.2 %
Mole Ratio (COOH /CHX)		50.2

5.6.8 Encapsulation Efficiency and Drug Loading Content

The encapsulation efficiency and the percentage of chlorhexidine loading in Carbopol Aqua SF1 was determined by UV-vis absorption spectrometry using the amount of chlorhexidine not encapsulated. The calibration can be seen in Figure 5.32. Table 5.4 depicts the encapsulation efficiency and the percentage of chlorhexidine loading content into Carbopol microgel. The equations used to calculate the encapsulation efficiency and drug loading content of chlorhexidine (CHX)¹² are as follows:

$$\text{CHX Encapsulation (\%)} = \frac{[w_{\text{CHX}} - w_{\text{U}}]}{w_{\text{CHX}}} \times 100$$

$$\text{CHX Loading Content (\%)} = \frac{[w_{\text{CHX}} - w_{\text{U}}]}{[w_{\text{CHX}} - w_{\text{U}} + w_{\text{C}}]} \times 100$$

Here w_{CHX} is the total amount of chlorhexidine added to the Carbopol Aqua SF1 at pH 8, w_{U} is the non-encapsulated amount of chlorhexidine obtained after the centrifugation, and w_{C} is the amount of Carbopol Aqua SF1 (wt.%).

It can be seen from the table that 90 % of total concentration of chlorhexidine was encapsulated into the microgel with a 47% chlorhexidine loading content. This high encapsulation efficiency is due to the fact that chlorhexidine is highly cationic with many nitrogen atoms that interact with carboxyl groups of Carbopol Aqua SF1.

Table 5.4: The encapsulation efficiency and chlorhexidine loading content for the encapsulation of 0.1 wt% chlorhexidine in 0.1 wt% Carbopol Aqua SF1.

Total CHX Concentration wt%	CHX Non-encapsulated wt%	CHX Encapsulated wt%	Encapsulation Efficiency %	Drug Loading Content %
0.1	0.01 ± 0.003	0.09 ± 0.003	90 ± 4	47 ± 1

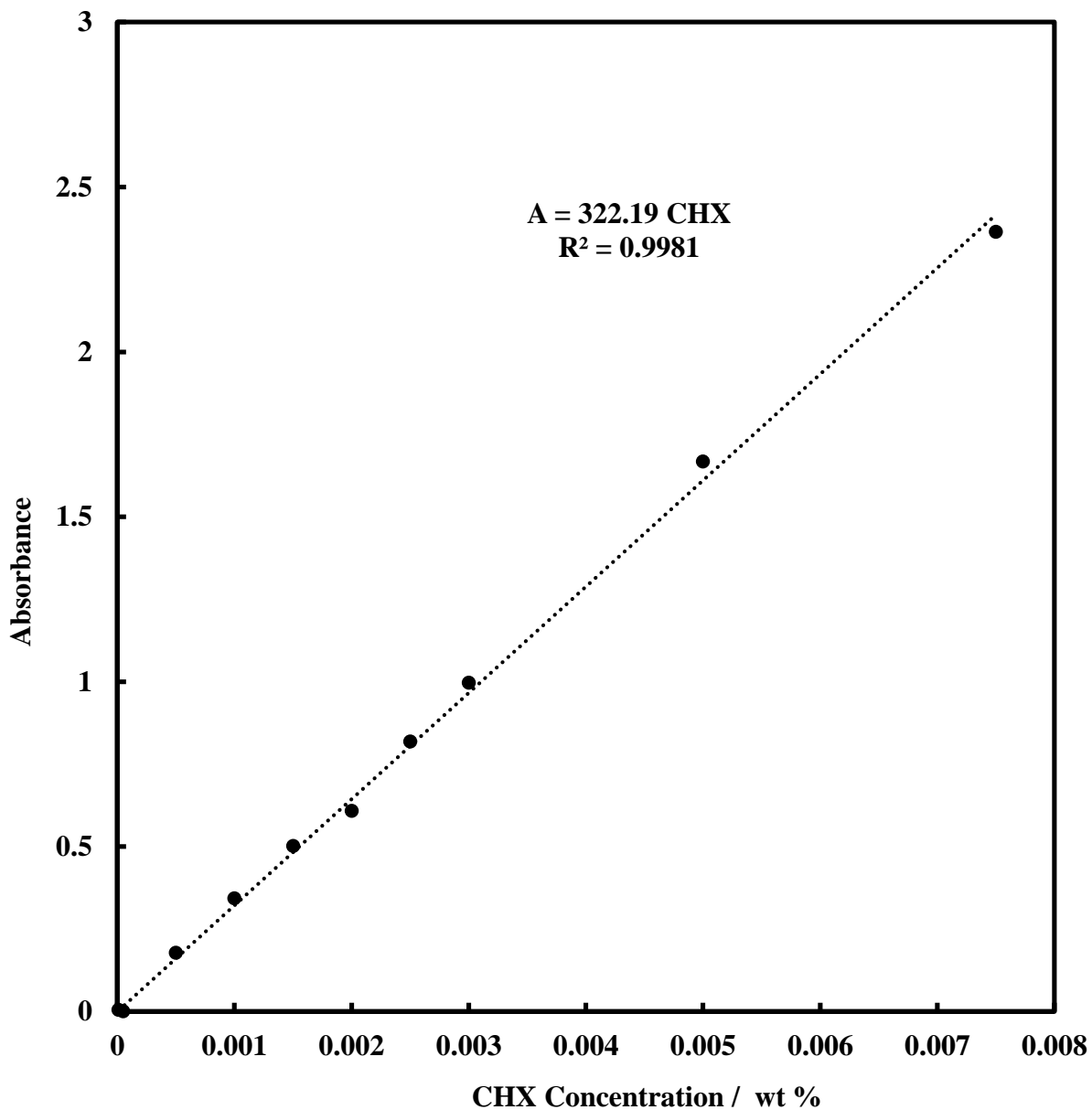


Figure 5.32: The standard curve of solutions of different concentrations of chlorhexidine di-gluconate at wavelength 254 nm using Perking Elmer Lambda 25 UV-Visible spectrophotometer. The solutions were prepared from 0.2 wt% stock solution of chlorhexidine digluconate.

5.6.9 Chlorhexidine Release Kinetics

The chlorhexidine release was studied in the same way as explained in Section 5.4.9 for berberine. The concentration of chlorhexidine loaded in the supernatant was used to study the amount of released chlorhexidine from the Carbopol microgel. The average particle diameter of the chlorhexidine loaded Carbopol suspension was 135 nm and the zeta potential was -35 mV. Figure 5.33 describes the percentage of cumulative chlorhexidine released as a function of time. At pH 5.5, 12 % of chlorhexidine was released within 2 h and 16% - after 5 h. Between 12 and 24 hour, the percentage of chlorhexidine release become around 20% where there was no significant release from Carbopol microgel. This happened because of the high interaction between anionic Carbopol Aqua SF1 and cationic chlorhexidine, causing slow release of the antimicrobial agent.

On the other hand, at pH 7.5 the % chlorhexidine release increased to 20% after 2 h. Between 12 h and 24 h, 45% of the chlorhexidine was released. This low release compared to berberine is due to the reduction of the zeta potential at pH 7.5, causing de-conjugation of chlorhexidine from the carboxyl groups of Carbopol Aqua SF1. One can also take into account that at pH 7.5 the microgel is swollen which would allow the de-conjugated chlorhexidine to diffuse out faster.

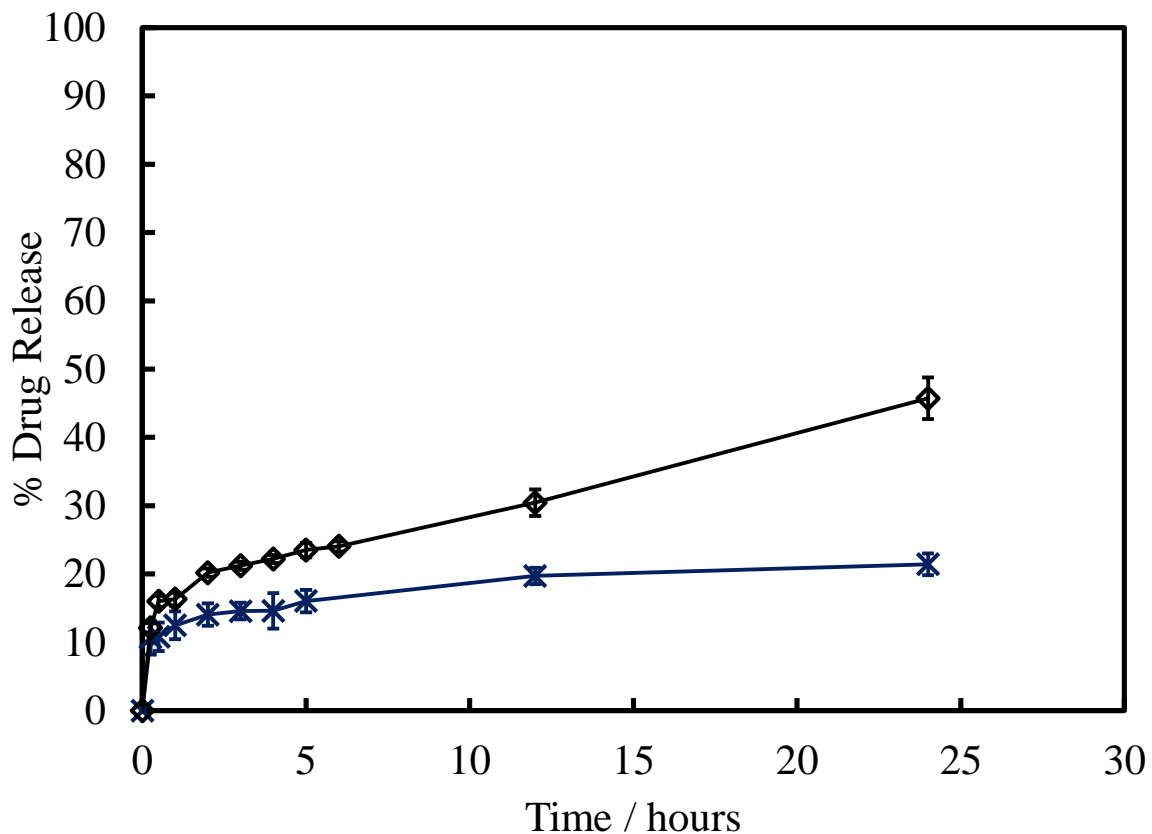


Figure 5.33: The percentage of *in vitro* chlorhexidine release as a function of time. The experiment was conducted using 10 K MWCO dialysis bag filled up with 50 mL of chlorhexidine loaded Carbopol Aqua SF1 suspension. The whole dialysis bag was dipped in a beaker filled with 500 mL of either acetate buffer solution at pH 5.5 or Phosphate buffer saline at pH 7.5. A 3 mL sample of loaded Carbopol microgel were pipetted from each buffer solution and in the same time, a 3 mL of fresh buffer solution was also added to the beaker. The pipetted amount was scanned in a range of wavelength (200 -700 nm) using Perkin Elmer UV-Visible Spectrophotometer.

5.7 Functionalization of Carbopol and Encapsulated Carbopol

Solutions of a specific concentration of a range of cationic polyelectrolytes including poly (allylamine hydrochloride) (PAH), branched poly (diallyldimethylammonium) chloride (PDAC) and polyethyleneimine (PEI) were mixed with a fixed concentration of carbopol Aqua SF1 microgel at a pH less than 5 to coat the microgel with a layer of cationic polyelectrolyte. Figure 5.34 shows the average particle hydrodynamic diameter of the cationic polyelectrolyte coated Carbopol Aqua SF1 microgels as a function of the type of cationic polyelectrolyte. PAH-coated and PDAC- coated Carbopol can be seen to have small particle diameters with a good stability in comparison with PEI which had much higher particle diameter (580 nm). PAH and PDAC were found to be the best cationic polyelectrolyte for the cationic functionalization of carbopol microgel with high colloidal stability.

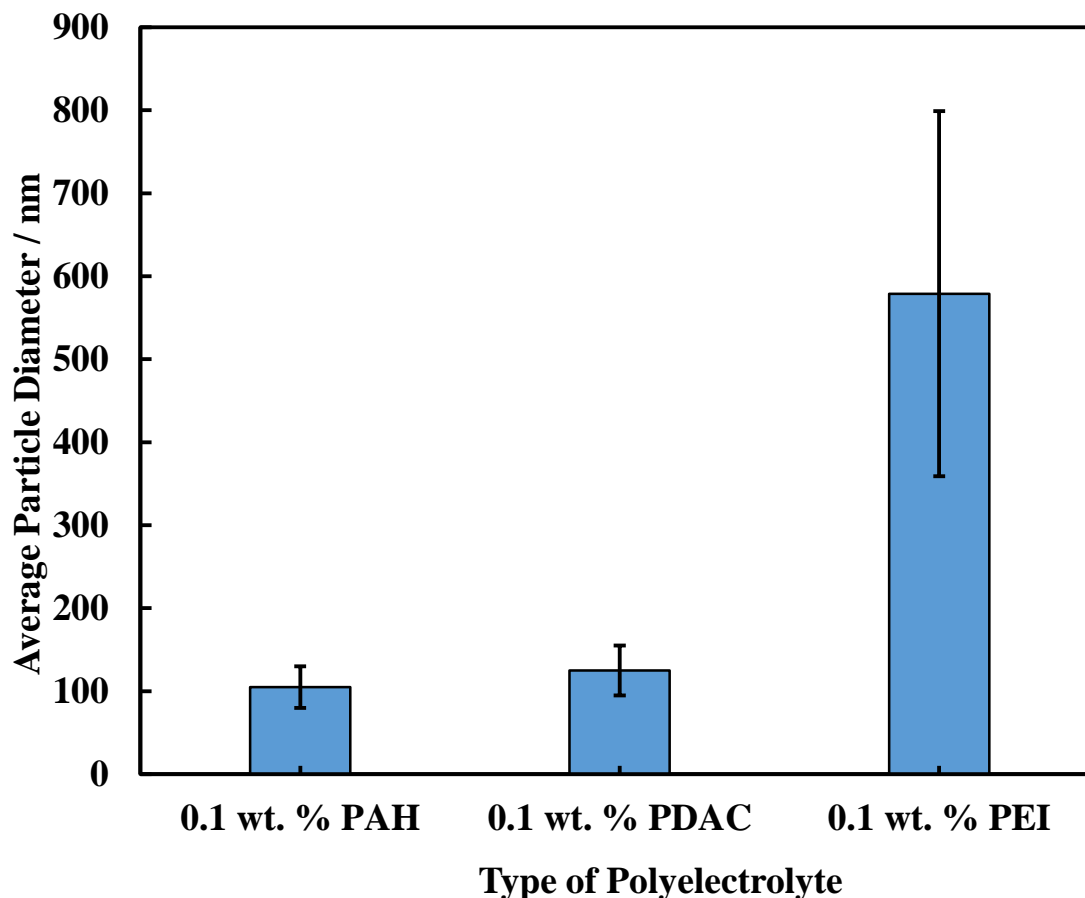


Figure 5.34: The average particle diameter of cationic polyelectrolyte functionalized Carbopol Aqua SF1 microgel versus the category of cationic polyelectrolyte. The experiment was achieved by mixing excess amount of either poly (allylamine hydrochloride) (PAH), or branched poly (diallyldimethylammonium) chloride (PDAC) or polyethyleneimine (PEI) with 0.1 wt. % Carbopol Aqua SF1 microgel, then gently stirred and ultra-sonicated for a minute.

In order to incubate the cationic polyelectrolyte PAH coated Carbopol Aqua SF1 microgel with microorganisms, they needed to be washed to remove any PAH polyelectrolyte not coating the particles as the free PAH would have a cytotoxic effect on the microorganisms. The suspension was therefore centrifuged for an hour at 10,000 rpm twice and washed each time before measuring the average particle diameter at each time. After the first wash, the average particle diameter was 106 nm with a zeta potential around 30 mV as shown in Figure 5.35.

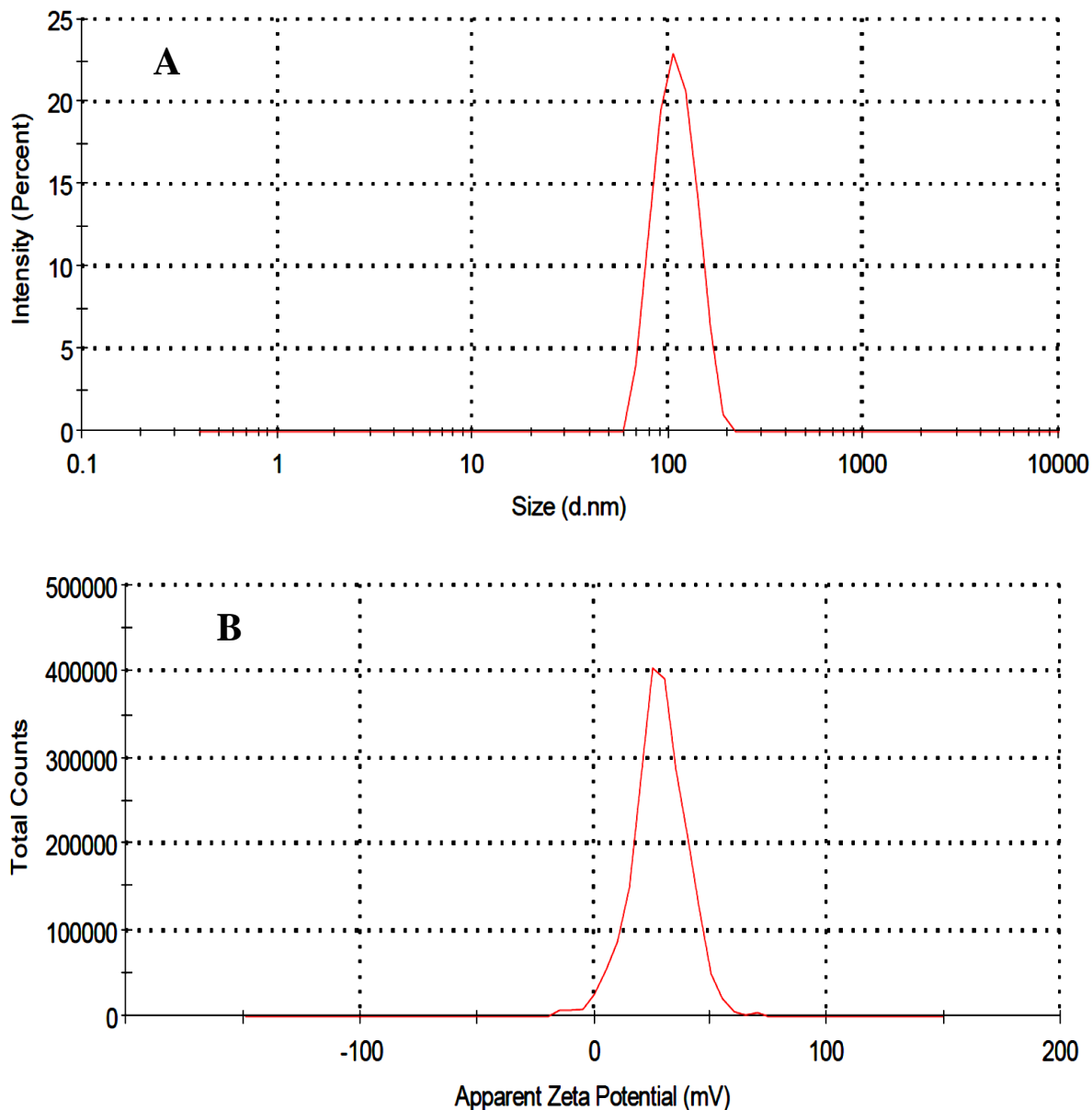


Figure 5.35: The average particle hydrodynamic diameter (A) and zeta potential (B) of PAH-coated Carbopol Aqua SF1 microgel at pH 5. This was achieved through mixing excess amount of solution of the cationic polyelectrolyte PAH with a fixed concentration of Carbopol Aqua SF1 suspension to form PAH-coated Carbopol Aqua SF1. The produced suspensions were stirred, ultra-sonicated and centrifuged once at 10,000 rpm for an hour.

Upon the second centrifugation, however as shown in Figure 5.36 that average particle diameter appeared too big at around 4 μ m and the zeta potential was -11 mV which means that the PAH-coating layer of carbopol microgel had washed off the particle and

was in the supernatant. Moreover, the coating of the microgel particles was damaged which did not allow them to be re-dispersed in the solution.

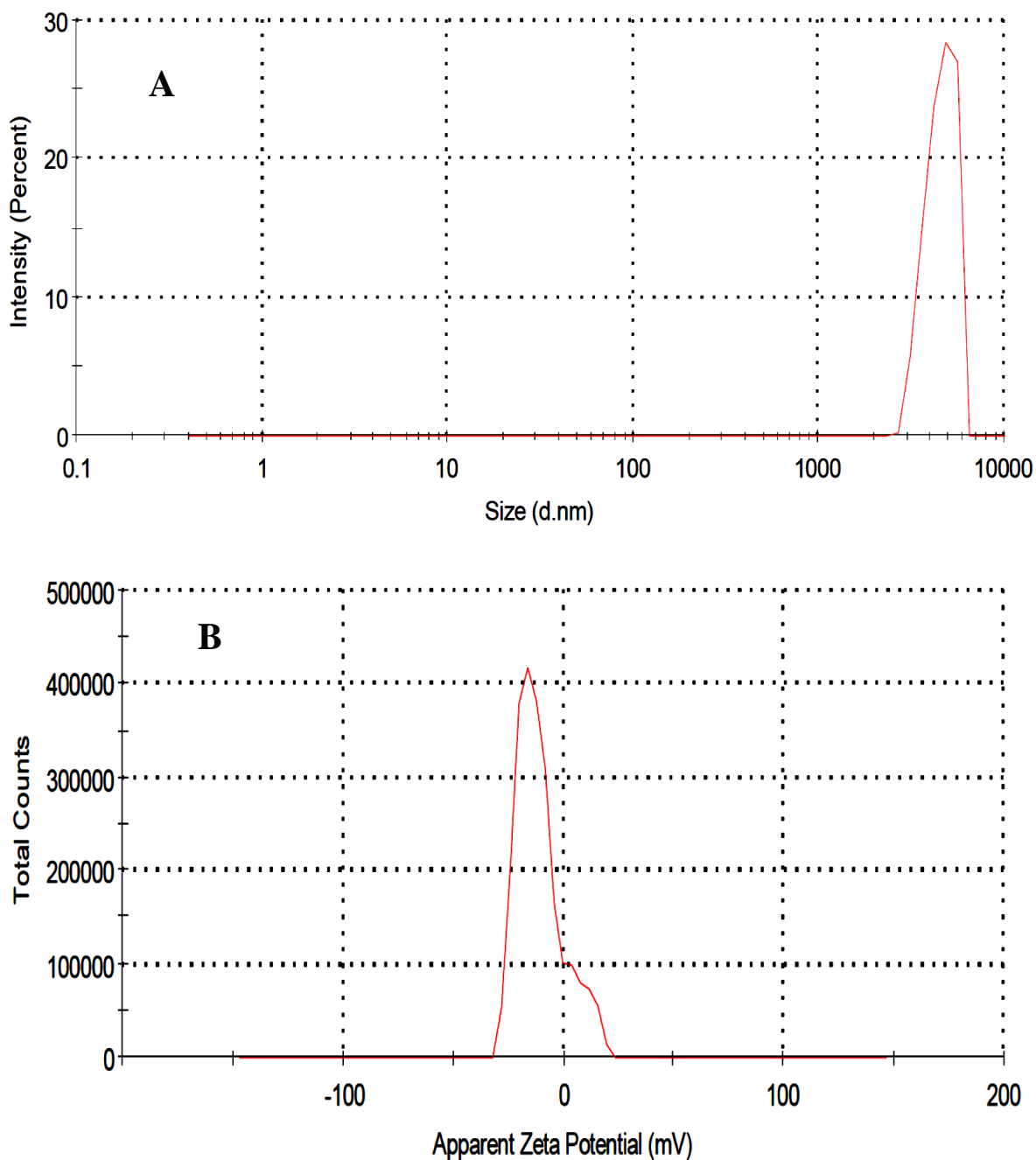


Figure 5.36: The average particle diameter (A) and zeta potential (B) of PAH-coated carbopol microgel at pH 5 which was conducted through stirring and ultra-sonicating of the suspension produced from the first centrifugation and then centrifuged again at 10,000 rpm for 1 hour.

5.7.1 Effect of PAH Concentration on Carbopol Coating

To overcome the problem outlined in the previous section, solutions of different concentrations of PAH were mixed with a solution with fixed concentration of Carbopol Aqua SF1 microgel to produce PAH-coated Carbopol Aqua SF1 microgel with equivalent amounts of cationic polyelectrolyte and Carbopol Aqua SF1 without any aggregation. Figure 5.37 shows the average particle hydrodynamic diameter and zeta potential of coated Carbopol Microgel as a function of PAH concentration. At 0.55 mg ml⁻¹ of PAH, the particle hydrodynamic diameter and zeta potential were 114 nm and -5 mV, respectively but for 1 mg ml⁻¹ PAH, the same parameters were 115 nm and -11 mV, respectively. Upon increasing the PAH concentration to 1.25 mg ml⁻¹, the particle size and zeta potential became 105 nm and +19 mV, respectively. Further increase in the concentration of PAH did not cause any pronounced change in the particle hydrodynamic diameter but the zeta potential kept increasing due to the increase in the ionic strength. 1.25 mg ml⁻¹ of PAH was selected as the optimal concentration to obtain maximum positive surface charge of the particle while maintaining the colloid stability of the PAH-coated carbopol microgel.

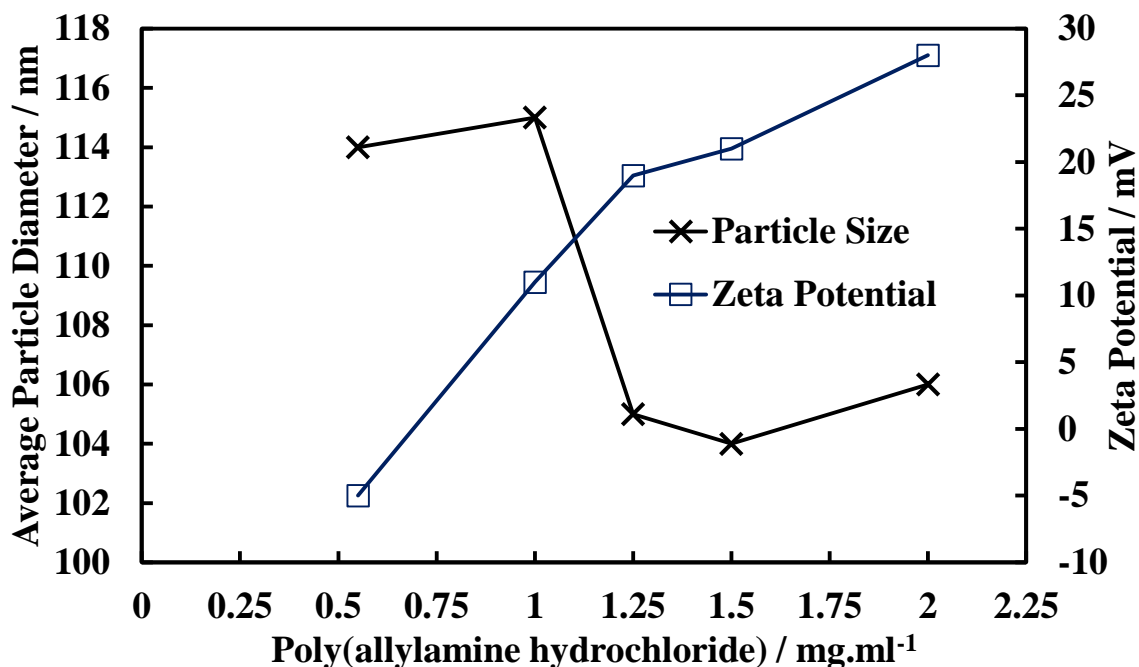


Figure 5.37: The average particle diameter and zeta potential of PAH coated Carbopol Aqua SF1 microgel as a function of PAH concentration in mg.ml⁻¹. The results were achieved through mixing different concentrations of PAH with 0.1 wt. % concentration of Carbopol microgel with gentle stirring and ultra-sonication for a minute.

5.7.2 Effect of the PDAC Concentration on the Carbopol Coating

The Carbopol Aqua SF1 microgel was also coated with the cationic polyelectrolyte PDAC by mixing solutions of different concentrations of PDAC with a solution of fixed concentration of Carbopol microgel to find a good balance between positive surface charge and colloidal stability of the PDAC-coated Carbopol microgel. Figure 5.38 depicts the average particle hydrodynamic diameter and zeta potential of PDAC-functionalized Carbopol microgel versus the PDAC concentration. Low concentrations of PDAC resulted in aggregation with low values for the zeta potential of around +12 mV while upon increase of the PDAC concentration up to 0.017 wt%, the average particle diameter and zeta potential of the PDAC-coated Carbopol were 228 nm and 15 mV, respectively. At 0.018 wt% PDAC concentration, the average particle size and zeta potential of Carbopol Aqua SF1 significantly decreased to 132 nm with a +18 mV. The particle diameter did not change for PDAC concentrations above 0.018 wt% but the zeta potential continued to increase to +44 mV at 0.1 wt% PDAC concentration. 0.018 wt% PDAC concentration was found to be the best compromise between positively charged microgel and colloidal stability of the PDAC-coated Carbopol Aqua SF1.

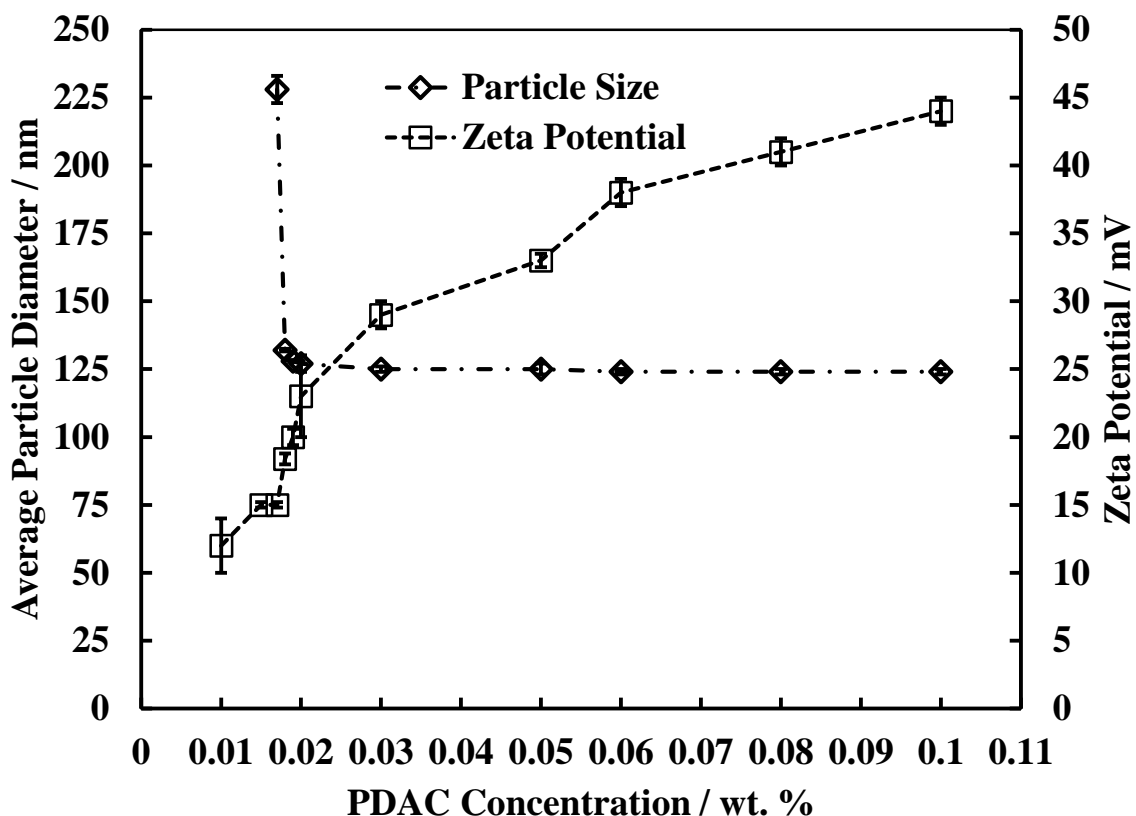


Figure 5.38: The average particle hydrodynamic diameter and zeta potential of PDAC-coated Carbopol Aqua SF1 suspension as a function of the PDAC concentration which were accomplished through mixing solutions of varied concentration of PDAC solutions with 0.1 wt% Carbopol microgel, followed by stirring and ultra-sonication for a minute. The particle diameter and zeta potential were measured by Malvern Zetasizer Nano ZS.

5.7.3 Cationic Functionalization of Antimicrobial-loaded Carbopol Microgel

PAH and PDAC are cationic polyelectrolytes which can kill microorganisms on their own through disrupting cell membranes¹⁶. In addition they can be utilized in promoting the adhesion of polyelectrolyte pre-coated particles to the cell membrane¹⁷ as well as to increase the antimicrobial activity of drug loaded nanoparticles.¹⁸. Both berberine-loaded Carbopol Aqua SF1 (BLC) and chlorhexidine-loaded Carbopol Aqua SF1 (CLC) were functionalized with PDAC to form PDAC-coated BLC and PDAC-coated CLC, respectively. Figure 5.39 and Figure 5.40 show the particle size distribution and zeta potential for both PDAC coated BLC- and PDAC-coated CLC. As shown in Figure 5.39

that the average particle diameter and zeta potential of PDAC coated BLC were 190 nm and +17 mV but 280 nm and +30 mV for PDAC coated CLC as stated in Figure 5.40.

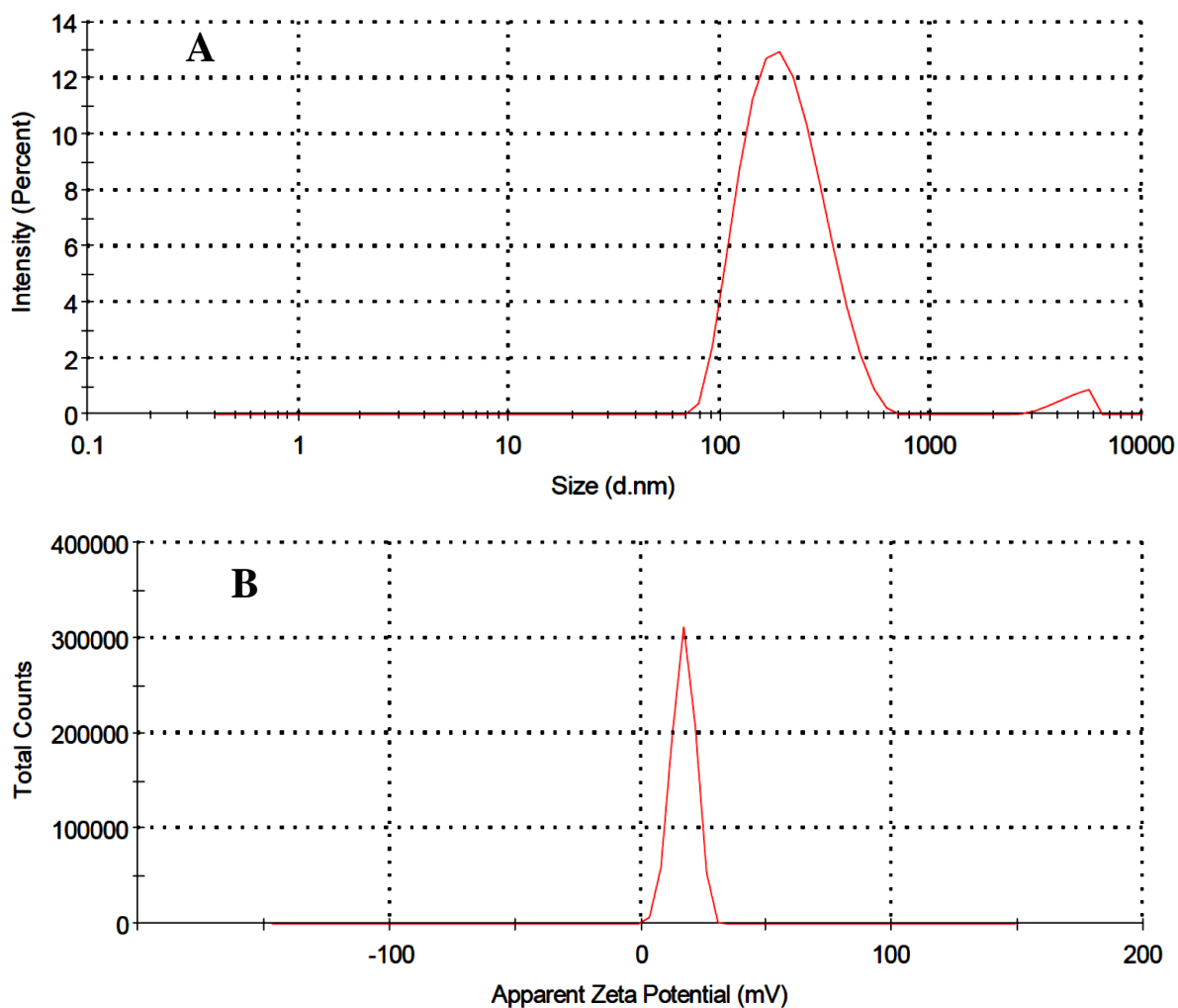


Figure 5.39: The particle size distribution (A) and zeta potential (B) of berberine-loaded carbopol coated with the cationic polyelectrolyte PDAC via addition of the cationic polyelectrolyte to the solution of berberine-loaded carbopol, followed by shaking of the solution for 5 minutes.

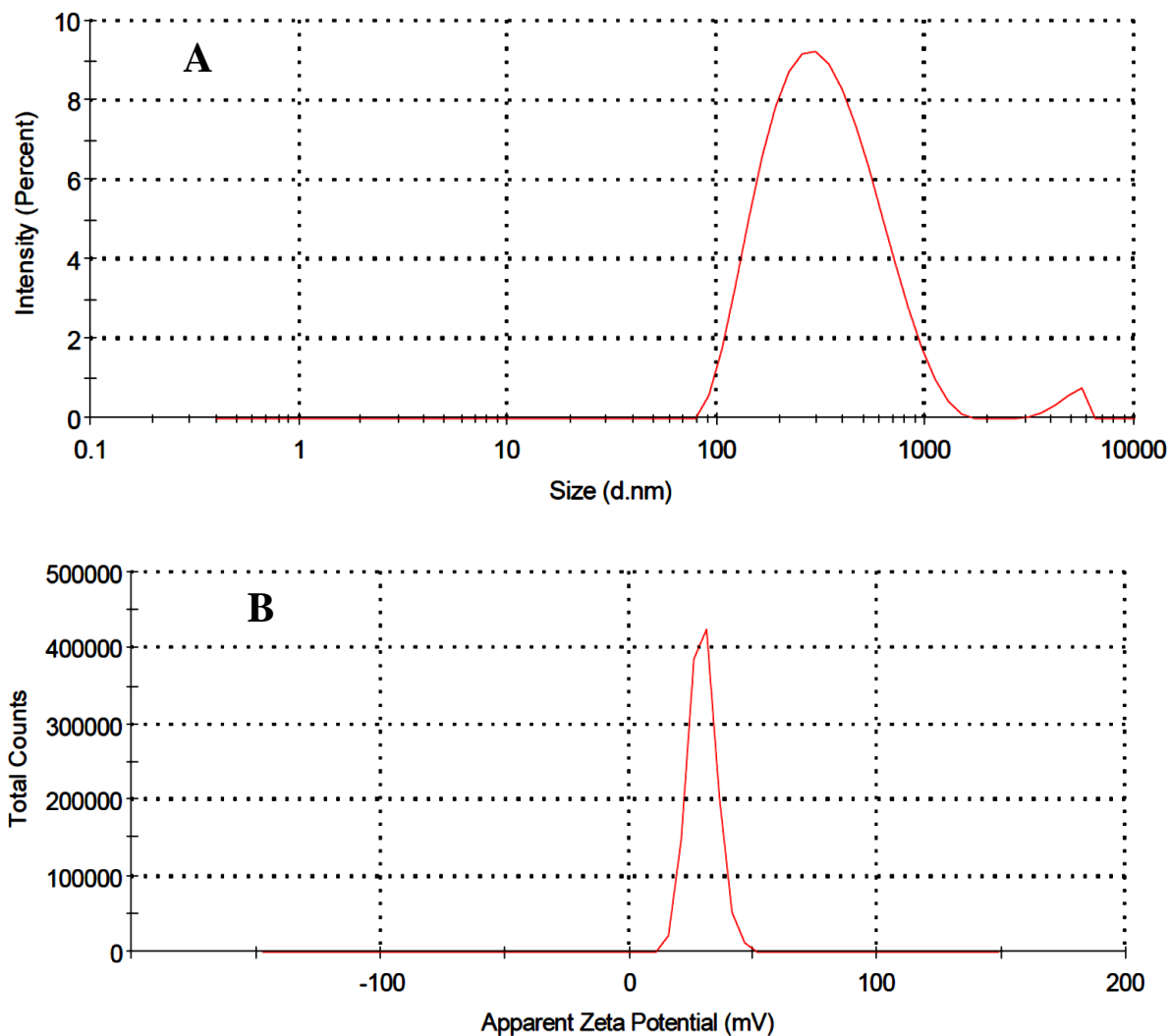


Figure 5.40: The particle size distribution (A) and zeta potential (B) of chlorhexidine-loaded carbopol coated with the cationic polyelectrolyte PDAC via addition of the cationic polyelectrolyte to the solution of Chlorhexidine-loaded carbopol, followed by shaking of the solution for 5 minutes.

It can be concluded that carbopol microgel has two refractive index according to the change in pH where the refractive index is 1.45 in case of collapsed carbopol microgel while it is 1.339 for the swelled microgel. The results also indicated that carbopol microgel can be used as a nanocarrier for drug delivery through encapsulation of berberine and chlorhexidine individually with high stability and improved drug release. It also indicated that the encapsulated berberine or chlorhexidine into carbopol microgel has the ability to be coated with cationic polyelectrolyte such as PAH and PDAC to increase the antimicrobial actions.

Bibliography

1. C. A. Lubrizol, *Noveon Consumer Specialties, Technical Data Sheet*, 2007, **294**.
2. A. Hirao, K. Sugiyama, Y. Tsunoda, A. Matsuo and T. Watanabe, *Journal of Polymer Science Part A: Polymer Chemistry*, 2006, **44**, 6659-6687.
3. T. M. Riddick, *Blood*, 1968, **10**, 1.
4. A. Kuo and Z. Pu, *Polymer Data Handbook*, 1999.
5. J. Kotz, P. Treichel and J. Townsend, *Chemistry and chemical reactivity*, Cengage Learning, 2011.
6. S. Bontha, A. V. Kabanov and T. K. Bronich, *Journal of controlled release*, 2006, **114**, 163-174.
7. S. Sahoo, C. K. Chakraborti and S. C. Mishra, *Journal of advanced pharmaceutical technology & research*, 2011, **2**, 195.
8. M. Moharram and M. Khafagi, *Journal of applied polymer science*, 2007, **105**, 1888-1893.
9. P.-L. Lam, K. K.-H. Lee, S. H.-L. Kok, G. Y.-M. Cheng, X.-M. Tao, D. K.-P. Hau, M. C.-W. Yuen, K.-H. Lam, R. Gambari and C.-H. Chui, *Soft Matter*, 2012, **8**, 5027-5037.
10. S.-J. Wu, T.-M. Don, C.-W. Lin and F.-L. Mi, *Marine drugs*, 2014, **12**, 5677-5697.
11. S. K. Battu, M. A. Repka, S. Maddineni, A. G. Chittiboyina, M. A. Avery and S. Majumdar, *Aaps Pharmscitech*, 2010, **11**, 1466-1475.
12. L. Wang, H. Li, S. Wang, R. Liu, Z. Wu, C. Wang, Y. Wang and M. Chen, *AAPS PharmSciTech*, 2014, **15**, 834-844.
13. A. Kovtun, D. Kozlova, K. Ganesan, C. Biewald, N. Seipold, P. Gaengler, W. H. Arnold and M. Epple, *RSC Advances*, 2012, **2**, 870-875.
14. K. Garala, P. Joshi, M. Shah, A. Ramkishan and J. Patel, *International journal of pharmaceutical investigation*, 2013, **3**, 29.
15. P. Larkin, *Infrared and Raman spectroscopy; principles and spectral interpretation*, Elsevier, 2011.
16. T. A. Kolesnikova, I. A. Fedorova, A. A. Gusev and D. A. Gorin, *Nanotechnol Russia*, 2011, **6**, 244-255.
17. S. Kidambi, N. Udpa, S. A. Schroeder, R. Findlan, I. Lee and C. Chan, *Tissue engineering*, 2007, **13**, 2105-2117.
18. A. P. Richter, J. S. Brown, B. Bharti, A. Wang, S. Gangwal, K. Houck, E. A. C. Hubal, V. N. Paunov, S. D. Stoyanov and O. D. Velev, *Nature nanotechnology*, 2015, **10**, 817-823.

6 Chapter Six: Antimicrobial Formulated in Nanocarriers: An Introduction

In the previous chapter, we developed a new protocol for loading of Carbopol Aqua SF1 microgels with two different antimicrobial agents, berberine and chlorhexidine and studied their properties in terms of optimization of their colloid stability, encapsulation efficiency and drug release. In this chapter, we examine the cytotoxic effect of Carbopol Aqua SF1 microgels after loading with antibacterial agents on microorganisms such as microalgae, yeast and *E.coli*. The study is complemented with an investigation into the antimicrobial activity of both berberine and chlorhexidine on these microorganisms at identical conditions as a reference for comparison with the microgel-formulated antimicrobials. Finally, the antimicrobial activity of cationic polyelectrolyte coated Carbopol microgels loaded with berberine or chlorhexidine was examined upon incubation with algae, yeast and *E.coli*. The aim of this work being to develop microgel-formulated antimicrobials in attempt to produce sustained release of antimicrobials as well as increase the antimicrobial activity of both berberine and chlorhexidine by their encapsulation at very low overall concentrations into Carbopol Aqua SF1 microgel particles. All cell viability experiments were conducted at room temperature through incubation of the Carbopol microgel with culture media free cells at pH 5.5 for up to 6 hours. Then a millilitre of the cell sample was pipetted, washed, centrifuged, and dispersed in Milli-Q water. After that, one drop of 5 mg ml⁻¹ FDA solution was added to the dispersed sample, the sample was shaken for 10 minutes, centrifuged twice and dispersed with Milli-Q water. A 20 µl of resulted sample was pipetted and placed in a chamber for cell counting. The cell viability assessment was done by using Cellometer Auto X4 based on the fluorescence of the FDA in-vivo hydrolysis (see Chapter 2 for more details).

6.1 Cytotoxicity Assay of Carbopol Aqua SF1 Microgel

Cytotoxic experiments were conducted through the incubation of suspensions of different concentrations of Carbopol microgel particles with a range of test microorganisms: *C.reinhardtii* (microalgae), *S.cerevisiae* (baker's yeast) and *E.coli*. The protocol used here was similar to that mentioned in Section 4.1, however, it included the incubation of Carbopol microgel suspensions with cells removed from the culture media to avoid any

interaction between Carbopol Aqua SF1 particles of culture media components. Figures 6.1 to 6.3 represent the cytotoxic effects of Carbopol Aqua SF1 microgel without any antimicrobial additives on *C.reinhardtii*, *S. cerevisiae*, and *E. coli*, respectively. As seen from Figure 6.1, we did not observe cytotoxic effect on the microalgae cells upon incubation with series of suspensions of different concentrations of Carbopol Aqua SF1 at room temperature and up to six hours incubation time. Similar results were obtained (Figure 6.2) for yeast with no measurable cytotoxic effect for 24 hours incubation time for solutions of different concentration of Carbopol Aqua SF1 microgel. Figure 6.3 also shows no pronounced cytotoxic effect of the unloaded microgel particles on *E.coli* cells. These results prove that Carbopol Aqua SF1 microgel does not apparently affect the viability of these microorganisms for the duration of these incubation experiments. Our results are in agreement technical data sheet provided by the manufacturer of this Carbopol microgel.¹

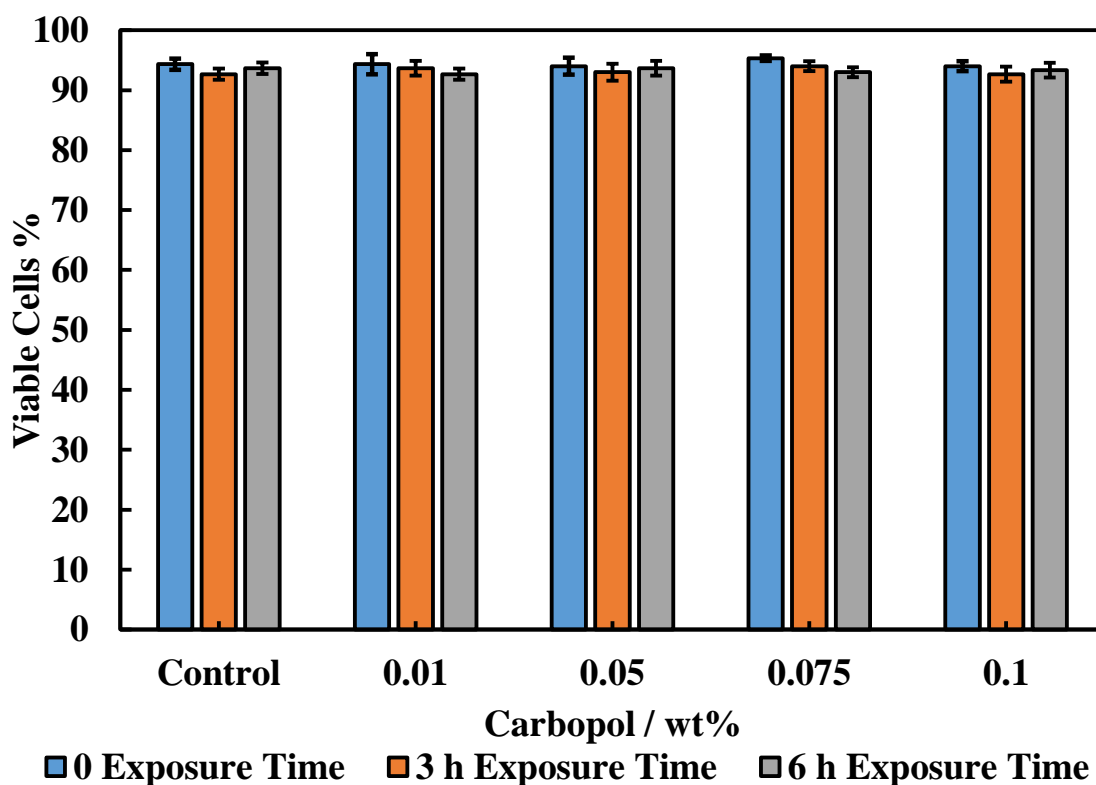


Figure 6.1: The change in cell viability of *C.reinhardtii* cells incubated in aqueous suspensions of varying concentrations of Carbopol Aqua SF1 microgel particles. The experiment was conducted at room temperature through incubation of Carbopol solutions with culture media free algal cells at pH 5.5 for up to 6 hours. The cells were washed by centrifugation and tested with FDA cell viability assay as described above.

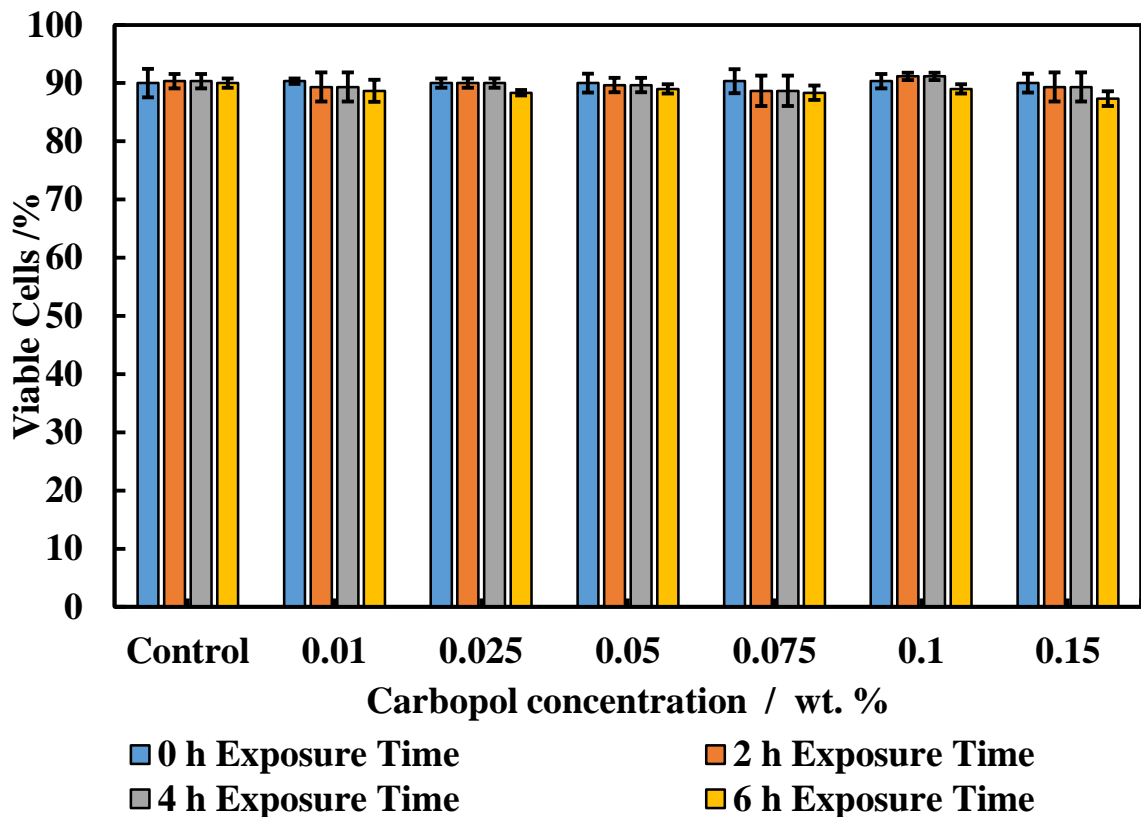


Figure 6.2: The cytotoxic effect of Carbopol Aqua SF1 on yeast cells whereby the cells were incubated with suspensions of different concentrations of Carbopol Aqua SF1 microgel particles at pH 5.5 at room temperature up to 24 hours. The cells were washed by centrifugation and tested with FDA cell viability assay as described above. .

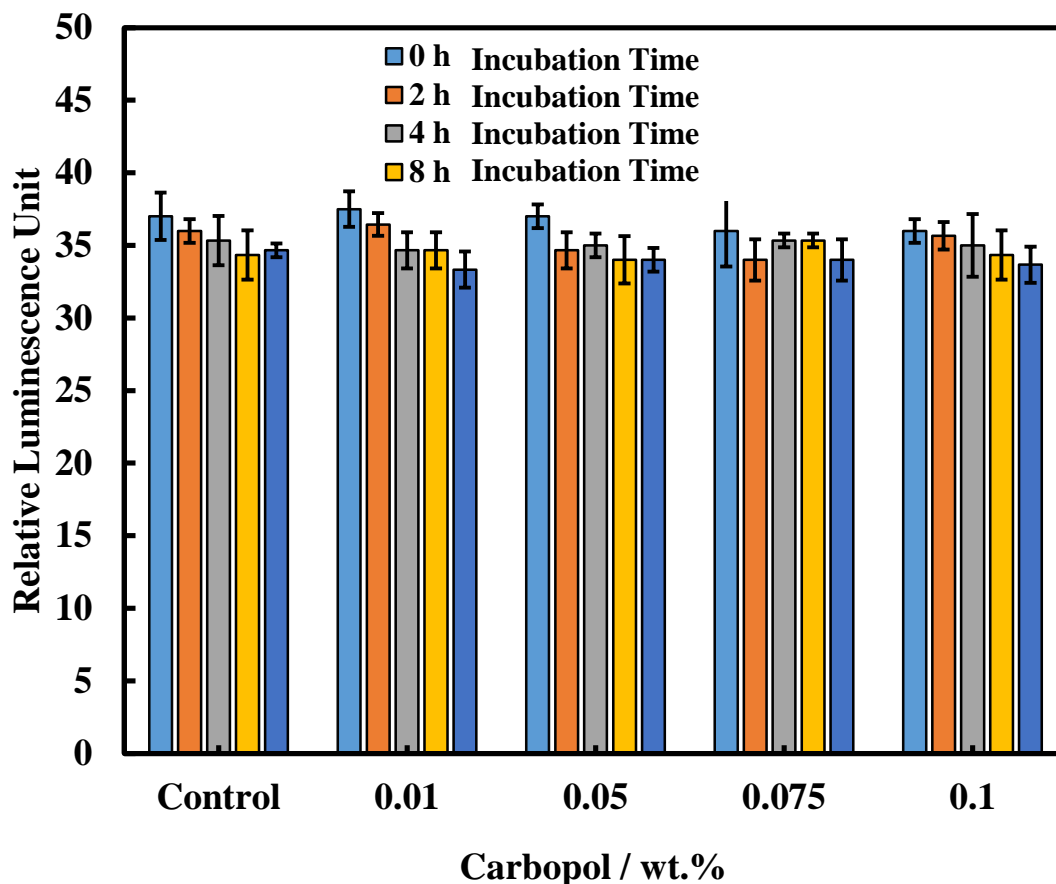


Figure 6.3: The cytotoxic effect of suspensions of different concentration of Carbopol Aqua SF1 microgel particles on *E. coli* cells at different incubation times. The experiment was conducted by incubation of the cells with solutions of different concentrations of Carbopol Aqua SF1 at pH 5.5 at room temperature for up to 24 hours. The assay was performed by pipetting a milliliter of the sample, washing, centrifuging and dispersing with Milli-Q water. After that, 100 μL of each sample was placed in 96-microwell plate and then, 100 μL leuciferin reagent was added to the 100 μL sample, shaken for 30 seconds, and incubated for 5 minutes at 25 $^{\circ}\text{C}$. The relative luminescence intensity which represents the percentage of viable cells was measured using a Luminometer.

6.2 TEM Image of Cells Incubated with Carbopol Microgel

The morphology of microalgae and yeast cells was studied by TEM. Through observation of the microstructure of these cells, the potential cytotoxic effects due to the incubation of the cells in suspensions of Carbopol Aqua SF1 microgel particles could be detected. Figure 6.4 shows the TEM images of microalgae cells incubated for 24 hours with 0.1 wt. % Carbopol Aqua SF1 microgel at pH 5.5. As seen in Figure 6.4B, the organelles of microalgae cells seem more or less intact in terms of chloroplast, nucleus and cell

membrane and that there was no visible disruption in the microstructure of the cells compared with the control sample as shown in Figure 6.4A.

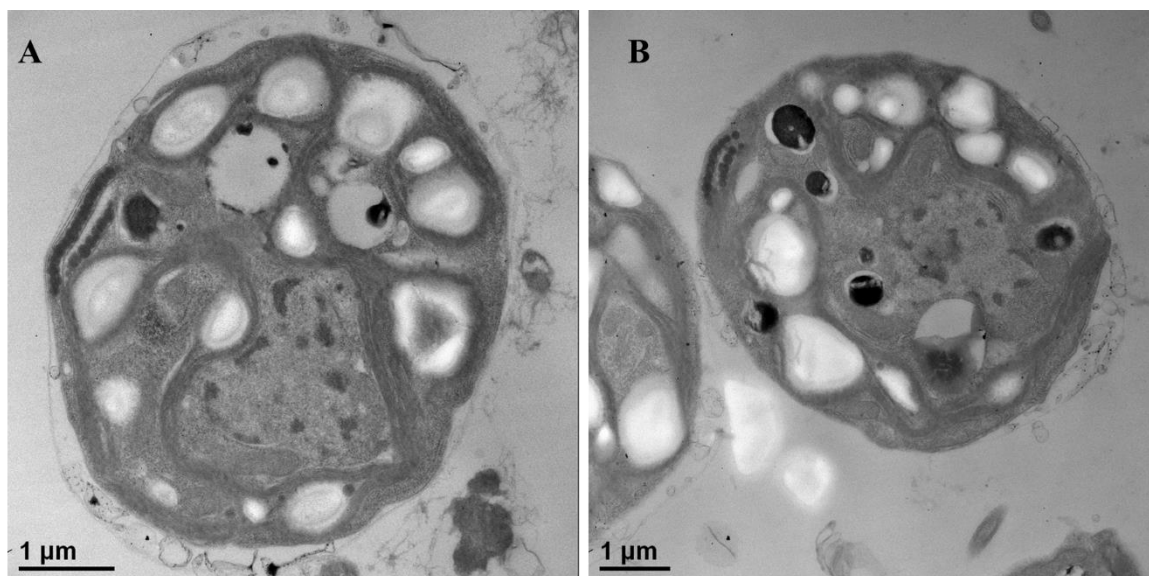


Figure 6.4: The TEM images of *C. reinhardtii* cells after incubation with 0.1 wt% Carbopol Aqua SF1 microgel. The TEM imaging was conducted with the similar way as it was mentioned in Section 2.2.7. Briefly, the cells were centrifuged at 500 rpm, washed with Milli-Q water, fixed in 2 wt% glutaraldehyde for 1 hour at room temperature, then treated with 1 wt% osmium tetroxide for 1 hour, followed by treatment with 2.5 wt% uranyl acetate for 1 hour and washed with solutions of different concentrations of ethanol. After that, the cell were embedded in fresh epoxy/araldite for 48 hours at 60 °C, left at room temperature for further 48 hours and sectioned using an ultra-microtome. The images were taken by using JOEL TEM machine.

The morphology of yeast cells was also investigated by capturing TEM and SEM images for cells that have been incubated with 0.15 wt% Carbopol Aqua SF1 microgel as seen in Figure 6.5. It can be seen in Figure 6.5B that the microstructures inside the yeast cells do not seem to change compared with the control sample, Figure 6.5A. The SEM images Figure 6.5C show the control yeast sample and Figure 6.5D shows a yeast cell after being incubated with Carbopol. We did not observe visible differences between the control sample and that of the Carbopol-exposed cell with respect to their outer cell membrane. These images suggest that Carbopol Aqua SF1 microgel does not have detectable cytotoxic effect at concentrations up to 0.15 wt% on both microalgae and yeast cells.

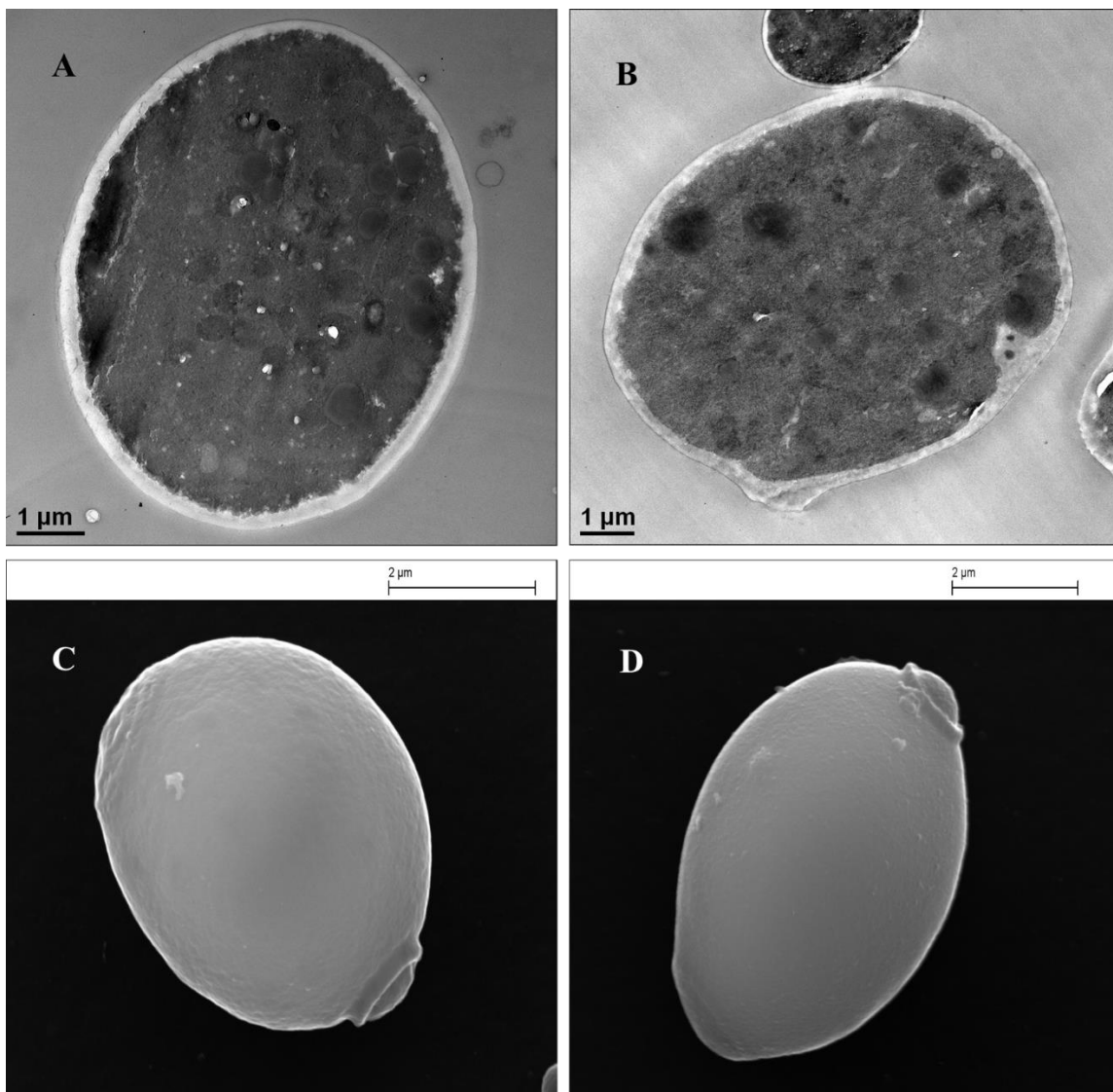


Figure 6.5: The TEM (A-B) and SEM (C-D) images of yeast cells incubated with a specific concentration of Carbopol Aqua SF1/ microgel at pH 5.5 for 24 hour incubation time. The experiment was conducted as described in Section 2.2.7. (A) TEM image of the control sample, (B) TEM image of the yeast cells after incubation in 0.15 wt% Carbopol Aqua SF1 for 24 hours, (C) SEM image of the control sample of yeast and (D) SEM image of yeast cell after incubation in 0.15 wt% Carbopol Aqua SF1 for 24 hours.

6.3 Antimicrobial Activity of Berberine-Loaded Carbopol (BLC)

The antimicrobial activity of free berberine and berberine-loaded Carbopol Aqua SF1 microgel on several microorganisms such as *C. reinhardtii* (microalgae), *S. cerevisiae* (yeast) and *E. coli* was studied. This approach might be helpful to boost the antimicrobial activity of berberine using very low overall concentrations encapsulated into Carbopol Aqua SF1 microgels. The next three sections 6.3.1, 6.3.2, and 6.3.3 describe the

investigation into the antimicrobial efficiency of berberine-loaded Carbopol Aqua SF1 with microalgae, yeast and E.coli in comparison with free berberine.

6.3.1 Antimicrobial Activity of Berberine Loaded Carbopol (BLC) on Algae

In order to increase the antimicrobial activity of berberine, a new method for encapsulating berberine into Carbopol aqua SF1 microgel was developed by using the swelling / shrinking of the microgel particles stimulated by a pH change.

Initially microalgae cells were separated from the culture media by centrifugation and a fixed amount of cells were incubated in solutions of different concentrations of free berberine at pH 5.5 supported using acetate buffer. The cell viability was then measured at different incubation times using FDA viability assay as described in Chapter 2 by an automatic cell counter. Figure 6.6 shows the cell viability of the microalgae as a function of free berberine concentration. The viability of the algal cells immediately upon incubation (0 hours) gradually declined from low to high berberine concentrations, (85% at 0.001 wt. % to around 10 % at 0.05 wt. %). After 2 hours incubation time the algal cells viability sharply decreased in comparison with the control sample with 0.05 wt. % being the minimal berberine concentration which kills all the cells, 5% viable algal cells were found at the concentration of 0.01 wt. % berberine after 2 hours incubation time. After 4 hours of incubation, the viability was significantly reduced to 20 % at 0.001 wt% berberine concentration and by 6 hours incubation time, no viable cells were observed at berberine concentrations from 0.007 wt% to 0.05 wt% while the viability went down to 15 % at 0.001 wt% berberine. This demonstrates that berberine tends to be an effective antimicrobial agent at moderate concentrations over sufficiently long period of time.

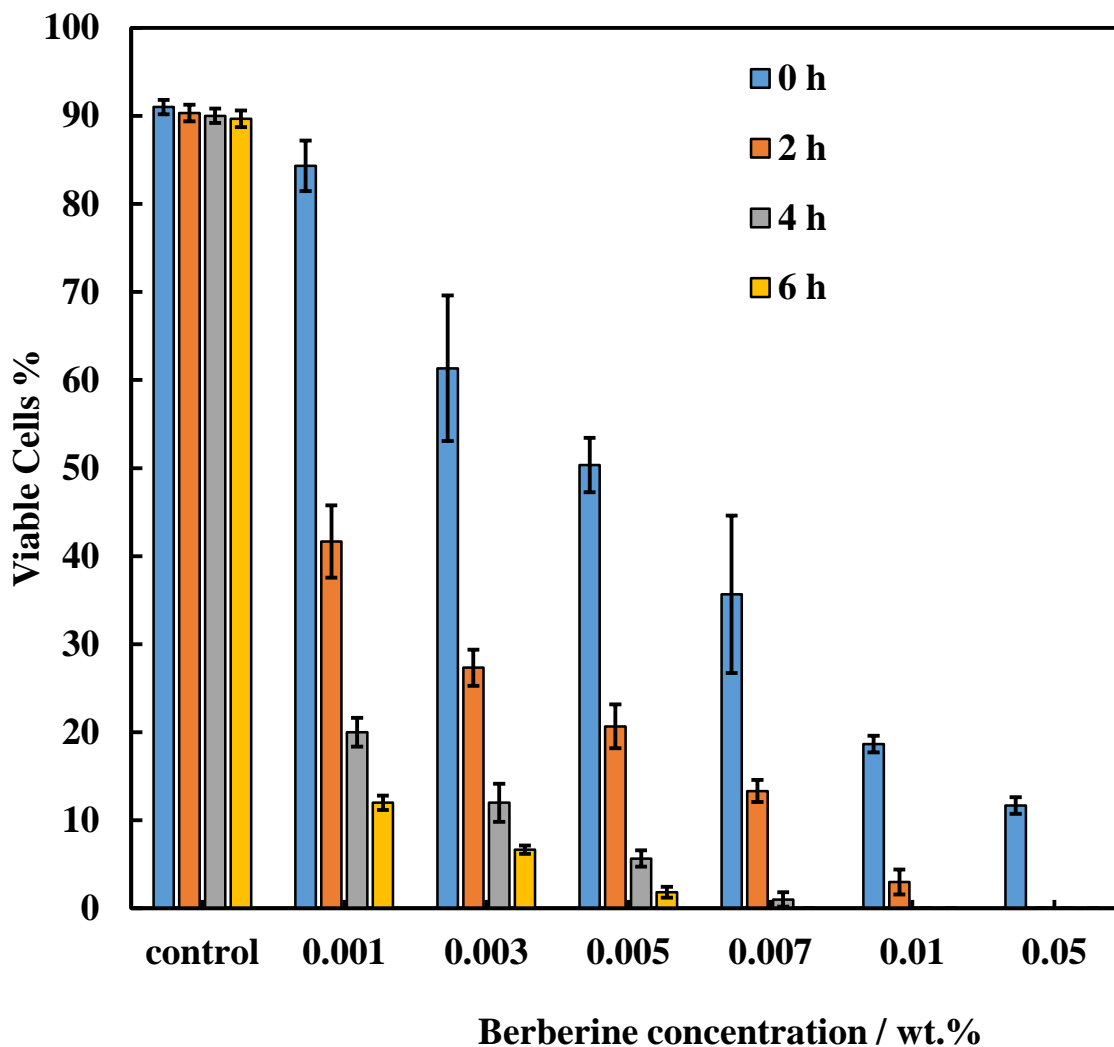


Figure 6.6: The viability of *C. reinhardtii* cells incubated with solutions of different concentrations of berberine at different incubation times. The pH of the solution was adjusted with acetate buffer solution (pH 5.5) to avoid any change in pH upon incubation. The incubation was conducted through mixing a solution of specific concentration of berberine with a fixed amount of culture media free microalgae cells in a 20 mL glass vial capped with cotton plug and placed in an incubator to avoid contamination. A 1.0 mL of each sample was pipetted, cells were centrifuged and washed with Milli-Q water and their viability was tested using FDA assay.

It also studied the same microalgae cells viability after being incubated with solutions of different overall concentrations of encapsulated berberine into Carbopol microgel. In Sections 5.8 and 5.9 the encapsulated berberine had been shown to have an encapsulation efficiency of around 10% with 65% of the total amount of berberine released at pH 5.5 over 24 hours. To avoid any interaction between the berberine-loaded Carbopol microgel

and components of culture media, the algal cells were washed prior to the experiments. Figure 6.7 shows the results for the viability of the microalgae cells when incubated with solutions of different concentrations of microgel-encapsulated berberine at room temperature with incubation time up to 2 hours. Figure 6.7 shows that the cell viability decreased slightly up to 0.005 wt% encapsulated berberine and then gradually declined from 0.0075 wt. % to 0.01 wt. % of encapsulated berberine at zero incubation time. Zero incubation time experiments corresponds to the cells mixed up with the berberine formulation and then immediately washed and tested with FDA assay. After 1 hour incubation time the cell viability was reduced progressively from 60% to 20% at 0.01 wt. % average encapsulated berberine.

After 2 hours incubation time, however, the viability decreased sharply from 37% at 0.001 wt% to 7% viability at 0.0025 wt% average encapsulated berberine, respectively. At concentrations above 0.01 wt. % all the cells were dead. Comparing the results for free berberine (Figure 6.6) and berberine-loaded Carbopol (Figure 6.7) encapsulation appeared to increase the antimicrobial activity of the berberine. This is because by encapsulating the berberine in the Carbopol Aqua SF1 microgel a concentrated local dose of berberine is delivered when a microgel particle is deposited to the outer cell membrane. This increases in the antimicrobial action attributed to the release of higher amount of berberine from the loaded Carbopol microgel on the membrane and possibly inside cytoplasm of the cell through formation of endosomes of berberine-loaded Carbopol microgel through endocytosis process, in which berberine molecules can be subsequently released in the cell cytoplasm leading to cell death. In addition to this antimicrobial mechanism, the locally increased berberine concentration leads to disruption of the outer membrane whose opening can also lead to the cell death. Thus, all these reasons increased the antimicrobial efficiency of berberine agent.

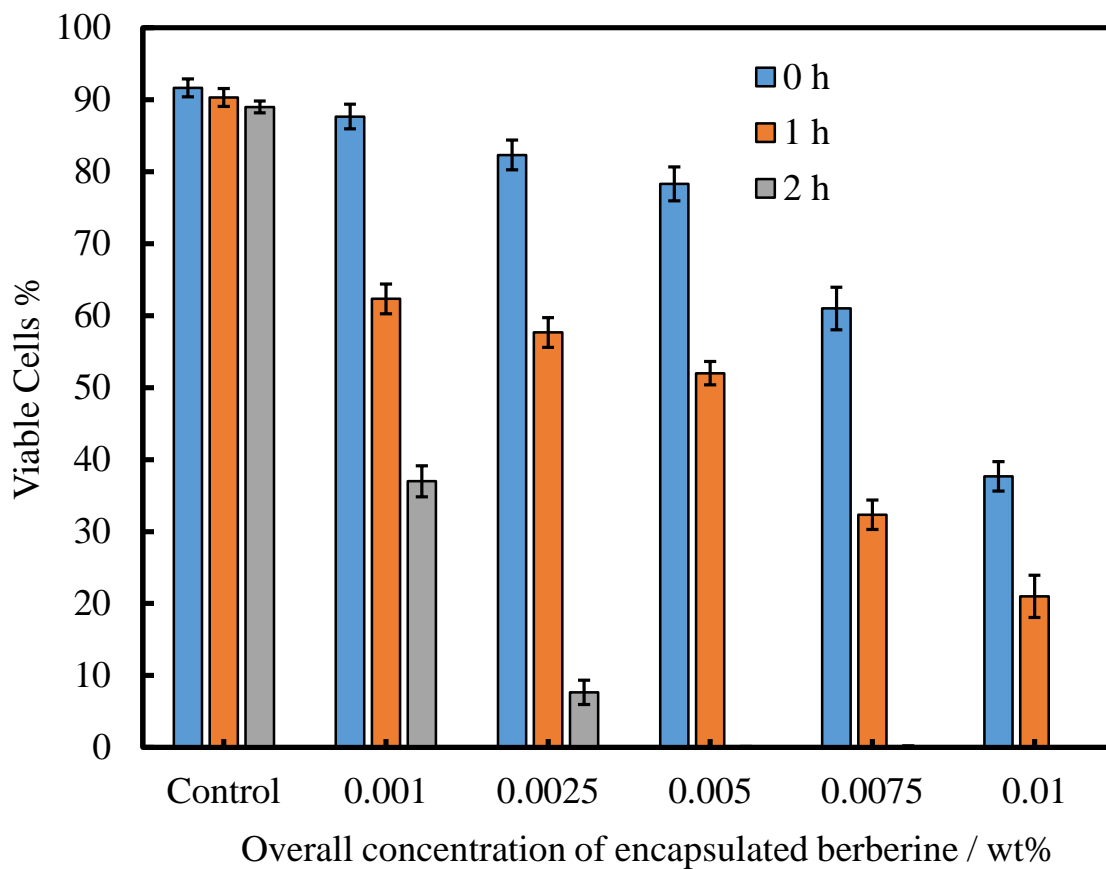


Figure 6.7: The viability of *C. reinhardtii* cells incubated with solutions of series of different overall concentration of berberine loaded into Carbopol Aqua SF1 microgel after different incubation times. The incubation was conducted at pH 5.5 by mixing a solution of a specific overall concentration of berberine loaded into Carbopol microgel with a fixed amount microalgae cells removed from the culture media in a 20 mL glass vial capped with a cotton plug and placed in an incubator to avoid contamination. A 1.0 mL of each sample was pipetted, washed with Milli-Q water and the viability was tested using FDA assay.

SEM images were taken of *C. reinhardtii* algal cells after incubation with 0.01 wt. % encapsulated berberine into Carbopol microgel for 2 hours as shown in Figure 6.8. It can be seen that the morphology of the cells had changed and showed irregular shapes as well as detachment of the flagella was observed for the treated algal cells (see fig. 6.8B, C, and D) in comparison with the control sample (Figure 6.8A). This change in the morphology might be attributed to the interaction between the cell membrane and berberine loaded Carbopol Aqua SF1 microgel to form endocytic cargos using clathrin/actin mediated-endocytosis² for these particles, which pass through the cell membrane and can potentially release more berberine inside the cytoplasm. Figure 6.9 shows schematic diagram of the interaction between berberine loaded Carbopol Aqua SF1 particles and the membrane of

cells and also details the mechanism of berberine released from the microgel particles loaded with the active material leading to the cell death. Note the dimples left on the cell membrane of the treated whose size matches approximately the size of the collapsed microgel particles. One may conclude that the cells treated with encapsulated berberine have been disrupted by one or more microgel particles attachment to their membrane. The curving of the membrane suggests that endocytosis of the berberine-loaded particles may also be a viable mechanism for antimicrobial action.

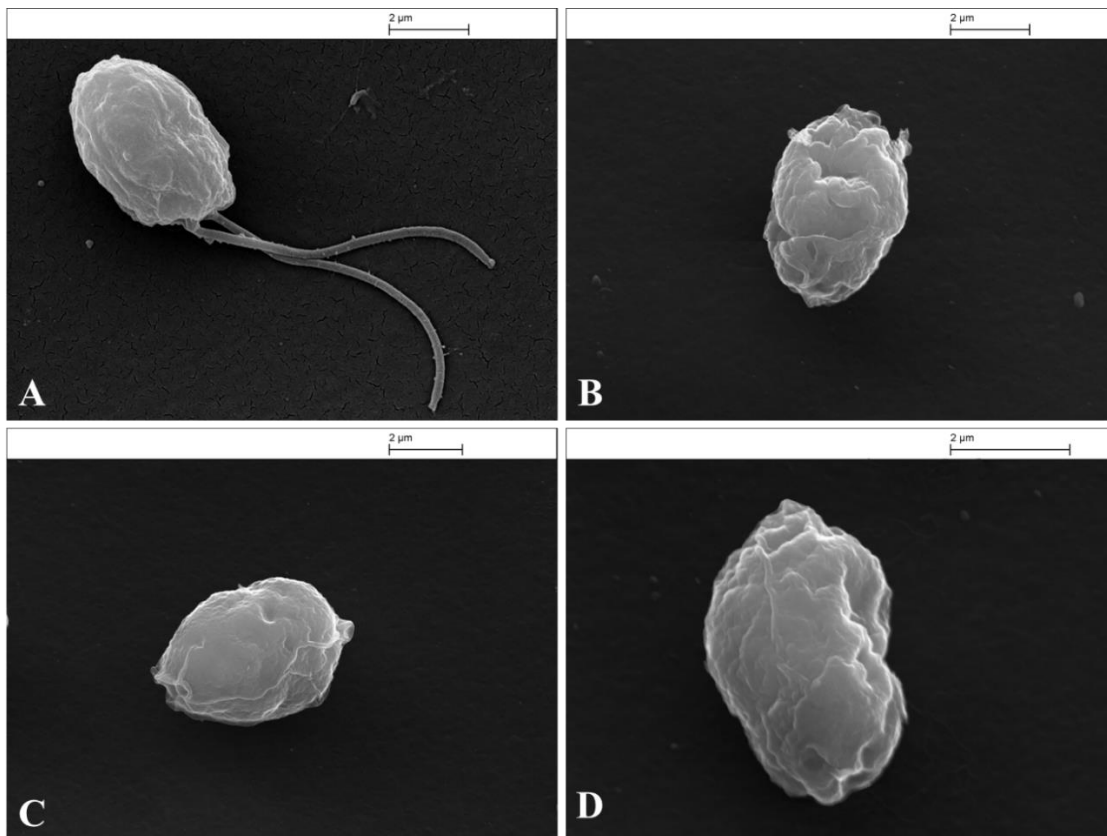


Figure 6.8: SEM images of *C.reinhardtii* cells upon incubation with 0.01 wt% encapsulated berberine into Carbopol Aqua SF1 particles whereby (A) represents the control sample and (B, C, and D) show the incubated cells with 0.01 wt% berberine loaded Carbopol Aqua SF1 for 2 hours. These cells were pre-treated after incubation as described in section 2.2.8.

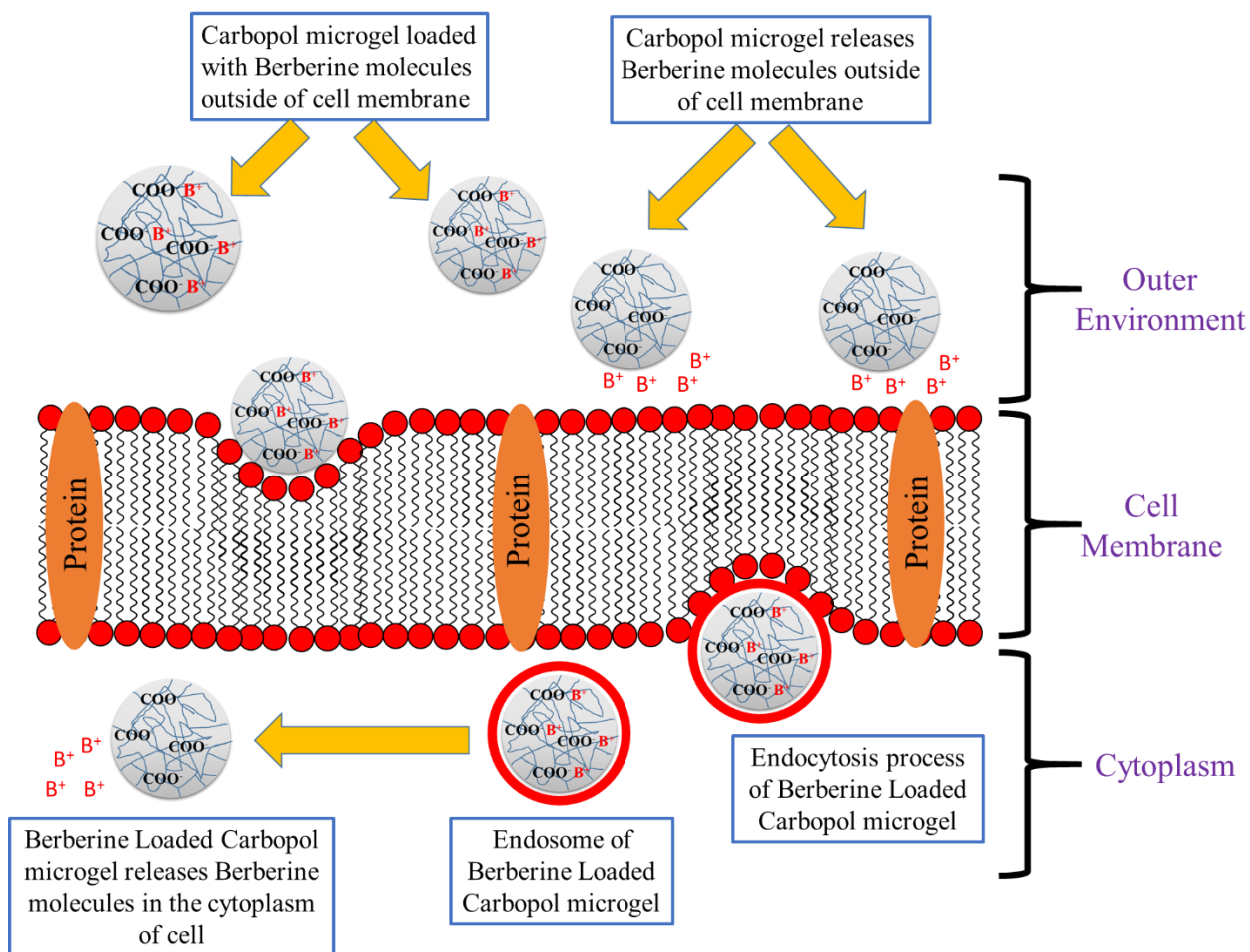


Figure 6.9: Schematic for the release of berberine from Carbopol microgel through direct diffusion in the outer cell membrane of cell as well as by the internalization of berberine-loaded Carbopol microgel through the cell membrane forming endosome of berberine loaded microgel particle by endocytosis whereby berberine molecules can be further released inside the cell's cytoplasm.

6.3.2 Antimicrobial Activity of Berberine-Loaded Carbopol (BLC) on Yeast

The antimicrobial activity of free berberine on yeast was studied through incubation of solutions of different concentrations of berberine with yeast cells removed from the culture media following same procedure as described for berberine with microalgae above (Figure 6.10). The study was conducted at room temperature and for incubation times up to 6 hours. It can be seen that free berberine did not appear to have any antimicrobial activity compared to the control sample where no berberine was used.

The antimicrobial activity of berberine-encapsulated into Carbopol Aqua SF1 microgel was then assessed with yeast at different incubation time. Figure 6.11 shows the results for the viability of yeast cells versus a range of overall concentrations of microgel-encapsulated berberine at various incubation times. It can be seen that the berberine encapsulated into the microgel also had no antimicrobial effect towards yeast cells, and these results are comparable with those for free berberine (Figure 6.10). The reason behind that is that the yeast cells have a very thick and rigid shell of glycoproteins around their cell membrane. This can be also be seen on the TEM images of incubated yeast cells after incubation with free and encapsulated berberine (Figure 6.12). The internal microstructure of the yeast cells seems undamaged and appears similar to the control sample. Interestingly, however the SEM images of yeast cells incubated with free and encapsulated berberine (Figure 6.13) did however display slight shrinkage of the outer cell membrane which means that berberine had affected the yeast cells but the cells have stayed viable along the incubation time (see Figure 6.13B) while at low concentration of encapsulated berberine (0.001 wt%), the SEM images of the treated cells showed no significant effect behind this incubation as shown in Figure 6.13C. Figure 6.13D, 6.13E, and 6.13F also showed that Carbopol Aqua SF1 microgel particles are being trapped on the surface of yeast cells, which explains that either Carbopol Aqua SF1 diffuses berberine outside of the cell or internalizes inside the cell through endocytosis process according to clathrin/actin mediated-endocytosis pathway³ which is as shown in Figure 9 for the antimicrobial activity of encapsulated berberine into algae.

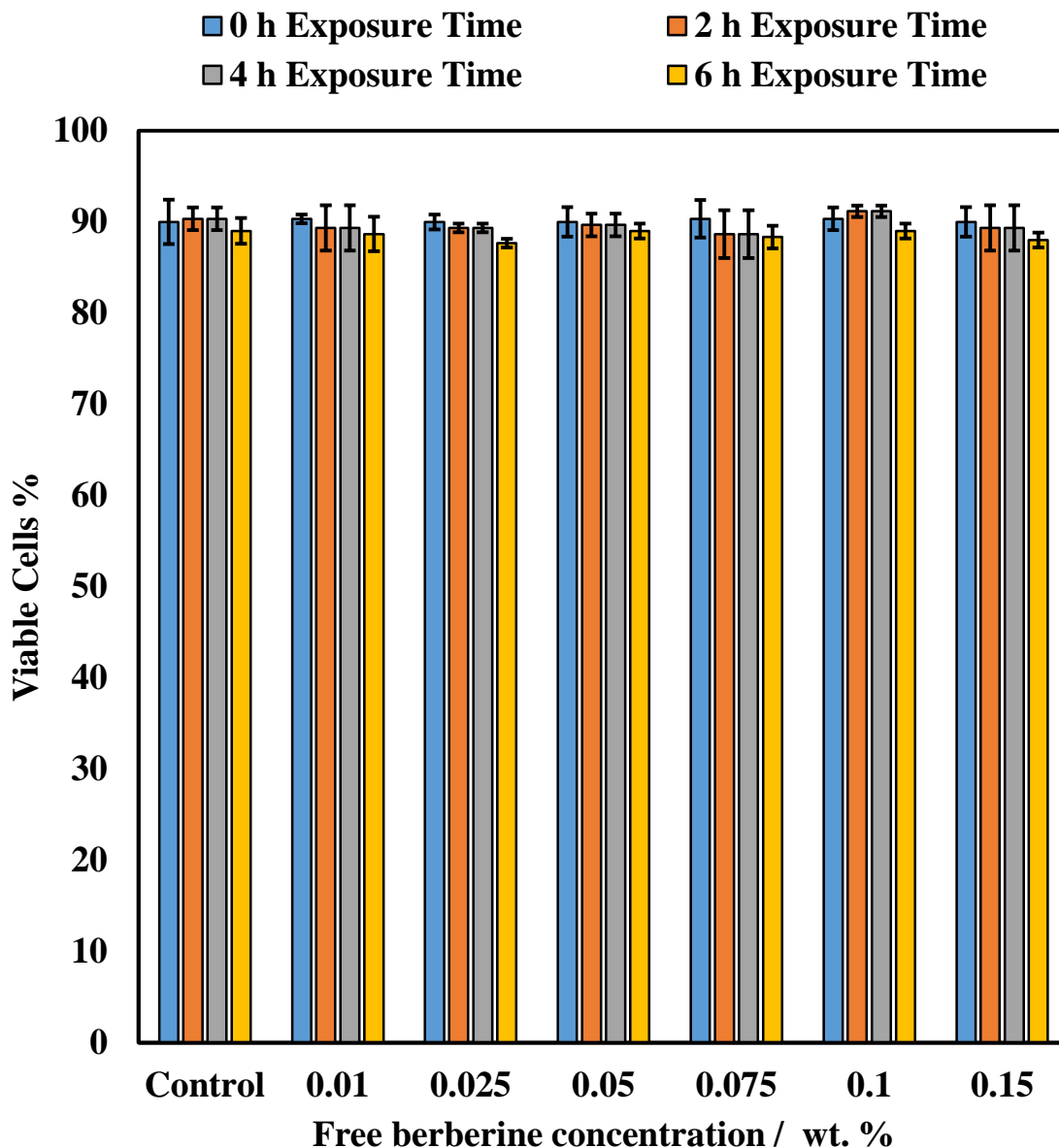


Figure 6.10: The viability of baker's yeast cells incubated with series of solutions of different concentrations of free berberine at pH 5.5 from 0 hours to 6 hours. The experiment was conducted by mixing yeast cells removed from the culture media with solutions of berberine concentrations from 0.01 wt% to 0.15 wt% in a 20 mL glass vial with gentle stirring. The cell viability was measured by using FDA assay whereby, 1 mL of sample was pipetted, washed and one drop of FDA acetone solution was added and stirred for 10 minutes, centrifuged and dispersed in PBS buffer solution. A 20 μ L of the sample was placed in a chip of measurement to determine the viability of cells.

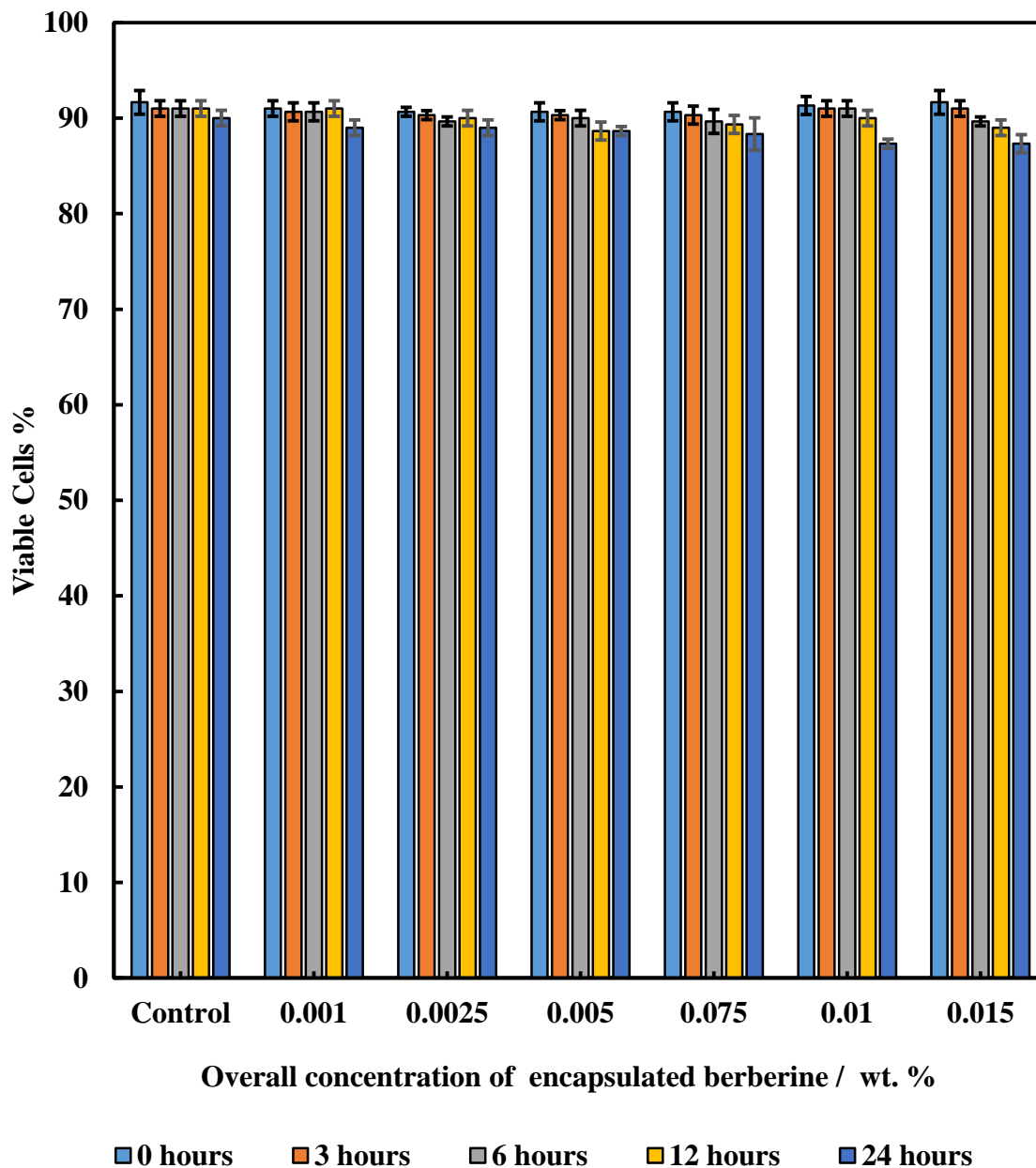


Figure 6.11: The viability of yeast cells incubated with series of average encapsulated Berberine concentrations at pH 5.5 from 0 hour to 6 hours incubation times. The experiment was conducted by mixing culture media free yeast cells with solutions of overall concentration of encapsulated berberine from 0.001 wt% to 0.015 wt% in a 20 mL glass vial with gentle stirring. The viability was measured by using FDA viability assay whereby, 1 mL of sample was pipetted, washed and one drop of FDA acetone solution was added and stirred for 10 minutes, centrifuged and dispersed in PBS buffer solution. A 20 μ L of the sample was placed in the Cell counter chip for measurement to determine the viability of cells.

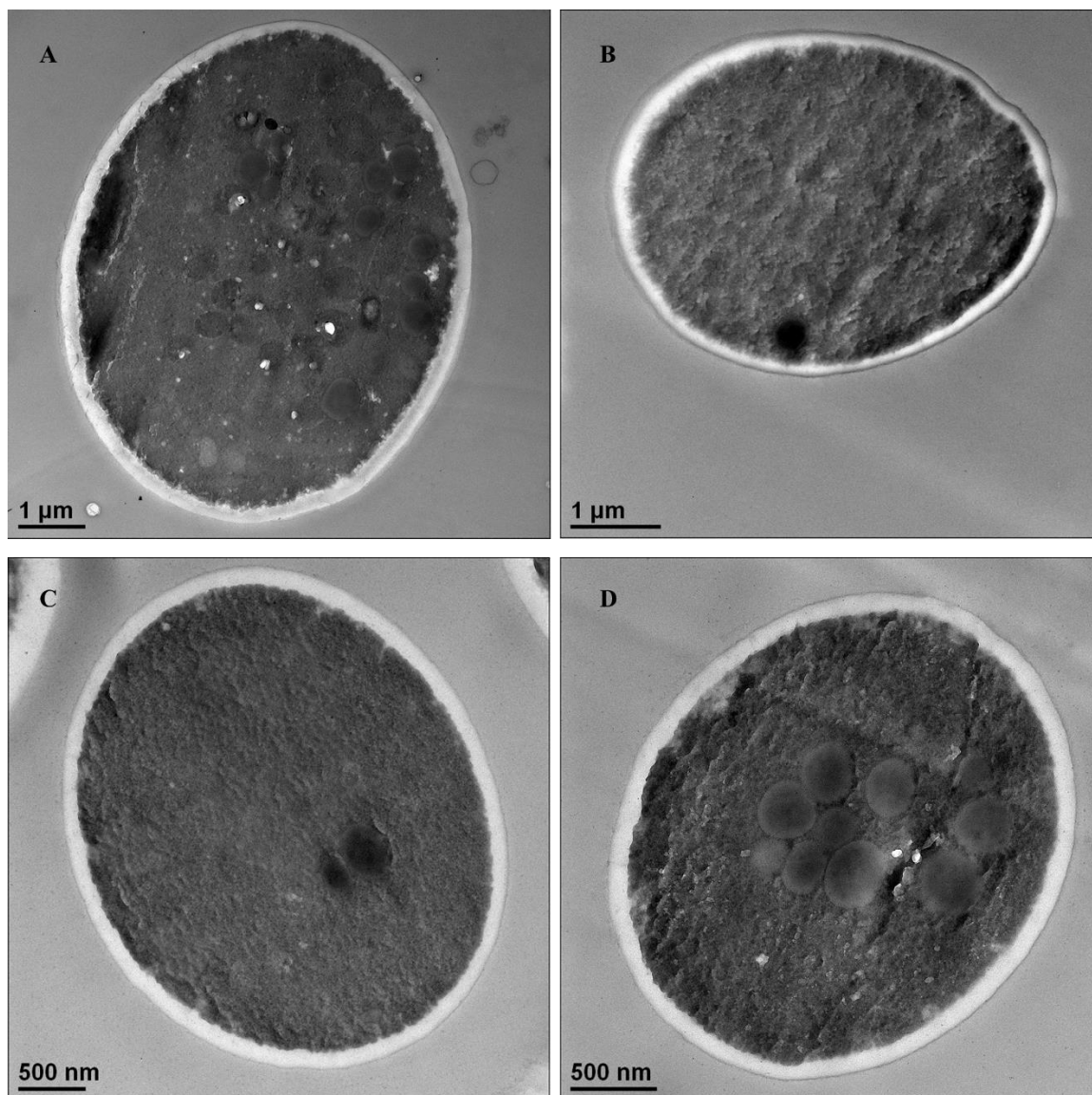


Figure 6.12: TEM images of culture media free yeast cells that have been incubated with solutions of different concentrations of berberine: (A) control sample without berberine, (B) 0.15 wt% berberine, and (C and D) 0.001 wt. % and 0.015 wt. % of overall encapsulated berberine into Carbopol Aqua SF1 microgel, respectively. The TEM images did not appear to show significant difference in comparison with the control in case of using both free or encapsulated berberine. The TEM samples were first treated with glutaraldehyde for 2 hours and washed with a buffer solution (pH 7.4) three times, then stained with uranyl acetate and washed with aqueous solutions of different concentrations of ethanol as explained in details in the experimental section (Chapter 2).

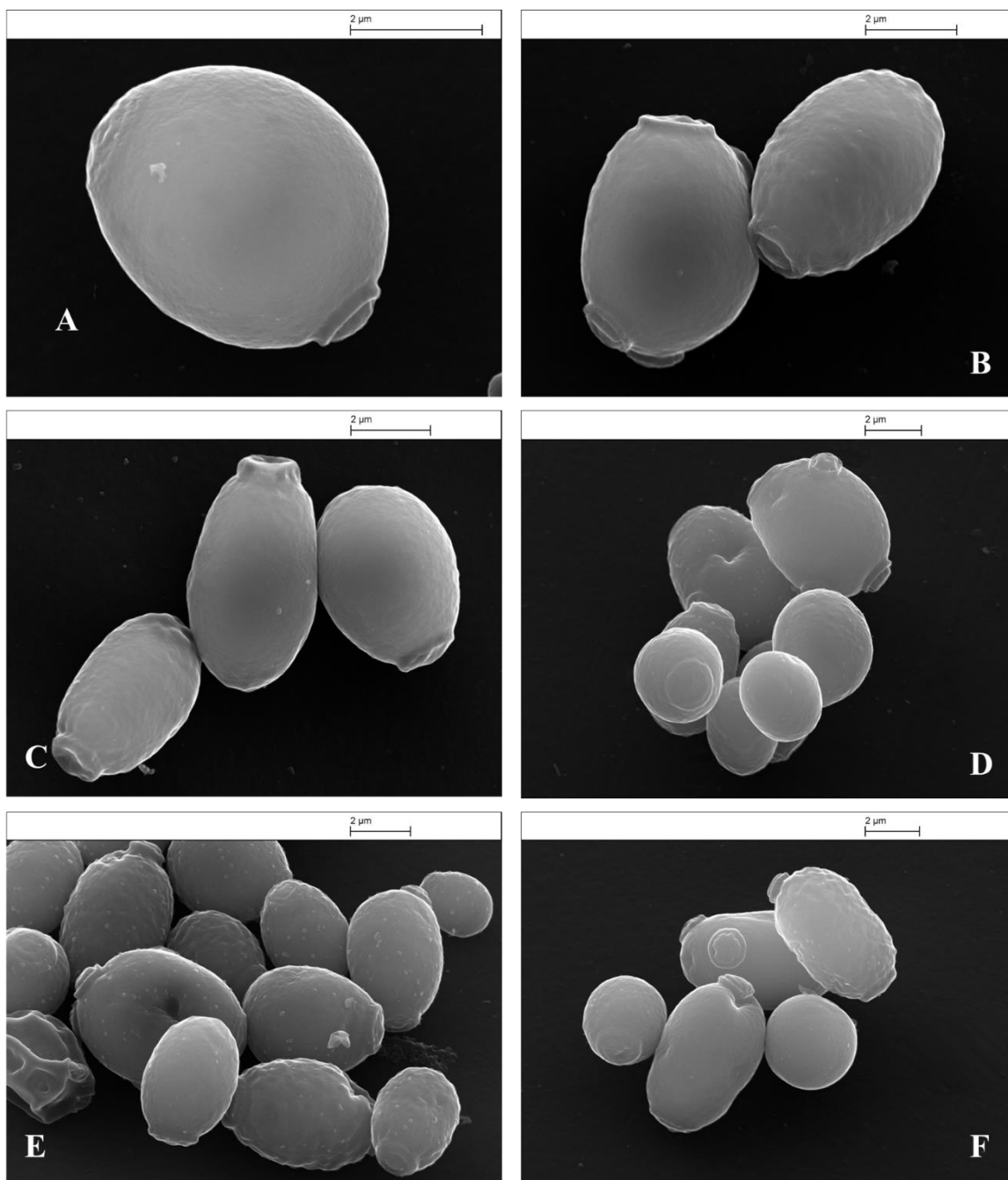


Figure 6.13: SEM images of yeast cells incubated for 6 and 24 hours with solutions of free and microgel-encapsulated berberine, respectively. (A) Control sample of yeast cells; (B) Yeast cells incubated with 0.15 wt% free berberine, (C) Yeast cells incubated with 0.001 wt% microgel-encapsulated berberine, and (D, E, and F) Yeast cells incubated with 0.015 wt. % of microgel-encapsulated berberine. Here the overall berberine concentration in the microgel formulation is quoted. The cells were pre-treated with glutaraldehyde for two hours and washed with buffer solution (pH 7.4) for three times, dried and then gold-sputtered to increase the imaging contrast.

6.3.3 Antimicrobial Activity of Berberine-Loaded Carbopol (BLC) on *E.coli*

The antimicrobial activity of berberine and berberine-loaded Carbopol Aqua SF1 on *E.coli* was investigated at various incubation times. Figures 6.14 and 6.15 show the results for the effect of the free berberine and berberine-encapsulated into Carbopol Aqua SF1 microgel, respectively. The experiments were conducted as previously, by mixing a fixed amount of the cells with each specific concentration of berberine and microgel-encapsulated berberine at room temperature. The results in Figure 13 for free berberine show that it had a strong effect on the viability of the *E. coli* cells. The viability of the *E.coli* decreased for berberine concentrations from 0.01 wt% to 0.1 wt% in the moment of addition of the cells to the solutions (0 hour incubation time). Upon increase of the incubation time to 1 hour, the viability of the cells became lesser in comparison with the control sample. Similarly, at 2 hours incubation time about 95% of the *E.coli* cells were killed at 0.075 wt% and 0.1 wt% free berberine, respectively.

The results for the antimicrobial activity of microgel-encapsulated berberine with *E.coli* are shown in Figure 6.15. Berberine-loaded Carbopol Aqua SF1 microgel can be seen to have a much lower antimicrobial activity than free berberine. From 0 hours to 4 hours incubation time there was a very low anti-bacterial effect. When the incubation time was increased up to 8 hours, the antimicrobial activity increased from 30 % at 0.001 wt. % to 70% at 0.01 wt. % of overall encapsulated berberine. After 24 hours of incubation, the viability of yeast cells sharply decreased to 5% at 0.01 wt% of overall concentration of microgel-encapsulated berberine. The difference in the antimicrobial activity between free berberine and berberine-loaded Carbopol microgel is attributed to the percentage of berberine release whereby berberine-loaded in the Carbopol microgel releases slower. In addition of that, Carbopol Aqua SF1 microgel at pH 5.5 has high negative zeta potential which interact strongly with the cationic berberine. The negatively charged loaded microgel also repels from the negatively charged surface of the bacterial cell wall which seems to reduce the effectiveness of the local berberine release in the cells near vicinity.

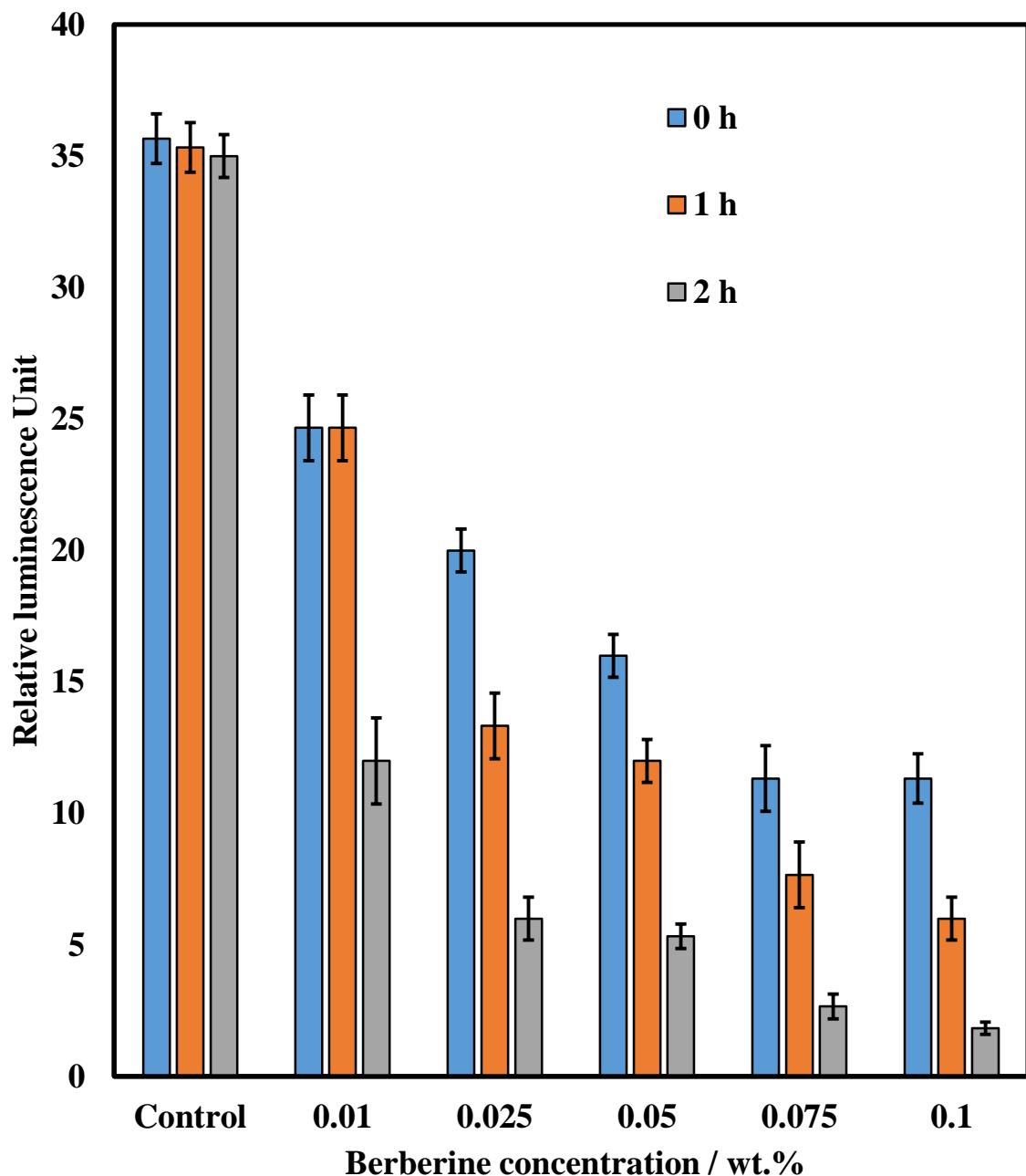


Figure 6.14: The relative luminescence intensities of viability of *E.coli* cells as a function of berberine concentrations for 2 hours incubation time. This experiment was performed through pipetting 1 mL of each sample was centrifuged thrice to get rid of the excess amount of berberine, then dispersed in Milli-Q water. After that, 100 μL of the sample was mixed with 100 μL of luciferase reagent in 96 microwell plate for 30 seconds, incubated for 5 minutes at 25 $^{\circ}\text{C}$, and the relative luminescence was measured by using a Luminometer.

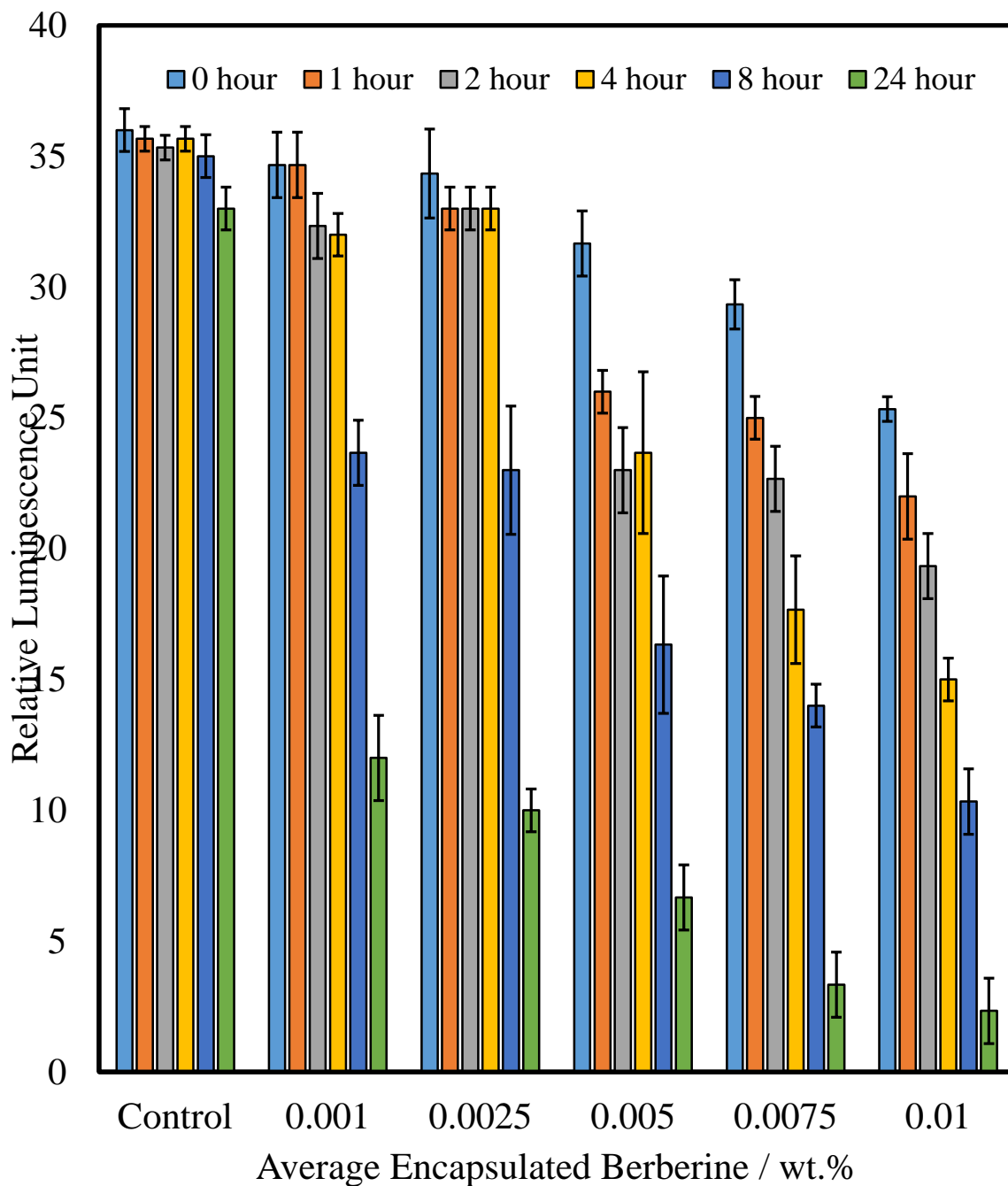


Figure 6.15: The relative luminescence intensities of viability of *E.coli* cells as a function of overall concentration of encapsulated berberine loaded into Carbopol Aqua SF1 microgel for different incubation times. This experiment was performed through pipetting 1 mL of each sample, centrifuged thrice to get rid of the excess amount of berberine, then dispersed in Milli Q water. After that, 100 μ L of the sample was mixed with 100 μ L of luciferase reagent in 96 microwell plate for 30 seconds, incubated for 5 minutes at 25 $^{\circ}$ C, and the luminescence intensity was measured by using Luminometer.

It can be seen in Figure 6.16, SEM images for *E.coli* cells that incubated with berberine loaded Carbopol Aqua SF1 for 24 hour where the cells had some cavities on the surface. The reason for this is owing to the interaction between cell membrane and berberine loaded Carbopol Aqua SF1 particles where the particles are either interacted with the cell membrane and released the active material or internalized into cells *via* caveolae endocytosis⁴ where this pathway is similar to that described for algae and yeast cells or *E.coli* cells sense to the changes in lateral tension in the bilayer of the cytoplasmic membrane produced by fast water flow into the cell causing filamentation due to osmotic shock.⁵

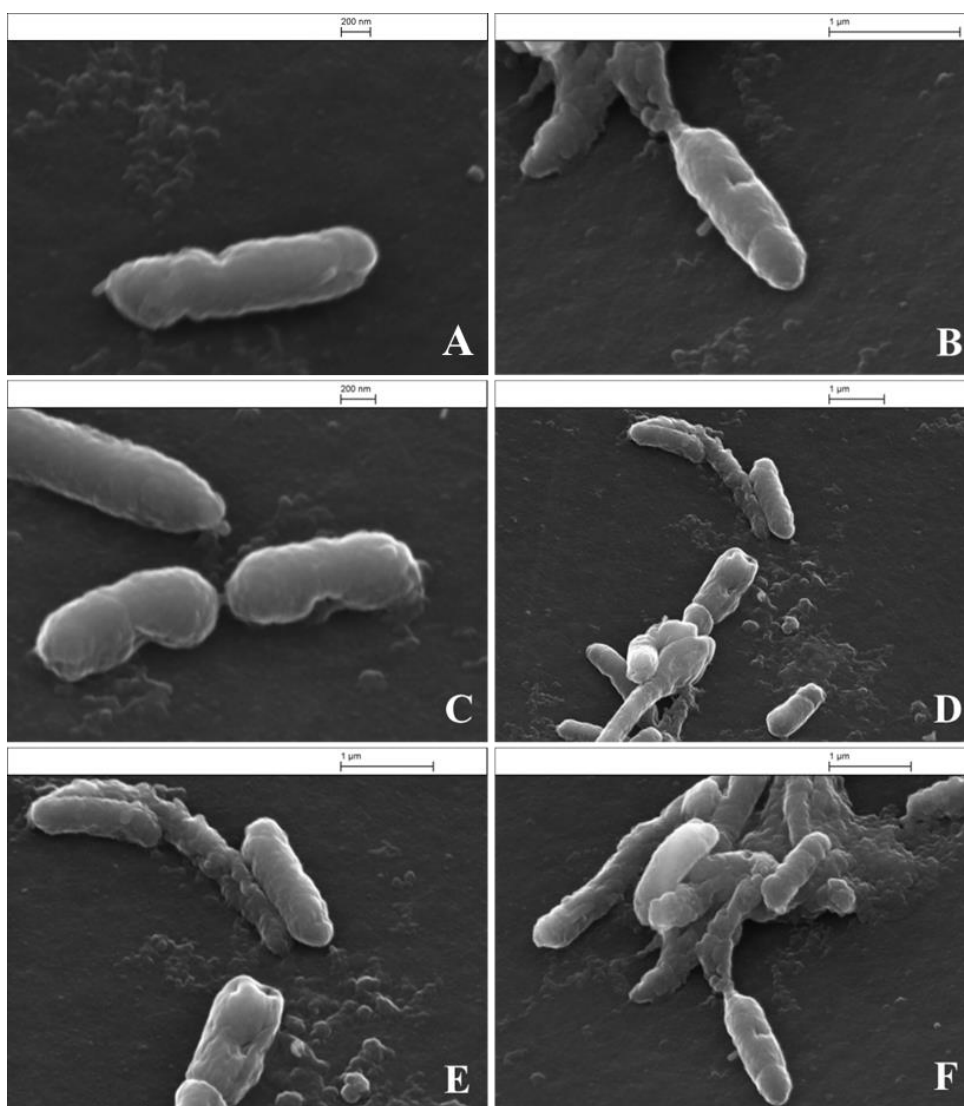


Figure 6.16: SEM images for *E.coli* cells incubated with a suspension of 0.01 wt% berberine-loaded Carbopol Aqua SF1 microgel. (A) Control sample and (B, C, D, E, and

F) represent *E.coli* cells incubated with 0.01 wt% berberine-loaded Carbopol Aqua SF1 microgel at room temperature for 24 hours incubation time.

6.4 Antimicrobial Activity of Chlorhexidine-Loaded Carbopol (CLC)

The antimicrobial activities of free chlorhexidine (CHX) and chlorhexidine-loaded Carbopol Aqua SF1 microgel (CLC) on *C. reinhardtii*, yeast and *E.coli* were then investigated. The reason behind encapsulation of chlorhexidine into Carbopol Aqua SF1 microgel is on the one hand, to increase the antimicrobial activity in comparison with free chlorhexidine and on the other hand to lessen the side effects of the antimicrobial agent.

6.4.1 Antimicrobial Activity of CHX-Loaded Carbopol (CLC) on microalgae

The antimicrobial activities of free chlorhexidine and microgel-encapsulated chlorhexidine was tested on microalgae at room temperature for different incubation times to examine their effects on algal cells as shown in Figures 6.17 and 6.18. Figure 6.17, for free chlorhexidine shows that at 0 hours incubation time, the viability sharply declined from 0.0001 wt% to 0.1 wt% concentrations of free chlorhexidine and that the cells were completely exterminated in the concentrations above 0.01 wt% free chlorhexidine. After 1 hour incubation the viability reduced to 20% at 0.005 wt% of chlorhexidine and after 2 hours the lethal effect of chlorhexidine expanded to concentration range above 0.005 wt%. In Figure 6.16 however, at 0 incubation time, the antimicrobial effect of Carbopol Aqua SF1 microgel-encapsulated chlorhexidine was reduced compared to free chlorhexidine (the cell viability decreased from 93% to around 40% whereas the viability reduced to 0 in the case of free chlorhexidine in the same concentration range). After 1 hour incubation time some antimicrobial affect was observed towards microalgae cells in the concentrations range from 0.045 wt% to 0.09 wt% but was still much reduced compared to free chlorhexidine. After two hours incubation time, the microalgae cells decreased for 9×10^5 to 0.009 wt% of overall concentration of microgel-encapsulated chlorhexidine. This difference in the viability of algal cells upon incubation with both free chlorhexidine and chlorhexidine-loaded Carbopol microgel is partly attributed to the slow release of chlorhexidine from the Carbopol Aqua SF1 microgel. Another important factor, however, is that there is an electrostatic repulsion between the negatively charged Carbopol Aqua SF1 particles and the cell surface which does not allow the encapsulated chlorhexidine to come too close to the cell membrane and disrupt it thus killing the cells. The SEM images

for *C. reinhardtii* cells in Figure 6.19 show that the chlorhexidine released from chlorhexidine-loaded Carbopol Aqua SF1 particles caused a damage for the membrane of the cells whereby cells have shrank and appeared wrinkled (see Figure 6.19B) in comparison with control sample as shown in Figure 6.19A. The interaction between the particles and microalgae cell membrane is similar to that for berberine for the same cell used.

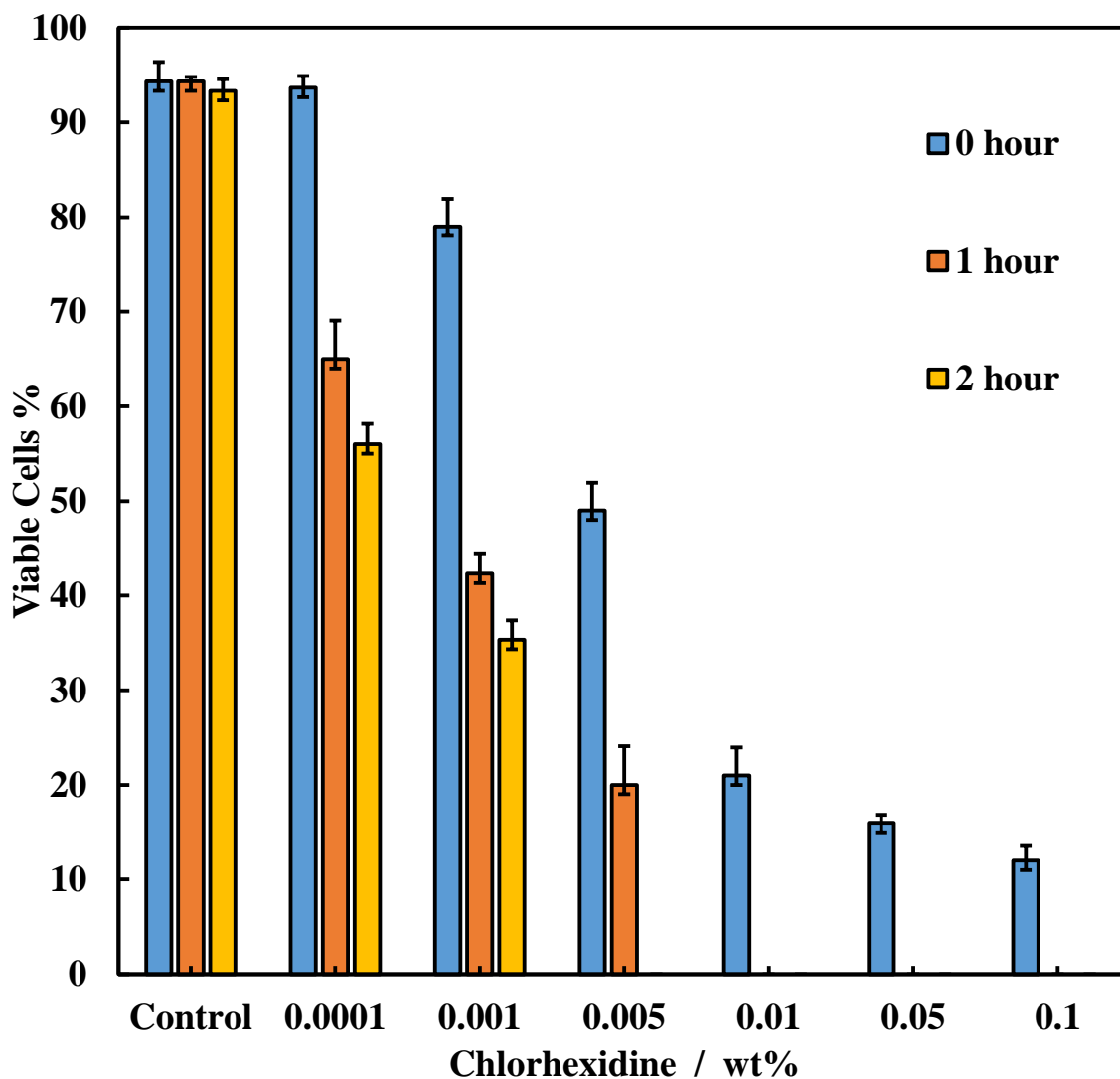


Figure 6.17: The viability of *C. reinhardtii* cells incubated with solutions of varied concentrations of free chlorhexidine at different incubation times. The incubation was conducted through mixing a solution of specific concentration of chlorhexidine with a fixed amount of microalgae cells remove from the culture media in a 20 mL glass vial caped with cotton and placed in an incubator. 1.0 mL of each sample was pipetted, washed with Milli-Q water and the cell viability was tested using FDA assay.

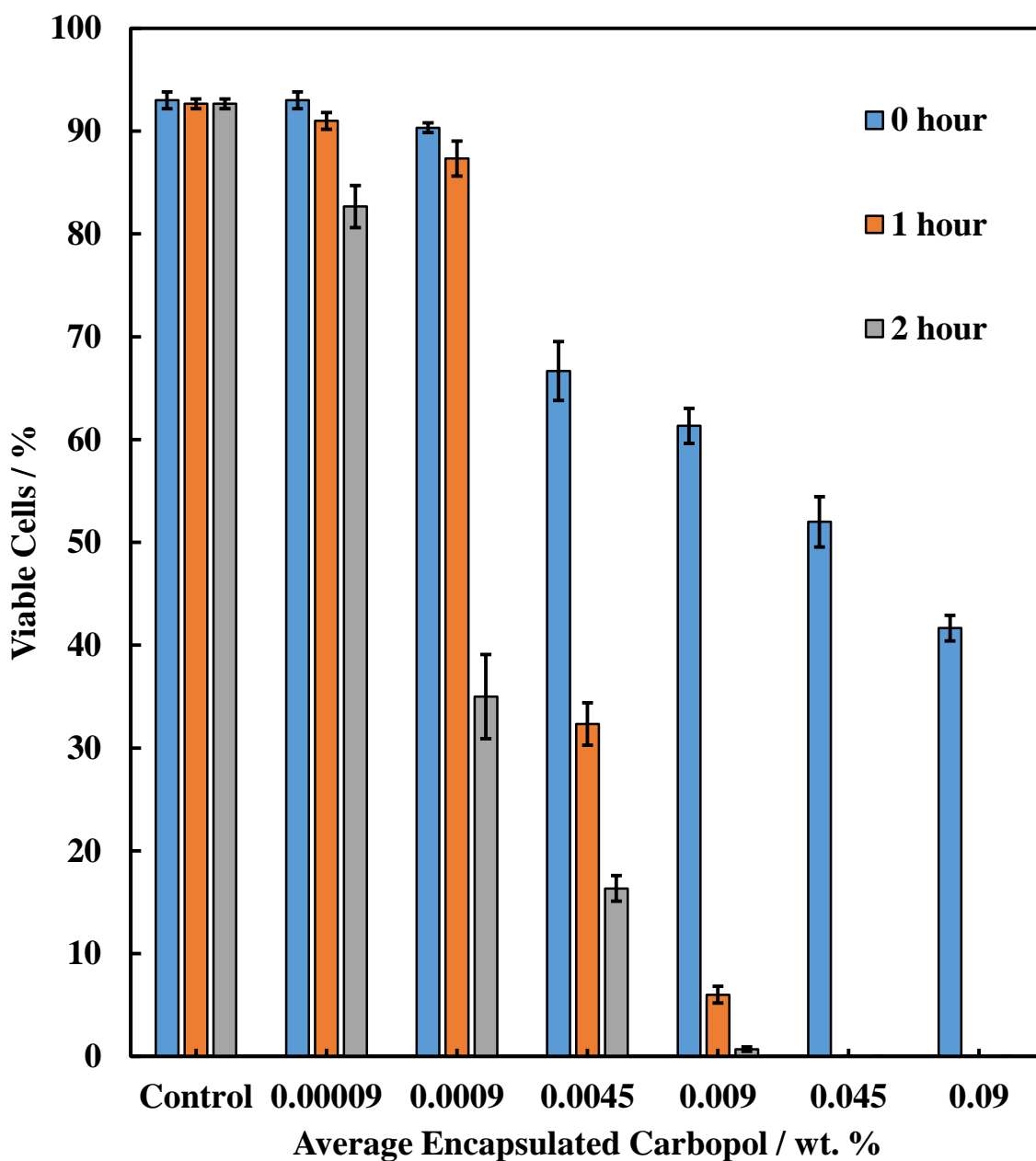


Figure 6.18: The viability of *C.reinhardtii* cells incubated with solutions of different overall concentrations of encapsulated chlorhexidine into Carbopol Aqua SF1 microgel after different incubation times. The incubation was conducted at pH 5.5 by mixing an aliquot of specific overall concentration of chlorhexidine-loaded Carbopol Aqua Sf1 microgel with a fixed amount of culture media free microalgae cells in a 20 mL glass vial capped with cotton and placed in an incubator. A 1.0 ml of each sample was pipetted, washed with Milli-Q water and the viability was tested using FDA assay.

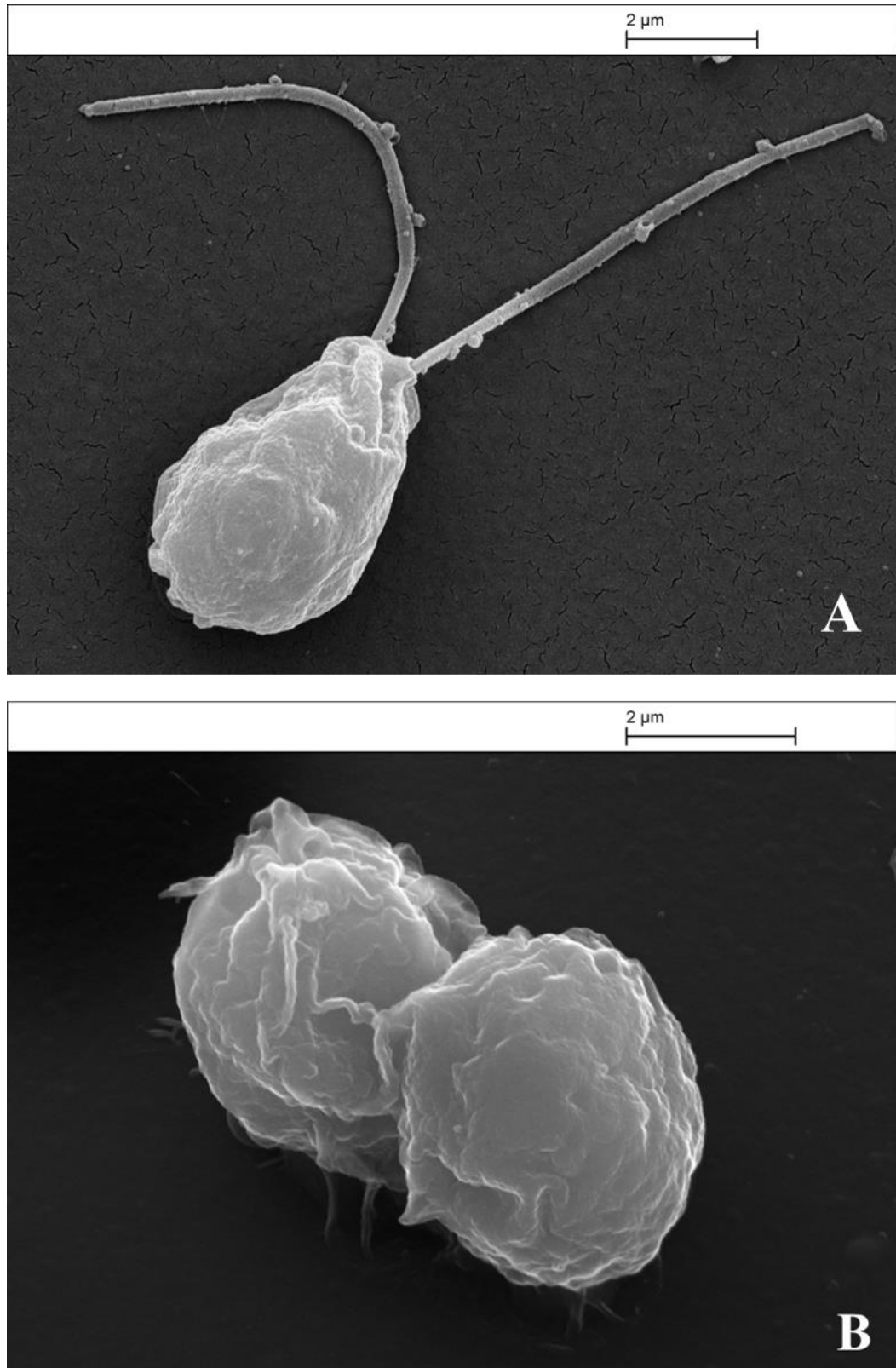


Figure 6.19: SEM images of *C.reinhardtii* cells. (A) Control sample of *E.coli*. (B) *E.coli* cells incubated with 0.09 wt% chlorhexidine-loaded Carbopol Aqua SF1 for two hours. The samples were pre-treated for SEM using the procedure described in section 2.2.8.

6.4.2 Antimicrobial Activity of Chlorhexidine-Loaded Carbopol (CLC) on Yeast

The effect of free chlorhexidine and microgel-encapsulated chlorhexidine was explored on baker's yeast cells which are known to have a very strong and rigid outer cell membrane. Figure 6.20 and 6.21 show the viability of the yeast cells after exposure to free chlorhexidine and chlorhexidine-loaded Carbopol microgel. At 0 hour incubation time (instant exposure), the viability of yeast cells decreased to 5% in the concentration range from 0.001 wt% to 0.05 wt% of free chlorhexidine di-gluconate, after an incubation time of one hour all cells were killed above concentrations 0.01 wt% chlorhexidine. The yeast viability had reduced sharply from 36% to 12% at chlorhexidine concentrations of 0.001 wt. % to 0.005 wt. % against the control sample.

Figure 6.21 indicates that the response of yeast cells towards microgel-encapsulated chlorhexidine is not pronounced probably due to the electrostatic repulsion of the negatively charged microgel from the yeast cell membrane which leads to release of chlorhexidine away from the cell. After 3 hours of incubation the cell viability decreased to around 70% for all concentrations of encapsulated chlorhexidine and this trend continued at 6 hours incubation. By 12 hours incubation time the viability had reduced to 50% compared to the control for concentrations of encapsulated chlorhexidine between 0.025 wt% and 0.05 wt%. After 24 hours, the effect become very noticeable for concentrations 0.001 wt% to 0.05 wt% to be around 40% at higher concentrations. These results also suggest a slow release of the encapsulated chlorhexidine due to its strong conjugation with the anionic microgel which does not allow the full amount of the cationic chlorhexidine to be released from the cross-linked network of negatively charged Carbopol. Figure 6.22 shows SEM images of yeast cells after incubation in a suspension of chlorhexidine-loaded Carbopol microgel particles for 24 hours at room temperature. It can be seen in Figure 6.22 (B, C, D, E, and F) that the morphology of the yeast cell's outer membrane has changed and cavities were appeared on the surface of the cells whereby these microgel particles have interacted with the cell membrane of the yeast cells. We cannot confirm based only on these SEM images whether microgel particles loaded with chlorhexidine have truly internalized into the cell cytoplasm using the similar way of endocytosis pathway as explained previously for antimicrobial action of microgel-encapsulated berberine with yeast cells. However, Figure 6.22A shows the control sample

of yeast cells where there was no chlorhexidine loaded particles in the solution and the surface of the membrane is free of cavities.

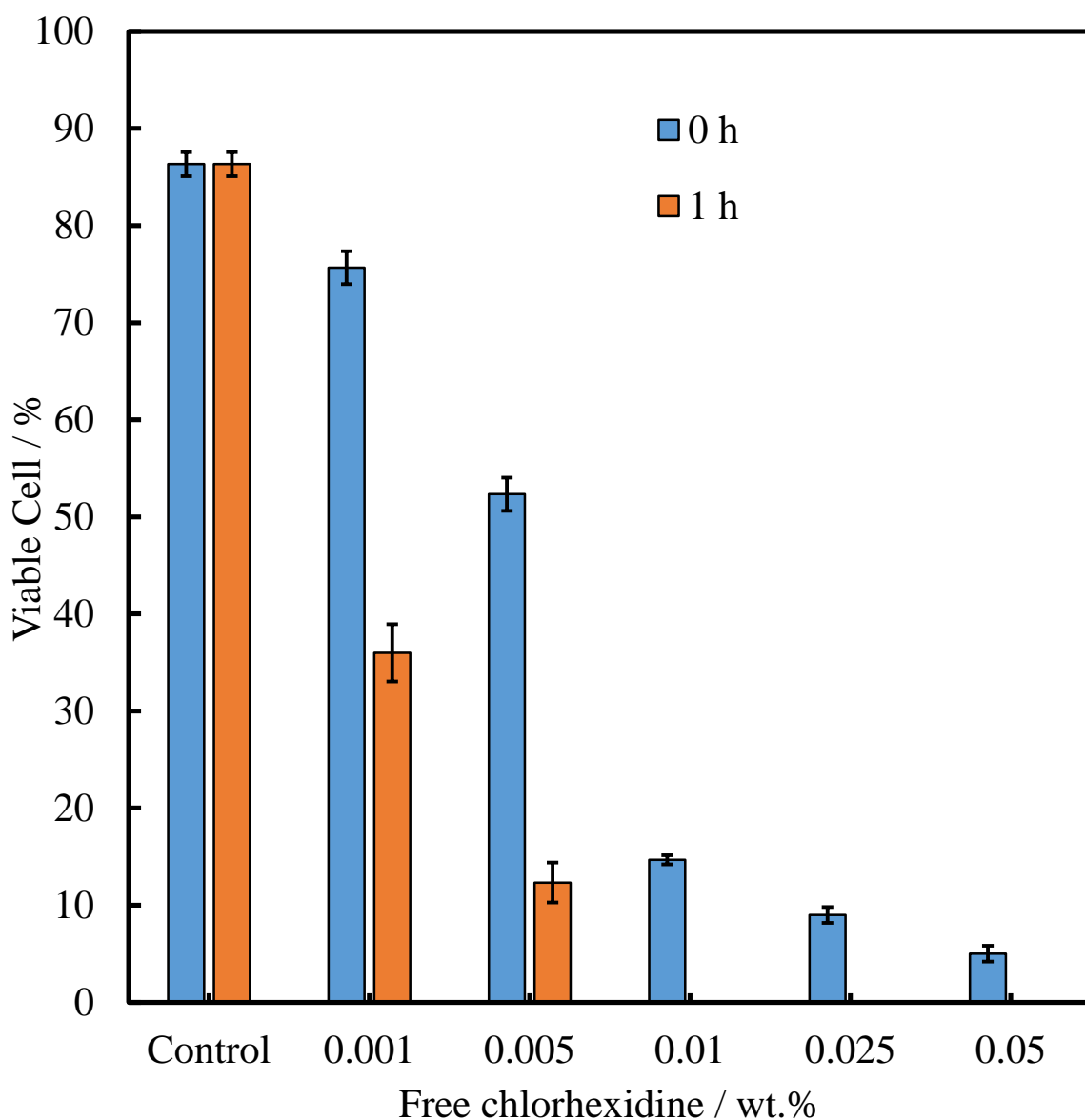


Figure 6.20: The viability of yeast cells incubated with series of solutions of free chlorhexidine with different concentrations at pH 5.5 after incubation from 0 to 1 hours. The experiment was conducted by mixing the yeast cells (removed from the media) with solutions of chlorhexidine concentrations from 0.001 wt% to 0.05 wt% in a 20 mL glass vial with gentle stirring. The cell viability was measured by using FDA viability assay whereby, 1 mL of sample was pipetted, washed and one drop of FDA acetone solution was added and stirred for 10 minutes and centrifuged and dispersed with PBS solution. A 20 μ L of the sample was placed in a cell counting chip to determine the cell viability.

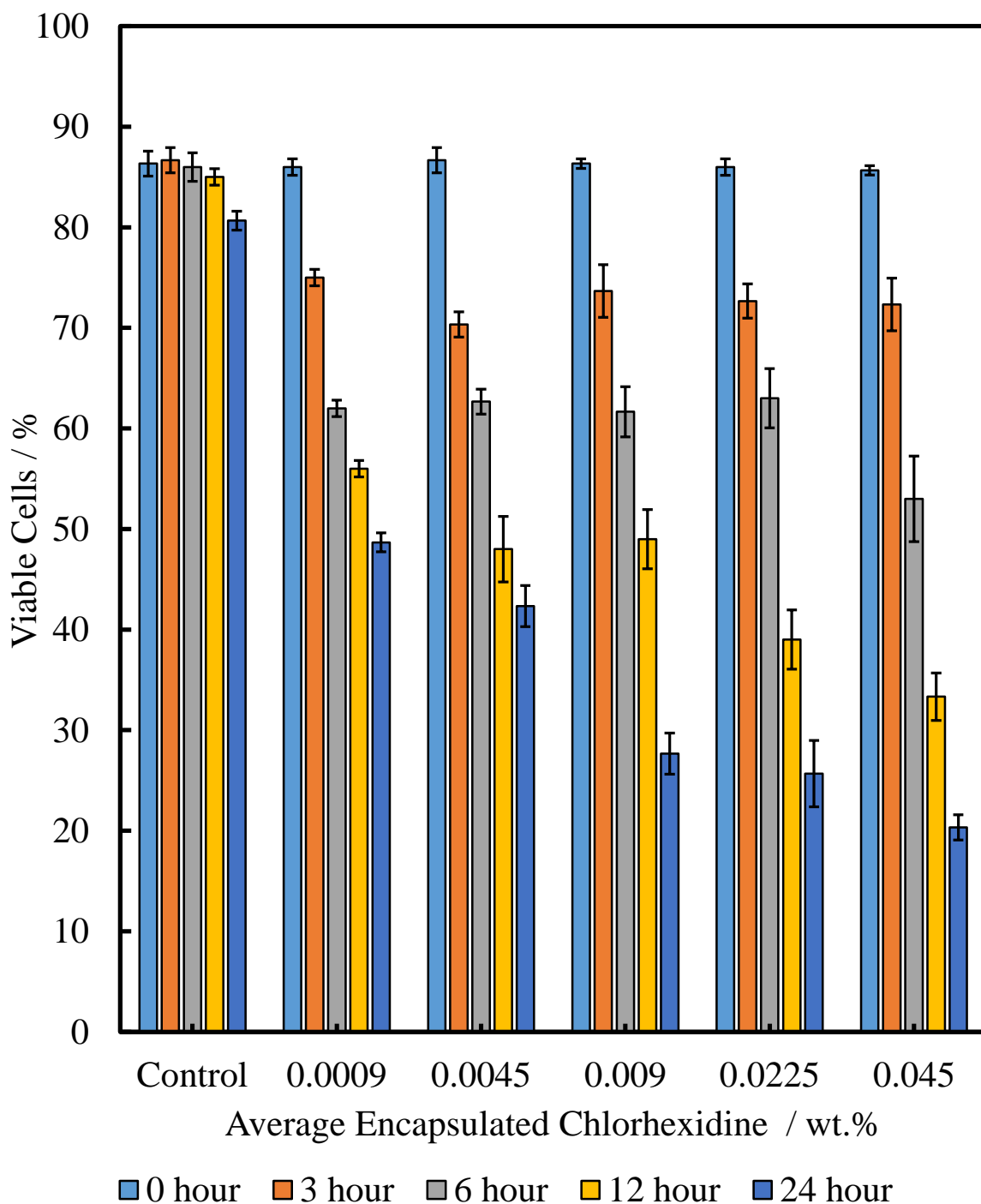


Figure 6.21: The viability of yeast cells incubated with series of average encapsulated chlorhexidine concentrations at pH 5.5 from 0 hour to 24 hours incubation times. The experiment was achieved through mixing culture media free yeast cells with solutions of Overall encapsulated chlorhexidine concentrations from 0.001 wt% to 0.05 wt%.

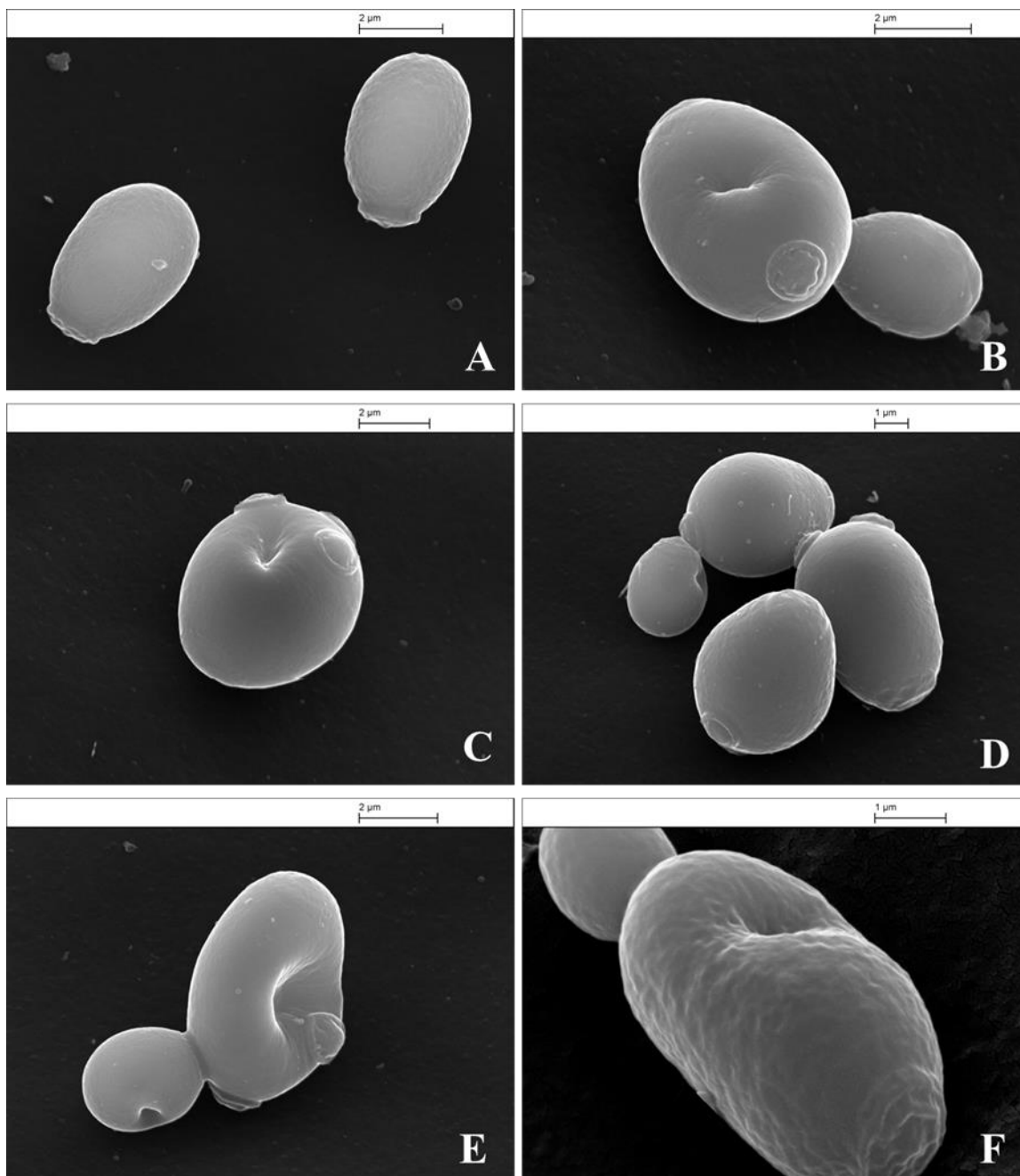


Figure 6.22: SEM images of yeast cells. (A) Control sample of yeast cells and (B, C, D, E and F) yeast cells after incubation in solution of 0.045 wt% chlorhexidine-loaded Carbopol Aqua SF1 microgel with yeast cells for 24 hours incubation time at room temperature. The cells were pre-treated for SEM using the procedure described in section 2.2.8.

6.4.3 Antimicrobial Activity of CHX-Loaded Carbopol (CLC) on *E.coli*

The testing of the antimicrobial activity of CLC was also checked on *E.coli* cells. The experiments were carried out using 20 mL glass vials capped with cotton to avoid contamination. *E.coli* cells were removed from the culture media prior to the experiment to avoid any interaction between the chlorhexidine-loaded Carbopol Aqua SF1 microgel and the culture media components. Figures 6.23 and 6.24 show the viability of *E.coli* cells when exposed to free- and microgel-encapsulated chlorhexidine at room temperature. There was a significant decrease in the viability of *E.coli* from 0.005 wt% to 0.1 wt% free chlorhexidine while no pronounced effect at 0.001 wt% at 0 hour incubation time. After 2 hour of incubation the *E.coli* viability has reduced for the same concentration to be about 50% and by 4 h exposure the reduction in the viability of the *E.coli* cells had expanded to cover all concentrations from 0.001 wt% to 0.1 wt% chlorhexidine and it was found to be 10 % of the maximum luminescence intensity of the control sample for the highest chlorhexidine concentration, by 4 hours incubation almost all cells died off.

As with the results for the microalgae and yeast, at 0 hour incubation time there was only a limited effect on *E.coli* cell viability. After 4 h incubation time, the viability was reduced at high chlorhexidine concentrations but the effect was much lower than for free chlorhexidine. At 8 hour incubation time, the luminescence intensity of viable cells dropped from 0.005 wt% to 0.05 wt% while the viability of *E.coli* cells was sharply down in the concentration ranged from 0.001 wt% to 0.05 wt%. After 24 hours incubation time 90% of *E.coli* cells were dead at 0.05 wt% in comparison with control sample where there was no chlorhexidine in the solution. As described previously, this is due to the slow release of chlorhexidine from Carbopol Aqua SF1 microgel.

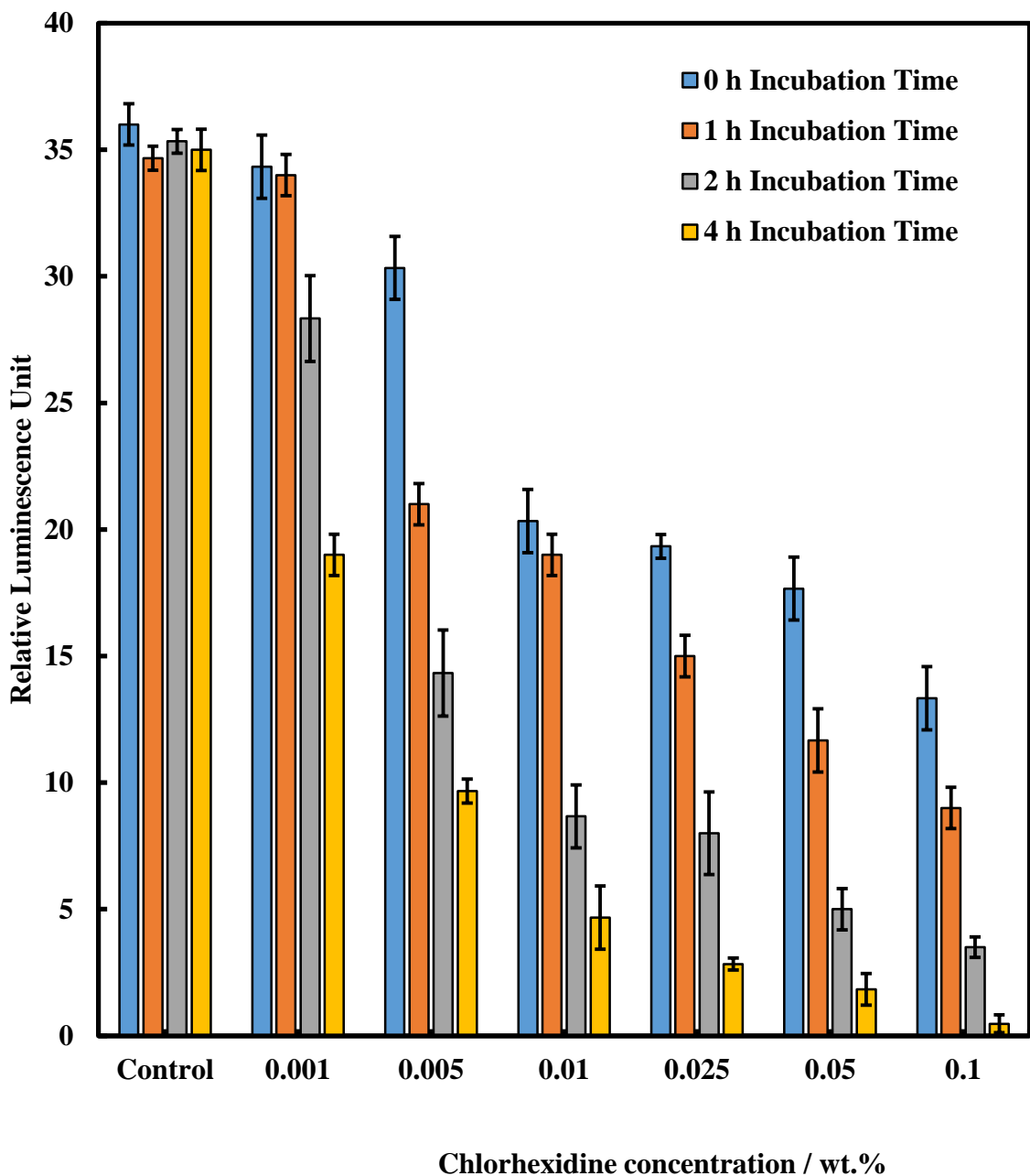


Figure 6.23: The relative luminescence intensities (a measure of the viability) of *E.coli* cells as a function of the free chlorhexidine concentration for up to 4 hours incubation time. This experiment was performed through pipetting 1 mL of each sample, centrifuged thrice to get rid of the excess amount of chlorhexidine and then dispersed in Milli-Q water. After that, 100 μ L of the sample was mixed with 100 μ L of luciferase reagent in 96 micro-well plate for 30 seconds, incubated for 5 minutes at 25 $^{\circ}$ C, and the luminescence was measured by using a luminometer.

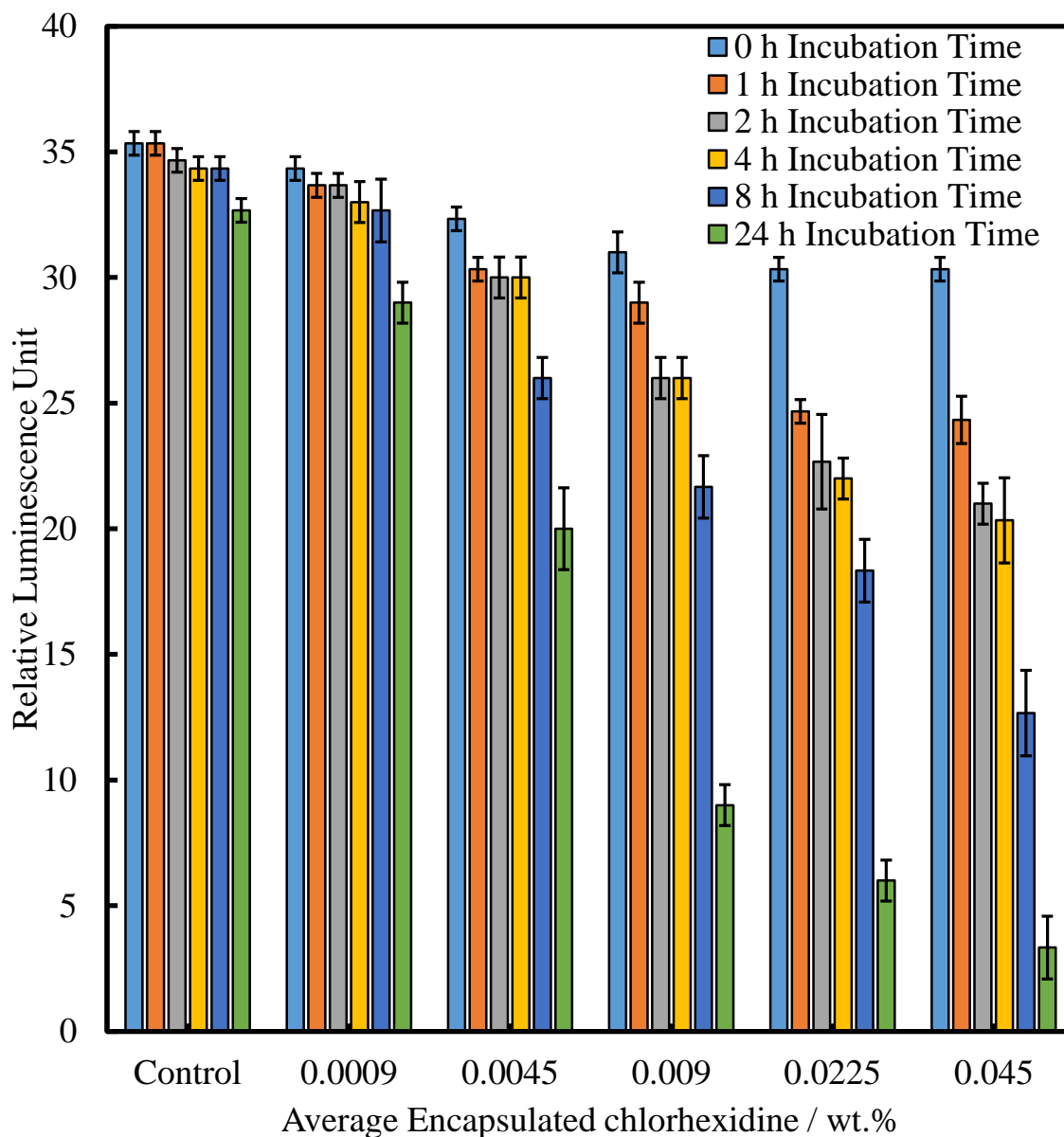


Figure 6.24: The relative luminescence intensities of viability of *E.coli* cells as a function of the overall concentration of chlorhexidine-loaded into Carbopol Aqua SF1 microgel for up to 24 hours incubation time. This experiment was performed at the same conditions as the one with free chlorhexidine (Figure 6.23).

Figure 6.25 shows SEM images of *E.coli* after their incubation in a suspension of 0.045 wt. chlorhexidine-loaded Carbopol Aqua SF1 microgel for 24 hours at room temperature. It can be seen that the cell membrane of the *E.coli* cells changed and shows some microgel particles aggregated on the bacteria surface which caused cavities on the cell membrane. These cavities refers to either the interaction between Carbopol Aqua SF1 particles and cell membrane leading to local release of chlorhexidine can disrupts the cell membrane and

kills the cells. The mechanisms for antimicrobial action seem to follow the same pathway described for berberine with *E.coli* cells.

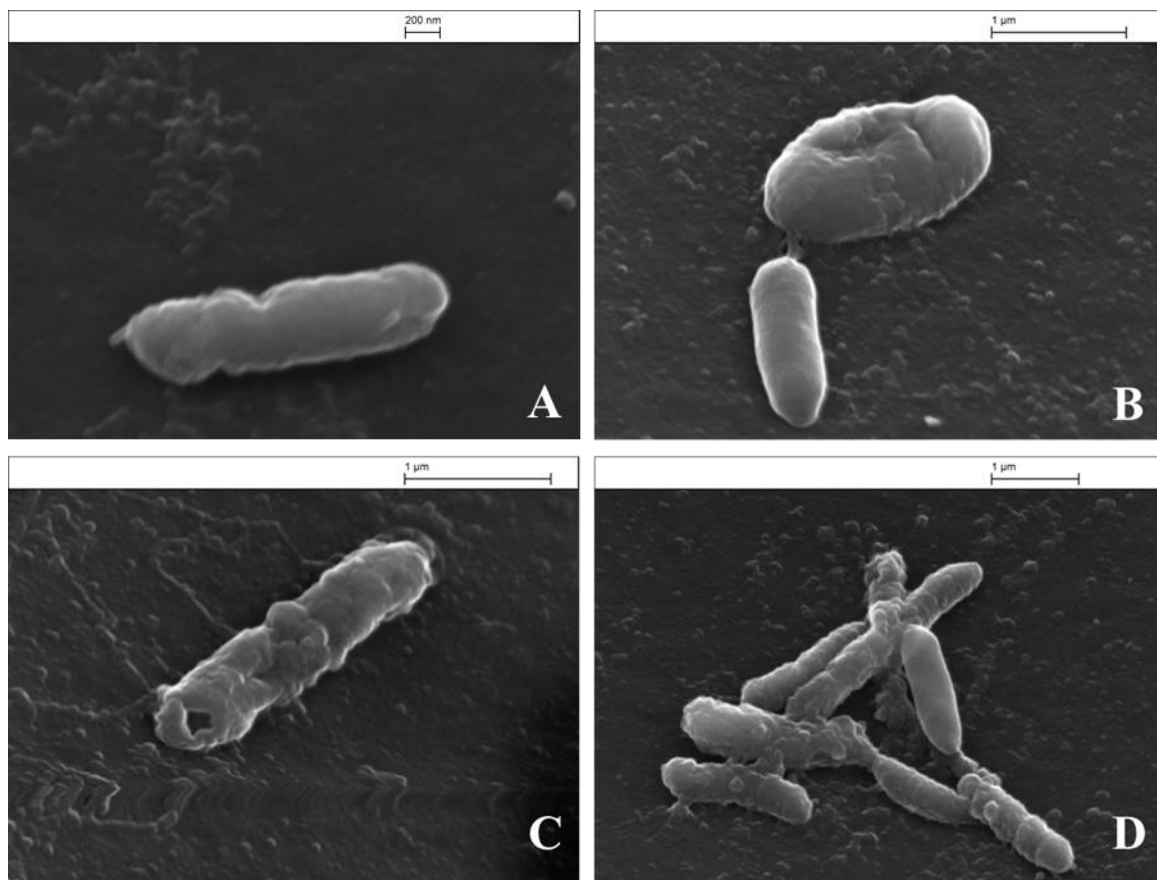


Figure 6.25: SEM images of *E.coli* cells. (A) Control sample of *E.coli* cells. (B, C, and D) *E.coli* cells incubated with 0.045 wt% chlorhexidine-loaded in Carbopol Aqua SF1 microgel. The cells were pre-treated with the procedure described in section 2.2.8.

6.5 Antimicrobial Activity of PDAC-coated Encapsulated Carbopol

Our previous experiments on the antimicrobial actions of encapsulated berberine or chlorhexidine showed that the Carbopol-encapsulated berberine and chlorhexidine have lower antimicrobial activity on a range of microorganisms in comparison with both free berberine and chlorhexidine. The main reason for this is that Carbopol microgel particles retain their negative surface charge even after the encapsulation takes place. The electrostatic repulsion with negatively charged cell surface does not allow them to release the encapsulated antimicrobial agent in near vicinity of the cell membrane. To overcome this problem, the Carbopol microgel particles encapsulating the berberine or the

chlorhexidine were coated with a cationic polyelectrolyte to increase their adhesion to cells and antimicrobial action.

6.5.1 Cytotoxic Effect of PDAC on Microalgae, Yeast and *E.coli*

We coated the berberine- or chlorhexidine-loaded Carbopol Aqua SF1 microgel with a cationic polyelectrolyte PDAC to reverse the surface charge of the microgel from negative to positive. However, we also needed to study the cytotoxic effect of the PDAC alone on the selected microorganisms (microalgae, yeast and *E.coli*). This was achieved by incubating such cells with solutions of different concentrations of PDAC to its threshold of cytotoxicity on these microorganisms. Figures 6.26, 6.27 and 6.28 show the cytotoxic effect of solutions of PDAC of different concentrations on *C.reinhardtii*, yeast and *E.coli*, respectively. It can be seen in these figures that the cationic polyelectrolyte (PDAC) has an extremely strong antimicrobial effect in a wide range of concentrations ranged from 0.0045 wt% to 0.05 wt%. To establish the toxicity of the antimicrobials-loaded microgel we therefore needed to remove the free PDAC from the microgel suspension before incubation with cells to differentiate between the cytotoxic effect of PDAC and the antimicrobial activities of microgel-encapsulated berberine or chlorhexidine. For microalgae and yeast (Figures 6.26 and 6.27), PDAC solutions of different concentrations were incubated with a fixed amount of cell sample. The cell viability was measured through pipetting a millilitre of each sample, centrifuged, dispersed in water, after that 1 drop of FDA solution was added and incubated for 10 minutes and centrifuged again two times. The cell viability of the resulted sample was measured by automatic cell counter using FDA viability assay. For *E.coli* (Figure 6.28), the cell viability was measured through pipetting a millilitre of each sample, centrifuged, dispersed in water, after that 100 μ L of each cell sample was placed in a 96-microplate wells and added 100 μ L of luminescence reagent. The 96 microplate wells were shaken for 30 second and incubated for 5 minutes and the luminescence intensity was measured by Luminometer.

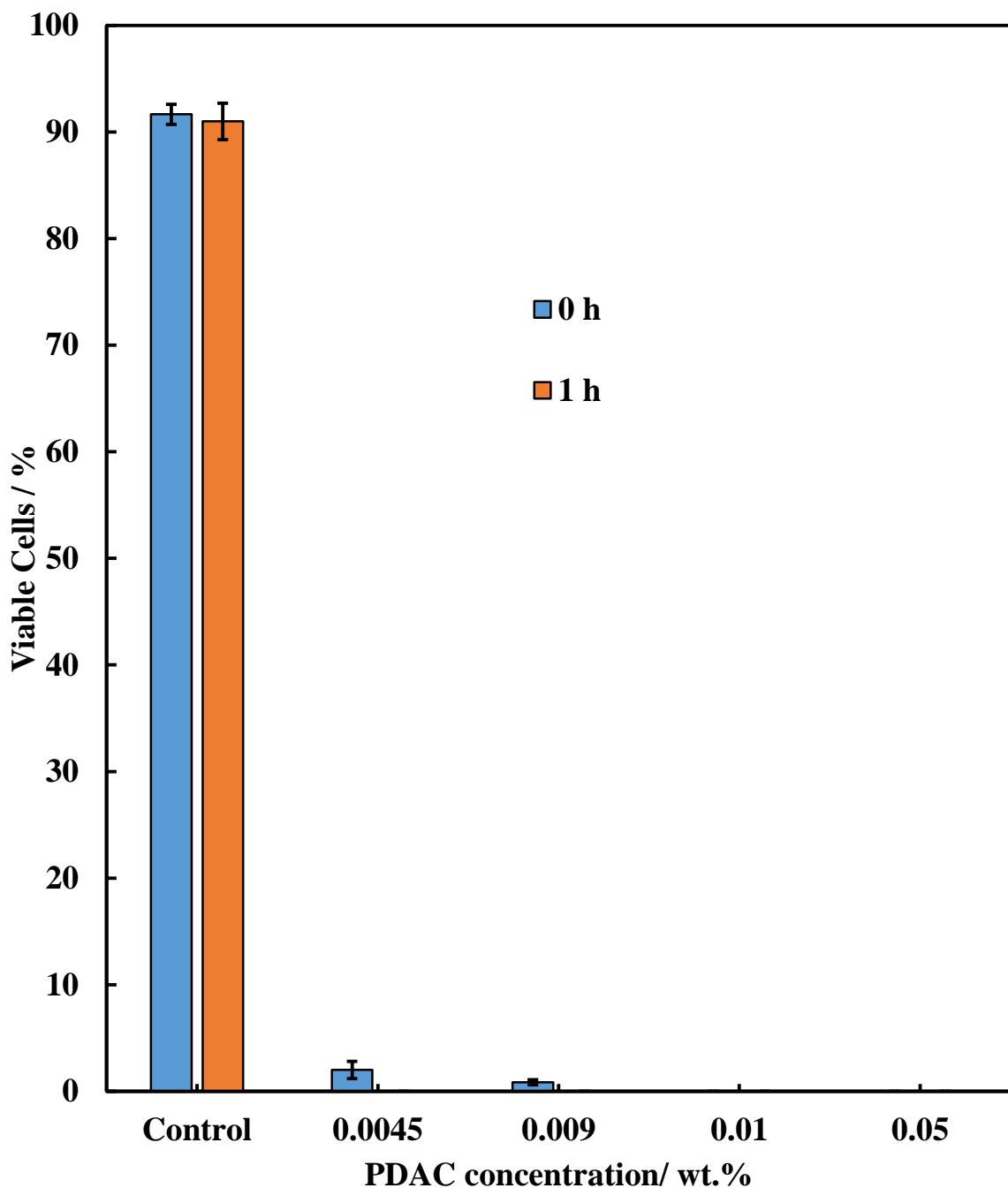


Figure 6.26: The cytotoxic effect of solutions of different PDAC concentration on microalgae cells (*C.reinhardtii*) for 1 hour incubation time at room temperature. PDAC solutions of different concentrations were incubated with a fixed amount of microalgae cells.

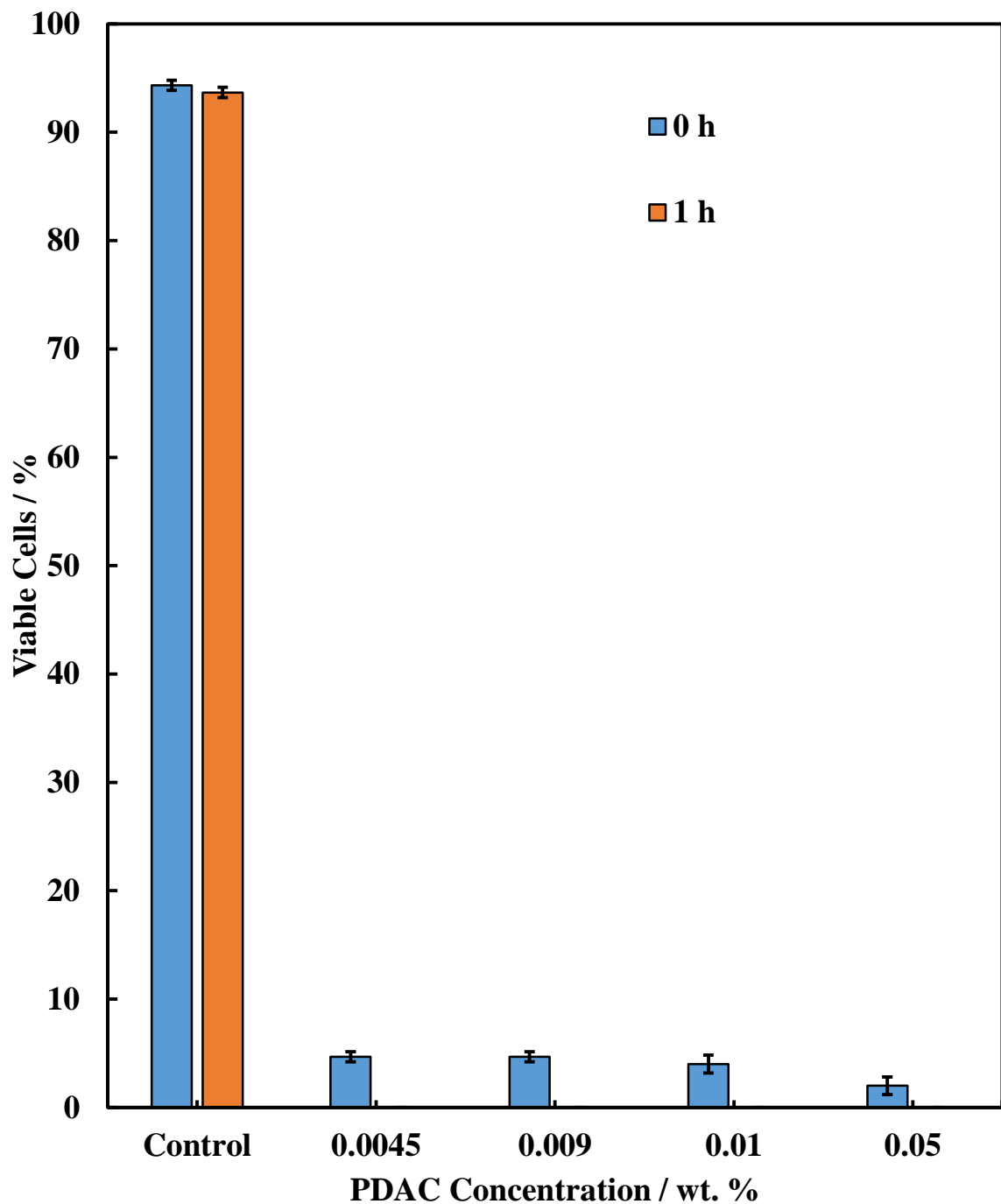


Figure 6.27: The cytotoxic effect of solutions of different PDAC concentration on yeast cells for up to 1 hour incubation time at room temperature. A fixed amount of yeast cells was incubated with a solution of different PDAC concentrations

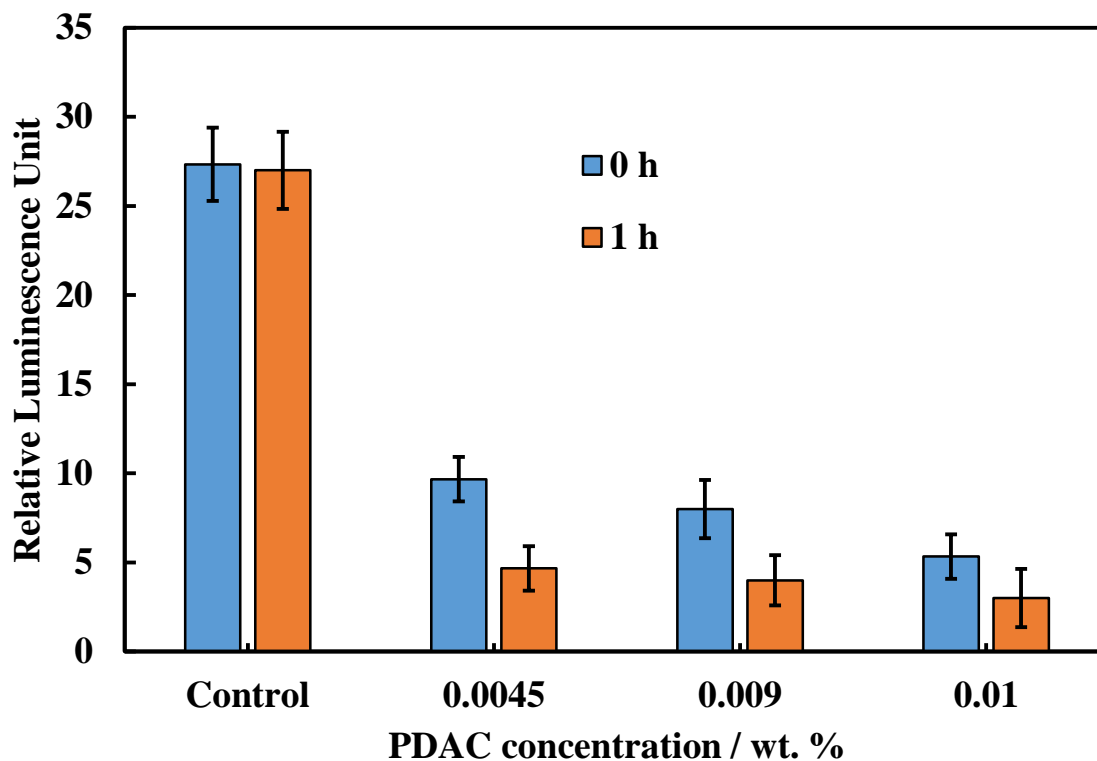


Figure 6.28: The cytotoxic effect of solutions of different PDAC concentration on *E.coli* cells for up to 1 hour incubation time at room temperature. Solutions of different PDAC concentrations were incubated with a fixed amount of *E.coli* cells.

6.5.2 Cytotoxic Effect of PDAC-Coated Carbopol on Algae, Yeast and *E.coli*

In order to measure the antimicrobial activity of PDAC-coated and berberine- or chlorhexidine-loaded Carbopol Aqua SF1 on microalgae, yeast and *E.coli*, the cytotoxic effect of PDAC coated-Carbopol Aqua SF1 (without berberine or chlorhexidine) towards these microorganisms had to be investigated. A specific quantity of each type of cell was incubated with suspensions varying concentrations of PDAC-coated Carbopol Aqua SF1 microgels at room temperature for selected incubation times. Figure 6.29 shows the results for algal cells where there is little effect until 0.009 wt% to 0.018 wt% at which point the viability is strongly affected. In this range even a 0 incubation time the coated Carbopol Aqua SF1 particles appear to be damaging the thin cell membrane of algae.

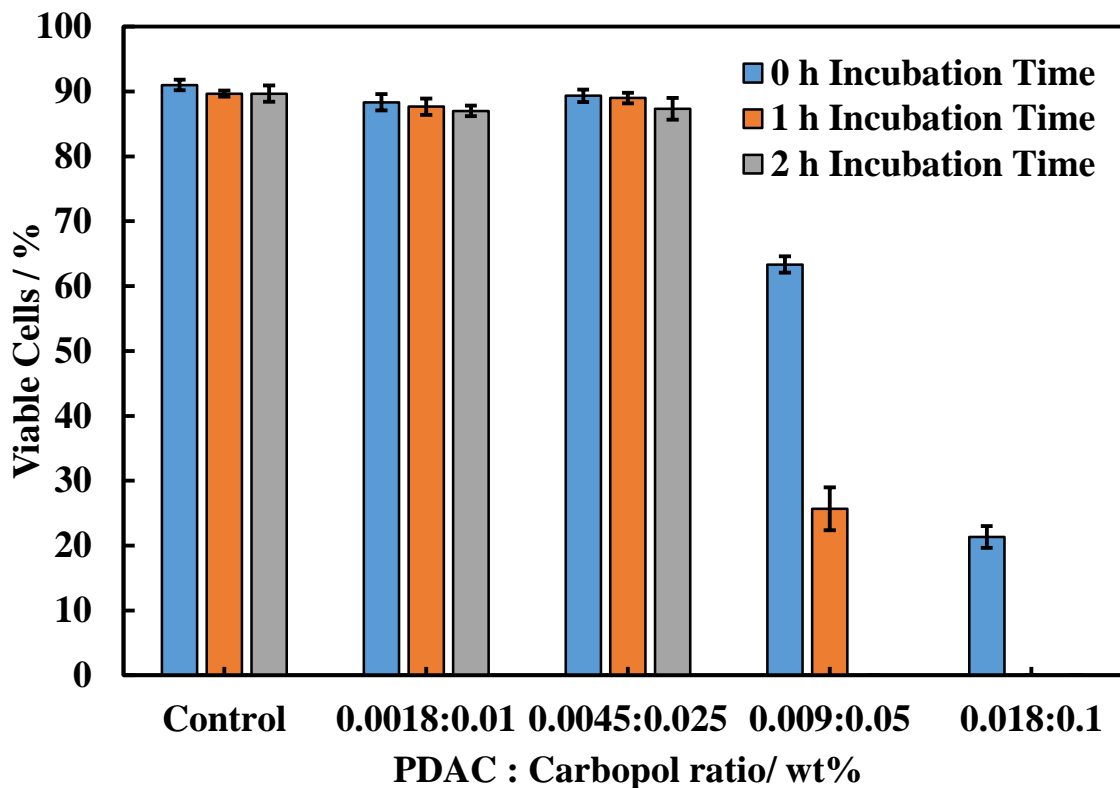


Figure 6.29: The cytotoxic effect of PDAC-coated Carbopol Aqua SF1 microgel upon incubation with microalgae cells for 2 hours at room temperature. The measurement was conducted through pipetting 1 mL of each sample, centrifuged twice, incubated with 1 drop of FDA solution for 10 minutes and then centrifuged and re-dispersed with PBS solution (pH 7.4). After that, the cell viability was measured by automatic cell counter.

Figure 6.30 shows the cytotoxic effect of the Carbopol microgel coated with the cationic polyelectrolyte PDAC on yeast cells after up to 6 hours incubation time at room temperature. In this case, there was no pronounced toxic effect for the incubation of yeast cells with each individual concentration, a slight decrease was seen for higher concentrations at 6 h. In the case of the yeast, the thicker cell membrane prevents the PDAC-coated Carbopol Aqua SF1 particles from disrupt it. Although PDAC can disrupt the cell membrane of yeast (see the section above), the microgel bonded PDAC does not seem to produce the same effect as free PDAC.

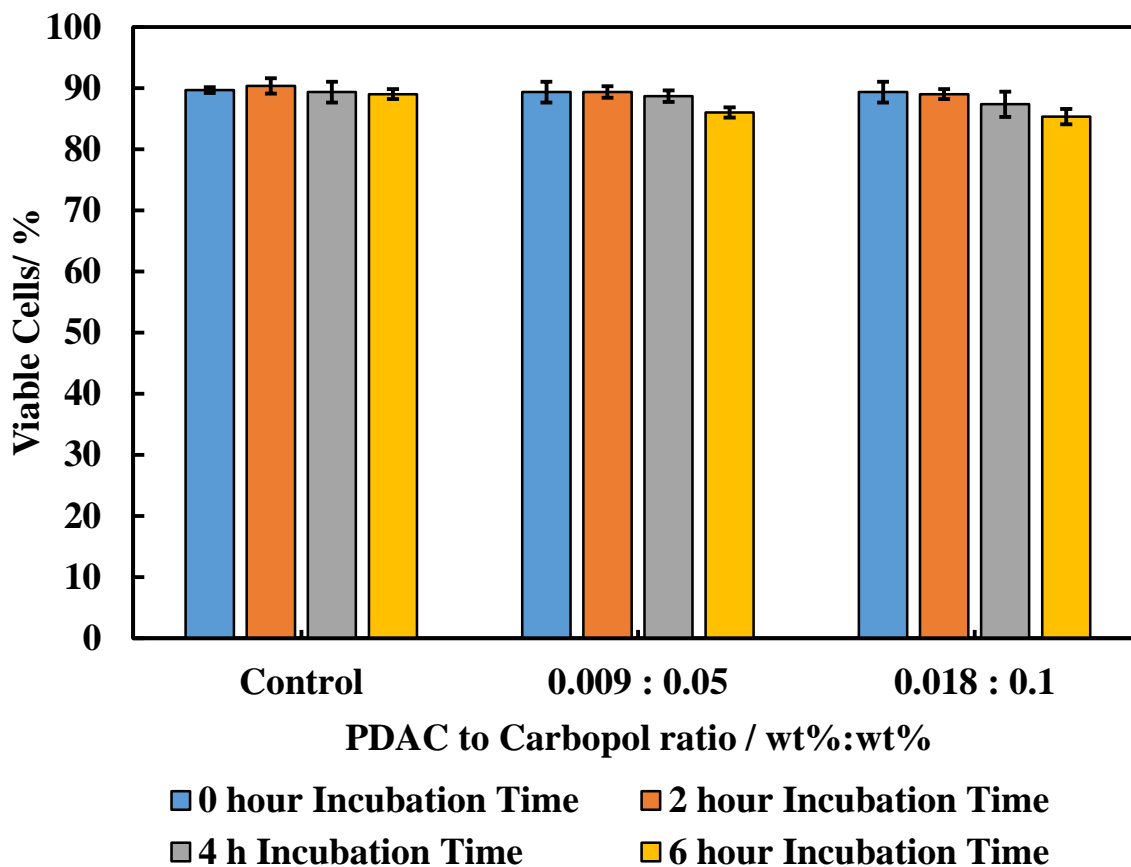


Figure 6.30: The cytotoxic effect of PDAC-coated Carbopol microgel upon incubation with yeast cells for up to 6 hours at room temperature. The measurement was conducted through pipetting 1 mL of each sample, centrifuged twice, incubated with FDA solution for 10 minutes and then centrifuged and dispersed with PBS solution (pH 7.4). After that, the cell viability was measured by automatic cell counter.

The cytotoxic effect of PDAC-coated Carbopol microgel particles was also tested on *E.coli*. Figure 6.31 shows that PDAC in the concentration range 0.0036 to 0.009 wt% is not toxic with up to a 2 h incubation time while at 0.018 wt% PDAC concentration there was a cytotoxic effect on *E.coli* cells. Therefore, it was utilized the concentrations from 0.0036 wt. % to 0.009 wt. % in the further experiments to incubate the cells with PDAC coated antimicrobial agent loaded Carbopol to measure the increase in the antimicrobial activity as well as to investigate the antimicrobial agent's ability to kill *E.coli* cells when delivered by using PDAC-coated microgel particles.

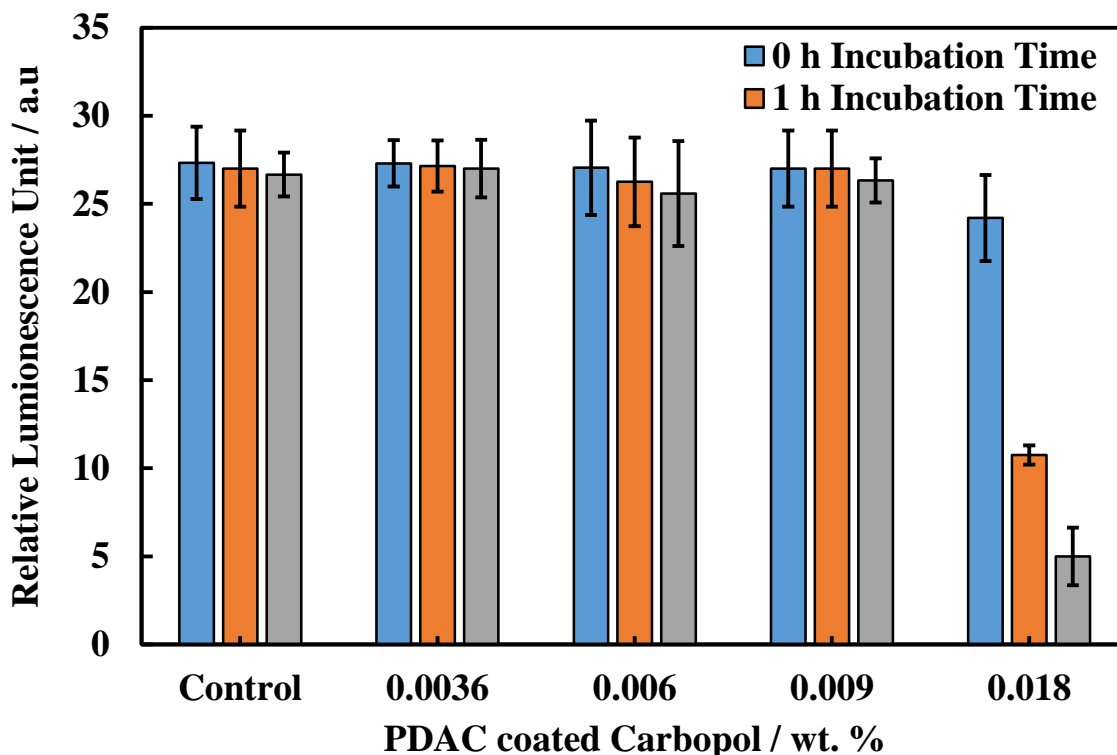


Figure 6.31: The cytotoxic effect of PDAC coated Carbopol Aqua SF1 microgel upon incubation with *E.coli* cells for 2 hours at room temperature. The measurement was carried out through pipetting 1 mL of each sample, centrifuged twice, after that 100 μ L of each cell sample was placed in a 96-microplate wells and added 100 μ L of luminescence reagent. The 96 microplate wells were shaken for 30 seconds, incubated for 5 minutes and the intensity was measured by Luminometer.

6.5.3 Antimicrobial Activity of PDAC-coated BLC on Microalgae

We studied the antimicrobial activity of berberine-loaded Carbopol Aqua SF1 which was additionally coated with the cationic polyelectrolyte PDAC to enhance the electrostatic adhesion between the negatively charged cell membrane and positively charged PDAC-coated Carbopol microgel loaded with berberine. Figure 6.32 shows the viability of *C.reinhardtii* cells incubated with suspensions of different concentration of PDAC-coated berberine loaded Carbopol Aqua SF1 (BLC). At 0 hour incubation time (instant exposure), the viability of the algal cells decreased from 82% at 0.0018 wt% PDAC - 0.0015 wt% berberine- Carbopol Aqua SF1 complex concentration to 50% at 0.0045 wt% PDAC-0.00375 berberine-Carbopol Aqua SF1 complex concentration and then sharply declined to 15% at 0.0045 wt% PDAC-0.00375 wt% berberine-Carbopol Aqua SF1 concentration. Upon increasing the incubation time to 1.5 hours, all the cells died for 0.0045 wt% PDAC-

0.00375 wt% Berberine-Carbopol Aqua SF1 concentration and the viability was 7% for the 0.003 wt% PDAC - 0.0025 wt% Berberine-Carbopol Aqua SF1 concentration. However, 40% of algal cells were viable after 1.5 hour for the 0.0018 wt% PDAC-0.0015 wt% Berberine-Carbopol complex. Therefore, 0.0045 wt% PDAC-0.00375 wt% berberine-Carbopol concentration was the most effective concentration to kill algal cells after 1.5 hour incubation time.

Figure 6.33 represents a comparison between the antimicrobial activities of PDAC-coated BLC complex, free berberine and Carbopol-encapsulated berberine. More than 90% of algal cells were dead at 0 h incubation time upon incubation with 0.0045 wt% of PDAC but for the same concentration of PDAC which had been used to coat the Carbopol Aqua SF1 to form PDAC-coated Carbopol microgel, there was no toxic effect. There was, however, an increase in the antimicrobial activity for the encapsulated berberine into PDAC-coated Carbopol microgel, in comparison with the uncoated BLC. The reason is that PDAC coated BLC was positively charged and is attracted to the negatively charged surface of the cells, allowing high local concentrations of encapsulated berberine to disrupt the cell membrane and kill the cells. Whereas, there was low biological activity from un-encapsulated berberine (0.00375 wt%) which slowly kills the cells while for the berberine-loaded Carbopol Aqua SF1, there was a slow release of berberine from Carbopol microgel causing delay in the death of cells after 1.5 hour incubation time. In the latter case there is unfavorable repulsion between the BLC and the cell membrane as they both carry negative surface charge.

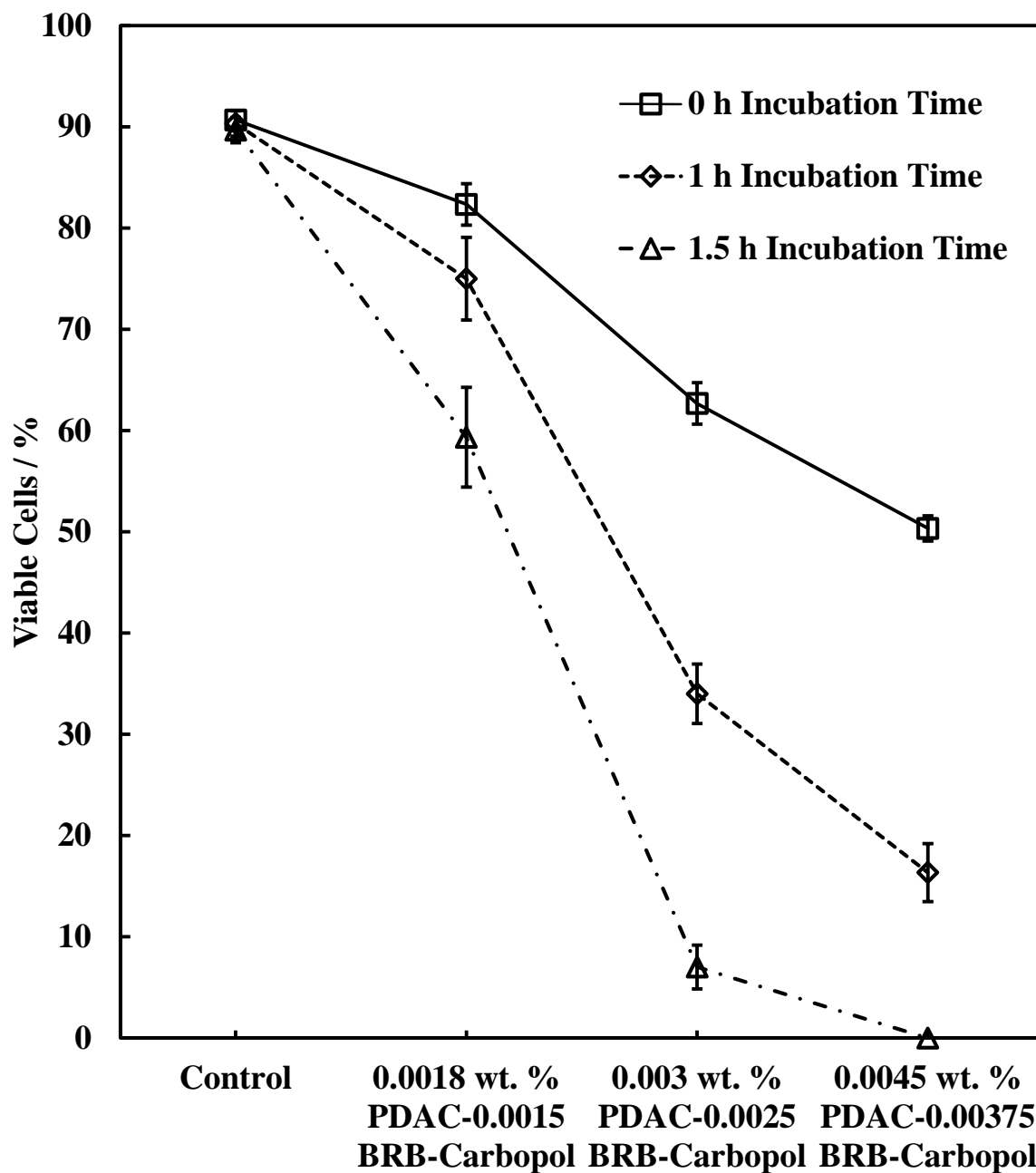


Figure 6.32: The viability of *C.reinhardtii* microalgae cells upon incubation with solutions of different concentrations of PDAC-coated berberine-loaded Carbopol Aqua SF1 microgel. The solutions were prepared depending on dilution from stock solution with the concentration 0.009 wt% PDAC-0.0075 wt%-0.075 wt% berberine-Carbopol Aqua SF1 complex. The measurement was conducted through pipetting 1 mL of each sample, centrifuged twice, incubated with a drop of FDA solution in acetone for 10 minutes, and then centrifuged and dispersed with PBS solution (pH 7.4). After that, the cell viability was measured by automatic cell counter.

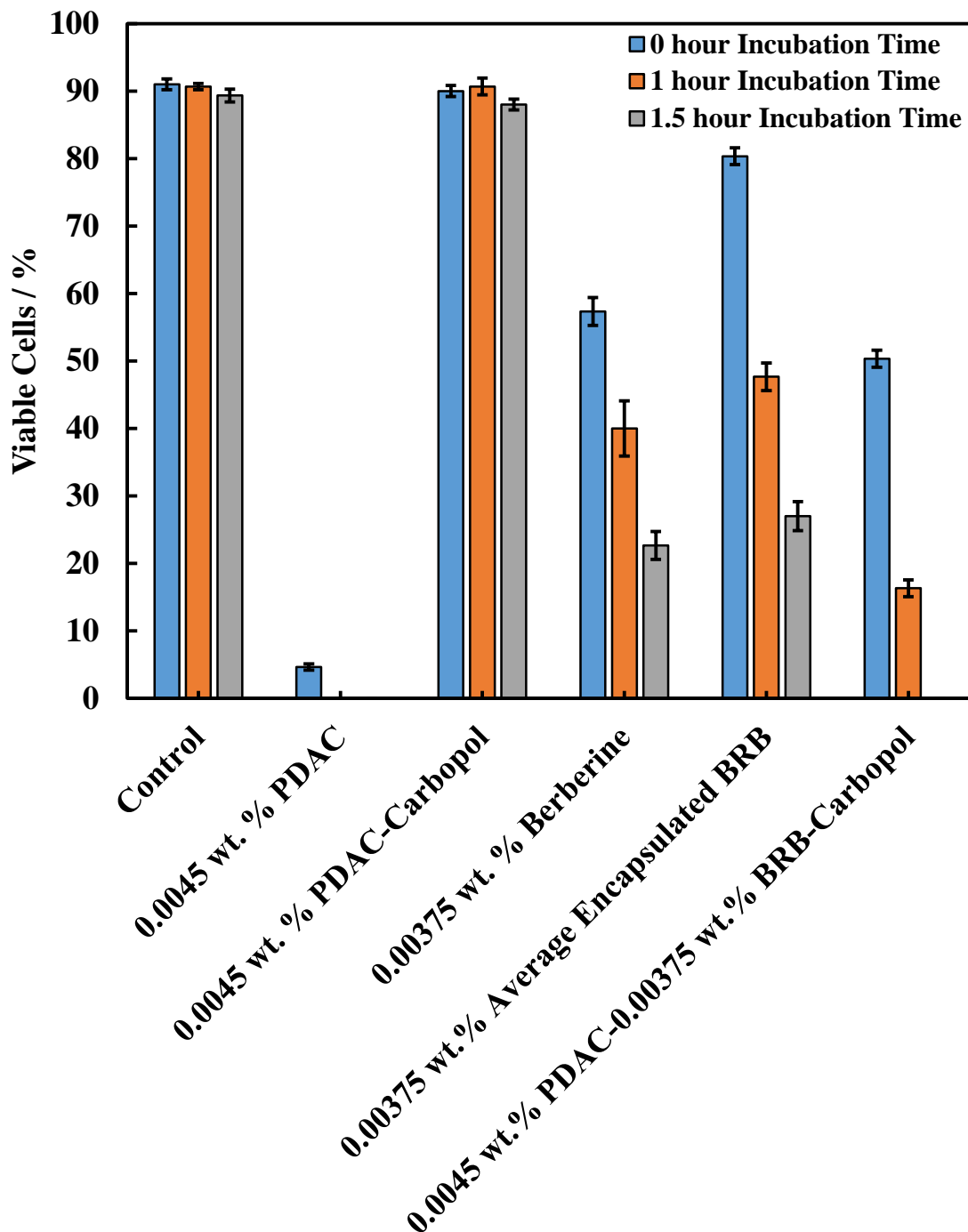


Figure 6.33: The viability of *C.reinhardtii* microalgae cells upon incubation with 0.0045 wt% PDAC, 0.0045 wt% PDAC-coated Carbopol, 0.0375 wt% berberine, 0.00375 wt% Carbopol-encapsulated berberine, and 0.0045 wt. % PDAC-coated 0.00375 wt% berberine-loaded Carbopol Aqua SF1 microgel complex. The measurement was conducted through pipetting 1 mL of each sample, centrifuged twice, incubated with 1 drop of FDA solution in acetone for 10 minutes and then centrifuged and dispersed with PBS solution (pH 7.4). After that, the viability was measured by an automatic cell counter.

Figure 6.34 shows SEM images for *C.reinhardtii* algal cells that had incubated with 0.0045 wt% PDAC-coated 0.00375 wt% berberine-loaded Carbopol Aqua SF1 microgel complex for one hour. From Figure 6.34B, C, and D one sees that microalgae cells were completely damaged by this complex and acquire an irregular shape in comparison with the control sample (see Figure 6.34A). The reason for this is due to the electrostatic interaction between the encapsulated cationic PDAC-coated Carbopol Aqua SF1 and the anionic cell membrane allows adhering particles to diffuse the active material in the local vicinity of the cell surface causing cell death as explained schematically in Figure 6.35.

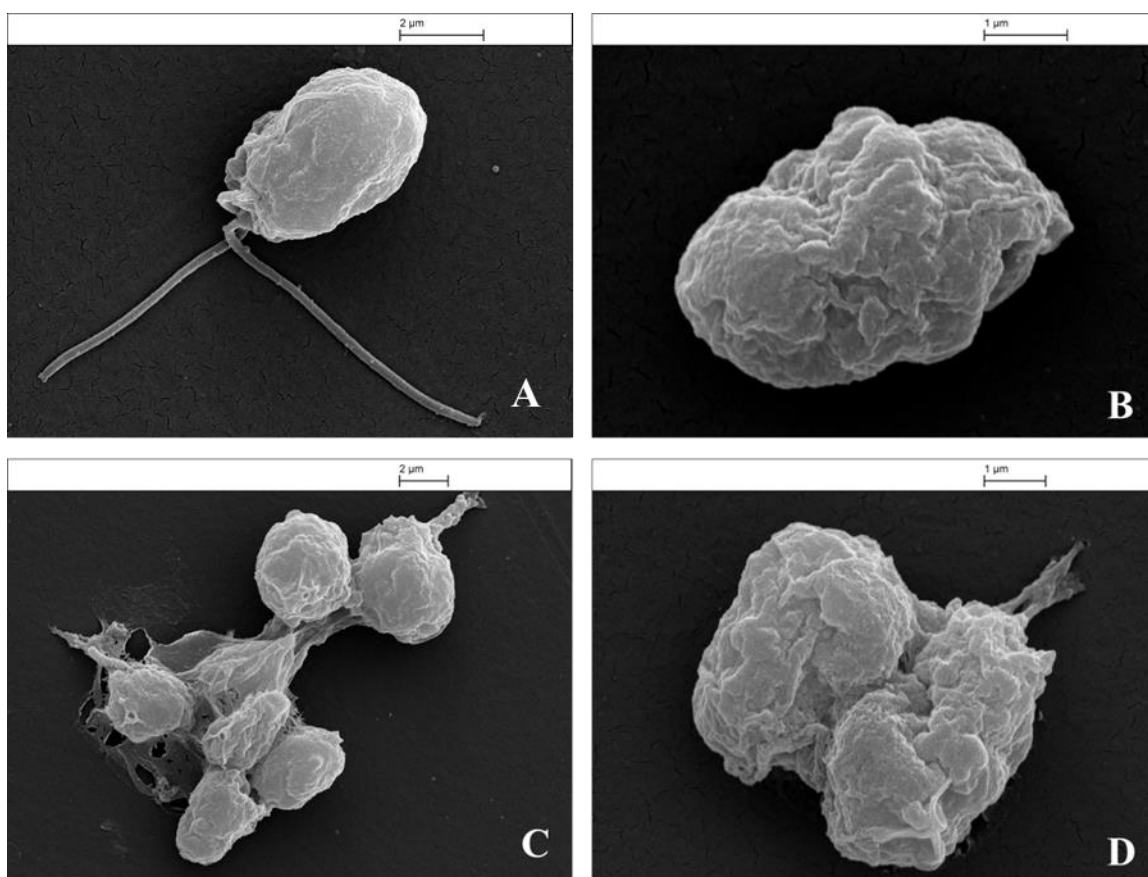


Figure 6.34: SEM images of *C.reinhardtii* microalgae cells. (A) Control sample of the microalgae cells. (B, C, and D) *C.reinhardtii* cells incubated with 0.0045 wt. % PDAC coated 0.00375 wt% berberine-loaded Carbopol Aqua SF1 microgel complex after one hour incubation time at room temperature. The experiment was conducted through incubation a suspension of microalgae cells with solution of PDAC-coated 0.00375 wt% berberine-loaded Carbopol Aqua SF1 particles. The cells were pre-treated for SEM using the procedure described in section 2.2.8.

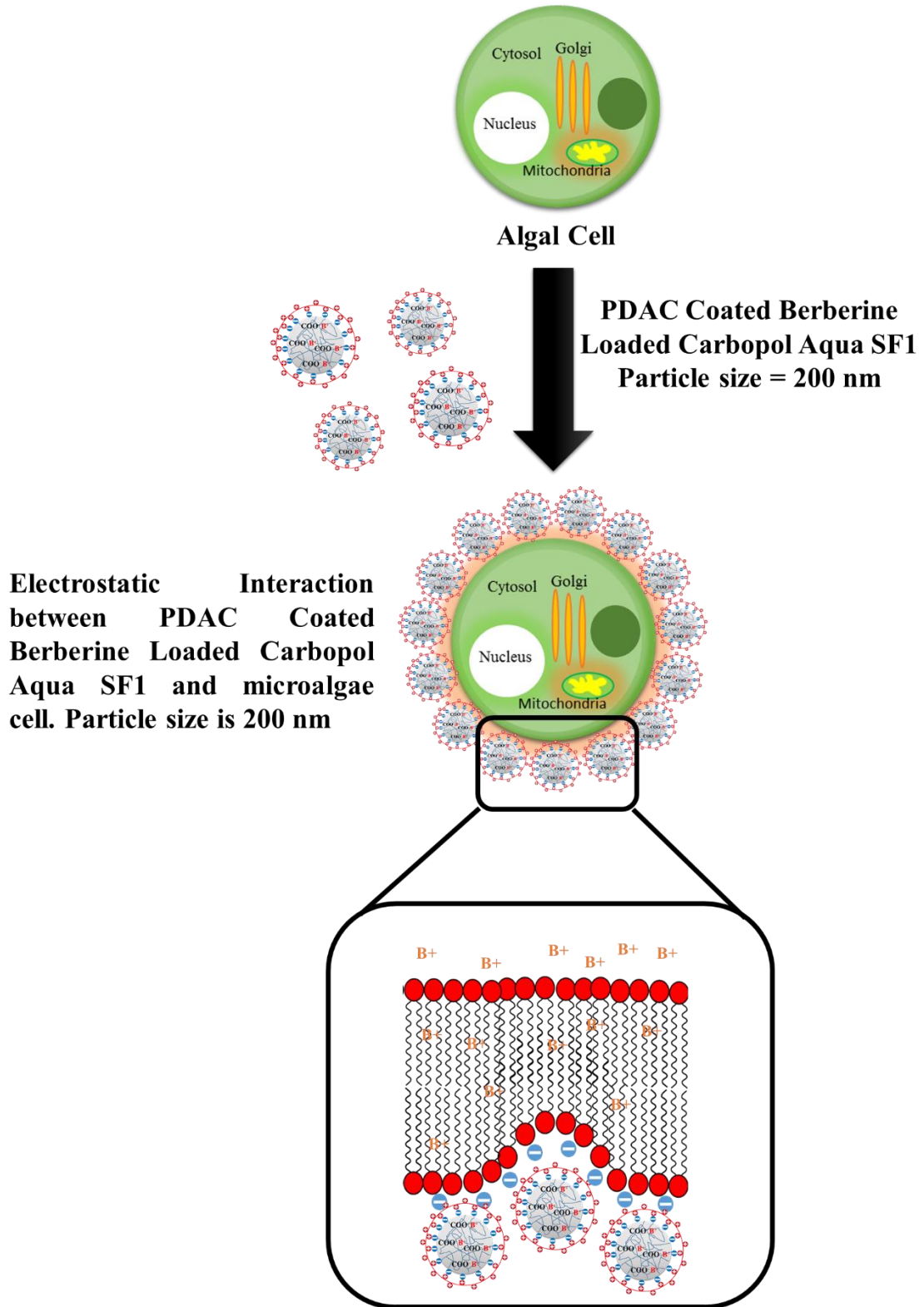


Figure 6.35: Schematic diagram for the electrostatic interaction between PDAC-coated berberine-loaded Carbopol Aqua SF1 particles and the anionic cell membrane of microalgae cells.

6.5.4 Antimicrobial Activity of PDAC coated BLC on Yeast

The antimicrobial activity of berberine-loaded Carbopol Aqua SF1 coated with PDAC was tested on yeast cells at room temperature for up to 2 h. From Figure 6.36 it can be seen that all the yeast cells survived when incubated with different concentrations of PDAC coated BLC particles. One possible explanation is that the cells remained viable because their thick and strong outer shell of the cell membrane which prevents the cationic antimicrobial from reaching the lipid bilayer. These results are in agreement with other studies in the literature⁶ where they tested berberine with yeast cells in the non-growth conditions and it were unable to demonstrate any cytotoxic or genotoxic effects.

Comparing with the results for berberine in the PDAC-coated Carbopol Aqua SF1 microgel with these with the same concentration of free berberine (0.0075 wt%) (Figure 6.37) it can be seen that for the same concentration of free berberine, berberine encapsulated within Carbopol Aqua SF1, and PDAC-coated berberine-loaded Carbopol complex, there was no cytotoxic effect towards yeast cells as compared with control sample. This was in contrast to 0.009 wt% free cationic polyelectrolyte PDAC which was a lethal concentration when incubated with yeast cells which is enough to disrupt the yeast cell membrane. The PDAC decreases its toxicity upon interacting with the anionic Carbopol microgel to form the PDAC-coated Carbopol Aqua SF1 microgel. Figure 38 displays the SEM images for yeast cells upon incubation with PDAC-coated berberine-loaded Carbopol particles. It can be seen in Figure 6.38B, C, D and E that yeast cells were appeared to have dimples and cavities on their surface due to the electrostatic attraction with cationic PDAC-coated berberine-loaded Carbopol microgel particles, allowing berberine to penetrate into the cells compared with the control sample of yeast as shown in Figure 6.38A. However, free berberine did not kill the yeast cells because they have rigid and thick outer membrane layer that prevents berberine molecules to disrupt the lipid bilayer.

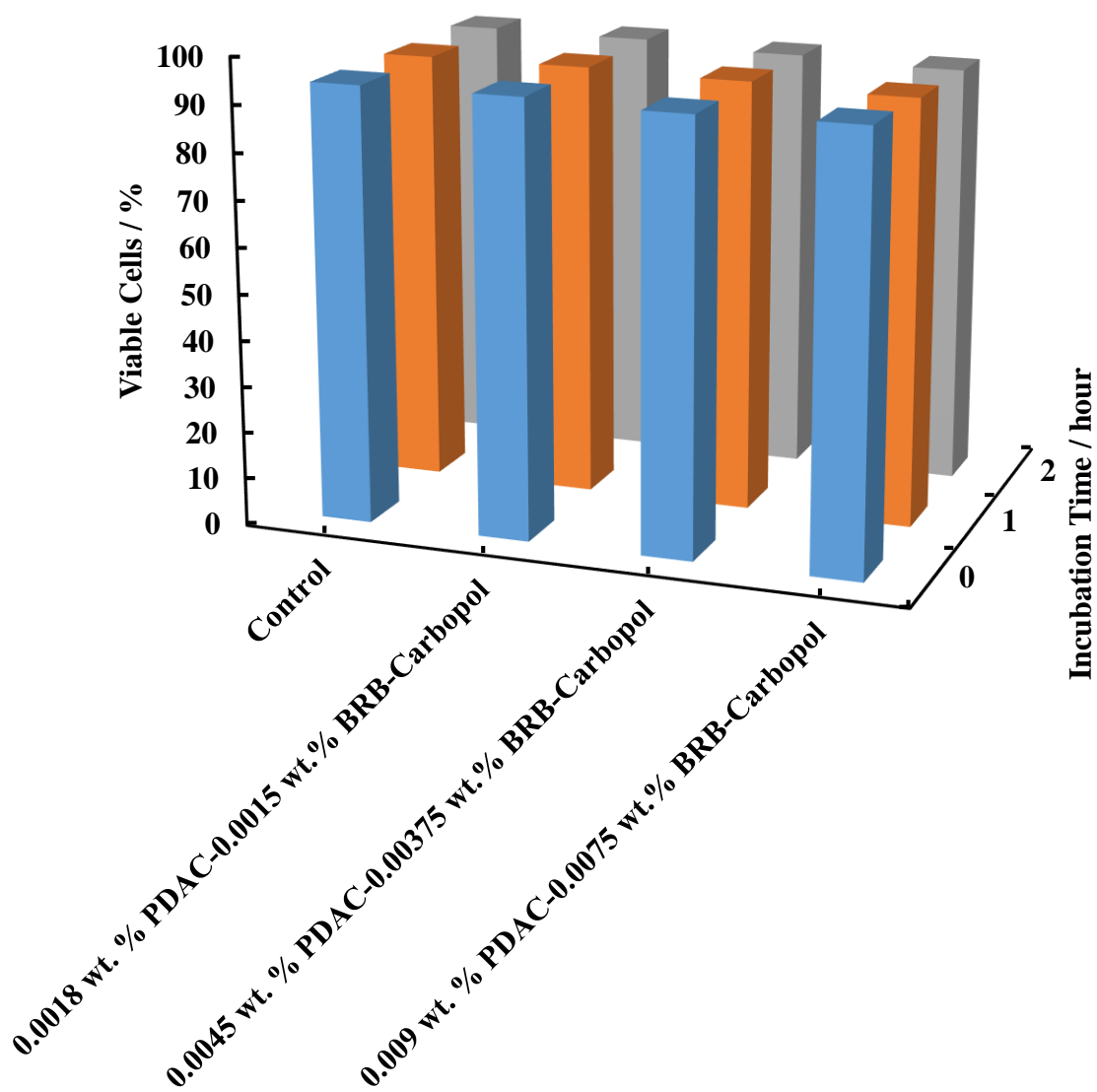


Figure 6.36: The viability of yeast cells upon incubation with solutions of different concentrations of PDAC-coated berberine-loaded Carbopol microgel. These suspensions were prepared by dilution from a stock solution with the concentration 0.009 wt% PDAC-0.0075 wt% berberine -0.075 wt% Carbopol Aqua SF1 complex.

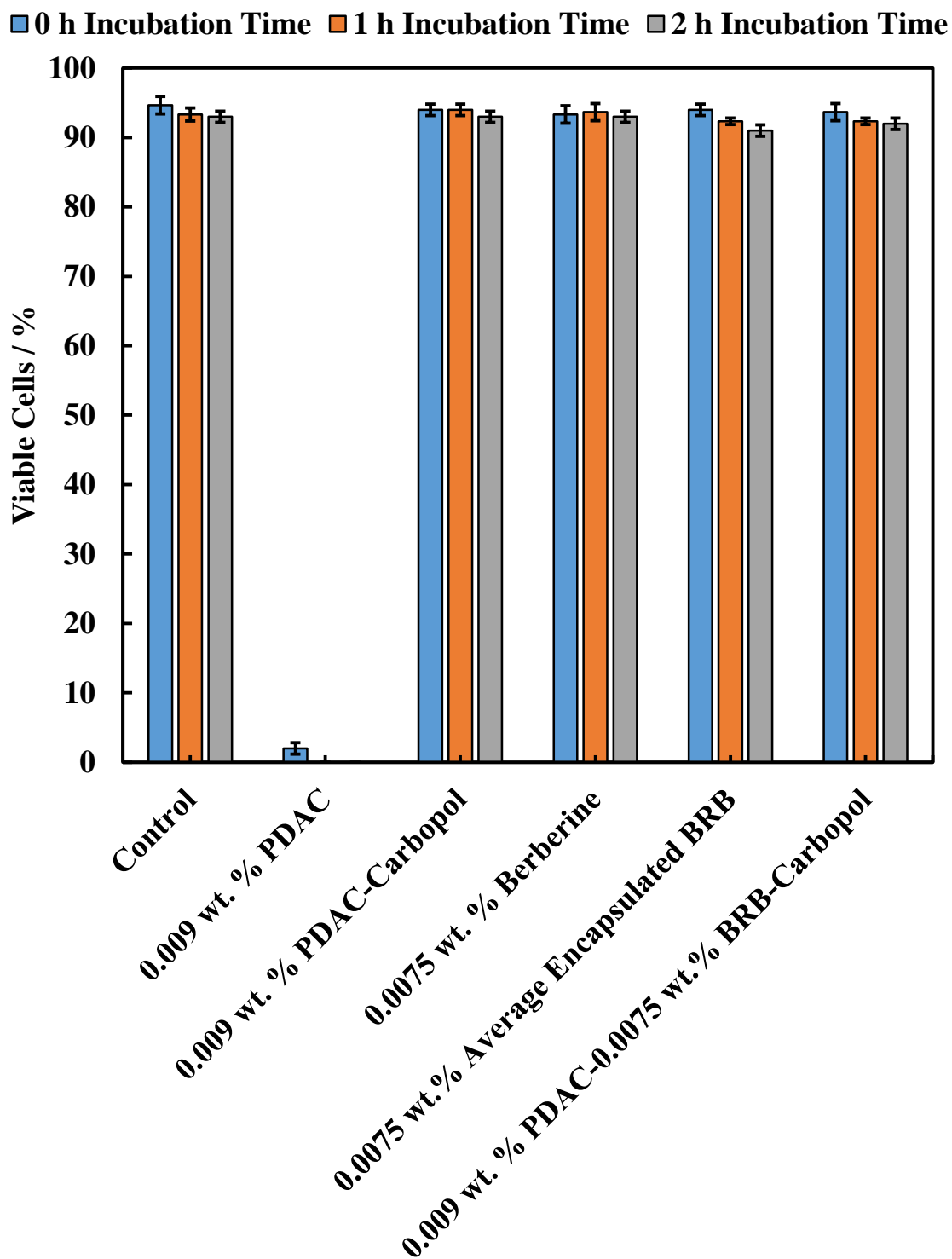


Figure 6.37: The viability of yeast cells upon incubation with 0.009 wt% PDAC, 0.009 wt% PDAC-coated Carbopol Aqua SF1, 0.0075 wt% berberine, 0.0075 wt% encapsulated berberine, and 0.009 wt% PDAC-coated 0.0075 wt% berberine-loaded Carbopol Aqua SF1 microgel complex.

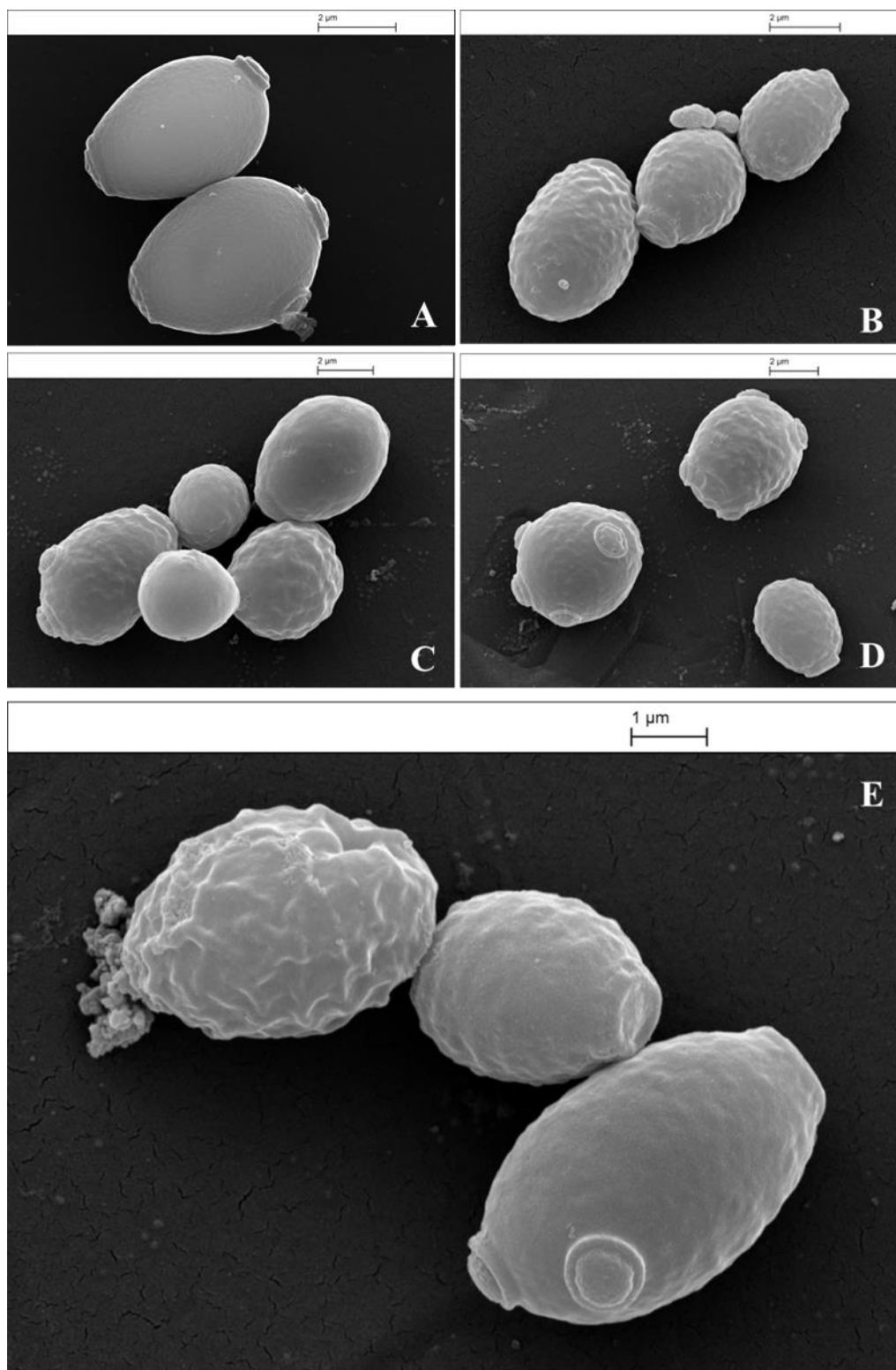


Figure 6.38: SEM images of yeast cells. (A) Control sample of yeast cell and (B, C, D, and E) yeast cells that incubated with 0.009 wt% PDAC-coated 0.0075 wt% berberine-loaded Carbopol Aqua SF1 microgel complex after two hours of incubation. The SEM samples were pretreated with the procedure described in section 2.2.8.

6.5.5 Antimicrobial Activity of PDAC Coated BLC on *E.coli*

The antimicrobial activity of PDAC-coated berberine-loaded Carbopol Aqua SF1 microgel complex (PDAC coated BLC) with *E.coli* was investigated by incubation of solutions of various concentration of PDAC coated BLC with a fixed amount of *E.coli* cells removed from their culture media for two hours at room temperature. Figure 6.39 shows that there was no noticeable antimicrobial activity for berberine concentrations from 0.0015 wt% to 0.0025 wt%. However, antimicrobial activity was seen for concentrations of 0.00375 wt% to 0.006 wt% berberine after two hours of incubation. Suspensions with 0.006 wt% Carbopol-encapsulated berberine appeared to have high antimicrobial activity, killing the cells. This increase in the antimicrobial efficiency towards the cells was attributed to the increase in the concentration of berberine encapsulated into the Carbopol microgel as well as the electrostatic interaction between PDAC-coated Carbopol-encapsulated berberine and the outer cell membrane of *E.coli*, in which the encapsulated berberine is released locally and disrupts the *E.coli* cells membrane causing cell death.

The comparison between the uncoated and the PDAC-coated microgel particles upon incubation with *E.coli* cells can be seen in in Figure 6.40. The uncoated particles were toxic after two hours period of incubation time. However, when we used same concentration of PDAC to coat the Carbopol Aqua SF1 microgel and incubated with the cells, it was found that all cells remained viable for the same period of time. The cells were also incubated with 0.006 wt% free and Carbopol encapsulated berberine and it was discovered that no significant antimicrobial activities was seen for both cases at the same overall concentration of berberine. Contrastingly, a considerable increase in the antimicrobial activity was observed after the incubation of the *E. coli* cells with PDAC-coated 0.006 wt% berberine-loaded Carbopol at the same incubation time. The reason is attributed to the interaction between cell membrane and the PDAC-coated berberine encapsulated particles which allowed the encapsulated berberine to get through and kill cells.

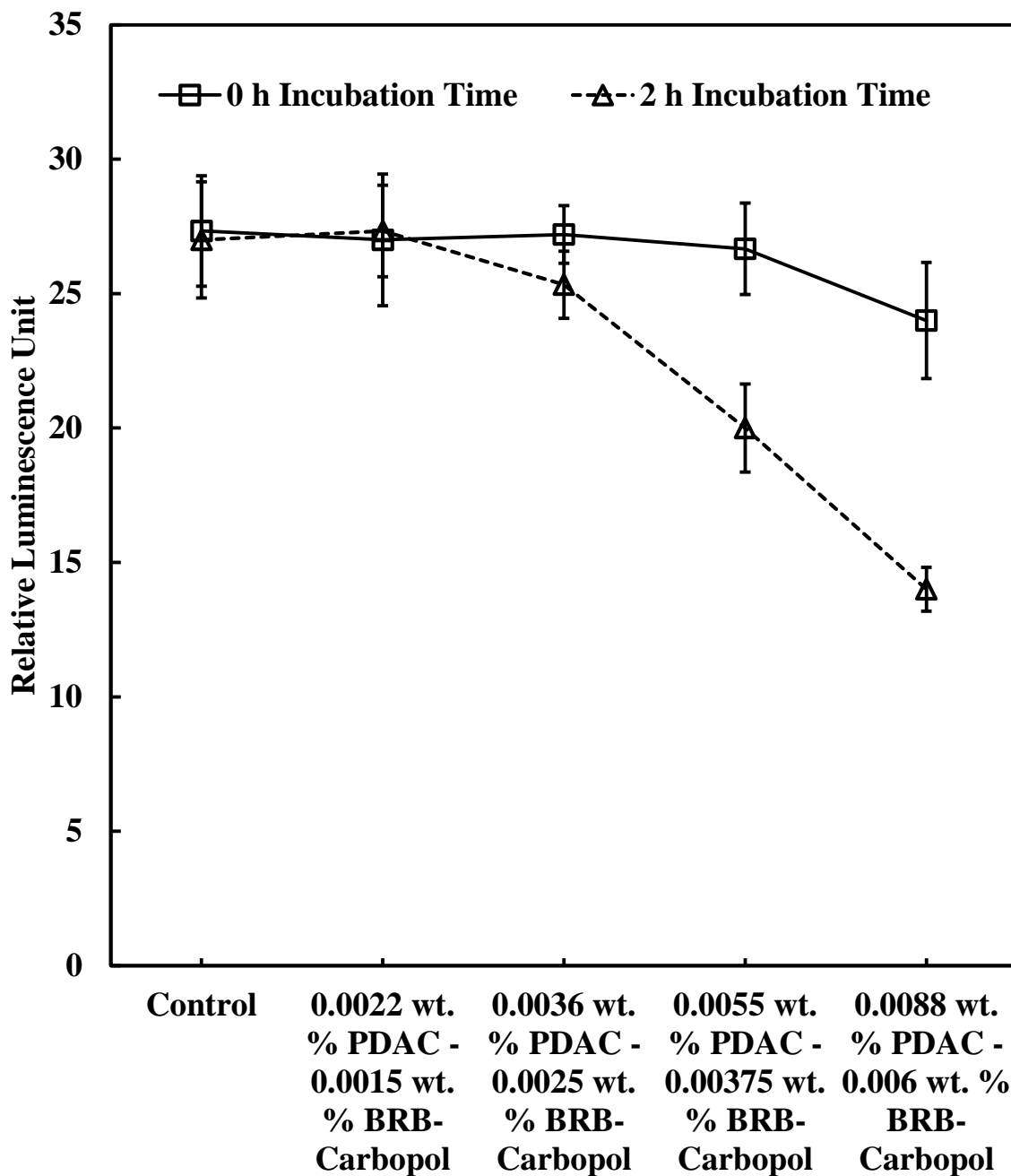


Figure 6.39: The antimicrobial activity of suspensions of different concentrations of PDAC-coated berberine-loaded Carbopol Aqua SF1 (PDAC coated BLC) against *E. coli* cells. The solutions were prepared from the stock solution (0.011 wt% PDAC-coated 0.0075 wt% berberine-loaded 0.05 wt% Carbopol Aqua SF1 complex).

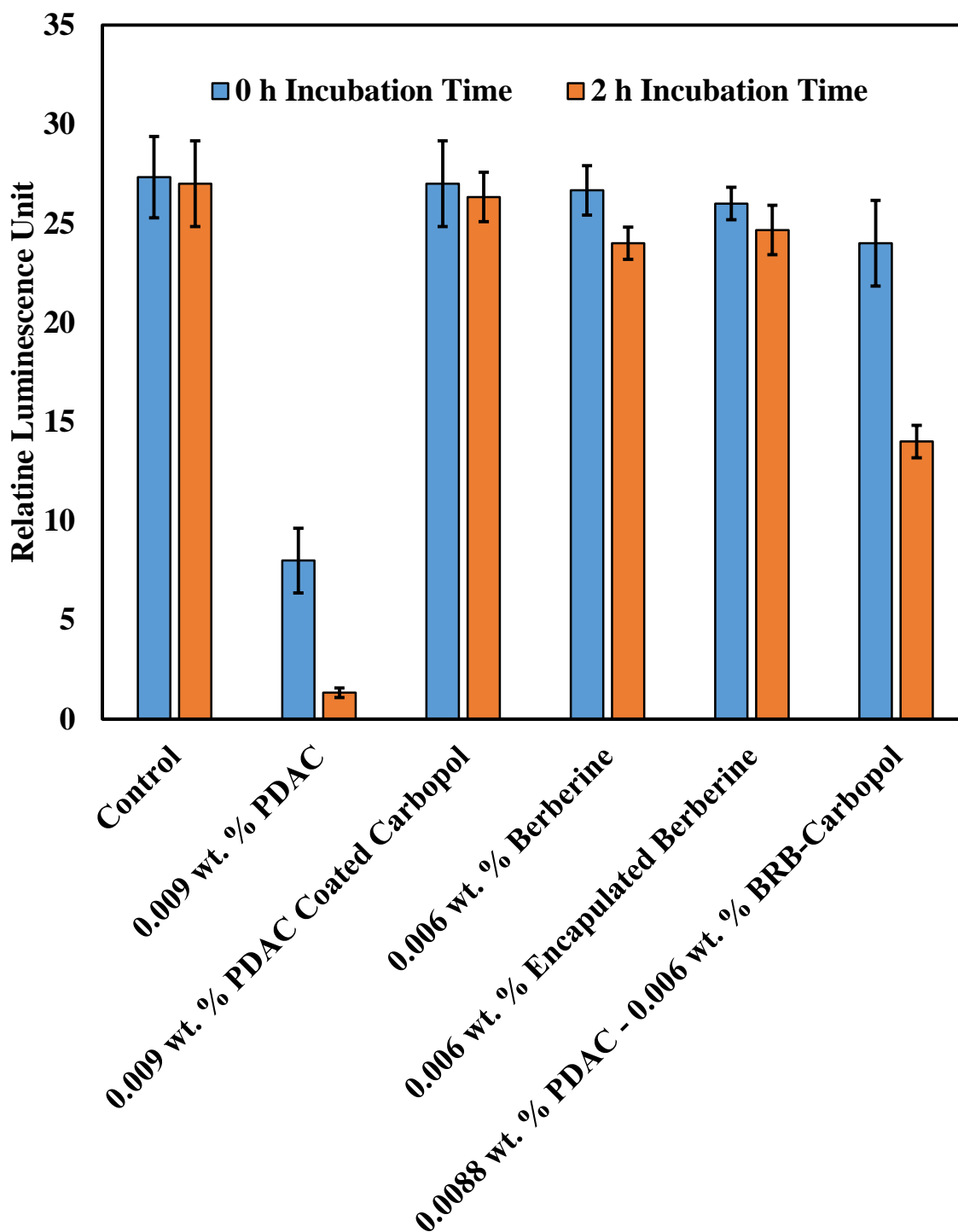


Figure 6.40: The antimicrobial activity of 0.0088 wt% PDAC-coated 0.006 wt% berberine-loaded Carbopol towards *E.coli* cells as a function of both the antimicrobial activity of free and Carbopol-encapsulated berberine and the cytotoxic effect of uncoated and PDAC-coated particles. The incubation was also performed through incubation each concentration with a fixed amount of *E.coli* cells after their removal from the culture media.

Figure 6.41 shows SEM images of *E.coli* cells that were incubated with 0.0088 wt% PDAC-coated 0.006 wt% berberine-loaded Carbopol particles for two hours at room temperature. It can be seen from Figure 6.41B, C, and D that particles of PDAC-coated berberine-loaded Carbopol are clustered on the surface of the cell membrane of *E.coli* cells compared with control sample where there was no berberine involved (see Figure 6.41A). This aggregation happened due to the electrostatic attraction between the cationic PDAC-coated berberine-loaded Carbopol particles and the anionic cell membrane of *E.coli* which contributed to the increase of the antimicrobial activity of berberine in comparison with the same concentration of free berberine over the same period of incubation.

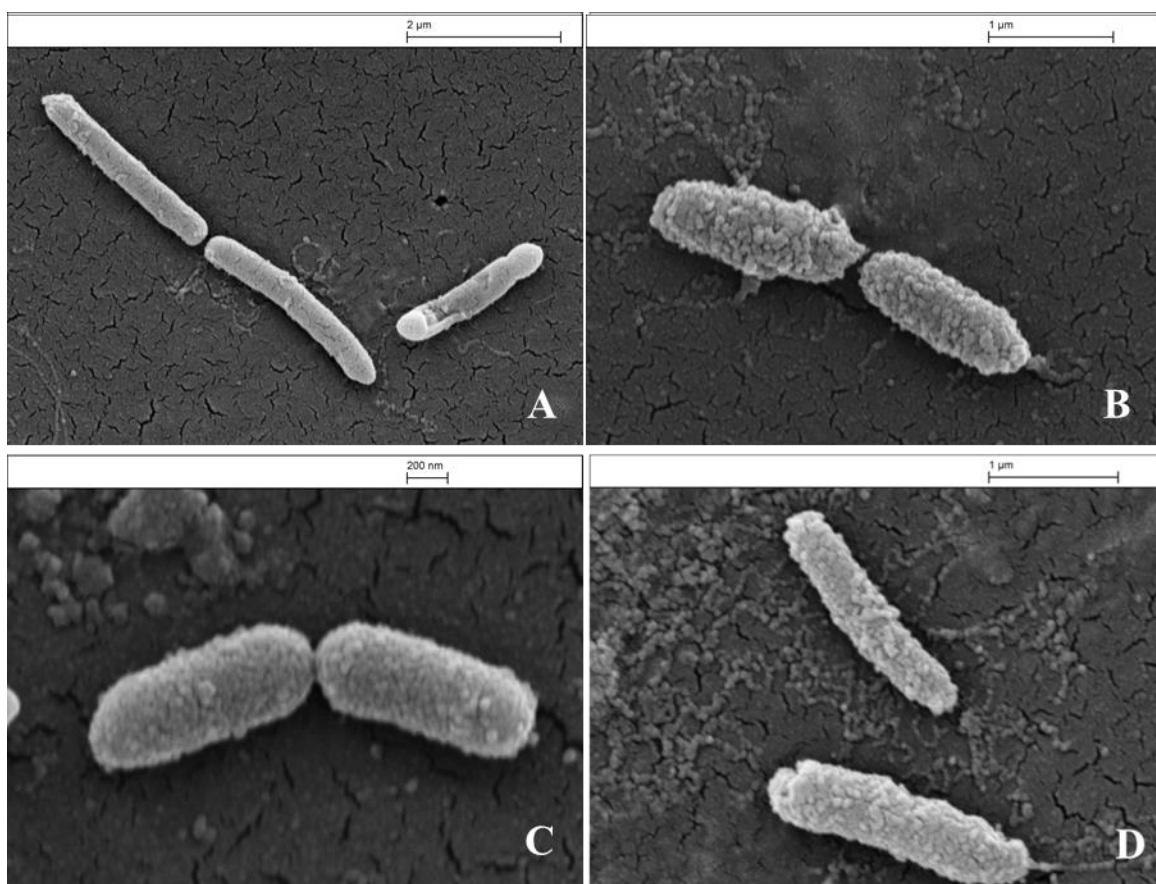


Figure 6.41: SEM images of *E.coli* cells. (A) Control sample of *E.coli* and (B, C, and D) incubation of *E.coli* cells with solution of 0.0088 wt% PDAC coated 0.006 wt% berberine-loaded Carbopol suspension.

6.5.6 Antimicrobial Activity of PDAC-coated CLC on Microalgae

The antimicrobial activity of chlorhexidine with microalgae cells was examined through incubation of suspensions of different concentrations of PDAC-coated chlorhexidine-loaded Carbopol microgel with microalgae cells for 1 hour. Figure 6.42 shows that at 0 hours incubation time (immediately upon incubation), the viability of the microalgae had sharply decreased to 41%, 32% and 25% at 0.0018 wt% PDAC-0.009 wt% Chlorhexidine-Carbopol Aqua SF1, 0.003 wt% PDAC-0.015 wt% Chlorhexidine-Carbopol, and 0.0045 wt% PDAC-0.0225 wt% Chlorhexidine-Carbopol, respectively. All the cells died for concentrations between 0.003 wt% and 0.0045 wt% PDAC-Chlorhexidine-Carbopol complex but approximately 10% viable cells remained from incubation of at the lower concentration after 1 hour. This means that both 0.003 wt% PDAC-0.015 wt% Chlorhexidine-Carbopol microgel and 0.0045 wt% PDAC-0.0225 wt% Chlorhexidine-Carbopol were effective in killing microalgae cells.

The antimicrobial activity of PDAC-coated chlorhexidine-loaded Carbopol was compared with that of free PDAC and PDAC-coated Carbopol Aqua SF1. We also compared these results with the antimicrobial activity of free chlorhexidine and uncoated chlorhexidine-loaded Carbopol microgel particles as shown in Figure 6.43. The free cationic polyelectrolyte PDAC was toxic and killed all the cells after one hour. The PDAC-coated Carbopol microgel did not have measurable cytotoxic effect on microalgae cells. There was, however, a significant increase in the antimicrobial activity of both free chlorhexidine (0.025 wt%) and 0.0045 wt% PDAC coated 0.0225 wt% chlorhexidine-loaded Carbopol towards microalgae cells in comparison with the uncoated chlorhexidine-loaded Carbopol microgel. This occurs because of the electrostatic attraction between the cationic PDAC-coated encapsulated chlorhexidine and the anionic cell membrane of the microalgae which allows for chlorhexidine to disrupt locally the cell membrane causing the cell death. Whereas, there was no interaction between the anionic chlorhexidine-loaded Carbopol particles and the cell membrane due to the electrostatic repulsion forces. Figure 6.44 shows SEM images of *C.reinhardtii* cells that were incubated with a suspension of 0.0045 wt% PDAC-0.0225 wt% Chlorhexidine-Carbopol complex for one hour. It can be illustrated in Figure 6.44B, C, and D that the particles of PDAC-coated chlorhexidine loaded Carbopol microgel were trapped on the cell membrane of the microalgae cells. This clustering and

accumulation of antimicrobial particles is attributed to the attraction between the cationic particle and anionic surface of the cells. The local release of chlorhexidine molecules increased the antimicrobial action. It can also be seen in Figure 6.44E, a high magnification of SEM image of 44D which explains the heterocoagulation of the antimicrobial particles on the cells.

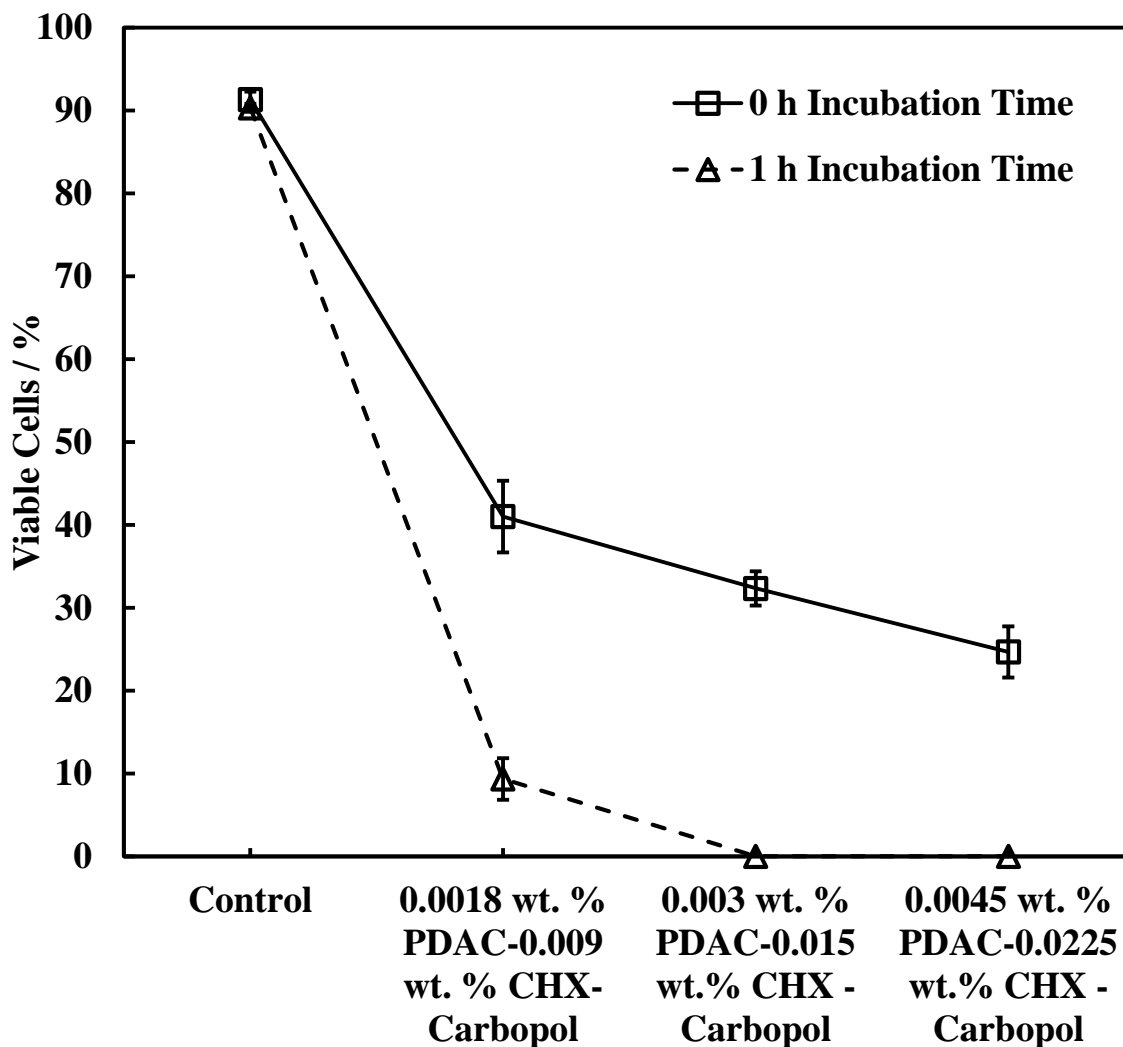


Figure 6.42: The viability of microalgae cells versus solution of several different concentrations of PDAC-coated chlorhexidine loaded Carbopol microgel which have been prepared from the stock solution 0.0045 wt% PDAC – 0.045 wt% Chlorhexidine – 0.05 wt% Carbopol dispersion.

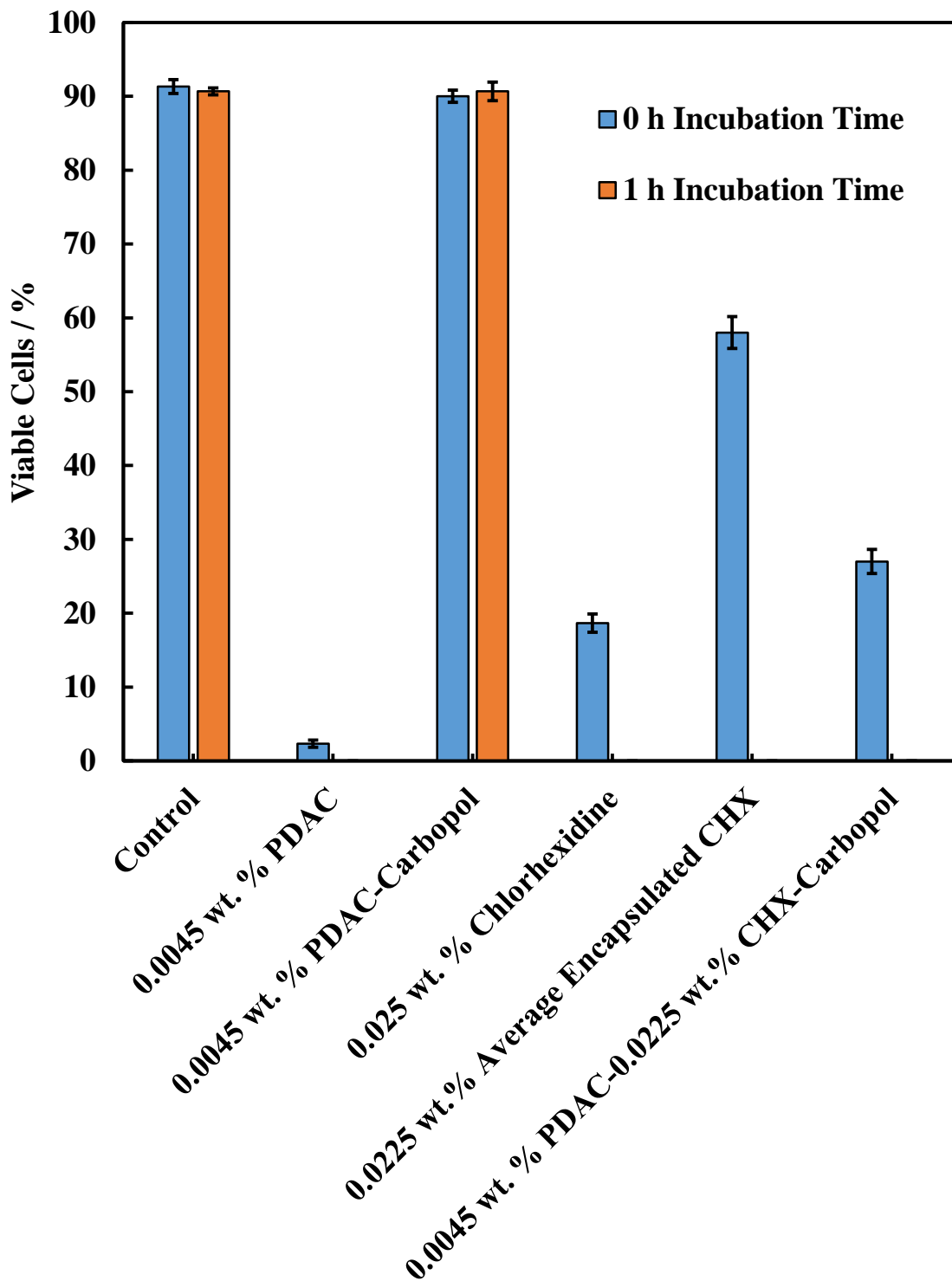


Figure 6.43: The comparison between the antimicrobial activity of 0.0045 wt% PDAC-0.0225 wt% Chlorhexidine-Carbopol microgel, the Carbopol-encapsulated chlorhexidine (0.0225 wt%), 0.025 wt% chlorhexidine and the cytotoxic effect of free 0.0045 wt% PDAC and 0.0045 wt% PDAC-coated Carbopol Aqua SF1 against the control sample of algal cells.

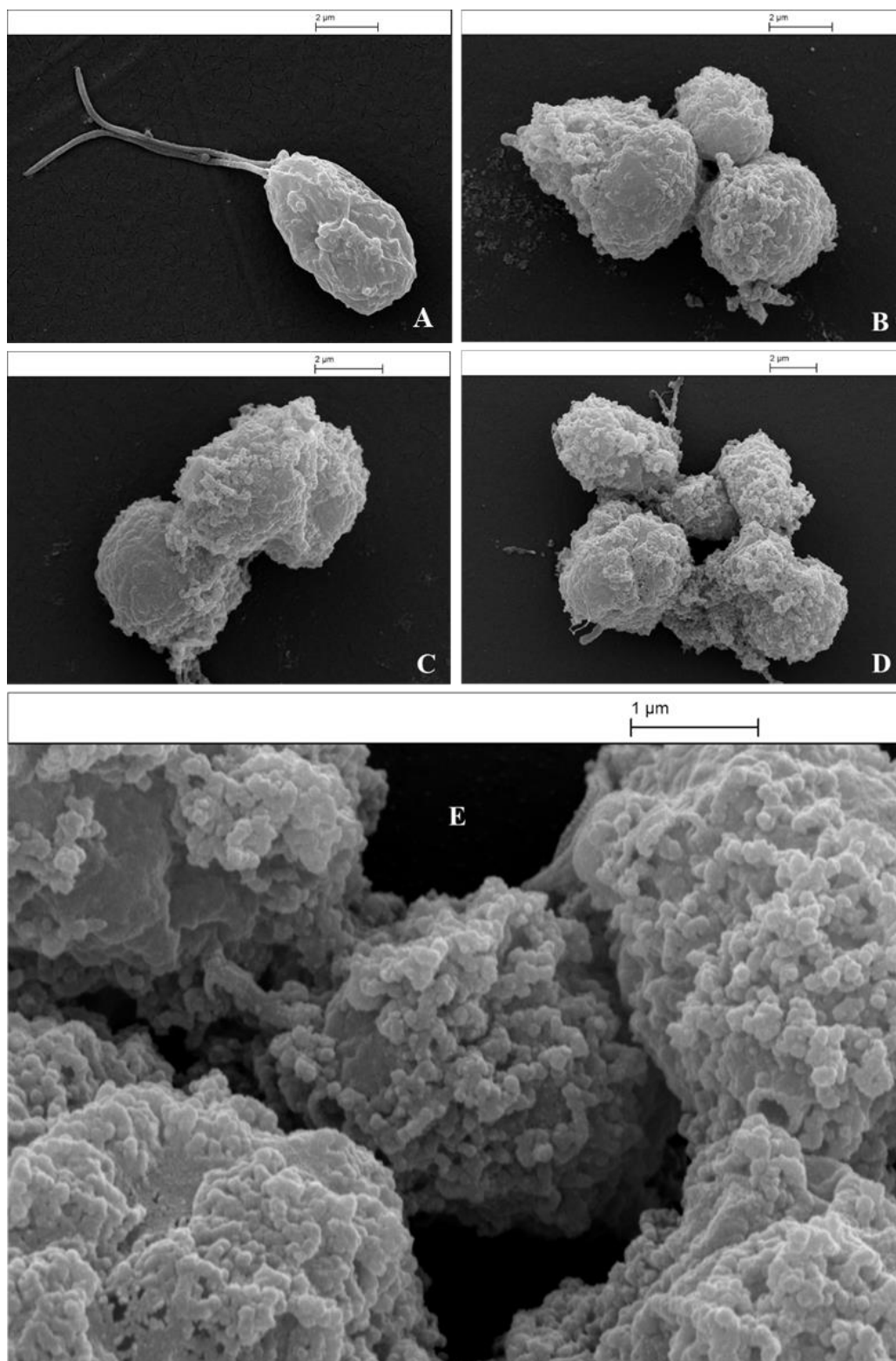


Figure 6.44: SEM images of *C. reinhardtii* cells. (A) Control sample and (B, C, D, and E) samples after incubation in a suspension of 0.0045 wt% PDAC-0.0225 wt% Chlorhexidine-Carbopol Aqua SF1 complex suspension with *C. reinhardtii* cells for one hour.

6.5.7 Antimicrobial Activity of PDAC-coated CLC on Yeast

The antimicrobial activity of PDAC coated chlorhexidine-loaded Carbopol Aqua SF1 microgel towards yeast cells was then investigated at room temperature for a 2 hours incubation period as shown in Figure 6.45. As previously, the cell culture media had been removed to prevent any unwanted interaction. It can be seen that the viability of yeast cells was reduced to 34% at high concentration while it was around 60% at low concentration at 0 h incubation. An hour later, the viability was considerably reduced to 35%, 23% and 15% for 0.0018 wt% PDAC-0.009 wt% Chlorhexidine-loaded Carbopol microgel, 0.0045 wt% PDAC-0.0225 wt% Chlorhexidine-loaded Carbopol microgel and 0.009 wt% PDAC-0.045 wt% Chlorhexidine-loaded Carbopol microgel, respectively. After 2 h both 0.0045 wt% PDAC-0.0225 wt% Chlorhexidine-loaded Carbopol and 0.009 wt% PDAC-coated 0.045 wt% Chlorhexidine-loaded Carbopol microgel had been the most active concentrations killing all cells because of the attraction between PDAC-coated microgel with encapsulated chlorhexidine and the cell membrane.

The antimicrobial activity towards yeast cells was best for 0.009 wt% PDAC-0.045 wt% Chlorhexidine-loaded Carbopol, free chlorhexidine (0.05 wt%) and 0.045 wt% chlorhexidine-loaded Carbopol Aqua SF1 microgel which are compared as shown in Figure 6.46. The figure also demonstrates the cytotoxic effect of each of 0.009 w% PDAC and 0.009 wt% PDAC-coated Carbopol microgel whereby 0.009 wt% free PDAC had appeared a toxic effect towards yeast cells while the PDAC-coated Carbopol did not affect the viability of yeast cells. PDAC-coated chlorhexidine-loaded Carbopol showed enhanced antimicrobial activity in comparison with the same concentration of uncoated chlorhexidine-loaded Carbopol which appeared to have a very low antimicrobial activity with 86% of the cells being viable after 2 hours. However, the free chlorhexidine seemed to have antimicrobial activity which is higher than that for PDAC-coated Carbopol with encapsulated chlorhexidine. The surface morphology of yeast cells incubated with 0.009 wt% PDAC-0.045 wt% Chlorhexidine-loaded Carbopol was examined using SEM as shown in Figure 6.47. It can be seen in Figure 6.47B, 6.47C, 6.47D, and 6.47E that yeast cells suffered a profound change of morphology from the interaction with PDAC-coated Carbopol with encapsulated chlorhexidine causing irregular surface shape with cavities as compared with control sample (Figure 6.47A) where there was no chlorhexidine. This

approach allowed enhancing of the antimicrobial action of chlorhexidine in comparison with free chlorhexidine at the same concentration.

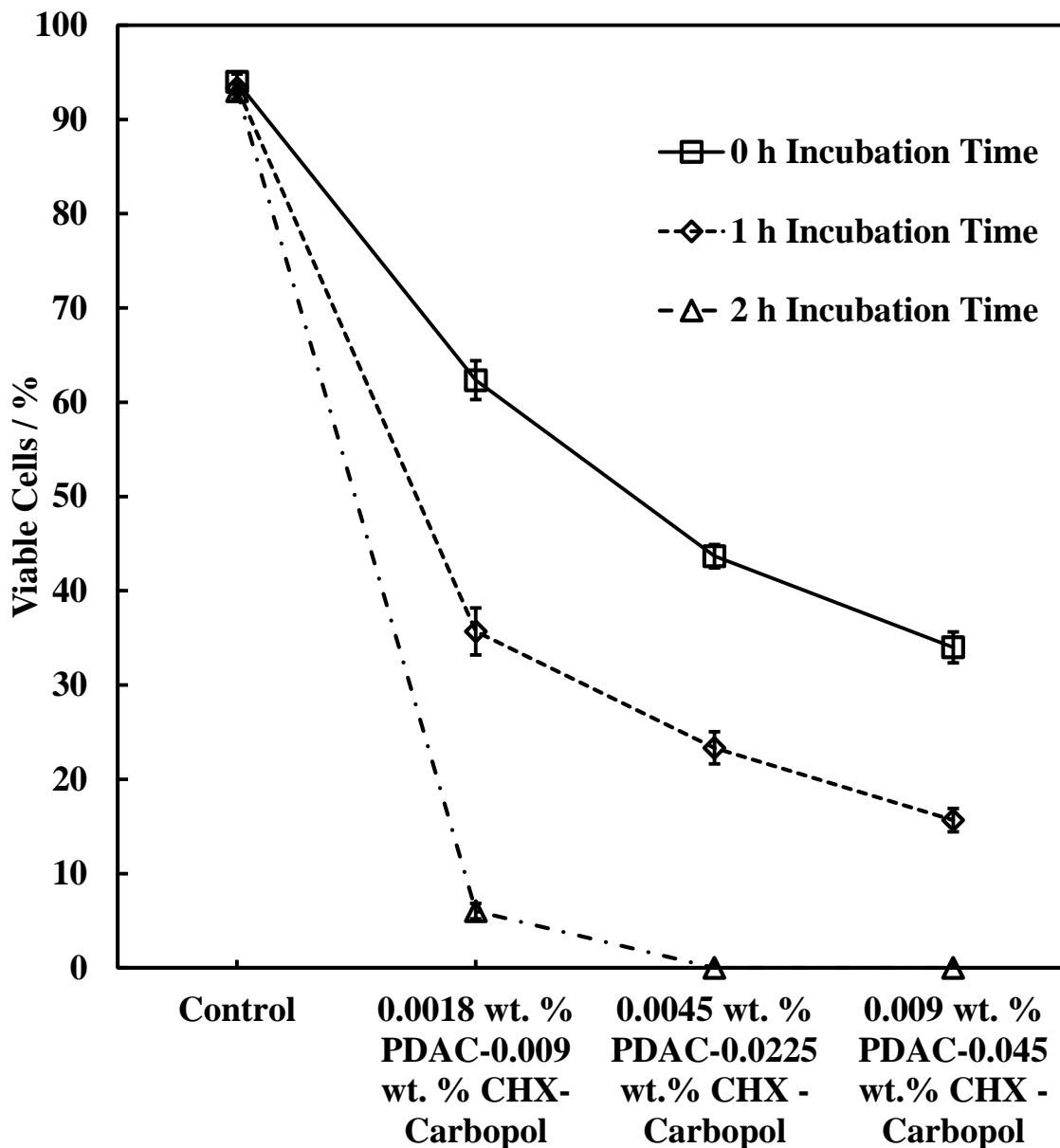


Figure 6.45: The viability of yeast cells versus suspensions of several concentrations of PDAC-coated chlorhexidine-loaded Carbopol prepared from a stock solution 0.0045 wt% PDAC – coated particles of 0.045 wt% Chlorhexidine – loaded in 0.05 wt. % Carbopol Aqua SF1 microgel.

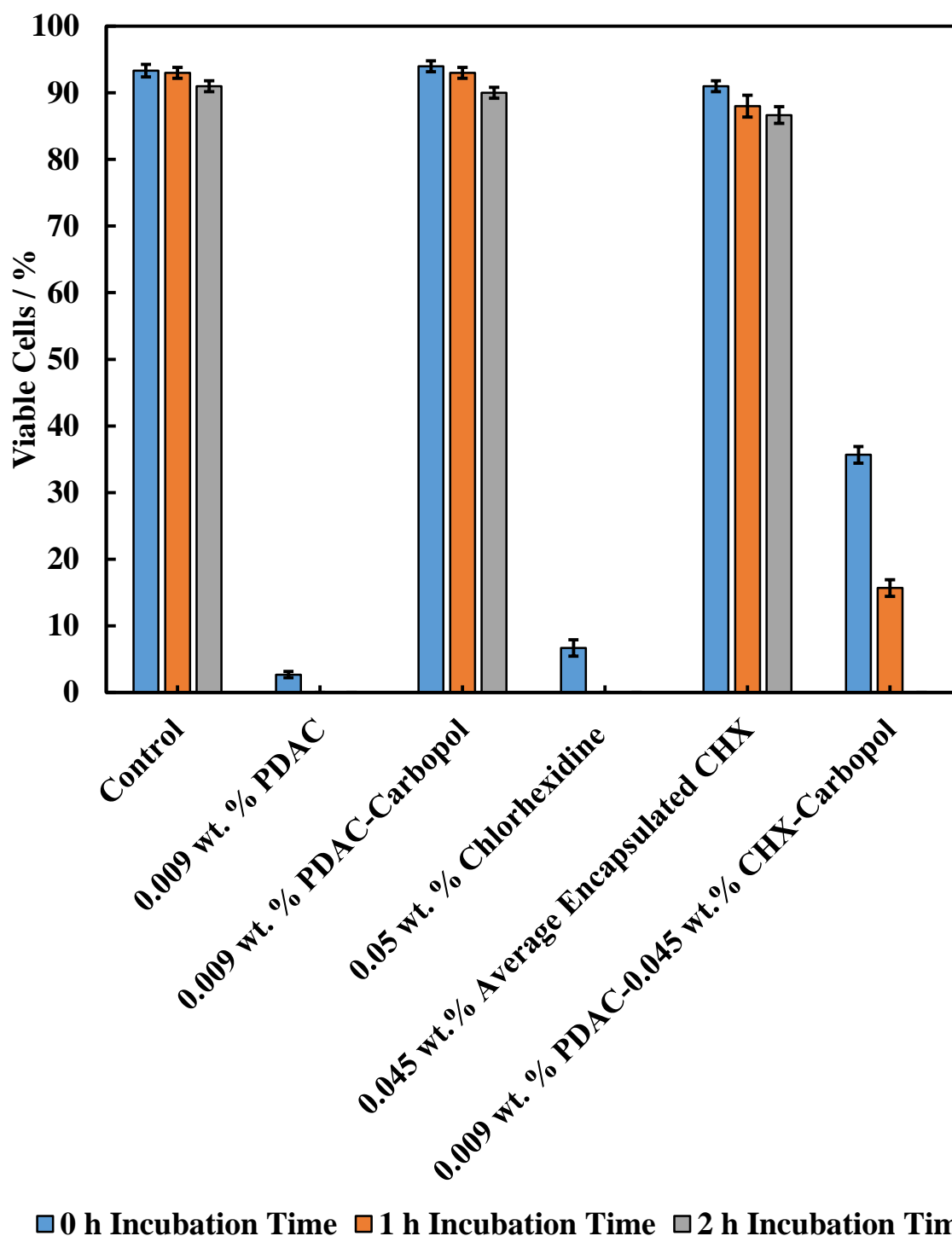


Figure 6.46: The comparison between the antimicrobial activity against yeast of 0.009 wt% PDAC-0.045 wt% Chlorhexidine-Carbopol microgel particles, the Carbopol-encapsulated chlorhexidine (of overall concentration 0.045 wt. %), 0.05 wt% chlorhexidine and the cytotoxic effect of free 0.009 wt. % PDAC and 0.009 wt. % PDAC-coated Carbopol against the control sample.

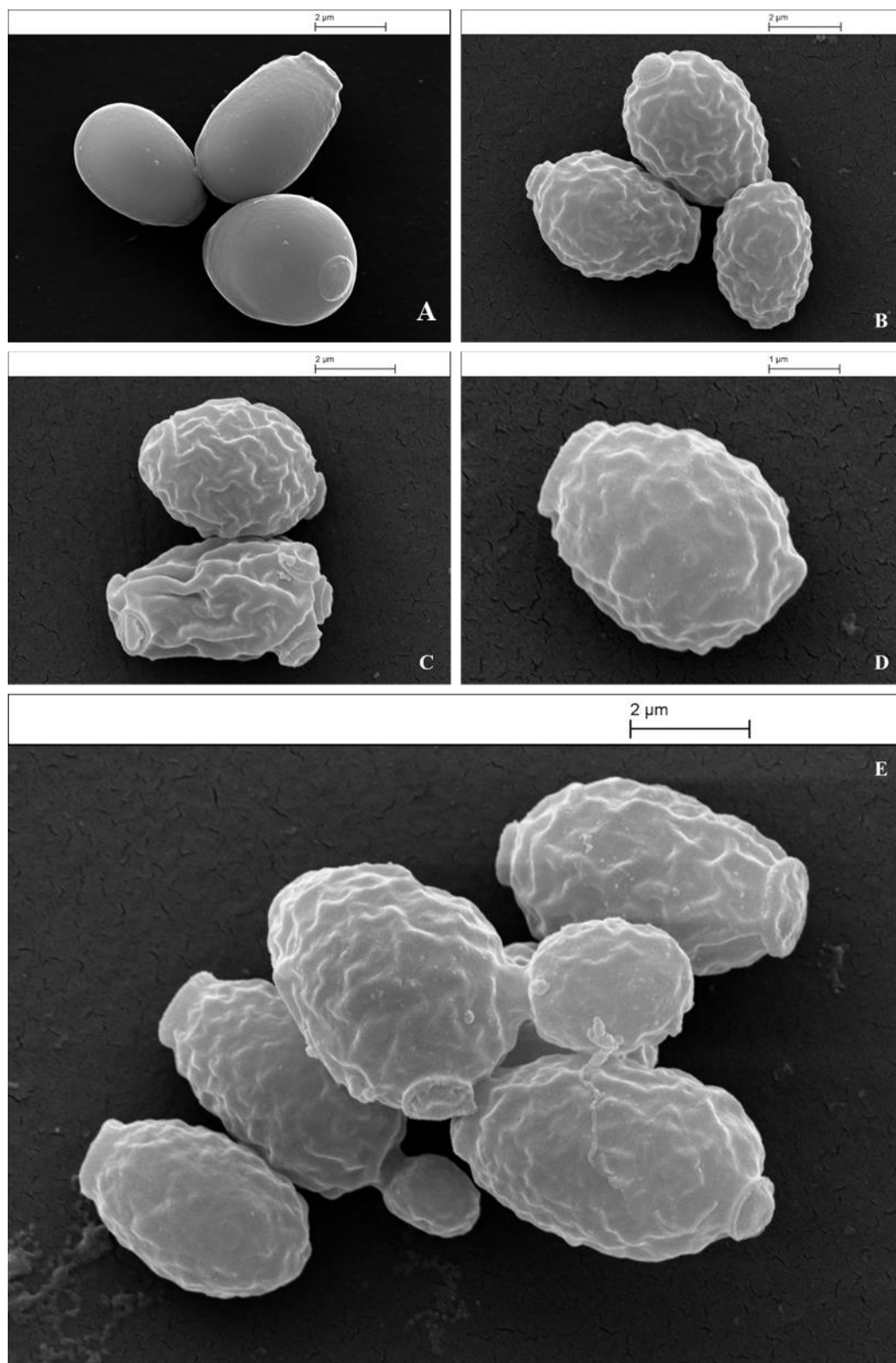


Figure 6.47: SEM images of yeast cells: (A) Control sample of yeast cell and (B, C, D, and E) represent the result of the incubation of yeast cells in suspension and 0.009 wt% PDAC-0.045 wt% Chlorhexidine-loaded Carbopol microgel particles after 2 hours.

6.5.8 Antimicrobial Activity of PDAC Coated CLC on *E.coli*

Finally, the antimicrobial activity of PDAC-coated chlorhexidine-loaded Carbopol microgel towards *E.coli* cells was studied for up to two hours of incubation. Figure 6.48 shows the relative luminescence intensity of *E.coli* cells upon incubation with series of PDAC coated CLC concentrations followed by exposure to luciferase.

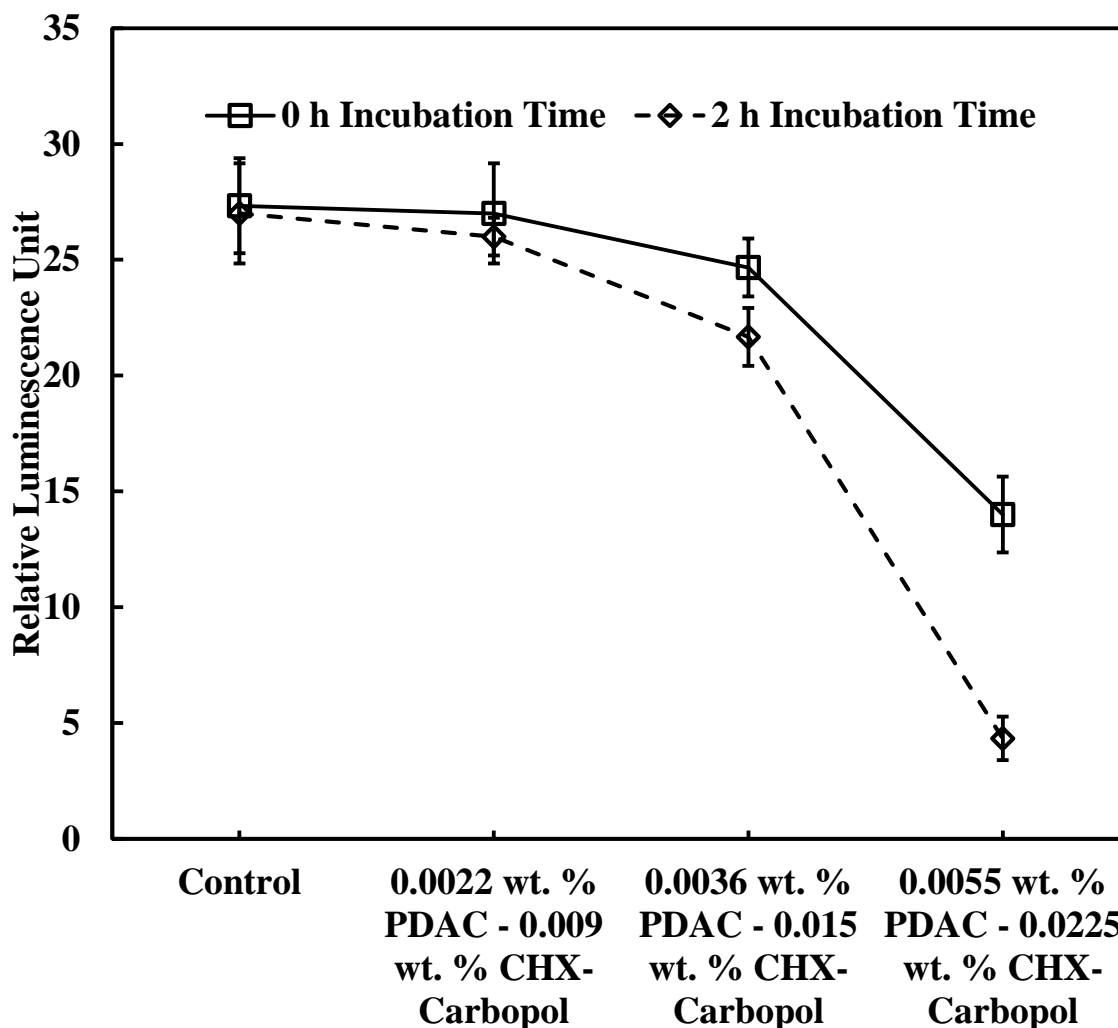


Figure 6.48: The relative luminescence intensity of *E.coli* incubated with suspensions of various concentrations of PDAC-coated chlorhexidine-loaded Carbopol for up to two hours of incubation. The diluted concentrations were prepared from the stock solution (0.011 wt% PDAC-coated 0.0075 wt% chlorhexidine-loaded 0.05 wt% Carbopol). The incubation was conducted through incubation each concentration with a fixed amount of culture media free *E.coli* cells.

A significant increase in the antimicrobial activity was seen at high concentrations of PDAC-loaded CLC (0.0055 wt% PDAC-coated 0.0225 wt% chlorhexidine-loaded

Carbopol) after incubation for 2 h and there was slight increase in the antimicrobial activity for PDAC coated 0.015 wt% chlorhexidine-loaded Carbopol. Therefore, the PDAC coating has a significant contribution in the increase of the antimicrobial activity of chlorhexidine because of the electrostatic interaction between the cationic PDAC and anionic cell membrane of the *E.coli* cells which leads to its successful disruption, and kills them.

The antimicrobial activity of 0.0055 wt% PDAC-coated 0.0225 wt% chlorhexidine-loaded Carbopol Aqua SF1 complex was also compared with the results at the same concentration of free chlorhexidine and chlorhexidine-loaded Carbopol with *E.coli* cells (Figure 6.49). There is a substantial increase in the antimicrobial activity of PDAC-coated CLC as compared with uncoated CLC but there was no pronounced change between PDAC-coated CLC and free chlorhexidine for the same concentration used. Figure 6.50 shows the morphology of the microstructure of *E.coli* cells that incubated with 0.0055 wt% PDAC-coated 0.0225 wt% chlorhexidine-loaded Carbopol for 2 hours of incubation. It can be seen in Figure 6.50B-F that the PDAC-coated particles are also heterocoagulated on the cell membrane of *E.coli* due to the cationic-anionic interaction between the particles and the surface of the cell, respectively. This interaction assisted in the increase the antimicrobial action of chlorhexidine through allowing penetration of high concentrations of encapsulated chlorhexidine to the intracellular fluid. This results were compared with the control sample of *E.coli* as shown in Figure 6.50A. The electrostatic interaction between the PDAC-coated CLC particles and the outer cell membrane of *E.coli* is shown in Figure 6.51 which explains the increase in the antimicrobial activity of chlorhexidine.

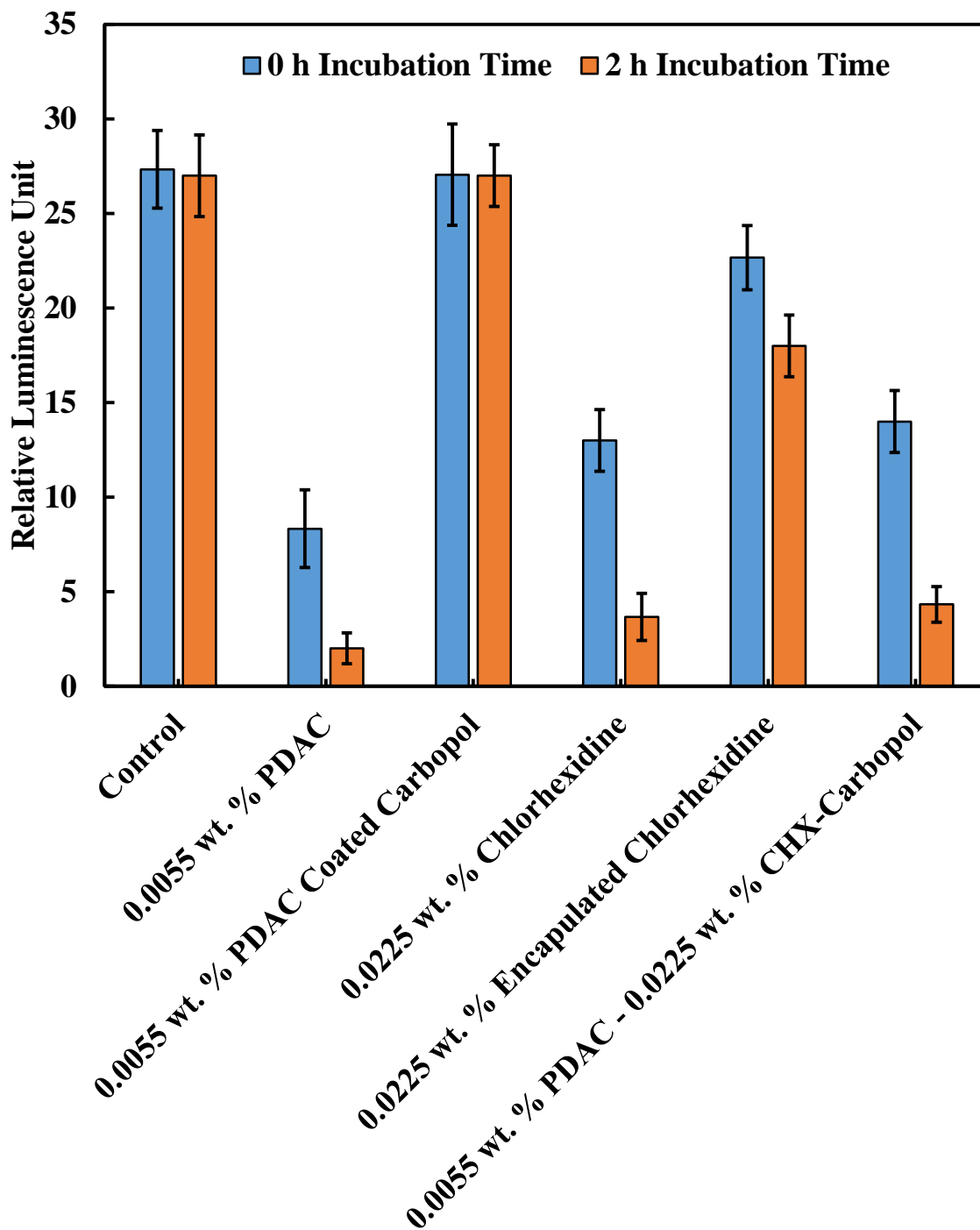
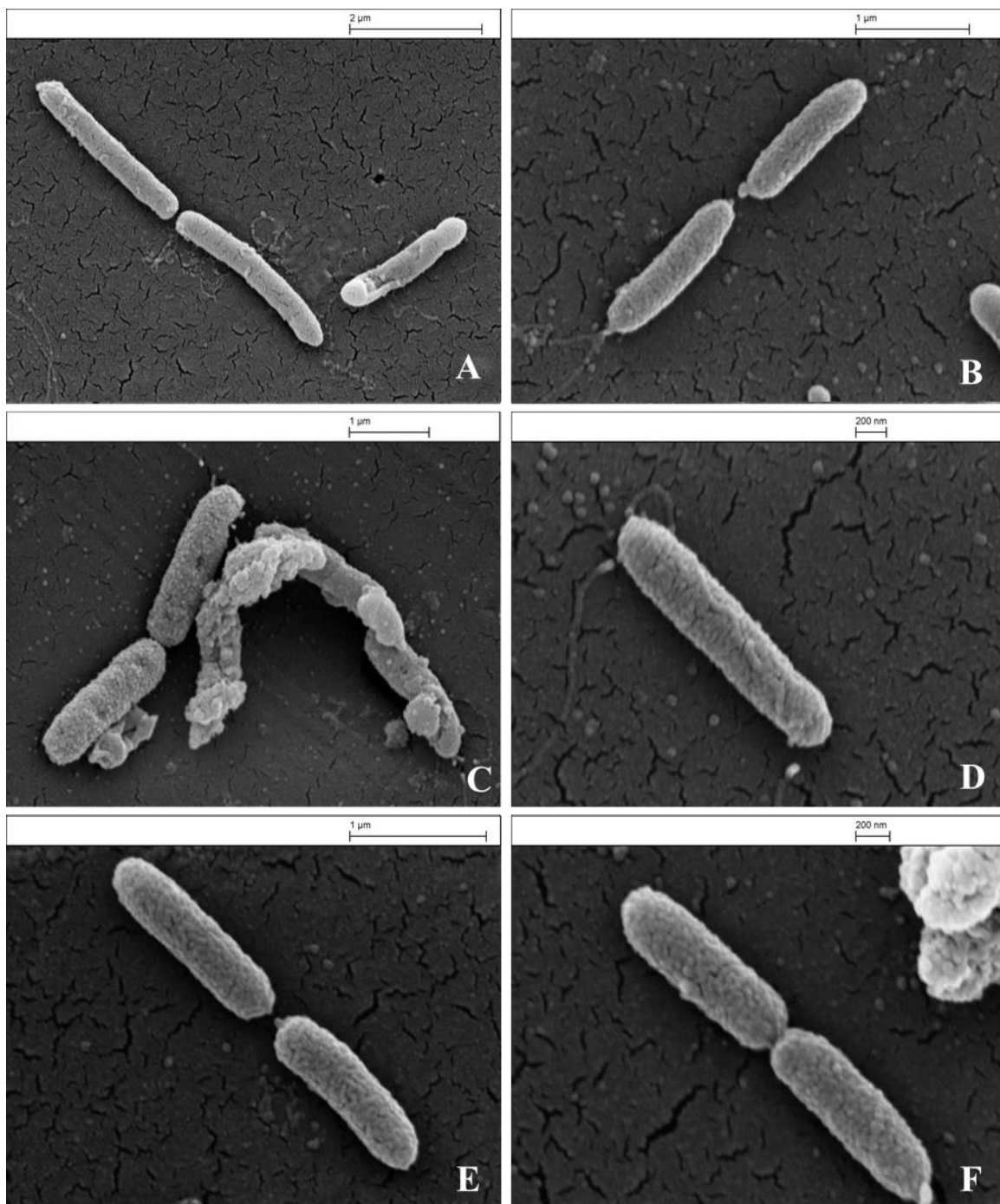


Figure 6.49: The antimicrobial activity of 0.0055 wt% PDAC-coated 0.0225 wt% chlorhexidine-loaded Carbopol microgel towards *E.coli* as a function of the antimicrobial activity of the free and Carbopol-encapsulated chlorhexidine. We also compare with cytotoxic effect of uncoated and coated CHX.



6.50: SEM images of *E.coli* cells. (A) Control sample of *E.coli* and (B, C, D, E, and F) represent the incubation of *E.coli* cells with a suspension of 0.0055 wt% PDAC coated 0.0225 wt% chlorhexidine-loaded Carbopol for 2 hours at room temperature. The cells were pre-treated with the procedure described in section 2.2.8.

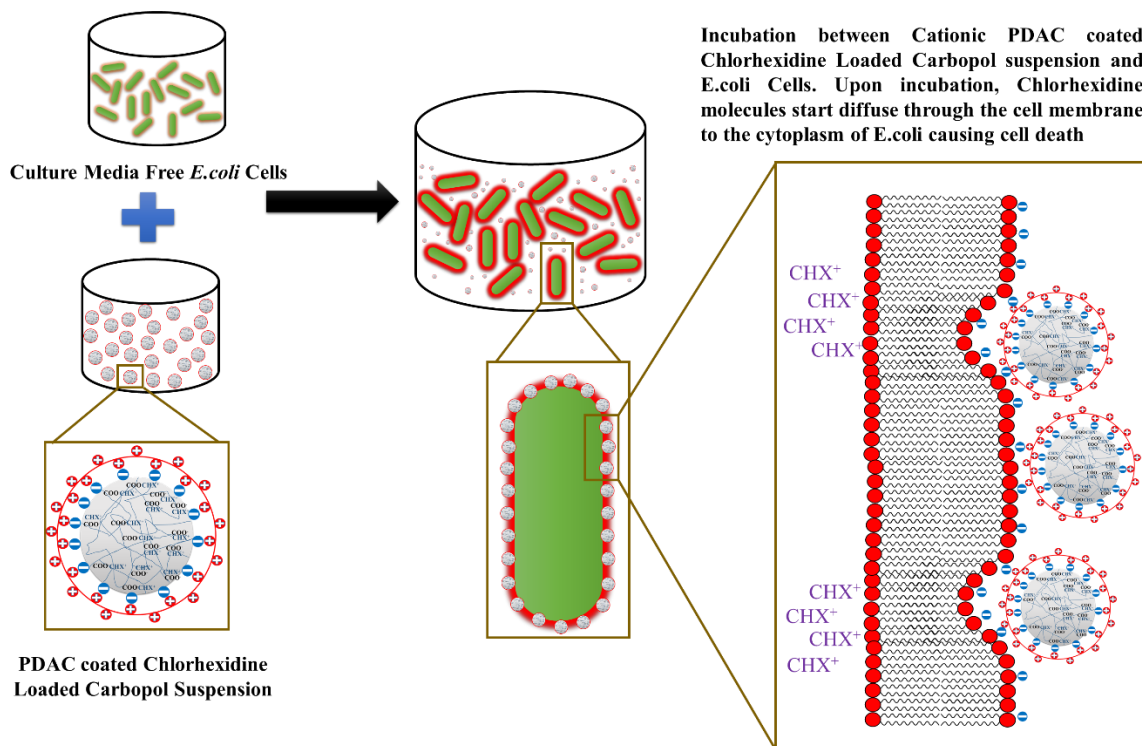


Figure 6.51: The schematic of the electrostatic interaction between PDAC-coated Chlorhexidine-loaded Carbopol microgel particles and the outer cell membrane of *E. coli* cells in which the chlorhexidine molecules are delivered locally at high concentrations on the cell membrane of *E. coli* cells.

It can be concluded that carbopol Aqua SF1 microgel is biodegradable and biocompatible material according to the toxicity testing of carbopol microgel suspensions with each of algae, yeast and *E. coli*. It can also be indicated that berberine or chlorhexidine loaded carbopol microgels have antimicrobial activities towards model microorganisms but this antimicrobial actions are significantly different from chlorhexidine to berberine for which it was noticed a considerably increase in the antimicrobial action for chlorhexidine which are much better than that for berberine. However, a significant increase in the antimicrobial actions were observed for both berberine and chlorhexidine towards algae, yeast and *E. coli*. This increase is attributed to the coating of encapsulated berberine and encapsulated chlorhexidine with cationic polyelectrolyte (PDAC) which cause electrostatic interaction between the coated encapsulated berberine or chlorhexidine and cell membrane within very short period of incubation time (less than one hour).

Bibliography

1. C. A. Lubrizol, *Noveon Consumer Specialties, Technical Data Sheet*, 2013, **294**.
2. L. Fan, R. Li, J. Pan, Z. Ding and J. Lin, *Trends in Plant Science*, 2015, **20**, 388-397.
3. C. P. Toret and D. G. Drubin, *Journal of Cell Science*, 2006, **119**, 4585-4587.
4. L. Pelkmans and A. Helenius, *Traffic*, 2002, **3**, 311-320.
5. I. R. Booth, *Current Opinion in Microbiology*, 2014, **18**, 16-22.
6. M. S. Pasqual, C. P. Lauer, P. Moyna and J. A. P. Henriques, *Mutation Research/Fundamental and Molecular Mechanisms of Mutagenesis*, 1993, **286**, 243-252.

7 Chapter Seven: Microfluidic Cell Based Assay: An Introduction

In the previous chapters the role of nanomaterials was studied in terms of either the toxicological effect of nanomaterials or their role as a nanocarrier for drug delivery. In both cases, the investigation was conducted through preparing solutions of different concentrations of nanomaterials and incubating them separately with microorganisms such as microalgae, yeast and E.coli cells. The batch method was utilized to investigate the viability of these cells and the cells were considered as whole cell biosensors to explore either the cytotoxic effect of metal nanoparticles or antimicrobial activity of encapsulated drug. The batch method was time-consuming and used high volumes of reagents. Using a microfluidic system it is possible to automate the process, reduce the amount of reagents and increase the throughput of screening.¹

7.1. Cell Adhesion using Poly-L-Lysine

The first approach investigated to trap the cells in the microfluidic device was cell adhesion to the micro chamber of the microchip device using the chemical adhesant such as poly-L-lysine.² A simple microfluidic device was utilized as shown in Figure 7.1, the microchip consists of two layers: the bottom plate is made of glass which was fabricated by photolithography. This plate involves two inlets, micro chamber in the centre of the chip and one outlet to collect the waste solution outside of the chip. The glass micro device was treated with alcoholic sodium hydroxide overnight, washed with water and ethanol thrice, and dried in the oven to prepare an active glass surface with a high distribution of negatively charged surface. After that, 2 μ l poly-L-lysine solution was added to the micro chamber and left overnight at 0°C to allow the poly-L-lysine to adhere to the glass surface as shown in Figure 7.2. On the other hand, the top plate is PDMS layer which is made of elastomer. This layer can be prepared from mixing elastomer with curing agent (10:1), then centrifuged and poured in a glass petri dish to form layer with thickness 3-4 mm and left overnight in an oven to be solidified at 60°C.

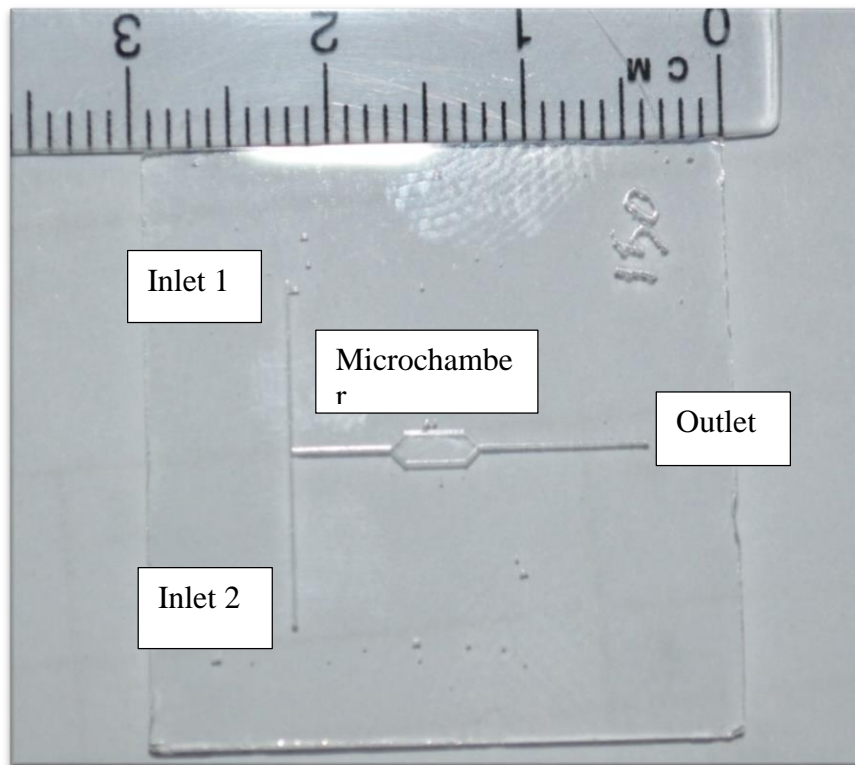
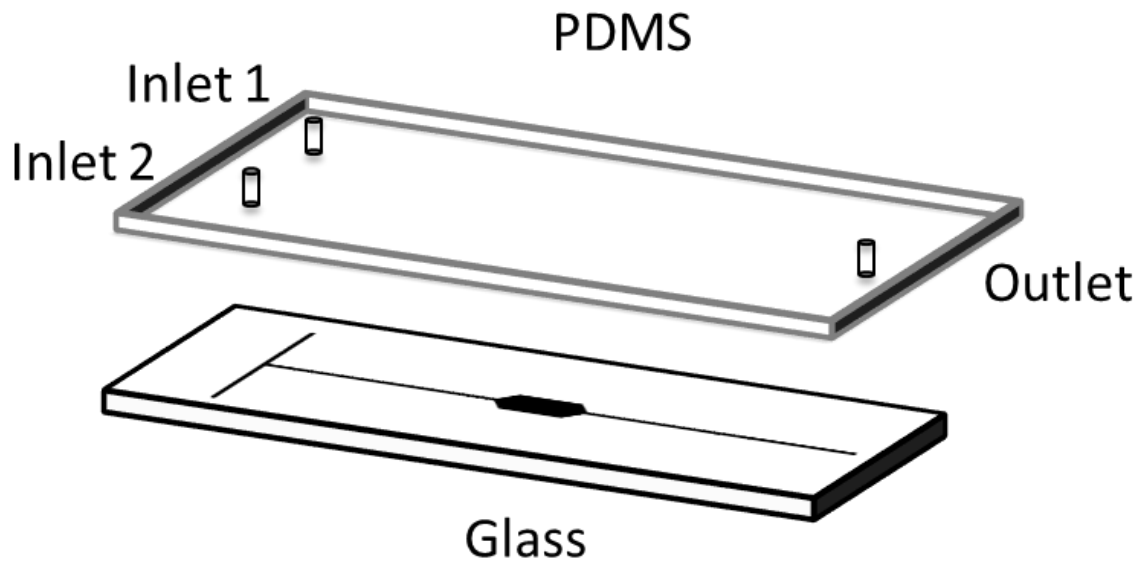


Figure 7.1: a) Schematic of a microfluidic chip; b) Photographic image of the microfluidic chip-cell based assay for trapping cells into a micro chamber.

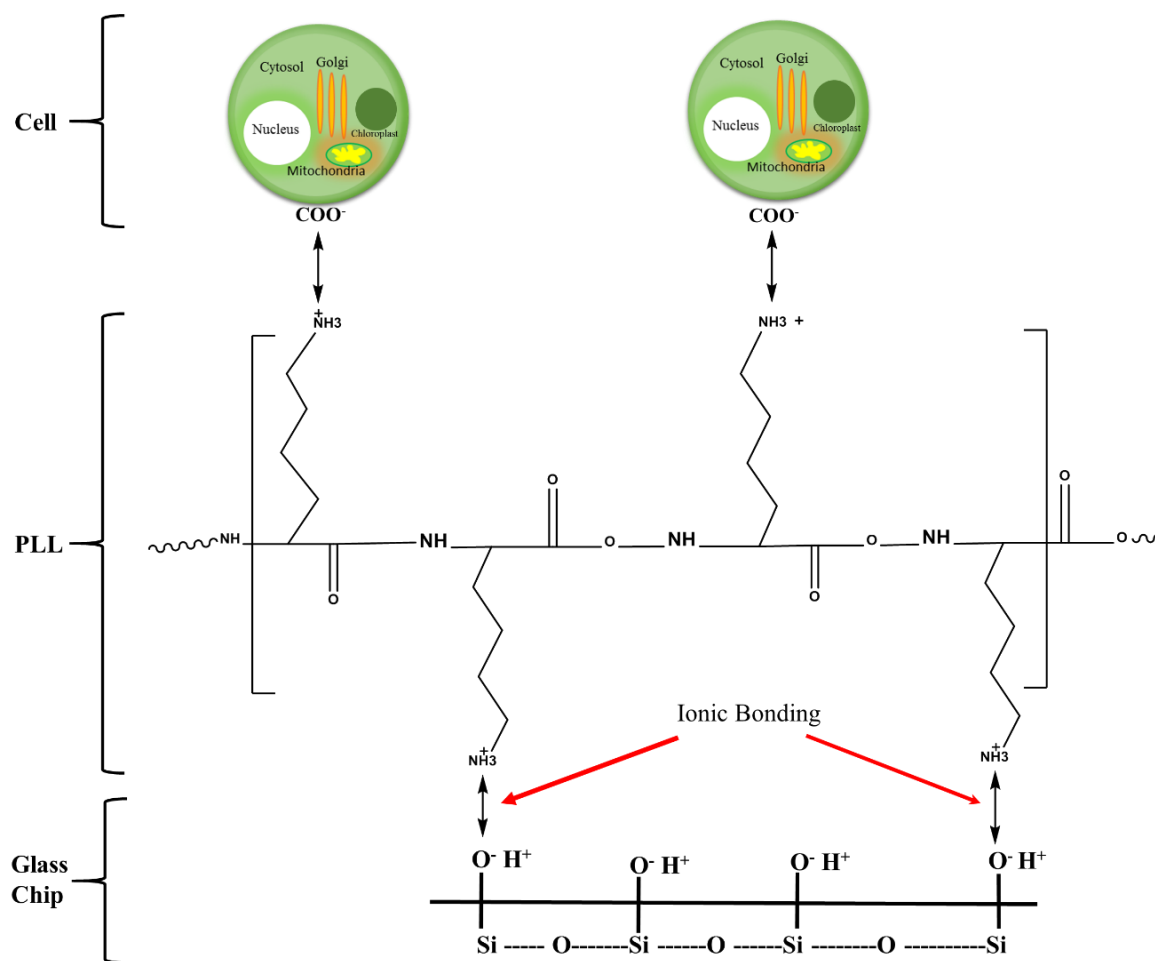


Figure 7.2: The schematic for the ionic bonding between poly-L-lysine and both of glass chip and cell.

The glass bottom plate of the microfluidic device was then bonded with a PDMS layer to prepare the channels and the device was placed in a chip holder and tubing was connected to the channels as displayed in Figure 7.3. Phosphate Buffered Saline (PBS, pH 7.4) was pumped at a flow rate $10 \mu\text{L}\cdot\text{min}^{-1}$ from inlet 1 and inlet 2 to wash and remove the excess unreacted amounts of poly-L-lysine for 30 minute, and also to provide a sterile microenvironment inside the chip. Then, a concentrated suspension of algae cells was pumped into the micro device at flow rate $10 \mu\text{L}\cdot\text{min}^{-1}$ for 10 minutes and then the pumping was stopped for 30 minutes to allow the algal cells to adhere to the surface of the micro chamber of the device. The trapped cells were then washed with phosphate buffer saline for 10 minutes to get rid of the unbound cells.

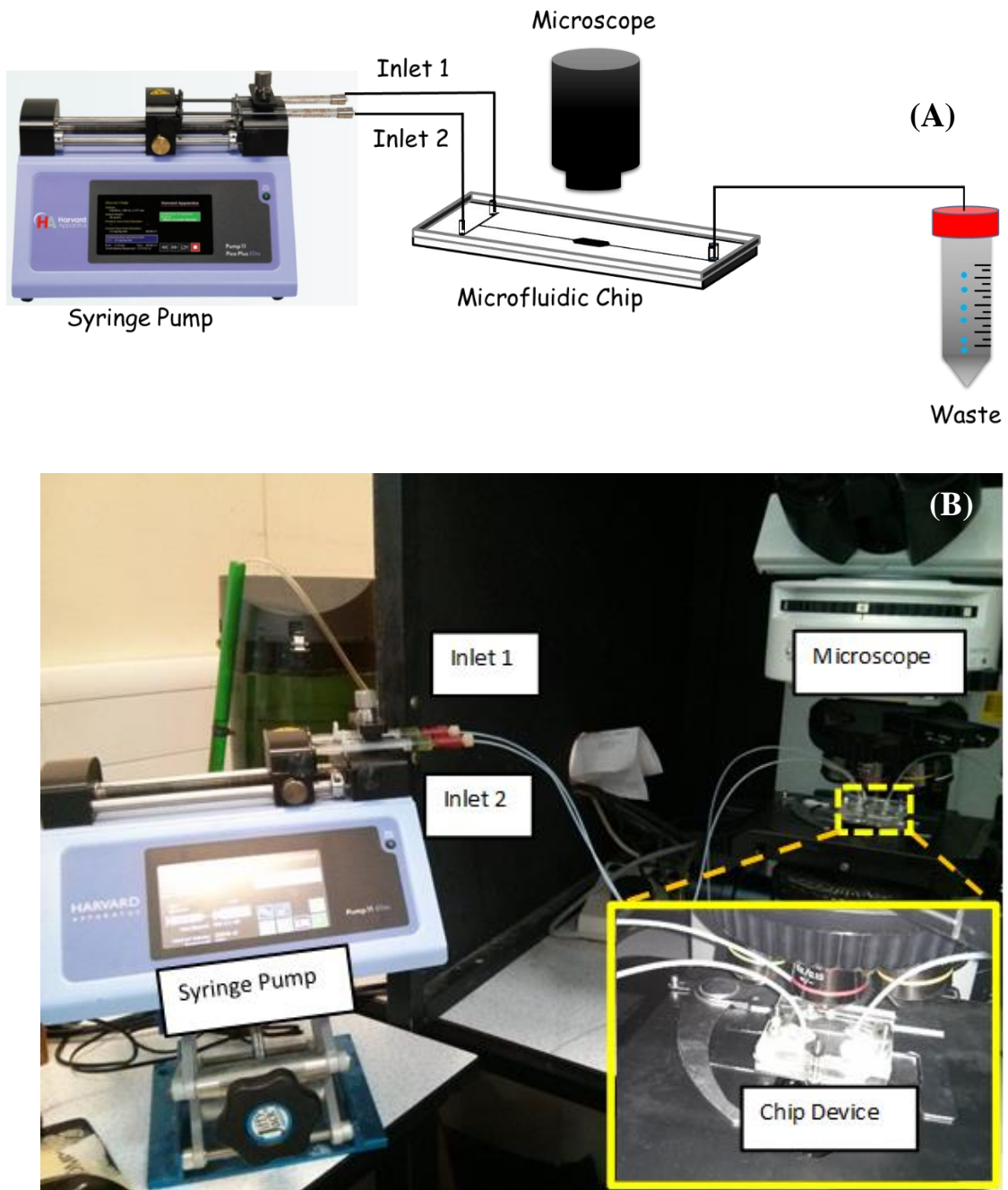


Figure 7.3: (A) A schematic flowgram of the microfluidics glass chip where the micro chamber is examined under microscope. (B) The experimental setup of algal cells trapping on the micro chamber of the microchip device using poly-l-lysine.

The trapped cells were examined under the microscope using the bright field position as shown Figure 7.4. It can be seen in Figure 7.4 (A, B and C) that algal cells were trapped in the micro chamber of the device with high distribution of the cells in the outlet (A), the centre (B), and the inlet of the micro chamber. Moreover, highly magnified images of trapped cells were also observed at D, E, and F of Figure 7.4.

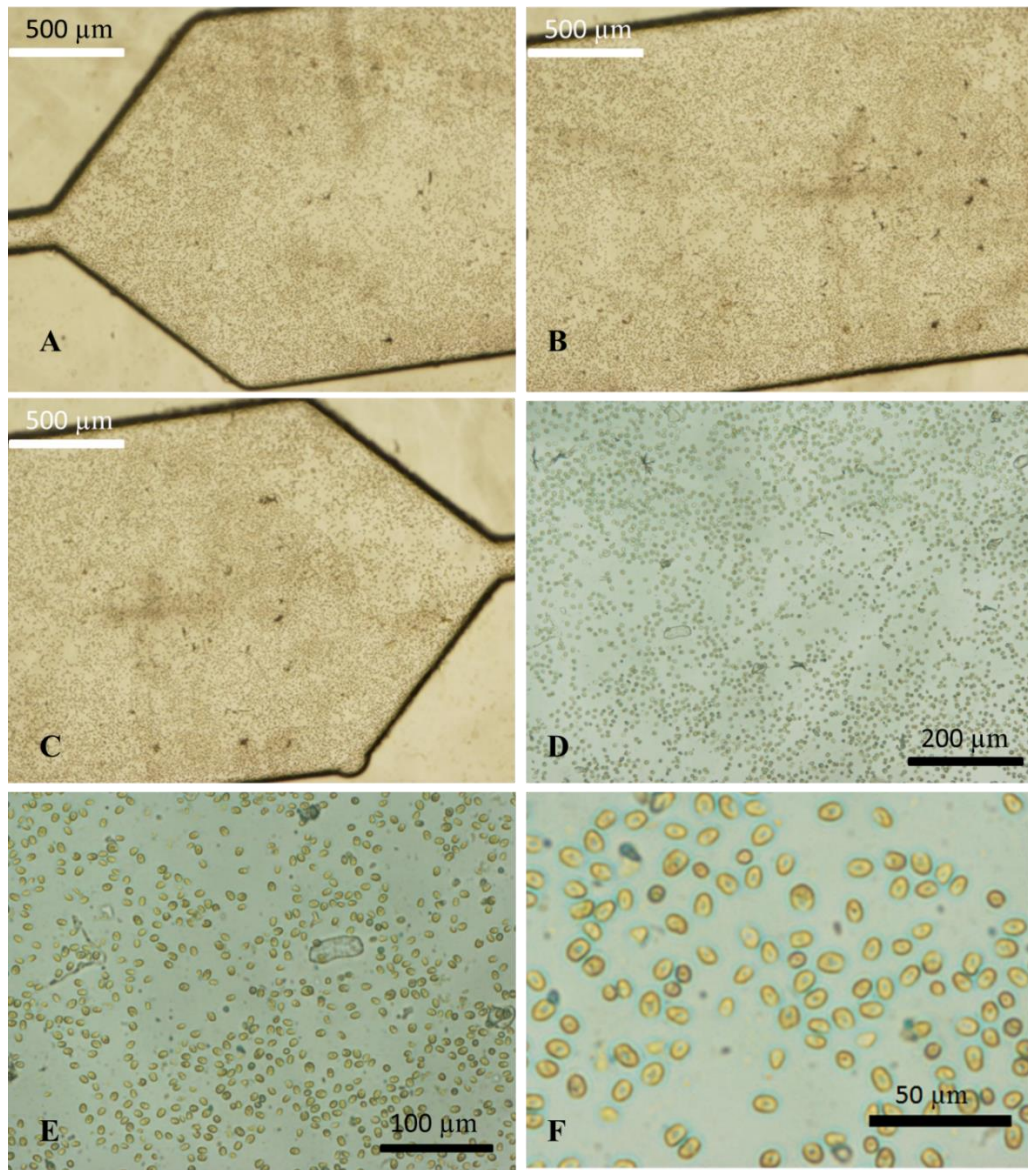


Figure 7.4: Bright field microscopic images of algal cells trapped in the micro chamber of the microfluidic chip using poly-l-lysine as an adhesant agent. (A) Trapped cells in the outlet of the micro chamber, (B) Trapped cells in the centre of the micro chamber, (C) Trapped cells in the inlet of the micro chamber, (D) On-chip trapped cells at 10X magnification, (E) On-chip trapped cells at 20X magnification, and (F) On-chip trapped cells at 50X magnification.

The viability of the trapped algal cells was tested using the fluorescein diacetate (FDA) viability assay. FDA was pumped through inlet 1 and inlet 2 using syringe pump at flow rate $10 \mu\text{l min}^{-1}$ for 5 minutes and incubated with the trapped cells for 10 minutes, then the remaining FDA solution was washed off with phosphate buffer saline (PBS). The viability of the cells was measured using the fluorescence microscope as shown in Figure 7.5. The figure shows that the algal cells trapped in the micro chamber of the chip were still viable but a significant decrease in the amount of trapped cells was observed. This decrease was attributed to the effect of shear stress forces from pumping reagents through the system because of the flow rate as well as the weak interaction between the cells and poly-L-lysine as shown in the white arrows in Figure 7.5 where cells detached from the surface of the microchamber. From these results it was clear that this method would not provide reproducible results.

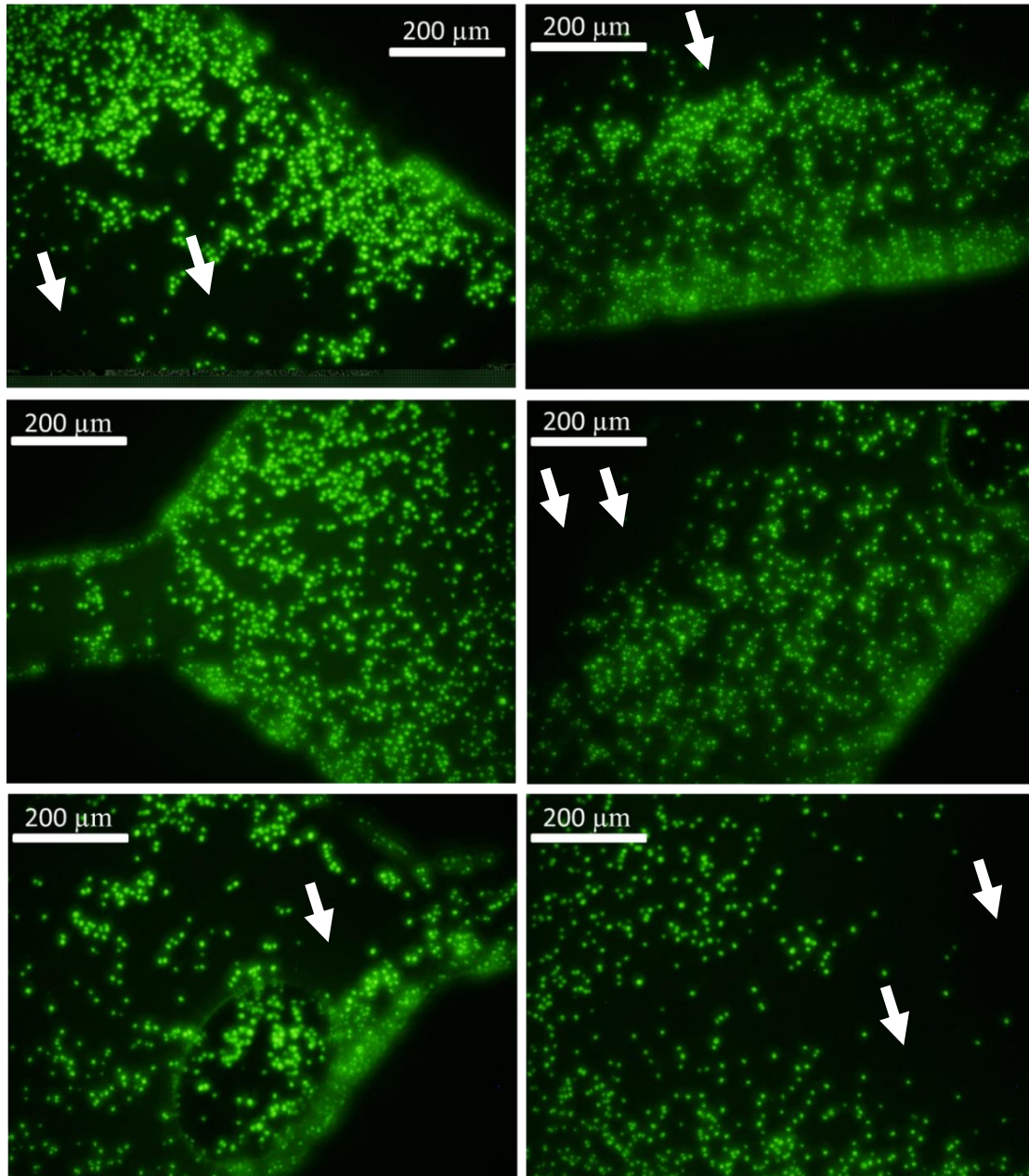


Figure 7.5: The Viability of on-chip trapped cells using chemical adhesion through the interaction between cells and glass chip adhered poly-L-lysine. The viability was measured by incubating cells with FDA solution for 10 minutes. White arrows refer to the detachment of cells from the surface of the microchamber due to the weak interaction where the effect of flow rate is dominant causing shear stress on the interaction between adhered cells and the surface.

7.2 Microfluidic Cell Trapping

It was clear an alternative method was needed and therefore it was decided to trap the cells physically using magnetic particles between 25 μm and 75 μm with strong magnetic response. A simple microfluidic chip design (channel width 100 μm , channel depth 50 μm and made of glass/PDMS plates) was used for the micro screening assay. Microorganisms were incubated with these nanomaterials to study either their toxicity or the antimicrobial action as shown in Figure 7.1.

Figure 7.6 describes a schematic diagram of the proposed cell trapping into the micro chamber of the micro device. The strategy of trapping cells is based on placing different sizes (25-75 μm) of fabricated magnetic microbeads into micro chamber of the chip device and then, trapping the beads at the end of the micro chamber using a high performance neodymium magnet as shown in Figure 7.6 (a and b). After that, the cells (size $\geq 3 \mu\text{m}$) are pumped at a slow flow rate using a syringe pump through inlet 1 and inlet 2 to be trapped before the gate keepers (magnetic beads). The magnet had to be kept in the place to avoid escaping cells and ensure a good distribution of trapped cells in the micro chamber as shown in Figure 7.6(c). A specific concentration of either titania nanoparticles or microgel particles are then pumped from the two inlets over the cells. The flow is then stopped to allow incubation with the trapped cells for a specific period. After that, PBS buffer solution (pH 7.4) is pumped from the two inlets to remove the nanomaterials and fluorescein diacetate is then introduced and incubated with the trapped cells for 10 minutes. Finally, the trapped cells are washed with PBS solution to remove the excess amount of FDA solution and the cell viability is measured as an overall intensity using the fluorescence microscope. The cells are then flushed from the chip by moving the magnet to the side as illustrated in Figure 7.6(d).

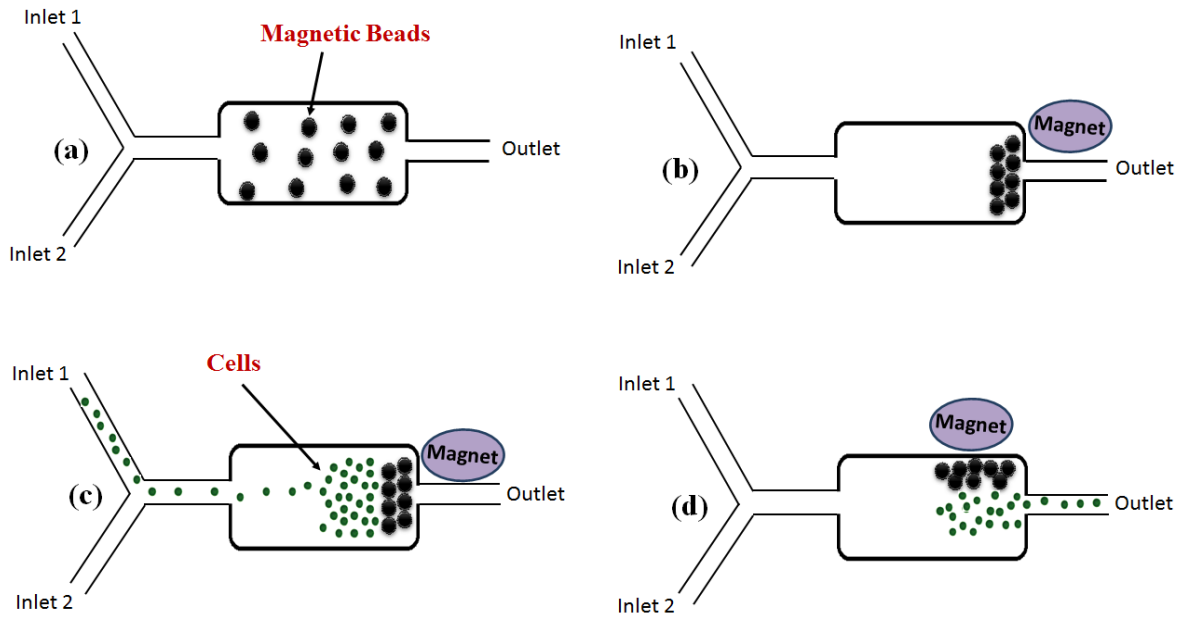


Figure 7.6: The schematic diagram of microfluidic cell trapping by gate keepers (magnetic microbeads) which are used for investigating the cytotoxic effect of nanoparticles or antimicrobial assay upon incubation with cells into the micro chamber for periods of incubation time. (a) Placing magnetic beads into micro chamber. (b) Attraction of magnetic beads by magnet (c) Passing and Trapping the cells into micro chamber (d) flushing out cells upon moving the magnet to the side.

Another design was also manufactured³ as shown in Figure 7.7. This design consisted of two layers: the upper layer was made of PDMS with three holes (Inner Diameter 1.6 mm) which were broken up using 1.25 mm biopsy punch device as shown in Figure 7.8 (A). However, the lower layer includes upstream part which can generate gradient concentrations from a stock solution allowing rapid experiments in which the cells are exposed to a range of different concentrations as shown in Figure 7.8 (B, C, and D).

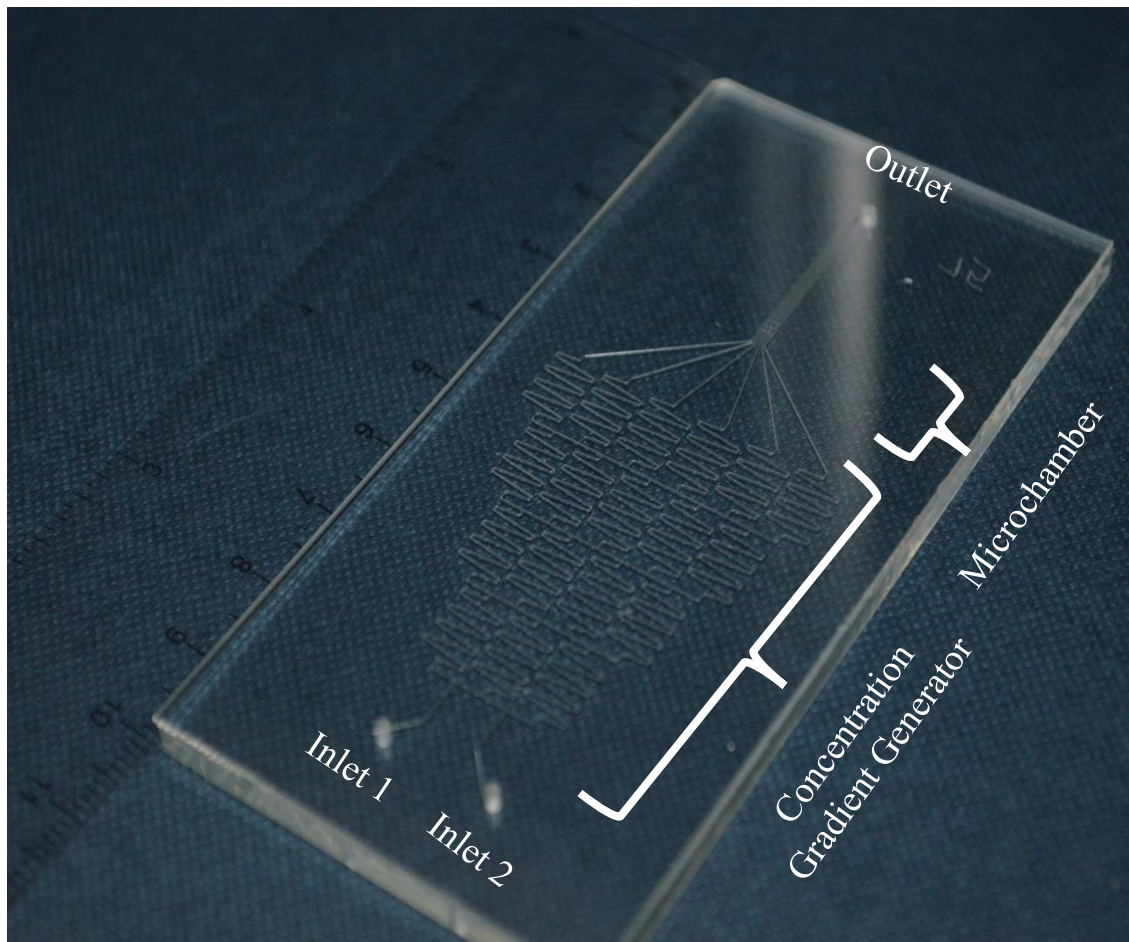


Figure 7.7: The microfluidic chip design which generates concentration gradients by pumping stock solution of a reagent from inlet 1 and water from inlet 2 with dilution occurring in the branched channels. This design was fabricated as mentioned in Chapter 2, Section of chip fabrication

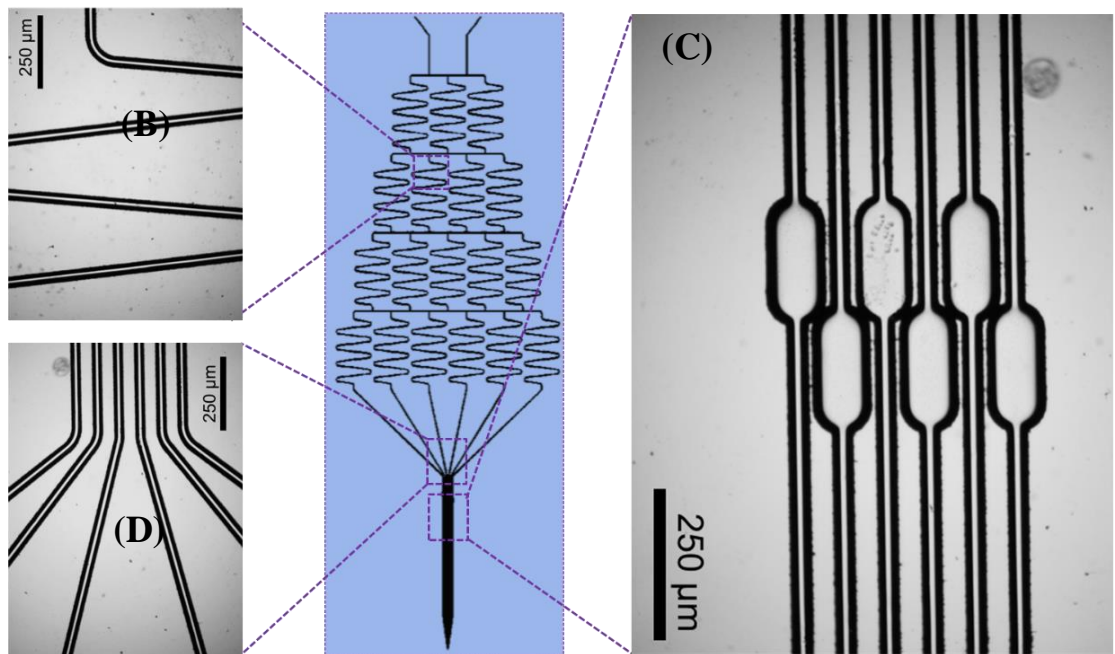
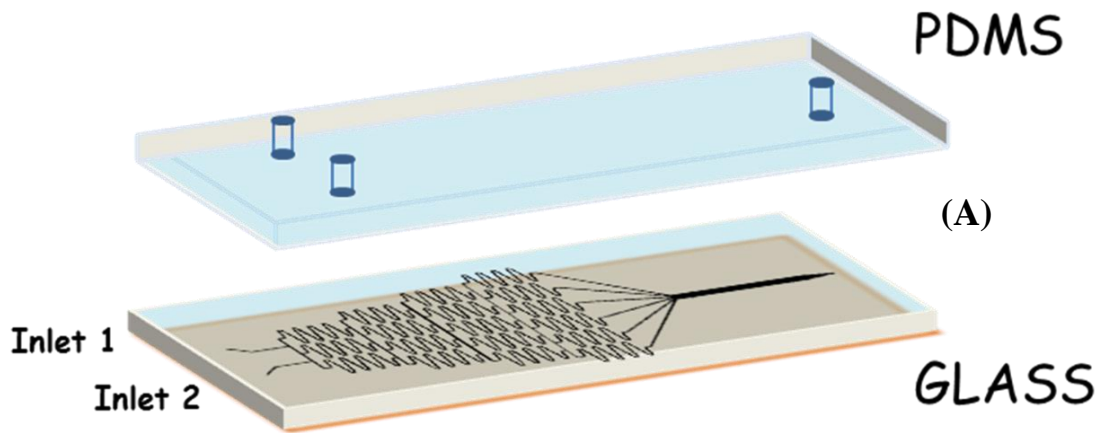


Figure 7.8: The microfluidic chip for high throughput micro screening cell based assay. (A) The whole microfluidics chip with concentration gradient generator. (B) The branched point for concentration gradient generator (CGG), (C) The micro chambers for trapping cells and (D) The cross channels between concentration gradient generator (CGG) and the micro chambers.

7.3 Fabrication of Magnetic Microbeads

A range of different magnetic particles were prepared to find the best type for this application.

7.3.1 Magnetic Glass Beads

To prepare these beads iron oxide nanoparticles were produced using the procedure described by Berger⁴ with some modification. 1M Ferrous chloride was vigorously mixed with 2M ferric chloride and then, ammonia solution was slowly added in drops to form magnetite, a black precipitate. The dark solid at the bottom of the beaker was the iron oxide magnetic nanoparticles which were washed three times until the solution gave a pH of 6.5-7. Then the magnetic particles were heated up to 80°C for one hour to convert hematite to magnetite. The precipitate was incubated at room temperature and washed three times with Milli Q water. Figure 7.9 shows the photographic images of the magnetic nanoparticles and Figure 7.10 displays their particle size distribution (41 nm) and zeta potential (-7 mV).

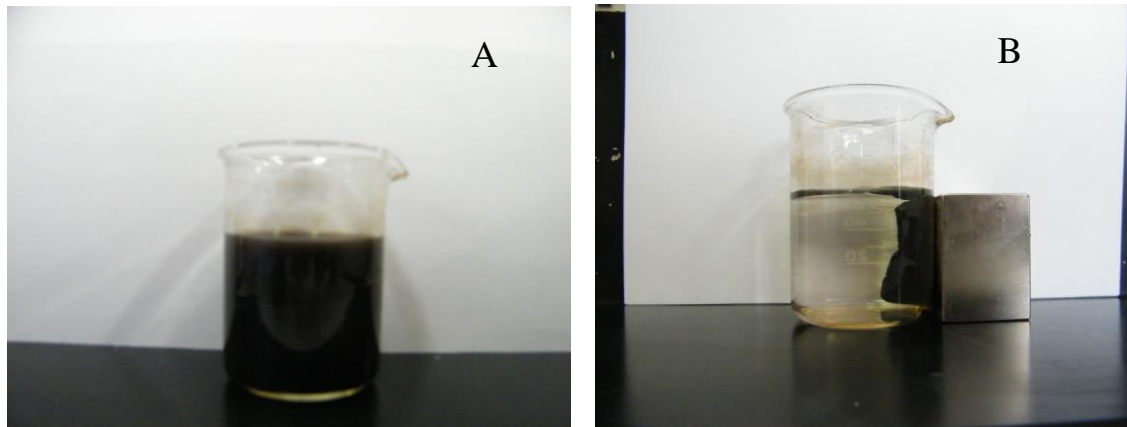


Figure 7.9: The photographic profile of black precipitate of magnetic nanoparticles dispersed in milli Q water (A) and particles attracted by magnet (B). The magnetic particles were prepared by mixing ferrous and ferric ions and ammonia solution was added drop wise to form iron oxide nanoparticles.

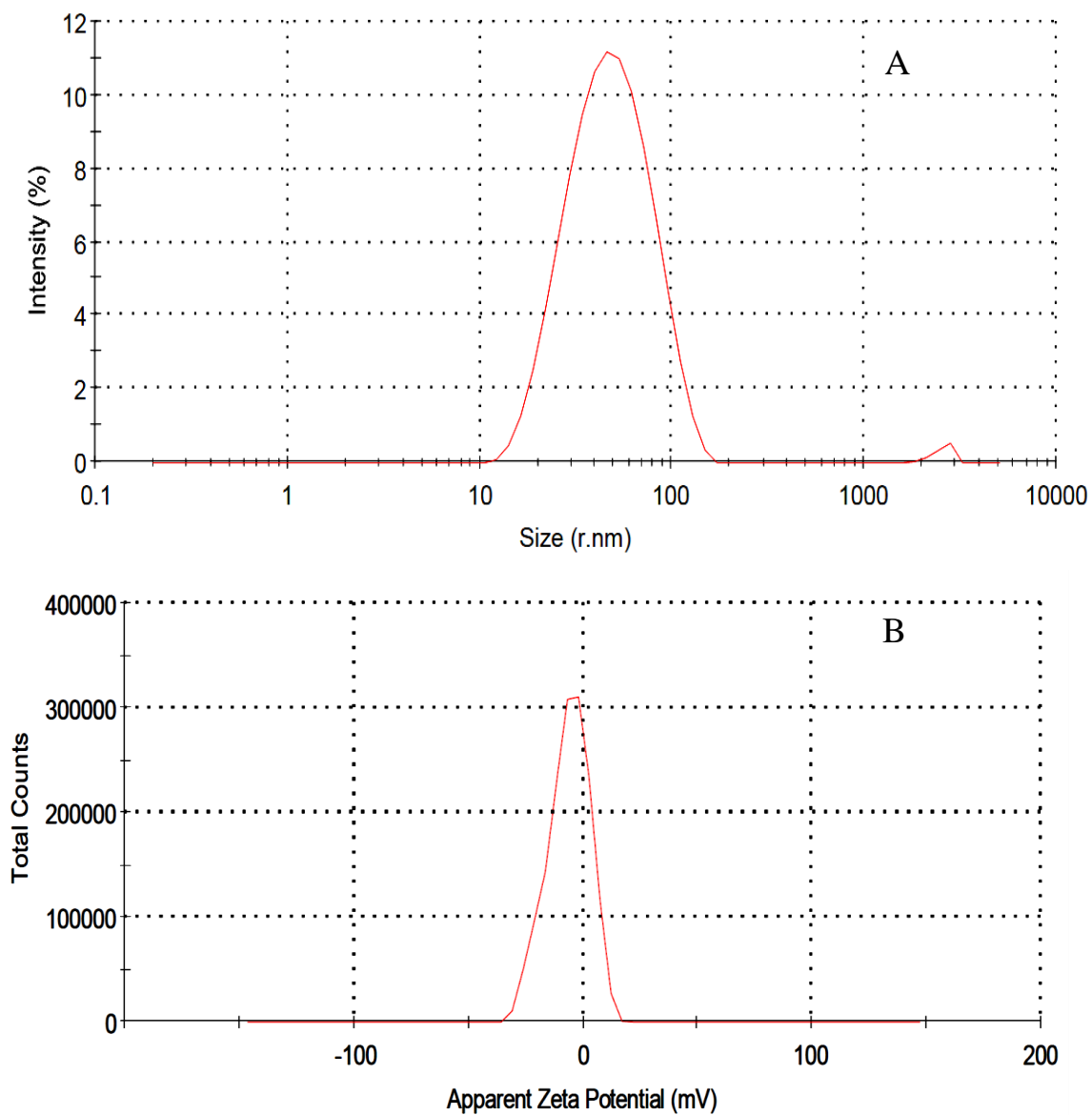


Figure 7.10: The average particle diameter (A) and zeta potential (B) of magnetic iron oxide nanoparticles prepared from mixing ferric and ferrous solutions in the basic medium.

The synthesized iron oxide nanoparticles was then coated with cationic polyelectrolyte (polyallylamine hydrochloride) to convert the surface charge of magnetic particles to positive by dispersing small amount of the nanoparticles with 10 mg/ml of PAH

for 20 minutes with an ultrasonic probe.³ The zeta potential was measured to be +60 mV as shown in figure 7.11.

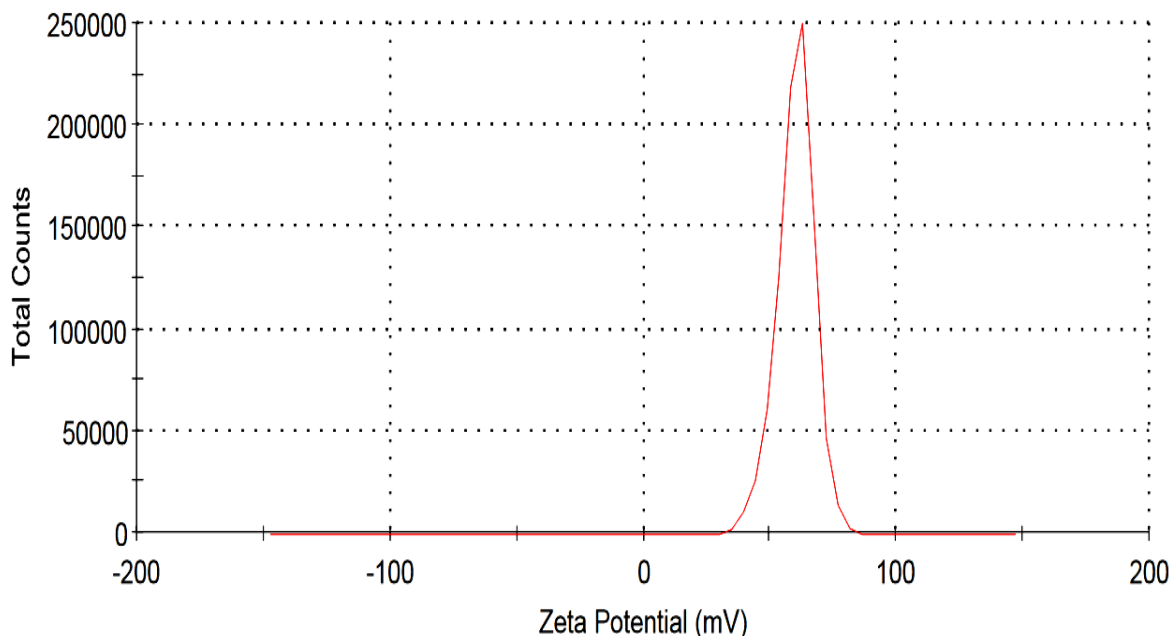


Figure 7.11 : The zeta potential of PAH coated magnetic iron oxide nanoparticles which were achieved through a specific amount of iron oxide nanoparticles solution with excess amount of cationic polyelectrolyte. The excess amount of polyelectrolytes was removed from the solution by separation with magnet.

To produce magnetic glass beads, the glass beads were cleaned to activate glass surface using piranha solution allowing increase the amount of hydroxyl groups on their surface. The activated glass beads were functionalized with cationic polyelectrolyte (PAH) and then it was further coated with anionic polyelectrolyte (PSS) to produce PSS coated PAH/ glass beads as shown in Figure 7.12. Then, the prepared PAH coated magnetic nanoparticles were mixed with PSS coated PAH/ glass beads and left for a while. The produced magnetic glass beads were tested with magnet and it was found few of these beads have magnetic response and they need further coating with magnetic nanoparticles to obtain strong magnetic response as demonstrated in Figure 7.13. Hence, it was required to synthesize another magnetic bead with lower size to enhance the magnetic response.

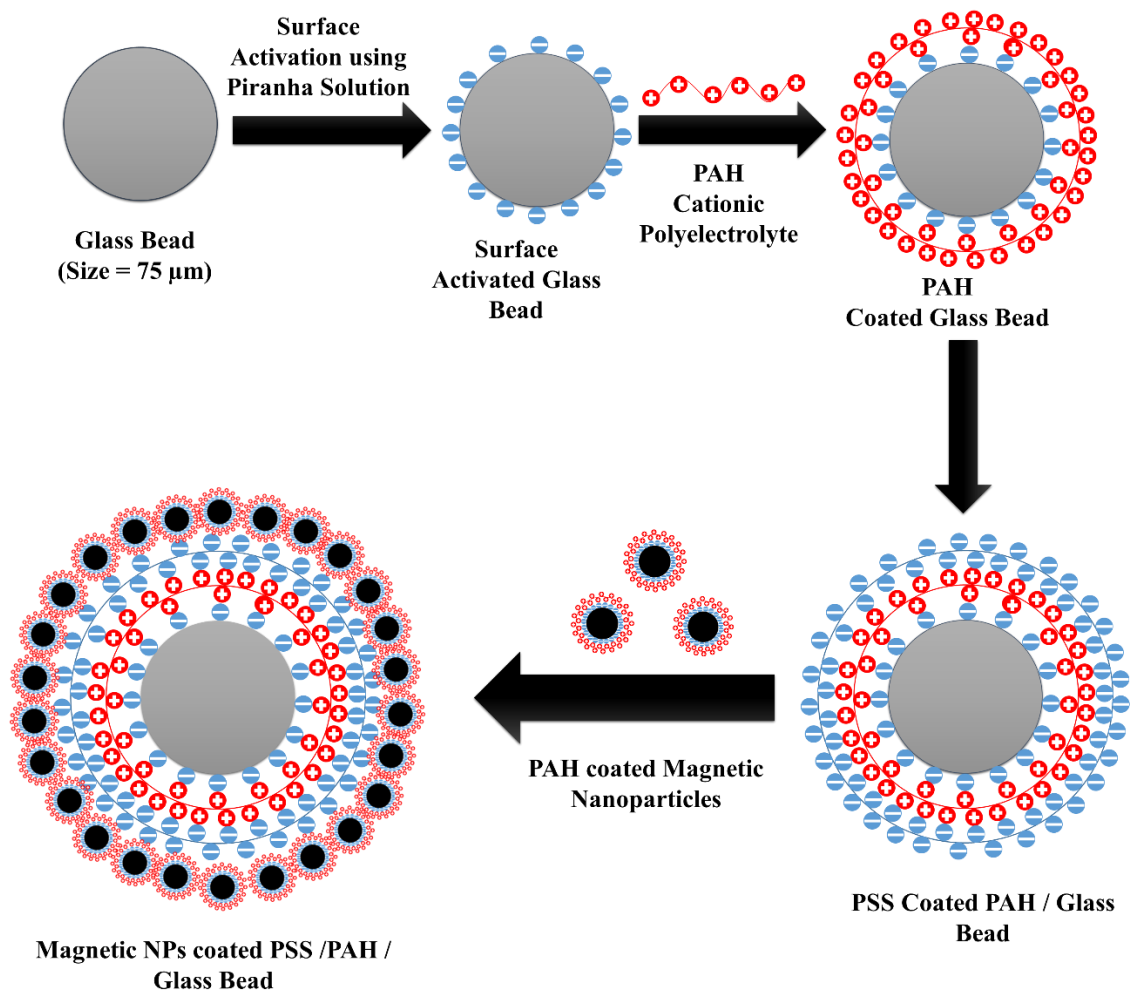


Figure 7.12: The schematic diagram for the functionalization of glass beads with magnetic nanoparticles in which the functionalization was achieved using cation and anionic polyelectrolyte such as poly (allylamine hydrochloride) and poly(styrene-4-sulfonate sodium).

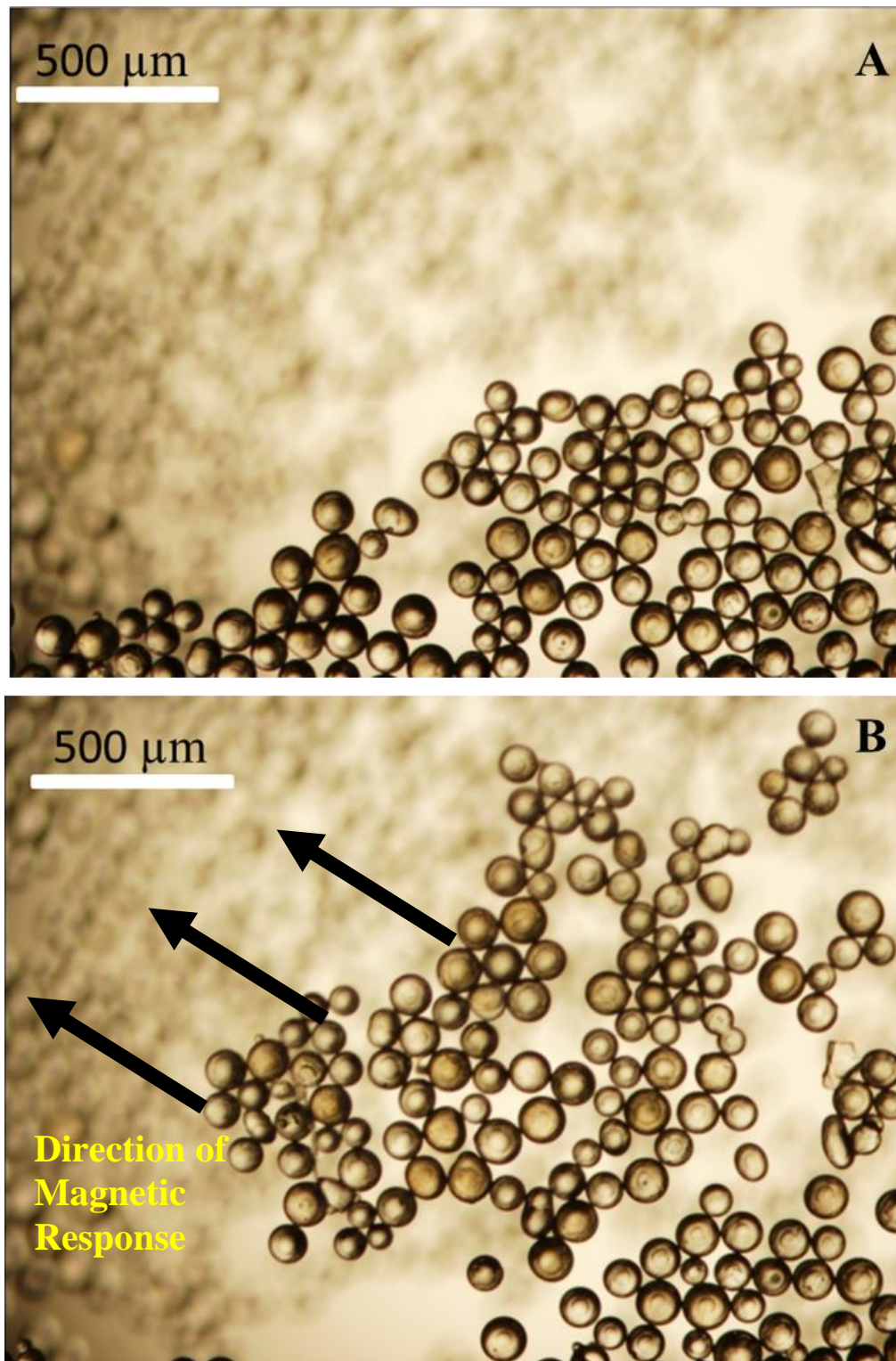


Figure 7.13: Bright field images of magnetic nanoparticles coated glass beads whereby (A) represents magnetic glass beads without any external operator and (B) denotes to the magnetic glass beads under the control of magnet

7.3.2 Magnetic Yeast Cells

Magnetic yeast cells were synthesized using electrostatic layer by layer coating.³ This method was conducted through coating of anionic magnetic nanoparticles with cationic polyelectrolyte poly (allylamine hydrochloride) (PAH) to form PAH coated magnetic nanoparticles. The latter was utilized to magnetize yeast cells by drop wise addition of yeast cells to the solution of PAH coated magnetic nanoparticles which then washed many times to get rid of the excess amount of polyelectrolyte by approaching magnet. Figure 7.15 shows microscopic image of magnetic nanoparticles functionalised yeast cells in comparison with normal yeast cells and it seems from the figure that magnetized yeast cells appeared aggregated and attached to each other due to the electrostatic interaction between anionic outer cell membrane and cationic PAH coated magnetic nanoparticles as well as the interaction between non-magnetized and magnetized yeast cells that allowed yeast cells to be aggregated.

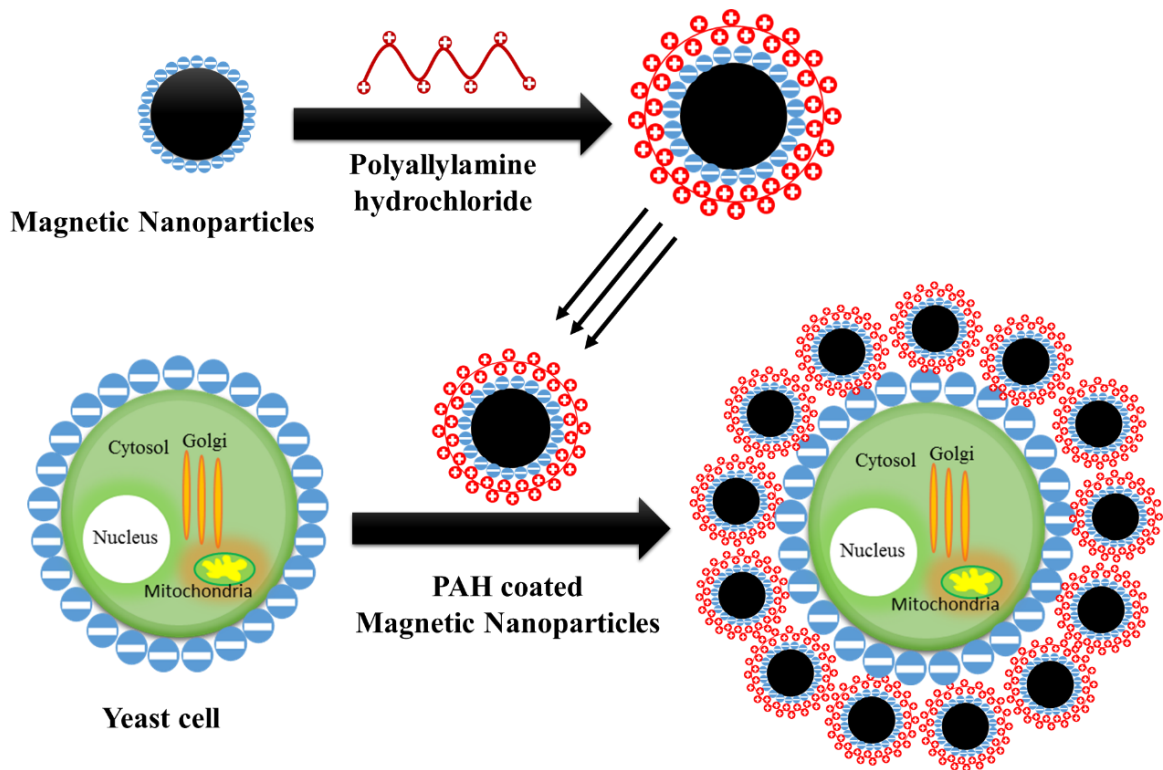


Figure 7.14: Schematic diagram for the magnetization of yeast cells using magnetic nanoparticles that previously coated with cationic polyelectrolyte (PAH) to form PAH coated Fe_3O_4 nanoparticles with stirring for 20 minutes. The magnetic nanoparticles were prepared from precipitation of ferrous and ferric ions in the basic medium of ammonia solution, then heated up to 80°C for an hour to get superparamagnetic nanoparticles which then separated by approaching neodymium magnet.

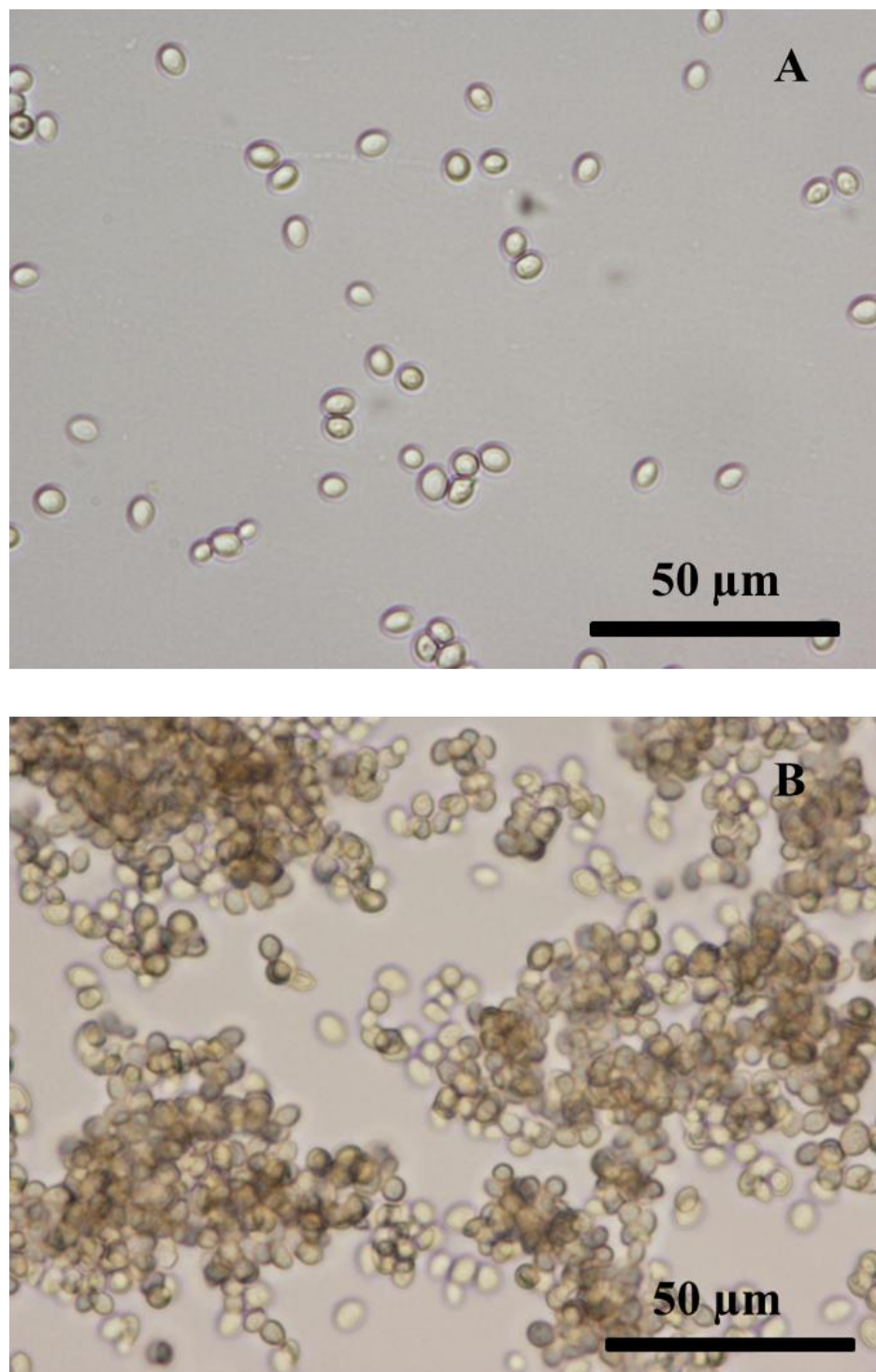


Figure 7.15: The bright field microscopic images of (A) normal yeast cells and (B) yeast cells that magnetized using Poly (allylamine hydrochloride) coated magnetic nanoparticles which in turn functionalized yeast cells to form magnetic yeast cells.

The magnetized yeast cells then were pumped at flow rate $25 \mu\text{l}\cdot\text{min}^{-1}$ from inlet 1 and inlet 2 as described in Figure 7.16A. Then, the magnetized cells were trapped into the micro chambers of the chip device using neodymium magnet which already placed on top of the micro chambers and process was carried on for an hour. The figures 7.16B and 7.16C describe the micro chambers in case of before and after trapping magnetized yeast cells, respectively. It can be observed from Figure 7.16C that magnetized yeast cells were trapped irregularly in the micro chamber because of the configuration of etched channel of the chip which hinder magnetic cells to accumulate properly. Moreover, a back pressure happened because of the small sizes of trapped magnetized cells which does not allow fluids to pass through pores of the magnetized cells. In addition of that, this method cannot be used for trapping cell where these magnetic coated cells might interact with trapped cells causing damaging of the cell membrane.

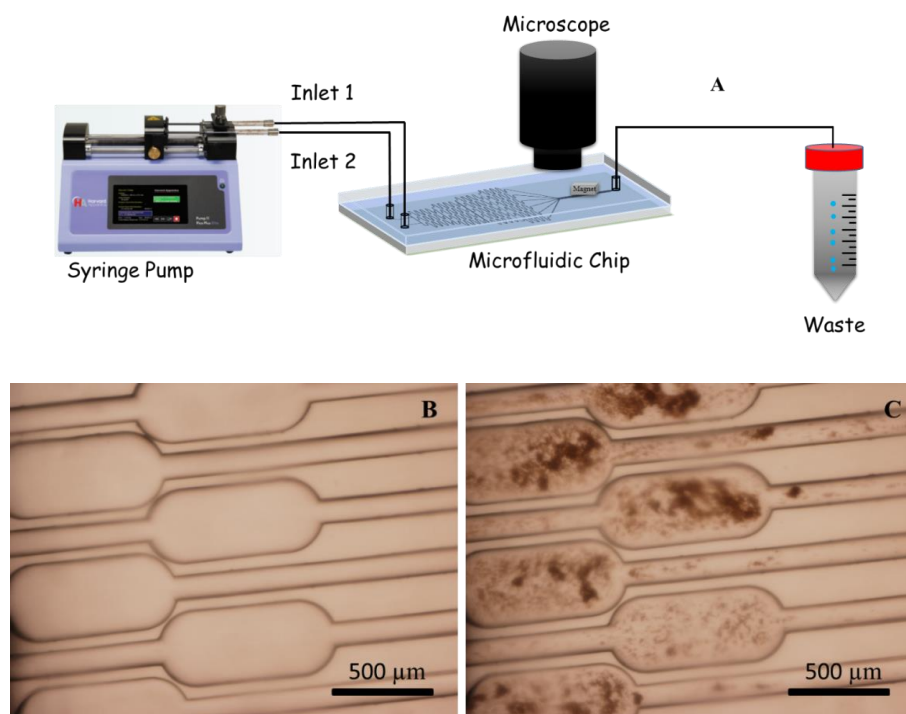


Figure 7.16: (A) Experimental setup of trapping magnetized yeast cells into the micro chambers of the micro device using neodymium magnetic on top of the micro chambers. This experiment was achieved by pumping the cells using syringe pump from inlet 1 and inlet 2 at flow rate $25 \mu\text{l}\cdot\text{min}^{-1}$ and trapping cells in the micro chambers following that flushing out trapped cells to the outlet upon removal the magnet from the chip, (B) A bright field microscopic image of the micro chambers before the trapping process, and (C) A microscopic image of trapped cells into the micro chambers of the chip after trapping upon placing the magnet of the top of the chambers.

7.3.3 PDMS stabilized oleic acid coated magnetic nanoparticles

To obtain smaller particles PDMS stabilized oleic acid functionalized magnetic nanoparticles were prepared by heating the prepared magnetic nanoparticles to 80°C (see Section 7.3.1) and then rapidly adding to them a millilitre of oleic acid to coat the particles and make them hydrophobic.⁵ The hydrophobized nanoparticles were dried to remove any residues of water molecules and then dispersed in a low density silicone oil which in turn mixed with equal amount of poly (dimethyl siloxane) (PDMS) as shown in Figure 7.17. The particles were then dispersed with low density silicone oil to decrease the viscosity of PDMS.

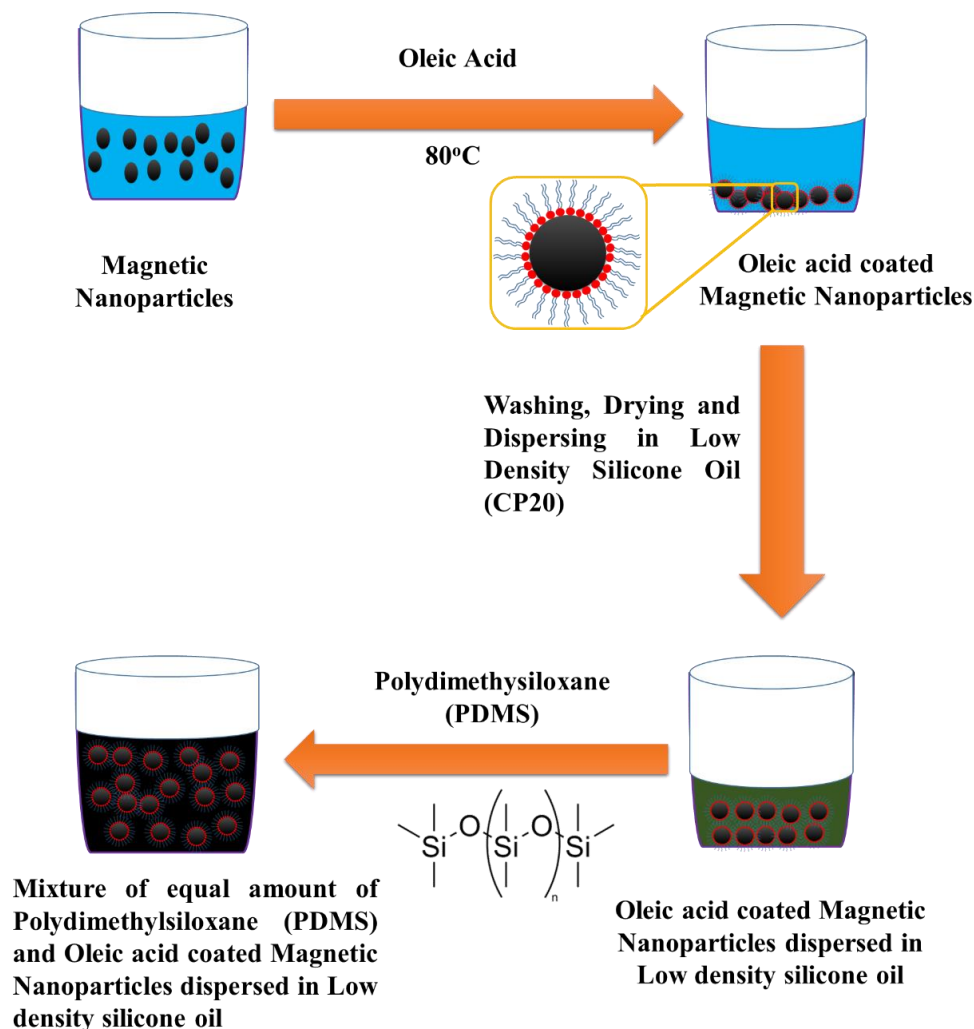


Figure 7.17: The schematic of synthesis of PDMS stabilized oleic acid coated magnetic nanoparticles which were synthesized using oleic acid coated magnetic nanoparticles and then dispersed in low density silicone oil and mixed with PDMS to form hydrophobic magnetic nanoparticles.

Polymerised magnetic micro beads could then be produced *via* filling a 50 μl glass syringe (Needle gauge 22S) with the coated nanoparticles. To make the method work a petri dish was prepared with two layers as shown in Figure 7.18. The upper layer was prepared by mixing 1% wt. % of both xanthan gum and sodium dodecyl sulphate (SDS) to make a highly hydrophilic wet solution and the other layer was solidified agar which works as a solid hydrophilic support as depicted in Figure 7.18A. The glass syringe was filled with PDMS stabilized oleic acid coated magnetic nanoparticle which were slowly, manually discharged in the interface between the top layer which contains xanthan gum and SDS to increase the shear stress forces between PDMS droplet and the hydrophilic

components of the top layer, and the agarose layer as a solid support. The PDMS droplets generated were warmed up to 60°C in the oven overnight to polymerize them to form solidified magnetic PDMS microbeads as shown in Figure 7.18B.

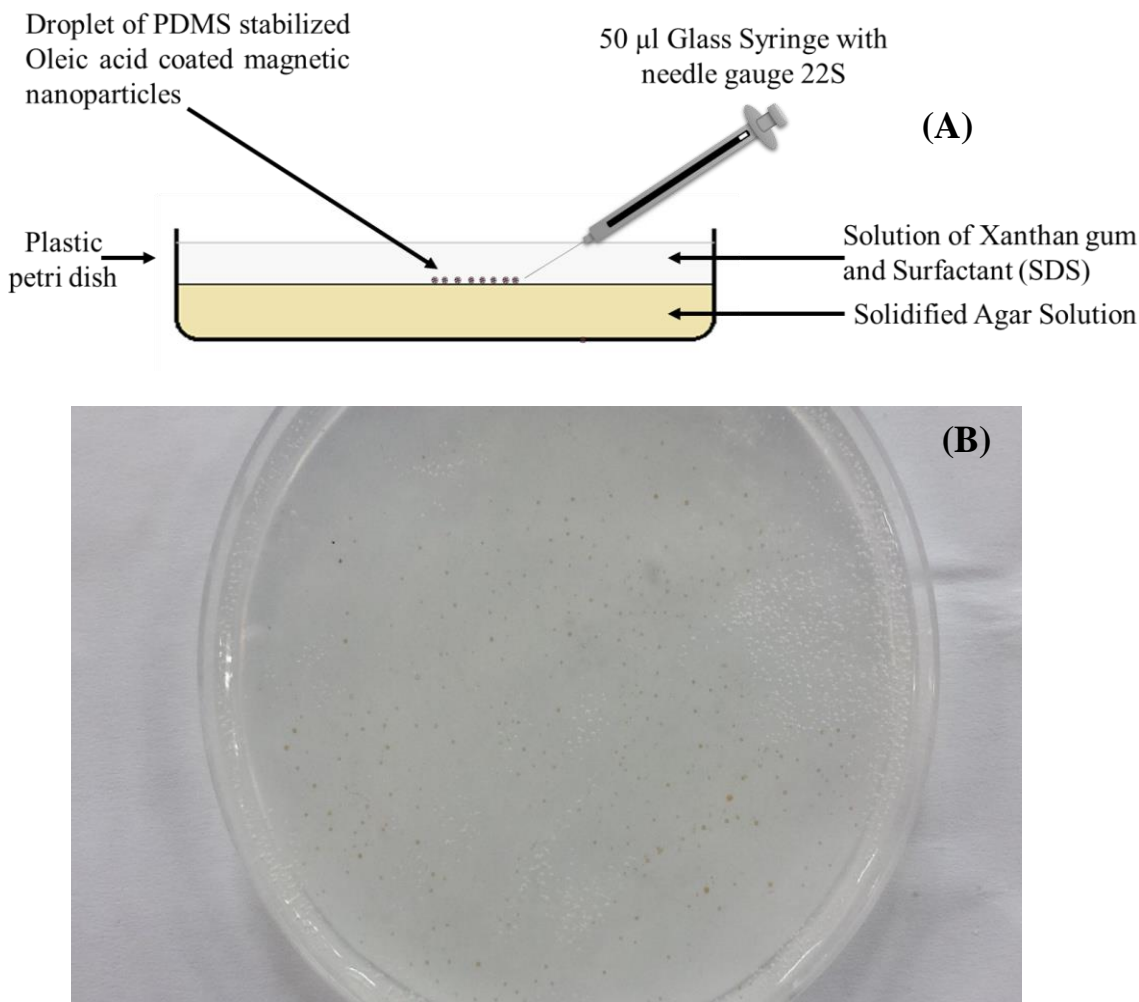


Figure 7.18: (A) Scheme of the synthesis of solidified magnetic PDMS micro beads in a plastic petri dish in which the upper layer includes 1 wt. % of both xanthan gum and sodium dodecyl sulphate (SDS) and the lower layer is solidified agar. (B) Photographic image of polymerised magnetic PDMS micro beads on the top layer of petri dish.

The synthesized magnetic PDMS microbeads were well washed with Milli Q water to remove the xanthan gum and sodium dodecyl sulphate (SDS) by attracting the beads with a neodymium magnet. The magnetic beads were then examined under the microscope and the bead sizes were found to be in the range from 50 µm to 500 µm (Figure 7.19).

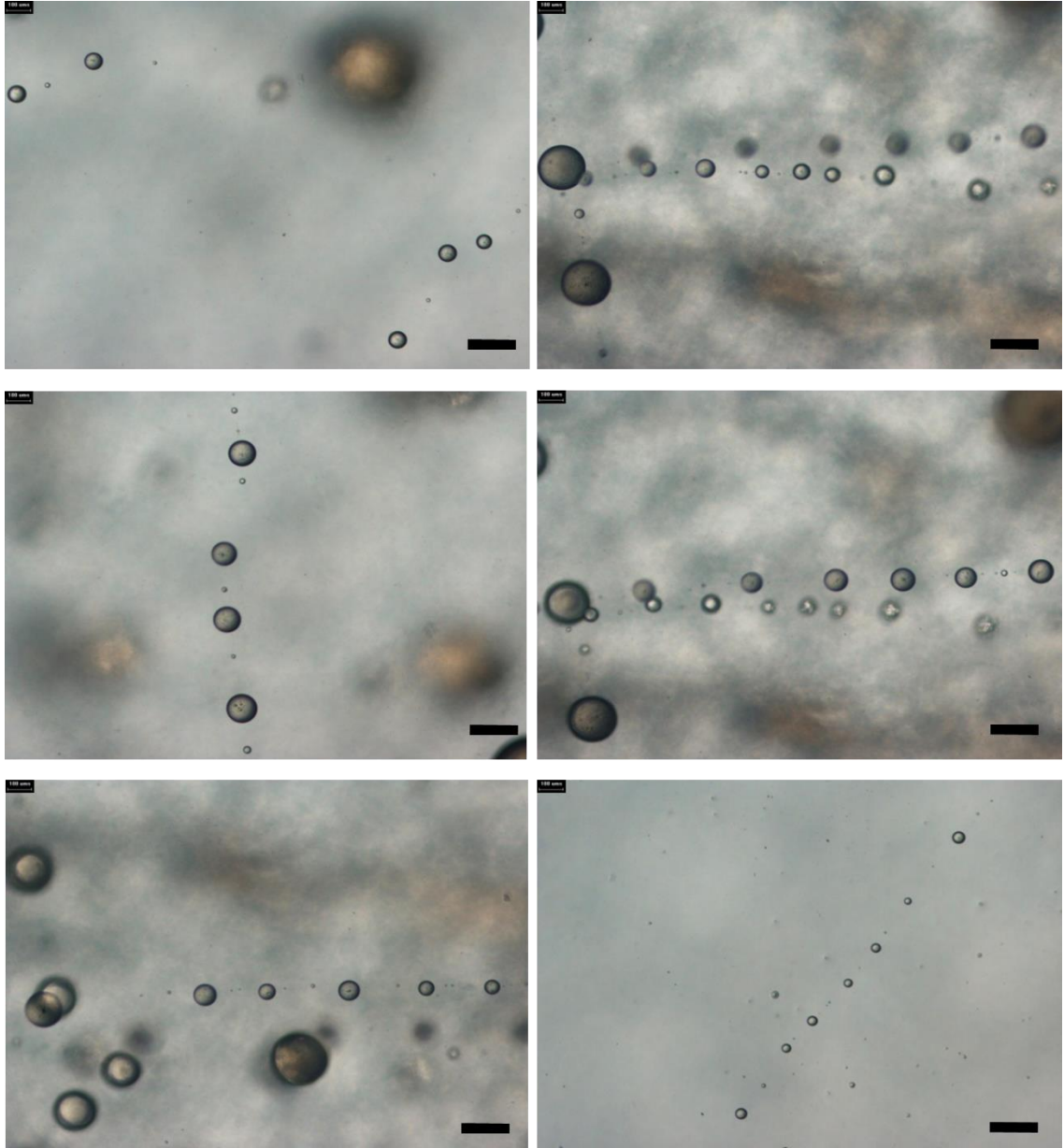


Figure 7.19: The bright field microscopic images of solidified magnetic PDMS micro beads which were prepared from generation of droplet of PDMS stabilised Oleic acid coated magnetic nanoparticles using glass microsyringe in the presence of mixture of xanthan gum and the surfactant SDS, and then these droplets were thermally polymerised to form solidified magnetic PDMS micro beads. The scale bar is 200 μm .

The solidified magnetic PDMS micro beads were tested on microfluidic chip device (3 cm x 3 cm, 100 μm width and 50 μm depth) towards magnet to investigate the magnetic response. It can be seen in Figure 7.20 A, B and C that the magnetic micro beads had a weak response to the neodymium magnet. Another problem that was noticed was that volume of magnetic PDMS bead was larger than the channel depth (Figure 7.20D) which meant that smaller magnetic beads with a strong magnetic response were needed. Moreover, it was observed that the beads were adhering to the surface of the microfluidic device.

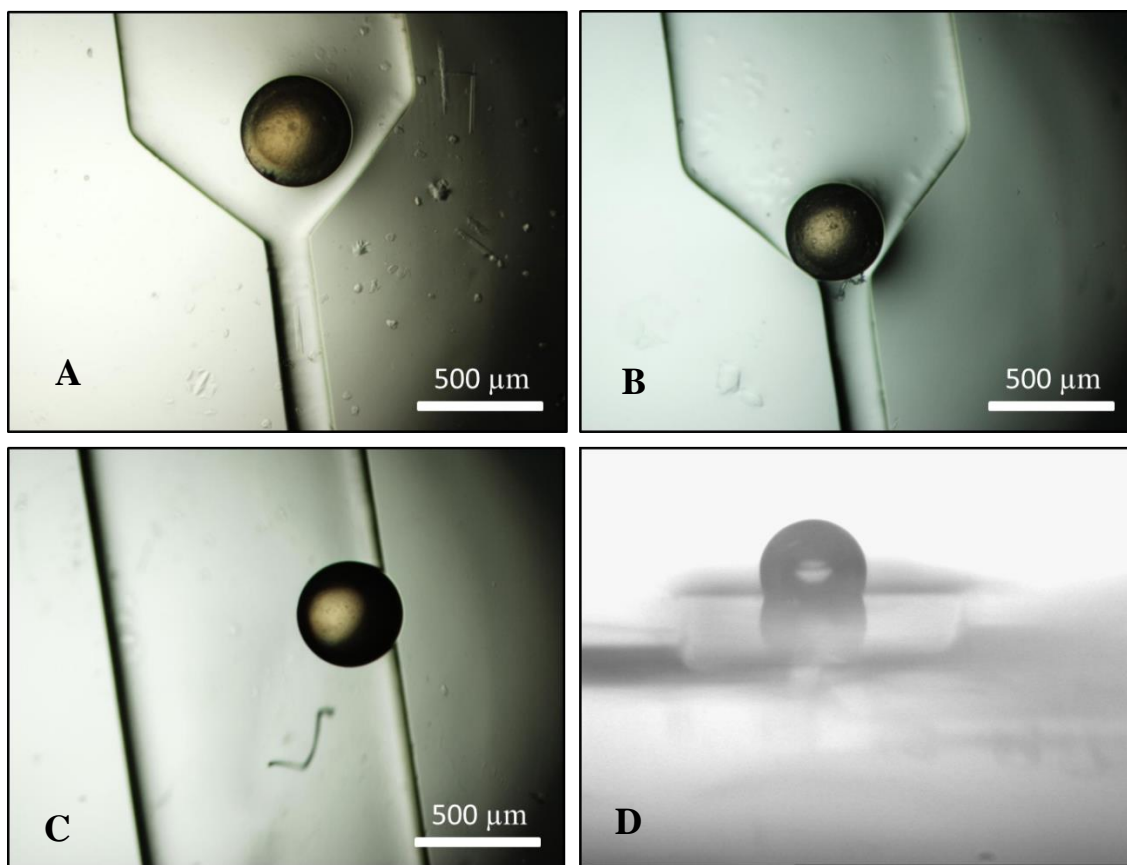


Figure 7.20: On-chip microfluidic interaction between magnetic PDMS micro beads and the neodymium magnet. (A-C) represent the response of the magnetic beads upon approaching the magnet whereby they showed weak magnetic response and (D) represents the horizontal flat surface of the microfluidic chip showing part of the magnetic beads on the top of the chip.

7.3.4 Flow Focusing Microfluidic Device

A microfluidic flow focusing technique was then investigated to prepare smaller monodispersed magnetic microbeads.⁶ This method was optimised by changing the flow rate for both the continuous and dispersed phase and also the depth and the width of the flow focusing device. Figure 7.21 shows the process for the synthesis of styrene based oleic acid coated magnetic nanoparticles using a flow focusing microchip. The dispersed phase was styrene based oleic acid coated magnetic nanoparticles (OCMNP) which was synthesized according to the scheme described in Figure 7.21A⁷. The synthesis are similar to that described in section 7.3.3 in Figure 7.17 but the produced oleic acid coated superparamagnetic iron oxide nanoparticles were then dispersed in styrene to form a styrene based ferrofluid. 2 wt. % thermal initiator 1, 1-azobis(cyclohexanecarbonitrile) (Vazo) was then added to the styrene based ferrofluid to obtain polymerized magnetic micro beads. The continuous phase was the surfactant (SDS) as an aqueous phase.

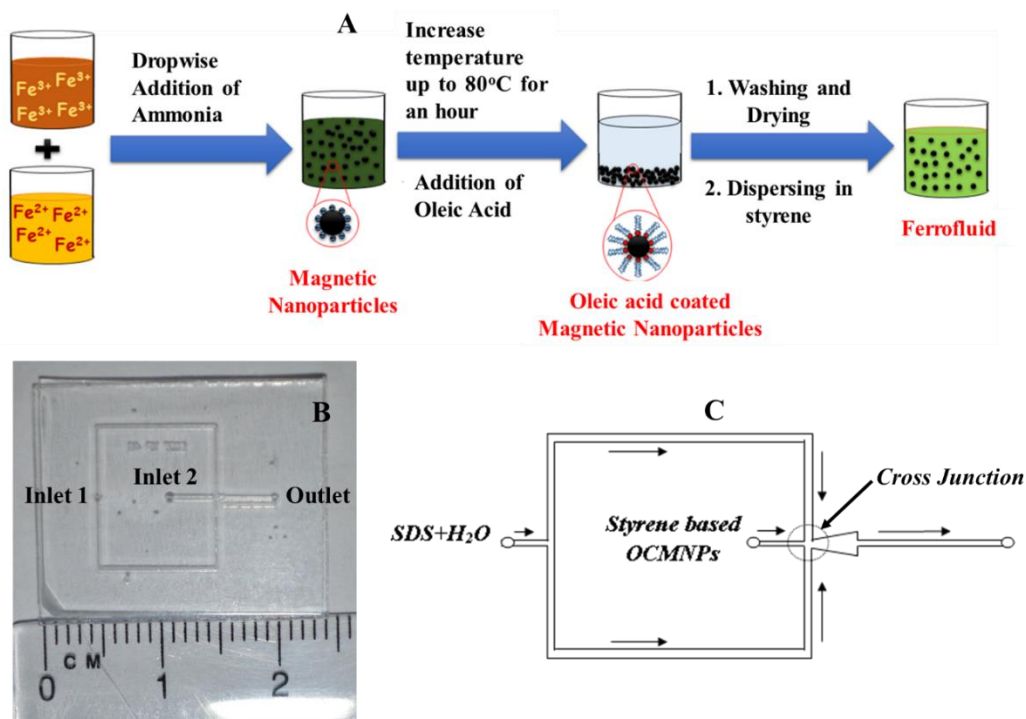


Figure 7.21: (A) the schematic diagram for the synthesis of styrene based ferrofluid which was synthesized from mixing the precursors ferrous and ferric ions in basic medium of ammonia which then dispersed in styrene. (B) A photographic image of microfluidic flow focusing used for the generation of magnetic microbeads. (C) The flow gram of components of continuous and dispersed phase in the flow focusing microchip.

Figure 7.21B describes the microfluidic flow focusing chip with dimensions of the channel are 50 μm in depth and 100 μm in width and the length of the chip is about 2.5 cm that was fabricated using photolithography as it was mentioned in chapter 2, Section of chip fabrication. The chip consisted of two layers of glass, the lower layer contained etched micro channels with flow focusing while the top layer was the bottom of the chip with tubing holes. Figure 7.21C shows the flow focusing chip⁸ where the continuous phase (SDS + Water) passes through two sides of the chip inlet whereas, the styrene based oleic coated magnetic nanoparticles are accommodated in the centre of flow focusing. The droplet generation was conducted by pumping sodium dodecyl sulphate at flow rate 5 $\mu\text{l}\cdot\text{min}^{-1}$ and the styrene based ferrofluid at 0.1 $\mu\text{l}\cdot\text{min}^{-1}$ with the droplets being generated at the cross junction as shown in Figure 7.22. To obtain monodispersed magnetic droplets which then can be thermally polymerised using initiator to form solidified magnetic micro beads, it is very important to optimize the flow rate of both continuous and dispersed phase and also the concentration of SDS surfactant.

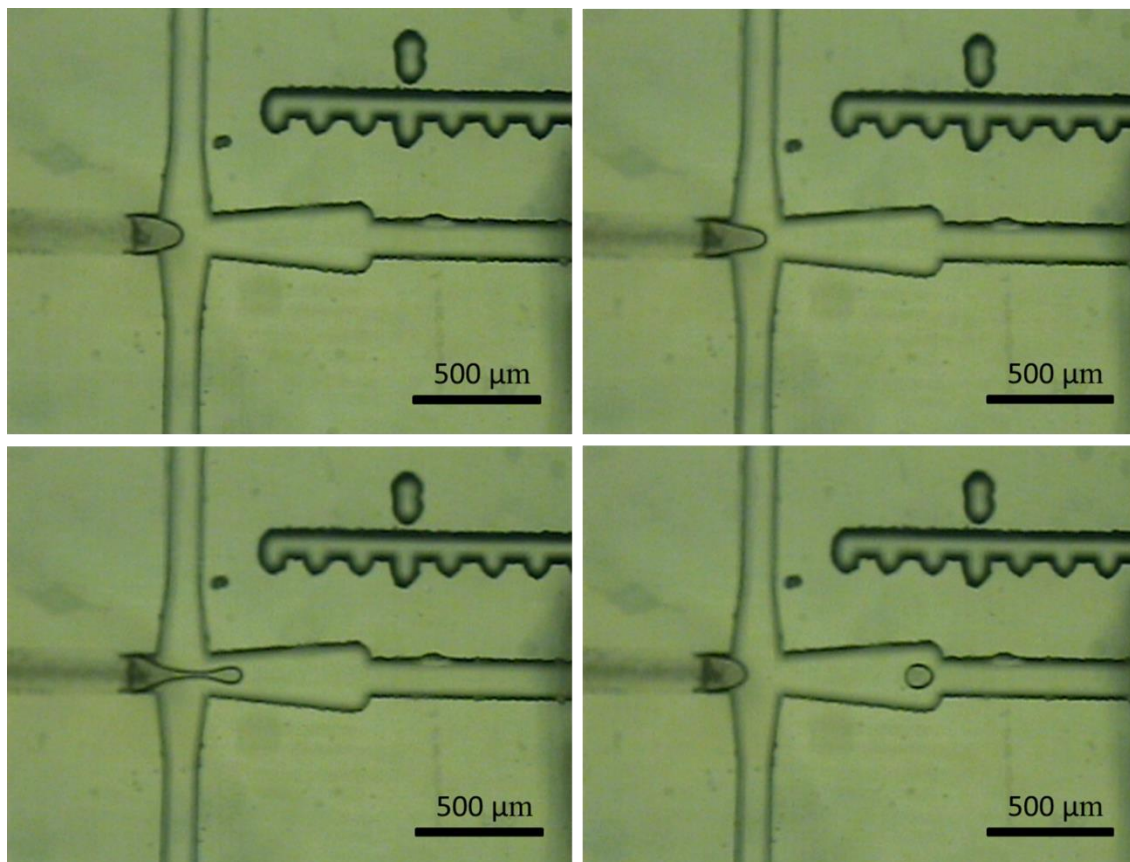


Figure 7.22: The droplet generation using microfluidic flow focusing technique depending on pumping sodium dodecyl sulphate on both sides of the inlet1 at flow rate $5 \mu\text{l}\cdot\text{min}^{-1}$ and styrene based ferrofluid in the centre of the chip (inlet 2) with flow rate $1 \mu\text{l}\cdot\text{min}^{-1}$ and the droplets were generated in the cross junction area to be collected in a glass tube from the outlet of the chip.

A plastic syringe was used for loading the continuous phase while a glass syringe was needed for loading the disperse phase because it contained styrene that could react with a plastic syringe in case of using it. Silica capillary tubes also had to be used to introduce solutions to avoid any reactions. The chip design had channel dimensions, depth $50 \mu\text{m}$ and width $100 \mu\text{m}$. Figure 7.23 shows a schematic of the microfluidic flow focusing chip, chip dimensions and the experimental setup of the droplet generation using flow focusing technique.

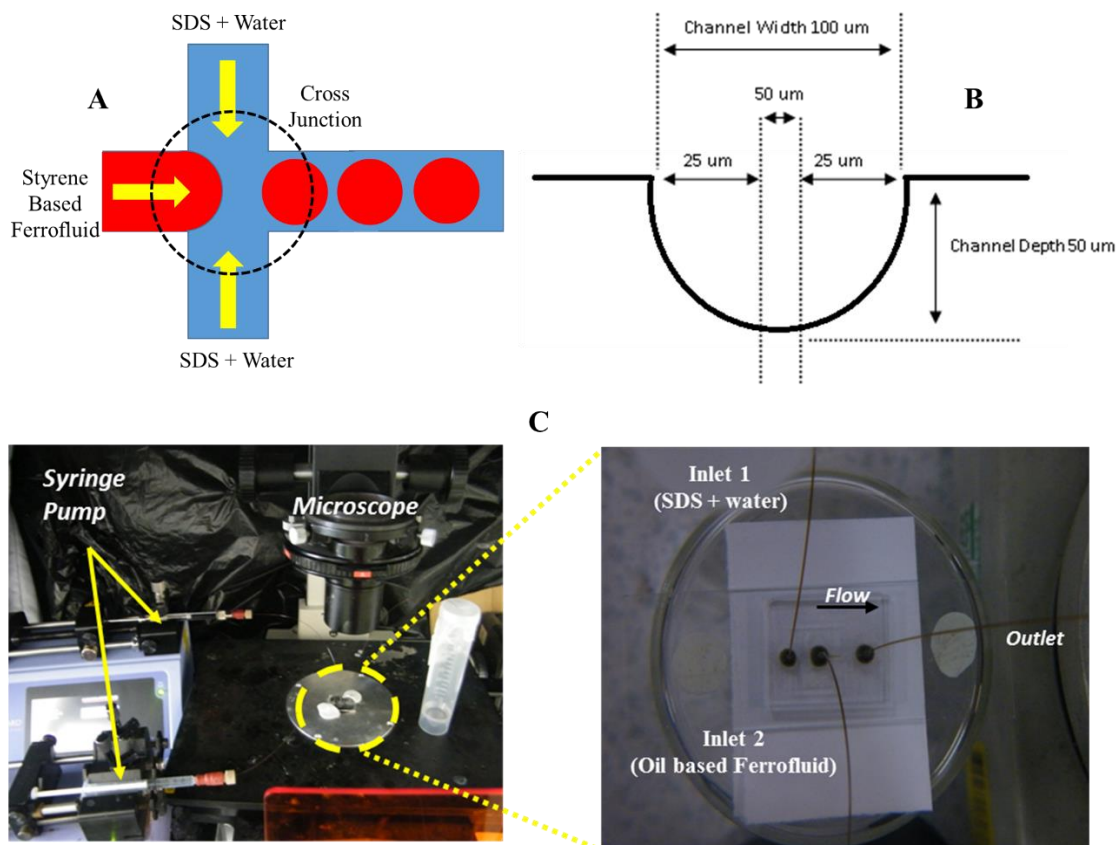


Figure 7.23: (A) profile for the flow gram of SDS as a continuous phase and styrene based Ferrofluid in the microfluidic flow focusing technique for generating droplet. (B) The channel dimensions of the chip which explained that the width is 100 μm and the depth is μm . (C) Photographic image of the experimental setup for the generation of magnetic droplets using microfluidic flow focusing.

- **Effect of SDS Concentration**

Different concentrations (0.035 M – 0.17 M) of SDS were used as a continuous phase at flow rate $5 \mu\text{l}\cdot\text{min}^{-1}$ with the dispersed phase (styrene based ferrofluid) at flow rate $0.1 \mu\text{l}\cdot\text{min}^{-1}$ to obtain the optimum concentration of SDS for the formation of micro beads. Figure 7.24 illustrates the droplet collected off at different concentrations of anionic surfactant. It can be seen from the figure that (A) which represents 0.035 M SDS gave mono dispersed droplet without any flocculation while B and C gave flocculated droplet generation with mono dispersed micro particles at SDS concentration 0.052 M SDS and 0.07 M SDS because of the attraction forces between each particle. However, D, E and F demonstrated highly mono dispersed magnetic micro particles with slightly flocculated

micro particles. Therefore, 0.035 M solution of SDS concentration is the best value to generate mono dispersed magnetic droplet.

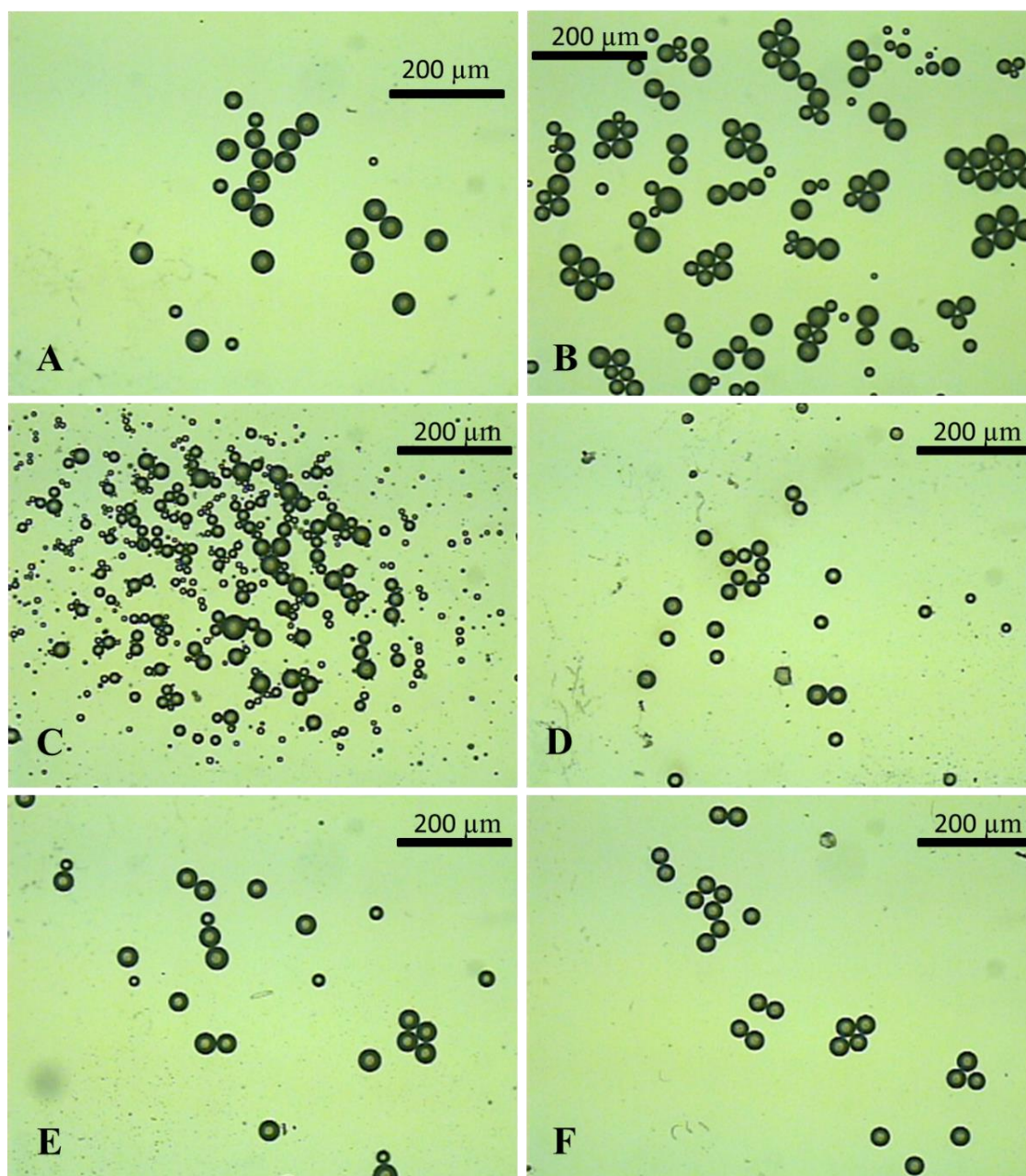


Figure 7.24: The effect of surfactant (SDS) on the size of the droplet generated from microfluidic flow focusing technique. (A) 0.035 M SDS (B) 0.052 M SDS, (C) 0.07 M SDS, (D) 0.07 M SDS, (E) 0.14 M SDS and (F) 0.17M SDS.

- **Effect of Flow rate**

Various flow rates of continuous phase (1 $\mu\text{l}/\text{min}$ – 5 $\mu\text{l}/\text{min}$) were studied. Figure 7.25 shows chip profile for the generation of droplet at different flow rate of continuous phase (SDS+ Water) with fixed flow rate of dispersed phase (0.1 $\mu\text{l}/\text{min}$). It was noticed that at low flow rate of continuous phase (1-2 $\mu\text{l}/\text{min}$) that large sizes of micro beads were generated but they were aggregated and poly dispersed as is shown in (A and B). However, at high flow rates of continuous phase, small sizes of micro particles were formed with relevant mono dispersion (C, D, E and F). Thus, 5 $\mu\text{l}/\text{min}$ flow rate of SDFS was chosen as an optimal flow rate for the generation of droplets.

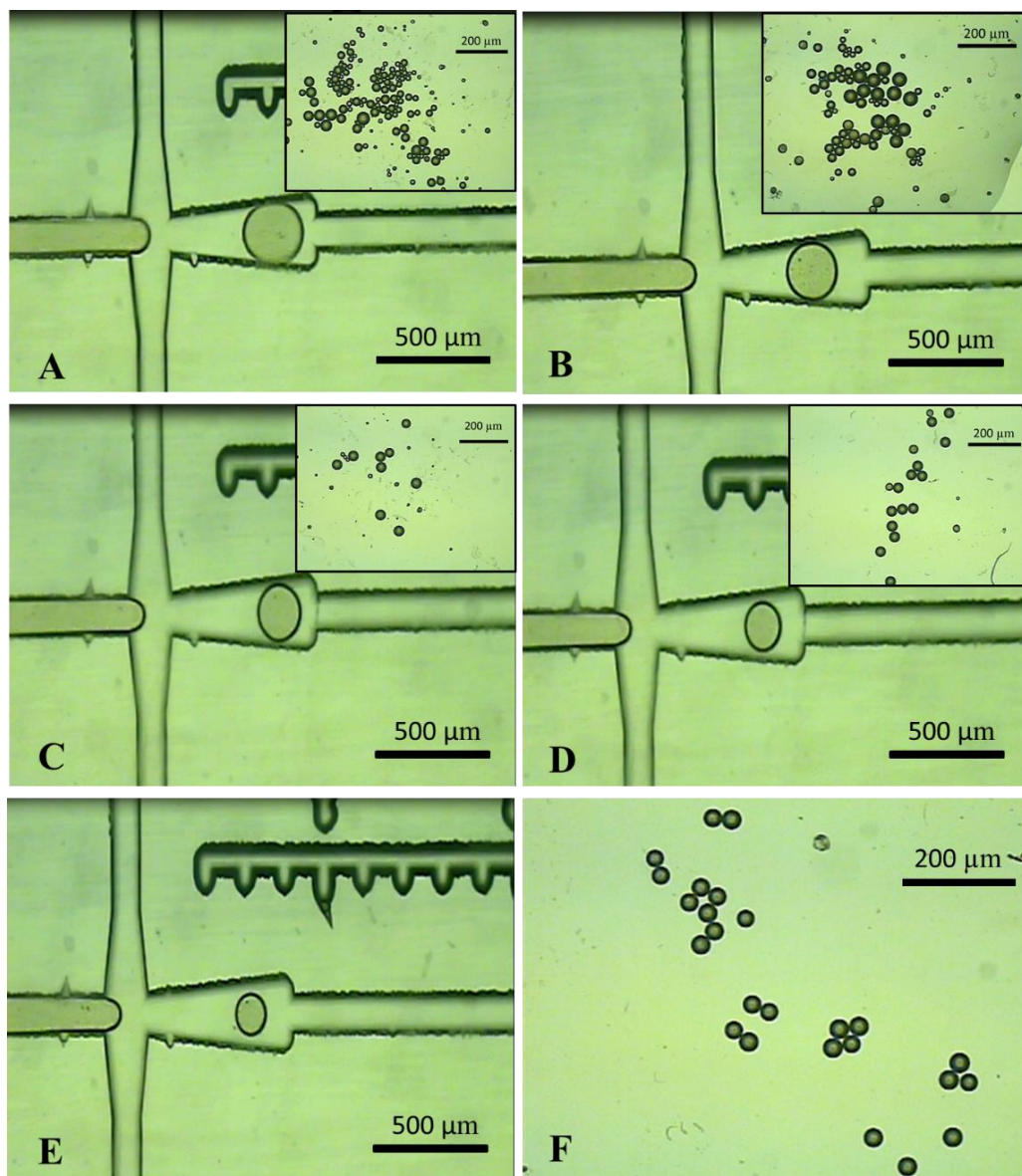


Figure 7.25: Effect of flow rate of continuous phase of sodium dodecyl sulphate (SDS) on the size of magnetized droplet using flow focusing microfluidic technique while the dispersed phase (styrene based ferrofluid) being kept at $0.1 \mu\text{L}/\text{min}$. (A) $1 \mu\text{L}/\text{min}$, (B) $2 \mu\text{L}/\text{min}$, (C) $3 \mu\text{L}/\text{min}$, (D) $4 \mu\text{L}/\text{min}$, and E and F represent the flow gram and droplet generated at flow rate of SDS at $5 \mu\text{L}/\text{min}$.

The magnetized droplets collected off chip at 1 % SDS concentration, $5 \mu\text{L}/\text{min}$ flow rate of SDS and $0.1 \mu\text{L}/\text{min}$ flow rate of styrene based ferrofluid were then thermally polymerised off chip at 70°C for three hours as displayed in the setup in Figure 7.26. It was observed that the droplets generated had a strong magnetic response but were unstable,

therefore, the droplets need more mixing on-chip to increase their stability and at the same time, they need more powerful surfactant to be more stable.

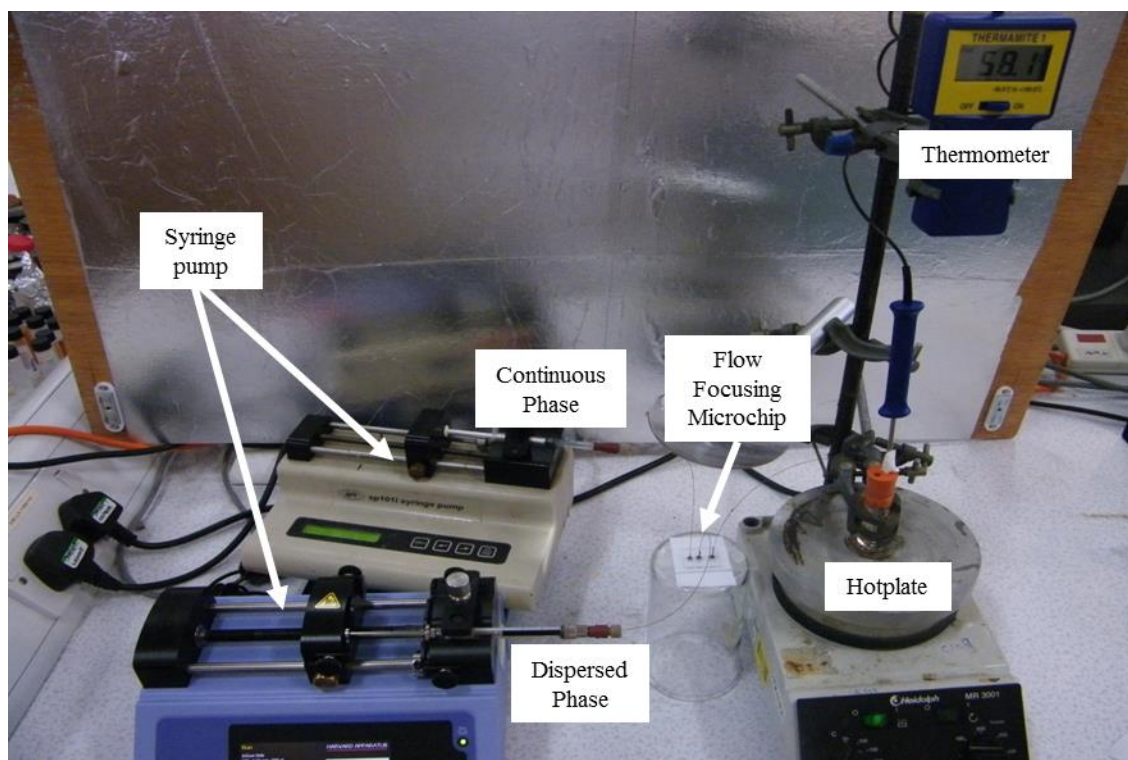


Figure 7.26: The experimental setup for the thermal polymerization of generated magnetized droplets from the system dispersed phase (styrene based Ferrofluid) and the continuous phase SDS solution using microfluidic flow focusing technique at 70oC for three hours.

7.3.5 Flow focusing Microfluidic with Serpentine

A new microfluidic flow focusing chip was then designed to generate magnetized droplet through adding serpentine mixing coil which allow droplets to interact with the surfactant for longer time so they could become more stable.^{9, 10} The polymerisable surfactant Hitenol BC20 was also used rather than SDS because the latter hydrolysed as the temperature was increased for polymerization.. Figure 7.27 shows the flow focusing microchip with the serpentine. The chip contained inlet 1 which accommodated 2% wt. % Hitenol BC20 as a continuous phase while inlet 2 was used for the styrene based ferrofluid as shown in Figure 7.27A and 7.27B. As before silica capillary tubes were used in the holes of the top layer of glass to deliver fluids to the lower layer of the chip. The chip dimensions were 7 cm in

length and 2.5 cm in width while for the micro channels were depth 50 μm and width 100 μm with a wider 150 μm channel for the serpentine. To generate more stable magnetized droplets, the concentration and the flow rate of Hitenol BC20 was investigated. Figure 7.28 shows the droplet generation using 1% Hitenol solution at flow rate 0.1 $\mu\text{l. min}^{-1}$ as a continuous phase and styrene based ferrofluid at 5 $\mu\text{l. min}^{-1}$ as a dispersed phase.

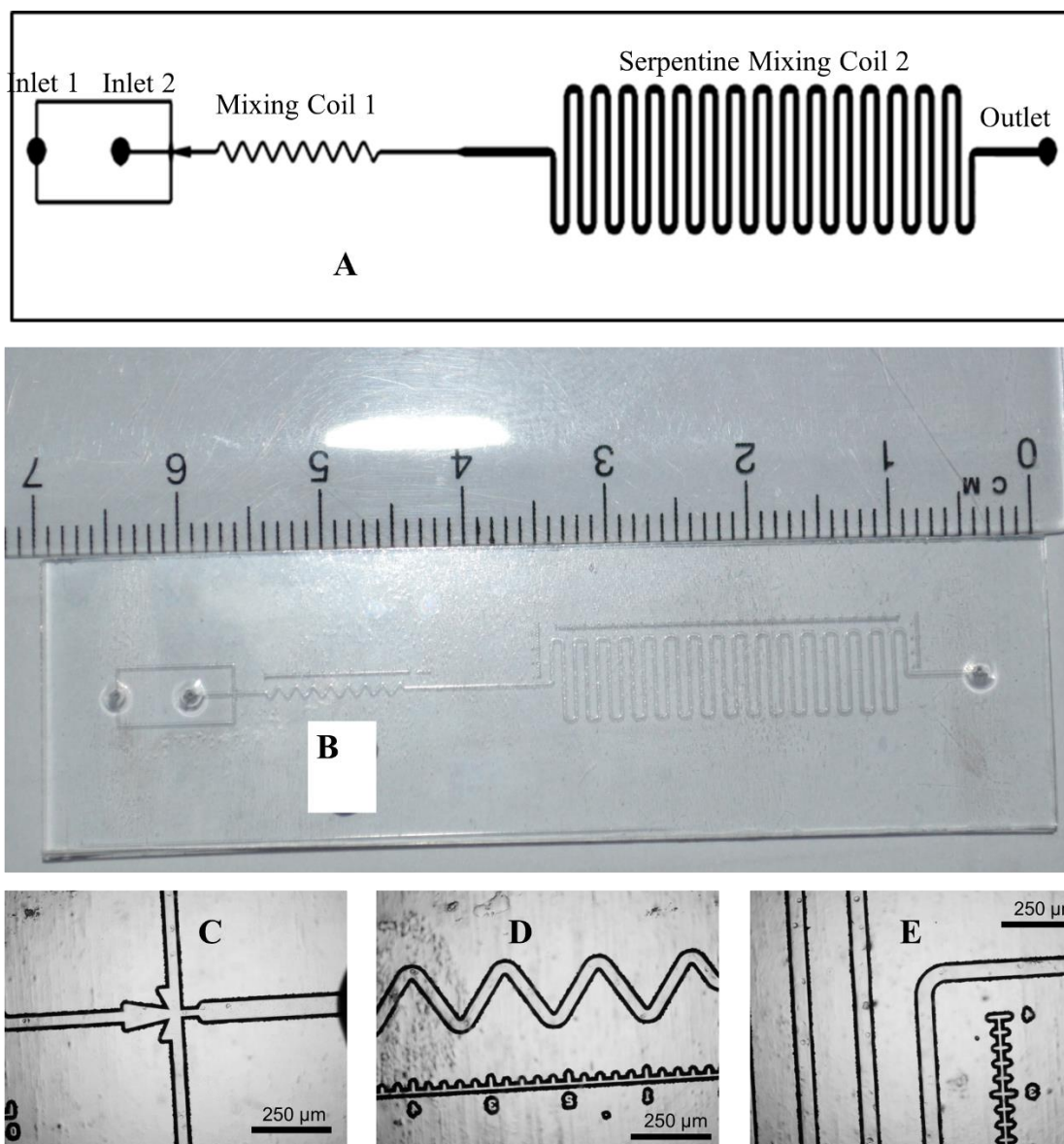


Figure 7.27: The microfluidic flow focusing with serpentine mixing part for the generation of magnetized droplets. (A) Flow gram of flow focusing technique with serpentine, (B) photographic image of the developed microchip for flow focusing technique. (C) Flow focusing cross junction, (D) mixing coil 1 and (E) serpentine mixing coil 2.

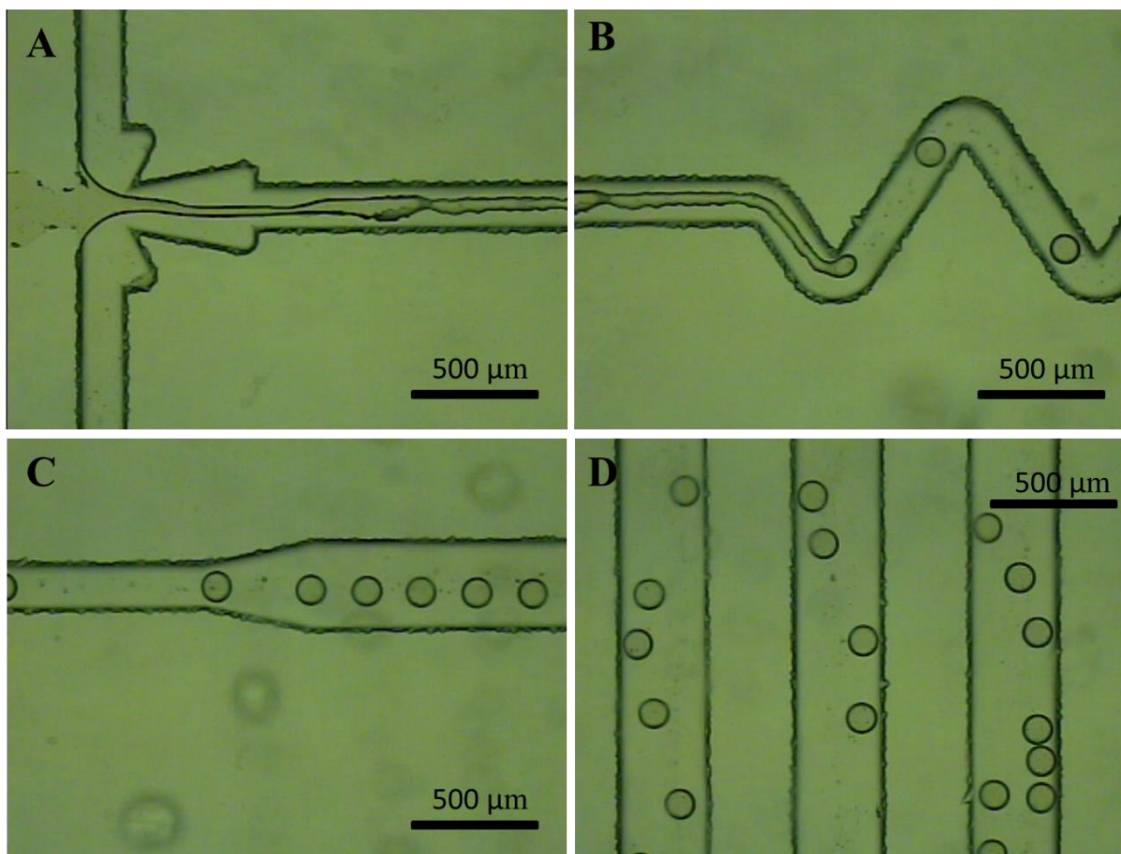


Figure 7.28: The droplet generation using flow focusing technique with serpentine mixing part. (A) Droplet generation in the cross junction, (B) The generated droplets in the mixing coil 1, (C) The generated magnetized droplet before entering the serpentine part, and (D) the generated droplet in the serpentine part as actually seen in the microscope.

- **Effect of Hitenol Concentration**

Different concentration (1%, 2 %, 3 % and 4 % wt. %) of the surfactant Hitenol BC20 were used as the continuous phase in inlet 1 at a flow rate $5 \mu\text{l min}^{-1}$ while styrene based ferrofluid was the dispersed phase being kept at flow rate $0.5 \mu\text{l min}^{-1}$ in inlet 2 of the microchip. Figure 7.29 shows that there was no significant difference in the generated magnetized droplets which means that the concentration of Hitenol BC20 did not affect the sizes of the magnetized droplet.

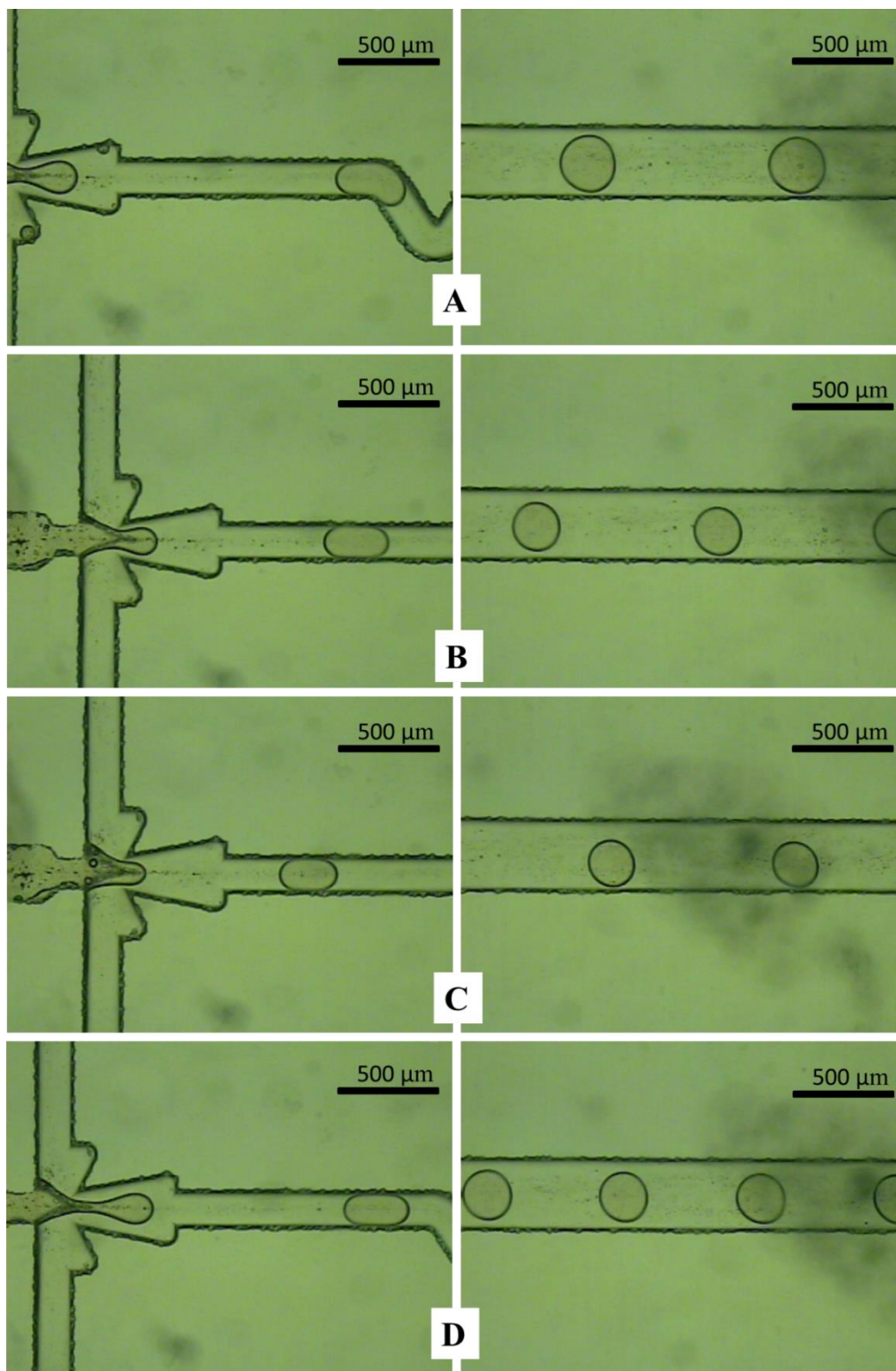


Figure 7.29: The effect of Hitenol BC20 on the size of the magnetized droplet generated from the system that consists of Hitenol as a continuous phase and styrene based ferrofluid as a dispersed phase. (A) 1 wt. % Hitenol BC20, (B) 2 wt. % Hitenol BC20, (C) 3 wt. % Hitenol BC20, and (D) 4 wt. % Hitenol BC20.

- **Effect of flow rate of Styrene based Ferrofluid**

Various flow rates of dispersed phase ($0.1 \mu\text{l min}^{-1}$, $0.5 \mu\text{l min}^{-1}$, $0.75 \mu\text{l min}^{-1}$, and $1 \mu\text{l min}^{-1}$) were utilized to study the effect of the flow rate of the dispersed phase on the size of the magnetized droplet while the flow rate of the continuous phase was $5 \mu\text{l min}^{-1}$. Figure 7.30 shows the effect of flow rate of the dispersed phase on the size of the magnetic micro beads for the system which consists of 2 wt. % Hitenol BC20 as a continuous phase at flow rate $5 \mu\text{l min}^{-1}$ and styrene based ferrofluid as a dispersed phase. It can be seen from the figure that as the flow rate of the dispersed phase increases, the size of magnetized particles increased where at 0.1 to $0.5 \mu\text{l min}^{-1}$ flow rates of the dispersed phase, the sizes were around $50 \mu\text{m}$ to $65 \mu\text{m}$ while at flow rate $0.75 \mu\text{l min}^{-1}$, the size increased to $90 \mu\text{m}$ and at $1 \mu\text{l min}^{-1}$, the size has become bigger than $100 \mu\text{m}$. These results were promising to obtain mono dispersed magnetic micro beads, however, they were still unstable even when using different surfactant. Therefore, this system needs to be further optimization by adding another channel to pump warmed agarose which then cooled down to keep the micro beads separate and avoid the coalescence between droplets. As time was running it out and it was decided to use the synthetic method in batch mode.

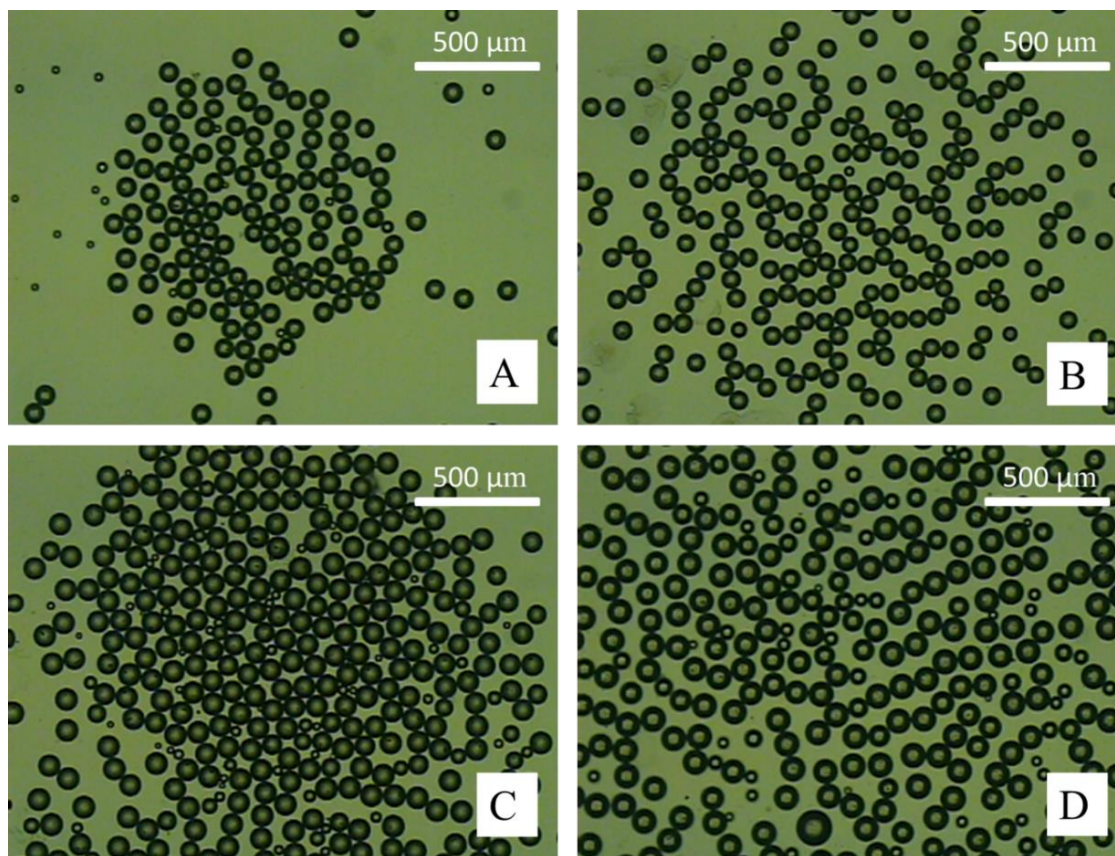


Figure 7.30: The effect of flow rate of the dispersed phase of styrene based ferrofluid on the size of the generated magnetized micro beads at fixed flow rate of continuous phase of Hitenol BC20. (A) $0.1 \mu\text{l min}^{-1}$, (B) $0.5 \mu\text{l min}^{-1}$, $0.75 \mu\text{l min}^{-1}$, and (D) $1 \mu\text{l min}^{-1}$.

7.3.6 Fabrication of Magnetized Micro Beads by Emulsification

Magnetic micro beads were synthesized according to the emulsification method described by Dyab *et al*¹¹ with some modifications as shown in Figure 7.31. The synthesis is similar to that mentioned in Figure 7.22A but styrene based ferrofluid was emulsified with anionic polymerisable surfactant Hitenol BC20 to produce hydrophobic micro beads after thermal polymerisation. The emulsion was homogenised manually using plastic pipette to make sure obtaining poly dispersed micro beads. It can be seen in figure 7.32A, the formation of magnetic micro droplets before thermal polymerisation as well as parallel chains were produced upon approaching strong neodymium magnet from magnetic micro droplets (see fig. 7.32(B)). In addition of that, figure 7.32(C and D) also display the fabricated magnetic micro beads after thermal polymerisation.

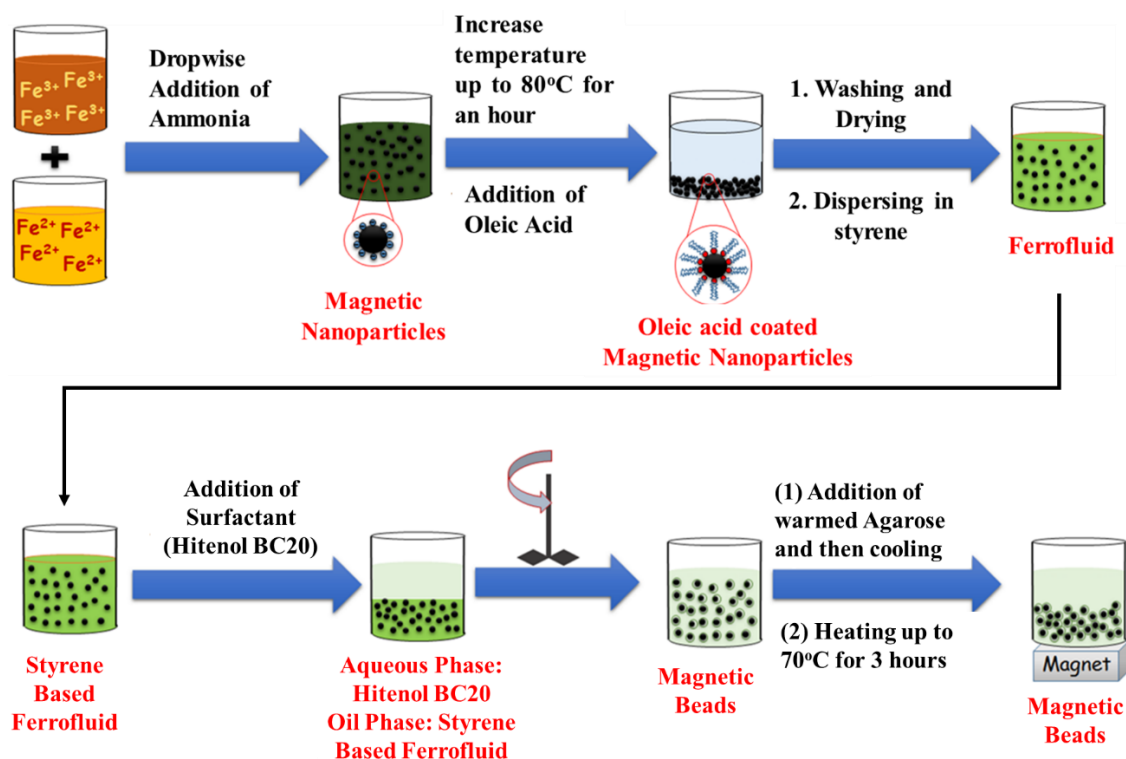


Figure 7.31: The schematic diagram for the manual synthesis of magnetized micro beads using the precursor's ferrous and ferric ions in the basic medium of ammonia to form magnetic nanoparticles which in turn functionalized with oleic acid and dispersed in styrene to form styrene based Ferrofluid. The latter then homogenized with equal amount of 2% Hitenol BC20 to form oil in water emulsion using pipette. After that, the emulsion was added to warmed agarose and cooled down to room temperature, which then heated up to 70°C for three hours to polymerise the beads.

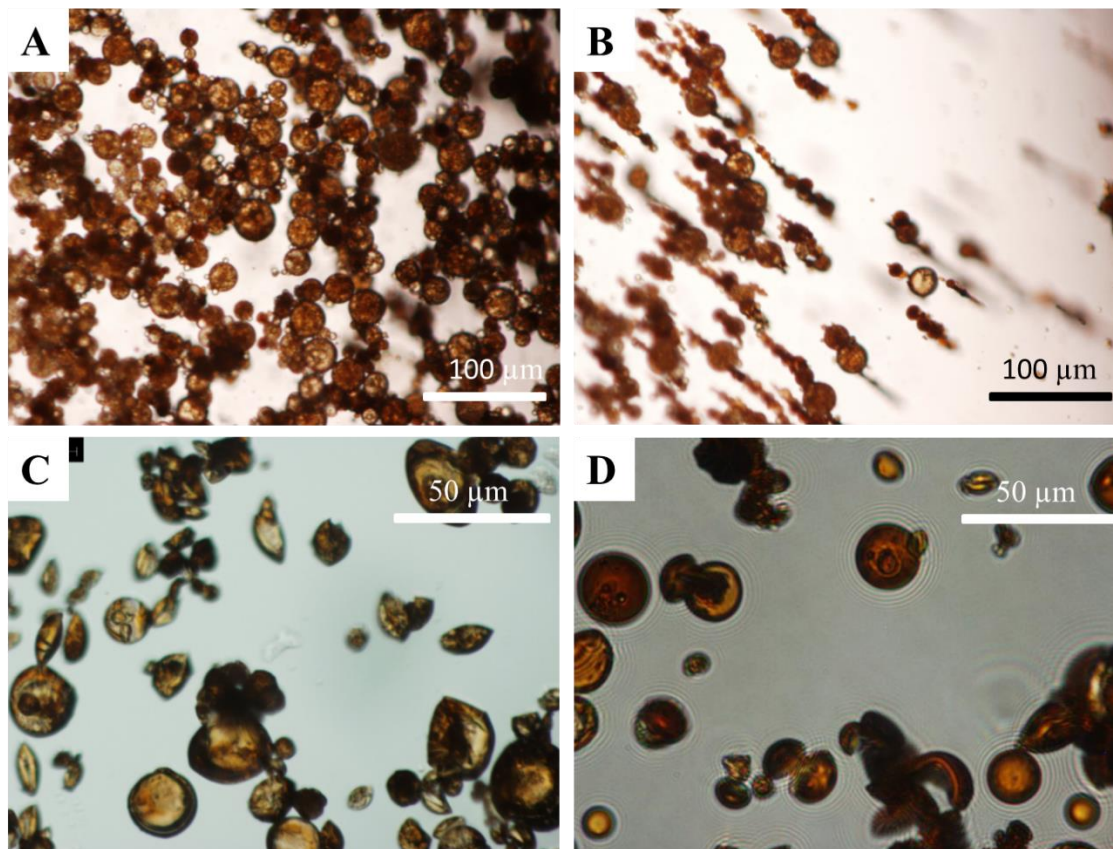


Figure 7.32: The generation of magnetic micro beads from the emulsification of the system Hitenol BC20 as a continuous phase and styrene based ferrofluid as a dispersed phase and thermally polymerised using thermal initiator. (A) The prepared oil in water magnetized droplets, (B) The parallel chains of magnetized micro beads before thermal polymerization and (C and D) The fabricated magnetic micro beads after thermal polymerization.

7.4 Magnetic Gate Keepers in Microchip

The generated magnetic micro beads had sizes ranged from 10-30 μm which means that these beads were poly dispersed micro particles allowing fluids to pass through the pores between micro beads to avoid the back pressure in case of pumping liquids from inlets of the chip. The magnetic response was tested and it was found to be very strong upon approaching neodymium magnet where the beads can be controlled and attracted in different directions. Therefore, these beads could be utilized for trapping cells into the micro chambers of microchip. Figure 7.33A and 7.33B show the different dimensions of the cell trapping microchip with the micro chamber which accommodates these beads as gate keepers at the outlet. The bottom plate of the glass chip consists of two inlets, one

outlet, and micro chamber of Microfluidic chip that is used for trapping cells while the upper plate accommodates PDMS layer. After that, the magnetic beads were placed in the micro chamber of the chip. The glass chip was bonded to PDMS plate using chip holder as shown in Figure 7.33C.

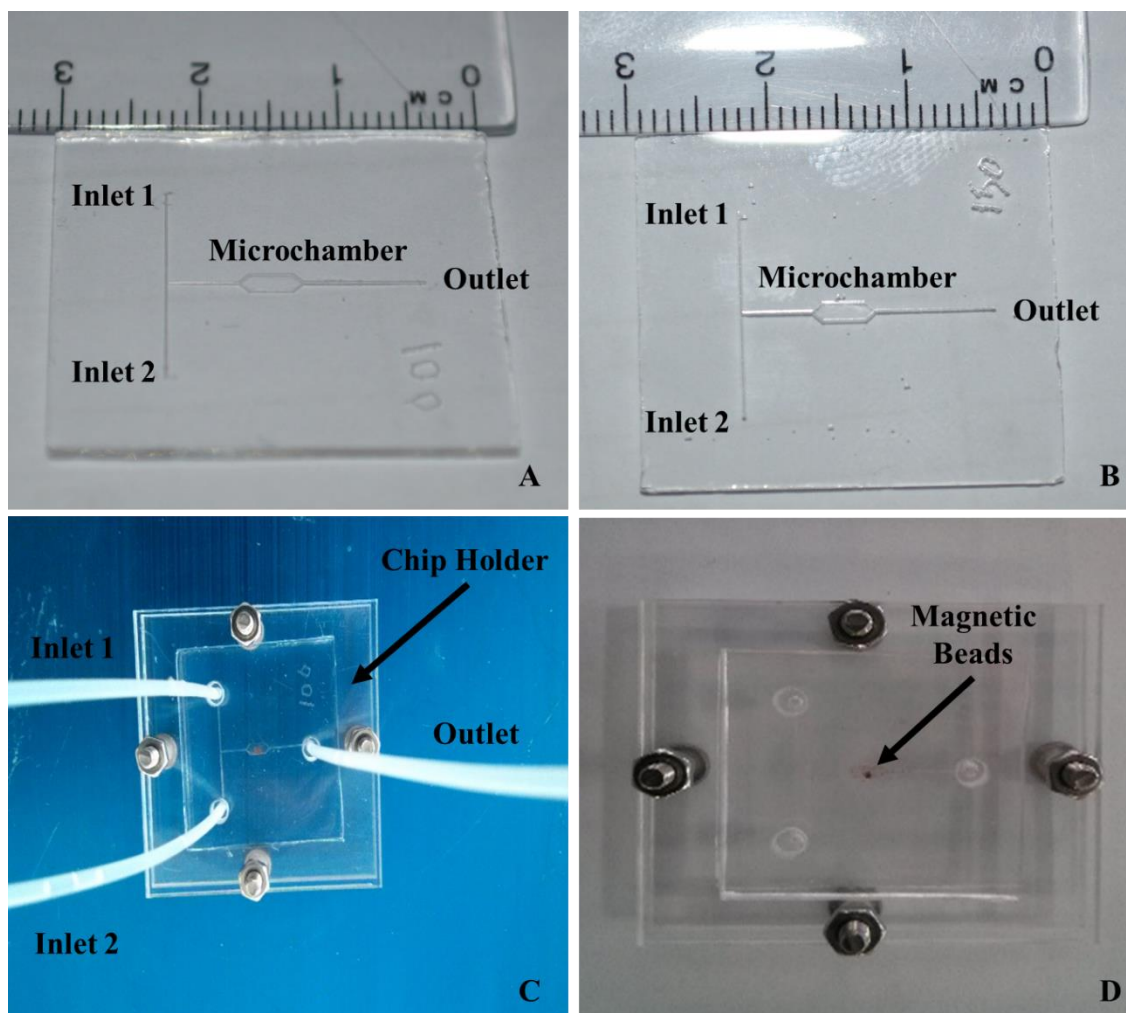


Figure 7.33: The PDMS/glass microfluidic cell based assay for trapping cells using magnetic micro beads as gate keepers into the micro chamber of the microchip. (A) Microfluidics chip cell trapping with 100 μm in depth, (B) microfluidics chip cell trapping with 150 μm in depth, (C) microfluidics glass chip cell trapping with 100 μm in depth as a lower plate bonded with PDMS using chip holder where all tubing holes were achieved by punch device and the tubing was 1.6 mm PTFE. (D) PDMS/glass microfluidic chip bonded with chip holder and magnetic micro beads are in the micro chamber of the chip

Various different channel depths (50 μm , 100 μm and 150 μm) were investigated to accommodate the magnetic beads into the micro chamber of the chip as shown in Figure 7.33A and 7.33B. However, it was observed that these beads do not have the ability to

move freely inside the micro chamber, even though they have strong magnetic response as explained in Figure 7.33D. The reason behind that is attributed to the configuration, the depth, and the width of the micro channel where there was not possibility to control precisely these parameter upon etching glass plate. In addition of that, the upper plate is made of PDMS and it was noticed that upon approaching neodymium magnet from the micro chamber from the top layer, the magnetic response of these beads were weak.

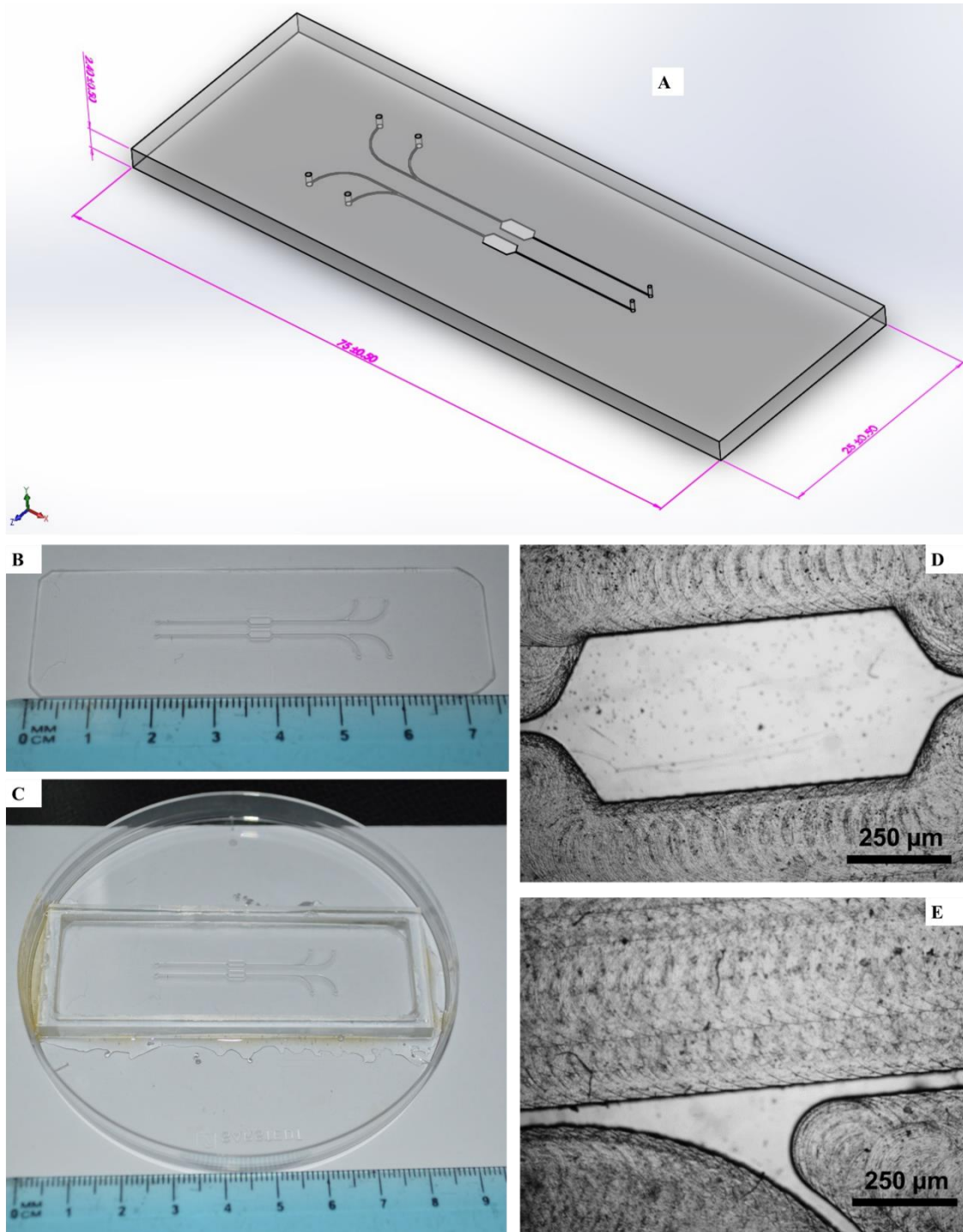


Figure 7.34: Microfluidics chip design that made of PMMA polymer from a CAD file designed by computer software that constructed by CNC machine to form three dimension micro channels. (A) The CAD file of the chip design. (B) The master design made of PMMA polymer by CNC machine. (C) The master design placed in rectangular block which can be used for making replica that made of PDMS (D) The micro chamber of the master PMMA design. (E) The micro channels of the master PMMA polymer design.

On the other hand, the magnetic response become extremely strong upon using magnet from the glass plate side. Therefore, it was tried another design of microchip with different dimensions (75 mm length and 25 mm width) by making the lower chip made of PDMS which contains the micro channels and chambers and the upper chip is made of glass (B270) with 1.6 mm inner diameter of each hole. Figure 7.34 describes microfluidic chip design as a master mold which made of PMMA polymer and the channels were created by CNC machine according to drawing CAD file using computer software. Additionally, it contains the rectangular block to construct the replica after pouring PDMS with curing agent on top of the master, then peeled off. It can also be displayed in Figure 7.35A that the PDMS plate contains the microchannel with 175 μm in depth alongside of the microchip while the glass plate includes the holes of inlets and outlets which then bonded on top of the PDMS plate using oxygen plasma cleaner as shown in Figure 7.35B.

The magnetic micro beads were placed into the micro chamber before bonding the two plates together where the face up of PDMS and glass plates were exposed to oxygen plasma cleaner for a minute at 0.6 watt RF power. The glass/PDMS chip was left in an oven for 24 hour at 60°C to strengthen the chemical bonding between the plates. Figure 7.36A describes the glass / PDMS microfluidic chip and magnetic beads are inside the micro chamber of PDMS plate which were placed after plasma bonding while the glass chip contains the holes of inlets and outlets. PTFE tubing (ID, 0.5 mm and OD, 1.6 mm) was utilized to pump fluids from syringe pump to the inlets of the microchip where they were glued to the chip using Araldite glue and left for a while to be solidified. The glass/PDMS chip was experimentally set up under bright field microscope with 2X magnification with neodymium magnet on top of the glass plate as explained in the photographic images for the whole setup and the side and the top of the microfluidic device in Figure 7.36B, 7.36C and 7.36D, respectively. The micro chamber placed magnetic beads were drive and controlled by neodymium magnet and moved to different directions as shown in Figure 7.37. It can be seen in Figure 7.37 that magnetic beads follow the magnet to each side where it was placed, and this feature are important for trapping cells.

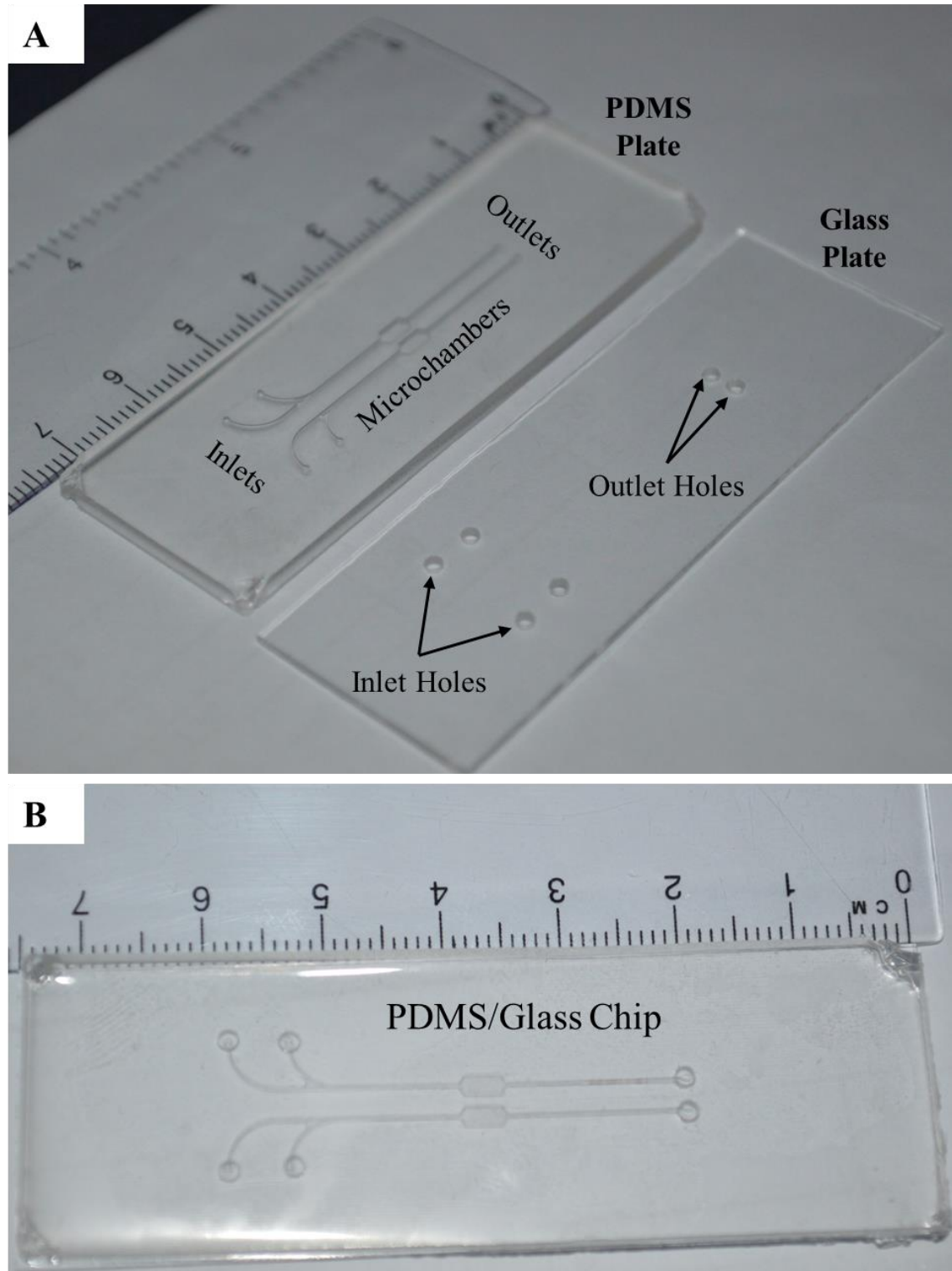


Figure 7.35: Glass/PDMS microfluidics cell trapping chip. (A) the microfluidics chip which consists of PDMS plate with micro channels and glass plate with holes. (B) Oxygen plasma bonded glass/PDMS microfluidics chip.

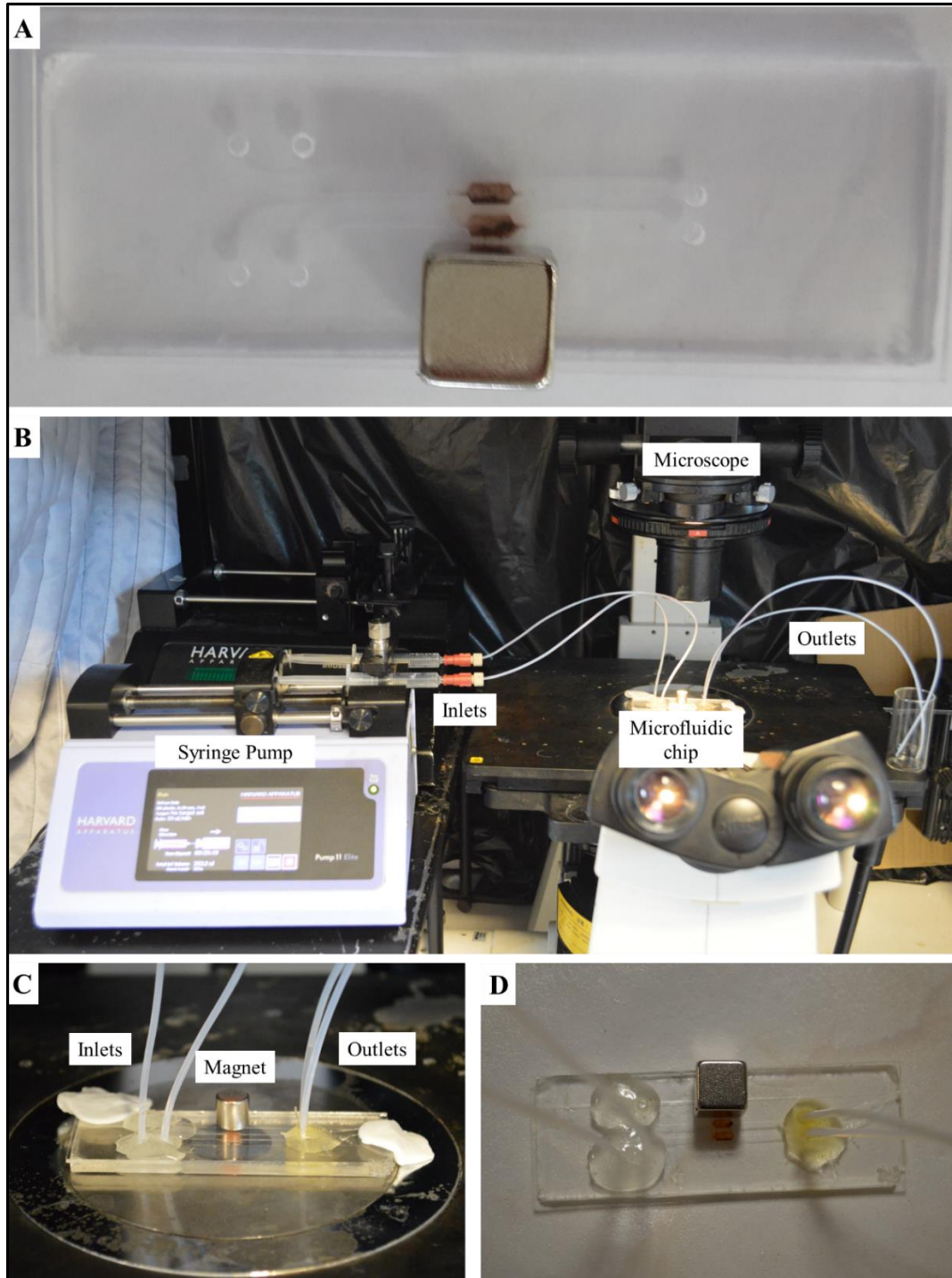


Figure 7.36: Glass / PDMS microfluidic chip for cell based assay which was conducted through bonding glass to PDMS using plasma cleaner and magnetic beads placed inside the micro chamber. (A) Glass/PDMS microfluidics chip with magnetic beads attracted by neodymium magnet. (B) The experimental setup of the microfluidic glass beads trapping into the micro chambers. (C) Photographic image of the side of the Glass/PDMS microchip with the magnet on top. (D) Photographic image of the top of Glass/PDMS microchip with the magnet on top of the glass plate trapping magnetic beads inside the micro chamber.

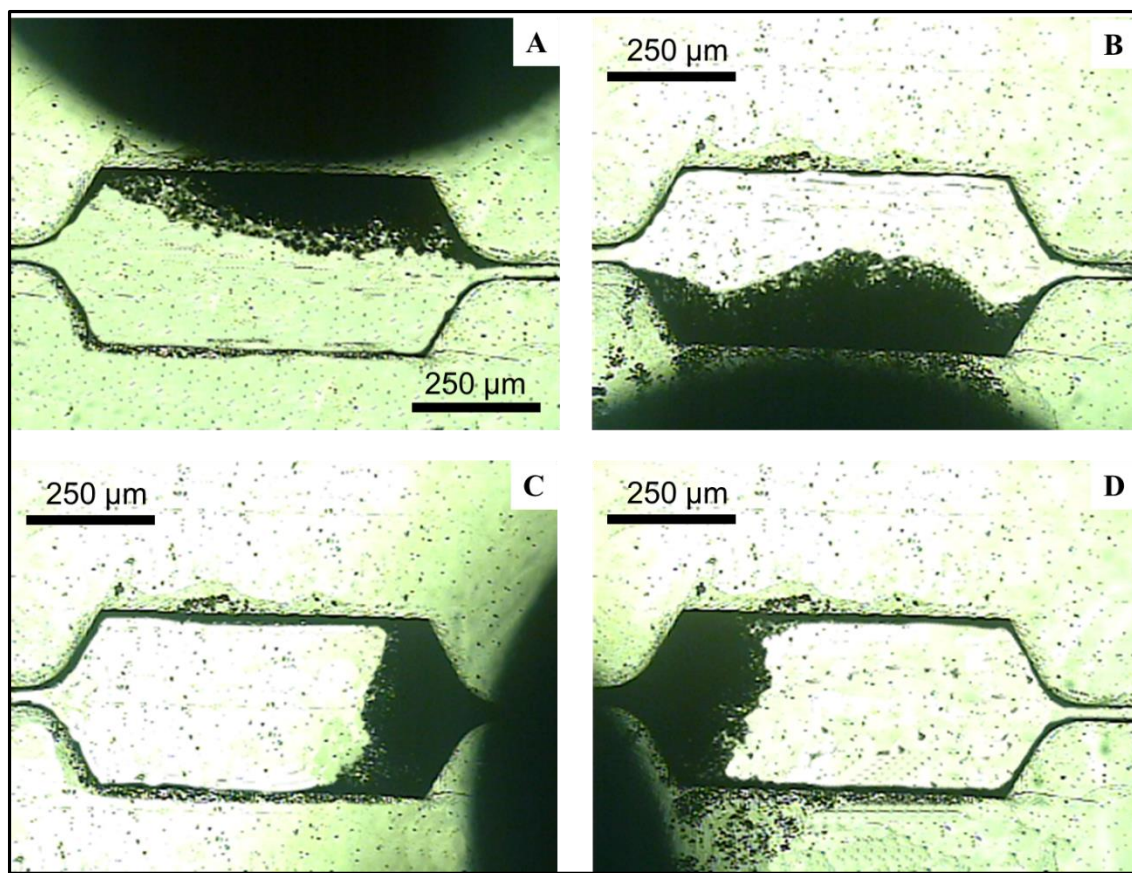


Figure 7.37: Bright field microscopic images of the micro chamber of glass / PDMS microfluidic chip where magnetic beads are inside the micro chamber and attracted by neodymium magnet upon approaching the magnet from the micro beads. (A) Magnetic beads upon approaching the magnet from the upper side of the chip. (B) Magnetic beads upon approaching the magnet from the down side of the chip. (C) Magnetic beads upon approaching the magnet from the right hand side of the chip. (D) Magnetic beads upon approaching the magnet from the left hand side of the chip.

It can be concluded that magnetized gate keepers were synthesized from thermal polymerization of emulsified styrene based ferrofluid in Hitenol BC20. These magnetized gate keepers have the ability to be trapped into the micro chamber of the chip upon approaching neodymium magnet. This developed method could overcome most problems of cell trapping methods into microfluidic chip which suffer some drawbacks such as electric and magnetic field and some mechanical forces.¹² Additionally, the new method does not have any interaction with the trapped cells as the magnetic Janus beads are hydrophobic and biocompatible.¹³ Several approaches were tried and had come up with a simple solution but ran out of time to achieve toxicity or antimicrobial testing which would be further work.

Bibliography

1. L. R. Volpatti and A. K. Yetisen, *Trends in Biotechnology*, 2014, **32**, 347-350.
2. D. Mazia, G. Schatten and W. Sale, *The Journal of cell biology*, 1975, **66**, 198-200.
3. J. García-Alonso, R. F. Fakhrullin, V. N. Paunov, Z. Shen, J. D. Hardege, N. Pamme, S. J. Haswell and G. M. Greenway, *Analytical and bioanalytical chemistry*, 2011, **400**, 1009-1013.
4. P. Berger, N. B. Adelman, K. J. Beckman, D. J. Campbell, A. B. Ellis and G. C. Lisensky, *Journal of Chemical Education*, 1999, **76**, 943.
5. N. V. Jadhav, A. I. Prasad, A. Kumar, R. Mishra, S. Dhara, K. Babu, C. Prajapat, N. Misra, R. Ningthoujam and B. Pandey, *Colloids and Surfaces B: Biointerfaces*, 2013, **108**, 158-168.
6. C. Zhou, P. Yue and J. J. Feng, *Physics of Fluids (1994-present)*, 2006, **18**, 092105.
7. A. K. Dyab, M. Ozmen, M. Ersoz and V. N. Paunov, *Journal of Materials Chemistry*, 2009, **19**, 3475-3481.
8. B. Lu, T. Georgiou and N. Pamme, 2014.
9. X. Gong, S. Peng, W. Wen, P. Sheng and W. Li, *Advanced Functional Materials*, 2009, **19**, 292-297.
10. M. T. Rahman and E. V. Rebrov, *Processes*, 2014, **2**, 466-493.
11. A. K. F. Dyab, M. Ozmen, M. Ersoz and V. N. Paunov, *Journal of Materials Chemistry*, 2009, **19**, 3475-3481.
12. R. M. Johann, *Analytical and bioanalytical chemistry*, 2006, **385**, 408-412.
13. M. Yoshida, K. H. Roh, S. Mandal, S. Bhaskar, D. Lim, H. Nandivada, X. Deng and J. Lahann, *Advanced materials*, 2009, **21**, 4920-4925.

8. Chapter Eight: Conclusions and Future Works

8.1 Conclusions

Nanomaterials play an important role in many industrial and biological applications as they have unique chemical and physical properties such as small size and high surface area. However, the huge production of these nanomaterials which might release to the environment causing damage ecological system. The aim of this thesis was to investigate nanoparticles, both in terms of their toxic effects on model microorganisms and their application for drug delivery. Metal nanoparticles such as titania nanoparticles have the ability to scatter and reflect light in cosmetics and in the same time, they are not biodegradable which may have toxic effect while polymer nanoparticles are biodegradable and biocompatible and they are commonly used in drug delivery systems.

In chapter three and four, a range of titania nanoparticles of different crystallite size were synthesised and characterised in terms of their surface charge and average hydrodynamic diameter in aqueous solutions. The effect of the TiO₂NPs hydrodynamic diameter on their toxicity for *C.reinhardtii* microalgae and yeast was studied. The cells were separated from their growth media to avoid any interferences with the TiO₂NPs. The results indicated that smaller TiO₂NPs have a higher toxicity than larger ones, with the anatase form of the TiO₂NPs having a higher impact on the cell viability than the rutile form. It was found that the bare anatase TiO₂NPs were cationic below pH 6.5 which explains their adhesion to the cell walls of both microalgae and yeast.

Irradiation of the microalgae cells with UV light (peak at 365 nm) had bigger impact on their viability in the presence of TiO₂NPs compared with the same experiments conducted in dark conditions. Surprisingly, illumination with visible light also made the TiO₂NPs more toxic to the microalgae compared to the ones in dark conditions. The experiment presented that TiO₂NPs at concentrations above 50 µg mL⁻¹ noticeably affect the microalgae viability while nanoparticle concentrations higher than 250 µg mL⁻¹ led to complete loss of viability. The tests also showed a decrease in the chlorophyll content after prolonged exposure to TiO₂NPs in UV and visible light. This indicated that TiO₂NPs can not only disrupt the cell membranes but also can interfere with the cell chloroplasts. The results with yeast cells showed similar trends but due to the much thicker yeast cells walls

the nanotoxicity concentration threshold TiO₂NPs was about one order of magnitude higher.

Polyelectrolyte-coated TiO₂NPs with up to 4 layers of polyelectrolytes of alternating charge (PSS and PAH) were also produced using the layer-by-layer technique. Cell viability tests showed that their nanotoxicity alternated with the particles surface charge and depended on the last coat of polyelectrolytes. Anionic nanoparticles as TiO₂NPs/PSS and TiO₂NPs/PSS/PAH/PSS showed much lower nanotoxicity than the cationic ones, TiO₂NPs/PSS/PAH and bare TiO₂NPs, respectively. This was explained by the poor adhesion of the anionic particles to the cell walls due to their electrostatic repulsion and the amplification of the particle-cell adhesion in the case of cationic TiO₂NPs. These results were backed by TEM images of sectioned microalgae and yeast cells. The results of this study contributed to the understanding of the interaction mechanisms of surface modified TiO₂NPs/PSS with living cells and determined the factors which control their nanotoxicity.

In Chapter five and six a polyacrylic acid based microgel (Carbopol Aqua SF1) was used as a nanocarrier for drug delivery using a swelling/deswelling technique. The encapsulation includes increase the pH of carbopol microgel to 8 and then the berberine or chlorhexidine is added to the swelled microgel. The complex formed was adjusted to pH 5.5, centrifuged three times and then dispersed in acetate buffer solution (pH 5.5). The results indicated that the Carbopol microgel has the ability to encapsulate berberine and chlorhexidine with 10% and 90% encapsulation efficiency with slow release, respectively. Carbopol Aqua SF1 was stable with zeta potential +33 mV and was also stable upon encapsulation with berberine and chlorhexidine and coating with polyelectrolytes (PAH and PDAC). The Carbopol Aqua SF1 was shown to be non-toxic upon incubation with algae, yeast and *E.coli*.

Carbopol microgel with encapsulated berberine and chlorhexidine were tested with algae and *E.coli* and it was found that that there were less effect in the antimicrobial actions due to the slow release of both berberine and chlorhexidine from carbopol microgel even at different incubation time as well as the repulsion interaction between encapsulated berberine or chlorhexidine into carbopol and cell membrane. However, there was no antimicrobial activity of berberine loaded carbopol microgel towards yeast due to the repulsion forces between the encapsulated berberine into the microgel and the big thickness

of cell membrane of yeast that prevent the cell membrane to be disrupted. Additionally, berberine is inactive to kill yeast cells in comparison with the encapsulated chlorhexidine which appeared also less antimicrobial action towards yeast. However, the antimicrobial activity for both encapsulated berberine and encapsulated chlorhexidine did increase upon coating the carbopol microgel with cationic polyelectrolyte (PDAC). The carbopol microgel was coated with PDAC to form PDAC coated carbopol microgel which played important role in the dramatic increase the antimicrobial actions upon incubation with algae and *E.coli* where they killed within 2 hours incubation time. This is due to the electrostatic interaction between the cationic PDAC coated berberine or chlorhexidine loaded carbopol microgel and the cell membranes of algae, yeast and *E.coli*. This interaction allows encapsulated berberine or chlorhexidine to diffuse into cell membrane causing cell death within short periods of time.

In Chapter 7 microfluidics cell based assays were explored in which cells were trapped in a micro chamber and then exposed to toxins to study the antimicrobial action or toxicity. Using chemical adhesion as an approach was not successful as the adhesant poly-l-lysine was not able to immobilize the cells due to the effect of shear stress forces, which caused them to detach from the surface of micro chamber. Magnetic glass beads and magnetic yeast cells were also found to be unsuitable for trapping cells in the micro chamber of the microfluidics chip due to the electrostatic interaction between the cells and either magnetic glass beads and magnetic yeast cells. An approach in which magnetized hydrophobic beads were used as gate keepers to trap cells into microfluidic consisting of glass/PDMS was most successful as these beads did not interact with the cells. The chip had two layers: the lower layer made of PDMS which accommodated channels with micro chamber while the upper layer was glass with holes for tubing. The results indicated that these magnetized gate keepers inside the micro chamber of the chip could be placed in position using a neodymium magnet, whilst allowing liquid flow without high back pressures.

8.2 Future Works

1. Investigation the toxicity effects of bare and coated titania nanoparticles upon incubation with *E.coli* in dark conditions and in the presence of UV light at different exposure times.
2. Study the toxicity effects of some heavy metals nanoparticles on algae, yeast and *E.coli*.
3. *In vivo* application of PDAC coated encapsulated berberine and encapsulated chlorhexidine into carbopol microgel.
4. Trapping cells such as algae and yeast into micro chamber of developed microfluidics chip to study the toxicity of titania nanoparticles and antimicrobial action of encapsulated berberine or encapsulated chlorhexidine into carbopol microgel.